



HAL
open science

Design, synthesis and study of functional organometallic ruthenium complexes for dye-sensitized solar cells and photoelectrochemical cells

Siliu Lyu

► **To cite this version:**

Siliu Lyu. Design, synthesis and study of functional organometallic ruthenium complexes for dye-sensitized solar cells and photoelectrochemical cells. Organic chemistry. Université de Bordeaux, 2018. English. NNT : 2018BORD0095 . tel-01897324

HAL Id: tel-01897324

<https://theses.hal.science/tel-01897324>

Submitted on 17 Oct 2018

HAL is a multi-disciplinary open access archive for the deposit and dissemination of scientific research documents, whether they are published or not. The documents may come from teaching and research institutions in France or abroad, or from public or private research centers.

L'archive ouverte pluridisciplinaire **HAL**, est destinée au dépôt et à la diffusion de documents scientifiques de niveau recherche, publiés ou non, émanant des établissements d'enseignement et de recherche français ou étrangers, des laboratoires publics ou privés.

THESIS

Presented at

UNIVERSITY OF BORDEAUX

DOCTORAL SCHOOL OF CHEMICAL SCIENCES

BY

Siliu LYU

TO OBTAIN THE DEGREE OF

DOCTOR

**Design, synthesis and study of functional organometallic ruthenium
complexes for dye-sensitized solar cells and photoelectrochemical cells**

Defend On: 6th July 2018 (plan)

In front of a jury composed of:

Mme Alessia COLOMBO	Chargé de Recherche, Università degli Studi di Milano	Reviewer
M. Frédéric PAUL	Director of research CNRS, Institut des Sciences Chimiques de Rennes, University of Rennes	Reviewer
Mme Corine MATHONIERE	Professor, ICMCB, University of Bordeaux	Examiner
M. Julien MASSIN	Maître de Conférences, ISM, University of Marseille	Examiner
M. Thierry TOUPANCE	Professor, ISM, University of Bordeaux	Supervisor
Mme Céline OLIVIER	Chargé de Recherche, ISM, University of Bordeaux	Co-supervisor

Acknowledgements

This work has been performed in Molecular Chemistry and Materials group, Institute of Molecular Sciences, University of Bordeaux. Here, I hope to express my sincere gratitude to some organizations and a number of people, without whom it would have not been possible for me to undertake such a novel and huge academic programme during my four years in France.

First of all, I sincerely thank “China Scholarship Council” for providing me financial support. I could have the opportunity to study abroad and finally get my doctor degree because of the strong support of my country. I will keep in mind the ardent expectations of my country and take them as an encouragement to keep working hard so as to serve the Motherland.

I would like to thank my thesis supervisors Prof. Dr. Thierry Toupance and Dr. Céline Olivier for their continuous support, encouragement and insightful guidance during my doctoral work in the last four years. I am very lucky and happy to be able to work with them. I sincerely thank Dr. Thierry Toupance and Dr. Céline Olivier for their reasoning and constructive criticisms that motivated me to delve deeper into my research. When I made mistakes in my work, they express their precious understanding and patience. I will never forget their unconditional support in and out of the lab to facilitate my stay in France.

This work is the result of a teamwork and collaboration of many people without whom this work could not have any real chance to execute well. I would like to thank our colleagues who helped me to characterize my samples: Samuel De Sousa, Laurent Ducasse, Yoann Farré, Yann Pellegrin, Fabrice Odobel, Tomofumi Hamamura, Julien Massin, Michele Pavone, Ana B. Muñoz-García, Brice Kauffmann, Murielle Chavarot-Kerlidou, Vincent Artero.

I am very happy in my last four years because I met many good colleagues in our lab. I would like to express my sincere gratitude to Emilie Genin, Yohann Nicolas, Luc Vellutini, Anne Thienpont, Karine Heuze, Marie-Anne Dourges, Svitlana Poix-Shinkaruk, Laurent Thomas, Imane Barbara, Camille Bertrand, Yannick Hermans, Shun Kashiwaya, Susanne Koch, Szu-Hsuan Lee, Yannick Mousli, Martin Palazzolo and Juan Angel Moreno Balderrama for their friendly help in the lab.

I would like to specially thank Qian Li, Changlong Wang, Jianguo Bai, Shilin Yu and Wenjing Ma for their help throughout my stay in Bordeaux in many ways. I consider myself fortunate to have them as my best friends forever. I thank you for being beside me in every critical phase in the last four years.

I deeply thank my parents for their unconditional love and support. Without their

encouragement I can never succeed in this endeavor.

SYNTHÈSE EN FRANÇAIS

L'objectif principal de ce travail était i) la conception et la synthèse de nouveaux colorants basés sur des complexes organométalliques présentant une architecture originale D-[M]-A, où [M] est le centre métallique riche en électrons $[\text{Ru}(\text{dppe})_2]$, pour les dispositifs DSSC de type n et de type p, ii) la caractérisation de leurs propriétés optiques et électroniques ainsi que l'évaluation de leurs performances photovoltaïques dans les dispositifs de type n à base de TiO_2 et les dispositifs de type p à base de NiO . Suite à ce travail, notre objectif a été d'élargir le champ d'application de ces photosensibilisateurs organométalliques à des DS-PEC (cellules photoélectrochimiques à colorants) à base de NiO pour la production photoinduite de dihydrogène.

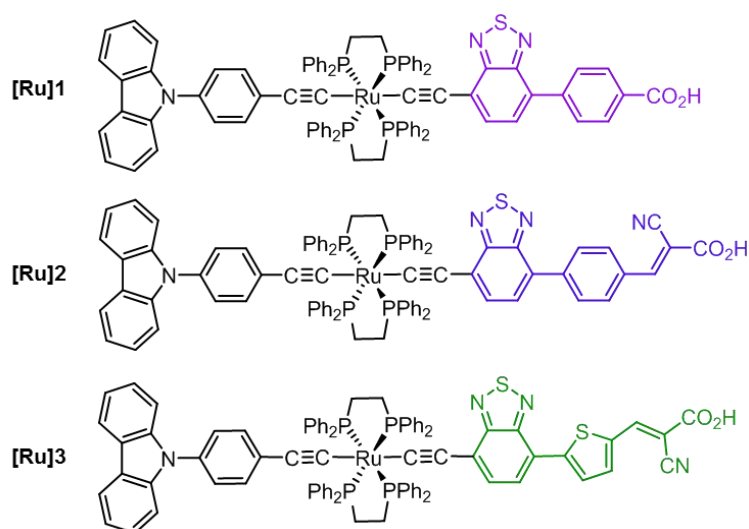


Figure I: Structure moléculaire des complexes Ru-diacétylures **[Ru]1**-**[Ru]3**

Ainsi, sur la base de travaux antérieurs menés dans notre groupe, le Chapitre II décrit la synthèse et l'étude d'une nouvelle série de colorants pour les DSSC de type n. En particulier, trois nouveaux colorants de type « push-pull » contenant le fragment organométallique $[\text{Ru}(\text{dppe})_2]$ ont été imaginés et préparés avec succès pour les applications en DSSC. Afin d'obtenir des colorants à faible bandgap, c'est à dire avec des propriétés d'absorption dans le proche IR, notre stratégie a consisté à moduler la partie électro-attractrice de systèmes D-[M]-A- π -A' où A est le motif benzothiadiazole (BTD), π représente un espaceur π -conjugué aromatique et A' représente à la fois l'accepteur secondaire et la fonction d'accroche acide carboxylique. Ainsi nous avons obtenu les trois nouveaux colorants organométalliques représentés Figure I. Le colorant **[Ru]1** présente un espaceur phényle entre l'unité BTD et le groupement d'ancrage acide carboxylique. **[Ru]2** et **[Ru]3** présentent quant à eux soit un

phényle soit un espaceur thiophène entre le BTD et le groupement accepteur/accroche acide cyanoacrylique.

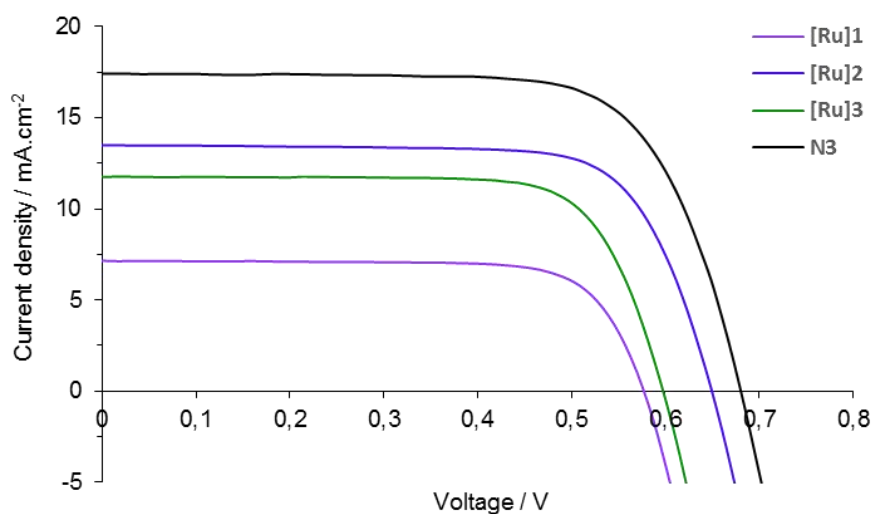


Figure II: Courbes J/V de [Ru]1-[Ru]3 et N3 en DSSC.

Tableau I: Performances photovoltaïques des dispositifs DSSC avec les colorants [Ru]1-[Ru]3 et N3. Taux de greffage des colorants sur TiO₂.

Dye	$J_{sc} / \text{mA.cm}^{-2}$	V_{oc} / mV	$ff / \%$	$\eta / \%$	$Q (\text{mol.cm}^{-2})$
[Ru]1	7.13	577	75.6	3.11	1.40×10^{-7}
[Ru]2	13.48	650	73.7	6.45	1.94×10^{-7}
[Ru]3	11.77	598	74.4	5.23	2.12×10^{-7}
N3	17.42	680	71.4	8.46	-

Performances photovoltaïques mesurées sous AM 1.5G, 1sun, $100 \text{ mW} \cdot \text{cm}^{-2}$: J_{sc} = densité de courant de court-circuit, V_{oc} = tension de circuit-ouvert, ff = facteur de forme, η = rendement de conversion photovoltaïque. Epaisseur du film de TiO₂ = 10 μm (couche transparente) + 5 μm (couche diffusante). Surface active = 0.159 cm² (masque). Q = quantité de colorant greffé sur une électrode de TiO₂ de 1 cm².

Cette ingénierie moléculaire a permis d'obtenir des photosensibilisateurs efficaces avec de fortes propriétés d'absorption dans le domaine visible, en particulier le colorant vert [Ru]3 présente une absorption large entre 500 et 800 nm. Les propriétés optiques et électroniques des trois nouveaux colorants sont décrites ainsi que leurs performances photovoltaïques dans

les dispositifs n-DSSC. En effet, les colorants **[Ru]1-[Ru]3** ont été chimisorbés sur des films minces transparents de TiO₂, en présence d'acide chéno-désoxycholique comme co-adsorbant, et les photoanodes ont été incorporées dans des dispositifs de cellules solaires selon la procédure décrite.¹ Les courbes densité de courant/tension (J/V) sont représentées sur la Figure II et les paramètres photovoltaïques sont rassemblés dans le Tableau I. Le colorant de référence N3 (cis-bis(isothiocyanato)bis(2,2'-bipyridyl-4,4'-dicarboxylato)ruthénium a été testé dans les mêmes conditions pour comparaison.

L'introduction d'un espaceur π -conjugué aromatique entre le BTD et le semi-conducteur, en empêchant la recombinaison de charges et le retour d'électrons de la surface, a permis d'améliorer les performances de **[Ru]2** par rapport au sensibilisateur Ru-BTD rapporté précédemment.² Les colorants **[Ru]2** et **[Ru]3**, associant BTD et fonction acide cyanoacrylique, ont donné des performances supérieures à celles du colorant **[Ru]1**, doté d'une fonction acide carboxylique simple, montrant ainsi que le choix du groupement d'ancrage est d'une grande importance pour optimiser le fonctionnement du dispositif. Dans l'ensemble, cette étude montre la pertinence d'utiliser des complexes organométalliques de type « push-pull » pour la conception de colorants à faible bandgap pour des dispositifs DSSC performants et une collecte efficace des photons de basse énergie.

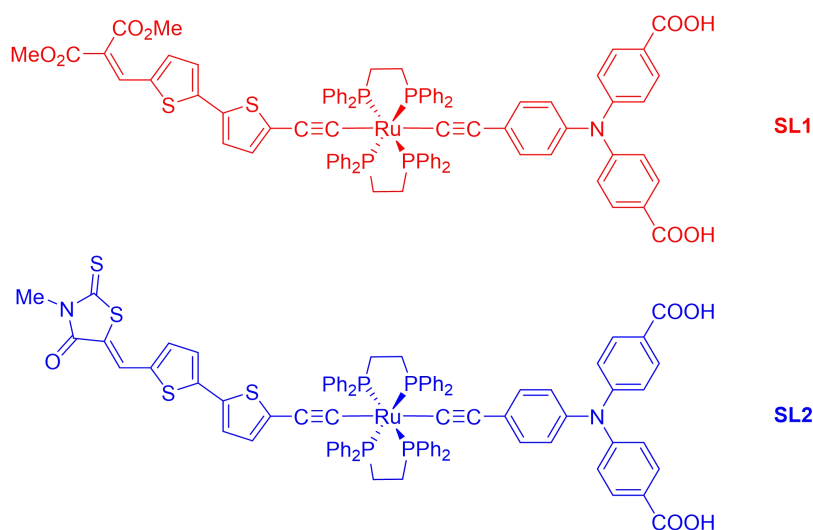


Figure III: Structure moléculaire des colorants organométalliques **SL1** et **SL2**.

Le Chapitre III décrit la synthèse et la caractérisation des premiers complexes diacétylures de ruthénium pour les DSSC de type p. Les deux premiers complexes, **SL1** et **SL2**, sont dotés d'un groupement d'accroche bidenté basé sur un motif triphénylamine donneur d'électrons (D) et fonctionnalisés par un groupement accepteur d'électrons (A) relié

au fragment organométallique [Ru(dppe)₂] par un motif bithiophène. La structure moléculaire des nouveaux photosensibilisateurs **SL1** et **SL2** est représentée sur la Figure III.

Une modification simple du ligand acétylure du côté accepteur a permis de moduler les propriétés optiques de ces complexes, conduisant ainsi à des colorants rouge et bleu avec de fortes propriétés d'absorption de la lumière visible. Les études spectroscopique et électrochimique de ces deux colorants ont mis en évidence des propriétés optiques et électroniques adaptées aux dispositifs p-DSSC. Des calculs théoriques ont également été effectués afin de rationaliser les données expérimentales.

Tableau II: Performances photovoltaïques des colorants **SL1** and **SL2** en dispositifs p-DSSC (AM 1.5G, 1sun, 100 mW·cm⁻²). Taux de greffage des colorants sur NiO.

<i>Dye</i>	$J_{SC}/\text{mA}\cdot\text{cm}^{-2}$	V_{OC}/mV	$ff/\%$	$\eta/\%$	Dye loading (nmol cm ⁻²)
SL1	2.25	104	34	0.079	31.9
SL2	1.50	77	33	0.038	10.1

Les performances photovoltaïques de ces colorants ont ensuite été étudiées dans des dispositifs p-DSSC à base de NiO, en collaboration avec le Dr Fabrice Odobel (Université de Nantes). Les paramètres des cellules solaires sont rassemblés dans le Tableau II. Bien que ces deux colorants ne soient pas parfaitement optimisés (force d'injection d'électrons modérée) leurs performances photovoltaïques sont comparables à d'autres colorants organométalliques rapportés dans la littérature pour cette même application (*ex.* des complexes ruthénium polypyridine). Dans notre étude, le colorant le plus performant, le colorant rouge **SL1**, a permis d'obtenir une densité de photocourant de 2,25 mA·cm⁻² et une valeur IPCE maximale de 18%. Ces résultats prometteurs nous ont permis d'envisager l'obtention d'autres colorants organométalliques efficaces pour une telle application. En effet nous avons imaginé que des colorants diacétylures de ruthénium plus performants pourraient être développés en abaissant le niveau d'énergie de leur HOMO afin d'améliorer le taux d'injection d'électrons du semi-conducteur vers le colorant photo-excité.

Par conséquent, deux nouveaux colorants à base de Ru-diacétylures ont été conçus et préparés, dans lesquels la partie donneuse d'électrons a été remplacée par un simple groupement phényle (**SL3**) ou thiophène (**SL4**) (voir Figure IV). Les deux colorants ont été fonctionnalisés par le même ligand électro-attracteur que **SL1**, le groupement diméthylmalonate. Comme prévu, l'utilisation de groupements moins riches en électrons

comme donneurs a conduit à des niveaux d'énergie HOMO inférieurs à ceux du colorant **SL1**, ce qui laissait envisager une amélioration des taux d'injection de charge. Cependant, l'efficacité des p-DSSC intégrant les colorants **SL3** ($\eta = 0,039\%$) et **SL4** ($\eta = 0,033\%$) est demeurée inférieure à celle intégrant 1 colorant **SL1** ($\eta = 0,096\%$). Ceci a été attribué à un taux de greffage inférieur pour les deux nouveaux colorants.

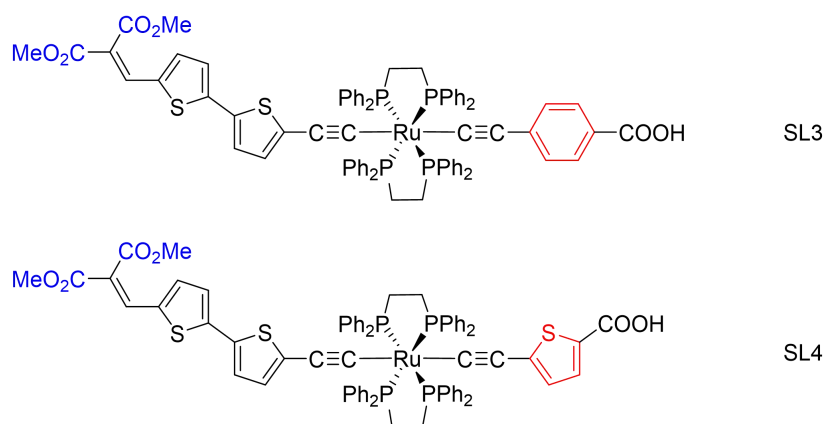


Figure IV: Structure moléculaire des colorants organométalliques **SL3** et **SL4**.

Nous avons donc cherché à obtenir un colorant Ru-diacétylure plus performant en modifiant la fonction d'ancrage. Le groupe acide phosphonique a ainsi été choisi afin d'améliorer la densité de greffage du colorant sur la photoélectrode. Le complexe **SL5**, représenté Figure V, est doté d'une fonction acide phosphonique et fonctionnalisé par le groupement électro-attracteur diméthylmalonate.

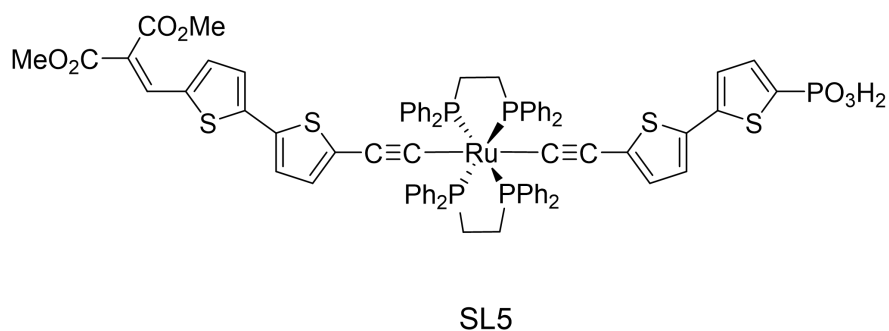


Figure V: Structure moléculaire du colorant organométallique **SL5**.

Comme prévu, une plus grande densité de greffage de colorant sur NiO a été observée avec le colorant **SL5**, comparé aux colorants **SL3** et **SL4**. En dispositifs p-DSSC, en présence du médiateur redox standard iodure/iodure, le colorant **SL5** présente des performances photovoltaïques légèrement améliorées ($\eta = 0,046\%$) par rapport à **SL3** ($\eta = 0,039\%$) et **SL4**

($\eta = 0,033\%$) mais une efficacité inférieure à celle obtenue avec **SL1** ($\eta = 0,096\%$). Cependant, le colorant **SL5** a également été testé avec un électrolyte à base de disulfure/thiolate, fournissant ainsi une photo-tension supérieure et la meilleure performance de la série, $\eta = 0,125\%$.

Sur la base des résultats encourageants obtenus avec **SL5** et un électrolyte disulfure/thiolate, nous avons finalement conçu de nouveaux complexes à base de Ru-diacétylure présentant une structure optimisée en vue d'augmenter à la fois la quantité de colorant sur l'électrode et le taux d'injection de charge au sein des dispositifs p-DSSC. La synthèse de ces nouveaux colorants est actuellement en cours dans notre groupe, en collaboration avec le groupe du Dr Fabrice Odobel.

Notre troisième objectif était d'étendre le champ d'application des photosensibilisateurs organométalliques à base de ruthénium aux dispositifs DS-PEC (dye-sensitized photo-electrochemical cells) à base de NiO pour la production d' H_2 . Ainsi, le Chapitre IV décrit la conception, la préparation et l'étude de chromophores organométalliques innovants comportant une structure π -conjuguée originale et pouvant s'adsorber sur un oxyde métallique semi-conducteur en vue d'applications photochimiques.

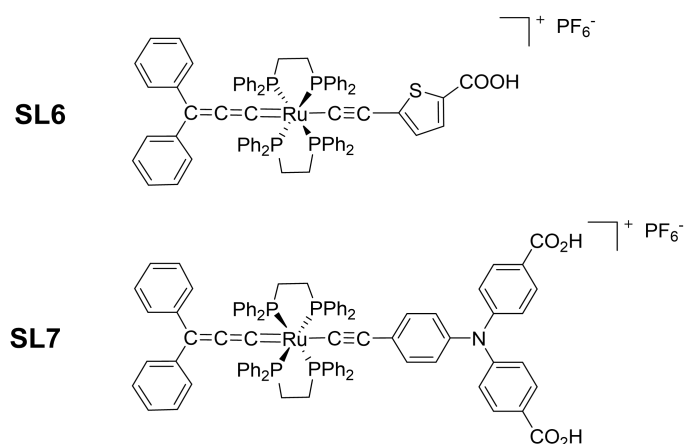


Figure VI: Structure moléculaire des colorants organométalliques **SL6** et **SL7**.

Dans un premier temps, nous avons employé des complexes mixtes allénylidène-acétylure de ruthénium pour la photosensibilisation d'électrodes de NiO afin d'étudier la génération photoinduite de courant dans des dispositifs photoélectrochimiques à colorant. Ainsi, les nouveaux colorants **SL6** et **SL7**, représentés Figure VI, présentent une structure fortement conjuguée comprenant le motif organométallique [Ru(dppe)₂] avec un ligand allénylidène délocalisé d'un côté, et un ligand σ -alkynyle portant un groupement riche

en électrons (thiophène ou triphénylamine) et une ou deux fonctions d'accroche acide carboxylique de l'autre côté.

Une étude systématique des propriétés optoélectroniques, électrochimiques et photoélectrochimiques des deux colorants a été réalisée. Une photoréponse large a été observée en absorption pour les deux colorants avec un maximum à environ 600 nm. En outre, la structure cristalline par diffraction des RX de l'un des précurseurs a été obtenue et des calculs théoriques ont été effectués afin de rationaliser les propriétés photo-physiques des nouveaux colorants. Ces photosensibilisateurs ont ensuite été employés pour préparer des photocathodes à base de NiO et testés en tant que générateurs de photocourant en conditions aqueuses et en présence d'un accepteur d'électrons sacrificiel, le complexe $[\text{Co}(\text{NH}_3)_5\text{Cl}]\text{Cl}_2$. Les électrodes et les mesures correspondantes ont été réalisées dans le groupe de Dr. Vincent Artero (CEA Grenoble). Les photocathodes ainsi obtenues ont fourni de bonnes densités de courant photoinduit (40 à $60 \mu\text{A}\cdot\text{cm}^{-2}$) à pH neutre (tampon phosphate) et une stabilité élevée a été observée pour les deux colorants (voir Figure VII).

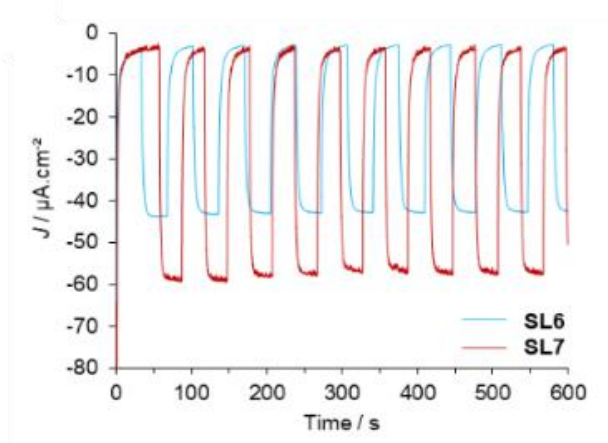


Figure VII: Photocourants cathodiques mesurés sous illumination intermittente avec des électrodes de NiO sensibilisées par SL6 (bleu) et SL7 (rouge) en présence de $[\text{Co}(\text{NH}_3)_5\text{Cl}]\text{Cl}_2$ (20 mM) en tampon phosphate (0.1 M ; pH 7) à +0.2 V vs. NHE.

Cette étude a donc permis de mettre en évidence la pertinence des colorants organométalliques push-pull pour la construction de photocathodes fonctionnant en milieu aqueux.

Ainsi, à la suite de ce travail, nous avons conçu et préparé un nouveau système photocatalytique mono-moléculaire par coordination axiale d'un catalyseur à base de cobalt actif pour la production d' H_2 (cobaloxime) sur un photosensibilisateur Ru-diacétylure fonctionnalisé par un groupement pyridyle. Ce système photocatalytique est représenté Figure VIII.

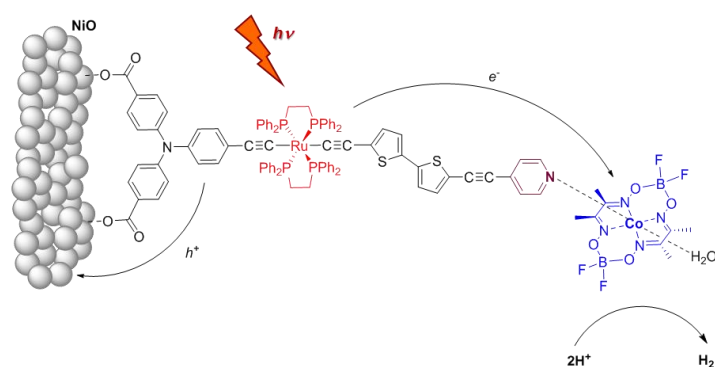


Figure VIII: Représentation du système photocatalytique Ru-diacétylure/Cobaloxime **SL8-Co** chimisorbé sur un film mince nanoparticulaire de NiO.

L'étude des propriétés optiques et électrochimiques du système photocatalytique **SL8-Co** a montré que celui-ci est parfaitement adapté à une utilisation dans des dispositifs DS-PEC à base de NiO. Des photocathodes à base de film mince nanoparticulaire de NiO ont donc été préparées en intégrant notre système photocatalytique [Ru-Co]. Ces électrodes et les mesures correspondantes ont une nouvelle fois été réalisées dans le groupe de Dr. Vincent Artero (CEA Grenoble). Des mesures chrono-ampérométriques ont été réalisées sous illumination intermittente à différents potentiels sur une période de 10 minutes montrant ainsi la génération de photocourant cathodique à l'équilibre. L'amplitude maximale a été obtenue à un potentiel appliqué de -0.2 V vs. NHE (-0.4 V vs. Ag/AgCl) avec une densité de photocourant d'environ $3.2 \mu\text{A}\cdot\text{cm}^{-2}$ (Figure IX).

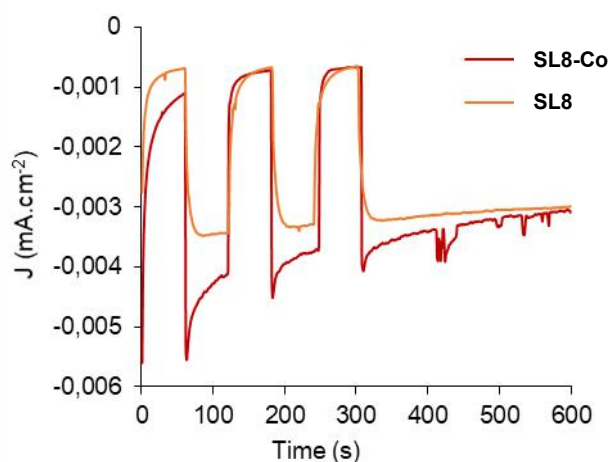


Figure IX: Mesures chrono-ampérométriques sous illumination visible intermittente (400-800 nm, $65 \text{ mV}\cdot\text{cm}^{-2}$, 1 sun) obtenues avec des électrodes de NiO sensibilisées par **SL8-Co** (rouge) et **SL8** seul (orange) en tampon acétate (0.1 M, pH 4.5) avec un potentiel appliqué de -0.2 V vs. NHE (-0.4 V vs. Ag/AgCl).

Une électrolyse prolongée en tampon acétate (0,1 M, pH 4,5) et sous irradiation continue a conduit à une génération photo-électrochimique de H₂ avec un rendement faradique de ~ 27%. Cette performance, comparable à d'autres rapportées dans la littérature,³⁻⁵ a pleinement validé notre approche consistant à utiliser des complexes de ruthénium organométalliques comme espèces photoactives pour construire des DS-PEC efficaces à base de NiO.

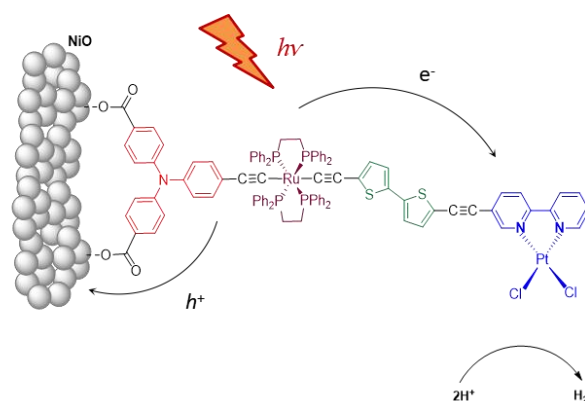


Figure X: Représentation du système photocatalytique Ru-diacétylure/PtCl₂ chimisorbé sur un film mince nanoparticulaire de NiO.

Enfin, nous avons récemment conçu un nouveau système photocatalytique mono-moléculaire par coordination d'un catalyseur à base de platine actif pour la production d'H₂ et incluant comme photosensibilisateur un complexe Ru-diacétylure fonctionnalisé par un motif bipyridyle, représenté Figure X. Les propriétés optiques et électrochimiques de ce nouveau système photocatalytique sont en cours d'étude, ce nouveau système sera ensuite utilisé pour la construction de photocathodes à base de NiO et la génération de H₂ en dispositifs DS-PEC.

References

- 1 S. Ito, T. N. Murakami, P. Comte, P. Liska, Carole Grätzel, M. K. Nazeeruddin, M. Grätzel. Fabrication of thin film dye sensitized solar cells with solar to electric power conversion efficiency over 10%. *Thin Solid Films*, **2008**, 516: 4613-4619.
- 2 S. D. Sousa, S. Lyu, L. Ducasse, T. Toupance, C. Olivier. Tuning visible-light absorption properties of Ru-diacetylde complexes: simple access to colorful efficient dyes for DSSCs. *J. Mater. Chem. A*, **2015**, 3: 18256-18264.
- 3 Z. Ji, M. He, Z. Huang, U. Ozkan, Y. Wu. Photostable p-Type Dye-Sensitized Photoelectrochemical Cells for Water Reduction. *J. Am. Chem. Soc.*, **2013**, 135, 32: 11696-11699.
- 4 N. Kaeffer, J. Massin, C. Lebrun, O. Renault, M. Chavarot-Kerlidou, V. Artero. Covalent Design for Dye-Sensitized H₂-Evolving Photocathodes Based on a Cobalt Diimine-Dioxime Catalyst. *J. Am. Chem. Soc.*, **2016**, 138, 38: 12308-12311.
- 5 J. Massin, M. Bräutigam, N. Kaeffer, N. Queyriaux, M. J. Field, F. H. Schacher, J. Popp, M. Chavarot-Kerlidou, B. Dietzek, V. Artero. Dye-sensitized PS-*b*-P2VP-templated nickel oxide films for photoelectrochemical applications. *Interface Focus*, **2015**, 5, 3: 20140083.

Table of Content

Chapter I: Introduction	p.1
<i>I.1. General Introduction</i>	p.2
<i>I.2. Overview of Solar Energy and Solar Cells</i>	p.4
<i>I.2.1. Solar Energy</i>	p.5
<i>I.2.2. Solar Radiation and Solar Spectrum</i>	p.6
<i>I.2.3. Solar Cells</i>	p.9
<i>I.2.3.1. Silicon-Based Solar Cells</i>	p.12
<i>I.2.3.1.1. Monocrystalline Silicon (mono-Si) Solar Cells</i>	p.12
<i>I.2.3.1.2. Polycrystalline Silicon (poly-Si) Solar Cells</i>	p.13
<i>I.2.3.1.3. Amorphous Silicon (a-Si) Solar Cells</i>	p.14
<i>I.2.3.2. III-V Solar Cells</i>	p.15
<i>I.2.3.3. CdTe/CdS Thin Film Solar Cells</i>	p.18
<i>I.2.3.4. CIGS Thin Film Solar Cells</i>	p.20
<i>I.2.3.5. Dye-Sensitized Solar Cells</i>	p.24
<i>I.2.3.6. Perovskite Solar Cells</i>	p.27
<i>I.3. TiO₂-Based n-Type Dye-Sensitized Solar Cells</i>	p.31
<i>I.3.1. Historical Background</i>	p.32
<i>I.3.2. Operational Principles and Electron Transfer Processes of n-Type Dye-Sensitized Solar Cells</i>	p.33
<i>I.3.3. Energetics of Operational Principles</i>	p.36
<i>I.3.4. Kinetics of Operational Principles</i>	p.38
<i>I.3.5. Characterization Techniques</i>	p.41
<i>I.3.5.1. Efficiency Measurements</i>	p.41
<i>I.3.5.2. Electrochemical Methods</i>	p.43
<i>I.3.6. Recent Improvements</i>	p.45
<i>I.3.6.1. Improvements in Photoanode</i>	p.45
<i>I.3.6.2. Improvements in Counter Electrode</i>	p.47
<i>I.3.6.3. Improvements in Electrolyte</i>	p.49
<i>I.3.6.3.1. Liquid Electrolytes</i>	p.50
<i>I.3.6.3.2. Organic-Solvent-Based Electrolytes</i>	p.50
<i>I.3.6.3.3. Ionic Liquid Electrolytes</i>	p.51
<i>I.3.6.3.4. Solid State Electrolytes</i>	p.51

I.3.6.3.5. <i>Quasi Solid State Electrolytes</i>	p.52
I.4. <i>NiO-Based p-Type Dye-Sensitized Solar Cells and NiO-Based Dye-Sensitized Photoelectrochemical Cells</i>	p.53
I.4.1. <i>Historical Background and Recent Improvements</i>	p.54
I.4.2. <i>Operational Principles</i>	p.60
I.5. <i>Research Objectives</i>	p.63
I.6. <i>References</i>	p.65
Chapter II: Ruthenium-Diacetylde Organometallic Complexes for n-Type Dye Sensitizers	p.105
II.1. <i>General Introduction</i>	p.106
II.2. <i>n-Type Dye Sensitizers</i>	p.107
II.2.1. <i>Ruthenium Complexes</i>	p.108
II.2.2. <i>Porphyrins and Phthalocyanines</i>	p.117
II.2.2.1. <i>Porphyrins</i>	p.117
II.2.2.2. <i>Phthalocyanines</i>	p.121
II.2.3. <i>Metal-Free Organic Dye Sensitizers</i>	p.124
II.3. <i>Molecular Engineering of Ruthenium-Diacetylde Organometallic Complexes for n-Type DSCs</i>	p.133
II.3.1. <i>Synthesis of the Dyes [Ru]1-[Ru]3</i>	p.134
II.3.2. <i>Optical and Electrochemical Properties</i>	p.137
II.3.3. <i>Theoretical Calculations</i>	p.139
II.3.4. <i>Photovoltaic Properties</i>	p.141
II.3.5. <i>Conclusions</i>	p.144
II.4. <i>References</i>	p.146
Chapter III: Ruthenium-Diacetylde Organometallic Complexes for p-Type Dye Sensitizers	p.165
III.1. <i>General Introduction</i>	p.166
III.2. <i>p-Type Dye Sensitizers</i>	p.167
III.3. <i>Push-Pull Ruthenium Diacetylde Complexes Including Triphenylamine Donor Moieties as New Dyes for p-Type Dye-Sensitized Solar Cells</i>	p.176
III.3.1. <i>Synthesis of the Dyes SL1 and SL2</i>	p.177
III.3.2. <i>Optical and Electrochemical Properties</i>	p.179

<i>III.3.3. Theoretical Calculations</i>	p.182
<i>III.3.4. Photovoltaic Measurements in p-Type DSCs</i>	p.185
<i>III.3.5. Conclusions</i>	p.187
<i>III.4. Push-Pull Ruthenium Diacetylide Complexes With Modified Electron-Donating Group</i>	p.187
<i>III.4.1. Synthesis of the Dyes SL3 and SL4</i>	p.188
<i>III.4.2. Optical and Electrochemical Properties</i>	p.190
<i>III.4.3. Theoretical Calculations</i>	p.192
<i>III.4.4. Photovoltaic Measurements in p-Type DSCs</i>	p.193
<i>III.4.5. Conclusions</i>	p.194
<i>III.5. Phosphonic Acid as a New Anchoring Function of Ru-Based Dyes for p-Type DSCs</i>	p.195
<i>III.5.1. Synthesis of the Dye SL5</i>	p.195
<i>III.5.2. Optical and Electrochemical Properties</i>	p.197
<i>III.5.3. Theoretical Calculations</i>	p.199
<i>III.5.4. Photovoltaic Measurements in p-Type DSCs</i>	p.200
<i>III.5.5. Conclusions</i>	p.201
<i>III.6. General Conclusion</i>	p.201
<i>III.7. References</i>	p.203
Chapter IV: Organometallic Ruthenium Complexes for NiO Sensitization and Photoelectrochemical Applications	p.209
<i>IV.1. General Introduction</i>	p.210
<i>IV.2. Sensitizers Utilized in NiO-Based DSPECs for Solar Hydrogen Production</i>	p.211
<i>IV.3. Organometallic Dyes for NiO Sensitization and Photoelectrochemical Applications</i>	p.215
<i>IV.3.1. Synthesis of the Dyes SL6 and SL7</i>	p.216
<i>IV.3.2. Crystallographic Study</i>	p.218
<i>IV.3.3. Optical and Electrochemical Properties</i>	p.219
<i>IV.3.4. Theoretical Calculations</i>	p.221
<i>IV.3.5. Electrode Preparation and Characterization</i>	p.224
<i>IV.3.6. Photoelectrochemical Properties of Dye-Sensitized NiO Films</i>	p.225
<i>IV.3.7. Conclusions</i>	p.227
<i>IV.4. Ru-diacetylide/Cobaloxime Photocatalytic System for H₂ Evolution from</i>	

<i>Dye-Sensitized Photoelectrochemical Cells</i>	p.227
<i>IV.4.1 Synthesis and Characterization</i>	p.228
<i>IV.4.2. Optical and Electrochemical Properties</i>	p.230
<i>IV.4.3. Theoretical Calculations</i>	p.233
<i>IV.4.4. Electrode Preparation and Characterization - XPS Analyses</i>	p.236
<i>IV.4.5. Photoelectrochemical Properties</i>	p.240
<i>IV.4.6. Conclusions</i>	p.242
<i>IV.5. Outlook</i>	p.243
<i>IV.6. References</i>	p.244
Chapter V: General Conclusion	p.251
Chapter VI: Experimental Part	p.257
<i>VI.1. Materials and Methods</i>	p.258
<i>VI.2. Synthesis</i>	p.259
<i>VI.2.1. Synthetic Routes to the Dyes [Ru]1-[Ru]3</i>	p.259
<i>VI.2.2. Synthetic Routes to the Dyes SL1 and SL2</i>	p.264
<i>VI.2.3. Synthetic Routes to the Dyes SL3 and SL4</i>	p.269
<i>VI.2.4. Synthetic Routes to the Dye SL5</i>	p.272
<i>VI.2.5. Synthetic Routes to the Dye SL6 and SL7</i>	p.274
<i>VI.2.6. Synthetic Routes to the Dye SL8 and SL8-Co</i>	p.276
<i>VI.3. Photovoltaic Characterization</i>	p.278
<i>VI.3.1. DSC Preparation and Characterization for [Ru]1-[Ru]3</i>	p.278
<i>VI.3.2. DSC Preparation and Characterization for SL1-SL5</i>	p.279
<i>VI.4. Determination of Dye-loading Amounts</i>	p.280
<i>VI.5. Crystallographic Study for Compound 48</i>	p.280
<i>VI.6. Electrode preparation method for SL6 and SL7</i>	p.282
<i>VI.7. Electrochemical and Photoelectrochemical Measurements for SL8-Co and SL8-Co@NiO</i>	p.282
<i>VI.8. References</i>	p.284
Annexes	p.287
<i>Abbreviation</i>	p.288
<i>Formulas</i>	p.290
<i>Published Articles</i>	p.296

Chapter I: Introduction

I.1. General Introduction

With the rapid development of the global economy, the growth of population, the acceleration of the urbanization process and the intensification of the environmental pollution, the pressing need for energy, especially clean, safe, and renewable energy, has inevitably become the most critical scientific and technological challenge confronting the entire mankind in 21st century. Despite the emerging world's astounding economic gains over in the past few decades, for a broad swath of mankind, access to sufficient electricity remains a remote dream. Figure I-1 lists the human development index (HDI) of more than 60 countries comprising over 90% of the global population and their per capita amount of electric power demand.¹

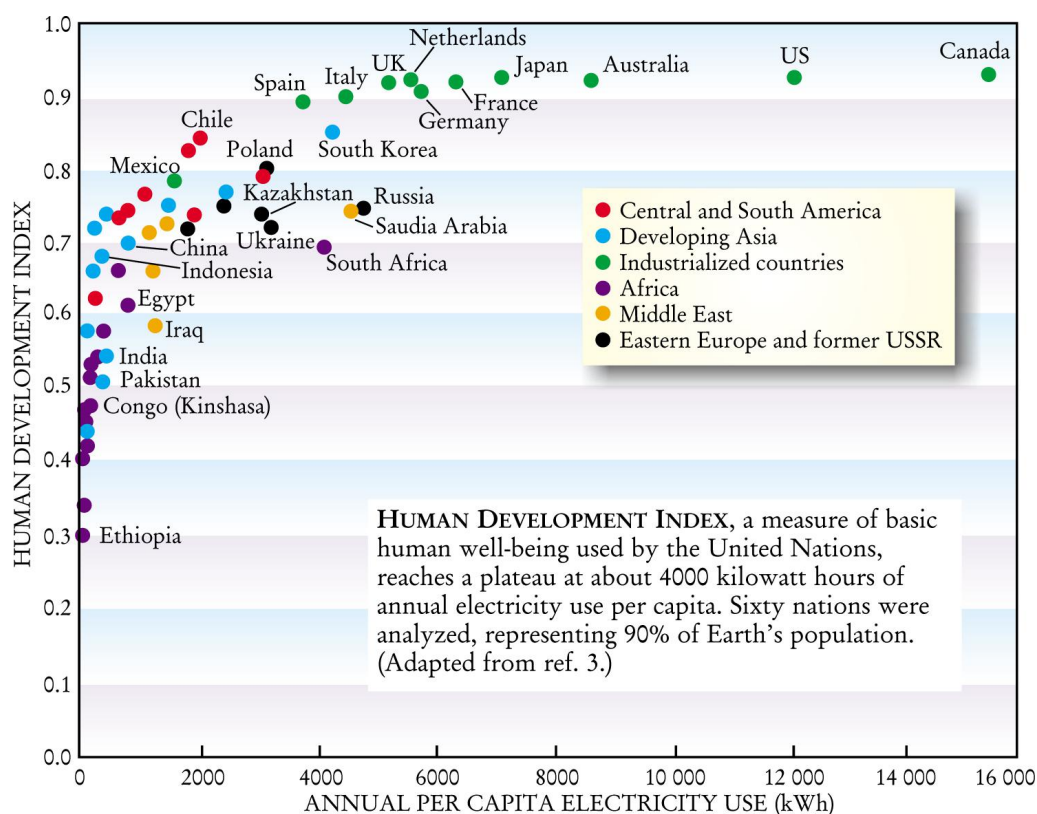


Figure I-1: Human Development Index (HDI), a measure of basic human well-being used by the United Nations, reaches a plateau at about 4000 kilowatt hours of annual electricity use per capita. Sixty nations were analyzed, representing 90% of Earth's population.¹

Fifteen terawatts is the energy of 150 billion 100-watt light bulbs burning 24 hours a day for a year, which is also how much energy humanity now uses annually. This is equivalent to consume 220 million barrels of oil per day to keep the world spinning.² Richard E. Smalley, a professor of Physics and Astronomy at Rice University who is the 1996 chemistry Nobel

Prize winner, found by calculating that the global population will reach ten billion by 2050. And by then, we would need to consume 60 terawatts on a global scale - the equivalent of 900 million barrels of oil per day. This most serious challenge facing mankind in this century was called “Terawatt Challenge” by Professor Smalley. Based on such research background, Professor Smalley generalized the major issues facing mankind into 10 issues (Energy, Water, Food, Environment, Poverty, Terrorism and war, Disease, Education, Democracy, Population), with energy at the top. Most notably, energy can be the key to solve all the other issues.³ For now, more than 85 percent of the energy consumed by humans comes from the incomplete combustion of the fossil fuels such as oil, coal, and natural gas. Through burning fossil fuels, carbon dioxide and sulfur dioxide have been emitted into the atmosphere which contribute to the global warming and cause the environmental pollution.⁴ It is learned that by the end of this century, a mere 82 years from now, we will need to have more infrastructures that run exclusively on renewable generated energy.⁵

Solar energy, as a renewable energy source, is inexhaustible in supply and always available for use. It is worth mentioning that solar energy has many unique advantages such as no transportation problems, can be stored in place, green pollution free and so on. Broadly speaking, there are three opportunities involving the conversion and storage of the sunlight in energy: solar-to-heat conversion, solar-to-chemistry conversion and solar-to-electricity conversion.⁶ Among them, the solar-to-electricity conversion is mainly realized through solar cells.

Up to now, solar cell production has increased at about 30% per year over decades.⁷ Conventional solar cells of today are based on crystalline silicon which are considered as the first generation of solar cells. The second generation of solar cells such as amorphous silicon, CIGS (Copper Indium Gallium Selenide) and CdTe (Cadmium Telluride) are based on thin film technologies. Single junction devices are the foundation of the first and the second generation solar cells. It should be noted that the calculated thermodynamic efficiency limit for single junction devices, *i.e.* 31%, suppose that a single electron-hole pair is formed when an individual photon is absorbed and all photon energy in excess of the energy gap is lost as heat. To overcome the so-called Shockley-Queisser limit, new concepts are developed which corresponds to third generation solar cells.^{7,8}

In this context, dye-sensitized solar cells (DSCs) can be regarded as a technology in the process of transition from the second generation to the third generation of solar cells.⁸ In the present stage, DSCs are attractive photovoltaic devices because their low production cost compared with conventional photovoltaic technologies, design opportunities such as

transparency and multi-color options, flexibility, lightweight, short energy payback time (< 1 year), low dependence both on the angle of incoming light and solar irradiance regarding power conversion efficiency (PCE) and so on.⁹⁻¹⁴ DSCs can be primitively categorized into n-type DSCs (n-DSCs), p-type DSCs (p-DSCs) and tandem DSCs on the basis of the working principles involved through the use of various dyes and nanostructured metal oxide electrodes.^{7,8,10,15} Furthermore, research efforts have been also devoted to dye-sensitized photoelectrochemical cells (DSPECs) which enable either proton reduction into hydrogen via water splitting or carbon dioxide reduction into carbon monoxide. In analogy to p-type DSCs, NiO-based photocathodes can be obtained by sensitization of nano-structured thin films with organic or metallo-organic dyes and display photoelectrochemical activity.^{12,16-18}

As is clear from the above descriptions, dye-sensitized solar cells (DSCs) is a promising technology in the field of solar electricity production since the seminal paper published by O'Regan and Grätzel in 1991¹⁹ which underpins the development of critical renewable energy and environmental technology. In this context, high efficiency/low cost solar cells and visible-light driven hydrogen production from photoactive cathodes based on molecular catalysts and dye-sensitized metal oxide semiconductors are of great interest. Following these earlier significant studies, in this thesis, we focused on the design, synthesis and properties of asymmetric ruthenium-diacetylidyde organometallic complexes as photosensitizers for a new series of n-type DSCs, p-type DSCs and DSPECs.

I.2. Overview of Solar Energy and Solar Cells

Natural society is composed of three elements: matter, energy and information. Since the beginning of human civilization, energy has been an indispensable element of survival and development which can undertake the necessary support to nature through energy transformation, such as mineral energy, nuclear energy, atmospheric circulation energy, terrestrial rational energy and so on. However, a series of environmental issues arising from fossil fuel consumption lead to global warming and ecological environmental deterioration.^{20,21} Within the global and national implications for poverty, economic development, and overall social progress, no country can afford to ignore the research on energy, especially on renewable energy. It is obvious that access to economically implemented renewable energy sources is promoted by the increasing public awareness that the Earth's fossil reserves will run out during this century, simultaneously the energy demand will be twofold within the next 50 years.²²⁻²⁶ In the field of renewable energies, solar energy appears as one of the most advantageous resources to fulfill the rising worldwide demand for

inexhaustible, clean, abundant and sustainable power sources.^{27,28} In this context, the attractive approaches that can facilitate the harness of the solar energy and mimic natural photosynthesis are very significant and valuable. Following this concept, solar cells have attracted worldwide interest which appear to be the large scale answer to solar energy utilization.^{7-9,29}

I.2.1. Solar Energy

The sun is a hot star with a surface temperature of 5777K (Figure I-2), which emits a generic form of radiation because of consistently nuclear fusion reactions inside. The light emitted outward from the sun has a range of wavelengths from the ultraviolet and visible to the infrared. A very small fraction of the sun's light is emitted and after passing unhindered through interplanetary space it hits the earth. According to estimates, the total energy of the sun's omnidirectional radiation into the universe is 4×10^{14} TW while the radiation to the surface of the earth's atmosphere can be estimated by solar constant.^{7,30,31} The solar constant is a flux density measuring mean solar electromagnetic radiation (solar irradiance) per unit area. It is measured on a surface perpendicular to the rays, one astronomical unit (AU) from the Sun (roughly the distance from the Sun to the Earth). The solar constant includes all types of solar radiation, not just the visible light. It is measured by satellite as being 1.361 kilowatts per square meter (kW/m^2) at solar minimum and approximately 0.1% greater (roughly 1.362 kW/m^2) at solar maximum.³² The solar "constant" is not a physical constant in the modern CODATA scientific sense; that is, it is not like the Planck constant or the speed of light which are absolutely constant in physics. The solar constant is an average of a varying value. In the past 400 years it has varied less than 0.2 percent.^{33,34} Hereby, the energy radiated from the sun to the surface of the earth can be estimated as approximate 1.74×10^5 TW — the equivalent of the heat given off by burning 1.86×10^{14} tons of standard coal per year. Moreover the energy of 1.74×10^5 TW goes so far as to be higher than the world's total reserves of fossil fuels (equivalent to about 1.00×10^{13} tons of standard coal).³⁵

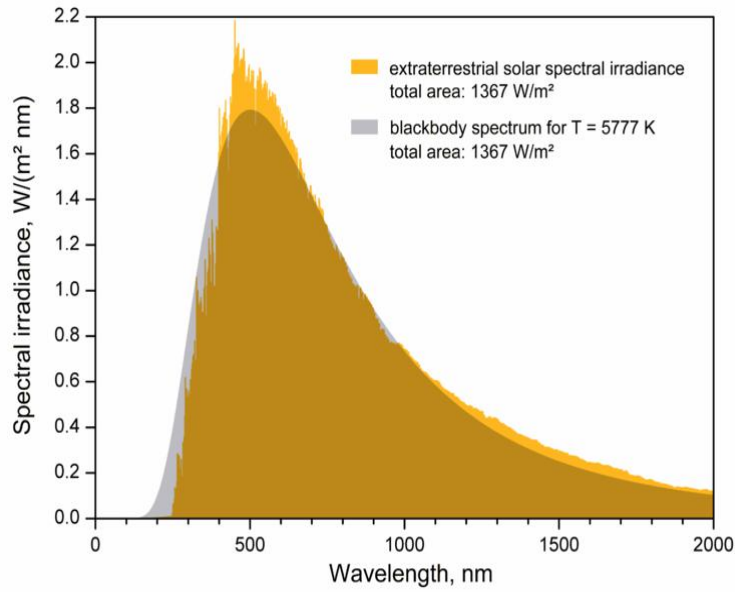


Figure I-2: The effective temperature, or black body temperature, of the Sun (5777 K) is the temperature a black body of the same size must have to yield the same total emissive power. (cited from Wikipedia)

Due to the progress of social civilization, the social level of industrialization will also continuously deepen accompanied by the problems of worldwide environmental pollution and energy shortage. Energy and environmental issues becoming more and more important, the development and utilization of solar energy are tuning into a key point as it possesses the advantages of being clean, safe and reliable.

I.2.2. Solar Radiation and Solar Spectrum

As mentioned above, solar constant is measured by artificial satellite in outer space, which is going to be equal to the sum of light energy versus all wavelengths of sunlight (within the range of 150-4000 nm) under the circumstance of no atmospheric absorption^{30,31,36,37}:

$$P_{in} = \int_{150}^{4000} P_{in}(\lambda)d\lambda = \int_{150}^{4000} \frac{hc}{\lambda} \times N_p(\lambda)d\lambda \quad (1)$$

The P_{in} in the formula refers to the luminous energy struck on solar cells in one minute offered by the light with a wavelength of λ while h stands for Plank constant and N_p represents photon flux (the amount of radiant energy received from the sun per unit area per unit time). In this way, the measured radiation under the circumstance of no atmospheric absorption is the solar constant. As a matter of fact, the absorption, reflection and scattering of

the sunlight by the earth atmosphere have influence on the solar radiation intensity and the distribution of the solar spectrum while the irradiance varies depending on the position of the sun, orientation of the earth and air quality of community. In order to measure this impact, the concept of air mass (AM) was introduced and can be approximated by $AM = P/P_0 \cdot \cos \theta_z$, where θ_z , P and P_0 represent the zenith angle, the local atmospheric pressure and the standard atmospheric pressure, respectively. The relationship between air mass and θ_z is shown in Figure I-3.

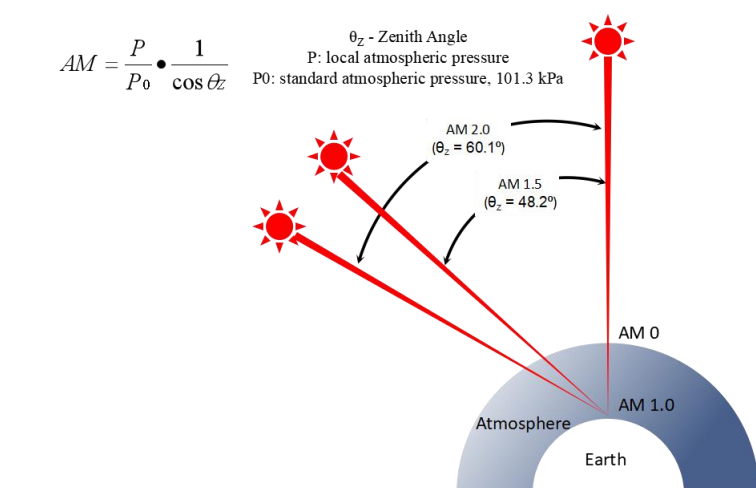


Figure I-3: The path length in units of air mass, changes with the zenith angle.

The experimental results show that the efficiency of a solar cell is highly sensitive to change of solar spectrum. It is significant to identify standard solar spectrum to accurately compare the performance of solar cells measured at different times in different places. The air mass coefficient is commonly used to characterize the performance of solar cells under standardized conditions, and is often referred to using the syntax “AM” followed by a number. The standard solar spectrum adopted outer space is called AM 0 corresponding to the situation that solar radiation is equal to solar constant, which is usually used to test performances of solar cells on artificial satellites and spaceships. Whereas the standard solar spectra served as efficiency measurements of solar cells are AM 1.5G (within the diffusion part of sunlight) and AM 1.5D (without the diffusion part of sunlight). The former spectrum is normalized in order that the integrated irradiance (the amount of radiant energy received from the sun per unit area per unit time) is $1000 \text{ W} \cdot \text{m}^{-2}$. The latter spectrum is commonly used to test the performance of concentrator solar cells.³⁶⁻³⁸ Figure I-4 gives these standard solar spectra.³⁹

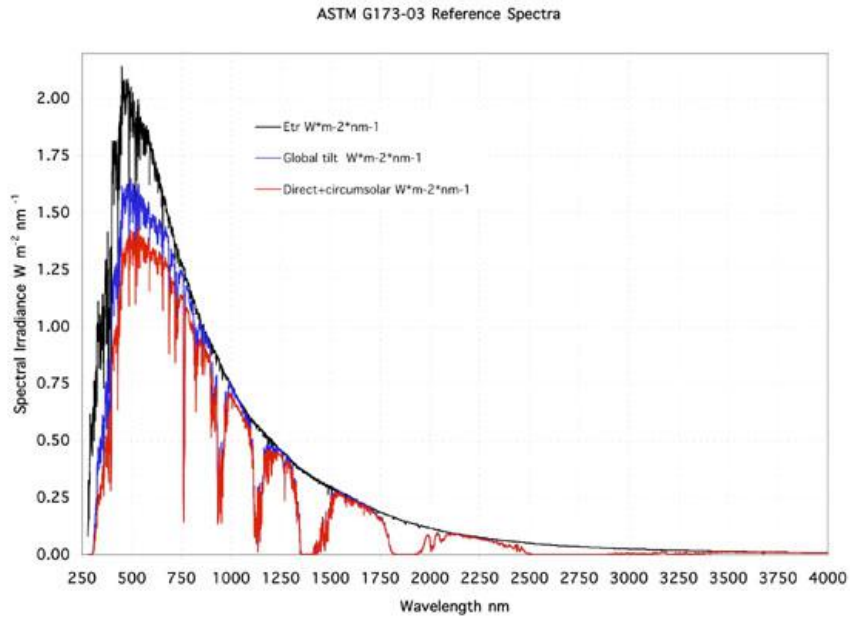


Figure I-4: Standard spectral irradiance spectra of AM 0 (black line), AM 1.5G (blue line) and AM 1.5D (red line).³⁹

Considering that the energy conversion efficiency mainly depends on electron-hole pair generation when the photons are absorbed, the solar photon flux spectra of Figure I-5 is thus more specifically suited to related discussions.^{7,40}

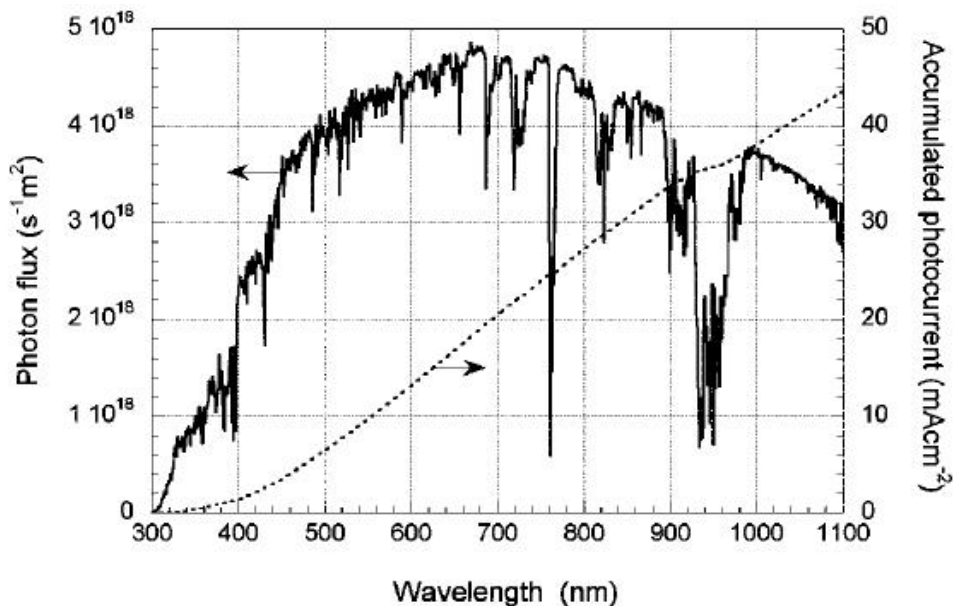


Figure I-5: Photon flux of the AM 1.5 G spectrum at $1000 \text{ W}\cdot\text{m}^{-2}$ (ASTM G173-03), and calculated accumulated photocurrent.⁷

I.2.3. Solar Cells

Since the French scientist Dr. E. Becquerel discovered "photoelectric effect" in 1839, the research on solar cells has never been stopped.^{12,41} In 1883, Dr. Charles Fritts successfully fabricated the first solar cell based on a gold/selenium rectifier.^{42,43} In 1954, the first monocrystalline silicon (mono-Si) solar cell with eventually conversion efficiency of 6.0% fabricated in American Bell Labs opened a new era of solar energy utilization.⁴⁴ In 1963, 242 W photovoltaic module array solar cell and its work system were designed and installed in Japan which was the global largest solar power station at that time. Starting from the year of 1973, solar cells have been used for civilian purpose along with their widely application.⁴³ Subsequently, the first amorphous silicon (a-Si) solar cell in the world was invented by D. E. Carlson and C. R. Wronski in 1976.⁴⁵ M. Grätzel and co-workers introduced the concept of dye-sensitized fractal type TiO₂ electrodes with high surface area in 1985 and the efficiency of solar cells based on nanostructured TiO₂ electrodes attained 7% in 1991.^{19,46-49}

In general, solar cells are electrical devices that convert the energy of light directly into electricity by the photovoltaic effects, which go through nearly 150 years. A solar cell includes a photoelectric cell, defined as a device whose electrical characteristics, such as current, voltage, or resistance, vary when exposed to light.^{50,51} As shown in Figure I-6⁵², solar cells can fall into three generations on the basis of their development stages.

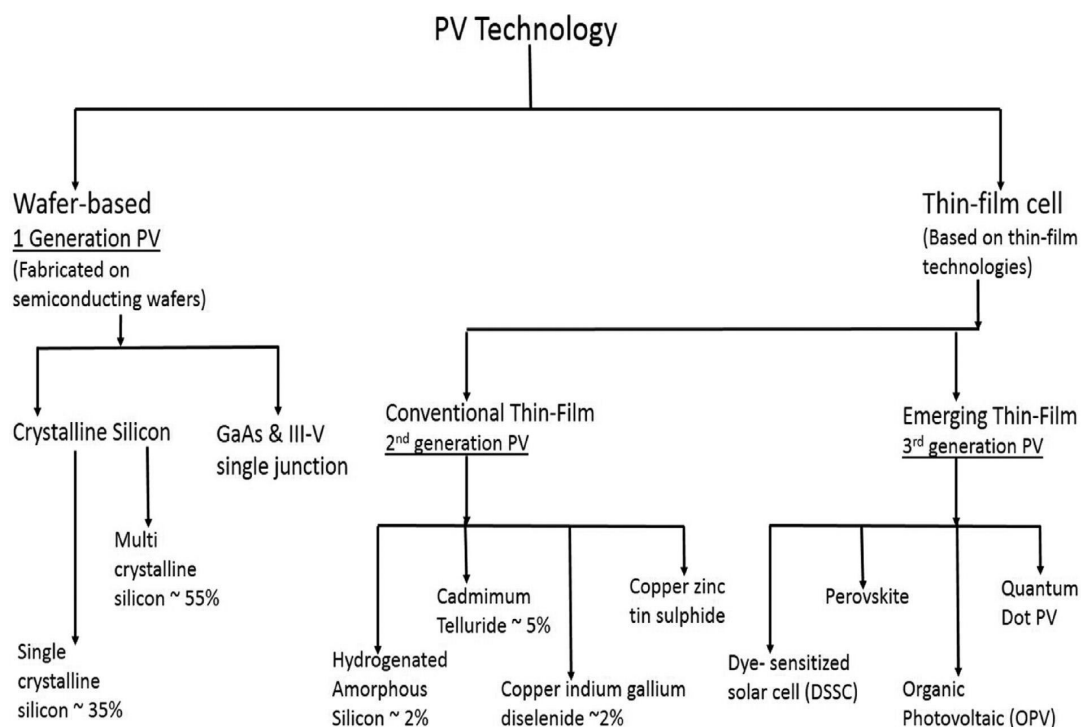


Figure I-6: Classification of photovoltaic technologies with their current market share in percentage until now.⁵²

Solar cells are described as being photovoltaic, irrespective of whether the source is sunlight or an artificial light. They are used as a photodetector (for example infrared detectors), detecting light or other electromagnetic radiation near the visible range, or measuring light intensity. The operation of a photovoltaic (PV) cell requires three basic attributes:⁵⁰⁻⁵⁶

- The absorption of light, generating either electron-hole pair or excitons;
- The separation of charge carriers of opposite types;
- The separate extraction of those carriers to an external circuit.

Solar cell efficiency refers to the portion of energy in the form of sunlight that can be converted via photovoltaics into electricity. Conversion efficiencies of best research solar cells worldwide from 1976 through 2017 for various photovoltaic technologies are shown in Figure I-7.⁵⁷

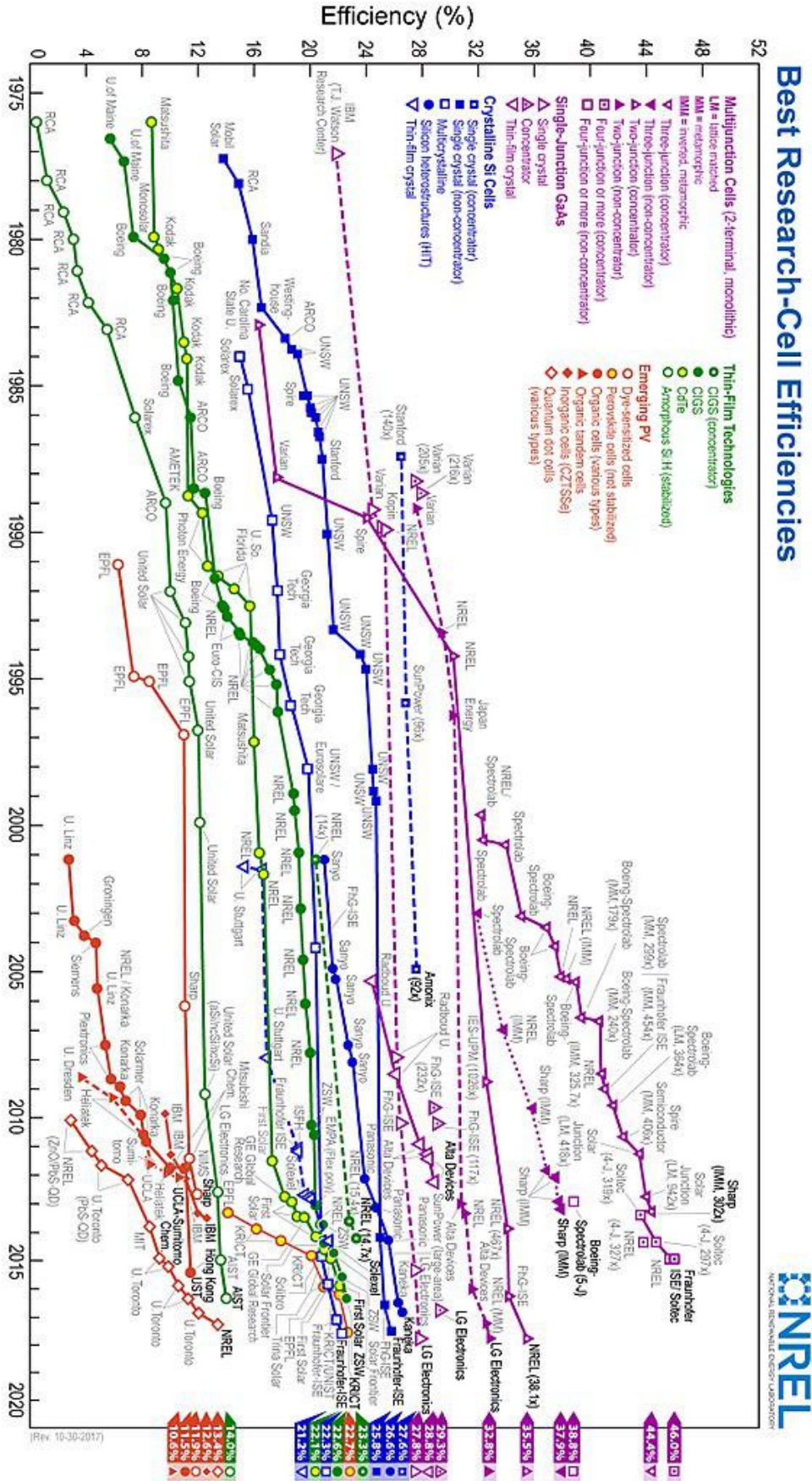


Figure I-7: Reported timeline of solar cell energy conversion efficiencies.⁵⁷

I.2.3.1. Silicon-Based Solar Cells

Nowadays, conventional solar cells, which are known as first generation solar cells, are based on silicon. It is noteworthy that most of the photons of sunlight have energies between 1 eV and 3 eV which means the optimum band gap for maximum power conversion is approximately 1.5 eV, while the band gap of crystalline silicon is only 1.14 eV. However, silicon based solar cells are the most studied, the ripest in technique and most commercialized civil solar cells for now. Perhaps the biggest advantage of silicon material, from a resource standpoint, lies in it is the world's second-largest element reserves in the earth's crust, let alone its stable performance, nontoxicity and environmental friendliness. So far, silicon based solar cells have accounted for about 90 percent global market share of solar cells. At the moment, silicon-based solar cells can be divided into three kinds: monocrystalline silicon (mono-Si) solar cell, polycrystalline silicon (poly-Si) solar cell and amorphous silicon (a-Si) solar cells.⁵⁸⁻⁶⁰

I.2.3.1.1. Monocrystalline Silicon (mono-Si) Solar Cells

Monocrystalline silicon (mono-Si) solar cells, as the earliest generation of silicon-based solar cells, have been widely used in people's production and life now relying on technology and production techniques (see Figure I-8).⁶¹

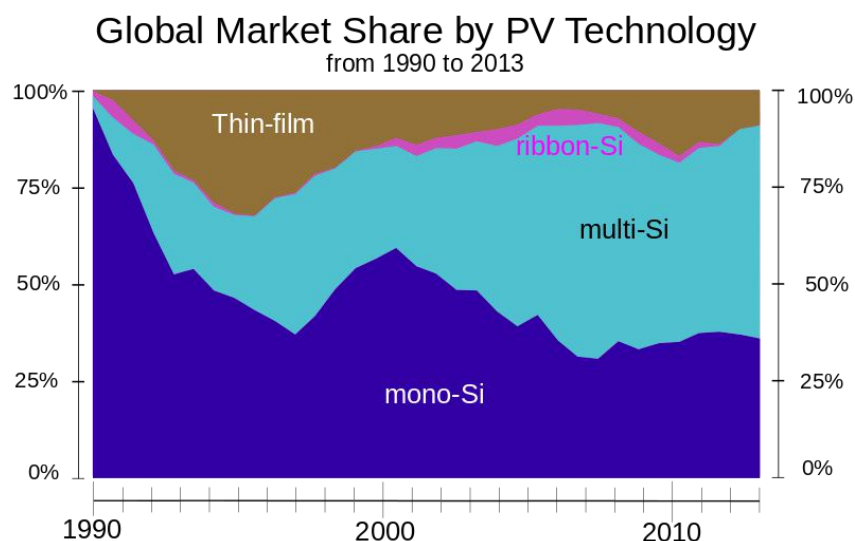


Figure I-8: Global market-share in terms of annual production by photovoltaic technology since 1990.⁶¹

Since the dawn of silicon based solar cells, the photoelectric conversion efficiency of mono-Si solar cells has been unceasingly improved.⁶² Lab efficiency of 26.6 percent for (heterojunction back-contact type) mono-Si cells is the highest in the commercial photovoltaic market while solar module efficiencies - which are always lower than those of their corresponding cells - crossed the 20 percent mark for mono-Si in 2012. These high efficiencies can be combined with other technologies, such as multi-layer solar cells in applications where space and weight become an issue such as powering satellites.^{61,63} However, the premise of high conversion efficiency is to use highly purified mono-Si material (over 99.999%) and quite demanding hot processing technology. Therefore, the theoretical boundary of efficiency based on mono-Si solar cells is 29%.⁶³ Moreover, it is a hardly practical option in terms of current technology to improve the efficiency of mono-Si solar cells. Although having high efficiencies and high market share, mono-Si solar cells have high production cost because they require highly purified mono-Si material and quite demanding hot processing technology. To reduce the production costs and simultaneously obtain high conversion efficiency, poly-Si solar cells and a-Si solar cells are the backup options for subsequent development in this field.

I.2.3.1.2. Polycrystalline Silicon (poly-Si) Solar Cells

Polycrystalline silicon (poly-Si) is the key feedstock in the crystalline silicon based photovoltaic industry and used for the production of conventional solar cells. For the first time, in 2006, over half of the world's supply of polysilicon was being used by PV manufacturers.⁶⁴ The solar industry was severely hindered by a shortage in supply of polysilicon feedstock and was forced to idle about a quarter of its cell and module manufacturing capacity in 2007.⁶⁵ Only twelve factories were known to produce solar-grade polysilicon in 2008, however, by 2013 the number increased to over 100 manufacturers.⁶⁶ The product manufacturing process of poly-Si solar cells is basically the same as mono-Si solar cells while the conversion efficiencies of both present differences. The conversion efficiency of poly-Si solar cells is around 12%-15% which is lower than mono-Si solar cells. Despite of this, poly-Si solar cells represent good prospects for development due to low dependence on silicon wafers and low production costs. In recent years, with the constant increase of photoelectric conversion efficiencies of the solar cell devices, poly-Si solar cells have been current mainstream products, whose market share has reached over 50% in silicon-based solar cells industry. Compared with mono-Si solar cells, the reasons for low conversion efficiency of poly-Si solar cells are mainly as follows:⁶⁷

- i. When produced for the electronics industry, polysilicon contains impurity levels of less than one part per billion (ppb), while polycrystalline solar grade silicon (SoG-Si) is generally less pure. This leads to reduction of free electrons when the light is absorbed, and furthermore, reduction of the photocurrent and the conversion efficiency.
- ii. The binding bonds between silicon atoms are weak and unstable which will be destroyed by the ultraviolet radiation of the sun as time goes on. Therefore the conversion efficiency of poly-Si solar cells will decrease with time.
- iii. The manufacturing technology of poly-Si is relatively simple which means the poly-Si will have more impurities and defects. The doping of polycrystalline silicon does have an effect on the resistivity which leads to the low efficiency of poly-Si solar cells.

I.2.3.1.3. Amorphous Silicon (a-Si) Solar Cells

Amorphous silicon (a-Si) thin film solar cells have a more than 40 years history in the course of invention and real industrialization, which present a strong vitality have already developed into a significant branch of solar cell industry.⁴⁵ Typically, amorphous silicon thin-film cells use a p-i-n structure, where p type layer and n type layer are composed of a boron-doped material and a phosphor-doped material, respectively and i represents an intrinsic material. The placement of the p-type layer on top is also due to the lower hole mobility, allowing the holes to traverse a shorter average distance for collection to the top contact.^{68,69} Typical panel structure includes front side glass, TCO, thin-film silicon, back contact, polyvinyl butyral (PVB) and back side glass (see Figure I-9).⁶⁹

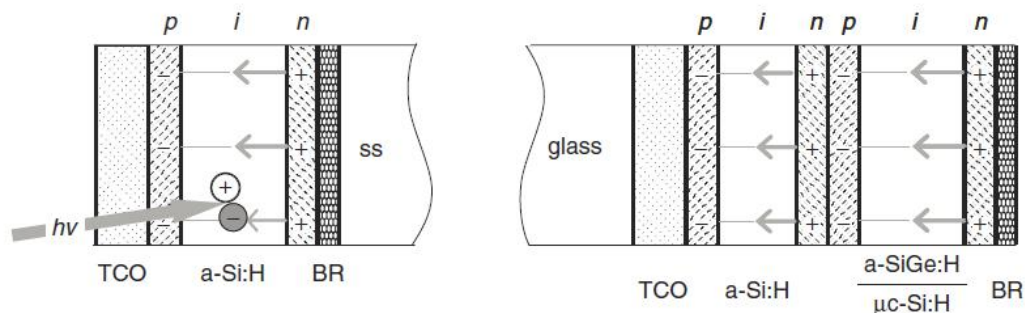


Figure I-9: (left) Single-junction *pin* solar cell with a stainless-steel (ss) substrate. In a *pin* structure in the dark, excess electrons are donated from the *n*-type doped layer to the *p*-type layer, establishing the space charges and electric fields as shown. Under illumination, each photon absorbed in the undoped,

intrinsic layer generates one electron and one hole photocarrier. The electric field causes these carriers to drift in the directions shown. (right) Tandem *pin* solar cell with a glass “superstrate”. The second intrinsic layer typically has a lower bandgap, and absorbs photons that are transmitted through the first layer. For amorphous silicon based cells, photons invariably enter through the *p*-type window layer as shown here.⁶⁹

Compared with silicon based solar cells, a-Si thin film solar cells have prominent advantages. First of all, the main advantage of a-Si in large scale production is not efficiency, but cost. A-Si cells use only a fraction of the silicon needed for conventional crystalline silicon (c-Si) cells, and the cost of the silicon has historically been a significant contributor to cell cost. Secondly, another significant advantage of a-Si thin film solar cells is to make the large area deposition become reality. Furthermore, in addition to the main advantages mentioned above, a-Si thin film solar cells can be deposited on flexible substrates, such as plastics, aluminium foil, stainless steel sheets and so on.⁶⁹ The “roll-to-roll” a-Si PV manufacturing process was exploited in 2003 by Energy Conversion Devices, Inc. (ECD)⁷⁰ and then has been used by ECD’s PV joint ventures and partners (United Solar Ovonic, Sovlux, and Canon) as well as Power Film.⁷¹

A-Si thin film solar cells come forth with certain incomparable advantages, and at the same time, have some insurmountable shortages and defects. On one hand, the solar conversion efficiencies of a-Si thin film solar cells are lower than mono-Si and poly-Si solar cells. To sum up all a-Si thin film solar cell devices based on different structures such as single-junction a-Si, tandem junction a-Si, or triple-junction a-Si/a-SiGe/a-SiGe, the commercial modules typically have stabilized efficiencies in the range of 5.5-6.5%.⁶⁹ On the other hand, the light-induced degradation cannot be negligible in a-Si thin film solar cells. For example, single crystalline silicon solar cells, the light-induced degradation can reach 30% which seriously limits its development scale and speed.^{68,69,72,73} If the critical issues mentioned above can be addressed, we can have faith in the increasing broad application of a-Si thin film solar cells significantly beyond today’s level.

I.2.3.2. III-V Solar Cells

III-V compounds are new semiconductors after the development of germanium (Ge) and silicon (Si). The elements in groups III and V of the periodic table can be put together in various way so that there is a wide range of III-V compounds. In recent years III-V compound semiconductor materials, including gallium arsenide (GaAs), gallium phosphide (GaP), and

indium phosphide (InP), are widely applied in electronic devices such as light-emitting diodes,⁷⁴ laser diodes,⁷⁵ photocatalysis^{76,77} and solar cells⁷⁸⁻⁸², because of their high saturated electron velocity, high electron mobility, and appropriate band gap. Among them, GaAs is identified to the optimal light absorption layer material, which band gap is 1.43 eV. The value is close to the band gap for maximum power conversion which is approximately 1.5 eV.⁸³ GaAs solar cells are promising due to their high efficiency and their resistance to the ionizing radiation in outer space.

To date, GaAs solar cells can reach the photoelectric conversion efficiencies of around 30% with the help of light concentrators and 28.8 ± 0.9 % under standard AM 1.5 sunlight, $100 \text{ mW}\cdot\text{cm}^{-2}$ irradiation.⁸⁴ In 1954, H. Welker first found photovoltaic effect of GaAs.⁸⁵ Soon afterwards, a 6% GaAs p-n junction solar cell was first reported by RCA laboratories in New Jersey, USA.⁸⁶ In 1970, Z. I. Alferov (2000 Nobel Prize in Physics) and co-workers at the Ioffe Institute developed a heteroface GaAlAs/GaAs solar cell which pointed the way to new device structures.⁸⁷ At the initial stage of study, liquid phase epitaxy (LPE) is used to manufacture the GaAs solar cells. However, the main issue for GaAs solar cells made by LPE is the high surface recombination velocity of GaAs material, which can greatly decrease the short circuit currents of GaAs solar cells. Until 1973, H. J. Hovel and J. M. Woodall put forward a way to add a thin, epitaxial layer of p-type $\text{Ga}_{1-x}\text{Al}_x\text{As}$ on the GaAs p-n junction surface which can solve the above problem (the high surface recombination velocity of GaAs material).⁸⁸ Recently, with the rapid increase of laminated cell efficiencies, the development of concentrating solar cell technology and the continuous improvement of installations, the terrestrial applications of GaAs solar cells have become into reality.⁸⁹ R. R. King and co-workers of multijunction solar cell team at Spectrolab in USA reported a metamorphic three-junction GaInP/GaInAs/Ge cell which had an efficiency of 40.7% under the standard spectrum for terrestrial concentrator solar cells at 240 suns ($24.0 \text{ W}/\text{cm}^2$, AM 1.5D, low aerosol optical depth, $25 \text{ }^\circ\text{C}$) in late 2007.⁹⁰ In January 2009, Fraunhofer ISE in Germany announced to obtain the efficiency of 41.1% for triple-junctions cells based on III-V semiconductor materials.⁹¹ Subsequently, in August 2009, Spectrolab in USA launched a press release announcing an efficiency of 41.6 % for a triple-junction concentrator solar cell which broke the record of 41.1% conversion efficiency.⁹² In June 2010, the excellent efficiency was demonstrated with InGaP/GaAs/InGaAs 3-junction solar cell with 35.8% and 42.1% at 1-sun and 230-suns, respectively by Sharp.⁹³ Figure I-10 shows theoretical conversion efficiencies of single-junction and multi-junction solar cells in comparison with experimentally realized efficiencies.⁹⁴ Finally, the record efficiency of about 46% at 234 suns was reached with

InGaP/GaAs/InGaAs/InGaAs four-junction solar cell device structure.⁹⁵

Although the new concentrator system is expected to open a door to a new age of high efficiency III-V based solar cells, there are still many issues which await to be solved. First of all, III-V solar cell devices are limited because of their complex fabrication. Secondly, the III-V materials are still inherently very expensive that results in a enormous challenge for large-area fabrication. Moreover some of the III-V materials are highly toxic such as arsenic and its compounds.⁶⁹ The environment, health and safety aspects of gallium arsenide sources (such as trimethylgallium and arsine) and industrial hygiene monitoring studies of metallo-organic precursors have been reported.⁶⁶ The stability and disposal methods of solid arsenic bearing wastes are important for environment pollution due to the toxicity of arsenic compounds. In short, from a long-term environmental perspective, III-V based solar cells do not remain as the first option regardless of their decent photoelectric conversion efficiency.

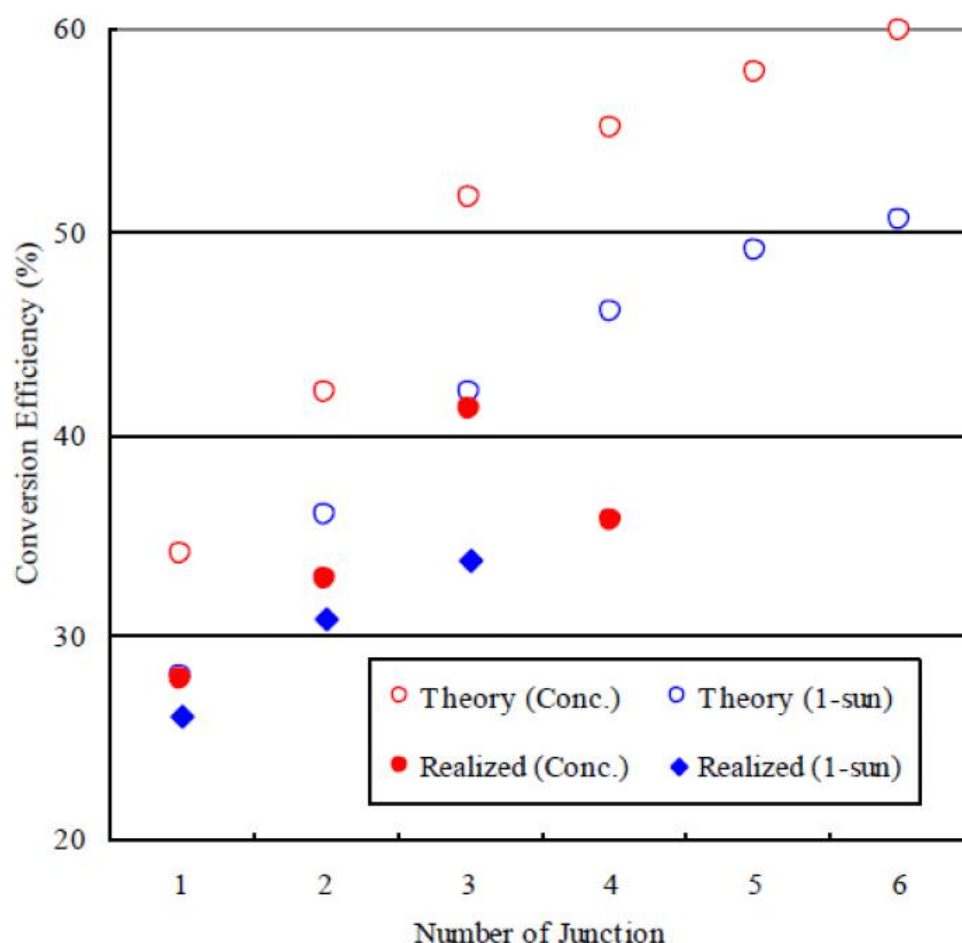


Figure I-10: Theoretical conversion efficiencies of single-junction and multi-junction solar cells in comparison with experimentally realized efficiencies. (Blue: single-junction solar cells; Red: multi-junction solar cells)⁹⁴

I.2.3.3. CdTe/CdS Thin Film Solar Cells

Cadmium telluride (CdTe) photovoltaics is known as the most commercial successful thin film photovoltaic technology, benefiting from some excellent physico-chemical peculiarities as follows⁹⁷⁻¹⁰⁵: (1) its band gap (1.45 eV) is almost a perfect match to the distribution of photons in the solar spectrum in terms of conversion to electricity, (2) 1 μm thick layer of CdTe can capture over 90% of the sunlight because of its high absorption coefficient in the visible part of the solar spectrum in the range of $(10^4 - 10^5) \text{ cm}^{-1}$, (3) it exhibits a great thermodynamic stability, (4) its high stability and congruent evaporation make it superior for the growth by means of various different preparation methods, (5) it is moderately p-type because it naturally grows with intrinsic stoichiometry defects, (6) its post-growth treatment can reduce defects and increase the crystallinity which make its boundaries electrically inactive.

The CdTe was deeply studied as a light absorber material in solar cells firstly by J. J. Loferski in 1956.¹⁰⁶ The first all thin film solar cell exhibiting a 6% efficiency based on CdTe/CdS was reported by D. Bonnet and H. Rabenhorst more than 45 years ago.¹⁰⁷ At the very beginning, a lot of early work on the CdTe/CdS solar cells - in which CdS as n-type partner for the junction formation with the p-type CdTe absorber - focused on the growth of the layers and the formation of the junction. However, with the post-deposition technology adapted to the as-deposited CdTe/CdS layer stacks, it has been obvious that the growth of the absorber and the formation of the junction were not of central importance. During the 1970s, the single crystals growth of II-VI elements in halogen was reported by C. Paorici *et al.* which was crucial and promising research result for the CdTe/CdS stack treatment in halogen atmosphere.^{108,109} In 1982, an efficient CdTe/CdS solar cell was developed in which CdTe/CdS films were prepared by a close-spaced-sublimation technique. The efficiency of this kind of CdTe/CdS solar cell was 10% which was considered as a threshold value for the large-scale development of thin film technology.¹¹⁰ And thereafter, by using CdS films prepared by chemical bath deposition and p-CdTe films deposited by close-spaced-sublimation, a CdTe/CdS solar cell of greater than 1cm^2 area with an AM 1.5 efficiency of 15.8% was reported by J. Britt and C. Ferekides in 1993.¹¹¹ From this research, a promising experience can be learned that the stability over-time issue could be settled by a very fine optimization of the back-contact formation. Recent years, the other layers were applied in CdTe/CdS solar cells such as cadmium stannate (CTO) to replace indium tin

oxide (ITO), aluminum doped zinc oxide (ZAO) and fluorine doped tin oxide (FTO) to improve the front-contact. And also, a second low-conductive and high-transparent layer such as zinc stannate (ZTO) layer, ZnO layer, and SnO₂ layer was added to improve the stability of the front-contact.¹¹² In the last two decades, the efficiency of CdTe/CdS solar cells went through from 16% to 22.1%¹¹³⁻¹³⁵ and lots of work have been done to push the conversion efficiency closer to the theoretical Shockley-Queisser limit of 33%^{133,136}. In the meantime, the industrial development based on CdTe/CdS thin film solar cells has become mature enough since 2000s and nowadays, the CdTe production capacity covers about 6% of the total photovoltaic production.^{103-105,126,137}

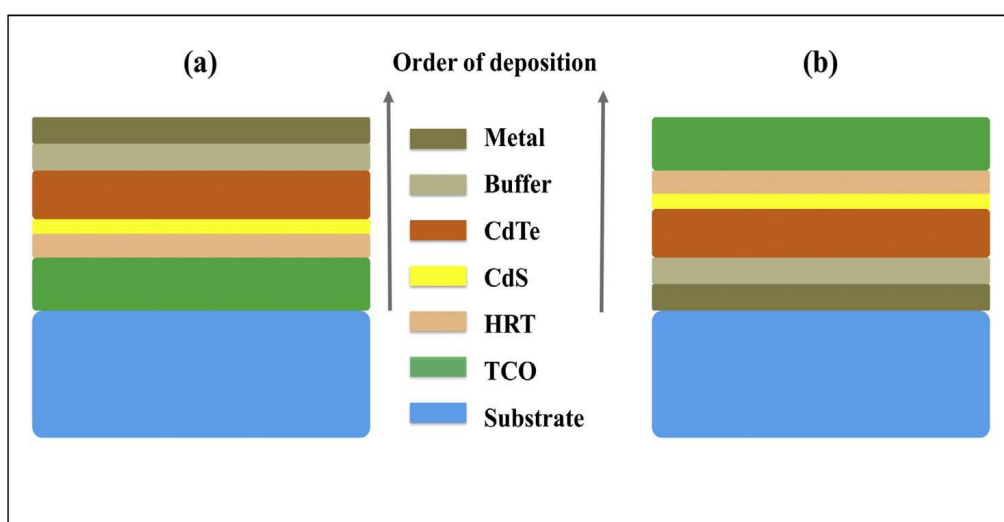


Figure I-11: Not in scale view of the sequence layers in a CdTe thin film solar cell highlighting the order of deposition: (a) superstrate configuration, (b) substrate configuration.¹⁰³

Compared to silicon based solar cells, CdTe/CdS thin film solar cells have a totally different design principle. Two conventional configurations of CdTe/CdS thin film solar cells including the substrate configurations and the superstrate configurations are shown in Figure I-11.¹⁰³ The main difference between the two conventional configurations lies in the sequence of individual thin layers which plays a decisive role in the final behavior of the CdTe/CdS solar cells.

Although huge progress has been made in the development of CdTe/CdS thin film solar cells since 1950s until now, some shortages and defects still remain such as interface defects and CdTe doping. Further studies based on CdTe/CdS thin film solar cells are in progress concerning to the toxicity of CdTe, the reduction of the absorber thickness, grain boundaries passivation, back-contact quality, CdTe doping, recombination/lifetime of the charge carriers,

interface defects and so on.^{70,103,129-135}

I.2.3.4. CIGS Thin Film Solar Cells

Copper indium gallium (di)selenide (CIGS) with the chalcopyrite crystal structure is a I-III-VI₂ tetrahedrally bonded semiconductor material composed of copper, indium, gallium, and selenium. Since the technology was first deployed, CIGS has always been one of the three mainstream thin-film photovoltaic technologies, alongside the cadmium telluride (CdTe) and amorphous silicon (a-Si). CIGS layers are thin enough to be flexible, adapting them to be deposited on flexible substrates.¹³⁸⁻¹⁴⁰ Upon heating from 805 °C to 1045 °C, CuIn_xGa_{1-x}Se₂ transforms from the zinc blende form (pure copper indium selenide, where x=1) to the chalcopyrite form (pure copper gallium selenide, where x=0) with bandgap from about 1.0 eV (for copper indium selenide) to about 1.7 eV (for copper gallium selenide).^{138,141}

Although CIGS can be applied on flexible supports, the best performance comes from solar cell devices deposited on glass as most of thin film technologies normally use high-temperature deposition techniques. CIGS can be employed as light absorption layer compared to silicon based material and CdTe despite its conversion efficiency is somewhat lower.¹³⁸ Figure I-12 shows the basic structure of a CIGS solar cell, with examples of the most commonly used material.¹⁴² The CIGS solar cells based on thin film technology are used to convert sunlight into electric power which are manufactured by depositing a thin layer of copper, indium, gallium and selenide on glass or plastic backing, along with electrodes on the front and back to collect current. Because the material has a high absorption coefficient and strongly absorbs sunlight, a further thinner film is required than of other semiconductor materials.^{138,142-146}

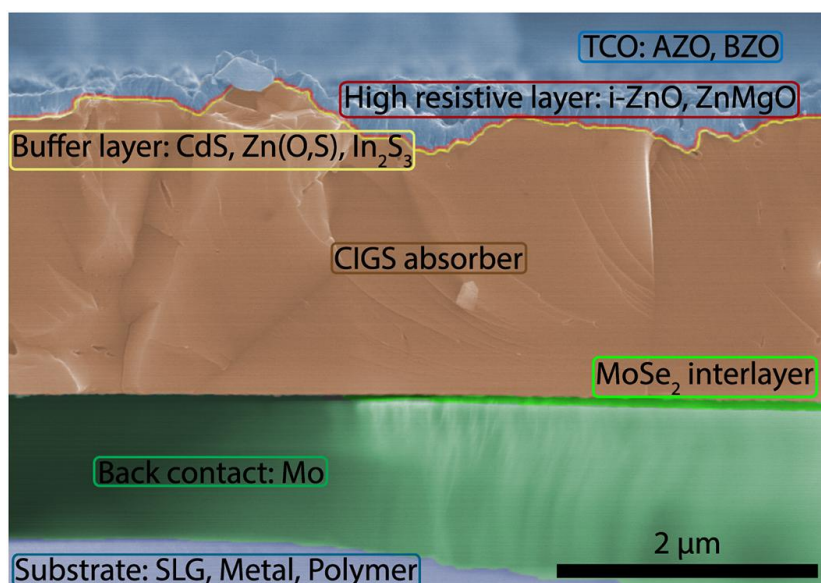


Figure I-12: Basic structure of a typical CIGS solar cell, with examples of the most commonly used materials.¹⁴²

The development history of CIGS solar cells can date back to the 1960s and 1970s, during that period the electrical, optical and structural properties of the semiconducting ternary chalcopyrites based on $(\text{Cu, Ag})(\text{Al, Ga, In})(\text{S, Se, Te})_2$ were firstly reported in the 1960s and 1970s.¹⁴⁷⁻¹⁴⁹ The first $\text{CuInSe}_2/\text{CdS}$ p-n heterojunction photovoltaic detectors by evaporating n-type CdS onto a single crystal of p-type CuInSe_2 which displayed uniform quantum efficiencies between 0.55 and 1.25 μm were reported by S. Wagner *et al.* in 1974 and at the same time the first solar device based on a single CuInSe_2 crystal was reported by them with a power conversion efficiency of 5%.¹⁵⁰ Subsequently, J. L. Shay and S. Wagner carried on this research through optimizing the device for application as a photovoltaic solar cell with an active area of 0.79 mm^2 and the solar intensity of 92 $\text{mW}\cdot\text{cm}^{-2}$ and finally obtained a better power conversion efficiency of 12%.¹⁵¹ In 1976, L. L. Kazmerski from university of Maine reported thin-film $\text{CuInSe}_2/\text{CdS}$ heterojunction solar cells with the efficiency of 4%~5% for the first time which opened the door to Copper indium diselenide (CIS) thin film solar cells. The CIS thin film was prepared by a two-source ($\text{CuInSe}_2 + \text{Se}$) co-evaporation technique in order to control carrier type. The p- CuInSe_2 film (5~6 μm) was subsequently grown on a Au-metallized glass substrate and then the CdS film (approximately 6 μm) was evaporated as window layer to form the heterojunction.¹⁵² However, there was limited interest in CIGS thin film solar cells because of underestimated significance of this p-n junction devices to photovoltaic field,^{153,154} until the first high-efficiency (9.4%) polycrystalline thin-film solar cell was reported in 1981 by R.A. Mickelsen of Boeing Aerospace Company.¹⁵⁵ One year later, R. A. Mickelsen, W. S. Chen and co-workers evaporated $\text{Cd}_{1-x}\text{Zn}_x\text{S}$ instead of CdS as a buffer

layer to attain the polycrystalline CIS thin-film solar cells with exceptionally high photocurrents ($>35 \text{ mA}\cdot\text{cm}^{-2}$), low open circuit voltages (about 400mV) and high quantum yields (>0.8) in the spectral range from 600 nm to 900 nm which reached the efficiency up to 10.6% in 1982¹⁵⁶, 10.98% in 1984¹⁵⁷ and 11.9% in 1986¹⁵⁸. After years of constant development, the emphasis of the CIS thin film turned into exploring the ways to increase the open circuit voltage while maintaining short circuit current. Through the use of wider energy band gap materials CuGaSe_2 (1.67 eV) and CuInS_2 (1.5 eV) compared to CuInSe_2 (1.04 eV), the band gaps of the absorbers can be widened and thus higher open circuit voltage can be achieved. By doping with Ga and S, the alloys $\text{Cu}(\text{In}, \text{Ga})\text{Se}_2$ and $\text{CuIn}(\text{S}, \text{Se})_2$ can be obtained which can also provide an optimal match to the solar spectrum resulting to an enhanced efficiency.¹⁵⁹⁻¹⁶¹ On the basis of this, a $\text{CdZnS}/\text{CuIn}_{0.73}\text{Ga}_{0.27}\text{Se}_2$ heterojunction cell, manufactured by Boeing Aerospace Company, was reported to achieve an efficiency of 12.9%. The significantly large open circuit voltage of the cell was 555 mV which was unattainable for non alloyed CIS solar cells.¹⁶²

Since 1990s, the CIS thin film solar cells has been rapidly developed. In 1993, L. Stolt *et al.* employed a quadrupole mass-spectrometer feedback system to make a CuInSe_2 thin film by co-evaporating elemental sources and then on the CuInSe_2 thin film covered a thin (10~20 nm) CdS buffer layer by a wet chemical dip process, which reached an active area efficiency of 14.8% with the cell structure n-ZnO/n-CdS/p-CuInSe₂ deposited on a soda-lime glass substrate. The achievement described the highest efficiency single junction thin-film cell reported to date at that time because the CdS layer deposited by chemical bath deposition improved the p-n junctions which finally resulted in reduced recombination rates, hence higher open circuit voltage (490 mV) and fill factor (71%).¹⁶³ In the same year, homogeneous bandgap (0.95 to 1.43 eV) and graded bandgap $\text{Cu}(\text{In}, \text{Ga})(\text{Se}, \text{S})_2$ (CIGSS) multinary absorber layers were fabricated by D. Tarrant and J. Ermer using a two-stage method. The thin film solar cell devices based on the structure of soda-lime glass/ Mo electrode/ graded bandgap CIGSS absorber/ CdS (50 nm) buffer layer/ ZnO window layer/ MgF_2 anti-reflection layer achieved the efficiency of 15.1% with an open circuit voltage of 728 mV. In this work, sulfur incorporation at grain boundaries or within the grains decreased the charge recombination and Ga incorporation forming an effective back surface field. The participation of sulfur and gallium, which both increased the band gap and improved the deposition, established the foundation for further improvement of CIGS solar cell efficiencies.¹⁶⁴ Among the CIGS thin film solar cell devices, the best-performing one had a CIGS absorber layer including 20~30% Ga with respect to $\text{In} + \text{Ga}$.^{159,165} The National Renewable Energy

Laboratory (NREL) was the world leader in the field of small-area CIGS thin film solar cell devices and reported record efficiencies increasing steadily over the years.¹⁶⁶⁻¹⁷⁰ The latest record efficiency of Cu(In, Ga)Se₂ solar cells by NREL was 23.3% at 14.7 suns optical concentration, whereas the devices yielded an efficiency of 20.8% under low flux optical concentration.¹⁷¹ The current world record for CIGS solar cell efficiency stands at 22.6% at 1 sun fabricated through a three-stage process reported by P. Jackson *et al.*. The alkali elements rubidium and cesium are used in this kind of CIGS solar cells in the place of sodium and potassium in the alkali post deposition treatment.¹⁷²

The development of CIGS photovoltaic modules can date from the year 2003, when the efficiency of small-area CIGS thin film solar cells has already overwhelm 23.3% under 15 suns.¹⁷³ There is no doubt that the transfer of the lab-scale processes into an industrial production encounters huge challenges which is obvious from the reported efficiency values. Even so, a number of companies such as Solar Frontier, AVANCIS, Solibro, Manz, Siemens Solar and others are pursuing commercial development of CuInSe₂ photovoltaic modules through employing a variety of process technologies and product design according to their perception of production costs and market demands.^{159,174-178} Moreover, flexible module manufacturing systems were fabricated through using polyimide or stainless steel as substrates reported by some companies with an efficiency above 20% achieved. The CIGS solar modules deposited on flexible substrates not only are advantageous for manufacturing (large area roll-to-roll deposition is possible) but also open up a new perspective for solar module design and application.^{142,179-183} Figure I-13 shows an example for the products based on module technology fabricated by Filsom AG.¹⁴² Anyhow, it will take more time to fully realize the technology transfer of lab-scale record high efficiency cells to average industrial production. In consideration of the great contribution in increasing the performance of industrial CIGS modules made by the significant and fast growing lab research results, the large-area, high-volume industrial CIGS modules with higher efficiencies will be attained in the near future. Furthermore, the large scale production of solar modules on flexible substrates creates a good chance to the development of novel applications such as building-integrated photovoltaics and concepts for solar electricity generation.

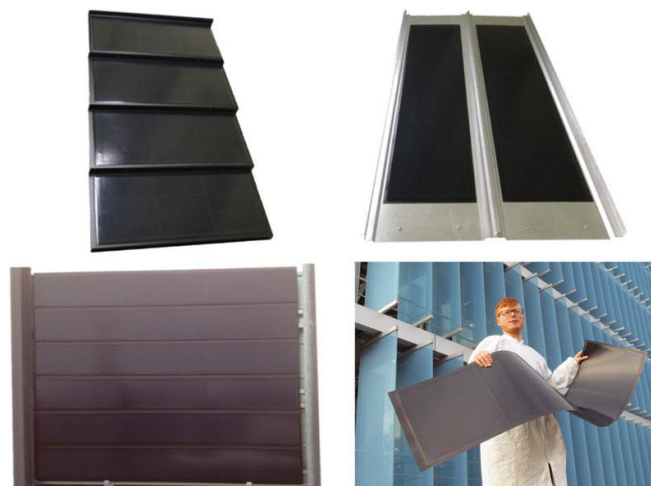


Figure I-13: Building-integrated photovoltaic product concepts based on flexible, lightweight monolithic CIGS solar modules on polyimide, from top left to bottom left: residential roof tile, architectural standing seam roof, and metal façade cladding elements. Bottom right: fully rollable module for application on rooftop membrane.¹⁴²

The development of CIGS thin film solar cells has expanded quickly over the past four decades and is now on the road to industrialization. Looking forward to the future, the conversion efficiencies of the CIGS solar cells will be further improved with in-depth research, new techniques and manufacturing technology. At the same time, material physics and device physics with respect to CIGS solar cells will have new progress in better performances.

I.2.3.5. Dye-Sensitized Solar Cells

The dye-sensitized solar cells (DSCs) are photoelectrochemical systems based on photo-sensitized semiconducting oxide anodes in contact with electrolytes and are low-cost solar cells belonging to the group of thin film solar cells.^{7,10} One major difference between conventional thin film cells and DSCs lies in the parts where the light is absorbed. In the thin film cells, the light is absorbed in the semiconductor layer while in DSCs light absorption is achieved by dye molecules grafted onto highly porous nanostructured metal oxide electrodes. Compared to traditional thin film solar cells, DSCs have different operating principles regarding charge separation and photoelectric conversion process. With regard to silicon based solar cells, for example, the silicon plays the role of the photoelectron source, as well as the donor of the electric field to separate the charges and produce the photocurrent, while in DSCs, the bulk of the semiconductor is used only for charge transport and the

separate photosensitive dye provides electrons to the semiconductor after light excitation. Therefore, charge separation takes place at the interfaces defined by the semiconductor, the dye and the electrolyte in DSCs. As a result of the unparalleled differential operational principles, DSCs can work even under low-light conditions by which it means DSCs are able to operate under cloudy skies and non-direct sunlight condition. By contrast, the traditional solar cells such as silicon based solar cells degrade at some lower limit of illumination and when charge carrier mobility is low, the recombination becomes a major issue for these classical thin film cells.^{69,184-188}

It is now established that DSCs are efficient photovoltaic devices that directly convert solar radiation into electric current. A schematic presentation of the operating principles of the DSCs is illustrated in Figure I-14.⁷

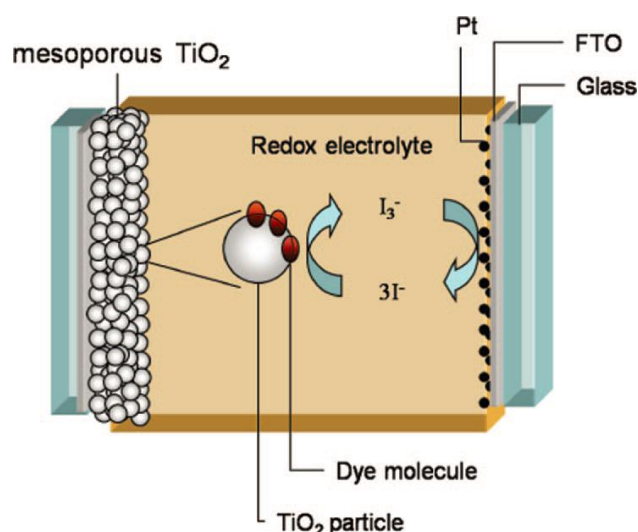


Figure I-14: Schematic diagram of the typical dye-sensitized solar cells.⁷

Dye-sensitized solar cells are made of three main contiguous components including a dye-sensitized nanocrystalline semiconductor-based mesoporous thin film, a platinized counter electrode and a redox electrolyte, which are sandwiched in between two conductive substrate materials. In detail, the typical system comprises the following parts:

1. The anode, which supports the dye-sensitized semiconducting oxide layer and helps in the electron transfer, is typically made by transparent conducting oxides (TCO).^{7,10,185-187} The TCO-coated glass is used as the substrate for the nanostructured metal oxide electrodes and hence is an imperative component. Theoretically, it should have high transparency and low sheet resistance which is less than $20\Omega/\square$. Moreover,

because of sintering of the electrode material (typically TiO_2), which is usually carried out between 450 and 500 °C, the sheet resistance should also be independent of temperature up to 500 °C. The two main types of conducting glass used as substrates are fluorine-doped tin oxide (FTO) and indium-doped tin oxide (ITO). Sometimes, it is difficult to choose a proper type due to the variety in cell configurations and materials.¹⁸⁹ High temperature processing during the device fabrication, in which a paste of TiO_2 is sintered at 400-600 °C, can degrade ITO properties because the exposure of ITO to temperature above 300°C in air usually increases its sheet resistance, whereas FTO is much more stable at 400-600 °C.^{69,189}

2. The nanostructured mesoporous oxide layer is deposited on the anode as electrodes to activate electronic conduction. The semiconductor electrode most commonly comprises nanocrystalline anatase TiO_2 layer. The TiO_2 thin film is deposited on the conducting glass with a thickness of 5-30 μm which plays an important part in both the exciton dissociation and the electron transfer process. The porosity and morphology of the TiO_2 layer have crucial influence on the amount of dye sensitizers adsorbed on its surface which can harvest incident light and further determine the conversion efficiencies of the solar cell devices, and hence are dominant factors. In order to adsorb a reasonable amount of the sunlight, the semiconductor layer needs to be made much thicker than the dye molecules themselves. To address this problem, a nanostructured material is used as a scaffold to hold large numbers of the dye molecules, increasing the number of molecules adsorbed on the surface of the TiO_2 layer.^{7,10} Some alternatives to TiO_2 have been reported such as ZnO , Nb_2O_5 , WO_3 , Ta_2O_5 , CdS , Fe_2O_3 , SnO_2 and so on. The more efficient semiconducting metal oxides reported so far are TiO_2 , ZnO , SnO_2 and Nb_2O_5 .^{47-49,69,190-198}
3. The monolayer of dyes which is covalently anchored to the surface of the nanostructured mesoporous oxide layer plays a very important role in the dye-sensitized solar cell devices. The dyes (photosensitizers or dye sensitizers) contribute to the primary steps of photon absorption and the subsequent electron injection.^{7,10,69,184-186} The historical context, molecular structures, classification, operational principles, recent progress and future outlook for the dyes are discussed in details in section II.2., III.2. and IV.2..
4. The electrolyte (or a hole-transporter for all-solid-state DSCs) includes redox mediator which is a ubiquitous and indispensable component of all DSCs. It plays an important role in the inner charge carrier transport between electrodes through

regenerating the dye during DSCs operation. Furthermore, the electrolyte has significant influence on the photovoltaic conversion efficiency, operational stability as well as long-term durability of dye-sensitized solar cell devices.^{15,188,199} Numbers of important parameters in DSCs can be relevantly affected by the electrolytes such as photocurrent density (J_{sc}), photovoltage (V_{oc}) and fill factor (FF).²⁰⁰ As a material that provides pure ionic conductivity between the electrodes in solar cell devices, the electrolyte must fulfill several essential requirements.^{15,188,201-203} Firstly, the electrolyte must ensure the charge carriers transport between the photoanode and the counter-electrode. Secondly, the electrolyte must have high conductivity and possess good interfacial contact with the dye-sensitized mesoporous layer and the counter-electrode. Thirdly, long-term stabilities such as chemical, thermal, optical, electrochemical, and interfacial stability are necessary. Last but not least, the absorption spectrum of the electrolyte should not cover the visible region. The electrolytes can be divided into liquid electrolytes, quasi-solid-state electrolytes and solid-state transport electrolytes. The most popular electrolyte is still the iodide/triiodide (I^-/I_3^-) redox couple in terms of solar cell device efficiency and device stability.^{7,10,15,188}

5. The cathode, also called counter-electrode, is made of a glass sheet treated with a catalyst to facilitate electron collection and electron transfer. The cathode employed in DSCs can directly affect the fill factor of the solar cell devices.^{7,10,69,186,200} Sputtered or calcined platinum (Pt) coated on a TCO substrate is popularly used as a cathode.²⁰⁴⁻²⁰⁸ Also, carbon materials²⁰⁹⁻²¹², polymer materials²¹³⁻²¹⁵ as well as other novel materials such as cobalt sulfide (CoS)²¹⁶ can be used as the cathodes instead of Pt.

As aforementioned in I.1, DSCs can be divided into n-type DSCs, p-type DSCs and tandem DSCs according to their operational principles. The historical contexts, the specific operational principles, recent progresses and future outlooks based on n-type DSCs and p-type DSCs are discussed in sections I.3. and I.4., respectively.

I.2.3.6. Perovskite Solar Cells

A promising new class of solar cells based on mixed organic-inorganic hybrid perovskite materials for converting solar energy into electrical energy have experienced unprecedentedly rapid emergence within less than a decade.^{52,217-229} The power conversion efficiencies of these solar cells are boosted from original 3.8%²³⁰ in 2009 up to 22.1%²³¹ (the highest power

conversion efficiency reported in a scientific article) in 2017, making them the fastest-advancing solar cells to date. The breakthrough solar cells fabricated based on perovskite materials are called perovskite solar cells (PSCs), which have revolutionized the third generation photovoltaic devices.

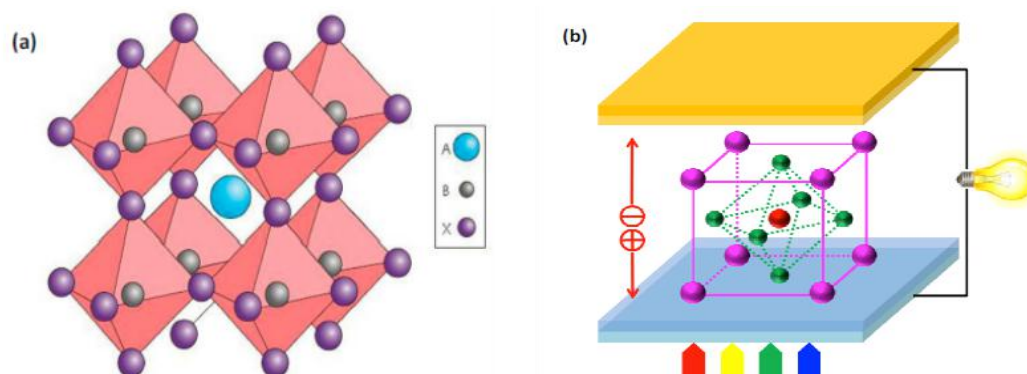


Figure I-15: (a) Crystal structure of cubic metal halide perovskite with generic chemical formula ABX_3 (A site: the large organic cations; B site: the small metal cations; and X site: halogen ions). (b) Organolead halide perovskite materials in PSCs.²²⁹

PSCs have emerged as a strong contender to conventional commercialized solar cells (Si or CdTe) in just a few years and have been in vogue in solar cell research attributable to the perovskite-structured organometal-halide materials. As shown in Figure I-15²²⁹, perovskite materials can be described by the formula ABX_3 , and typically one unit cell of ABX_3 include five atoms in a cubic structure, where cation B has six nearest neighbor anions X and cation A has twelve.²³² For the organic-inorganic hybrid halide perovskite materials, organic cations ($CH_3NH_3^+$, $HC(NH_2)_2^+$ *et al.*) occupy position A while metal cations (Pb^{2+} , Sn^{2+} *et al.*) and halogen ions (I^- , Br^- , Cl^-) occupy the B and X positions, respectively.²²² The crystallographic stability and correlative structure are deduced by a tolerance factor t . The relationship between the tolerance factor t and the ionic radii of A, B, X (R_A , R_B , R_X) should satisfy the following equation²³³:

$$t = (R_A + R_B) / \left\{ \sqrt{2} (R_B + R_X) \right\} \quad (2)$$

With respect to the high symmetry cubic structure under ideal conditions, the tolerance factor t should be close to 1. Otherwise, the perovskite material structures are pseudo-cubic because of distortion and the symmetry is degraded. For halide-structured perovskite materials, the tolerance factor t should be in the range of 0.81 through 1.11 and the defined octahedral factor μ (R_B/R_X) in the range of 0.44 through 0.90. At finite temperature, the cubic

structure is likely when t lies in the range of 0.89-1.0 while lower symmetry tetragonal or orthorhombic structures arise when $t < 0.89$. Despite these constraints, transitions between these different structures occur when heated and the cubic structure usually exists at high temperature. In particular, for the organic-inorganic halide perovskites, the position A is occupied by a larger organic cation²³⁴ which generally results in materials with good performance²³⁵⁻²³⁸.

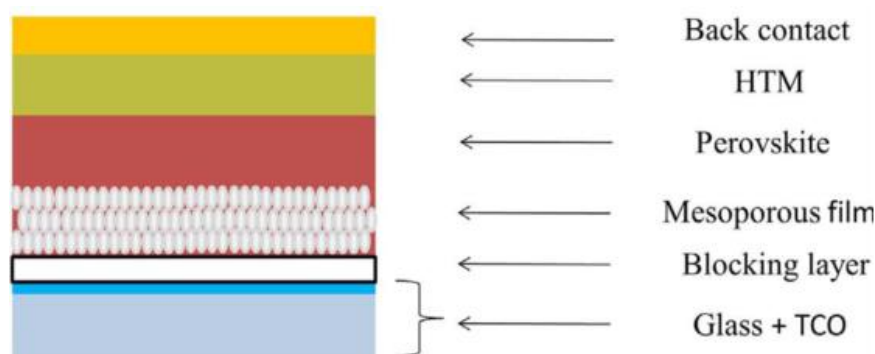


Figure I-16: The multilayer arrangement of a typical mesoporous perovskite solar cell.²²⁰

Fundamentally, similarly to typical DSCs, the most efficient PSCs present a configuration composed of five main thin layers as shown in Figure I-16²²⁰: 1) a TCO-coated glass substrate; 2) a compact layer which is also called blocking layer that forms a n-i junction selective to transfer electrons (typically compact TiO_2 layer); 3) a semiconducting mesoporous scaffold (most commonly TiO_2); 4) a perovskite material as a light absorber in the bulk of which most electron or hole transport occurs; 5) a hole transfer material; and 6) a conducting back contact. In the working process of PSCs, the perovskite material contributes to the primary steps of photoexcitation and charge separation. Under light illumination, the electron-hole pairs are created in the perovskite material. Then, the photogenerated electrons are injected into the mesoporous layer while the holes are driven into the hole transfer material. The injected electrons are further passed on to the back contact through the external circuit and at the same time the holes are transferred to the same back contact. Subsequently, the holes and the electrons recombine at the interface of the back contact and hole transfer layer which finally regenerates the system. For an effective charge extraction process, the band alignment of the perovskite material should satisfy the following requirements: 1) its conduction band must be higher than the conduction band edge of the electron transport layer and 2) its valence band must be lower than the valence band edge of the hole transport layer. However, some detrimental charge recombination can occur during the charge-transfer

process. Some photogenerated electrons can recombine with holes in the perovskite material layer and/or in the hole transfer material layer. What's more, the injected electrons may further recombine with the holes at the interface of electron transport layer/perovskite material layer and/or at the interface of electron transport layer/hole transfer material layer. Therefore, charge generation and extraction must operate on much faster timescales than charge recombination in order to get high performance PCSs.²³⁹⁻²⁴²

Research into halide perovskite materials can date back over a century²³², while present emergence of organic-inorganic halide PSCs benefit from the investigations of related thin film transistors and light-emitting diodes based on the electricity-to-light conversion ability of halide perovskites reported by the Mitzi's group.^{243,244} In 2006, Miyasaka *et al.* reported photovoltaic performances of perovskites for the first time by using organic-inorganic hybrid perovskite $\text{CH}_3\text{NH}_3\text{PbBr}_3$ as sensitizer in liquid DSCs with an efficiency of 2.2%.²⁴⁵ Three years later, in 2009, they increased the efficiency up to 3.8% by replacing $\text{CH}_3\text{NH}_3\text{PbBr}_3$ with $\text{CH}_3\text{NH}_3\text{PbI}_3$.²³⁰ However, the device life time was extremely short due to the instability of the hybrid perovskite in the presence of the liquid electrolyte. Subsequently, Park *et al.* employed $\text{CH}_3\text{NH}_3\text{PbI}_3$ perovskite nanoparticles to fabricate a cell architecture which is similar to the extremely thin absorber DSCs and by using TiO_2 treatments they achieved an efficiency of 6.5% in 2011.²⁴⁶ In 2012, by replacing the problematic liquid-based electrolytes with a solid-state hole transport material, *i.e.* spiro-OMeTAD, the efficiency of PSCs was boosted to 9.7%.²⁴⁷ By using a similar cell architecture based on mesoscopic structure, Snaith *et al.* also achieved an efficiency of 7.6%, and they further increased the reported efficiency up to 10.9% by replacing conducting nanoporous TiO_2 with non-conducting Al_2O_3 .²⁴⁸ After this work, a theory of hypothesis was put forward: the perovskite materials themselves may play a role in electrons and holes transfer. Based on this, Snaith *et al.* further fabricated efficient planar heterojunction PSCs based on $\text{CH}_3\text{NH}_3\text{PbI}_{3-x}\text{Cl}_x$ by two-source thermal evaporation and achieved an efficiency of 15.4%.²⁴⁹ By using a poly-triarylamine hole transport material and a mixed-halide perovskite material $\text{CH}_3\text{NH}_3\text{PbI}_{3-x}\text{Br}_x$, an efficiency of 16.2% was achieved by Seok's group at the end of 2013. This efficiency was increased to 17.9% by optimization.²²² The power conversion efficiency has been further improved to 19.3% in 2014 by Zhou *et al.* by adjusting the band alignment of hole transport materials to perovskite layer.²⁵⁰ In 2015, W. S. Yang *et al.* reported an approach for depositing high-quality formamidinium lead iodide perovskites films and fabricated PSCs with maximum power conversion efficiency of 20.1%.²⁵¹ Most recently, S. S. Shin *et al.* explored the superoxide colloidal solution route and prepared an lanthanum-doped BaSnO_3 electrode below 300°C. Based on this kind of electrode

and methylammonium lead iodide, an efficiency of 21.2% was achieved. This kind of PSCs retained 93% of their efficiencies after 1000h of full sun illumination.²⁵² Furthermore one of the highest power conversion efficiency reported in a scientific article comes from Prof. M. Grätzel's group. They introduced an approach to prepare perovskite thin films by using poly(methyl methacrylate) (PMMA) as a template for $(\text{HC}(\text{NH}_2)_2\text{I})_{0.81}(\text{PbI}_2)_{0.85}(\text{CH}_3\text{NH}_3\text{PbBr}_3)_{0.15}$ perovskite material to control nucleation and crystal growth and finally obtained stable PSCs which had excellent reproducibility with a power conversion efficiency up to 21.6% and a certified power conversion efficiency of 21.02% under AM 1.5G.²⁵³ More recently, Seok *et al.* reported an efficiency over 22% with PSCs containing the defect-engineered thin perovskite layers.²³¹

So far, various outstanding perovskite materials based on the formula $\text{CH}_3\text{NH}_3\text{PbX}_3/\text{HC}(\text{NH}_2)_2\text{PbX}_3$ ($X = \text{Cl}, \text{Br}, \text{I}$) have been prepared and studied. These perovskite materials have uplifted mobilities, diffusion lengths of electrons and holes, lower surface recombination rates and favorable grain boundary effects. These perovskite materials also have high optical absorptivity, excellent structural defect tolerance and electrically clear defect characteristics.^{254,255} What's more, these perovskite materials are promising for flexible devices.²¹⁷ PSCs as a rising star in the third generation photovoltaics, have attracted much attention from both academic and industrial fields, indicating a great possibility of mass production and commercialization in the near future. However, the stability of PSCs in moist environments, the interplay between the organic and inorganic components, the fundamental reasons for alloy stabilization of the structures and the replacement of toxic Pb atoms by environment-friendly components are still crucial challenges that require further developments.

I.3. TiO₂-Based n-Type Dye-Sensitized Solar Cells

The third generation solar cells conquer the limits of single junction devices and display high efficiency compared to the same production costs of the first and second generation solar cells which effectively drive down the US\$/W.²⁵⁶ Dye-sensitized solar cells can be identified as a technology between the second and third generation solar cells,⁸ and thus have been extensively studied since the pioneering work being reported by O'Regan and Grätzel in 1991.¹⁹ Owing to their low fabrication cost, variety of colors, large-scale manufacturing processes, environmental friendliness, earth-abundant materials and relatively high power conversion efficiency, the DSCs can fulfill all of the desired properties of conventional silicon based solar cells.^{7-15,185-188,199,200} Over the last few decades, TiO₂-based n-type DSCs have

attracted considerable attention and a substantial amount of experiments have been carried out to improve the device efficiency from 7.1% in 1991¹⁹ to 14.3% in 2015.²⁵⁷ In this section, n-type DSCs based on nanostructured mesoporous TiO₂ layer and the iodide/triiodide (I⁻/I₃⁻) redox couple are introduced.

I.3.1. Historical Background

Sensitization achieved by adsorption of dye molecules at semiconductor surface has become a research hot-spot since 1949, which can be attributed to the successful experiments described by Putzeiko and Terenin. They found the Dember effect (photocurrent response) of ZnO powder in the visible light region when xanthene and cyanine dyes were adsorbed on ZnO surface.²⁵⁸ In 1968, Gerischer *et al.* presented their experiments and a theoretical model rationalizing the photocurrent observed for electrodes of n-type zinc oxide and p-type perylene. They further put forward that the formation of associates of dye molecules at the semiconductor surface had an adverse effect on the photochemical activity of the dye. These promising work indicated that the photocurrent was created by dye-sensitized semiconductors under certain conditions according to charge transfer between organic dyes and semiconductors, which finally fetched up an important foundation of the photoelectrochemical cells.²⁵⁹ In 1972, A. Fujishima and K. Honda constructed an electrochemical cell to fulfill the hydrogen generation in which an electrode based on TiO₂ was connected with a platinum black electrode through the external circuit.²⁶⁰ From then on, TiO₂ was widely recognized as a crucial semiconductor material in the fields of photovoltaic solar cells. However, in preliminary research, the dye-sensitized photoelectrochemical cell devices were fabricated based on smooth semiconductor surfaces resulting in a rather low light-harvesting ability. The main reason is that a monolayer of the photosensitizer can absorb even less than 1% of the AM 1.5G spectrum.^{7,12,259} As to this background, before 1991 some researches were focused on the possibilities to increase the roughness of the semiconductor surface in order to increase the number of dye molecules adsorbed on the surface and in contact with a redox electrolyte. In 1977, M. Matsumura *et al.* studied the photocurrent generated by a dye-sensitized electrochemical system (zinc oxide / aq solution / platinum). In their experiments ZnO sintered disks sensitized with Rose Bengal and Rhodamine B dyes were used as electrodes. The results revealed that the photocurrent was caused by the dye adsorbed on the electrode and the Rose Bengal dye gave rise to a photoconversion quantum yield of 22% at maximum absorption wavelength.²⁶¹ In 1980 Alonson *et al.* also reported ceramics of ZnO obtained from commercial high grade zinc oxide powder by sintering in two

steps as semiconducting ZnO ceramic electrodes which were then sensitized with Rhodamine B and Ru(II) complex dyes. The I-V characteristics of a doubly sensitized (Rhodamine B and Ru(II) complex) cell under a broad (400-800nm) visible light displayed an open circuit voltage of 0.4 V and short-circuit photocurrents of 0.2 mA.²⁶² To improve the previous poor light energy harvesting as well as small quantum yields for charge injection, in 1985, M. Grätzel, J. Augustynski *et al.* employed Ru(II) complex dye-sensitized colloidal anatase particles and polycrystalline anatase electrodes with high surface area to achieve an incident photon-to-current conversion efficiency (IPCE) of 44% at λ_{\max} , which was unprecedented at that time.²⁶³ After almost a half-century of development, the photosensitization of wide band gap nanocrystalline semiconductors by adsorbed molecular dyes for solar cell applications still seemed impossible within the foreseeable future until a breakthrough in 1991,¹⁹ at which time O'Regan and Grätzel reported their pioneering work on this promising application by using nano-sized TiO₂ porous film electrodes. A photovoltaic cell was described in their seminal paper based on a 10 μ m-thick, optically nano-sized transparent TiO₂ layer, absorbed with a monolayer of a charge-transfer dye for light harvesting resulting in exceptionally more than 80% efficiencies for the conversion of incident photons to electrical current and an overall energy conversion yield of 7.1-7.9% under simulated sunlight. Since then, DSCs have entered public view and garnered ever-increasing research attention over the following decades, with efficiencies over 14% at the lab scale.²⁵⁷ Also, TiO₂ was commonly deployed as the semiconductor of choice because of its various advantages for sensitized photo-chemistry and photo-electrochemistry (low-cost, broadly available, non-toxic, biocompatible, etc...) and great progress was incremental in a synergy of structure, substrate roughness and morphology, dye photophysics as well as electrolyte redox chemistry.^{46-49,106,185-187,264,265}

I.3.2. Operational Principles and Electron Transfer Processes of n-Type Dye-Sensitized Solar Cells

A scheme of typical liquid-state DSCs showing their basic configuration has been mentioned above (I.2.3.5., Figure I-14). In 1993, cis - X₂bis(2,2' - bipyridyl - 4,4' - dicarboxylate) ruthenium(II) complexes were prepared and characterized in regard to their absorption, luminescence, and redox behavior by M. Grätzel *et al.*, where X = Cl⁻, Br⁻, I⁻, CN⁻ and SCN⁻. Among them, cis - di (thiocyanato) bis (2,2' - bipyridyl - 4,4' - dicarboxylate) ruthenium(II), coded as N3, exhibited the more promising properties including broad visible absorption spectrum, commendable photon-to-current conversion efficiency (IPCE),

remarkable long excited state lifetime, strong adsorption on the semiconductor surface and superior solar-to-electric energy conversion efficiency when employed in DSCs. Because of its excellent properties, the classical N3 dye is commonly used as a reference and yielded record efficiencies.^{7,200,266,267} On the other hand, as referred above (I.2.3.5.), the iodide/triiodide (I^-/I_3^-) redox couple is the most popular electrolyte because of different advantageous features such as easy preparation process, high conductivity, low viscosity and excellent interfacial wetting between the sensitized electrode and itself.¹⁵ The basic electron transfer processes and various potentials in a DSC device based on the N3 dye attached to the surface of the nanocrystalline TiO_2 semiconductor and the iodide/triiodide (I^-/I_3^-) redox couple in the electrolyte are depicted in Figure I-17.

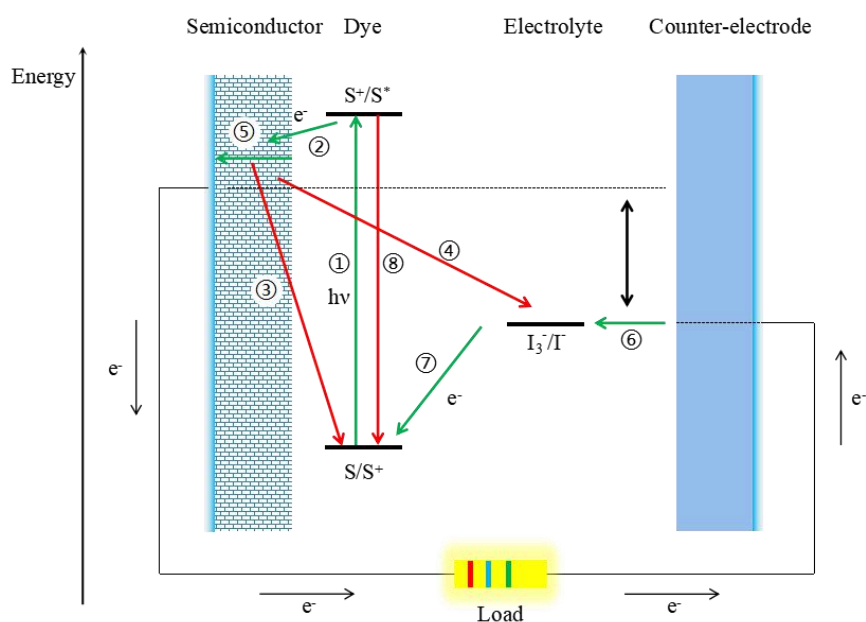


Figure I-17: Basic electron transfer processes and potentials in a DSC device. The basic electron transfer processes are denoted by numbers 1 to 8 and the potentials indicated correspond to the iodide/triiodide (I^-/I_3^-) redox couple, the HOMO/LUMO of N3 dye and the TiO_2 conduction band edge. Loss pathways are represented by red arrows. (Adapted from reference 7)

When exposed to the sunlight, the dyes on the surface of TiO_2 semiconductor film get excited. The electrons from photoexcited dyes are injected into the conduction band of TiO_2 , leaving the dyes in their oxidized state, and then flow through the mesoporous TiO_2 thin film to the transparent conducting oxide (TCO) substrate. Finally, these generated electrons diffuse via electron migration through an external load to the counter-electrode in contact with the electrolyte containing the redox mediator I^-/I_3^- , while the oxidized dyes are regenerated to

their ground state by the electrons diffused from the electrolyte to complete the cycle.^{7,10,13,185,186,268,269} In the process, the regeneration of the dye by iodide (I⁻) intercepts the adverse recapture of the conduction band electrons directly by the oxidized dye and the electron flow lies on the incident intensity and trapping-detrapping effect.^{7,185,270,271} The basic electron transfer processes can be represented with the following equations:^{7,9,185,272,273}

- i. Under illumination, the dye is photoexcited, resulting in the transition of the sensitizer from the ground state (S) to the excited state (S^{*}). (Figure I-17, Process 1)



- ii. Electron injection occurs from the excited dye (S^{*}) to the conduction band (CB) of TiO₂, leaving the dye in its oxidized state (S⁺). (Figure I-17, Process 2)



- iii. The oxidized state (S⁺) is unfavourably regenerated by the conduction band electrons (e⁻(CB)). (Figure I-17, Process 3)



- iv. The adverse electrons transfer to I₃⁻ from the conduction band (CB) of TiO₂. (Figure I-17, Process 4)



- v. The conduction band electrons (e⁻(CB)) diffuse through the mesoporous TiO₂ thin film to the transparent conducting oxide (bc: back contact), and then migrate to the external load. (Figure I-17, Process 5)



- vi. I₃⁻ ions diffuse to the counter electrode at which electrons transfer to reduce I₃⁻ ions to I⁻ ions. (Figure I-17, Process 6)



- vii. The oxidized dye (S⁺) is regenerated and the I₃⁻ ions form by oxidation of I⁻ ions. (Figure I-17, Process 7)



- viii. The adverse excited state (S^{*}) decay occurs resulting in the dye to the ground state (S). (Figure I-17, Process 8)



As mentioned above, the loss pathways of the electron transfer processes (3, 4 and 8) are indicated and must be minimized compared to the desired pathways of processes (1, 2, 5, 6 and 7). Process 8 represents the adverse recombination of the excited dye which can be characterized by the excited state lifetime while process 3 and process 4 represent the

recombination of the conduction band electrons with either the oxidized dye or I_3^- in the electrolyte, respectively.^{7,9,185,272,273} Actually, there is an alternative possibility not mentioned above that electron transfer to I_3^- can occur at the photoanode contact (transparent conducting oxides (TCO)) which borders on the electrolyte. However, this adverse electron transfer process can be prevented by using a compact TiO_2 blocking layer deposited on the photoanode. Also, some other semiconductors and insulating materials such as Nb_2O_5 , ZnO , WO_3 , $CaCO_3$, $BaCO_3$ and SnO_2 can be used as blocking layers which can effectively suppress the back reaction of photoinjected electrons with I_3^- ions in the electrolyte.^{7,10,190-198,274-277}

I.3.3. Energetics of Operational Principles

In general, charge separation in n-type DSCs can be considered as a two-step redox reaction including the electron injection into the TiO_2 semiconductor and the subsequent oxidation of the redox electrolyte respectively, while the latter reaction results in the dye sensitizers from the oxidized state to the ground state which is referred in I.3.2.. Also, the thermodynamically downhill for both electron injection and dye regeneration is schematized in Figure I-17. After charge separation processes, the transport processes of the photogenerated charges to both photoanode and counter-electrode are of great importance for charge collection processes which are primarily driven by diffusion processes because of concentration gradients. For an efficient n-type DSC device under optimum conditions (good TiO_2 nanoparticle interconnections and low-viscosity electrolyte in the presence of the redox mediator I/I_3^-), the modest concentration gradients can efficiently drive the charge transport processes of both photogenerated electrons toward the photoanode and redox ions toward the counter electrode, and therefore result in small free energy losses.^{7,9,272,273} Electron transfer to reduce I_3^- to I^- can occur by using an efficient catalyst at the counter electrode to enable the process to proceed with minimal overpotential. Analogously, the photogenerated electron diffusion toward the photoanode can occur through an excellent contact at the interface between TiO_2 and TCO. Hence, the positions of the energy levels, in other words the energetics, at the interfaces of both TiO_2 /dye and dye/electrolyte fundamentally enable to determine the overall device output. The standard measurements of the positions of the energy levels can be found in the refs 278 and 279.

Figure I-18 can be used to interpret and analyze the typical values for the interfacial energetic situation in DSCs. These values can be derived from the measurements of the individual components and the ordinate may represent the internal energy, that is to say, the conduction band energy is one-electron energy rather than a free energy. The meaningful

configurational entropy of charge carriers caused by the number of accessible energy states can be totally different in the different phases.⁷ The energy levels of the sensitizer are usually introduced in the form of HOMO/LUMO levels in some publications.^{204,280-283} For the solid-state physics, the energy scale with vacuum can be used as reference, while for solid-state electrochemistry, the potential scale with the standard hydrogen electrode (SHE) or normal hydrogen electrode (NHE) can be used as reference.^{7,9,272,273,278,279} In TiO₂ semiconductor, the electrochemical potential of electrons corresponds to the energy at the Fermi level (E_F), while in an electrolyte solution the electrochemical potential of electrons corresponds to the redox potential (U_{redox}). On the one hand, the efficient charge separation and collection by the photoanode and the counter electrode can determine the power output of DSCs and result in a photocurrent. On the other hand, the generation of the photovoltage can also determine the power output of DSCs which corresponds to the free energy difference between the photoanode and the counter electrode. At equilibrium, the electrochemical potential of the TiO₂ semiconductor (or the Fermi energy of the TiO₂ semiconductor) is equivalent to the midpoint potential of the redox couple, which finally results in zero output voltage. In the circumstances, the Fermi level of the TiO₂ semiconductor mainly lies in the band gap of the TiO₂ semiconductor, while the TiO₂ film is effectually insulating which means almost a negligible electron density in the TiO₂ conduction band. As known, the photoexcitation leads to the electron injection into the conduction band of TiO₂ and subsequent the oxidation of the redox electrolyte. On this occasion, the oxidized and reduced species are highly concentrated in the electrolyte, and thus the electrolyte photooxidation process will not give rise to a significant change in the potential of the electrolyte. By comparison, the process of electron injection into the TiO₂ conduction band can give rise to a dramatic increase of the electron density, which in turn can raise the TiO₂ Fermi level to the edge of the conduction band. Furthermore, such shift of the TiO₂ Fermi level signifies a significant increase in the stored free energy of the injected electrons which also plays a role in the photovoltage generation process in the external electrical circuit.^{7,273,278-283} The midpoint potential of the redox couple can be described by Nernst equation²⁷³, which hinges on the relative concentrations of iodide and iodine. An efficient n-type DSC device requires high concentrations of iodide and iodine. However, the kinetics of the dye regeneration process at the photoanode and the iodide regeneration process at the counter electrode inversely constrains the concentrations of iodide and iodine.²⁸⁴⁻²⁸⁹ Typically, the concentrations of iodide and iodine are in the range of 0.1-0.7 M and 10-200 mM, respectively, which as mentioned above, constrains the midpoint potential of the electrolyte to approximately 0.3V

versus NHE.^{273,290,291} Additionally it is worthwhile to mention that the iodine is primarily present in the form of I_3^- due to the presence of an excess of iodide, which results in the electrolyte usually being referred to as the iodide/triiodide (I^-/I_3^-) redox couple.^{15,272,273,292-295} Although the difference of an electron versus the NHE potential in vacuum is unmeasurable with thermodynamic rigor^{7,296}, an estimated equation reported by R. Memming gives the relationship in any redox couple between the Fermi level ($E_{F,redox}$) and the redox potential (U_{redox}) as follows²⁹⁷:

$$E_{F,redox} [\text{eV}] = - (4.6 \pm 0.1) - eU_{redox} [\text{V}] \quad (11)$$

The e in the equation refers to the elementary charge, with which the standard potentials of the other redox couples are able to be represented on the absolute scale.

I.3.4. Kinetics of Operational Principles

A schematic state diagram representing the kinetics of DSCs operating principle is illustrated in Figure I-18²⁷³ which gives the sequence of electron transfer processes, while the more detailed kinetic data for the diverse electron transfer processes corresponding to the processes 1 to 8 (see Figure I-17) taking place at the TiO_2 /dye/electrolyte interface for the state-of-the-art DSCs are shown in Figure I-19⁷. Figure I-18 illustrates not only the forward processes of light absorption, electron injection, dye regeneration and charge transport but also the unfavorable loss pathways (processes 3, 4 and 8; see Figure I-17). As referred in I.3.2., the unfavorable loss pathways comprise decay of the sensitizer excited state to ground, and charge recombination of injected in the TiO_2 with either oxidized dye or the redox couples in the electrolyte. The kinetic data in Figure I-19 have also been summarized in a number of publications and references therein.^{7,9,10,185,204,267,273,298,299} These charge transfer processes lead to an enhanced spatial separation of the electrons and the holes and thus increase the lifetime of the charge-separated state along with the reduction of the free energy stored in the state. This mechanism is quite similar to the function of the photosynthetic reaction centers. For the natural photosynthesis, the quantum efficiencies of charge separation and collection result from the competitions between the different forward processes and the loss pathways, which are therefore considered as key factors determining energy conversion efficiency.^{7,55,273,300-305}

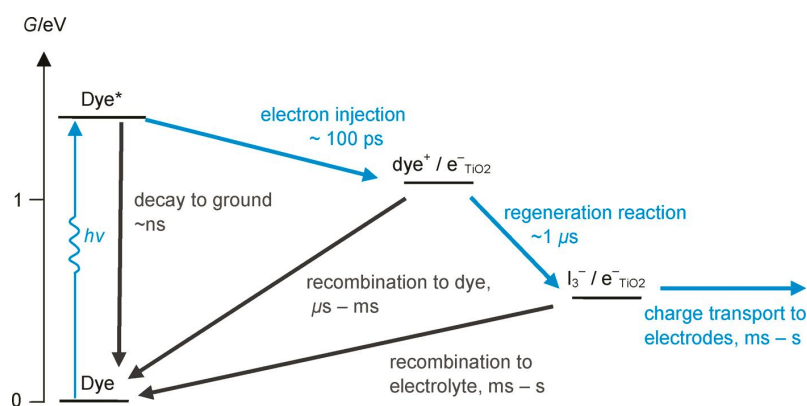


Figure I-18: State diagram representation of the kinetics of DSCs function. Blue arrows represent the forward processes of light absorption, electron injection, dye regeneration and charge transport. Gray arrows represent the unfavorable loss pathways. The ordinate corresponds to the free energy stored in the charge separated states. The free energy of injected electrons depends on the Fermi level of the TiO_2 , assuming that the TiO_2 Fermi level is 0.6 V above the chemical potential of the redox electrolyte.²⁷³

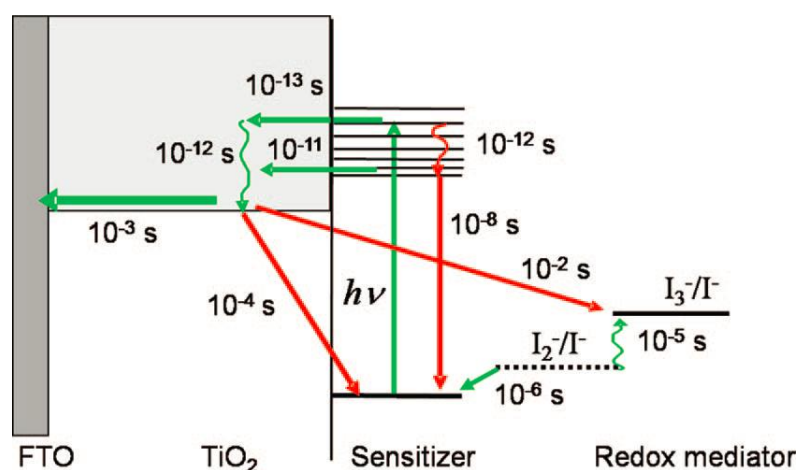


Figure I-19: Overview of processes and typical time constants under 1 sun simulated irradiation in DSCs based on Ru complex dye with iodide/triiodide electrolyte. Loss pathways are represented by red arrows.⁷

It is worthy to note that the electron injection efficiency in DSCs hinges on the magnitude of the injection kinetics relative to the excited-state decay to the ground-state, rather than the absolute kinetics of the electron injection. The excited state lifetimes of the sensitizers substantially differ from picoseconds to nanoseconds, which thus require on the different kinetics of the electron injection resulting in efficient device function.^{273,306-309} Another point to consider is that the potential for electron injection comes not only from dye

singlet but also triplet excited states. The triplet states are long-live and can be ascribed to intersystem crossing from the singlet excited state. However, the triplet states are less energetic than the relative singlet state. For example, the intersystem crossing from the singlet to triplet state based on ruthenium bipyridine coordination dyes can be as fast as $1 \times 10^{13} \text{ s}^{-1}$.³⁰⁹⁻³¹² Generally, depending on the solvent/electrolyte environments, the singlet state lifetimes are in the range of 1×10^{-13} to 1×10^{-9} s, while the triplet state lifetimes are in the range of nanoseconds to milliseconds.^{7,273,312,313} As discussed above, the efficiency of electron injection is dependent not only on the rate of electron injection but also on the kinetics of the excited-state decay.

The rate of electron injection from the dye excited state into the mesoporous TiO_2 semiconductor depends both on the electronic coupling between the dye LUMO orbital and accepting states of TiO_2 , and on the large density of states (DOS) in the TiO_2 energetically accessible from the dye excited state.^{7,314,315} After the electron injection process, the injected electrons play a role in fast thermal relaxation down to the electron Fermi level of the electrode. The thermalization process contributes to an adverse loss in free energy, which results in a limitation on the efficiencies of DSCs.^{7,203,273} As referred, the electron injection kinetics depends on the energy of TiO_2 conduction band compared to the dye excited-state oxidation potential. The electron injection kinetics also depends on the concentrations of the oxidized and reduced species in the electrolyte. Particularly, the presence of acidic ions can lead to a high metal oxide energy conduction band and thus a lower density of accessible acceptor states. The consequent low density of accessible acceptor states eventually results in a slow rate of electron injection, a low quantum yield of charge injection and a low device photocurrent.³¹⁶⁻³¹⁹

In order to obtain efficient dye regeneration, the rate of reduction of the oxidized dye cations by the redox couple must exceed that of charge recombination of the injected electrons with the oxidized dye cations. The dye regeneration process strongly depends on the iodide concentration in the electrolyte, the viscosity of the electrolyte and the dye structure. Employing the best-performing Ru-complexes and a low viscosity electrolyte such as I^-/I_3^- dissolved in acetonitrile, the regeneration process is sufficiently fast to compete with the recombination process which thereby guarantee the regeneration process can be attained with unity quantum efficiency.^{273,299,320} The recombination process is strongly dependent on the Fermi level of the TiO_2 film and thus on the light intensity and solar cell voltage, accelerating by an order of magnitude between short circuit and circuit conditions.³¹⁵ Furthermore, the recombination process depends on the spatial separation of the dye cation from the electrode

surface, with the rate constant decaying exponentially with the approximate distance of the excited state HOMO from the TiO₂ surface according to the electron-tunneling theory.²⁸⁰

In order to obtain efficient charge collection by the external circuit, the rate of the electron transport to the counter electrode must exceed the rate of charge recombination of injected electrons with the redox couple in the electrolyte. The electron trapping in localized sub-bandgap states plays a key role in the diffusive electron transport process. Therefore, the kinetics strongly hinges on the position of the TiO₂ electron Fermi level, that is, the higher Fermi level toward the conduction band edge the more trap filling.^{273,321,322}

There are coupled relationships between the charge separation and collection kinetics and the energetic losses involved in the basic electron transfer processes in DSCs. The energetic losses can cause the device output voltage being remarkably less than its optical bandgap, which thereby results in the maximized device output voltage being in the range of 0.6 to 0.75 V, less than half absorption onset of the typical dye sensitizers.^{7,273} The balance between the kinetics and the energetics have been reported in a number of publications^{7,55,273,301,319,323-327} which will not be considered further in this manuscript.

I.3.5. Characterization Techniques

Characterization techniques are essential to investigate internal processes of complete solar cell devices under normal solar light conditions. These techniques are also useful to measure and assist in the development of theoretical models accounting for the various electron transfer and transport processes, explore the stability and reproducibility of the solar cell devices and optimize their manufacturing based on different material components. Some efficiency measurements and electrochemical methods are reviewed in the following sections.

I.3.5.1. Efficiency Measurements

The current density-voltage (J-V) characteristics of DSCs are the most widespread method used to determine the power conversion efficiency (η) of DSCs.^{7,9-11,185-187} Because of high interfacial capacity, DSCs usually have a relatively slow electrical response. Therefore, the voltage scan should be at a slow speed to avoid errors happening in the current measurement. On the contrary, the currents from a rapid forward and reverse voltage scan can be at average speed.³²⁸ Figure I-20 illustrates a typical J-V curve, where J_{sc} , V_{oc} and P_{max} are indicated.

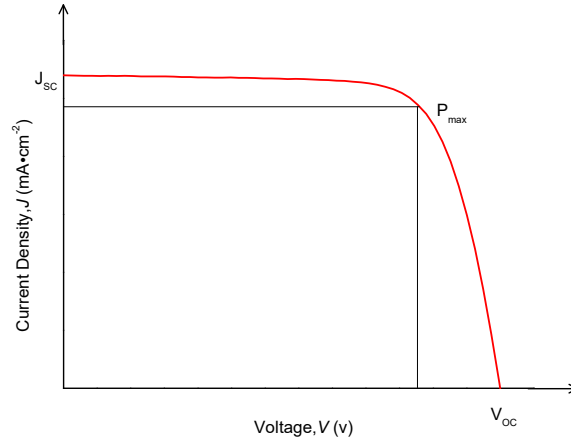


Figure I-20: A typical J-V curve.

From the J-V curve, the overall power conversion efficiency is given by¹⁰

$$\eta = \frac{|JV|_{\max}}{P_{in}} = \frac{J_{sc}V_{oc}FF}{P_{in}} \quad (12)$$

where P_{in} represents the power density of the incident light and FF represents the fill factor. Graphically, FF represents the shape of the J-V curve, also known as the “square-ness” of the solar cells, and its value is comprised between 0 and 1. A high value of FF reveals a more favorable rectangular shape. The short circuit current density J_{sc} , which corresponds to the highest photocurrent generated by the solar cell divided by the area illuminated, is determined at the $V=0$ intercept. The open-circuit potential V_{oc} is determined at the $J=0$ intercept.^{7,9,11,328}

The FF is given by the equation^{7,9,11,200}

$$FF = \frac{P_{\max}}{J_{sc}V_{oc}} \quad (13)$$

where P_{\max} represents the maximum power of the solar cell per unit area. Besides the two other parameters (V_{oc} and J_{sc}) the FF is another significant parameter which can reflect the quality of DSCs. A higher value of FF can be achieved by increasing the shunt resistance, decreasing the series resistance and reducing the overvoltage for diffusion and electron transfer processes.²⁶⁹

Another fundamental method used to measure the performance of a solar cell is the “external quantum efficiency (EQE)” which is usually called the incident photon-to-current conversion efficiency (IPCE). The value of IPCE is relative to the J_{sc} produced in the external circuit divided by the photon flux that strikes the solar cell. The IPCE as a function of wavelength can be calculated by^{7,10,11,15,200}

$$IPCE = \frac{J_{sc}(\lambda)}{e\Phi(\lambda)} = 1240 \frac{J_{sc}(\lambda)[Acm^{-2}]}{\lambda[nm]P_{in}(\lambda)[Wcm^{-2}]} \quad (14)$$

where e represents the elementary charge. The values of IPCE provide information about the monochromatic quantum efficiencies of a solar cell device.^{7,200}

With a view to the bandgap energy, the maximum voltage generated under illumination is dependent upon the difference between the quasi Fermi level of the TiO₂ film and the electrolyte redox potential. The V_{oc} value is dependent on the iodide concentration due to the recombination reaction occurring between the electrons on the conduction band of TiO₂ and I₃⁻ and thus can be given by^{10,331,332}

$$V_{oc} = \frac{kT}{q} \ln\left(\frac{\eta\Phi_0}{n_0 k_{et} [I_3^-]}\right) \quad (15)$$

where η represents the quantum yield of photogenerated electron for the given incident photon flux (Φ_0) and n_0 represents the electron density on the conduction band of TiO₂ in the dark. The k_{et} in equation (15) corresponds to the recombination reaction rate for a given I₃⁻ concentration. Higher V_{oc} can be achieved through using Co(II/III) redox couple which has more positive redox potential and thus increases the potential difference.^{10,269,331,332}

Similarly, the precise value of J_{sc} can be determined by integrating IPCE and the Φ_0 over the spectral distribution which is given by^{10,331,332}

$$J_{sc} = e \int IPCE(\lambda) \Phi_0(\lambda) (1 - r(\lambda)) d\lambda \quad (16)$$

where $r(\lambda)$ represents the incident light loss and e represents the elementary charge. According to equation (16), a good approach to improve J_{sc} is to increase the value of IPCE, which can be realized through using panchromatic dyes that can absorb broad sunlight covering visible to the near-infrared range in solar spectrum.^{10,269,331,332}

The IPCE can also be calculated by^{7,9}

$$IPCE(\lambda) = LHE(\lambda) \phi_{inj}(\lambda) \phi_{reg} \eta_{cc}(\lambda) \quad (17)$$

where $LHE(\lambda)$ represents the light-harvesting efficiency at wavelength λ , ϕ_{inj} represents the quantum yield for electron injection from the excited sensitizer in the conduction band of the TiO₂, ϕ_{reg} represents the quantum yield for dye regeneration and η_{cc} represents the efficiency for the charge collection where LHE is equal to $1 - 10^{-A}$ with A being the absorbance of the film.^{7,9,304}

I.3.5.2. Electrochemical Methods

The individual components of DSCs can be characterized by a range of electrochemical methods. Such methods afford the significant information on the energy levels of the

component, the reversibility and kinetics of the electrochemical processes. The standard equipment for electrochemical measurements comprise a potentiostat connected to a three electrode cell including one working electrode, one reference electrode and one counter electrode.^{7,328,333-336}

The most widespread electrochemical method is cyclic voltammetry. In such method, the potential is swept at a constant rate and reversed at a certain point, and at the same time the current is persistently monitored. The monitored current can arise from both the Faradaic processes such as the electron transfer at the electrode and the non-Faradaic processes such as capacitive charging at the electrode/electrolyte interface. In normal cyclic voltammograms, one can test the potentials of redox processes and obtain the reversibility of the electron transfer processes. Also, because the current peaks depend on the scan rate, one can get information on whether the redox active species are free in the solution or adsorbed to the electrode surface. There are some other electrochemical methods such as differential pulse voltammetry and square wave voltammetry. However, unlike the cyclic voltammetry, these referred techniques cannot give information on the reversibility.^{7,328,333-336}

The electrochemical impedance spectroscopy (EIS) is another powerful electrochemical method to fully understand the electronic and ionic processes occurring at the different interfaces in DSCs. Such method afford information on the series resistance, the charge transfer resistance of the counter electrode, the diffusion resistance of the electrolyte, the resistance of the electron transport process and recombination process in TiO₂ as well as the chemical capacitance of the mesoporous TiO₂ electrode. The impedance measured in a wide range of frequencies in a real system can be determined according to an equivalent circuit including the series and parallel connected elements (resistors, capacitors, inductors) and the Warburg element that indicates the diffusion processes.^{205,334,337,338-340}

The electrochemical method can be better applied if combined with different kinds of spectroscopy such as UV-Vis. From some reported publications, the electrochemistry combined with the UV-Vis spectroscopy has been employed to study the accumulation of electrons in mesoporous TiO₂ semiconductor electrodes.³⁴¹ The onset of the accumulation of electrons in TiO₂ electrodes can be related to the conduction band edge of mesoporous TiO₂. Such onset based on a number of organic electrolytes have been reported by G. Redmond and D. Fitzmaurice.³⁴² They found that some cations in the electrolytes such as Li⁺ and Mg²⁺ can determine the position of the conduction band of TiO₂ on account of their specific adsorption on the mesoporous TiO₂ electrode. Particularly, the electrochemistry combined with spectroscopy can be employed to determine the spectra of the oxidized and reduced dye

sensitizers, which is significant in laser spectroscopy studies.^{7,343-345}

I.3.6. Recent Improvements

In this section, the various improvements achieved in the recent years in the field of DSCs are exposed. The rapid strides in the development of DSCs performance now demand attention to be paid to architectural improvements on individual component. With supporting data, the recent improvements on different components of DSCs including photoanodes, electrolytes, counter electrodes and some parameters of DSCs are compared to provide ideas for further modification. These comparative studies can help to compile and apply a few of the discussed works and give suggestions to enhance the overall power conversion efficiency of DSCs. Furthermore, the progress of DSCs has stimulated research efforts for the development of feasible commercial products including this technology. Also, the life-time of DSCs is a key factor which holds back their developments. Therefore, some important research works referred in this section have been done in terms of enhancing the life-time of DSCs. The improvements on various sensitizers are introduced in II.2., III.2. and IV.2..

I.3.6.1. Improvements in Photoanode

As indicated in I.2.3.5., the photoanode which supports the sensitizers, is involved in the electron transfer processes, and thus plays as an important role on the overall power conversion efficiency and is an indispensable component of DSCs. Most commonly, TiO₂, ZnO and SnO₂ are used to coat on TCO substrates such as FTO and ITO.^{186,268} Fundamentally, compared with the SnO₂, the lower isoelectric point of TiO₂ can restrain the adsorption of sensitizers with carboxyl groups.³⁴⁶ However, the DSCs based on SnO₂ semiconductor films are prone to severe recombination losses. That the reason why SnO₂-based core-shell heterostructures have been investigated. Thus, solar cell devices based on SnO₂/MgO films where SnO₂ crystallites are covered with an ultra-thin shell of MgO, showed a maximum overall power conversion efficiency (PCE) of 7%.³⁴⁷

In recent years, a lot of research work have been done on modification of photoanodes through using nanoparticles, nanorods, nanotubes^{7,10,13,268,269,348,349} in order to enhance the light absorption,^{350,351} scattering,³⁵²⁻³⁵⁴ charge transport³⁵⁵ and by improving the interfaces energy by restraining the charge recombination processes³⁵⁶. Ag nanowires and graphene can be used in order to modify the photoanodes on the FTO glass which was reported by H. Yan *et al.* in 2015. In this publication, a novel multistage structure of DSCs which was comprised of Ag

nanowires, TiO₂ nanoparticles and graphene wrapped TiO₂ mesoporous microspheres was designed and fabricated by using simple spin coating methods. The resulting PCE based on the novel solar cell structure was up to 7.42% which was about twice as much as that for the solar cell devices only with a TiO₂ nanoparticle layer.³⁵⁷ Generally, both the dye adsorption and the optical absorption via surface plasmon resonance can be enhanced through employing metal nanoparticles such as Ag nanoparticles.³⁵⁸⁻³⁶⁰ Because of the flexibility and low cost, the polymers such as polyethylene terephthalate (PET) and polyethylene naphthalate (PEN) can act as an alternative to glass substrates. The solar cell devices by using PET coated with ITO showed an efficiency of 3.8% and the solar cell devices by using PEN coated with ITO showed an efficiency of 7.8%.^{361,362} Apart from polymers, metals such as tungsten, stainless steel and titanium can also be used as substrates.³⁶³⁻³⁶⁵

In order to obtain a better performance of DSCs, a novel Sr, Cr co-doped TiO₂ xerogel film was employed as a constituent part of photoanode. The performances of solar cell devices varied with the different ratios of strontium and chromium along with the FTO glasses.³⁶⁶ Similarly, the performance of DSCs can be optimized through employing a novel Sr, V co-doped TiO₂ film.³⁶⁷ Also, the nanoparticles such as Au-TiO₂ and Pt-TiO₂ along with the FTO glasses can be employed as photoanodes to show a better performance compared to the solar cell devices using pure TiO₂ along with the FTO glasses as photoanodes.²⁶⁸

The semiconductor layers of ZnO nanoparticles, ZnO powders and nanopowders along with FTO glasses were designed to fabricate double-layered semiconducting photoanodes for DSCs. The under-layer was ZnO nanoparticles prepared by simple and cost-effective sparking technique onto the FTO glass substrate. The thickness of the under-layer was controlled by the number of sparking cycles under atmospheric pressure. Subsequently, the double-layered photoanode was formed through screen-printing the ZnO powders and nanopowders onto the under-layer. The best results of DSCs based on such photoanodes were achieved 50 sparking cycles for ZnO powders and ZnO nanopowders over-layers with the efficiencies of 1.11% and 1.14%, respectively.³⁶⁸ The hybrid films such as carbon nanotubes/ZnO by blending multi walled carbon nanotubes or single wall carbon nanotubes with ZnO can be employed to act as photoanodes and enhance the efficiencies of DSCs.³⁶⁹⁻³⁷² Notably, few high efficiency ZnO-based DSCs have been reported because of Zn²⁺-dye aggregations at the interface between ZnO and the dye that result in blocking of the electron transfer processes.³⁷³ To solve this problem, L. Loh *et al.* reported a heterogeneous architecture of ZnO and bismuth ferrite prepared through using a technique which allows the synthesis using purely chemical solution techniques. The performance of DSCs can be improved by using bismuth ferrite with the ZnO

nanoparticles along with FTO glass as photoanodes.³⁷⁴ Y. Yin and L. Chen reported the employment of ZnO nanowires and ZnO nanoparticles composites coated onto the ITO glass substrates as photoanodes of DSCs. In their study, 4-tert-butylpyridine and water vapor was employed on the ZnO composite photoanodes to improve the performance of DSCs and finally the efficiency of 6.60% was achieved.³⁷⁵ M. Moradzaman *et al.* reported the light scattering, harvesting and adsorption effects in DSCs through preparing carbon nanotubes coated with TiO₂ and Zr-doped TiO₂ nanoparticles as constituent parts of mono- and double-layer solar cell devices. The best result was achieved based on the double layer solar cell device consisting of 0.025 mol% Zr-doped TiO₂ nanoparticles as the under-layer and mixtures of TiO₂ and Zr-doped TiO₂ nanoparticles and 0.025 wt% coated carbon nanotubes with TiO₂ as the over-layer and showed a highest efficiency of 8.19%.³⁷⁶

Finally, J. T. Kim *et al.* reported lithium silicate modified TiO₂ electrodes prepared by a soaking process which were employed as photoanodes in DSCs. Compared to the reference solar cell device without any surface modification, the solar cell device with the photoanode composed of the lithium silicate modified TiO₂ along with FTO glass substrate showed a better efficiency of 10.58%. In this study, the lithium silicate acting as a surface modifier played an important role in the performance of the DSCs.³⁷⁷

I.3.6.2. Improvements in Counter Electrode

Overall, the counter electrode is a key component of DSCs.^{7,10,13,268,348,349} FTO or ITO substrate coated with standard Pt is used as the most common and effective counter electrode because of its remarkable catalytic activity and high conductivity. However, improvements are required on developing alternative Pt-free electrodes due to the high cost and scarcity of Pt.^{186,268} For now, studies have been reported on modification and development of the counter electrode by using different types of nanoparticles, novel metals and surface modification such as single or double layer.

More specifically, the counter electrode can be modified by using different materials such as graphite, activated carbon, platinum, carbon black, single wall carbon nanotubes, polypyrrole, polyaniline and poly(3,4-ethylene dioxythiophene) which are used as catalysts for reduction of triiodide.^{186,210,268} Numerous metals materials were tried as substrates in DSCs such as stainless steel, W, Ti, Co, Ni, Al, Pt, Cu and Zn because of their promising electrical conductivity, good flexibility and/or ductility, thermal stability withstanding high temperature treatment, or also lower sheet resistance compared to ITO or FTO. However, when used as substrate materials of counter electrodes, metal substances are demonstrably prone to

corrosion in the aggressive redox electrolyte medium.^{186,268,284,378-381}

Intrinsic conducting polymers may have metallic conductivity or semiconducting properties. The electrical properties of such compounds can be finely-tuned through organic synthesis and advanced dispersion techniques.²⁸⁴ Most of the conductive polymers are derivatives of polyacetylene, polyaniline, polypyrrole or polythiophenes, the structures of which are usually conjugated double bonds for conduction.³⁸¹⁻³⁸⁴ The reported conductive polymers such as poly(3,4-ethylenedioxythiophene) (PEDOT) doped with p-toluenesulfonate (PEDOTTsO) or polystyrenesulfonate (PEDOT-PSS) can be employed for Pt-free counter electrode materials in DSCs.^{214,215} K. Takayuki *et al.* reported the carbon-based electrodes using carbon composites such as polypyrrole and polyaniline as composite catalysts along with carbon black coated on the FTO glasses for solid state DSCs. In their study, carbon-based counter electrode showed a promising electric contact with the hole transport layer of polypyrrole to give higher cell performance compared to the cell with gold or platinum counter electrode.³⁸⁵ N. Ikeda designed and prepared a clay-like conductive material comprising polyaniline-loaded carbon black particles with the ionic liquid ethyleneoxide substituted imidazolium iodide which was sandwiched between mesoporous TiO₂ film and the FTO glass substrate to form a solid-state dye-sensitized solar cell device showing an efficiency of 3.48%.³⁸⁶ Similarly, solar cell device based on a Ti-metal foil substrate for photoanode, a Pt counter electrode deposited by electrochemical deposition method on ITO/polyethylene naphthalate of 5 mM H₂PtCl₆ aqueous solution showed an efficiency of 7.2%.³⁶² J. Burschka *et al.* proposed a PEDOT film deposited onto ITO-polyethylene terephthalate(PET) substrates as the counter electrode by electro polymerization proving that polymer PET films are suitable for counter electrode.³⁸⁷ In another publication, the deposition of platinum was reported to result in the lower charge transfer resistance and lower ohmic serial resistance. The charge transfer resistance and ohmic serial resistance were 0.175 Ωcm² and 3.16 Ωcm² for solar cell devices using electrospun carbon nanofibers (ECNs)/Pt as counter electrodes, 1.15 Ωcm² and 3.31 Ωcm² for Pt, 0.44 Ωcm² and 4.12 Ωcm² for ECNs.³⁸⁸

Graphene-based composite materials along with FTO glass substrate were also reported to act as counter electrodes.³⁸⁹⁻³⁹⁵ For example graphene modified vanadium pentoxide nanobelts can be employed as an efficient counter electrode for DSCs and showing efficiency of 4.94%.³⁹⁶ NiCu bimetallic nanoparticle decorated graphene prepared by hydrothermal treatment can be used to act as an efficient and alternative Pt-free counter electrode for DSCs, as reported by M. Motlak *et al.*. In their study, the performance of the prepared modified graphene as counter electrode was strongly dependent on the composition of the metallic

nanoparticles. Compared to the other introduced formulations (Ni-, Ni_{0.25}Cu_{0.75} and Ni_{0.6}Cu_{0.4}) as well as pristine graphene, the graphene decorated by Ni_{0.75}Cu_{0.25} nanoparticles showed the best efficiency of 5.1%.³⁹⁷

The single wall carbon nanotubes (CNTs) were used as a carbon counter electrode because of the high longitudinal conductivity and showed a conversion efficiency of 4.5%, as reported by S. Kazuharu *et al.*²¹² Carbon-black-loaded stainless steel electrode used as a novel counter electrode can also display a good efficiency if a suitable thickness of carbon black is chosen. Such counter electrode is low cost and can be used for large scale production, the efficiency of DSCs based on which showed a high efficiency of 9.15%, as reported by T. N. Murakami *et al.*³⁹⁸ Compared to stainless steel materials, the carbon catalysts on metal surface are suitable for counter electrode because of their low cost and high stability towards corrosion.²⁰⁹ A low cost nanoscale carbon/TiO₂ composite was reported to be used as counter electrode for DSCs with an efficiency of 5.5%. In such composite, carbon acted as a catalyst and the TiO₂ as a binder.³⁹⁹ A nickel incorporated carbon nanotube/nanofiber composite can also be used as a low cost counter electrode for DSCs, as reported by P. Joshi *et al.* In their study, polyacrylonitrile (PAN) was employed to fabricate Ni(AcAc)₂ nanofibers by electrospinning and a mixture of Ar and C₂H₄ was employed to form carbon nanotubes (CNTs) and carbon nanofibers (CNFs) which were expected to significantly increase the surface area for triiodide reduction. The solar device based on the Ni-CNTs-CNFs composite counter electrode yielded an efficiency of 7.96%.⁴⁰⁰ X. Mei *et al.* reported a high performance dye-sensitized solar cell device based on a binder-free film of CNTs including both single walled and multi walled CNTs as the counter electrode. Compared to the solar cell device based on multi walled CNTs, the solar cell device based on single walled CNTs showed a slightly higher efficiency of 7.81%.⁴⁰¹

I.3.6.3. Improvements in Electrolyte

As referred in I.2.3.5., the electrolyte is a ubiquitous and indispensable component in DSCs. The main function of the electrolyte is to inject electrons into the conduction band of the semiconductor to accomplish the dye regeneration and to transfer positive charges to the counter electrode. The properties of the electrolyte are responsible for the photovoltaic conversion efficiency, operational stability and long-term durability of DSCs. Therefore, the electrolyte should have (1) a high electrical conductivity and a low viscosity for electron diffusion processes, (2) an excellent interfacial contact with the semiconductor and the counter electrode, (3) a non-desorption characteristic in oxidization surface and the

degradation of the dye sensitizer, and (4) a non-light-absorbing characteristic in the visible region.^{7,15,188,199,205,285}

Generally, the electrolytes used in DSCs can be classified into three types: (1) liquid electrolytes, (2) solid-state electrolytes and (3) quasi-solid electrolytes.

I.3.6.3.1. Liquid Electrolytes

Z. Yu *et al.* reviewed the liquid electrolytes in 2011.²⁹⁵ According to their work the liquid electrolytes can be further classified into two types: (1) the organic solvent based electrolytes and (2) the ionic liquid based electrolytes. Although the conventionally used electrolyte in DSCs is liquid, the major drawbacks of liquid electrolytes are poor long-term stability due to volatility, leakage and flammability of the liquids.^{7,15,186,295} In this context, electrolytes including liquid ionic as low-volatile solvents were successfully designed.

I.3.6.3.2. Organic-Solvent-Based Electrolytes

An organic electrolyte is usually composed of a solvent, a redox couple and some additives. There are a number of redox couples for the organic electrolytes which have already been reported such as $\text{Br}^-/\text{Br}_3^-$,⁴⁰⁵ $\text{SCN}^-/(\text{SCN})_2$, $\text{SeCN}^-/(\text{SeCN})_2$ ^{406,407} and substituted bipyridyl cobalt(II/III)⁴⁰⁸. Anyway, the most ideal redox couple is still I^-/I_3^- because of its good solubility, rapid ion diffusion, low light absorption in the visible region, fast dye regeneration, appropriate redox potential and slow dynamics of recombination for electron injection into the semiconductor and the triiodide.^{15,188,409}

The solvents for the organic electrolytes play an important role in the electron diffusion and the dissolution of the iodide/triiodide ions. For now, many organic solvents for the organic electrolytes such as acrylonitrile (AcN), propylene carbonate (PC), ethylene carbonate (EC), 3-methoxypropionitrile (MePN) and N-methylpyrrolidone (NMP) have already been reported.^{13,410} The solvents with large donor number can enhance the V_{oc} but reduce the J_{sc} . By controlling the donor number one can control the equilibrium of iodine and triiodide ions in the solvents.⁴¹¹ Therefore, the electric additives can optimize the photovoltaic properties of DSCs because the additives can adsorb on the photoanode/electrolyte interface and restrain the recombination of injected electrons with the triiodide ions. For now, 4-*tert*-butylpyridine (TBP), guanidinium thiocyanate (GuNCS) and N-methylbenzimidazole (NMBI) are reported to be the most efficient additives.⁴¹²⁻⁴¹⁴

I.3.6.3.3. Ionic Liquid Electrolytes

Due to their volatility, liquid electrolytes usually have high evaporation rate. The evaporation issue and the leakage of the liquid electrolyte further lead to poor long term stability. The use of ionic liquid-based electrolytes can minimize the above drawbacks. Room-temperature ionic liquids can act as alternative electrolytes for DSCs and other electrochemical devices because of their excellent chemical and thermal stability, negligible vapor pressure, non-flammability, high ionic conductivity, and a wide electrochemical window.⁴¹⁵ The ionic liquid electrolytes are conventionally composed of various organic salts containing cations such as imidazolium, pyridinium and anions from the halides or pseudo halides.⁴¹⁶ The most used ionic electrolyte for DSCs contains N,N' bis-alkyl-substituted imidazolium iodides. The viscosity of the organic salts was proved to decrease with the reduction of the alkyl chain length due to the decrease of Van der Waals forces. On the other hand, if the viscosity increases, the conductivity of the ionic liquid electrolytes decreases.⁴¹⁵⁻⁴¹⁷

Therefore, an unprecedented efficiency of 8.2% under AM1.5G illumination was obtained by M. Grätzel's group through using a solvent-free ionic liquid electrolyte including 3-alkylimidazolium based salts which opened up possibilities for large-scale outdoor applications of mesoscopic DSCs.⁴⁰⁴

I.3.6.3.4. Solid State Electrolytes

Solid state electrolytes have also been studied to overcome the leakage issue and improve the stability, compared to the liquid electrolytes.^{7,338,418} In solid state electrolytes, a p-type semiconductor or a hole transfer material takes the place of the liquid electrolyte. The band gap of the p-type semiconductor should be compatible with the HOMO level of the dye and the conduction band of the n-type semiconductor.^{7,10,268} Copper based compounds such as CuI, CuBr and CuSCN can be used as inorganic hole transfer materials because of their excellent conductivity.¹⁸⁸ However, organic hole transport materials are superior to their inorganic counterpart because of their easy processing characteristics. The amorphous organic hole transfer material 2,2',7,7'-tetrakis(N,N-di-p-methoxyphenylamine)9,9'-spirobifluorene, commonly named as spiro-OMeTAD, was for the first time employed as organic hole transfer material in 1998 by U. Bach *et al.* showing a low efficiency of 0.74% when a Ru-complex was used as sensitizer.⁴¹⁹ Further development of tailored-made sensitizers combined with the introduction of new dopants allowed for a continuous increase in the PCE of the

corresponding cells over 7%.

Up to now, spiro-OMeTAD is still used in state-of-the-art dye-sensitized solar cell devices. The solid state p-type DSCs were reported to obtain a best efficiency of 7.51% employing spiro-OMeTAD as a hole transport photocathode and a novel benzothiadiazole-based D-A- π -A organic material as a dye sensitizer.⁴⁵⁵ However, there are some drawbacks of the molecular hole conductor spiro-OMeTAD which are low hole-conductivity, difficult infiltration into mesoporous photoanodes and high material cost. Therefore, alternative hole conductors have garnered growing interest. J. Zhang *et al.* reported a conducting polymer poly(3,4-ethylenediothiophene) (PEDOT) hole transport material in 2016. The solid state dye-sensitized solar cell device based on PEDOT and a diketopyrrolopyrrole-based dye showed an efficiency of 5.5% while the device based on the small molecular spiro-OMeTAD hole conductor showed a lower efficiency of 2.9%. The higher power conversion efficiency for PEDOT-based p-type DSCs can be attributed to the significantly enhanced charge collection efficiency due to the three-order-of-magnitude higher hole conductivity compared with that of the hole conductor spiro-OMeTAD.⁴⁵⁶ A low-cost spiro[fluorene-9,90-xanthene] based organic hole transport material, which is the first example of an easily synthesized spiro-structured hole conductor, was designed and employed for highly efficient solid state p-type DSCs by B. Xu *et al.*. Solar devices based on such hole transport material showed an best efficiency of 7.30% under 100 mW·cm⁻² AM1.5G solar illumination. Furthermore, the simple synthesis of spiro[fluorene-9,90-xanthene] from cheap commercially available starting material paved the way for the large-scale industrial production of solid state p-type DSCs in future.⁴⁵⁷ The copper complexes as redox mediators in DSCs were first reported by Fukuzumi *et al.* which showed an efficiency of 2.2%.⁴⁵⁸ Bis(2,9-dimethyl-1,10-phenanthroline)-copper(I/II) (Cu(dmp)₂) in the solid phase were reported to replace the typical I⁻/I₃⁻ electrolyte and employed as efficient molecular hole transport material. This Copper phenanthroline complex-based solar cell device showed the best efficiency of 8.2% in all Cu-mediated DSCs.⁴⁵⁹ Some other Cu-mediated hole transport materials such as [Co(bpyPY4)](OTf)₂ and Co(bpyPY4)](OTf)₃ where bpyPY4 represents the hexadentate ligand 6,6'-bis(1,1-di(pyridin-2-yl)ethyl)-2,2'-bipyridine and OTf represents the trifluoromethanesulfonate anion were also reported.⁴⁶⁰

I.3.6.3.5. Quasi Solid State Electrolytes

The existing difficulty in penetrating into the mesopores of the semiconductor for solid state electrolytes limits their applications. Therefore, the quasi solid electrolytes rose in

response to the difficulty. A quasi-solid electrolyte can be considered as a composite of a polymer and a liquid electrolyte.^{7,186,188,268} The quasi-solid electrolytes display a better performance and long term stability, excellent interfacial contact and high electrical conductivity because of the unique network structure of polymers which is strongly dependent on the molecular weight and the morphology. It is worth noting that the cell performances obtained with quasi-solid electrolytes are closely related to the working temperature because an increase in temperature results in a phase transition from a gel state to a solution state.¹⁸⁸

I.4. NiO-Based p-Type Dye-Sensitized Solar Cells and NiO-Based Dye-Sensitized Photoelectrochemical Cells

In recent years, DSCs based on the sensitization of a p-type semiconductor have strengthened the increasing interest in photovoltaic science because the new type of photoelectrochemical devices paves the way for the conversion of solar energy into both electricity and chemical energy.⁴²⁰ In contrast to conventional n-type DSCs, p-type DSCs operate in an inverse mode where the rapid electron transfer process from a p-type semiconductor to the dye sensitizer occurs after dye excitation.²⁶⁹ The photoelectrochemical devices share some structural similarities with the conventional n-type DSCs due to their mirror-image relationship. However, they use different materials and have different charge transfer kinetics. In p-type DSCs, the photoexcited dye sensitizer is reductively quenched by hole injection into the valence band of a p-type semiconductor. Therefore, the research on the p-type DSCs plays an important role in understanding both the key factors which control the rate of hole injection and the rational design of efficient p-type DSCs.⁴²⁰⁻⁴²² Moreover, improving the performance of p-type DSCs is a crucial part of the development of high performance tandem DSCs. The tandem DSCs which can be fabricated by pairing a typical TiO₂ based photoanode with a dye-sensitized photocathode were proposed to improve the conversion efficiency of DSCs.^{7,18,421,425-427} Although the pn-type tandem DSCs are calculated to reach the energy conversion efficiencies of approximate 43% in theory, the practical maximum energy conversion efficiency achieved is only 4.1%,^{421,427-429} which is far from ideal. Similarly, the best up-to-date NiO based p-type DSCs device shows an efficiency of 2.51%.⁴³⁰ The low efficiencies of tandem DSCs can be prevalingly attributed to the practical performances of the p-type semiconductors. Particularly, the low energy conversion efficiency of p-type DSCs can be attributed to the low J_{sc} and V_{oc} produced by the p-type semiconductors.^{7,18,430,423-429} Up to now, the most frequently used semiconductor for p-type

DSCs is nickel oxide (NiO).^{421,423,424,431,432} However, some other inorganic oxide materials such as CuO⁴³³⁻⁴³⁵ can be employed as p-type semiconductors, as well as delafossites (CuMO₂, M = Al, Ga, Cr, Fe, In, Sc, etc.)^{429,431,432} and non-delafossites materials (SrCu₂O₂, LaCuOCh where Ch = chalcogen, etc.).^{431,432}

In addition, the production of fuels from solar energy and other renewable raw materials is an attractive solution to the constant depletion of fossil fuels and satisfy the world's increasing energy demand. As an example, water splitting can produce molecular hydrogen with O₂ as a side product, while light driven reduction of CO₂ can produce carbon-based fuels, with a net zero-carbon footprint. Theoretically, these processes can be implemented in dye-sensitized photoelectrochemical cells (DSPEC).^{16,437,438} To date, a number of architectures have been designed for DSPEC, all of which contains photoelectrodes.⁴³⁹ In this thesis, in analogy to p-type DSCs, DSPEC based on NiO photocathode have been focused which display photoelectrochemical activity for hydrogen production.

In this section, the historical background, recent improvements and operational principles for NiO-based p-DSCs and NiO-based DSPEC are introduced. Characterization techniques of n-type DSCs described in section I.3. can be adapted to p-DSCs and thus will not be described further in this section. Relevant contents for the characterization techniques of NiO-based DSPEC will be introduced in Chapter IV.

I.4.1. Historical Background and Recent Improvements

Compared to classical n-type DSCs, the field of p-type DSCs is much younger, with far fewer studies being reported: less than one hundred publications dealing with this type of cells since 2012, and before 2005 only 2 publications referring to DSCs based on the sensitization of p-type metal oxide.⁴²³ However, scientific interest has been rapidly growing over the past decade.

The earliest study on dye-sensitization of p-type semiconductors can date back to 1984. K. Tennakone *et al.* reported cuprous thiocyanate as a p-type semiconductor, which was found to adsorb thiocyanated cationic dyes and show high photoresponse in aqueous KCNS.⁴⁴⁰ In 1995, a method for the preparation of thin polycrystalline films of cuprous thiocyanate onto ITO glass substrates by electrochemical deposition was reported by K. Tennakone *et al.*. In this study, CuSCN was employed as a p-type semiconductor which was sensitized with SCN⁻ salts of cationic dyes and the typical I⁻/I₃⁻ redox couple was used. Illuminated by a 60 W tungsten filament lamp, the constructed photoelectrochemical cell device displayed low photocurrents of approximate 100 μA·cm⁻² which was attributed to the low porosity of the

CuSCN film.⁴⁴¹ A seminal publication was then reported by J. He *et al.*, in which p-type nanostructured NiO film was prepared by depositing nickel hydroxide slurry on conducting glass as a photocathode for DSCs. The highest IPCE of solar cell devices based on tetrakis(4-carboxyphenyl)porphyrin (TPPC) and erythrosin B-coated NiO films were 0.24% and 3.44%. The valence band of NiO was approximately 0.54 V vs. NHE at pH = 7.0.⁴⁴² Another publication was subsequently reported by the same group in 2001 in which nanostructured NiO thin film was further investigated and the conclusions were given that nanostructured NiO film was optically transparent with a band gap of ~3.55 eV. In this study, the nanostructured NiO photocathodes were obtained by heating Ni(OH)₂ sol-gel films at a high temperature of 300-320 °C.⁴⁴³

The charge transport studies of dye-sensitized NiO photocathodes are also important. For p-NiO semiconductor, the hole transport was reported to occur by a hopping mechanism between localized surface states which enhance the interfacial charge recombination losses with the electrolyte.⁴⁴⁴⁻⁴⁴⁷ The enhancement of charge collection efficiency of p-DSCs can be realized by increasing the hole diffusion coefficient or decreasing the collection time.⁴⁴⁸⁻⁴⁵⁰ In contrast to TiO₂ based n-DSCs, it was investigated that the transport time in NiO based p-DSCs would not vary significantly with the incident photo intensity.^{444,446,451} Theoretically, the conductivity of the semiconductors should be enhanced by increasing the concentration of the photogenerated charges. This is often the case for the typical n-DSCs. However, for NiO based p-DSCs, the hole transport rate is almost invariant and the hole lifetime drops severely with the increase in the photogenerated charge concentration. And therefore, when the hole lifetime is close to the transport time, the effective diffusion length of the hole limits the thickness of the NiO photocathode to 2-3 μm.^{444,446,451,452} The peculiar charge transport mechanism of dye-sensitized NiO photocathodes involves hole hopping between Ni(III) cations located at the surface and also assists the recombination with the electrolyte.^{446,453} Another drawback of NiO stems from its peculiar ability to catalyze oxidation reaction when employed in heterogeneous catalysts. Actually, it has been already investigated that the overpotential of iodide oxidation is reduced on dye-sensitized NiO photocathode compared to that on FTO or platinum electrodes. The photogenerated hole charges are excited on NiO and subsequently react quickly with the reduced form of the electrolyte, which finally results in the primary photocurrent loss especially at voltages close to the V_{oc}. On the basis of the above theories, either the typical I⁻/I₃⁻ electrolyte or the NiO photocathode should be replaced or modified in order to improve the efficiencies of p-type DSCs.

In 2009, E. A. Gibson *et al.* presented a three-fold increase in V_{oc} (0.35 V) while maintaining a J_{sc} of $1.7 \text{ mA}\cdot\text{cm}^{-2}$ for a p-type NiO dye-sensitized solar cell device. Contrary to earlier publications, a novel electrolyte composed of Co(II/III) tris(4,4'-di-tert-butyl-2,2'-dipyridyl) perchlorate (0.1 M/ 0.1 M) and LiClO_4 (0.1 M) in propylene carbonate was employed to replace the typical I/I_3^- electrolyte. The efficiency of NiO-based p-type DSCs based on the novel electrolyte and a carefully designed “dyad” dye sensitizer was up to 0.20%.⁴⁵⁴

In addition to the replacement of the typical I/I_3^- electrolyte, an alternative approach to bring further improvements to the efficiency of p-type DSCs is to improve the quality and conductivity of NiO based photocathodes. An excellent review was reported to explore the effect of the preparation of NiO surfaces on their efficiencies as photocathodes.⁴²⁴ As referred in I.3., there are several optional semiconductors which can be employed as photoanodes in n-type DSCs. However, only few metal oxides can exhibit p-type semiconductivity. In this thesis, nickel oxide is employed as photocathode in p-type DSCs and DSPEC and some other p-type semiconductors or NiO-based semiconductors in doped forms will not be introduced.

Nickel oxide is an intrinsic nonstoichiometric p-type semiconductor which has a wide bandgap ($E_g = 3.6\text{-}4.0 \text{ eV}$) and possesses excellent thermal and chemical stability.^{18,420,421,422,424,443,444,448,450} The valence band of nickel oxide semiconductor is positioned at 0.54 V vs. NHE in neutral environment,^{425,442} which endows itself a promising electron donating property for a number of dye sensitizers and also makes the reductive quenching process of the dye sensitizers easier. However, the low-lying valence band potential of nickel oxide results in a low V_{oc} for NiO-based dye-sensitized solar cell devices. Moreover, NiO exhibits lower electrical conductivity than n-type metal oxide semiconductors and the TCO such as fluorine-doped tin oxide and indium-doped tin oxide are mostly n-type. The hole diffusion coefficient of NiO semiconductor films is in the range of 10^{-8} to $10^{-7} \text{ cm}^2\cdot\text{s}^{-1}$ while that of TiO_2 semiconductor films is in the range of 10^{-6} to $10^{-5} \text{ cm}^2\cdot\text{s}^{-1}$, which were determined by photoinduced absorption spectroscopy.^{445,460} The slow hole diffusion rate results in a long time delay between hole injection process into NiO and hole collection process, which finally increases their potential scavenging by the redox couples.^{18,420,421,424,445} In general, the nanostructured NiO photocathodes for p-type DSCs are prepared in two steps: i) synthesis of $\text{Ni}(\text{OH})_2$ precursor, and ii) heat $\text{Ni}(\text{OH})_2$ sol-gel films at high temperature.⁴⁴³ Simultaneously, some other alternative routes including chemical vapor deposition, electrodeposition, hydrothermal synthesis, sputtering and sol-gel were also reported. J. Velevska *et al.* reported their methods to prepare nickel oxide (NiO_x) thin films through a low

vacuum evaporation onto FTO glass substrates. These NiO_x semiconductor films exhibited anodic electrochromism, changing color from transparent white-yellowish to dark brown.⁴⁶¹ Through spin-coating, dipping and electrochemically, F. Vera *et al.* fabricated nickel oxide (NiO) thin films onto ITO glass substrates. The NiO grown onto ITO glass substrates by dipping method exhibited excellent morphological properties. The semiconductor properties of these nanostructured NiO thin films showed p-type behaviors characterized by photoelectrochemical and optical experiments.⁴⁶² A nanostructured NiO photoelectrode was also synthesized through initial deposition of layered basic nickel acetate having a yarn-ball-shaped morphology and subsequent heat-treatment at 500 °C in oxygen, which was reported by Y. Mizoguchi and S. Fujihara in 2008.⁴⁶³ Porous and nanostructured NiO thin films can be fabricated onto FTO glass substrates by annealing nickel acetate films obtained by recrystallization under hydrothermal conditions in the presence of hexamethylenetetramine. The excellent reproducibility of this method offered a reliable strategy to explore various dye sensitizers and other parameters to improve the power conversion efficiency of p-DSCs.⁴⁶⁴ Through a hydrothermal process, D.-B. Kuang *et al.* designed and prepared the hierarchical β-Ni(OH)₂ microspheres with 6-8 μm diameter assembled from nanoplate/nanosheet building blocks in the presence of an anion surfactant poly(ethylene glycol) 4-nonylphenyl 3-sulfopropylether potassium salt. They also prepared NiO microspheres assembled from nanoplate/nanosheet through thermal decomposition of the as-synthesized β-Ni(OH)₂ at 320 °C for 3 h in air. These novel hierarchical single crystalline Ni(OH)₂ and NiO microsphere structures were all investigated to be suitable for p-DSCs.⁴⁶⁵ Y. Y. Xi *et al.* in 2008 also reported their synthesis of NiO nanostructured thin films through both hydrothermal and electrodeposition methods at different deposition temperatures. For both fabrication methods, annealing was indispensable treatment for conversion of the films to NiO.⁴⁶⁶

In the photocatalytic or DSPEC systems for light driven water splitting, the semiconductor materials should meet certain requirements. Theoretically, the conduction band position of the suitable semiconductor should be more negative than the redox potential of H⁺/H₂ which is ~-0.42 V *vs.* NHE at pH = 7. Simultaneously, the valence band of the suitable semiconductor should be more positive than the redox potential of O₂/H₂O which is ~0.81 V *vs.* NHE at pH = 7. As a result, the band gap of a suitable semiconductor must be minimum 1.23 eV. Moreover, if the overpotentials which drive the oxygen and hydrogen evolution reactions is taken into account, then the value of band gap should be larger than 1.23 eV.^{27,467-472} On the other hand, the band gap of a suitable semiconductor must be smaller than

3.0 eV for the sake of visible light ($\lambda > 400$ nm) absorption. The difficulty of finding suitable semiconductor materials lies in the dilemma that few semiconductors can possess both a sufficiently narrow band gap and suitable energy levels for catalytic reactions. Most of the semiconductor materials have either poor absorption characteristic or additional undesirable external bias.⁴⁷³ Also, the energy levels of inorganic semiconductor materials are intrinsically hard to be finely-tuned. The employment of molecular dye sensitizers can be a solution for extending absorption into the visible light region for semiconductors.^{7,474} Anyway, as mentioned above, NiO can be employed as an effective semiconductor for DSPEC. Similarly to DSCs, DSPEC based on dye-sensitized n-type semiconductors or dye-sensitized p-type semiconductors are both possible. Compared to the p-DSCs, hydrogen evolving catalysts instead of redox mediators are employed as electron acceptors in p-DSPEC based on p-type semiconductors, such as NiO. Our work concerning the design, fabrication and study of p-type DSPEC based on NiO semiconductor and metallo-organic dye sensitizers will be described in Chapter IV. The dye sensitizers used in NiO-based DSPEC should fulfill some general requirements to obtain functional dye-sensitized photocathodes. On one hand, in addition to the suitable absorption and stability characteristics, the HOMO level of the dye must be more positive than the valence band position of the p-type semiconductors for the sake of efficient hole transfer processes after photoexcitation. On the other hand, the LUMO level of the dye sensitizers must be more negative than the catalytic onset reduction potential of the hydrogen evolving catalysts.^{27,437} Some promising dye sensitizers for NiO-based DSPEC are introduced in the following. Up to now, a large number of hydrogen evolving catalysts for proton reductions in homogeneous systems have been designed and investigated.^{437,475-479} Here, the details of the hydrogen evolving catalysts will not be further introduced.

The first example of a p-type DSPEC for visible light-driven proton reduction based on the earth-abundant and inexpensive p-type NiO semiconductor was reported by L. Sun *et al.* in 2012.¹⁷ The photo-active cathode used in their work was composed of a nanostructured NiO electrode which was sensitized with a push-pull p-type organic dye. A molecular H₂-evolving catalyst, Co(dmgbF₂)₂(H₂O)₂ (where dmgbF₂ represents difluoroboryldimethyl glyoximate), was employed. In connection with a Pt wire anode, the p-type DSPEC devices based on such photocathode and cobaloxime catalyst realized visible light driven hydrogen generation and showed a transient short-circuit photocurrent density of $\sim 22.5 \mu\text{A}\cdot\text{cm}^{-2}$ under illumination with a light-emitting-diode at -0.4 V bias potential vs. Ag/AgCl and pH = 7.0 phosphate buffer solution. Unfavourably, photocurrent decay with time was observed under

illumination, which can be attributed to the decomposition and/or leaching of the catalyst and the organic dye from the surface of the photoelectrode. In their work, a modified Clark-type electrode sensor for hydrogen detection was employed to confirm the light-driven H₂ formation on the photocathode. In the same year 2012, A. J. Mozer *et al.* reported their work to design and prepare a novel dye-sensitized photocathode comprised of a donor-acceptor type dye adsorbed onto the nanostructured NiO electrode. The donor-acceptor type dye was comprised of a perylenemonoimide electron acceptor, a regioregular 3-hexyl substituted sexithiophene unit, and triphenylamine as electron donor.⁴⁸⁰ Interestingly, no hydrogen evolving catalyst was used in this system. Their research work indicated that hydrogen evolution can occur in the absence of a catalyst if the dye sensitizer has a large negative potential. The light-driven proton reduction in this system directly occurred at the photocathode by photogenerated dye anions. In connection with a Pt wire anode, such dye-sensitized photocathode in Na₂SO₄ buffer solution (pH 7) with zero bias exhibited a photocurrent density of 1.7 μA·cm⁻² which subsequently increased to 3.9 μA·cm⁻² after 4 h. After 2 h illumination, the Faradaic efficiency of H₂ generation was investigated to be 97 ± 7 %. Through using the dye-sensitized NiO photocathode and BiVO₄ photoanode (which was selected due to its visible response up to λ = 500 nm and its good photocatalytic properties for O₂ evolution reaction) connected in a tandem configuration, the tandem DSPEC showed a photocurrent density of 1.8 μA·cm⁻² without any external bias in a 0.1 M Na₂SO₄ buffer solution at pH = 7. The photocurrent density increased up to 2.7 μA·cm⁻² after 4h. Also, the Faradaic efficiency of H₂ generation was investigated to be 79 ± 3 % after 4h. However, O₂ evolution could not be detected in their work due to the low sensitivity of their gas chromatography detector to oxygen.

In 2013, Y. Wu *et al.* designed and prepared a stable sensitizer-catalyst dyad assembly, in which the Ru polypyridyl sensitizer acted as a molecular bridge between the alumina coated NiO film and the cobaloxime H₂-evolving catalyst CodmgBF₂.⁴⁸¹ On one side of the dye molecule, a phenylpyridyl ligand with a carboxylic acid anchoring group was designed to be covalently attached onto the surface of the nanostructured NiO film to facilitate the hole injection to NiO. On the other side of the dye molecule, a vinylpyridyl substituent at the 4,4'-bipyridine ligand was designed to axially coordinate to the cobalt metal center of CodmgBF₂. The oxidation potential of the bifunctional cyclometalated Ru sensitizer was investigated to be 0.6 V *vs.* NHE, which was more positive than the valence band of NiO (0.54 V). The first reduction potential of the dye sensitizer was investigated to be -1.36 V *vs.* NHE, which was more negative than the redox potential of CodmgBF₂ (-0.46 V). Therefore,

hole injection from the dye to NiO as well as electron transfer from the dye to $\text{Co}(\text{mg})\text{BF}_2$ are thermodynamically favorable. Irradiation with a 300 W Xe lamp on the sensitizer-catalyst dyad photocathode based on the bifunctional cyclometalated ruthenium sensitizer and $\text{Co}(\text{mg})\text{BF}_2$ catalyst in a neutral aqueous solution, led to a stable photocurrent density of $9 \mu\text{A}\cdot\text{cm}^{-2}$ under an applied bias of 0.1 V for 1h. Hydrogen generation was also measured through gas chromatography to exhibit a Faradaic efficiency of 68% under an applied bias of 0.1 V for 2.5 h. In 2014, K. Fan *et al.* in 2014 reported a Pt-free tandem molecular DSPEC device, for the first time, employing molecular ruthenium- and cobalt-catalysts with strong dipicolinic acid anchoring groups on the respective photoanode (TiO_2 was used) and photocathode (NiO was used) for total water splitting.⁴⁸² Before this work, all the dye-sensitized photoanodes reported employed passive Pt cathodes to fabricate DSPEC. Therefore, their study paved the way for the Pt-free tandem molecular DSPEC for light-driven total-water splitting. A novel dye-sensitized p-type NiO photocathode with a hexaphosphonated $\text{Ru}(2,2'\text{-bipyridine})_3$ based dye and a tetraphosphonated molecular $[\text{Ni}(\text{P}_2\text{N}_2)_2]^{2+}$ type proton reduction catalyst (NiP) for light-driven H^+ reduction to H_2 was reported by E. Reisner *et al.* in 2016.⁴⁸³ They employed a layer-by-layer deposition method which utilized Zr^{4+} ions to link the phosphonate units in the dye sensitizer and NiP in a supramolecular assembly on the NiO photocathode. This layer-by-layer deposition method effectively locked the dye sensitizer in close proximity to the catalyst and semiconductor surface, but spatially separated the NiP from NiO for favorable electron transfer dynamics. More recently, V. Artero *et al.* reported an original noble-metal and covalent dye-catalyst assembly to realize photoelectrochemical visible-light-driven proton reduction to H_2 in mildly acidic aqueous conditions where p-type NiO semiconductor was employed as photoelectrode.⁴⁸⁴ Although some of efficient catalytic systems reported for solar hydrogen production employed the dye sensitizer molecular assemblies containing a sacrificial electron donor such as triethylamine or triethanolamine in aqueous solutions,⁴⁸⁵⁻⁴⁸⁷ the use of NiO-based photocathodes to fabricate DSPEC is sparking growing interest in the research field of solar fuel production. An excellent review reported by J. Willkomm *et al.* summarized strategies and challenges for the assembly of functional dye-sensitized photocatalysis systems and experimental techniques for their evaluation based on NiO-based photocathodes.⁴⁸⁸

I.4.2. Operational Principles

Similarly to n-DSCs, light absorption and charge transport in p-DSCs are performed by separate materials. However, the p-DSCs operate in an inverse fashion compared to

conventional n-DSCs. The operational principles of NiO-based p-DSCs are illustrated in Figure I-21.¹⁸

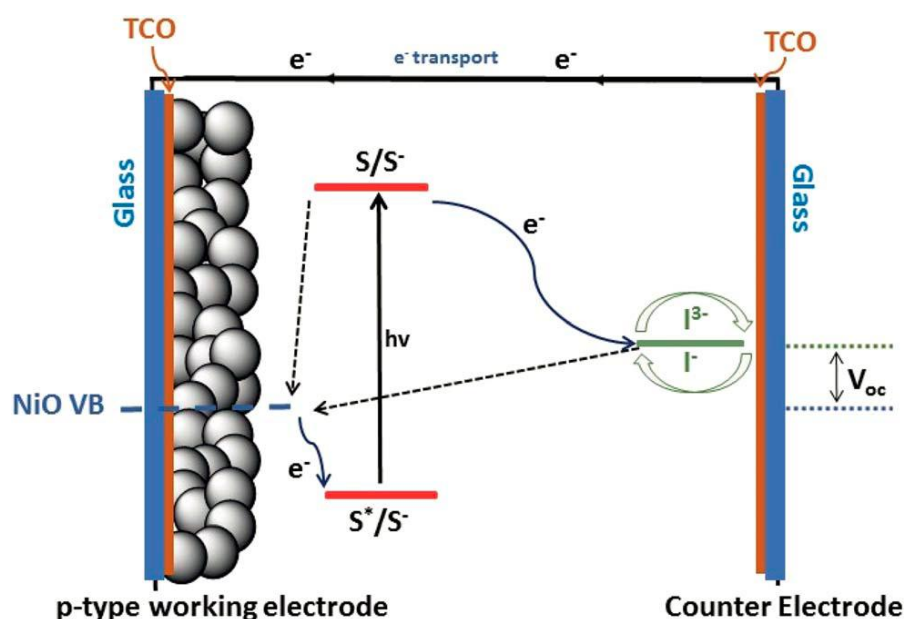


Figure I-21: Operational Principles of NiO-based p-type DSCs. Dashed arrows represent the two recombination processes between: (i) the dye and NiO, (ii) the redox couple and NiO. Straight blue arrows stand for electron transfer processes, while TCO stands for transparent conductive oxide.¹⁸

Upon light absorption, the dye sensitizer (S) adsorbed on the surface of NiO semiconductor film is photoexcited, leaving the dye sensitizer in its excited state (equation 18). The excited sensitizer (S^*) injects a hole into the valence band of the NiO semiconductor (p-SC) which results in the reduction of the dye sensitizer (S^-) (equation 19). The injected hole further diffuses to the back contact of the transparent conducting TCO substrate. If the charge recombination process between S^- and the hole in the valence band (h^+/VB_{p-sc}) is slow enough (equation 20), the reduced dye molecule is restored to its ground state (S) by giving an electron to the redox mediator (M) in the electrolyte (equation 21). At the counter electrode, the reduced form of the redox mediator (M^-) finally yields an electron to an external load to complete the whole circuit, and at the same time the redox mediator is oxidized back to its original state by the hole (h^+/CE) (equation 22).^{18,27,420,421,424,489} To sum up, the reactions involved in the operational principles of NiO-based p-DSCs can be represented as follows:





For a p-DSC device under illumination, the open-circuit potential (V_{oc}) indicates the difference between the quasi-Fermi level close to the NiO valence band and the redox potential of the electrolyte. The quasi-Fermi level mainly depends on the concentration of the photogenerated charge carriers in NiO semiconductor, which is affected by charge recombination at the interfaces of both dye/NiO and electrolyte/NiO.^{445,490} On the basis of the above operational principles, the free energies of the hole injection (ΔG_{inj}) can be determined by the equation as follows:

$$\Delta G_{inj} = e[E_{VB}(p-SC) - (E_{00}(S^*) + E(S/S^{\cdot}))] \quad (23)$$

The free energies of the dye regeneration (ΔG_{reg}) can be determined by the following equation:

$$\Delta G_{reg} = e[E(M/M^{\cdot}) - E(S/S^{\cdot})] \quad (24)$$

The free energies of the charge recombination (ΔG_{CR}) can be determined by

$$\Delta G_{CR} = e[E(S/S^{\cdot}) - E_{VB}(p-SC)] \quad (25)$$

In equations 23-25, the E_{VB} , $E_{00}(S^*)$, $E(S/S^{\cdot})$, $E(M/M^{\cdot})$ and e represent the valence band potential of the NiO semiconductor, the energy of the excited state dye sensitizer, the reduction potential of the dye sensitizer, the reduction potential of the redox mediator and the elementary charge, respectively.⁴²⁰ According to these equations, the maximum open circuit voltage (V_{oc}^{max}) can be determined by the difference of the Fermi levels (E_f) of both the photocathode and the counter electrode as follows⁴²⁰:

$$V_{oc}^{max} = E(M/M^{\cdot}) - E_{VB}(p-SC) \quad (26)$$

The concept of dye sensitization extends to the field of photosynthetic solar cells, making the emergence of the so-called DS-PEC. A NiO based p-DSPEC device operates in an analogous fashion to a NiO-based p-DSC except two catalytic reactions which take place in a DS-PEC. Instead of using redox mediators like in DSCs, hydrogen evolving catalysts coupled to the dye sensitizers are employed to act as electron acceptors in DS-PEC to restore the reduced forms of dye molecules to their ground states. Protons are subsequently reduced to generate hydrogen by the H₂-evolving catalysts. The photogenerated holes migrate through an external circuit to the counter electrode, where water molecules are oxidized to generate oxygen and protons.^{18,27,437,439,456,473,481} According to the Nernst equation, the free energy change for the conversion of one molecule of H₂O to H₂ and 1/2 O₂ under standard conditions is $\Delta G = 237.2$ kJ/mol, which corresponds to the fact that the reduction potential for both (H⁺/H₂) and (O₂/H₂O) redox couples (E^0) is 1.23 V for one electron transfer. The photoelectrochemical process should generate two electron-hole pairs per molecule of H₂ or

four electron-hole pairs per molecule of O₂. As discussed above, NiO semiconductor can drive the hydrogen evolution reaction and oxygen evolution reaction because its band gap energy is large enough to split water as well as its conduction band-edge energy and valence band-edge energy straddle the electrochemical potentials E⁰ (H⁺/H₂) and E⁰ (O₂/H₂O).^{437,442,443-446,450,452,491}

1.5. Research Objectives

DSCs which is an innovative, modern and growing technology, has a number of attractive features. It is simple to manufacture using conventional coating techniques and most of the raw materials employed are low-cost. The semi-transparency and colour of the device can be controlled for aesthetic integration into a variety of surfaces including flexible substrates, which is not applicable to Si-based systems. Moreover, DSCs can work efficiently under low-light conditions, even during overcast periods, and exhibit no angular dependence. Although its solar-to-electric power conversion efficiency is still lower than the best Si-based cells, in theory its price/performance ratio should be good enough to allow DSC to compete with fossil fuel electrical generation by achieving grid parity.^{7,9,10,185,187} To achieve efficient light-harvesting, the DSC device therefore relies on pigment molecules that play the role of visible-light absorbing antennae. In addition, inspired by the architectures of DSCs, DSPEC based on molecular sensitizer-functionalized metal oxide semiconductors in association with water-oxidation catalysts or hydrogen-evolving catalysts are now being designed and tested as promising approaches to generate hydrogen via solar-driven water splitting. The aim of the present work is to find novel dyes for DSCs and DSPEC, and its main objectives are:

1. To design and synthesize new colorful dyes based on organometallic complexes featuring the original D-[M]-A architecture where [M] is the electron-rich [Ru(dppe)₂] metal center for n-type DSCs and to characterize their optical and electronic properties as well as their photovoltaic performance in DSC devices.
2. To design and synthesize novel donor- π -acceptor dyes based on organometallic Ru-diacetylide complexes for use in NiO-based p-type DSCs, and to subsequently assess their optical and electrochemical properties as well as their photovoltaic performance in p-DSC devices.
3. To design and synthesize new dyes for DSPECs. The first dye design showed an original π -conjugated structure containing the [Ru(dppe)₂] metal fragment with an allenylidene ligand on one side and a σ -alkynyl ligand bearing an electron-rich group (*i.e.* a thiophene or triphenylamine unit) and one or two anchoring functions on the other side. The aim was to investigate the optoelectronic, electrochemical and

photoelectrochemical properties of the new target dyes. The second objective of this part was to design and synthesize a mono-molecular photocatalytic system comprising a Ru-diacetylide photosensitizer and a cobalt-based H₂-evolving catalyst, and to subsequently implement the new photocatalytic system in NiO-based photocathodes for H₂ generation tests in DSPEC.

I.6. References

- 1 S. G. Benka. The Energy Challenge. *Physics Today*, **2002**, 55: 38-39.
- 2 (a) M. Grätzel. Powering the planet. *Nature*, **2000**, 403, 363. (b) N. S. Lewis, D G Nocera. Powering the planet: Chemical challenges in solar energy utilization. *Proc. Natl. Acad. Sci.*, **2006**, 103(43): 15729-15735. (c) N. Armaroli, V. Balzani. The future of energy supply: Challenges and opportunities. *Angew. Chem. Int. Ed.*, **2007**, 46(1-2):52-66.
- 3 R. E. Smalley. Future global energy prosperity: The Terawatt Challenge. *Mrs Bulletin*, **2005**, 30(6): 412-417.
- 4 P. Würfel. Physics of Solar Cells. *Weinheim: Wiley-VCH Verlag GmbH*, **2007**.
- 5 A. Correljé, C. V. D. Linde. Energy supply security and geopolitics: A European perspective. *Energy Policy*, **2006**, 34(5): 532-543.
- 6 (a) N. S. Lewis. Introduction: Solar Energy Conversion. *Chem. Rev.*, **2015**, 115: 12631-12632. (b) T. R. Cook, D. K. Dogutan, S. Y. Reece, Y. Surendranath, T. S. Teets, D.G. Nocera. Solar Energy Supply and Storage for the Legacy and Nonlegacy Worlds. *Chem. Rev.*, **2010**, 110: 6474-6502.
- 7 A. Hagfeldt, G. Boschloo, L. C. Sun, L. Kloo, H. Pettersson. Dye-sensitized Solar Cells. *Chem. Rev.*, **2010**, 110: 6595-6663.
- 8 M. A. Green. Third Generation Photovoltaics: Advanced Solar Energy Conversion. *Springer-Verlag: Berlin, Heidelberg*, **2003**
- 9 M. K. Nazeeruddin, E. Baranoff, M. Grätzel. Dye-sensitized solar cells: A brief overview. *Solar Energy*, **2011**, 85: 1172-1178.
- 10 J. W. Gong, J. Liang, K. Sumathy. Review on dye-sensitized solar cells (DSSCs): Fundamental concepts and novel materials. *Renewable and Sustainable Energy Reviews*, **2012**, 16: 5848-5860.
- 11 Q. Wang, S. Ito, M. Grätzel, F. Fabregat-Santiago, I. Mora-Seró, J. Bisquert, T. Bessho, H. Imai. Characteristics of High Efficiency Dye-Sensitized Solar Cells. *J. Phys. Chem. B*: **2006**, 110: 25210-25221.
- 12 M. Grätzel. Photoelectrochemical cells. *Nature*, **2001**, 414: 338-344.
- 13 S. Sharma, B. Siwach, S. K. Ghoshal, D. Mohan. Dye sensitized solar cells: From genesis to recent drifts. *Renewable and Sustainable Energy Reviews*, **2017**, 70: 529-537.
- 14 G. Richhariya, A. Kumar, P. Tekasakul, B. Gupta. Natural dyes for dye sensitized solar cell: A review. *Renewable and Sustainable Energy Reviews*, **2017**, 69: 705-718.
- 15 J. H. Wu, L. Zhang, J. M. Lin, M. L. Huang, Y. F. Huang, L. Q. Fan, G. G. Luo. Electrolytes in Dye-Sensitized Soar Cells. *Chem. Rev.*, **2015**, 115: 2136-2173.

-
- 16 J. Massin, S. Lyu, M. Pavone, A. B. Muñoz-Garcia, B. Kauffmann, T. Toupance, C. Olivier. Design and synthesis of novel organometallic dyes for NiO sensitization and photo-electrochemical applications. *Dalton Trans.*, **2016**, 45: 12539-12547.
 - 17 L. Li, L. L. Duan, F. Y. Wen, C. Li, M. Wang, A. Hagfeld, L. C. Sun. Visible light driven hydrogen production from a photo-active cathode based on a molecular catalyst and organic dye-sensitized p-type nanostructured NiO. *Chem. Commun.*, **2012**, 48: 988-990.
 - 18 V. Nikolaou, A. Charisiadis, G. Charalambidis, A. G. Coutsolelos, F. Odobel. Recent advances and insights in dye-sensitized NiO photocathodes for photovoltaic devices. *J. Mater. Chem. A*, **2017**, 5: 21077.
 - 19 B. O'Regan, M. Grätzel. A low-cost, high-efficiency solar cell based on dye-sensitized colloidal TiO₂ films. *Nature*, **1991**, 353: 737-740.
 - 20 P. Nejat, F. Jomehzadeh, M. M. Taheri, M. Gohari, M. Z. Abd. Majid. A global review of energy consumption, CO₂ emissions and policy in the residential sector (with an overview of the top ten CO₂ emitting countries). *Renewable and Sustainable Energy Reviews*, **2015**, 43: 843-862.
 - 21 J. Popp, Z. Lakner, M. Harangi-Rákos, M. Fári. The effect of bioenergy expansion: Food, energy, and environment. *Renewable and Sustainable Energy Reviews*, **2014**, 32: 559-578.
 - 22 R. F. Service. Is It Time to Shoot for the Sun? *Science*, **2005**, 309, 5734: 548-551.
 - 23 J. Potočník. Renewable Energy Sources and the Realities of Setting and Energy Agenda. *Science*, **2007**, 315, 5813: 810-811.
 - 24 S. E. Hosseini, M. A. Wahid. Hydrogen production from renewable and sustainable energy resources: Promising green energy carrier for clean development. *Renewable and Sustainable Energy Reviews*, **2016**, 57: 850-866.
 - 25 M. Hosenuzzaman, N. A. Rahim, J. Selvaraj, M. Hosenuzzaman, A. B. M. A. Malek, A. Nahar. Global prospects, progress, policies, and environmental impact of solar photovoltaic power generation. *Renewable and Sustainable Energy Reviews*, **2015**, 41: 284-297.
 - 26 A. Goepfert, M. Czaun, G. K. Surya Prakash, G. A. Olah. Air as the renewable carbon source of the future: an overview of CO₂ capture from the atmosphere. *Energy Environ. Sci.*, **2012**, 5: 7833-7853.
 - 27 Z. Yu, F. Li, L. C. Sun. Recent advances in dye-sensitized photoelectrochemical cells for solar hydrogen production based on molecular components. *Energy Environ. Sci.*, **2015**, 8: 760-775.
-

-
-
- 28 X. X. Zou, Y. Zhang. Nobel metal-free hydrogen evolution catalysts for water splitting. *Chem. Soc. Rev.*, **2015**, 44: 5148-5180.
- 29 Q. Schiermeier, J. Tollefson, T. Scully, A. Witze, O. Morton. Energy alternatives: Electricity without carbon. *Nature*, **2008**, 454: 816-823.
- 30 M. A. Green, K. Emery, Y. Hishikawa, W. Warta, E. D. Dunlop. Solar cell efficiency tables (Version 43). *Prog Photovolt Res Appl*, **2014**, 22, 1: 1-9.
- 31 J. Nelson. The physics of solar cells. *Imperial College Press: London*, **2003**.
- 32 G. Kopp, J. L. Lean. A new, lower value of total solar irradiance: Evidence and climate significance. *Geophysical Research Letters*, **2011**, 38, L01706.
- 33 G. Kopp, A. Fehlmann, W. Finsterle, D. Harber, K. Heuerman, R. Willson. Total solar irradiance data record accuracy and consistency improvements. *Metrologia*, **2012**, 49, 2.
- 34 G. Kopp, G. Lawrence, G. Rottman. The Total Irradiance Monitor (TIM): Science Results. *Springer, New York, NY*, **2005**: 129-139.
- 35 S. Mathew, A. Yella, P. Gao, R. Humphry-Baker, B. F. E. Curchod, N. Ashari-Astani, I. Tavernelli, U. Rothlisberger, M. K. Nazeeruddin, M. Grätzel. Dye-sensitized solar cells with 13% efficiency achieved through the molecular engineering of porphyrin sensitizers. *Nature Chemistry*, **2014**, 6: 242-247.
- 36 N. R. Thomson, C. J. Rodger, M. A. Clilverd. Daytime D region parameters from long-path VLF phase and amplitude. *Journal of Geophysical Research*, **2011**, 116, A11305.
- 37 A. R. Thompson, J. M. Moran, G. W. Swenson. Interferometry and Synthesis in Radio Astronomy, Second Edition. *Wiley-VCH Verlag GmbH*. **2007**.
- 38 Y. Chiba, A. Islam, Y. Watanabe, R. Komiya, N. Koide, L. Y. Han. Dye-sensitized Solar Cells with Conversion Efficiency of 11.1%. *Japanese Journal of Applied Physics*, **2006**, 45, 25: L638-L640.
- 39 <http://rredc.nrel.gov/solar/spectra/am1.5>.
- 40 Standard Tables for Reference Solar Spectral Irradiances: Direct Normal and Hemispherical on 37° Tilted Surface. *ASTM Standard G173*, **2012**
- 41 A. E. Becquerel. Recherches sur les effets de la radiation chimique de la lumière solaire, au moyen des courants électriques. *C. R. Acad. Sci.*, **1839**, 9: 145-149.
- 42 C. E. Fritts. On a new form of selenium cell, and some electrical discoveries made by its use. *Am J Sci.*, **1883**, 3, 26: 465-472.
- 43 M. Grundmann. The physics of Semiconductors: An Introduction Including Nanophysics and Applications. *Springer*, **2006**.
-
-

-
-
- 44 D. M. Chapin, C. S. Fuller, G. L. Pearson. An New Silicon p-n Junction Photocell for Converting Solar Radiation into Electrical Power. *Journal of Applied Physics*, **1954**, 25: 676-677.
 - 45 D. E. Carlson, C. R. Wronski. Amorphous silicon solar cell. *Appl. Phys. Lett.*, **1976**, 28: 671.
 - 46 J. Desilvestro, M. Grätzel, L. Kavan, J. Moser, J. Augustynski. Highly efficient sensitization of titanium dioxide. *J. Am. Chem. Soc.*, **1985**, 107, 10: 2988-2990.
 - 47 T. W. Hamann, R. A. Jensen, A. B. F. Martinson, H. V. Ryswyk, J. T. Hupp. Advancing beyond current generation dye-sensitized solar cells. *Energy Environ. Sci.*, **2008**, 1: 66-78.
 - 48 M. Pagliaro, G. Palmisano, R. Ciriminna, V. Loddo. Nanochemistry aspects of titania in dye-sensitized solar cells. *Energy Environ. Sci.*, **2009**, 2: 838-844.
 - 49 R. Jose, V. Thavasi, S. Ramakrishna. Metal Oxides for Dye-sensitized Solar Cells. *J. Am. Ceram. Soc.*, **2009**, 92: 289-301.
 - 50 M. F. Hohmann-Marriott, R. E. Blankenship. *Evolution of Photosynthesis. Annual Review of Plant Biology*. **2011**, 62: 548-515.
 - 51 J. Xiong, C. E. Bauer. Blankenship. *Complex Evolution of Photosynthesis. Annual Review of Plant Biology*. **2002**, 53: 503-521.
 - 52 M. I. H. Ansari, A. Qurashi, M. K. Nazeeruddin. Frontiers, opportunities, and challenges in perovskite solar cells: A critical review. *J. Photochem. Photobiol. C: Photochem. Rev.*, **2018**, 35: 1-24.
 - 53 G. J. Hedley, A. Ruseckas, I. D. W. Samuel. Light Harvesting for Organic Photovoltaics. *Chem. Rev.*, **2017**, 2, 117: 837-796.
 - 54 O. Ostroverkhova. Organic Optoelectronic Materials: Mechanisms and Applications. *Chem. Rev.*, **2016**, 2, 116: 13279-13412.
 - 55 T. M. Clarke, J. R. Durrant. Charge Photogeneration in Organic Solar Cells. *Chem. Rev.*, **2010**, 11, 110: 6736-6767.
 - 56 C. S. Ponseca Jr., P. Chábera, J. Uhlig, P. Persson, Villy Sundström. Ultrafast Electron Dynamics in Solar Energy Conversion. *Chem. Rev.*, **2017**, 16, 117: 10940-11024.
 - 57 D. Levi. National Renewable Energy Laboratory (NREL), Golden, CO, **2017**.
 - 58 A. V. Shah, J. Meier, E. Vallat-Sauvain, N. Wyrsh, U. Kroll, C. Droz, U. Graf. Material and solar cell research in microcrystalline silicon. *Sol. Energy Mater. Sol. Cells*, **2003**, 78, 1-4: 469-491.
 - 59 S. Y. Myong, S. W. Kwon, J. H. Kwak, K. S. Lim, J. M. Pearce, M. Konagai. Good
-
-

-
- Stability of Protocrystalline Silicon Multilayer Solar Cells Against Light Irradiation Originating from Vertically Regular Distribution of Isolated Nano-Sized Silicon Grains. *Photovoltaic Energy Conversion, Conference Record of the 2006 IEEE 4th World Conference on*, **2006**.
- 60 S. Y. Myong. Fast light-induced metastability and thermal recovery for protocrystalline silicon multilayers proved by sub-bandgap absorption spectra. *Solar Energy*, **2014**, 106: 43-47.
- 61 Fraunhofer Institute for Solar Energy Systems, ISE. Photovoltaics Report. *Fraunhofer*, **2017**.
- 62 S. R. Wenham, M. A. Green, M. E. Watt, R. Corkish. Applied Photovoltaics. *Earthscan*, **2007**.
- 63 M. A. Green, K. Emery, Y. Hishikawa, W. Warta, E. D. Dunlop. Solar cell efficiency tables (Version 43). *Prog Photovolt Res Appl*, **2017**, 25, 4: 333-334.
- 64 S. Singer. Photovoltaics: Getting Cheaper. *Eco Queen of Green*. **2007**.
- 65 R. Bernstein. A Shortage Hits Solar Power. *The Wall Street Journal*, **2006**.
- 66 <http://www.ensolar.com/directory/material/polysilicon>.
- 67 Y. Kolic, R. Gauthier, M. A. G. Perez, A. Sibai, J. C. Dupuy, P. Pinard, R. M’Ghaieth, H. Maaref. Electron powder ribbon polycrystalline silicon plates used for porous layer fabrication. *Thin Solid Films*, **1995**, 255, 1-2: 159-162.
- 68 O. A. O. Gassim. The Effect of Hydrogen Amorphous Silicon on the Optical Properties of Solar Cells. *International Journal of Science and Research*. **2017**, 6, 4: 1670-1675.
- 69 A. Luque, S. Hegedus. Handbook of Photovoltaic Science and Engineering (Second Edition). *John Wiley & Sons, Ltd*. **2011**.
- 70 M. Izu, T. Ellison. Roll-to-roll manufacturing of amorphous silicon alloy solar cells with in situ cell performance diagnostics. *Sol. Energy Mater. Sol. Cells*, **2003**, 78: 613-626.
- 71 S. Guha, J. Yang. Amorphous silicon alloy materials, cells and modules. *Proceedings 29th IEEE Photovoltaic Specialists Conference, New Orleans*, **2002**: 1070-1075.
- 72 A. H. Mahan, J. Carapella, B. P. Nelson, R. S. Crandall. Deposition of device quality, low H content amorphous silicon. *Journal of Applied Physics*, **1991**, 69: 6728-6730.
- 73 B. J. Yan, G. Z. Yue, X. X. Xu, J. Yang, S. Guha. High efficiency amorphous and nanocrystalline silicon solar cells. *Status Solidi A*, **2010**, 207, 3: 671-677.
- 74 S. Prasad. Optoelectronics: A Deep-Level LED. *Nature Materials*, **2003**, 2: 359–360.
- 75 H. Y. Liu, T. Wang, Q. Jiang, R. Hogg, F. Tutu, F. Pozzi, A. Seeds. Long-wavelength InAs/GaAs quantum-dot laser diode monolithically grown on Ge substrate. *Nature*
-

-
- Photonics*, **2011**, 5: 416-419.
- 76 S. Hu, C. Chi, K. T. Fountaine, M. Yao, H. A. Atwater, P. D. Dapkus, N. S. Lewis, C. W. Zhou. Optical, electrical, and solar energy-conversion properties of gallium arsenide nanowire-array photoanodes. *Energy Environ. Sci.*, **2013**, 6: 1879-1890.
- 77 L. Gao, Y. C. Cui, J. Wang, A. Cavalli, A. Standing, T. T. T. Vu, M. A. Verheijen, J. E. M. Haverkort, E. P. A. M. Bakkers, P. H. L. Notten. Photoelectrochemical hydrogen production on InP nanowire arrays with molybdenum sulfide electrocatalysts. *Nano Lett.*, **2014**, 14: 3715-3719.
- 78 J. Yoon, S. Jo, I. S. Chun, I. Jung, H. Kim, M. Meitl, E. Menard, X. L. Li, J. J. Coleman, U. Paik, J. A. Rogers. GaAs photovoltaics and optoelectronics using releasable multilayer epitaxial assemblies. *Nature*, **2010**, 465: 329-333.
- 79 D. C. Bobela, L. Gedvilas, M. Woodhouse, K. A. W. Horowitz, P. A. Basore. Economic competitiveness of III-V on silicon tandem one-sun photovoltaic solar modules in favorable future scenarios. *Prog. Photovoltaic*, **2017**, 25: 41-48.
- 80 M. Woodhouse, A. Goodrich, R. Margolis, T. L. James, M. Lokanc, R. Eggert. Supply-chain dynamics of tellurium, indium and gallium within the context of PV module manufacturing costs. *J. Photovoltaic*, **2013**, 3: 833-837.
- 81 M. Q. Yao, N. F. Huang, S. Cong, C. Chi, M. A. Seyed, Y. T. Lin, Y. Cao, M. L. Povinelli, P. D. Dapkus, C. W. Zhou. GaAs Nanowire Array Solar Cells with Axial p-i-n Junctions. *Nano Lett.*, **2014**, 14, 3293-3303.
- 82 D. V. Dam, N. J. J. V. Hoof, Y. C. Cui, P. J. V. Veldhoven, E. P. A. M. Bakkers, J. G. Rivas, J. E. M. Haverkort. High-Efficiency Nanowire Solar Cells with Omnidirectionally Enhanced Absorption Due to Self-Aligned Indium-Tin-Oxide Mie Scatterers. *ACS Nano*, **2016**, 10: 11414-11419.
- 83 T. S. Lay, M. Hong, J. Kwo, J. P. Mannaerts, W. H. Hung, D. J. Huang. Energy-band parameters at the GaAs- and GaN- Ga₂O₃(Gd₂O₃) interfaces. *Solid-State Electronics*, **2001**, 45, 9: 1679-1682.
- 84 B. M. Kayes, H. Nie, R. Twist, S. G. Spruytte, F. Reinhardt, I. C. Kizilyalli, G. S. Higashi. 27.6% conversion efficiency, a new record for single-junction solar cells under 1 sun illumination. *Proceedings of the 37th IEEE Photovoltaic Specialists Conference*, **2011**.
- 85 H. Welker. Semiconducting intermetallic compounds. *Physica*, **1954**, 20, 7-12: 893-909.
- 86 D. A. Jenny, J. J. Loferski, P. Rappaport. Photovoltaic Effect in GaAs p-n Junctions and Solar Energy Conversion. *Phys. Rev.*, **1956**, 101: 1208-1209.
- 87 Z. I. Alferov. Nobel Lecture: The double heterostructure concept and its applications in
-

-
- physics, electronics, and technology. *Rev. Mod. Phys.*, **2001**, 73: 767.
- 88 H. J. Hovel, J. M. Woodall. Ga_{1-x}Al_xAs-GaAs P-P-N heterojunction solar cells. *Journal of The Electrochemical Society*, **1973**, 120, 9: 1246-1252.
- 89 J. W. Woodall and H. J. Hovel. Outlooks for GaAs terrestrial photovoltaics. *Journal of Vacuum Science and Technology*. **1975**, 12, 1000.
- 90 R. R. King, D. C. Law, K. M. Edmondson, C. M. Fetzer, G. S. Kinsey, H. Yoon. 40% efficient metamorphic GaInP/GaInAs/Ge multijunction solar cells. *Applied Physics Letters*, **2007**, 90: 183516.
- 91 W. Gutera, J. Schöne, S. P. Philipps, M. Steiner, G. Siefer, A. Wekkeli, E. Welsler, E. Oliva, A. W. Bett, F. Dimroth. Current-matched triple-junction solar cell reaching 41.1% conversion efficiency under concentrated sunlight. *Appl. Phys. Lett.*, **2009**, 94: 223504.
- 92 A. W. Bett, F. Dimroth, W. Guter, R. Hoheisel, E. Oliva, S. P. Philipps, J. Schöne, G. Siefer, M. Steiner, A. Wekkeli, E. Welsler, M. Meusel, W. Köstler, G. Strobl, Fraunhofer ISE. Highest efficiency multi-junction solar cell for terrestrial and space applications. *24th European Photovoltaic Solar Energy Conference, Hamburg, Germany*, **2009**.
- 93 T. Takamoto, T. Agui, A. Yoshida, K. Nakaido, H. Juso, K. Sasaki, K. Nakamora, H. Yamaguchi, T. Kodama, H. Washio, M. Imaizumi, M. Takahashi. World's highest efficiency triple-junction solar cells fabricated by inverted layers transfer process. *Proceedings of the 35th IEEE Photovoltaic Specialists Conference, Hawaii, USA*, **2010**.
- 94 M. Yamaguchi, T. Takamoto, K. Araki, M. Imaizumi, N. Kojima, and Y. Ohshita. Present and Future of High Efficiency Multi-Junction Solar Cells. *Laser Applications to Photonic Applications, OSA*, **2011**: CMT5.
- 95 M. A. Green, Y. Hishikawa, E. D. Dunlop, D. H. Levi, J. Hohl-Ebinger, A. W. Y. Ho-Baillie. Solar cell efficiency tables (version 51). *Prog Photovolt Res Appl*, **2018**, 26: 3-12.
- 96 D. V. Shenai-Khatkhate, R. Goyette, R. L. DiCarlo, G. Dripps. Environment, health and safety issues for sources used in MOVPE growth of compound semiconductors. *Journal of Crystal Growth*, **2004**, 272, 1-4: 816-821.
- 97 K. Zweibel, J. Mason, V. Fthenakis. A Solar Grand Plan. *Scientific American*, **2008**.
- 98 D. A. Jenny, R. H. Bube. Semiconducting Cadmium Telluride. *Phys. Rev.*, **1954**, 96: 1190-1191.
- 99 R. H. Bube. Photoconductivity of the Sulfide, Selenide, and Telluride of Zinc or Cadmium. *Proceedings of the IRE*, **1955**, 43, 12: 1836-1850.
- 100 D. A. Cusano. CdTe solar cells and photovoltaic heterojunctions in II-VI compounds.
-

-
- Solid-State Electronics*, **1963**, 6, 3: 217-232.
- 101 B. Goldstein. Properties of Photovoltaic Films of CdTe. *Phys. Rev.*, **1958**, 109, 2: 601-603.
- 102 Y. A. Vodakov, G. A. Lomakina, G. P. Naumov, Y. P. Maslakovets. A P-N Junction photocell made of CdTe. *Soviet Physics, Solid State*, **1960**, 2, 1: 1.
- 103 A. Bosio, G. Rosa, N. Romeo. Past, present and future of the thin film CdTe/CdS solar cells. *Solar Energy*, **2018**, in press.
- 104 A. Morales-Acevedo. Physical basis for the design of CdTe/CdS thin film solar cells. *Solar Energy Materials & Solar Cells*, **2006**, 90: 678-685.
- 105 K. Durose, P. R. Edwards, D. P. Halliday. Materials aspects of CdTe/CdS solar cells. *Journal of Crystal Growth*, **1999**, 197: 733-742.
- 106 J. J. Loferski. Theoretical considerations governing the choice of the optimum semiconductor for photovoltaic solar energy conversion. *J. Appl. Phys.*, **1956**, 27, 7: 777-784.
- 107 D. Bonnet and H. Rabenhorst. CdS/CdTe thin film solar cells by DLTS. *J. Phys. Chem. Solids*, **1972**, 65, 11: 1817-1822.
- 108 C. Paorici, C. Pelosi, G. Zuccalli. Epitaxial growth of CdTe on CdS substrates. *Phys. Status Solidi (a)*, **1972**, 13, 1: 95-100.
- 109 C. Paorici, G. Attolini, C. Pelosi, G. Zuccalli. Chemical-transport properties of the Cd: Te: H: Cl: N system. *Journal of Crystal Growth*, **1973**, 18, 3: 289-293.
- 110 Y. S. Tyan, E. A. Perez-Alburne. Efficient thin-film CdS/CdTe solar cells. *16th IEEE photovoltaics specialists conference, San Diego, CA, USA*, **1982**: 794.
- 111 J. Britt, C. Ferekides. Thin-film CdS/CdTe solar cell with 15.8% efficiency. *Appl. Phys. Lett.*, **1993**, 62, 22: 2851-2852.
- 112 X. Z. Wu. High-efficiency polycrystalline CdTe thin-film solar cells. *Solar Energy*, **2004**, 77, 6: 803-814.
- 113 D. W. Niles, D. Waters, D. Rose. Chemical reactivity of CdCl₂ wet-deposited on CdTe films studied by X-ray photoelectron spectroscopy. *Appl. Surf. Sci.*, **1998**, 136, 3: 221-229.
- 114 X. Li, R. Ribelin, Y. Mahathongdy, D. Albin, R. Dhere, D. Rose, S. Asher, H. Moutinho, P. Sheldon. The effect of high-resistance SnO₂ on CdS/CdTe device performance. *AIP Conf. Proceed*, **1999**, 462: 230-235.
- 115 T. Minami. New n-type transparent conducting oxides. *MRS Bull.*, **2000**, 25, 8: 38-44.
- 116 M. D. G. Potter, D. P. Halliday, M. Cousins, K. Durose. A study of the effects of varying
-

- cadmium chloride treatment on the luminescent properties of CdTe/CdS thin film solar cells. *Thin Solid Films*, **2000**, 361: 248–252.
- 117 A. Romeo, D. L. Bätzner, H. Zogg, C. Vignali, A. N. Tiwari. Influence of CdS growth process on structural and photovoltaic properties of CdTe/CdS solar cells. *Sol. Energy Mater. Sol. Cells*, **2001**, 67, 1: 311–321.
- 118 T. Potlog, L. Ghimpu, P. Gashin, A. Pudov, T. Nagle, J. Sites. Influence of annealing in different chlorides on the photovoltaic parameters of CdS/CdTe solar cells. *Sol. Energy Mater. Sol. Cells*, **2003**, 80, 3: 327–334.
- 119 T. Minami. Transparent conducting oxide semiconductors for transparent electrodes. *Semicond. Sci. Technol.*, **2005**, 20, 4: S35.
- 120 R. Mamazza, U. Balasabramanian, S. Gayam, S. Bapanapalli, L. Nemani, M. Jayabal, H. Zhao, D. L. Morel, C. S. Ferekides. The influence of various front-contact materials on the performance of CdTe solar cells. *Photovoltaic Specialists Conference 2005, Conference Record of the Thirty-First IEEE*, **2005**: 283–286.
- 121 N. Romeo, A. Bosio, A. Romeo. An innovative process suitable to produce high efficiency CdTe/CdS thin-film modules. *Sol. Energy Mater. Sol. Cells*, **2010**, 94, 1: 2–7.
- 122 A. Kumar, C. Zhou. The race to replace tin-doped indium oxide: which material will win? *ACS Nano*, **2010**, 4, 1: 11–14.
- 123 V. M. Nikale, S. S. Shinde, C. H. Bhosale, K. Y. Rajpure. Physical properties of spray deposited CdTe thin films: PEC performance. *J. Semicond.*, **2011**, 32, 3: 033001.
- 124 N. R. Paudel, K. A. Wieland, A. D. Compaan. Ultrathin CdS/CdTe solar cells by sputtering. *Sol. Energy Mater. Sol. Cells*, **2012**, 105: 109–112.
- 125 L. Kranz, C. Gretener, J. Perrenoud, R. Schmitt, F. Pianezzi, F. L. Mattina, P. Blösch, E. Cheah, A. Chirilă, C. M. Fella, H. Hagendorfer, T. Jäger, S. Nishiwaki, A. R. Uhl, S. Buecheler, A. N. Tiwari. Doping of polycrystalline CdTe for high-efficiency solar cells on flexible metal foil. *Nat. Commun.*, **2013**, 4: 2306.
- 126 J. D. Major, R. E. Treharne, L. J. Phillips, K. Durose. A low-cost non-toxic post-growth activation step for CdTe solar cells. *Nature*, **2014**, 511, 7509: 334.
- 127 B. L. Williams, J. D. Major, L. Bowen, W. Keuning, M. Creatore, K. Durose. A comparative study of the effects of nontoxic chloride treatments on CdTe solar cell microstructure and stoichiometry. *Adv. Energy Mater.*, **2015**, 5, 21: 1500554-1500563.
- 128 G. Kartopu, A. J. Clayton, W. S. Brooks, S. D. Hodgson, V. Barrioz, A. Maertens, D. A. Lamb, S. J. Irvine. Effect of window layer composition in Cd_{1-x}Zn_xS/CdTe solar cells. *Prog. Photovoltaics Res. Appl.*, **2014**, 22, 1: 18–23.

-
-
- 129 J. D. Poplawsky. Record-breaking voltages. *Nat. Energy*, **2016**, 16021: 1–2.
- 130 J. D. Poplawsky, W. Guo, N. Paudel, A. Ng, K. More, D. Leonard, Y. Yan. Structural and compositional dependence of the CdTe_xSe_{1-x} alloy layer photoactivity in CdTe-based solar cells. *Nat. Commun.*, **2016**, 7, 12537: 1–9.
- 131 A. A. Ojo, I. M. Dharmadasa. 15.3% efficient graded band gap solar cells fabricated using electroplated CdS and CdTe thin films. *Sol. Energy*, **2016**, 136: 10–14.
- 132 S. Menga, Y. Yanb. Band gap optimization of CdTeSe thin-film solar cells. *J. Adv. Phys.*, **2016**, 12, 2: 4213-4218.
- 133 A. Polman, M. Knight, E. C. Garnett, B. Ehrler, W. C. Sinke. Photovoltaic materials: present efficiencies and future challenges. *Science*, **2016**, 352, 6283: aad4424.
- 134 M. Tuteja, P. Koirala, V. Palekis, S. MacLaren, C. S. Ferekides, R. W. Collins, A. Rockett, A. A. Angus. Direct observation of CdCl₂ treatment induced grain boundary carrier depletion in CdTe solar cells using scanning probe microwave reflectivity based capacitance measurements. *J. Phys. Chem. C*, **2016**, 120: 7020–7024.
- 135 A. Kanevce, M. O. Reese, T. M. Barnes, A. S. Jensen, W. K. Metzger. The roles of carrier concentration and interface, bulk, and grain-boundary recombination for 25% efficient CdTe solar cells. *J. Appl. Phys.*, **2017**, 121: 214506.
- 136 W. Shockley, H. J. Queisser. Detailed balance limit of efficiency of p-n junction solar cells. *J. Appl. Phys.*, **1961**, 32, 3: 510–519.
- 137 P. Singh, N. M. Ravindra. Temperature dependence of solar cell performance - an analysis. *Sol. Energy Mater. Sol. Cells*, **2012**, 101: 36-45.
- 138 M. A. Green, K. Emery, Y. Hishikawa, W. Warta. Solar cell efficiency tables (Version 50). *Prog Photovolt Res Appl*, **2017**, 25, 7: 668-676.
- 139 S. Niki, M. Contreras, I. Repins, M. Powalla, K. Kushiya, S. Ishizuka, K. Matsubara. CIGS absorbers and processes. *Prog. Photovolt: Res. Appl.*, **2010**, 18: 453-466.
- 140 L. Kronik, D. Cahen, H. W. Schock. Effects of sodium on polycrystalline Cu(In, Ga)Se₂ and its solar cell performance. *Adv. Mater.*, **1998**, 10, 1: 31-36.
- 141 T. Tinoco, C. Rincón, M. Quintero, G. S. Pérez. Phase diagram and optical energy gaps for CuIn_yGa_{1-y}Se₂ alloys. *Phys. Stat. Sol. (a)*, **1991**, 124: 427-434.
- 142 T. Feuerer, P. Reinhard, E. Avancini, B. Bissig, J. Löckinger, P. Fuchs, R. Carron, T. P. Weiss, J. Perrenoud, S. Stutterheim, S. Buecheler, A. N. Tiwari. Progress in thin film CIGS photovoltaics - Research and development, manufacturing, and applications. *Prog. Photocolt: Res. Appl.*, **2017**, 25: 645-667.
- 143 L. L. Yan, Y. M. Bai, B. Yang, N. F. Chen, Z. A. Tan, T. Hayat, A. Alsaedi. Extending
-
-

- absorption of near-infrared wavelength range for high efficiency CIGS solar cell via adjusting energy band. *Current Applied Physics*, **2018**, in press.
- 144 B. J. Stanbery. Copper indium selenides and related materials for photovoltaic devices. *Critical Reviews in Solid State and Materials Sciences*, **2002**, 27, 2: 73-117.
- 145 J. C. Mikkelsen. Ternary phase relations of the chalcopyrite compound CuGaSe₂. *Journal of Electronic Materials*, **1981**, 10, 3: 541-558.
- 146 M. A. Green, K. Emery, Y. Hishikawa, W. Warta. Solar cell efficiency tables (Version 33). *Prog Photovolt Res Appl*, **2009**, 17, 1: 85-94.
- 147 E. Parthé. Crystal chemistry of tetrahedral structures. *Gordon and Breach, New York*, **1964**.
- 148 J. L. Shay, J. H. Wernick. Ternary Chalcopyrite Semiconductors: Growth, Electronic Properties, and Applications. *Pergamon*, **1974**.
- 149 B. R. Pamplin, T. Kiyosawa, K. Masumoto. Ternary chalcopyrite compounds. *Prog. Crystal Growth Charact.*, **1979**, 1, 4: 331-387.
- 150 S. Wagner, J. L. Shay, P. Migliorato. CuInSe₂/CdS heterojunction photovoltaic detectors. *Appl. Phys. Lett.*, **1974**, 25: 434-435.
- 151 J. L. Shay, S. Wagner, H. M. Kasper. Efficient CuInSe₂/CdS solar cells. *Appl. Phys. Lett.*, **1975**, 27: 89-90.
- 152 L. L. Kazmerski, F. R. White, G. K. Morgan. Thin-film CuInSe₂/CdS heterojunction solar cells. *Appl. Phys. Lett.*, **1976**, 29: 268-270.
- 153 L. L. Kazmerski, F. R. White, M.S. Ayyagari, Y. J. Juang, R. P. Patterson. Growth and characterization of thin-film compound semiconductor photovoltaic heterojunctions. *Journal of Vacuum Science and Technology*, **1977**, 14, 1: 65-8.
- 154 J. J. Loferski, J. Shewchun, B. Roessler, R. Beaulieu, J. Piekoszewski, M. Gorska, G. Chapman. Investigation of thin film cadmium sulfide/mixed copper ternary heterojunction photovoltaic cells. *Proceedings of 13th IEEE PVSC*, **1978**: 190-194.
- 155 R. A. Mickelsen, W. S. Chen. Development of a 9.4% efficient thin-film CuInSe₂/CdS solar cell. *Proceedings of 15th IEEE PVSC*, **1981**: 800-804
- 156 R. A. Mickelsen, W. S. Chen. Polycrystalline thin-film CuInSe₂/sub 2/ solar cells. *Conf. Rec. IEEE Photovoltaic Spec. Conf.*, **1982**.
- 157 R. A. Mickelsen, W. S. Chen, Y. R. Hsiao, V. E. Lowe. Polycrystalline thin-film CuInSe₂/CdZnS solar cells. *IEEE Transactions on Electron Devices*, **1984**, 31, 5: 542-546.
- 158 J. M. Stewart, W. S. Chen, W. E. Devaney, R. A. Mickelsen. Thin film polycrystalline

- CuIn_{1-x}Ga_xSe₂ solar cells. *Proceedings of 7th International Conference on Ternary and Multinary Compounds, Snowmass, Colorado, 1986*.
- 159 R. W. Birkmire. Compound polycrystalline solar cells: Recent progress and Y2K perspective. *Sol. Energy Mater. Sol. Cells*, **2011**, 65: 17-28.
- 160 W. S. Chen, J. M. Stewart, B. J. Stanbery, W. E. Devaney, R. A. Mickelsen. Development of thin film polycrystalline CuIn_{1-x}Ga_xSe₂ solar cells. *Proceedings of 19th IEEE PVSC*, **1987**: 1445-1447.
- 161 T. Walter, M. Ruckh, K. O. Velthaus, H. Schock. Solar cells based on CuIn(S, Se)₂ - A promising alternative. *Proceedings of 11th European PVSEC*, **1992**: 124-127.
- 162 A. Rockett, R. W. Birkmire. CuInSe₂ for photovoltaic applications. *J. Appl. Phys.*, **1991**, 70: R81-R97.
- 163 L. Stolt, J. Hedström, J. Kessler, M. Ruckh, K. Velthaus, H. Schock. ZnO/CdS/CuInSe₂ thin-film solar cells with improved performance. *Appl. Phys. Lett.*, **1993**, 62: 597-599.
- 164 D. Tarrant, J. Ermer. I-III-VI/ sub 2/ multinary solar cells based on CuInSe/ sub 2/. *Proc. of 23th IEEE PVSC*, **1993**: 372-378.
- 165 P. Jackson, D. Hariskos, E. Lotter, S. Paetel, R. Wuerz, R. Menner, W. Wischmann, M. Powalla. New world record efficiency for Cu(In,Ga)Se₂ thin-film solar cells beyond 20%. *Prog. Photovolt: Res. Appl.*, **2011**, 19: 894-897.
- 166 A. M. Gabor, J. R. Tuttle, D. S. Albin, M. A. Contreras, R. Noufi. High-efficiency CuIn_xGa_{1-x}Se₂ solar cells made from (In_xGa_{1-x})₂Se₃ precursor films. *Appl. Phys. Lett.*, **1994**, 65:198-200.
- 167 M. A. Contreras, B. Egaas, K. Ramanathan, J. Hiltner, A. Swartzlander, F. Hasoon, R. Noufi. Progress toward 20% efficiency in Cu(In, Ga)Se₂ polycrystalline thin-film solar cells. *Prog. Photovolt: Res. Appl.*, **1999**, 7: 311-316.
- 168 K. Ramanathan, M. A. Contreras, C. L. Perkins, S. Asher, F. S. Hasoon, J. Keane, D. Young, M. Romero, W. Metzger, R. Noufi, J. Ward, A. Duda. Properties of 19.2% efficiency ZnO/CdS/CuInGaSe₂ thin-film solar cells. *Prog. Photovolt: Res. Appl.*, **2003**, 11: 225-230.
- 169 I. Repins, M. A. Contreras, B. Egaas, C. Dehart, J. Scharf, C. L. Perkins, B. To, R. Noufi. 19.9%-efficient ZnO/CdS/CuInGaSe₂ solar cell with 81.2% fill factor. *Prog. Photovolt: Res. Appl.*, **2008**, 16: 235-230.
- 170 L. M. Mansfield, R. Noufi, C. P. Muzzillo, C. DeHart, K. Bowers, B. To, J. W. Pankow, R. C. Reedy, K. Ramanathan. Enhanced performance in Cu(In,Ga)Se₂ solar cells fabricated by the two-step selenization process with a potassium fluoride postdeposition treatment.

-
- IEEE Journal of Photovoltaics*, **2014**, 4, 6: 1650-1654.
- 171 J. S. Ward, B. Egaas, R. Noufi, M. Contreras, K. Ramanathan, C. Osterwald, K. Emery. Cu(In,Ga)Se₂ solar cells measured under low flux optical concentration. *Proceedings of 40th IEEE PVSC*, **2014**: 2934-2937.
- 172 P. Jackson, R. Wuerz, D. Hariskos, E. Lotter, W. Witte, and M. Powalla. Effects of heavy alkali elements in Cu(In,Ga)Se₂ solar cells with efficiencies up to 22.6%. *Phys. Status Solidi RRL*, **2016**, 10: 583-586.
- 173 J. S. Ward, K. Ramanathan, F. S. Hasoon, T. J. Coutts, J. Keane, M. A. Contreras, T. Moriarty, R. Noufi. A 21.5% efficient Cu(In,Ga)Se₂ thin-film concentrator solar cell. *Prog. Photovolt. Res. Appl.*, **2002**, 10, 1: 41-46.
- 174 M. Powalla, B. Dimmler. Process development of high performance CIGS modules for mass production. *Thin Solid Films*, **2001**, 387, 1-2: 251-256.
- 175 M. Powalla, B. Dimmler. Scaling up issues of CIGS solar cells. *Thin Solid Films*, **2000**, 361-362: 540-546.
- 176 M. Powalla, M. Cemernijak, J. Eberhardt, F. Kessler, R. Kniese, H. D. Mohring, B. Dimmler. Large-area CIGS modules: Pilot line production and new developments. *Sol. Energy Mater. Sol. Cells*, **2006**, 90, 18-19: 3158-3164.
- 177 A. E. Delahoy, D. Chorobski, F. Ziobro, Z. J. Kiss. Baseline process development for pilot line production of CIGS modules. *AIP Conference Proceedings*, **1999**, 462: 144-151.
- 178 P. Reinhard, F. Pianezzi, B. Bissig, A. Chirila, P. Blosch, S. Nishiwaki, S. Buecheler, A. N. Tiwari. Cu(In,Ga)Se thin-film solar cells and modules - a boost in efficiency due to Potassium. *IEEE Journal of Photovoltaics*, **2015**, 5, 2: 656-663.
- 179 S. Aksu, S. Pethe, A. Kleiman-Shwarsctein, S. Kundu, M. Pinarbasi. Recent advances in electroplating based CIGS solar cell fabrication. *38th IEEE Photovoltaic Specialists Conference (PVSC)*, **2012**: 003092-003097.
- 180 M. Powalla, W. Witte, P. Jackson, S. Paetel, E. Lotter, R. Wuerz, F. Kessler, C. Tschamber, W. Hempel, D. Hariskos, R. Menner, A. Bauer, S. Spiering, E. Ahlswede, T. M. Friedlmeier, D. Blázquez-Sánchez, I. Klugius, W. Wischmann. CIGS Cells and Modules With High Efficiency on Glass and Flexible Substrates. *IEEE Journal of Photovoltaics*, **2014**, 4, 1: 440-446.
- 181 K. Moriwaki, M. Nomoto, S. Yuuya, N. Murakami, T. Ohgoh, K. Yamane, S. Ishizuka, S. Niki. Monolithically integrated flexible Cu(In,Ga)Se₂ solar cells and submodules using newly developed structure metal foil substrate with a dielectric layer. *Sol. Energy Mater.*
-

- Sol. Cells*, **2013**, 112: 106-111.
- 182 K. Otte, L. Makhova, A. Braun, I. Konovalov. Flexible Cu(In,Ga)Se₂ thin-film solar cells for space application. *Thin Solid Films*, **2006**, 511-512: 613-622.
- 183 P. Reinhard, A. Chirilă, P. Blösch, F. Pianezzi, S. Nishiwaki, S. Buecheler, A. N. Tiwari. Review of Progress Toward 20% Efficiency Flexible CIGS Solar Cells and Manufacturing Issues of Solar Modules. *IEEE Journal of Photovoltaics*, **2013**, 3, 1: 572-580.
- 184 Z. Guo, Y. Chen, N. L. Lu. Multifunctional Nanocomposites for Energy and Environmental Applications. *Wiley-VCH Verlag GmbH & Co. KGaA*, **2018**.
- 185 M. Grätzel. Dye-sensitized solar cells. *Journal of Photochemistry and Photobiology C: Photochemistry Reviews*, **2003**, 4: 145-153.
- 186 V. Sugathan, E. John, K. Sudhakar. Recent improvements in dye sensitized solar cells: A review. *Renewable and Sustainable Energy Reviews*, **2015**, 52: 54-64.
- 187 C. Lee, R. Y. Lin, L. Lin, C. Li, T. Chu, S. Sun, J. T. Lin, K. Ho. Recent progress in organic sensitizers for dye-sensitized solar cells. *RSC ADV.*, 2015, 5: 23810-23825.
- 188 J. H. Wu, Z. Lan, S. C. Hao, P. J. Li, J. M. Lin, M. L. Huang, L. Q. Fang, Y. F. Huang. Progress on the electrolytes for dye-sensitized solar cells. *Pure and Applied Chemistry*, **2009**, 80, 2241-2258.
- 189 C. Sima, C. Grigoriu, S. Antohe. Comparison of the dye-sensitized solar cells performances based on transparent conductive ITO and FTO. *Thin Solid Films*, **2010**, 519, 2: 595-597.
- 190 J. L. Xu, K. Fan, W. Y. Shi, K. Li, T. Y. Peng. Application of ZnO micro- flowers as scattering layer for ZnO-based dye-sensitized solar cells with enhanced conversion efficiency. *Solar Energy*, **2014**, 101: 150-159.
- 191 K. Song, I. Jang, D. Song, Y. S. Kang, S. Oh. Echinoid-like particles with high surface area for dye-sensitized solar cells. *Solar Energy*, **2014**, 105: 218-224.
- 192 M. R. Golobostanfard, H. Abdizadeh. Hierarchical porous titania/carbon nanotube nanocomposite photoanode synthesized by controlled phase separation for dye sensitized solar cell. *Sol. Energy Mater. Sol. Cells*, **2014**, 120: 295-302.
- 193 S. Satapathi, H. S. Gill, S. Das, L. Li, L. Samuelson, M. J. Green, J. Kumar. Performance enhancement of dye-sensitized solar cells by incorporating graphene sheets of various sizes. *Applied Surface Science*, **2014**, 314, 30: 638-641.
- 194 J. J. Fan, Z. Z. Li, W. Y. Zhou, Y. C. Miao, Y. J. Zhang, J. H. Hu, G. S. Shao. Dye-sensitized solar cells based on TiO₂ nanoparticles/nanobelts double layered film with

- improved photovoltaic performance. *Applied Surface Science*, **2014**, 319, 30: 75-82.
- 195 M. Zi, M. Zhu, L. Chen, H. M. Wei, X. P. Yang, B. Q. Cao. ZnO photoanodes with different morphologies grown by electrochemical deposition and their dye-sensitized solar cell properties. *Ceramics International*, **2014**, 40, 6: 7965-7970.
- 196 S. B. Zhu, L. M. Shan, X. Tian, X. Y. Zheng, D. Sun, X. B. Liu, L. Wang, Z. W. Zhou. Hydrothermal synthesis of oriented ZnO nanorod-nanosheets hierarchical architecture on zinc foil as flexible photoanodes for dye-sensitized solar cells. *Ceramics International*, **2014**, 40, 8, A: 11663-11670.
- 197 F. Xu, Y. Wu, X. Y. Zhang, Z. Y. Gao, K. Jiang. Controllable synthesis of rutile TiO₂ nanorod array, nanoflowers and microspheres directly on fluorine-doped tin oxide for dye-sensitized solar cells. *Micro & Nano Letters*, **2012**, 7, 8: 826-80.
- 198 L. Cojocar, C. Olivier, T. Toupance, E. Sellier, L. Hirsch. Size and shape fine-tuning of SnO₂ nanoparticles for highly efficient and stable dye-sensitized solar cells. *J. Mater. Chem. A*, **2013**, 1: 13789-13799.
- 199 L. M. Gonçalves, V. D. Z. Bermudez, H. A. Ribeiro, A. M. Mendes. Dye-sensitized solar cells: A safe bet for the future. *Energy Environ. Sci.*, **2008**, 1: 655-667.
- 200 M. Grätzel. Recent Advances in Sensitized Mesoscopic Solar Cells. *Acc. Chem. Res.*, **2009**, 42, 11: 1788-1798.
- 201 M. Winter, R. J. Brodd. What Are Batteries, Fuel Cells, and Supercapacitors? *Chem. Rev.*, **2004**, 104, 10: 4245-4270.
- 202 A. F. Nogueira, C. Longo, M. A. D. Paoli. Polymers in dye sensitized solar cells: overview and perspectives. *Coord. Chem. Rev.*, **2004**, 248, 13-14: 1455-1468.
- 203 S. Ardo, G. J. Meyer. Photodriven heterogeneous charge transfer with transition-metal compounds anchored to TiO₂ semiconductor surfaces. *Chem. Soc. Rev.*, **2009**, 38: 115-164.
- 204 N. Papageorgiou, W. F. Maier, M. Grätzel. An Iodine/Triiodide Reduction Electrocatalyst for Aqueous and Organic Media. *J. Electrochem. Soc.*, **1997**, 144, 3: 876-884.
- 205 A. Hauch, A. Georg. Diffusion in the electrolyte and charge-transfer reaction at the platinum electrode in dye-sensitized solar cells. *Electrochimica Acta*, **2001**, 46, 22: 3457-3466.
- 206 E. Olsen, G. Hagen, S. E. Lindquist. Dissolution of platinum in methoxy propionitrile containing LiI/I₂. *Sol. Energy Mater. Sol. Cells*, **2000**, 63, 3: 267-273.
- 207 A. Iefanova, J. Nepal, P. Poudel, D. Davoux, U. Gautam, V. Mallam, Q. Q. Qiao, B. Logue, M. F. Baroughi. Transparent platinum counter electrode for efficient

- semi-transparent dye-sensitized solar cells. *Thin Solid Films*, **2014**, 562: 578-584.
- 208 M. Wang, Y. Zhao, S. Yuan, Z. Y. Wang, X. Ran, M. H. Zhang, L. Y. Shi, D. D. Li. High electro-catalytic counter electrode based on three-dimensional conductive grid for dye-sensitized solar cell. *Chemical Engineering Journal*, **2014**, 255: 424-430.
- 209 T. N. Murakami, S. Ito, Q. Wang, M. K. Nazeeruddin, T. Bessho, I. Cesar, P. Liska, R. Humphry-Baker, P. Comte, P. Péchy, M. Grätzel. Highly Efficient Dye-Sensitized Solar Cells Based on Carbon Black Counter Electrodes. *J. Electrochem. Soc.*, **2006**, 153, 12: A2255-A2261.
- 210 E. Ramasamy, W. J. Lee, D. Y. Lee, J. S. Song. Nanocarbon counterelectrode for dye sensitized solar cells. *Appl. Phys. Lett.*, **2007**, 90: 173103.
- 211 K. Imoto, K. Takahashi, T. Yamaguchi, T. Komura, J. Nakamura, K. Murata. High-performance carbon counter electrode for dye-sensitized solar cells. *Sol. Energy Mater. Sol. Cells*, **2003**, 79, 4: 459-469.
- 212 S. Kazuharu, Y. Makoto, K. Mikio, Y. Shozo. Application of Carbon Nanotubes to Counter Electrodes of Dye-sensitized Solar Cells. *Chem. Lett.*, **2003**, 32, 1: 28-29.
- 213 L. Bay, K. West, B. Winther-Jensen, T. Jacobsen. Electrochemical reaction rates in a dye-sensitised solar cell - the iodide/tri-iodide redox system. *Sol. Energy Mater. Sol. Cells*, **2006**, 90, 3: 341-351.
- 214 Y. Saito, T. Kitamura, Y. Wada, S. Yanagida. Application of Poly (3,4-ethylenedioxythiophene) to Counter Electrode in Dye-Sensitized Solar Cells. *Chem. Lett.*, **2002**, 31, 10: 1060-1061.
- 215 Y. Saito, W. Kubo, T. Kitamura, Y. Wada, S. Yanagida. I⁻/I₃⁻ redox reaction behavior on poly(3,4-ethylenedioxythiophene) counter electrode in dye-sensitized solar cell. *Journal of Photochemistry and Photobiology A: Chemistry*, **2004**, 164, 1-3: 153-157.
- 216 M. K. Wang, A. M. Anghel, B. Marsan, N. C. Ha, N. Pootrakulchote, S. M. Zakeeruddin, M. Grätzel. CoS Supersedes Pt as Efficient Electrocatalyst for Triiodide Reduction in Dye-Sensitized Solar Cells. *J. Am. Chem. Soc.*, **2009**, 131, 44: 15976-15977.
- 217 L. B. Li, S. S. Zhang, Z. C. Yang, E. E. S. Berthold, W. Chen. Recent advances of flexible perovskite solar cells. *Journal of Energy Chemistry*, **2018**, in press.
- 218 Q. Wali, N. K. Elumalai, Y. Iqbal, A. Uddin, R. Jose. Tandem perovskite solar cells. *Renewable and Sustainable Energy Reviews*, **2018**, 84: 89-110.
- 219 W. J. Yin, J. H. Yang, J. Kang, Y. F. Yan, S. H. Wei. Halide perovskite materials for solar cells: a theoretical review. *J. Mater. Chem. A*, **2015**, 3: 8926-8942.
- 220 I. Msequita, L. Andrade, A. Mendes. Perovskite solar cells: Materials, configurations and

-
- stability. *Renewable and Sustainable Energy Reviews*, **2018**, 82: 2471-2489.
- 221 M. K. Assadi, S. Bakhoda, R. Saidur, H. Hanaei. Recent progress in perovskite solar cells. *Renewable and Sustainable Energy Reviews*, **2018**, 81: 2812-2822.
- 222 M. A. Green, A. Ho-Baillie, H. J. Snaith. The emergence of perovskite solar cells. *Nature Photonics*, **2014**, 8: 506-514.
- 223 J. Sunarso, S. S. Hashim, N. Zhu, W. Zhou. Perovskite oxides applications in high temperature oxygen separation, solid oxide fuel cell and membrane reactor: A review. *Progress in Energy and Combustion Science*, **2017**, 61: 55-57.
- 224 X. L. Yang, X. W. Zhang, J. X. Deng, Z. M. Chu, Q. Jiang, J. H. Meng, P. Y. Wang, L. Q. Zhang, Z. G. Yin, J. B. You. Efficient green light-emitting diodes based on quasi-two-dimensional composition and phase engineered perovskite with surface passivation. *Nature Communications*, **2018**, 9: 570.
- 225 G. E. Eperon, M. T. Hörantner, H. J. Snaith. Metal halide perovskite tandem and multiple-junction photovoltaics. *Nature Reviews Chemistry*, **2017**, 1: 0095.
- 226 J. C. Yu, J. A. Hong, E. D. Jung, D. B. Kim, S. Baek, S. Lee, S. Cho, S. S. Park, K. J. Choi, M. H. Song. Highly efficient and stable inverted perovskite solar cell employing PEDOT:GO composite layer as a hole transport layer. *Scientific Reports*, **2018**, 8: 1070.
- 227 M. Adnan, J. K. Lee. All Sequential Dip-Coating Processed Perovskite Layers from an Aqueous Lead Precursor for High Efficiency Perovskite Solar Cells. *Scientific Reports*, **2018**, 8: 2168.
- 228 C. H. Ng, T. S. Ripolles, K. Hamada, S. H. Teo, H. N. Lim, J. Bisquert, S. Hayase. Tunable Open Circuit Voltage by Engineering Inorganic Cesium Lead Bromide/Iodide Perovskite Solar Cells. *Scientific Reports*, **2018**, 8: 2482.
- 229 S. N. Yun, Y. Qin, A. R. Uhl, V. Nikolaos, M. Yin, D. D. Li, X. G. Han, A. Hagfeldt. New-Generation Integrated Devices based on Dye-Sensitized and Perovskite Solar Cells. *Energy Environ. Sci.*, **2018**, in press.
- 230 A. Kojima, K. Teshima, Y. Shirai, T. Miyasaka. Organometal Halide Perovskites as Visible-Light Sensitizers for Photovoltaic Cells. *J. Am. Chem. Soc.*, **2009**, 131, 17: 6050–6051.
- 231 W. S. Yang, B.-W. Park, E. H. Jung, N. J. Jeon, Y. C. Kim, D. U. Lee, S. S. Shin, J. Seo, E. K. Kim, J. H. Noh, S. I. Seok. Iodide management in formamidinium-lead-halide-based perovskite layers for efficient solar cells. *Science*, **2017**, 356, 6345: 1376-1379.
- 232 M. Grätzel. The light and shade of perovskite solar cells. *Nature Materials*, **2014**, 13: 838-842.
-

-
- 233 C. Li, X. Lu, W. Ding, L. Feng, Y. Gao, Z. Guo. Formability of ABX₃ (X= F, Cl, Br, I) halide perovskites. *Acta Cryst.*, **2008**, B64: 702-707.
- 234 N. K. McKinnon, D. C. Reeves, M. H. Akabas. 5-HT₃ receptor ion size selectivity is a property of the transmembrane channel, not the cytoplasmic vestibule portals. *Journal of General Physiology*, **2011**, 138, 4: 453-466.
- 235 J. Im, J. Chung, S. Kim, N. Park. Synthesis, structure, and photovoltaic property of a nanocrystalline 2H perovskite-type novel sensitizer (CH₃CH₂NH₃)PbI₃. *Nanoscale Res Lett.*, **2012**, 7: 353-359.
- 236 T. M. Koh, K. F., Y. N. Fang, S. Chen, T. C. Sum, N. Mathews, S. G. Mhaisalkar, P. P. Boix, T. Baikie. Formamidinium-Containing Metal-Halide: An Alternative Material for Near-IR Absorption Perovskite Solar Cells. *J. Phys. Chem. C*, **2014**, 118, 30: 16458-16462.
- 237 G. E. Eperon, S. D. Stranks, C. Menelaou, M. B. Johnston, L. M. Herza, H. J. Snaith. Formamidinium lead trihalide: a broadly tunable perovskite for efficient planar heterojunction solar cells. *Energy Environ. Sci.*, **2014**, 7: 982-988.
- 238 S. P. Pang, H. Hu, J. L. Zhang, S. L. Lyu, Y. M. Yu, F. Wei, T. S. Qin, H. X. Xu, Z. H. Liu, G. L. Cui. NH₂CH=NH₂PbI₃: An Alternative Organolead Iodide Perovskite Sensitizer for Mesoscopic Solar Cells. *Chem. Mater.*, **2014**, 26, 3: 1485-1491.
- 239 J. B. Xia, S. Yanagida. Strategy to improve the performance of dye-sensitized solar cells: Interface engineering principle. *Solar Energy*, **2011**, 85, 12: 3143-3159.
- 240 J. J. Shi, X. Xu, D. M. Li, Q. B. Meng. Interfaces in Perovskite Solar Cells. *Small*, **2015**, 11: 2472-2486.
- 241 M. Grätzel, R. A. J. Janssen, D. B. Mitzi, E. H. Sargent. Materials interface engineering for solution-processed photovoltaics. *Nature*, **2012**, 488: 304-312.
- 242 Z. Ye, L. S. Sun. Recent Progress on Hole-Transporting Materials for Emerging Organometal Halide Perovskite Solar Cells. *Adv. Energy Mater.*, **2015**, 5: 1500213.
- 243 D. B. Mitzi, S. Wang, C. A. Feild, C. A. Chess, A. M. Guloy. Conducting Layered Organic-inorganic Halides Containing <110> - Oriented Perovskite Sheets. *Science*, **1995**, 267, 5203: 1473-1476.
- 244 D. B. Mitzi, K. Chondroudis, C. R. Kagan. Organic-inorganic electronics. *IBM Journal of Research and Development*, **2001**, 45, 1: 29-45.
- 245 A. Kojima, K. Teshima, T. Miyasaka, Y. Shirai. Novel photoelectrochemical cell with mesoscopic electrodes sensitized by lead-halide compounds (2). *210th ECS Meeting*, **2006**, abstract # 397.
-

-
- 246 J. Im, C. Lee, J. Lee, S. Park, N. Park. 6.5% efficient perovskite quantum-dot-sensitized solar cell. *Nanoscale*, **2011**, 3: 4088-4093.
- 247 H. Kim, C. Lee, J. Im, K. Lee, T. Moehl, A. Marchioro, S. Moon, R. Humphry-Baker, J. Yum, J. E. Moser, M. Grätzel, N. Park. Lead iodide perovskite sensitized all-solid-state submicron thin film mesoscopic solar cell with efficiency exceeding 9%. *Sci. Rep.* **2**, **2012**: 591.
- 248 M. M. Lee, J. Teuscher, T. Miyasaka, T. N. Murakami, H. J. Snaith. Efficient Hybrid Solar Cells Based on Meso-Superstructured Organometal Halide Perovskites. *Science*, **2012**, 338: 643-647.
- 249 M. Z. Liu, M. B. Johnston, H. J. Snaith. Efficient planar heterojunction perovskite solar cells by vapour deposition. *Nature*, **2013**, 501: 395-398.
- 250 H. Zhou, Q. Chen, G. Li, S. Luo, T. Song, H. Duan, Z. Hong, J. You, Y. Liu, Y. Yang. Interface engineering of highly efficient perovskite solar cells. *Science*, **2014**, 345, 6196: 542-546.
- 251 W. S. Yang, J. H. Noh, N. J. Jeon, Y. C. Kim, S. Ryu, J. Seo, S. I. Seok. High-performance photovoltaic perovskite layers fabricated through intramolecular exchange. *Science*, **2015**, 348, 6240: 1234-1237.
- 252 S. S. Shin, E. J. Yeom, W. S. Yang, S. Hur, M. G. Kim, J. Im, J. Seo, J. H. Noh, S. I. Seok. Colloidally prepared La-doped BaSnO₃ electrodes for efficient, photostable perovskite solar cells. *Science*, **2017**, 356, 6334: 167-171.
- 253 D. Q. Bi, C. Y. Yi, J. S. Luo, J. Décoppet, F. Zhang, S. M. Zakeeruddin, X. Li, A. Hagfeldt, M. Grätzel. Polymer-templated nucleation and crystal growth of perovskite films for solar cells with efficiency greater than 21%. *Nature Energy*, **2016**, 1: 16142.
- 254 W. J. Yin, T. Shi, Y. Yan. Unique Properties of Halide Perovskites as Possible Origins of the Superior Solar Cell Performance. *Adv. Mater.*, **2014**, 26: 4653-4658.
- 255 Q. Chen, N. D. Marco, Y. Yang, T. Song, C. Chen, H. Zhao, Z. Hong, H. Zhou, Y. Yang. Under the spotlight: The organic-inorganic hybrid halide perovskite for optoelectronic applications. *Nanotoday*, **2015**, 10, 3: 355-396.
- 256 D. M. Bagnall, M. Boreland. Photovoltaic technologies. *Energy Policy*, **2008**, 36, 12: 4390-4396.
- 257 K. Kakiage, Y. Aoyama, T. Yano, K. Oya, J. Fujisawa, M. Hanaya. Highly-efficient dye-sensitized solar cells with collaborative sensitization by silyl-anchor and carboxy-anchor dyes. *Chem. Commun.*, **2015**, 51: 15894-15897.
- 258 E. K. Putseiko, A. N. Terenin. Photosensitization of the internal photoeffect in zinc oxide
-

- and other semiconductors by adsorbed dyes. *Zhurnal Fizicheskoi Khimii*, **1949**, 23: 676.
- 259 H. Gerischer, M. E. Michel-Beyerle, F. Rebentrost, H. Tributsch. Sensitization of charge injection into semiconductors with large band gap. *Electrochimica Acta*, **1968**, 13, 6: 1509-1515.
- 260 A. Fujishima, K. Honda. Electrochemical Photolysis of Water at a Semiconductor Electrode. *Nature*, **1972**, 238: 37-38.
- 261 M. Matsumura, Y. Nomura, H. Tsubomura. Dye-sensitization on the Photocurrent at Zinc Oxide Electrode in Aqueous Electrolyte Solution. *Bulletin of the Chemical Society of Japan*, **1977**, 50, 10: 2533-2537.
- 262 N. Alonso V., M. Beley, P. Chartier. Dye sensitization of ceramic semiconducting electrodes for photoelectrochemical conversion. *Revue Phys. Appl.*, **1981**, 16: 5-10.
- 263 J. Desilvestro, M. Grätzel, L. Kavan, J. Moser, J. Augustynski. Highly efficient sensitization of titanium dioxide. *J. Am. Chem. Soc.*, **1985**, 107, 10: 2988-2990.
- 264 P. P. Kumavat, P. Sonar, D. S. Dalal. An overview on basics of organic and dye sensitized solar cells, their mechanism and recent improvements. *Renewable and Sustainable Energy Reviews*, **2017**, 78: 1262-1287.
- 265 T. W. Hamann, J. W. Ondersma. Dye-sensitized solar cell redox shuttles. *Energy Environ. Sci.*, **2011**, 4: 370-381.
- 266 D. Kuang, C. Klein, S. Ito, J. E. Moser, R. Humphry-Baker, N. Evans, F. Durrant, C. Grätzel, S. M. Zakeeruddin, M. Grätzel. High-Efficiency and Stable Mesoscopic Dye-Sensitized Solar Cells Based on a High Molar Extinction Coefficient Ruthenium Sensitizer and Nonvolatile Electrolyte. *Adv. Mater.*, **2007**, 19: 1133-1137.
- 267 D. Kuang, S. Ito, B. Wenger, C. Klein, J. E. Moser, R. Humphry-Baker, S. M. Zakeeruddin, M. Grätzel. High Molar Extinction Coefficient Heteroleptic Ruthenium Complexes for Thin Film Dye-Sensitized Solar Cells. *J. Am. Chem. Soc.*, **2006**, 128, 12: 4146-4154.
- 268 M. Z. H. Khan, M. R. Al-Mamun, P. K. Halder, M. A. Aziz. Performance improvement of modified dye-sensitized solar cells. *Renewable and Sustainable Energy Reviews*, **2017**, 71: 602-617.
- 269 J. Gong, K. Sumathy, Q. Qiao, Z. Zhou. Review on dye-sensitized solar cells (DSSCs): Advanced techniques and research trends. *Renewable and Sustainable Energy Reviews*, **2017**, 68: 234-246.
- 270 L. M. Peter, K. G. U. Wijayantha. Electron transport and back reaction in dye sensitised nanocrystalline photovoltaic cells. *Electrochimica Acta*, **2000**, 45, 28: 4543-4551.

-
- 271 K. Fredin, J. Nissfolk, A. Hagfeldt. Brownian dynamics simulations of electrons and ions in mesoporous films. *Sol. Energy Mater. Sol. Cells*, **2005**, 86, 2: 283-297.
- 272 L. M. Peter. Characterization and Modeling of Dye-Sensitized Solar Cells. *J. Phys. Chem. C*, **2007**, 111: 6601-6612.
- 273 A. Listorti, B. O'Regan, J. R. Durrant. Electron Transfer Dynamics in Dye-Sensitized Solar Cells. *Chem. Mater.*, **2011**, 23: 3381-3399.
- 274 A. Yella, H.-W. Lee, H. N. Tsao, C. Yi, A. K. Chandiran, M. Nazeeruddin, E. W. Diau, C. Yeh, S. M. Zakeeruddin, M. Grätzel. Porphyrin-Sensitized Solar Cells with Cobalt (II/III)-Based Redox Electrolyte Exceed 12 Percent Efficiency. *Science*, **2011**, 334, 6056: 629-634.
- 275 H. Yu, S. Zhang, H. Zhao, G. Will, P. Liu. An efficient and low-cost TiO₂ compact layer for performance improvement of dye-sensitized solar cells. *Electrochimica Acta*, **2009**, 54, 4: 1319-1324.
- 276 P. J. Cameron, L. M. Peter. Characterization of Titanium Dioxide Blocking Layers in Dye-Sensitized Nanocrystalline Solar Cells. *J. Phys. Chem. B*, **2003**, 107, 51: 14394-14400.
- 277 S. Y. Huang, G. Schlichthörl, A. J. Nozik, M. Grätzel, A. J. Frank. Charge Recombination in Dye-Sensitized Nanocrystalline TiO₂ Solar Cells. *J. Phys. Chem. B*, **1997**, 101, 14: 2576-2582.
- 278 A. Hagfeldt, G. Boschloo, H. Lindström, E. Figgemeier, A. Holmberg, V. Aranyos, E. Magnusson, L. Malmqvist. A system approach to molecular solar cells. *Coordination Chemistry Reviews*, **2004**, 248, 13-14: 1501-1509.
- 279 A. J. Bard, L. R. Faulkner. *Electrochemical Methods: Fundamentals and Applications*, Second Edition. *John Wiley & Sons, Inc.: New York*, **2001**.
- 280 S. A. H. Dr., S. Handa, K. Peter, E. P. Dr., M. T. Dr., J. R. D. Dr. Supermolecular Control of Charge Transfer in Dye-Sensitized Nanocrystalline TiO₂ Films: Towards a Quantitative Structure-Function Relationship. *Angewandte Chemie International Edition*, **2005**, 44, 35: 5740-5744.
- 281 D. Kuciauskas, M. S. Freund, H. B. Gray, J. R. Winkler, N. S. Lewis. Electron Transfer Dynamics in Nanocrystalline Titanium Dioxide Solar Cells Sensitized with Ruthenium or Osmium Polypyridyl Complexes. *J. Phys. Chem. B*, **2001**, 105, 2: 392-403.
- 282 J. N. Clifford, E. Palomares, Md. K. Nazeeruddin, M. Grätzel, J. Nelson, X. Li, N. J. Long, J. R. Durrant. Molecular Control of Recombination Dynamics in Dye-Sensitized Nanocrystalline TiO₂ Films: Free Energy vs Distance Dependence. *J. Am. Chem. Soc.*,
-

- 2004, 126, 16: 5225-5233.
- 283 C. Kleverlaan, M. Alebbi, R. Argazzi, C. A. Bignozzi, G. M. Hasselmann, G. J. Meyer. Molecular Rectification by a Bimetallic Ru-Os Compound Anchored to Nanocrystalline TiO₂. *Inorg. Chem.*, **2000**, 39, 7: 1342-1343.
- 284 J. Wu, Z. Lan, J. Lin, M. Huang, Y. Huang, L. Fan, G. Luo, Y. Lin, Y. Xie, Y. Wei. Counter electrodes in dye-sensitized solar cells. *Chemical Society Reviews*, **2017**, 46, 11: 5975-6023.
- 285 J. N. D. Freitas, A. D. S. Gonçalves, M.-A. D. Paoli, J. R. Durrant, A. F. Nogueira. The role of gel electrolyte composition in the kinetics and performance of dye-sensitized solar cells. *Electrochimica Acta*, **2008**, 53, 24: 7166-7172.
- 286 P. Yadav, K. Pandey, B. Tripathi, P. V. V. Jayaweera, S. Kaneko, M. Kumar. Electroanalytical investigation of the losses during interfacial charge transport in dye-sensitized solar cell. *Solar Energy*, **2016**, 129: 207-216.
- 287 D. Zhang, M. Ye, X. Wen, N. Zhang, C. Lin. Electrochemical methods for the characterization and interfacial study of dye-sensitized solar cell. *Science Bulletin*, **2015**, 60, 9: 850-863.
- 288 B. Tripathi, P. Yadav, M. Kumar. Charge transfer and recombination kinetics in dye-sensitized solar cell using static and dynamic electrical characterization techniques. *Solar Energy*, **2014**, 108: 107-116.
- 289 W. Gao, M. Liang, Y. Tan, M. Wang, Z. Sun, S. Xue. New triarylamine sensitizers for high efficiency dye-sensitized solar cells: Recombination kinetics of cobalt(III) complexes at titania/dye interface. *Journal of Power Sources*, **2015**, 283: 260-269.
- 290 Z. Yang. Fundamental studies of nanoarchitected dye-sensitized solar cells. *Northern Illinois University, ProQuest Dissertations Publishing*, **2011**: 3473119.
- 291 M. Grätzel, J. R. Durrant. Chapter 9: Dye- And Perovskite-Sensitised Mesoscopic Solar Cells. *Clean Electricity From Photovoltaics: 2nd*, **2015**: 413-452.
- 292 G. Schmitz. Kinetics and mechanism of the iodate-iodide reaction and other related reactions. *Phys. Chem. Chem. Phys.*, **1999**, 1: 1909-1914.
- 293 H. Song, H. Rao, X. Zhong. Recent advances in electrolytes for quantum dot-sensitized solar cells. *J. Mater. Chem. A*, **2018**, Advance Article.
- 294 Y. Fu, S. Ng, G. Qiu, T. Hung, C. L. Wu, C. Lee. A redox-controlled electrolyte for plasmonic enhanced dye-sensitized solar cells. *Nanoscale*, **2017**, 9: 10940-10947.
- 295 Z. Yu, N. Vlachopoulos, M. Gorlov, L. Kloo. Liquid electrolytes for dye-sensitized solar cells. *Dalton Trans.*, **2011**, 40: 10289-10303.

-
- 296 D. Fitzmaurice. Using spectroscopy to probe the band energetics of transparent nanocrystalline semiconductor films. *Sol. Energy Mater. Sol. Cells*, **1994**, 32, 3:289-305.
- 297 R. Memming. Electron Transfer Theories. *Semiconductor Electrochemistry, 2nd Edition*, **2015**.
- 298 L. M. Peter. Dye-sensitized nanocrystalline solar cells. *Phys. Chem. Chem. Phys.*, **2007**, 9, 2630-2642.
- 299 P. Wang, B. Wenger, R. Humphry-Baker, J.-E. Moser, J. Teuscher, W. Kantlehner, J. Mezger, E. V. Stoyanov, S. M. Zakeeruddin, M. Grätzel. Charge Separation and Efficient Light Energy Conversion in Sensitized Mesoscopic Solar Cells Based on Binary Ionic Liquids. *J. Am. Chem. Soc.*, **2005**, 127, 18: 6850-6856.
- 300 M. D. Archer, A. J. Nozik. Nanostructured And Photoelectrochemical Systems For Solar Photon Conversion. *Imperial College Press: London*, **2008**.
- 301 R. Katoh, A. Furube, A. V. Barzykin, H. Arakawa, M. Tachiya. Kinetics and mechanism of electron injection and charge recombination in dye-sensitized nanocrystalline semiconductors. *Coordination Chemistry Reviews*, **2004**, 248, 13-14: 1196-1213.
- 302 K. Hara, T. Sato, R. Katoh, A. Furube, Y. Ohga, A. Shinpo, S. Suga, K. Sayama, H. Sugihara, H. Arakawa. Molecular Design of Coumarin Dyes for Efficient Dye-Sensitized Solar Cells. *J. Phys. Chem. B*, **2003**, 107, 2: 597-606.
- 303 B. Wenger, M. Grätzel, J.-E. Moser. Rationale for Kinetic Heterogeneity of Ultrafast Light-Induced Electron Transfer from Ru(II) Complex Sensitizers to Nanocrystalline TiO₂. *J. Am. Chem. Soc.*, **2005**, 127, 35: 12150-12151.
- 304 G. Zanotti, N. Angelini, S. Notarantonio, A. M. Paoletti, G. Pennesi, G. Rossi, A. Lembo, D. Colonna, A. D. Carlo, A. Reale, T. M. Brown, G. Calogero. Bridged Phthalocyanine Systems for Sensitization of Nanocrystalline TiO₂ Films. *International Journal of Photoenergy*, **2010**, 2010: No.268035.
- 305 H. Lu, C. Tsai, W. Yen, C. Hsieh, C. Lee, C. Yeh, E. W. Diau. Control of Dye Aggregation and Electron Injection for Highly Efficient Porphyrin Sensitizers Adsorbed on Semiconductor Films with Varying Ratios of Coadsorbate. *J. Phys. Chem. C*, **2009**, 113, 49: 20990-20997.
- 306 M. Hilgendorff, V. Sundström. Dynamics of Electron Injection and Recombination of Dye-Sensitized TiO₂ Particles. *J. Phys. Chem. B*, **1998**, 102, 51: 10505-10514.
- 307 R. Katoh, A. Furube, T. Yoshihara, K. Hara, G. Fujihashi, S. Takano, S. Murata, H. Arakawa, M. Tachiya. Efficiencies of Electron Injection from Excited N3 Dye into Nanocrystalline Semiconductor (ZrO₂, TiO₂, ZnO, Nb₂O₅, SnO₂, In₂O₃) Films. *J. Phys.*
-

- Chem. B*, **2004**, 108, 15: 4818-4822.
- 308 S. E. Koops, B. C. O'Regan, P. R. F. Barnes, J. R. Durrant. Parameters. Influencing the Efficiency of Electron Injection in Dye-Sensitized Solar Cells. *J. Am. Chem. Soc.*, **2009**, 131, 13: 4808-4818.
- 309 C. Bauer, G. Boschloo, E. Mukhtar, A. Hagfeldt. Electron Injection and Recombination in Ru(dcbpy)₂(NCS)₂ Sensitized Nanostructured ZnO. *J. Phys. Chem. B*, **2001**, 105, 24: 5585-5588.
- 310 F. E. Lytle, D. M. Hercules. Luminescence of tris (2,2'-bipyridine) ruthenium(II) dichloride. *J. Am. Chem. Soc.*, **1969**, 91, 2: 253-257.
- 311 S. Yoon, P. Kukura, C. M. Stuart, R. A. Mathies. Direct observation of the ultrafast intersystem crossing in tris(2,2'-bipyridine)ruthenium(II) using femtosecond stimulated Raman spectroscopy. *Molecular Physics*, **2006**, 104, 8: 1275-1282.
- 312 J. N. Demas, D. G. Taylor. On the "intersystem crossing" yields in ruthenium(II) and osmium(II) photosensitizers. *Inorg. Chem.*, **1979**, 18, 11: 3177-3179.
- 313 K. J. Morris, M. S. Roach, W. Xu, J. N. Demas, B. A. DeGraff. Luminescence Lifetime Standards for the Nanosecond to Microsecond Range and Oxygen Quenching of Ruthenium(II) Complexes. *Anal. Chem.*, **2007**, 79, 24: 9310-9314.
- 314 N. A. Anderson, T. Lian. Ultrafast electron transfer at the molecule-semiconductor nanoparticle interface. *Annu. Rev. Phys. Chem.*, **2005**, 56: 491-519.
- 315 B. C. O'Regan, K. Bakker, J. Kroeze, H. Smit, P. Sommeling, J. R. Durrant. Measuring Charge Transport from Transient Photovoltage Rise Times. A New Tool To Investigate Electron Transport in Nanoparticle Films. *J. Phys. Chem. B*, **2006**, 110, 34: 17155-17160.
- 316 C. A. Kelly, F. Farzad, D. W. Thompson, J. M. Stipkala, G. J. Meyer. Cation-Controlled Interfacial Charge Injection in Sensitized Nanocrystalline TiO₂. *Langmuir*, **1999**, 15, 20: 7047-7054.
- 317 J. B. Asbury, N. A. Anderson, E. Hao, X. Ai, T. Lian. Parameters Affecting Electron Injection Dynamics from Ruthenium Dyes to Titanium Dioxide Nanocrystalline Thin Film. *J. Phys. Chem. B*, **2003**, 107, 30: 7376-7386.
- 318 D. F. Watson, G. J. Meyer. Cation effects in nanocrystalline solar cells. *Coord. Chem. Rev.*, **2004**, 248: 1391-1406.
- 319 Y. Tachibana, S. A. Haque, I. P. Mercer, J. E. Moser, D. R. Klug, J. R. Durrant. Modulation of the Rate of Electron Injection in Dye-Sensitized Nanocrystalline TiO₂ Films by Externally Applied Bias. *J. Phys. Chem. B*, **2001**, 105, 31: 7424-7431.
- 320 A. N. M. Green, E. Palomares, S. A. Haque, J. M. Kroon, J. R. Durrant. Charge Transport

- versus Recombination in Dye-Sensitized Solar Cells Employing Nanocrystalline TiO₂ and SnO₂ Films. *J. Phys. Chem. B*, **2005**, 109, 25: 12525-12533.
- 321 L. Peter. "Sticky Electrons" Transport and Interfacial Transfer of Electrons in the Dye-Sensitized Solar Cell. *Acc. Chem. Res.*, **2009**, 42, 11: 1839-1847.
- 322 P. R. F. Barnes, B. C. O'Regan. Electron Recombination Kinetics and the Analysis of Collection Efficiency and Diffusion Length Measurements in Dye Sensitized Solar Cells. *J. Phys. Chem. C*, **2010**, 114, 44: 19134-19140.
- 323 A. J. Morris, G. J. Meyer. TiO₂ Surface Functionalization to Control the Density of States. *J. Phys. Chem. C*, **2008**, 112, 46: 18224-18231.
- 324 K. Hara, Z. Wang, T. Sato, A. Furube, R. Katoh, H. Sugihara, Y. Dan-oh, C. Kasada, A. Shinpo, S. Suga. Oligothiophene-Containing Coumarin Dyes for Efficient Dye-Sensitized Solar Cells. *J. Phys. Chem. B*, **2005**, 109, 32: 15476-15482.
- 325 J. Kallioinen, G. Benkő, V. Sundström, J. E. I. Korppi-Tommola, A. P. Yartsev. Electron Transfer from the Singlet and Triplet Excited States of Ru(dcbpy)₂(NCS)₂ into Nanocrystalline TiO₂ Thin Films. *J. Phys. Chem. B*, **2002**, 106, 17: 4396-4404.
- 326 J. B. Asbury, E. Hao, Y. Wang, H. N. Ghosh, T. Lian. Ultrafast Electron Transfer Dynamics from Molecular Adsorbates to Semiconductor Nanocrystalline Thin Films. *J. Phys. Chem. B*, **2001**, 105, 20: 4545-4557.
- 327 S. Pelet, M. Grätzel, J.-E. Moser. Femtosecond Dynamics of Interfacial and Intermolecular Electron Transfer at Eosin-Sensitized Metal Oxide Nanoparticles. *J. Phys. Chem. B*, **2003**, 107, 14: 3215-3224.
- 328 N. Koide, L. Han. Measuring methods of cell performance of dye-sensitized solar cells. *Review of Scientific Instruments*, **2004**, 75, 9: 2828-2831.
- 329 M. K. El-Adawi, I. A. Al-Nuaim. A method to determine the solar cell series resistance from a single I-V. Characteristic curve considering its shunt resistance-new approach. *Vacuum*, **2001**, 64, 1: 33-36.
- 330 K. Bouzidi, M. Chegaar, A. Bouhemadou. Solar cells parameters evaluation considering the series and shunt resistance. *Sol. Energy Mater. Sol. Cells*, **2007**, 91, 18: 1647-1651.
- 331 Z. Lan, J. Wu, D. Wang, S. Hao, J. Lin, Y. Huang. Quasi-solid-state dye-sensitized solar cells based on a sol-gel organic-inorganic composite electrolyte containing an organic iodide salt. *Solar Energy*, **2007**, 81, 1: 117-122.
- 332 E. Stathatos, P. Lianos, S. M. Zakeeruddin, P. Liska, M. Grätzel. A Quasi-Solid-State Dye-Sensitized Solar Cell Based on a Sol-Gel Nanocomposite Electrolyte Containing Ionic Liquid. *Chem. Mater.*, **2003**, 15, 9: 1825-1829.

-
-
- 333 C. H. Yoon, R. Vittal, J. Lee, W.-S. Chae, K.-J. Kim. Enhanced performance of a dye-sensitized solar cell with an electrodeposited-platinum counter electrode. *Electrochimica Acta*, **2008**, 53, 6: 2890-2896.
- 334 A. Hauch, A. Georg. Diffusion in the electrolyte and charge-transfer reaction at the platinum electrode in dye-sensitized solar cells. *Electrochimica Acta*, **2001**, 46, 22: 3457-3466.
- 335 D. O. Wipf, E. W. Kristensen, M. R. Deakin, R. M. Wightman. Fast-scan cyclic voltammetry as a method to measure rapid heterogeneous electron-transfer kinetics. *Anal. Chem.*, **1988**, 60, 4: 306-310.
- 336 R. S. Nicholson. Theory and Application of Cyclic Voltammetry for Measurement of Electrode Reaction Kinetics. *Anal. Chem.*, **1965**, 37, 11: 1351-1355.
- 337 J. V. D. Lagemaat, N.-G. Park, A. J. Frank. Influence of Electrical Potential Distribution, Charge Transport, and Recombination on the Photopotential and Photocurrent Conversion Efficiency of Dye-Sensitized Nanocrystalline TiO₂ Solar Cells: A Study by Electrical Impedance and Optical Modulation Techniques. *J. Phys. Chem. B*, **2000**, 104, 9: 2044-2052.
- 338 F. Fabregat-Santiago, J. Bisquert, L. Cevey, P. Chen, M. Wang, S. M. Zakeeruddin, Michael Grätzel. Electron Transport and Recombination in Solid-State Dye Solar Cell with Spiro-OMeTAD as Hole Conductor. *J. Am. Chem. Soc.*, **2009**, 131, 2: 558-562.
- 339 L. Han, N. Koide, Y. Chiba, A. Islam, R. Komiya, N. Fuke, A. Fukui, R. Yamanaka. Improvement of efficiency of dye-sensitized solar cells by reduction of internal resistance. *Appl. Phys. Lett.*, **2005**, 86: 213501.
- 340 F. Fabregat-Santiago, J. Bisquert, G. Garcia-Belmonte, G. Boschloo, A. Hagfeldt. Influence of electrolyte in transport and recombination in dye-sensitized solar cells studied by impedance spectroscopy. *Sol. Energy Mater. Sol. Cells*, **2005**, 87, 1-4: 117-131.
- 341 Brian O'Regan, M. Grätzel, D. Fitzmaurice. Optical electrochemistry I: steady-state spectroscopy of conduction-band electrons in a metal oxide semiconductor electrode. *Chem. Phys. Lett.*, **1991**, 183, 1-2: 89-93.
- 342 G. Redmond, D. Fitzmaurice. Spectroscopic determination of flatband potentials for polycrystalline titania electrodes in nonaqueous solvents. *J. Phys. Chem.*, **1993**, 97, 7: 1426-1430.
- 343 U. B. Cappel, E. A. Gibson, A. Hagfeldt, G. Boschloo. Dye Regeneration by Spiro-MeOTAD in Solid State Dye-Sensitized Solar Cells Studied by Photoinduced
-
-

- Absorption Spectroscopy and Spectroelectrochemistry. *J. Phys. Chem. C*, **2009**, 113, 15: 6275-6281.
- 344 C. Hsieh, H. Lu, C. Chiu, C. Lee, S. Chuang, C. Mai, W. Yen, S. Hsu, E. W. Diau, C. Yeh. Synthesis and characterization of porphyrin sensitizers with various electron-donating substituents for highly efficient dye-sensitized solar cells. *J. Mater. Chem.*, **2010**, 20: 1127-1134.
- 345 Y. Diamant, S. Chappel, S. G. Chen, O. Melamed, A. Zaban. Core-shell nanoporous electrode for dye sensitized solar cells: the effect of shell characteristics on the electronic properties of the electrode. *Coord. Chem. Rev.*, **2004**, 248: 1271-1276.
- 346 G. A. Parks. The Isoelectric Points of Solid Oxides, Solid Hydroxides, and Aqueous Hydroxo Complex Systems. *Chem. Rev.*, **1965**, 65, 2: 177-198.
- 347 M. K. I. Senevirathna, P. K. D. D. P. Pitigala, E. V. A. Premalal, K. Tennakone, G. R. A. Kumara, A. Konno. Stability of the SnO₂/MgO dye-sensitized photoelectrochemical solar cell. *Sol. Energy Mater. Sol. Cells*, **2007**, 91, 6: 544-547.
- 348 M. Ye, X. Wen, M. Wang, J. Iocozzia, N. Zhang, C. Lin, Z. Lin. Recent advances in dye-sensitized solar cells: from photoanodes, sensitizers and electrolytes to counter electrodes. *Materials Today*, **2015**, 18, 3: 155-162.
- 349 U. Sulaemana, A. Z. Abdullah. The way forward for the modification of dye-sensitized solar cell towards better power conversion efficiency. *Renewable and Sustainable Energy Reviews*, **2017**, 74: 438-452.
- 350 Q. Zhang, T. P. Chou, B. Russo, S. A. Jenekhe, G. Cao. Polydisperse Aggregates of ZnO Nanocrystallites: A Method for Energy - Conversion - Efficiency Enhancement in Dye-Sensitized Solar Cells. *Adv. Funct. Mater.*, **2008**, 18:1654-1660.
- 351 S. Zhu, L. Shan, X. Chen, L. He, J. Chen, M. Jiang, X. Xie, Z. Zhou. Hierarchical ZnO architectures consisting of nanorods and nanosheets prepared via a solution route for photovoltaic enhancement in dye-sensitized solar cells. *RSC Adv.*, **2013**, 3: 2910-2916.
- 352 A. H. G. Niaki, A. M. Bakhshayesh, M. R. Mohammadi. Double-layer dye-sensitized solar cells based on Zn-doped TiO₂ transparent and light scattering layers: Improving electron injection and light scattering effect. *Solar Energy*, **2014**, 103: 210-222.
- 353 K. Park, Q. Zhang, B. B. Garcia, X. Zhou, Y. Jeong, G. Cao. Effect of an Ultrathin TiO₂ Layer Coated on Submicrometer-Sized ZnO Nanocrystallite Aggregates by Atomic Layer Deposition on the Performance of Dye-Sensitized Solar Cells. *Adv. Mater.*, **2010**, 22, 21: 2329-2332.
- 354 H. Li, J. Bai, B. Feng, X. Lu, J. Weng, C. Jiang, J. Wang. Dye-sensitized solar cells with a

- tri-layer ZnO photo-electrode. *Journal of Alloys and Compounds*, **2013**, 578: 507-511.
- 355 X. C. Lau, C. Desai, S. Mitra. Functionalized nanodiamond as a charge transporter in organic solar cells. *Solar Energy*, **2013**, 91: 204-211.
- 356 J. Xia, N. Masaki, K. Jiang, S. Yanagida. Sputtered Nb₂O₅ as a Novel Blocking Layer at Conducting Glass/TiO₂ Interfaces in Dye-Sensitized Ionic Liquid Solar Cells. *J. Phys. Chem. C*, **2007**, 111, 22: 8092-8097.
- 357 H. Yan, J. Wang, B. Feng, K. Duan, J. Weng. Graphene and Ag nanowires co-modified photoanodes for high-efficiency dye-sensitized solar cells. *Solar Energy*, **2015**, 122: 966-975.
- 358 Y. Gao, P. Fang, F. Chen, Y. Liu, Z. Liu, D. Wang, Y. Dai. Enhancement of stability of N-doped TiO₂ photocatalysts with Ag loading. *Applied Surface Science*, **2013**, 265: 796-801.
- 359 S. P. Lim, N. M. Huang, H. N. Lim, M. Mazhar. Aerosol assisted chemical vapour deposited (AACVD) of TiO₂ thin film as compact layer for dye-sensitised solar cell. *Ceramics International*, **2014**, 40, 6: 8045-8052.
- 360 D. M. Schaadt, B. Feng, E. T. Yu. Enhanced semiconductor optical absorption via surface plasmon excitation in metal nanoparticles. *Appl. Phys. Lett.*, **2005**, 86: 63106.
- 361 U. Mehmood, S. Rahman, K. Harrabi, I. A. Hussein, B. V. S. Reddy. Recent Advances in Dye Sensitized Solar Cells. *Adv. Mater. Sci. Eng.*, **2014**, 2014: 1-12.
- 362 S. Ito, N. C. Ha, G. Rothenberger, P. Liska, P. Comte, S. M. Zakeeruddin, P. Péchy, M. K. Nazeeruddina, M. Grätzel. High-efficiency (7.2%) flexible dye-sensitized solar cells with Ti-metal substrate for nanocrystalline-TiO₂ photoanode. *Chem. Commun.*, **2006**, 0: 4004-4006.
- 363 Y. Jun, J. Kim, M.G. Kang. A study of stainless steel-based dye-sensitized solar cells and modules. *Sol. Energy Mater. Sol. Cells*, **2007**, 91, 9: 779-784.
- 364 K. Lee, L. Lin, V. Suryanarayanan, C. Wu. Titanium dioxide coated on titanium/stainless steel foil as photoanode for high efficiency flexible dye-sensitized solar cells. *Journal of Power Sources*, **2014**, 269: 789-794.
- 365 S. Sheehan, P. K. Surolia, O. Byrne, S. Garner, P. Cimo, X. Li, D. P. Dowling, K. R. Thampi. Flexible glass substrate based dye sensitized solar cells. *Sol. Energy Mater. Sol. Cells*, **2015**, 132: 237-244.
- 366 A. M. Bakhshayesh, N. Bakhshayesh. Enhanced performance of dye-sensitized solar cells aided by Sr,Cr co-doped TiO₂ xerogel films made of uniform spheres. *Journal of Colloid and Interface Science*, **2015**, 460: 18-28.

-
-
- 367 A. M. Bakhshayesh, N. Bakhshayesh. Enhanced short circuit current density of dye-sensitized solar cells aided by Sr,V co-doped TiO₂ particles. *Materials Science in Semiconductor Processing*, **2016**, 41: 92-101.
- 368 K. Hongsith, N. Hongsith, D. Wongratanaphisan, A. Gardchareon, S. Phadungdhitidhada, P. Singjai, S. Choopun. Sparking deposited ZnO nanoparticles as double-layered photoelectrode in ZnO dye-sensitized solar cell. *Thin Solid Films*, **2013**, 539: 260-266.
- 369 H. Abdullah, A. Omar, M. A. Yarmo, S. Shaari, M. R. Taha. Structural and morphological studies of zinc oxide incorporating single-walled carbon nanotubes as a nanocomposite thin film. *J. Mater. Sci. Mater. Electron.*, **2013**, 24, 9: 3603-3610.
- 370 A. Omar, H. Abdullah, M. A. Yarmo, S. Shaari, M. R. Taha. Morphological and electron transport studies in ZnO dye-sensitized solar cells incorporating multi- and single-walled carbon nanotubes. *J. Phys. D Appl. Phys.*, **2013**, 46, 16: 165503.
- 371 A. Omar, H. Abdullah, S. Shaari, M. R. Taha. Characterization of zinc oxide dye-sensitized solar cell incorporation with single-walled carbon nanotubes. *J. Mater. Res.*, **2013**, 28, 13: 1753-1760.
- 372 H. Abdullah, A. Omar, M. Z. Razali, M. A. Yarmo. Photovoltaic properties of ZnO photoanode incorporating with CNTs for dye-sensitized solar cell application. *Ionics*, **2014**, 20, 7: 1023-1030.
- 373 M. Wang, C. Huang, Y. Cao, Q. Yu, W. Guo, Q. Liu, J. Liang, M. Hong. A plasma sputtering decoration route to producing thickness-tunable ZnO/ TiO₂ core/shell nanorod arrays. *Nanotechnology*, **2009**, 20, 28: 285311.
- 374 L. Loh, J. Briscoe, S. Dunn. Bismuth Ferrite Enhanced ZnO Solid State Dye-sensitised Solar Cell. *Procedia Engineering*, **2016**, 139: 15-21.
- 375 Y. Yin, L. Chen. Promising Surface Modification Strategies for High Power Conversion Efficiency Dye Sensitized Solar Cell Based on ZnO Composite Photoanode. *Energy Procedia*, **2014**, 61: 2042-2045.
- 376 M. Moradzaman, M. R. Mohammadi, H. Nourizadeh. Efficient dye-sensitized solar cells based on CNTs and Zr-doped TiO₂ nanoparticles. *Materials Science in Semiconductor Processing*, **2015**, 40: 383-390.
- 377 J. T. Kim, S. H. Lee, Y. S. Han. Enhanced power conversion efficiency of dye-sensitized solar cells with Li₂SiO₃-modified photoelectrode. *Applied Surface Science*, **2015**, 333: 134-140.
- 378 T. Ma, X. Fang, M. Akiyama, K. Inoue, H. Noma, E. Abe. Properties of several types of novel counter electrodes for dye-sensitized solar cells. *J. Electroanal. Chem.*, **2004**, 574,
-
-

- 1: 77-83.
- 379 M. Toivola, F. Ahlskog, P. Lund. Industrial sheet metals for nanocrystalline dye-sensitized solar cell structures. *Sol. Energy Mater. Sol. Cells*, **2006**, 90, 17: 2881-2893.
- 380 S. K. Balasingam, M. G. Kang, Y. Jun. Metal substrate based electrodes for flexible dye-sensitized solar cells: fabrication methods, progress and challenges. *Chem. Commun.*, **2013**, 49, 98: 11457-11475.
- 381 S. Yun, A. Hagfeldt, T. Ma. Pt-Free Counter Electrode for Dye-Sensitized Solar Cells with High Efficiency. *Adv. Mater.*, **2014**, 26, 36: 6210-6237.
- 382 K. Saranya, M. Rameez, A. Subramania. Developments in conducting polymer based counter electrodes for dye-sensitized solar cells - An overview. *Eur. Polym. J.*, **2015**, 66: 207-227.
- 383 J. Theerthagiri, A. R. Senthil, J. Madhavan, T. Maiyalagan. Recent Progress in Non-Platinum Counter Electrode Materials for Dye-Sensitized Solar Cells. *ChemElectroChem*, **2015**, 2, 7: 928-945.
- 384 S. Yun, J. N. Freitas, A. F. Nogueira, Y. Wang, S. Ahmad, Z. Wang. Dye-sensitized solar cells employing polymers. *Prog. Polym. Sci.*, **2016**, 59: 1-40.
- 385 T. Kitamura, M. Maitani, M. Matsuda, Y. Wada, S. Yanagida. Improved Solid-State Dye Solar Cells with Polypyrrole using a Carbon-Based Counter Electrode. *Chem. Lett.*, **2001**, 30, 10: 1054-1055.
- 386 N. Ikeda, K. Teshima, T. Miyasaka. Conductive polymer - carbon - imidazolium composite: a simple means for constructing solid-state dye-sensitized solar cells. *Chem. Commun.*, **2006**, 0: 1733-1735.
- 387 J. Burschka, V. Brault, S. Ahmad, L. Breau, M. K. Nazeeruddin, B. Marsan, S. M. Zakeeruddin, M. Grätzel. Influence of the counter electrode on the photovoltaic performance of dye-sensitized solar cells using a disulfide/thiolate redox electrolyte. *Energy Environ. Sci.*, **2012**, 5: 6089-6097.
- 388 P. Poudel, Q. Qiao. Carbon nanostructure counter electrodes for low cost and stable dye-sensitized solar cells. *Nano Energy*, **2014**, 4: 157-175.
- 389 Y. Y. Dou, G. R. Li, J. Song, X. P. Gao. Nickel phosphide-embedded graphene as counter electrode for dye-sensitized solar cells. *Phys. Chem. Chem. Phys.*, **2012**, 14:1339-1342.
- 390 R. Bajpai, S. Roy, N. kulshrestha, J. Rafiee, N. Koratkar, D. S. Misra. Graphene supported nickel nanoparticle as a viable replacement for platinum in dye sensitized solar cells. *Nanoscale*, **2012**, 4: 926-930.
- 391 F. Gong, H. Wang, Z. Wang. Self-assembled monolayer of graphene/Pt as counter

- electrode for efficient dye-sensitized solar cell. *Phys. Chem. Chem. Phys.*, **2011**, 13: 17676-17682.
- 392 T. Battumur, S. H. Mujawar, Q. T. Truong, S. B. Ambade, D. S. Lee, W. Lee, S. Han, S. Lee. Graphene/carbon nanotubes composites as a counter electrode for dye-sensitized solar cells. *Curr. Appl. Phys.*, **2012**, 12: e49-e53.
- 393 J. Velten, A. J. Mozer, D. Li, D. Officer, G. Wallace, R. Baughman, A. Zakhidov. Carbon nanotube/graphene nanocomposite as efficient counter electrodes in dye-sensitized solar cells. *Nanotechnology*, **2012**, 23: 85201.
- 394 G. Wang, S. Zhuo, W. Xing. Graphene/polyaniline nanocomposite as counter electrode of dye-sensitized solar cells. *Mater. Lett.*, **2012**, 69:27-29.
- 395 S. Stankovich, D. A. Dikin, G. H. B. Dommett, K. M. Kohlhaas, E. J. Zimney, E. A. Stach, R. D. Piner, S. T. Nguyen, R. S. Ruoff. Graphene-based composite materials. *Nature*, **2006**, 442: 282-286.
- 396 M. Lee, S. K. Balasingam, Y. Ko, H. Y. Jeong, B. K. Min, Y. J. Yun, Y. Jun. Graphene modified vanadium pentoxide nanobelts as an efficient counter electrode for dye-sensitized solar cells. *Synthetic Metals*, **2016**, 215: 110-115.
- 397 M. Motlak, N. A. M. Barakat, A. G. El-Deen, A. M. Hamza, M. Obaid, O. B. Yang, M. S. Akhtar, K. A. Khalil. NiCu bimetallic nanoparticle-decorated graphene as novel and cost-effective counter electrode for dye-sensitized solar cells and electrocatalyst for methanol oxidation. *Applied Catalysis A: General*, **2015**, 501, 41-47.
- 398 T. N. Murakami, M. Grätzel. Counter electrodes for DSC: Application of functional materials as catalysts. *Inorganica Chimica Acta*, **2008**, 361, 3: 572-580.
- 399 P. Joshi, Y. Xie, M. Ropp, D. Galipeau, S. Bailey, Q. Qiao. Dye-sensitized solar cells based on low cost nanoscale carbon/TiO₂ composite counter electrode. *Energy Environ. Sci.*, **2009**, 2: 426-429.
- 400 P. Joshi, Z. Zhou, P. Poudel, A. Thapa, X. Wu, Q. Qiao. Nickel incorporated carbon nanotube/nanofiber composites as counter electrodes for dye-sensitized solar cells. *Nanoscale*, **2012**, 4: 5659-5664.
- 401 X. Mei, S. J. Cho, B. Fan, J. Ouyang. High-performance dye-sensitized solar cells with gel-coated binder-free carbon nanotube films as counter electrode. *Nanotechnology*, **2010**, 21, 39: 395202.
- 402 C. Chou, C. Huang, R. Yang, C. Wang. The effect of SWCNT with the functional group deposited on the counter electrode on the dye-sensitized solar cell. *Adv. Powder Technol.*, **2010**, 21: 542-550.

-
- 403 M. Fitra, I. Daut, M. Irwanto, N. Gomesh, Y. M. Irwan. TiO₂ Dye Sensitized Solar Cells Cathode Using Recycle Battery. *Energy Procedia*, **2013**, 36: 333-340.
- 404 Y. Bai, Y. Cao, J. Zhang, M. Wang, R. Li, P. Wang, S. M. Zakeeruddin, M. Grätzel. High-performance dye-sensitized solar cells based on solvent-free electrolytes produced from eutectic melts. *Nature Materials*, **2008**, 7: 626-630.
- 405 Z. Wang, K. Sayama, H. Sugihara. Efficient Eosin Y Dye-Sensitized Solar Cell Containing Br⁻/Br₃⁻ Electrolyte. *J. Phys. Chem. B*, **2005**, 109, 47: 22449-22455.
- 406 B. V. Bergeron, A. Marton, G. Oskam, G. J. Meyer. Dye-Sensitized SnO₂ Electrodes with Iodide and Pseudohalide Redox Mediators. *J. Phys. Chem. B*, **2005**, 109, 2: 937-943.
- 407 G. Oskam, B. V. Bergeron, G. J. Meyer, P. C. Searson. Pseudohalogens for Dye-Sensitized TiO₂ Photoelectrochemical Cells. *J. Phys. Chem. B*, **2001**, 105, 29: 6867-6873.
- 408 S. A. Sapp, C. M. Elliott, C. Contado, S. Caramori, C. A. Bignozzi. Substituted Polypyridine Complexes of Cobalt(II/III) as Efficient Electron-Transfer Mediators in Dye-Sensitized Solar Cells. *J. Am. Chem. Soc.*, **2002**, 124, 37: 11215-11222.
- 409 G. Boschloo, A. Hagfeldt. Characteristics of the Iodide/Triiodide Redox Mediator in Dye-Sensitized Solar Cells. *Acc. Chem. Res.*, **2009**, 42, 11: 1819-1826.
- 410 A. Fukui, R. Komiya, R. Yamanaka, A. Islam, L. Han. Effect of a redox electrolyte in mixed solvents on the photovoltaic performance of a dye-sensitized solar cell. *Sol. Energy Mater. Sol. Cells*, **2006**, 90, 5: 649-658.
- 411 J. Wu, Z. Lan, J. Lin, M. Huang, P. Li. Effect of solvents in liquid electrolyte on the photovoltaic performance of dye-sensitized solar cells. *Journal of Power Sources*, **2007**, 173, 1: 585-591.
- 412 X. Yin, W. Tan, J. Zhang, Y. Weng, X. Xiao, X. Zhou, X. Li, Y. Lin. The effect mechanism of 4-ethoxy-2-methylpyridine as an electrolyte additive on the performance of dye-sensitized solar cell. *Colloids Surf., A*, **2008**, 326, 1-2: 42-47.
- 413 C. Zhang, J. Dai, Z. Huo, X. Pan, L. Hu, F. Kong, Y. Huang, Y. Sui, X. Fang, K. Wang, S. Dai. Influence of 1-methylbenzimidazole interactions with Li⁺ and TiO₂ on the performance of dye-sensitized solar cells. *Electrochimica Acta*, **2008**, 53, 17: 5503-5508.
- 414 T. Stergiopoulos, E. Rozi, C. Karagianni, P. Falaras. Influence of electrolyte co-additives on the performance of dye-sensitized solar cells. *Nanoscale Research Letters*, **2011**, 6: 307.
- 415 P. Wang, S. M. Zakeeruddin, J. Moser, M. Grätzel. A New Ionic Liquid Electrolyte Enhances the Conversion Efficiency of Dye-Sensitized Solar Cells. *J. Phys. Chem. B*,
-

- 2003, 107, 48: 13280-13285.
- 416 S. M. Zakeeruddin, M. Grätzel. Solvent-Free Ionic Liquid Electrolytes for Mesoscopic Dye-Sensitized Solar Cells. *Adv. Funct. Mater.*, **2009**, 19, 14: 2187-2202.
- 417 W. Kubo, T. Kitamura, K. Hanabusa, Y. Wada, S. Yanagida. Quasi-solid-state dye-sensitized solar cells using room temperature molten salts and a low molecular weight gelator. *Chem. Commun.*, **2002**, 0: 374-375.
- 418 B. Li, L. Wang, B. Kang, P. Wang, Y. Qiu. Review of recent progress in solid-state dye-sensitized solar cells. *Sol. Energy Mater. Sol. Cells*, **2006**, 90, 5: 549-573.
- 419 U. Bach, D. Lupo, P. Comte, J. E. Moser, F. Weissörtel, J. Salbeck, H. Spreitzer, M. Grätzel. Solid-state dye-sensitized mesoporous TiO₂ solar cells with high photon-to-electron conversion efficiencies. *Nature*, **1998**, 395: 583-585.
- 420 F. Odobel, L. L. Pleux, Y. Pellegrin, Errol Blart. New Photovoltaic Devices Based on the Sensitization of p-type Semiconductors: Challenges and Opportunities. *Acc. Chem. Res.*, **2010**, 43, 8: 1063-1071.
- 421 F. Odobel, Y. Pellegrin, E. A. Gibson, A. Hagfeldt, A. L. Smeigh, L. Hammarström. Recent advances and future directions to optimize the performances of p-type dye-sensitized solar cells. *Coordination Chemistry Reviews*, **2012**, 256: 2414-2423.
- 422 P. Qin, H. Zhu, T. Edvinsson, G. Boschloo, A. Hagfeldt, L. Sun. Design of an Organic Chromophore for P-Type Dye-Sensitized Solar Cells. *J. Am. Chem. Soc.*, **2008**, 130, 27: 8570-8571.
- 423 F. Odobel, Y. Pellegrin. Recent Advances in the Sensitization of Wide-Band-Gap Nanostructured p-Type Semiconductors. Photovoltaic and Photocatalytic Applications. *J. Phys. Chem. Lett.*, **2013**, 4, 15: 2551-2564.
- 424 D. Dini, Y. Halpin, J. G. Vos, E. A. Gibson. The influence of the preparation method of NiO_x photocathodes on the efficiency of p-type dye-sensitized solar cells. *Coordination Chemistry Reviews*, **2015**, 304-305: 179-201.
- 425 J. He, H. Lindström, A. Hagfeldt, S.-E. Lindquist. Dye-sensitized nanostructured tandem cell-first demonstrated cell with a dye-sensitized photocathode. *Sol. Energy Mater. Sol. Cells*, **2000**, 62: 265-273.
- 426 N. Akihiko, U. Hisanao, S. Seiichi, H. Satoshi, K. Toshiki, S. Eiji. A High Voltage Dye-sensitized Solar Cell using a Nanoporous NiO Photocathode. *Chem. Lett.*, **2005**, 34: 500-501.
- 427 A. Nattestad, A. J. Mozer, M. K. R. Fischer, Y.-B. Cheng, A. Mishra, P. Bäuerle, U. Bach. Highly efficient photocathodes for dye-sensitized tandem solar cells. *Nature Materials*,

- 2010, 9: 31-35.
- 428 Y. Farré, M. Raissi, A. Fihey, Y. Pellegrin, E. Blart, D. Jacquemin, F. Odobel. A Blue Diketopyrrolopyrrole Sensitizer with High Efficiency in Nickel-Oxide-based Dye-Sensitized Solar Cells. *ChemSusChem*, **2017**, 10, 12: 2618-2625.
- 429 M. Yu, T. I. Draskovic, Y. Wu. Cu(I)-based delafossite compounds as photocathodes in p-type dye-sensitized solar cells. *Phys. Chem. Chem. Phys.*, **2014**, 16: 5026-5033.
- 430 I. R. Perera, T. Daeneke, S. Makuta, Z. Yu, Y. Tachibana, A. Mishra, P. Bäuerle, C. A. Ohlin, U. Bach, L. Spiccia. Application of the Tris(acetylacetonato)iron(III)/(II) Redox Couple in p-Type Dye-Sensitized Solar Cells. *Angew. Chem., Int. Ed.*, **2015**, 54, 12: 3758-3762.
- 431 S. Sheng, G. Fang, C. Li, S. Xu, X. Zhao. P-type transparent conducting oxides. *Phys. Stat. Sol. (a)*, **2006**, 203, 8: 1891-1900.
- 432 K. H. L. Zhang, K. Xi, M. G. Blamire, R. G. Egdell. P-type transparent conducting oxides. *J. Phys.: Condens. Matter*, **2016**, 28: 383002.
- 433 O. Langmar, C. R. Ganivet, A. Lennert, D. Costa, G. D. L. Torre, T. Torres, D. M. Guldi. Combining Electron-Accepting Phthalocyanines and Nanorod-like CuO Electrodes for p-Type Dye-Sensitized Solar Cells. *Angew. Chem., Int. Ed.*, **2015**, 127, 26: 7798-7802.
- 434 O. Langmar, C. R. Ganivet, G. D. L. Torre, T. Torres, R. D. Costa, D. M. Guldi. Optimizing CuO p-type dye-sensitized solar cells by using a comprehensive electrochemical impedance spectroscopic study. *Nanoscale*, **2016**, 8: 17963-17975.
- 435 T. Jiang, M. Bujoli-Doeuff, Y. Farré, E. Blart, Y. Pellegrin, E. Gautron, M. Boujtita, L. Cario, F. Odobel, S. Jobic. Copper borate as a photocathode in p-type dye-sensitized solar cells. *RSC Adv.*, **2016**, 6: 1549-1553.
- 436 S. Sumikura, S. Mori, S. Shimizu, H. Usami, E. Suzuki. Photoelectrochemical characteristics of cells with dyed and undyed nanoporous p-type semiconductor CuO electrodes. *J. Photochem. Photobiol. A*, **2008**, 194: 143-147.
- 437 M. G. Walter, E. L. Warren, J. R. McKone, S. W. Boettcher, Q. Mi, E. A. Santori, N. S. Lewis. Solar Water Splitting Cells. *Chem. Rev.*, **2010**, 110, 11: 6446-6473.
- 438 J. R. McKone, N. S. Lewis, H. B. Gray. Will Solar-Driven Water-Splitting Devices See the Light of Day? *Chem. Mater.*, **2014**, 26, 1: 407-414.
- 439 N. Queyriaux, N. Kaeffer, A. Morozan, M. Chavarot-Kerlidou, V. Artero. Molecular cathode and photocathode materials for hydrogen evolution in photoelectrochemical devices. *J. Photochem. Photobiol. C*, **2015**, 25: 90-105.
- 440 K. Tennakone, M. Kahanda, C. Kasige, P. Abeysooriya, R. H. Wijayanayaka, P. Kaviratna.

- Dye Sensitization of Cuprous Thiocyanate Photocathode in Aqueous KCNS. *J. Electrochem. Soc.*, **1984**, 131, 7: 1574-1577.
- 441 K. Tennakone, A. R. Kumarasinghe, P. M. Sirimanne, G. R. R. A. Kumara. Deposition of thin polycrystalline films of cuprous thiocyanate on conducting glass and photoelectrochemical dye-sensitization. *Thin Solid Films*, **1995**, 261, 1-2: 307-310.
- 442 J. He, H. Lindström, A. Hagfeldt, S.-E. Lindquist. Dye-Sensitized Nanostructured p-Type Nickel Oxide Film as a Photocathode for a Solar Cell. *J. Phys. Chem. B*, **1999**, 103, 8940-8943.
- 443 G. Boschloo, A. Hagfeldt. Spectroelectrochemistry of Nanostructured NiO. *J. Phys. Chem. B*, **2001**, 105: 3039-3044.
- 444 H. Zhu, A. Hagfeldt, G. Boschloo. Photoelectrochemistry of Mesoporous NiO Electrodes in Iodide/Triiodide Electrolytes. *J. Phys. Chem. C*, **2007**, 111, 47: 17455-17458.
- 445 S. Mori, S. Fukuda, S. Sumikura, Y. Takeda, Y. Tamaki, E. Suzuki, T. Abe. Charge-Transfer Processes in Dye-Sensitized NiO Solar Cells. *J. Phys. Chem. C*, **2008**, 112, 41: 16134-16139.
- 446 G. Natu, P. Hasin, Z. Huang, Z. Ji, M. He, Y. Wu. Valence Band-Edge Engineering of Nickel Oxide Nanoparticles via Cobalt Doping for Application in p-Type Dye-Sensitized Solar Cells. *ACS Appl. Mater. Interfaces*, **2012**, 4, 11: 5922-5929.
- 447 M. Yu, G. Natu, Z. Ji, Y. Wu. P-Type Dye-Sensitized Solar Cells Based on Delafossite CuGaO₂ Nanoplates with Saturation Photovoltages Exceeding 460 mV. *J. Phys. Chem. Lett.*, **2012**, 3, 9: 1074-1078.
- 448 S. Uehara, S. Sumikura, E. Suzukia, S. Mori. Retardation of electron injection at NiO/dye/electrolyte interface by aluminium alkoxide treatment. *Energy Environ. Sci.*, **2010**, 3: 641-644.
- 449 Z. Bian, T. Tachikawa, S. Cui, M. Fujitsuka, Tetsuro Majima. Single-molecule charge transfer dynamics in dye-sensitized p-type NiO solar cells: influences of insulating Al₂O₃ layers. *Chem. Sci.*, **2012**, 3: 370-379.
- 450 I. Hod, Z. Tachan, M. Shalom, A. Zaban. Characterization and control of the electronic properties of a NiO based dye sensitized photocathode. *Phys. Chem. Chem. Phys.*, **2013**, 15: 6339-6343.
- 451 E. A. Gibson, A. L. Smeigh, L. Le Pleux, L. Hammarström, F. Odobel, G. Boschloo, A. Hagfeldt. Cobalt Polypyridyl-Based Electrolytes for p-Type Dye-Sensitized Solar Cells. *J. Phys. Chem. C*, **2011**, 115, 19: 9772-9779.
- 452 L. L. Pleux, A. L. Smeigh, E. Gibson, Y. Pellegrin, E. Blart, G. Boschloo, A. Hagfeldt, L.

- Hammarström, F. Odobel. Synthesis, photophysical and photovoltaic investigations of acceptor-functionalized perylene monoimide dyes for nickel oxide p-type dye-sensitized solar cells. *Energy Environ. Sci.*, **2011**, 4: 2075-2084.
- 453 Z. Huang, G. Natu, Z. Ji, M. He, M. Yu, Y. Wu. Probing the Low Fill Factor of NiO P-Type Dye-Sensitized Solar Cells. *J. Phys. Chem. C*, **2012**, 116, 50: 26239-26246.
- 454 E. A. Gibson, A. L. Smeigh, L. L. Pleux, J. Fortage, G. Boschloo, E. Blart, Y. Pellegrin, F. Odobel, A. Hagfeldt, L. Hammarström. A p-Type NiO-Based Dye-Sensitized Solar Cell with an Open-Circuit Voltage of 0.35 V. *Angew. Chem., Int. Ed.*, **2009**, 121, 24: 4466-4469.
- 455 X. Zhang, Y. Xu, F. Giordano, M. Schreier, N. Pellet, Y. Hu, C. Yi, N. Robertson, J. Hua, S. M. Zakeeruddin, H. Tian, M. Grätzel. Molecular Engineering of Potent Sensitizers for Very Efficient Light Harvesting in Thin-Film Solid-State Dye-Sensitized Solar Cells. *J. Am. Chem. Soc.*, **2016**, 138, 34, 10742-10745.
- 456 J. Zhang, N. Vlachopoulos, Y. Hao, T. W. Holcombe, G. Boschloo, E. M. J. Johansson, M. Grätzel, A. Hagfeldt. Enhanced Charge Collection by Using an in Situ Photoelectrochemically Generated Conducting Polymer Hole Conductor. *ChemPhysChem*, **2016**, 17, 10: 1441-1445.
- 457 B. Xu, D. Bi, Y. Hua, P. Liu, M. Cheng, M. Grätzel, L. Kloo, A. Hagfeldt, L. Sun. A low-cost spiro[fluorene-9,9'-xanthene]-based hole transport material for highly efficient solid-state dye-sensitized solar cells and perovskite solar cells. *Energy Environ. Sci.*, **2016**, 9: 873-877.
- 458 S. Hattori, Y. Wada, S. Yanagida, S. Fukuzumi. Blue Copper Model Complexes with Distorted Tetragonal Geometry Acting as Effective Electron-Transfer Mediators in Dye-Sensitized Solar Cells. *J. Am. Chem. Soc.*, **2005**, 127, 26: 9648-9654.
- 459 M. Freitag, Q. Daniel, M. Pazoki, K. Sveinbjörnsson, J. Zhang, L. Sun, A. Hagfeldt, G. Boschloo. High-efficiency dye-sensitized solar cells with molecular copper phenanthroline as solid hole conductor. *Energy Environ. Sci.*, **2015**, 8: 2634-2637.
- 460 L. Li, E. A. Gibson, P. Qin, G. Boschloo, M. Gorlov, A. Hagfeldt, L. Sun. Double-Layered NiO Photocathodes for p-Type DSSCs with Record IPCE. *Adv. Mater.*, **2010**, 22, 15: 1759-1762.
- 461 J. Velevska, M. Ristova. Electrochromic properties of NiO_x prepared by low vacuum evaporation. *Sol. Energy Mater. Sol. Cells*, **2002**, 73: 131-139.
- 462 F. Vera, R. Schrebler, E. Muñoz, C. Suarez, P. Cury, H. Gómez, R. Córdova, R. E. Marotti, E. A. Dalchiele. Preparation and characterization of Eosin B- and Erythrosin J-sensitized

- nanostructured NiO thin film photocathodes. *Thin Solid Films*, **2005**, 490, 2: 182-188.
- 463 Y. Mizoguchi and S. Fujihara. Fabrication and Dye-Sensitized Solar Cell Performance of Nanostructured NiO/Coumarin 343 Photocathodes. *Electrochem. Solid-State Lett.*, **2008**, 11, 8: K78-K80.
- 464 L. Lepleux, B. Chavillon, Y. Pellegrin, E. Blart, L. Cario, S. Jobic, F. Odobel. Simple and Reproducible Procedure to Prepare Self-Nanostructured NiO Films for the Fabrication of P-Type Dye-Sensitized Solar Cells. *Inorg. Chem.*, **2009**, 48, 17: 8245-8250.
- 465 D.-B. Kuang, B.-X. Lei, Y.-P. Pan, X.-Y. Yu, C.-Y. Su. Fabrication of Novel Hierarchical β -Ni(OH)₂ and NiO Microspheres via an Easy Hydrothermal Process. *J. Phys. Chem. C*, **2009**, 113, 14: 5508-5513.
- 466 Y. Y. Xi, D. Li, A. B. Djurišić, M. H. Xie, K. Y. K. Man, W. K. Chan. Hydrothermal Synthesis vs Electrodeposition for High Specific Capacitance Nanostructured NiO Films. *Electrochem. Solid-State Lett.*, **2008**, 11, 6: D56-D59.
- 467 P. Salvador, C. Gutiérrez, J. B. Goodenough. Photoelectrochemical properties of n-type NiTiO₃. *Journal of Applied Physics*, **1982**, 53, 10: 7003.
- 468 J. Wu, J. Zheng, C. L. Zacherl, P. Wu, Z. Liu, R. Xu. Hybrid Functionals Study of Band Bowing, Band Edges and Electronic Structures of Cd_{1-x}Zn_xS Solid Solution. *J. Phys. Chem. C*, **2011**, 115, 40: 19741-19748.
- 469 M. L. Pegis, J. A. S. Roberts, D. J. Wasylenko, E. A. Mader, A. M. Appel, J. M. Mayer. Standard Reduction Potentials for Oxygen and Carbon Dioxide Couples in Acetonitrile and N,N-Dimethylformamide. *Inorg. Chem.*, **2015**, 54, 24: 11883-11888.
- 470 K. A. Vincent, A. Parkin, O. Lenz, S. P. J. Albracht, J. C. Fontecilla-Camps, R. Cammack, B. Friedrich, F. A. Armstrong. Electrochemical Definitions of O₂ Sensitivity and Oxidative Inactivation in Hydrogenases. *J. Am. Chem. Soc.*, **2005**, 127, 51: 18179-18189.
- 471 S. Canaguier, V. Artero, M. Fontecave. Modelling NiFe hydrogenases: nickel-based electrocatalysts for hydrogen production. *Dalton Trans.*, **2008**, 0: 315-325.
- 472 H. R. Pershad, J. L. C. Duff, H. A. Heering, E. C. Duin, S. P. J. Albracht, F. A. Armstrong. Catalytic Electron Transport in Chromatium vinosum [NiFe]-Hydrogenase: Application of Voltammetry in Detecting Redox-Active Centers and Establishing That Hydrogen Oxidation Is Very Fast Even at Potentials Close to the Reversible H⁺/H₂ Value. *Biochemistry*, **1999**, 38, 28: 8992-8999.
- 473 R. Abe. Recent progress on photocatalytic and photoelectrochemical water splitting under visible light irradiation. *J. Photochem. Photobiol. C*, **2010**, 11: 179-209.
- 474 A. Hagfeldt, M. Grätzel. Molecular Photovoltaics. *Acc. Chem. Res.*, **2000**, 33, 269-277.

-
- 475 S. Berardi, S. Drouet, L. Francàs, C. Gimbert-Suriñach, M. Guttentag, C. Richmond, T. Stoll, A. Llobet. Molecular artificial photosynthesis. *Chem. Soc. Rev.*, **2014**, 43: 7501-7519.
- 476 J. L. Dempsey, B. S. Brunschwig, J. R. Winkler, H. B. Gray. Hydrogen Evolution Catalyzed by Cobaloximes. *Acc. Chem. Res.*, **2009**, 42, 12: 1995-2004.
- 477 W. T. Eckenhoff, R. Eisenberg. Molecular systems for light driven hydrogen production. *Dalton Trans.*, **2012**, 41: 13004-13021.
- 478 S. Fukuzumi, Y. Yamada, T. Suenobu, K. Ohkubo, H. Kotani. Catalytic mechanisms of hydrogen evolution with homogeneous and heterogeneous catalysts. *Energy Environ. Sci.*, **2011**, 4: 2754-2766.
- 479 M. Wang, L. Chen, L. Sun. Recent progress in electrochemical hydrogen production with earth-abundant metal complexes as catalysts. *Energy Environ. Sci.*, **2012**, 5: 6763-6778.
- 480 L. Tong, A. Iwase, A. Nattestad, U. Bach, M. Weidelener, G. Götz, A. Mishra, P. Bäuerle, R. Amal, G. G. Wallace, A. J. Mozer. Sustained solar hydrogen generation using a dye-sensitized NiO photocathode/BiVO₄ tandem photo-electrochemical device. *Energy Environ. Sci.*, **2012**, 5: 9472-9475.
- 481 Z. Ji, M. He, Z. Huang, U. Ozkan, Y. Wu. Photostable p-Type Dye-Sensitized Photoelectrochemical Cells for Water Reduction. *J. Am. Chem. Soc.*, **2013**, 135, 32: 11696-11699.
- 482 K. Fan, F. Li, L. Wang, Q. Daniel, E. Gabrielsson, L. Sun. Pt-free tandem molecular photoelectrochemical cells for water splitting driven by visible light. *Phys. Chem. Chem. Phys.*, **2014**, 16: 25234-25240.
- 483 M. A. Gross, C. E. Creissen, K. L. Orchard, E. Reisner. Photoelectrochemical hydrogen production in water using a layer-by-layer assembly of a Ru dye and Ni catalyst on NiO. *Chem. Sci.*, **2016**, 7: 5537-5546.
- 484 N. Kaeffer, J. Massin, C. Lebrun, O. Renault, M. Chavarot-Kerlidou, V. Artero. Covalent Design for Dye-Sensitized H₂-Evolving Photocathodes Based on a Cobalt Diimine-Dioxime Catalyst. *J. Am. Chem. Soc.*, **2016**, 138, 38: 12308-12311.
- 485 A. Fihri, V. Artero, M. Razavet, C. Baffert, W. Leibl, M. Fontecave. Cobaloxime-Based Photocatalytic Devices for Hydrogen Production. *Angew. Chem. Int. Ed.*, **2008**, 47: 564-567.
- 486 A. Fihri, V. Artero, A. Pereira, M. Fontecave. Efficient H₂-producing photocatalytic systems based on cyclometalated iridium- and tricarbonylrhenium-diimine photosensitizers and cobaloxime catalysts. *Dalton Trans.*, **2008**, 0: 5567-5569.
-

- 487 P. Du, J. Schneider, G. Luo, W. W. Brennessel, R. Eisenberg. Visible Light-Driven Hydrogen Production from Aqueous Protons Catalyzed by Molecular Cobaloxime Catalysts. *Inorg. Chem.*, **2009**, 48, 11: 4952-4962.
- 488 J. Willkomm, K. L. Orchard, A. Reynal, E. Pastor, J. R. Durrant, E. Reisner. Dye-sensitised semiconductors modified with molecular catalysts for light-driven H₂ production. *Chem. Soc. Rev.*, **2016**, 45: 9-23.
- 489 C. J. Wood, C. A. McGregor, E. A. Gibson. Does Iodine or Thiocyanate Play a Role in a p-Type Dye-Sensitized Solar Cells? *ChemElectroChem*, **2016**, 3, 11: 1827-1836.
- 490 C. E. Richards, A. Y. Anderson, S. Martiniani, C. Law, B. C. O'Regan. The Mechanism of Iodine Reduction by TiO₂ Electrons and the Kinetics of Recombination in Dye-Sensitized Solar Cells. *J. Phys. Chem. Lett.*, **2012**, 3, 15: 1980-1984.
- 491 J. A. Turner. A Realizable Renewable Energy Future. *Science*, **1999**, 285, 5428: 687-689.

**Chapter II:
Ruthenium-Diacetylide Organometallic
Complexes for n-Type Dye Sensitizers**

II.1. General Introduction

As discussed in the first chapter, n-type DSCs as sub-species of DSCs have attracted worldwide attention in the field of photovoltaics since the seminal paper reported by B. O'Regan and M. Grätzel¹ due to cost-effective and easy manufacturing process. The extensive fascination n-type DSCs arouse primarily stems from the tunability of the main components of the solar cell device that stimulates huge emulation in various areas of research. In particular, advanced molecular engineering afforded finely tailored organometallic and fully-organic dyes that raised the current record power conversion efficiency above 13%.^{2,3} To achieve efficient light-harvesting, the solar cell device therefore relies on pigment molecules that play the role of visible-light absorbing antennae. In this important respect, ruthenium can operate as a connector allowing electron flow to occur between different elements in *trans*-ditopic architectures.^{4,6} Up to now, ruthenium coordination complexes such as N3 or N719 remain to be the most efficient chromophores which therefore represent one of the main families of dye sensitizers. However, ruthenium complexes usually have modest molar extinction coefficient as well as exclusively polypyridyl derivatives which finally limit the development of their applications for DSCs.⁷⁻⁹ In order to overcome the drawback of moderate light absorption, organic dye sensitizers or so-called push-pull materials bearing electron-donating (D) and electron-withdrawing (A) fragments linked by π -conjugated bridges have been designed and reported for DSCs.¹⁰⁻¹³ The organic dye sensitizers featuring a D- π -A architecture notoriously afford efficient charge transfer from their ground state to the excited state which results in the enhancement of their absorption properties. Furthermore, the prototypical push-pull design can allow reduction of the electronic recombination processes in the solar cell devices. The reason may be that the photons with short wavelengths will create electrons in the TiO₂ which are closer to the back contact and thus less prone to recombination during transport.¹⁴ Since the cutting-edge dye sensitizers play an important role in the future of DSCs, this thesis focuses on the design and synthesis of innovative ruthenium-diacetylide organometallic dye sensitizers to obtain efficient DSCs and DSPEC.

In this chapter, various dominant n-type dye sensitizers are reviewed, including ruthenium complexes, porphyrins, phthalocyanines and metal-free organic dyes. Then, our work dealing with the design and synthesis of innovative ruthenium-diacetylide organometallic dye sensitizers is described in section II.3.. Optical and electrochemical properties, theoretical calculations as well as photovoltaic properties based on these novel dyes are then discussed.

II.2. n-Type Dye Sensitizers

From the working principles of DSCs referred in the previous section, the dye-sensitizer is crucial for DSCs by playing an important role in the photovoltaic properties of the solar cell device. The reason for the importance of dye-sensitizers is because their photophysical and electrochemical properties can firsthand determine and influence the related factors of short-circuit current density such as $LHE(\lambda)$, η_{ED} , Φ_{inj} , η_{reg} and so on.¹⁵ Consequently, rational design and optimization of the dyes have been the key factors of this field and opportunity-filled challenges. Theoretically, efficient photosensitizers should fulfill some essential characteristics^{7,16-18}:

- i. The dye-sensitizers should have high molar extinction coefficients and their absorption spectra should have wide absorption spectrum which cover visible region and even the part of the near-infrared.
- ii. The photosensitizers should have at least one anchoring group ($-\text{COOH}$, $-\text{H}_2\text{PO}_3$, $-\text{SO}_3\text{H}$, $-\text{Si}(\text{OEt})_3$, etc.) to strongly bind the dye onto the semiconductor surface which make sure the photoinduced electron injection from the excited dye into the conduction band (CB) of the semiconductor.
- iii. For n-type DSCs, the conduction band (CB) edge of semiconductor should be lower in energy than the excited level of photosensitizer to make sure that the efficient electron transfer process can take place between the conduction band (CB) of the semiconductor and the excited dye.
- iv. The oxidized state level of the photosensitizer should be lower (more positive) than the redox potential of the electrolyte to ensure the process of dye regeneration.
- v. Dye aggregation is unfavorable process which should be prevented through the molecular structure optimization or addition of cosensitizer. Controlling of dye aggregation is to the benefit of good performance of the photosensitizer.
- vi. The ground state, excited state and oxidized state should have photostable, electrochemical and thermal stability which can enable the dye repetitive work for 10^8 times (equivalent to be exposed under natural daylight for 20 years).

Based on the above-mentioned essential requirements, many different photosensitizers have been designed and applied to n-type DSCs in the past decades. These published photosensitizers have various types and numerous examples exist that can be broadly separated into metal complexes (mainly ruthenium complexes), porphyrins, phthalocyanines and metal-free organic dyes. The above-mentioned requirements are also our clues when we designed, synthesized and optimized our target products.

II.2.1. Ruthenium Complexes

Metal complexes, especially ruthenium complexes, have been extensively investigated in recent decades. Metal complexes have excellent performances such as their broad absorption spectra and outstanding photovoltaic properties when used for dye sensitized solar cell devices. The heart of metal complexes comprises a central metal ion and auxiliary ligands having at least one anchoring group. Charge separation and electron transport from the central metal ion to its ligand determine the absorption spectrum of the photosensitizer and kinetic competition which means that the central metal ion is a crucial part of the overall properties.^{7,16,19-21} On the other hand, the auxiliary ligands (typically bipyridines, terpyridines, etc.) of metal complexes play an important role in photophysical and electrochemical properties through changing different substituents (alkyl, aryl, heterocycle, etc.).²²⁻²⁵ Meanwhile, the function of anchoring groups of metal complexes is to link the photosensitizer and the semiconductor and make sure that excited electron injects into the conduction band (CB) of the semiconductor. Therefore, modification of any part of metal complexes can tune the excited level of photosensitizers, optimize the electron injection, charge separation and regeneration kinetics.²⁶⁻³⁰ So far, lots of photosensitizers based on metal complexes have been designed and synthesized including most used ruthenium complexes and other complexes where the central metal ions are osmium (Os),³¹⁻³³ platinum (Pt),³⁴⁻³⁶ rhenium (Re),³⁷ copper (Cu),^{38,39} and iron (Fe).^{40,41} Here, ruthenium complexes are mainly introduced, while other metal complexes will not be detailed.

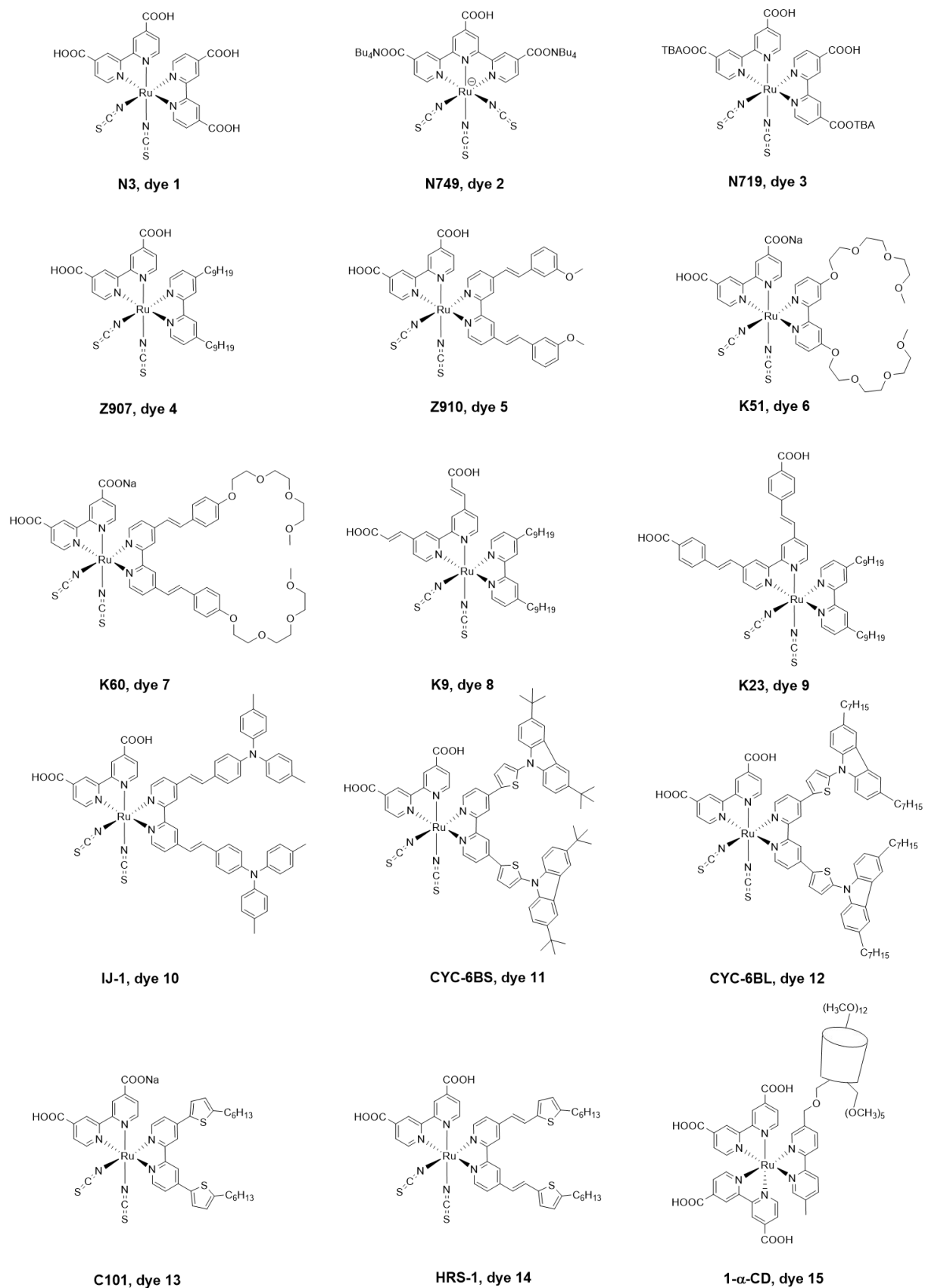


Figure II-1: Some representative ruthenium complex photosensitizers.

Some representative ruthenium complex photosensitizers are shown in Figure II-1. In 1991, O'Regan and Grätzel built the first dye-sensitized nanocrystalline solar cells using a trinuclear ruthenium complex, a novel mesoporous TiO₂ electrode and an organic solvent based electrolyte. The photoelectric energy conversion rate reached 7.1% and the incident photon to electrical current conversion efficiency was approximately 80%.¹ Since then, ruthenium complex photosensitizer has become one of the most extensively researched and uppermost used photosensitizers because of the broad absorption spectrum which can cover part of the near-infrared (NIR), suitable oxidation-reduction potential, comparatively long excited-state life time and good electrochemical stability.^{8,42-44} Two years later, Grätzel *et al.* adopted the thiocyanato derivative as the auxiliary ligand to synthesize high performing ruthenium complex cis-(SCN)₂bis(2,2'-bipyridyl-4,4'-dicarboxylate) ruthenium(II) (coded as N3, see Figure II-1, dye 1) which showed an incident photon-to-current conversion efficiency (IPCE) spectrum extending to 80% in the wavelength range between 480 and 600 nm, attaining a plateau of 85-90% between 510 and 570 nm. In view of the losses due to the conducting glass support, this indicated that the conversion of photon flux arriving onto the film into electrical current in the external circuit was practically quantitative in the wavelength domain. Moreover, the dye N3 had a broad visible light absorption spectrum, whose absorption threshold was around 800 nm. The solar-to-electric energy conversion efficiency of the sensitized solar cell device based on the N3 photosensitizer reached 10% for the first time.⁴⁵ Different strategies were subsequently developed for the replacement of the ligands of Ru complexes to optimize the dye sensitizers. In 1999, M. Grätzel *et al.* reported a black trithiocyanato-ruthenium(II) terpyridyl complex where the terpyridyl ligand was substituted by three carboxyl groups in 4,4',4''-positions (see Figure II-1, dye 2).²⁴ This so-called N749 dye, also called "black dye", displayed very efficient panchromatic sensitization over the whole visible range extending into the NIR region up to 920 nm. Light absorption in the visible part of the solar spectrum can be attributed to a metal-to-ligand charge-transfer (MLCT) process.^{7,46,47} Based on this theory, the red-shifted MLCT absorption band in the visible region was attributed to the decrease in the π^* level of the 4,4',4''-tricarboxy-2,2': 6',2''-terpyridine ligand and an increase in the energy of the t_{2g} metal orbital. The N749 dye which displayed enhanced light harvesting in the red and NIR region paved a way for the improvement of the overall efficiency of DSCs. In their subsequent work, the absorption and emission maxima of the N749 dye was investigated to show a bathochromic shift with decreasing pH and display pH-dependent excited-state lifetimes. Furthermore, IPCE over 80% was observed with the N749 dye when anchored to

nanocrystalline TiO₂ films and an overall efficiency of 10.4% ($J_{sc} = 20.5 \text{ mA}\cdot\text{cm}^{-2}$, $V_{oc} = 720 \text{ mV}$, $FF = 0.7$) under standard AM 1.5 sunlight, $100 \text{ mW}\cdot\text{cm}^{-2}$ irradiation was attained with this system.⁴⁸ M. K. Nazeeruddin *et al.* synthesized the bis (4,4'-dicarboxy-2,2'-bipyridine) ruthenium(II) complexes with different degrees of protonation and systematically studied their absorption, emission, electrochemical and photoelectrochemical properties. Among them, the doubly protonated form of the complex $(\text{Bu}_4\text{N})_2[\text{Ru}(\text{dcbpyH})_2(\text{NCS})_2]$, which was called N719 (see Figure II-1, dye 3), displayed an improved IPCE and an efficient power conversion efficiency superior to those of the other dyes. Furthermore, deprotonation of the COOH groups of the N3 dye was found to shift the oxidation and reduction potentials to more negative potentials for dyes in solution. Due to the excellent performances of the devices, the N3 and N719 dyes are usually used as reference dyes for the characterization of the photovoltaic properties of DSCs.⁴⁹ An amphiphilic heteroleptic ruthenium dye sensitizer $\text{cis-RuLL}'(\text{SCN})_2$ ($L = 4,4'$ - dicarboxylic acid - 2,2'-bipyridine, $L' = 4,4'$ - dinonyl - 2,2' - bipyridine), which was coded as Z907 (see Figure II-1, dye 4), was reported to display an excellent thermostability due to the introduction of two hydrophobic alkyl chains on the bipyridyl ligand. The solar cell devices based on Z907 dye and a quasi-solid-state polymer gel electrolyte showed an unprecedented stable performance under both thermal stress and soaking with light and reached an efficiency of over 6% under standard AM 1.5 sunlight, $100 \text{ mW}\cdot\text{cm}^{-2}$ irradiation. Moreover, the solar cell device maintained 94% of its initial performance when sustainably heated for 1000 h at 80 °C and also displayed prominent stability under light soaking for 1000 h at 55 °C under a solar simulator ($100 \text{ mW}\cdot\text{cm}^{-2}$) equipped with an ultraviolet filter.^{50,51} The solar cell device based on nanocrystalline TiO₂ films covered by a mixed self-assembled monolayer of the Z907 dye and 1-decylphosphonic acid (DPA) as a co-absorbent showed a sustainable power conversion efficiency of over 7% for 1000 h aging at 80 °C and displayed an excellent photostability when submitted to accelerated testing under a solar simulator at $100 \text{ mW}\cdot\text{cm}^{-2}$ illumination.⁵² Despite the long-term thermal device stability, the molar extinction coefficient of the amphiphilic polypyridyl ruthenium (II) complexes such as the Z907 dye are somewhat lower than the analogous N719 dye.^{53,54} One approach to enhance the molar extinction coefficient is to increase the conjugation length of the ligand, and thus to increase the light-harvesting efficiency. In order to achieve this, M. Grätzel *et al.* designed and synthesized a new heteroleptic dye through introducing 3-methoxystyryl into the ancillary ligand of the Z907 dye. The obtained $\text{Ru}(\text{dcbpy})(\text{dmsbpy})(\text{NCS})_2$ ($\text{dcbpy} = 4,4'$ -dicarboxylic acid-2,2'-bipyridine), which was named as Z910 (see Figure II-1, dye 5), displayed an excellent

light-harvesting efficiency because of the extended π -conjugated system of the bipyridine and therefore the MLCT absorption bands of the Z910 dye were red-shifted compared to the Z907 dye to show a higher molar extinction coefficient. The solar cell device based on the Z910 dye yielded an overall efficiency of 10.2% ($J_{sc} = 17.2 \text{ mA}\cdot\text{cm}^{-2}$, $V_{oc} = 777 \text{ mV}$, $FF = 0.764$) under AM 1.5 full sunlight. This study indicated that enhancing the molar extinction coefficient of dye sensitizers can be an elegant strategy to improve the photovoltaic performance of DSCs.⁵⁵ Through introduction of the tri(ethylene oxide) methyl ether into the 2,2'-bipyridine ligand, a Li^+ coordinating sensitizer, NaRu(4-carboxylic acid-4'-carboxylate) (4,4'-bis [(triethylene glycol methyl ether) methyl ether] -2,2'-bipyridine) - $(\text{NCS})_2$ (coded as K51, see Figure II-1, dye 6), has been designed and synthesized by M. Grätzel *et al.* When incorporating a nonvolatile liquid electrolyte or an organic hole-transporter, the solar cell devices based on the K51 dye showed best efficiencies of 7.8% and 3.8%, respectively, under simulated sunlight. Compared to a non-ion coordinating dye displaying a large drop in potential with the addition of Li^+ , a significant increase in the photocurrent density and only a small decrease in the open-circuit voltage were investigated with the addition of Li^+ to a nonvolatile liquid electrolyte.⁵⁶ One year later, another novel high molar extinction coefficient ion-coordinating ruthenium sensitizer, Ru (4,4 - dicarboxylic acid - 2,2' - bipyridine) (4,4' - bis (2- (4- (1,4,7,10 - tetraoxyundecyl) phenyl) ethenyl) - 2,2'-bipyridine) $(\text{NCS})_2$ (coded as K60, see Figure II-1, dye 7), was designed and synthesized thus extending the π -conjugation of the ligand of the K51 dye. Under standard AM 1.5 sunlight, $100 \text{ mW}\cdot\text{cm}^{-2}$ irradiation, the solar cell device based on the K60 dye and a nonvolatile organic-solvent electrolyte exhibited a best photovoltaic power conversion efficiency of 8.4%. Furthermore, the DSC devices displayed prominent stability when submitted to long-term high-temperature stress and light-soaking tests.⁵⁷ On the other hand, S.-R. Jang *et al.* designed, synthesized and characterized two novel ruthenium sensitizers, Ru (4,4' - dicarboxyvinyl) - 2,2' - bipyridine) (4,4' - dinonyl - 2,2' - bipyridine) $(\text{NCS})_2$ (coded as K9, see Figure II-1, dye 8) and Ru (4,4' - dicarboxy (phenylethenyl) - 2,2' - bipyridine) (4,4' - dinonyl - 2,2' - bipyridine) $(\text{NCS})_2$ (coded as K23, see Figure II-1, dye 9), which contained hydrophobic alkyl chains and an extended π -conjugation bridge between carboxylic acid groups and the ruthenium chromophore center. Both K9 and K23 displayed enhanced red response and higher molar extinction coefficients compared to the Z907 dye. The nanocrystalline TiO_2 -based thin film solar cell devices based on the K9 and K23 dye sensitizers showed short-circuit photocurrent densities (J_{sc}) of 7.70 and 8.31 mA/cm^2 , and power conversion efficiencies of 4.14 and 4.41%, respectively. The investigated higher J_{sc} of the devices based on the K9 and K23 dye sensitizers compared to

that based on the Z907 dye can be attributed to the enhanced molar extinction coefficient of the new dyes and the increased absorptions in the visible and near-IR spectral region.⁵⁸ In order to improve the molar extinction coefficient, suppress dye aggregation on TiO₂ and optimize the redox potential of the dye, the ruthenium photosensitizers with triarylamine based electron donor groups at the bipyridyl ligands and with alkyl thiophene, ethylene-dioxythienyl or carbazole groups at the bipyridyl ligands were also widely investigated.⁵⁹⁻⁶⁴ J.-H. Yum *et al.* reported a highly efficient heteroleptic ruthenium (II) complex, cis - di (thiocyanato) (4,4' - dicarboxylic acid - 2,2' - bipyridine) (4,4' - di - (2 - (4-ditolylamine phenyl) ethenyl) - 2,2' - bipyridine) ruthenium (II) (coded as IJ-1, see Figure II-1, dye 10), where the secondary electron donor moiety triphenylamine was finely tuned by substituting methyl groups. Through using a liquid electrolyte, the solar cell devices based on the IJ-1 dye showed a high power conversion efficiency of 10.3% and an incident photon-to-electron conversion efficiency of 87%.⁶⁵ The thiophene-derived species were investigated to be good candidates for increasing the conjugation length of the ancillary ligand to improve the light-harvesting ability and red-shift the MLCT band of a ruthenium complex. Furthermore, the thiophene-derived units can be easily functionalized with a alkyl-substituted hole-transport moiety, such as bis(heptyl)carbazole.^{62,64} Two new ruthenium based dyes, which was coded as CYC-B6S (see Figure II-1, dye 11) and CYC-B6L (see Figure II-1, dye 12), were reported by C.-Y. Chen *et al.* in 2008. In the structures of the two ruthenium based dyes, the alkyl-substituted carbazole moieties were incorporated in the thiophene-substituted bipyridine ligands. The absorption data of CYC-B6S and CYC-B6L were in parallel which indicated that the difference in the alkyl chain on carbazole was of no importance for the light-absorption ability of dye molecules. The solar cell devices based on CYC-B6S and CYC-B6L showed photovoltaic power conversion efficiencies of 9.72% and 8.98%, respectively.⁶⁶ The conjugated electron-rich species such as alkyl thiophene, alkyl furan, alkyl selenophene and alkyl thieno[3,2-b]thiophene can be applied in the ancillary ligands of heteroleptic ruthenium dye sensitizers to further enhance the molar extinction coefficient.^{9,67-69} In order to increase the optical absorptivity of mesoporous TiO₂ film and charge collection yield in DSCs, a new heteroleptic polypyridyl ruthenium complex, coded as C101 (see Figure II-1, dye 13), was reported by M. Grätzel *et al.*⁹ The solar cell devices based on the C101 dye and an acetonitrile-based electrolyte showed notably high efficiencies of 11.0-11.3% under AM 1.5 global sunlight. Significantly, when incorporating a low volatility 3-methoxypropionitrile electrolyte and a solvent-free ionic liquid electrolyte, the devices based on the C101 dye showed corresponding efficiencies of more than 9.0%, which indicated

that over 95% of the initial performance after 1000 h full sunlight soaking at 60°C was retained. Through introducing 2-thiophene-2-yl-vinyl into the ancillary ligand of the ruthenium complexes, S. Yanagida *et al.* designed and synthesized a novel hydrophobic ruthenium complex, which was coded as HRS-1 (see Figure II-1, dye 14).⁷⁰ The molar extinction coefficient of the lowest energy absorption band of the HRS-1 dye was increased by 33% and its absorption maximum wavelength was red-shifted of about 10 nm compared to that of the N719 dye. Under standard AM 1.5 sunlight, 100 mW·cm⁻² irradiation, the solar cell device based on the HRS-1 dye showed an overall conversion efficiency of 9.5% ($J_{sc} = 20$ mA·cm⁻², $V_{oc} = 680$ mV, FF = 0.69). To facilitate dye/redox couple interaction and dye regeneration in nanocrystalline TiO₂-based DSCs, J. Faiz *et al.* introduced a cyclodextrin unit into the ancillary ligand of the ruthenium tri-bipyridyl core to obtain a supramolecular complex which was coded as 1- α -CD (see Figure II-1, dye 15). Incorporating a composite polymer electrolyte, the solar cell devices based on the 1- α -CD dye showed a higher short-circuit photocurrent ($J_{sc} = 4.21$ mA·cm⁻²), open-circuit photovoltage ($V_{oc} = 590$ mV), and overall conversion efficiency (1.64%) compared to those of solar cell devices based on the dye without the cyclodextrin unit ($J_{sc} = 3.84$ mA·cm⁻², $V_{oc} = 521$ mV, $\eta = 1.17\%$). The enhanced performances of the solar devices based on the 1- α -CD dye can be attributed to guest-host interactions between the dye and the iodide/triiodide redox couple. This study indicated that the regeneration of the dye can be facilitated through binding of the iodide/triiodide redox couple into the CD cavity.⁷¹

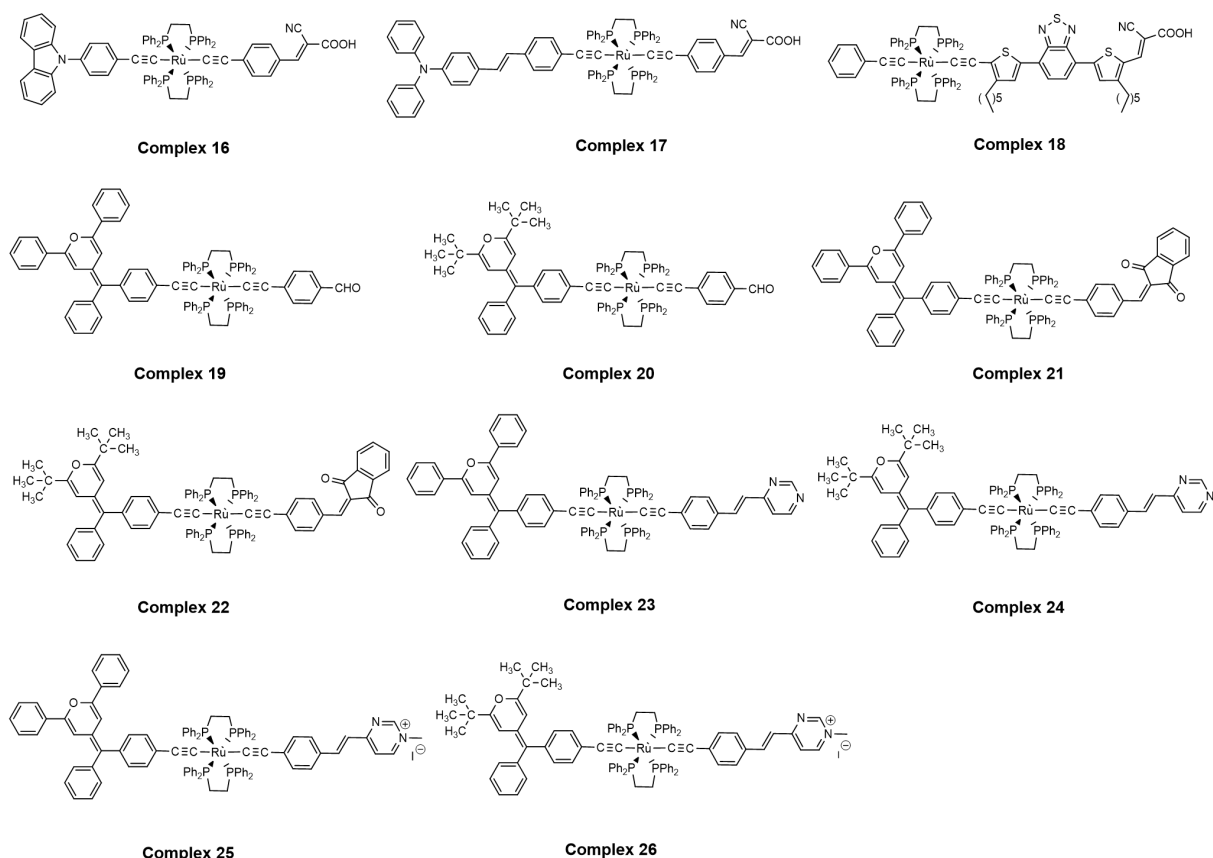


Figure II-2: Several representative asymmetrical σ -dialkynyl ruthenium complexes containing original D- π -Ru- π -A architectures

Organometallic complexes have been considered as promising materials for light absorption due to their higher electroconductibility and weaker π -conjugated bridge length dependence than their purely organic counterparts of comparable length. Furthermore, the metal complexes can act as redox switchable units because of their strong ligand-mediated electronic effects.^{10,72-75} In this context, the incorporation of the ruthenium metal fragment into the π -conjugated scaffold of push-pull chromophores have been investigated to be a promising method to improve the intramolecular charge transfer and enhance the performance of DSCs.^{6,10,76,77} In view of the advantage of the linear geometry of the *trans*-ditopic ruthenium-based unit such as [Ru(dppe)₂] (dppe: bisdiphenylphosphinoethane) or [Ru(dppm)₂] (dppm: bisdiphenylphosphinomethane) and their π -conjugated characters, such organometallic complexes may present outstanding electronic and structural properties that lead to a wide range of applications.^{7,77} Several representative asymmetrical σ -dialkynyl ruthenium complexes containing original D- π -Ru- π -A architectures are shown in Figure II-2. In 2011, A. Colombo *et al.* reported a novel dinuclear ruthenium(II) complex where two Ru atoms were separated by a bridge consisting of a 2,1,3-benzothiadiazole acceptor moiety

flanked on either side by 2,5-thienyl donor units. This rather simple rodlike diruthenium-acetylide complex was the first example which employed Ru-acetylide as a tool for the design of donor materials. The bulk heterojunction solar cell device based on this dye showed a power conversion efficiency of 0.1% upon blending with a methanofullerene derivative.⁷⁸ This study paved the way for the employment of rodlike Ru-acetylide complexes as the dye sensitizers for DSCs. Despite the reported unsymmetrical diacetylide-transition-metal complexes, asymmetric diacetylide push-pull complexes containing strong donor and/or acceptor groups have barely been reported before 2014.⁷⁹⁻⁸⁴ In 2014, the first example of chromophores for DSCs presenting a ruthenium-diacetylide moiety embodied within a push-pull architecture (see Figure II-2, complex 16) was reported by our group. Such an innovative photosensitizer based on the D- π -[M]- π -A design concept in which [M] was the [Ru(dppe)₂] metal fragment, appropriately end-capped with an anchoring carboxylic acid function, was further adsorbed onto a semiconducting TiO₂ porous thin film to serve as a photosensitizer in hybrid solar cells. The solar cell devices based on the complex 16 along with chenodeoxycholic acid as a co-adsorbent showed a good spectral response with a broad IPCE and overall power conversion efficiency of 7.32% ($J_{sc} = 15.56 \text{ mA}\cdot\text{cm}^{-2}$, $V_{oc} = 680 \text{ mV}$, $FF = 0.692$).⁶ Due to the decent optoelectronic and photovoltaic properties, this asymmetric Ruthenium-diacetylide organometallic complex paved the way to a new generation of organometallic photosensitizers for photovoltaic applications. A series of dipolar π -delocalized Ru(II) dialkynyl complexes were designed, synthesized and characterized by F. Nisic *et al.* in 2015 in order to get a better understanding of the 2,1,3-benzothiadiazole as acceptor moiety and to study new “Donor-phenylalkynyl-Ru-alkynylphenyl-Acceptor” architectures.⁸⁵ In this study, the second-order nonlinear optical properties and the dipole moments of these complexes were investigated by the electric field induced second harmonic generation technique and density functional theory calculations. Among these complexes, two most promising push-pull ruthenium diacetylide complexes (see Figure II-2, complex 17 and 18) bearing a carboxylic acid anchoring group were investigated as photosensitizers in DSCs. The solar cell devices based on the complex 17 and the appropriate electrolyte showed a best overall power conversion efficiency of 1.5% ($J_{sc} = 4.6 \text{ mA}\cdot\text{cm}^{-2}$, $V_{oc} = 578 \text{ mV}$, $FF = 0.561$) while the devices based on the complex 18 showed that of 0.3% ($J_{sc} = 1.5 \text{ mA}\cdot\text{cm}^{-2}$, $V_{oc} = 432 \text{ mV}$, $FF = 0.3$). This study indicated that D- π -[M]- π -A structured metal acetylide complexes were positively suitable for dye sensitizers in DSCs with the aim to obtain the right compromise between the best efficiency together with a satisfactory stability and the introduction of selected functional groups along the push-pull chain may play a key role in

acquisition of good efficiencies in DSCs. Recently, R. J. Durand *et al.* reported a series of dipolar π -delocalized Ru(II) dialkynyl chromophores (see Figure II-2, complexes 19 to 26) based on the innovative asymmetrical D- π -[Ru]- π -A push-pull design concept which incorporated pyranilidene ligands as pro-aromatic electron-donating groups and formaldehyde, indane-1,3-dione, pyrimidine or pyrimidinium as electron-withdrawing groups separated by ruthenium bis-acetylidate fragments and π -conjugated linkers.¹⁰ Through the investigation of their electrochemical, photophysical and second-order nonlinear optical properties compared to those of purely organic compounds, it can be concluded that the [Ru(dppe)₂] metal fragment merged into the π -conjugated core of pyranilidene-N-methylated pyrimidine ring push-pull complexes resulted in the enhancement of the second-order nonlinear optical responses and the nonlinear optical properties of the easily modulated push-pull diacetylidate ruthenium-based complexes in return resulted in versatility of such complexes. Complex 25 and 26 containing pyrimidinium species displayed significantly high $\mu\beta$ values which indicated that the excited states of the two complexes were more polarized than their ground states.

Section II.3. of this manuscript focuses on our work relative to new Ru-diacetylidate organometallic complexes designed for n-type DSCs and their relevant optical and electrochemical properties, theoretical calculations as well as photovoltaic characterization.

II.2.2. Porphyrins and Phthalocyanines

The limited absorption in the near-infrared region of the solar spectrum is one of the short boards of the ruthenium complexes as photosensitizers, while porphyrins and phthalocyanines have intense spectral response in the near-infrared region and exhibit excellent thermal stability, optoelectronic and electrochemical properties, which provide great advantage for photovoltaic applications.^{7,86-88}

II.2.2.1. Porphyrins

In the last decade, many extensive research efforts have been devoted to the design, synthesis and characterization of porphyrin sensitizers for DSCs. As a consequence, porphyrin sensitizers exhibit remarkable solar cell performances which can be comparable to conventional ruthenium sensitizers such as N3 and N719.^{89,90} At the very beginning, the research of porphyrins as potential sensitizers for DSCs focused on their intense absorption bands in the visible region, versatile modifications of their core, and facile tuning of the

electronic structures. However, the overall power conversion efficiencies of DSCs based on typical porphyrin sensitizers were much lower than those based on conventional ruthenium sensitizers because of the poor light-harvesting ability at around 500 nm and beyond 600 nm of porphyrin sensitizers. To tackle this drawback, the push-pull structure and/or the elongation of porphyrin π -conjugated system were introduced in follow-up studies to improve the light-harvesting property which finally resulted in highly efficient porphyrin DSCs.⁸⁹⁻⁹⁵ Some representative porphyrin photosensitizers can be found in Figure II-3.

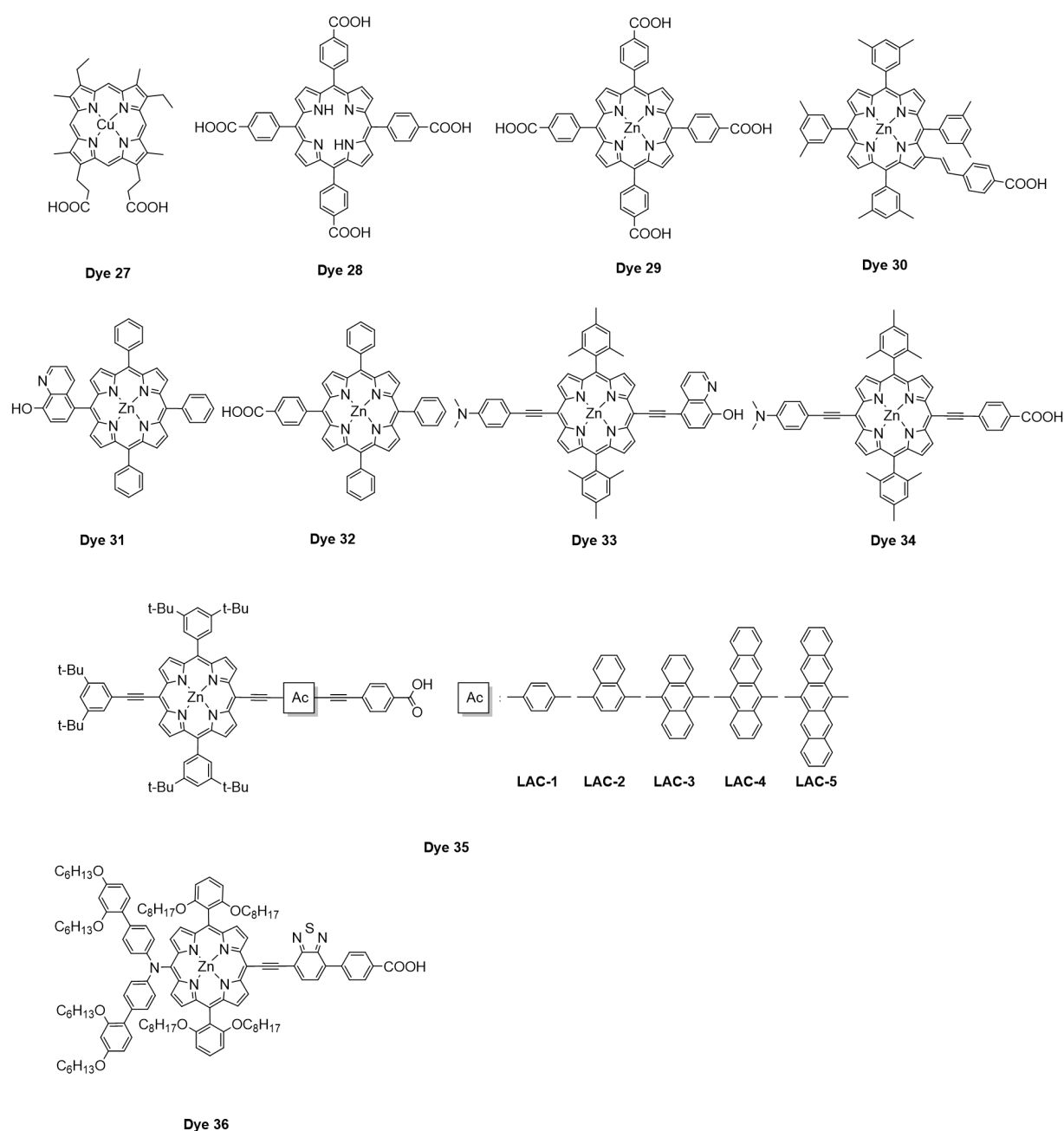


Figure II-3: Some representative porphyrin photosensitizers.

In 1993, A. Kay and M. Grätzel reported the pioneering work to design and synthesize a novel copper mesoporphyrin dye sensitizer (see Figure II-3, dye 27). With a 12- μm -thick TiO_2 film sensitized by the dye 27, the IPCE was investigated up to 83% in the Soret peak at 400 nm which corresponded to nearly unity quantum efficiency of charge separation when light reflection losses were taken into account. The overall power conversion efficiency of DSCs based on the dye 27 reached up to 2.6% ($J_{\text{sc}} = 9.4 \text{ mA}\cdot\text{cm}^{-2}$, $V_{\text{oc}} = 520 \text{ mV}$). The free carboxyl groups were proved to be important for adsorption and sensitization on TiO_2 through the comparison of different chlorophyll derivatives while π -conjugated system of the carboxyl groups in the chromophores were proved to be dispensable for efficient electron transfer process. Moreover, the employment of co-adsorbents such as cholanic acids was found to significantly prevent unfavorable dye aggregation.⁹⁶ Another commonly used porphyrin photosensitizer for DSCs, tetra (4-carboxyphenyl) porphyrin (coded as TCPP, see Figure II-3, dye 28), was reported by S. Cherian and C. C. Wamser in 2000. At one sun light simulating, the solar cell device based on TCPP-sensitized TiO_2 electrodes showed a short-circuit photocurrent of about $6 \text{ mA}\cdot\text{cm}^{-2}$, an open-circuit photopotential of 485 mV and a decent overall energy conversion efficiency of about 3%. The IPCE was also investigated up to 55% at the Soret peak and 25-45% at the Q-band peaks.⁹⁷ In the same year, Y. Tachibana *et al.* reported their work to compare the different electron injection and charge recombination properties of the N3 dye, TCPP and zinc based tetracarboxyphenyl porphyrins (ZnTCPP) (see Figure II-3, dye 29) because all of the three dyes displayed large differences in their oxidation potentials and photophysics, while retaining similar carboxyl groups for anchoring onto the TiO_2 semiconductor. Significantly, the differences in photophysics and redox chemistry of the three dyes were proved to be of no importance in the interfacial electron transfer kinetics observed following adsorption of these dyes to the nanocrystalline TiO_2 films. The kinetics of electron injection into the TiO_2 conduction band were found to be indistinguishable while the kinetics of electron recombination were found to be weakly sensitive for all three dyes. Moreover, they attributed the lower efficiency of porphyrin-sensitized DSCs to an increased excited-state decay caused by dye aggregation on the TiO_2 surface.⁹⁸ Zinc/free base porphyrin heterodimers were also designed and employed in TiO_2 -based DSCs. The antenna effects of such zinc/free base porphyrin heterodimers on DSC performance were investigated to result in the similar IPCE values.⁹⁹ A series of porphyrin dyes with different central metal ions including Cu(II) and Zn(II) and different anchoring groups including $-\text{COOH}$ and $-\text{PO}_3\text{H}_2$ were designed and synthesized by M. K. Nazeeruddin *et al.* In this study, the resultant photovoltaic data indicated that for porphyrin sensitizers with carboxylic anchoring groups,

the Zn containing diamagnetic metalloporphyrins showed much higher IPCE values than those observed for the Cu containing paramagnetic metalloporphyrins. Solar cell devices based on porphyrin sensitizers with a phosphonate anchoring group showed lower efficiencies than those with a carboxylate anchoring group. The solar cell device based on the reported porphyrin sensitizer with Zn(II) and -COOH anchoring group (see Figure II-3, dye 30) showed the highest power conversion efficiency of 4.8% than those based on the other dyes and a higher IPCE value of 75% at λ_{\max} . This study paved the way for improving the efficiency of nanocrystalline injection solar cells through employing suitable porphyrins with a small band gap and which absorb in the visible and near IR regions of the solar spectrum.¹⁰⁰

In most cases, carboxylic acids such as benzoic acid and cyanoacrylic acid are used as anchoring groups for attaching dye sensitizers onto the semiconductors. However, under severe conditions such as exposure to aqueous and alkaline electrolytes, the carboxylic acids maybe dissociate from the semiconductor surface which results in the detachment of adsorbed dyes from TiO₂ and finally results in adverse effect on the durability of DSCs for photovoltaic applications.¹⁰¹ In 2012, H. He *et al.* for the first time reported their work to employ 8-Hydroxylquinoline (HOQ) as a strong alternative anchoring group porphyrin dyes to improve the long-term stability of solar cells. Through the comparison of an 8-hydroxylquinoline modified porphyrin, TPPZn-HOQ, (see Figure II-3, dye 31) and a benzoic acid modified porphyrin, TPPZn-COOH (see Figure II-3, dye 32), it was found that HOQ was a more reliable anchoring group compared to the benzoic acid group for porphyrin dyes. Moreover, when employing a complementary dye boron dipyrromethene (BET), the overall power conversion efficiency can be significantly improved.¹⁰² Two years later, they reported another three porphyrin dyes including DPZn-HOQ and DPZn-COOH (see Figure II-3, dyes 33 and 34) for DSCs. Both DPZn-HOQ and DPZn-COOH exhibited a D- π -A configuration through employing N,N-dimethylaniline as a donor group and HOQ and para-benzoic acid (BZA) as acceptor groups. As a better photosensitizer, DPZn-HOQ showed a broader and stronger light absorption in the red region than DPZn-COOH. Under the same conditions, the solar cell device based on DPZn-HOQ exhibited a higher power conversion efficiency compared to that based on DPZn-COOH, which was 3.09% and 1.76%, respectively. When employing a complementary dye boron dipyrromethene (BET), the efficiency of DPZn-HOQ-sensitized solar cells was further improved up to 3.41%.¹⁰³

A possible strategy to achieve a better light-harvesting ability in the visible and near infrared (NIR) regions for porphyrin sensitizers is to develop π -extended porphyrins. For example, C.-Y. Lin *et al.* designed and prepared a series of acene-modified zinc porphyrins

(benzene to pentacene, denoted as LAC-1 to LAC-5, see Figure II-3, dye 35) and studied their absorption spectra, electrochemical properties, and photovoltaic properties. With respect to the performances of DSCs using LAC serial porphyrins, the solar cell devices based on LAC-1 to LAC-5 showed the overall power conversion efficiencies of 2.95%, 3.31%, 5.44%, 2.82% and 0.10%, respectively. The IPCE data indicated that the gap between B and Q bands of LAC-3 was minimized due to its broadened absorption bands, which resulted in the best performance of DSCs. The very poor performance of LAC-5 was deduced to be result from rapid non-radiative relaxation of the molecule in the singlet excited state.¹⁰⁴

As referred above, porphyrin sensitizers have been research hotspot from their birth until now. Up to date, the record efficiency for solar-energy-to- electricity conversion based on porphyrin sensitizers associated with a cobalt-based redox mediator is 13% and was reported by S. Mathew *et al.* in 2014. In their study, a molecularly engineered porphyrin dye, coded as SM315 (see Figure II-3, dye 36), which features the prototypical structure of a D- π -A was employed in order to maximize electrolyte compatibility and improve light-harvesting properties.² However, there are still remaining challenges for practical applications of porphyrin-based DSCs such as further improvement of the light-harvesting ability in the visible and NIR regions, suppression of porphyrin aggregation on TiO₂ to reduce undesirable quenching of the excited singlet state, optimization of electron injection and inhibition of charge recombination processes at the interface by controlling the adsorption structures on TiO₂ and so on.^{7,86-90}

II.2.2.2. Phthalocyanines

Phthalocyanines are planar 18 π -electron macroheterocycles that consist of four isoindole subunits linked together through nitrogen atoms.¹⁰⁶ Their specially conjugated system endow them with intense absorption spectra, presenting two major bands including the Q-band (620-700 nm) and the Soret B band (near 350 nm). Therefore, phthalocyanines, with high molar extinction coefficients in a wide region of electromagnetic spectrum, can be promising targets as photosensitizers for DSCs. Through the addition of a metal into the ring and axial and/or peripheral substitution with a variety of ligands, the physical and optical properties of phthalocyanines can be easily tailored. Moreover, phthalocyanines are thermally and chemically stable and exhibit appropriate redox properties for sensitization of TiO₂ films, thus representing perfect light-harvesting systems for solar-energy-to-electricity conversion devices.^{7,92,105-111} Some phthalocyanine sensitizers used in DSCs are shown in Figure II-4.

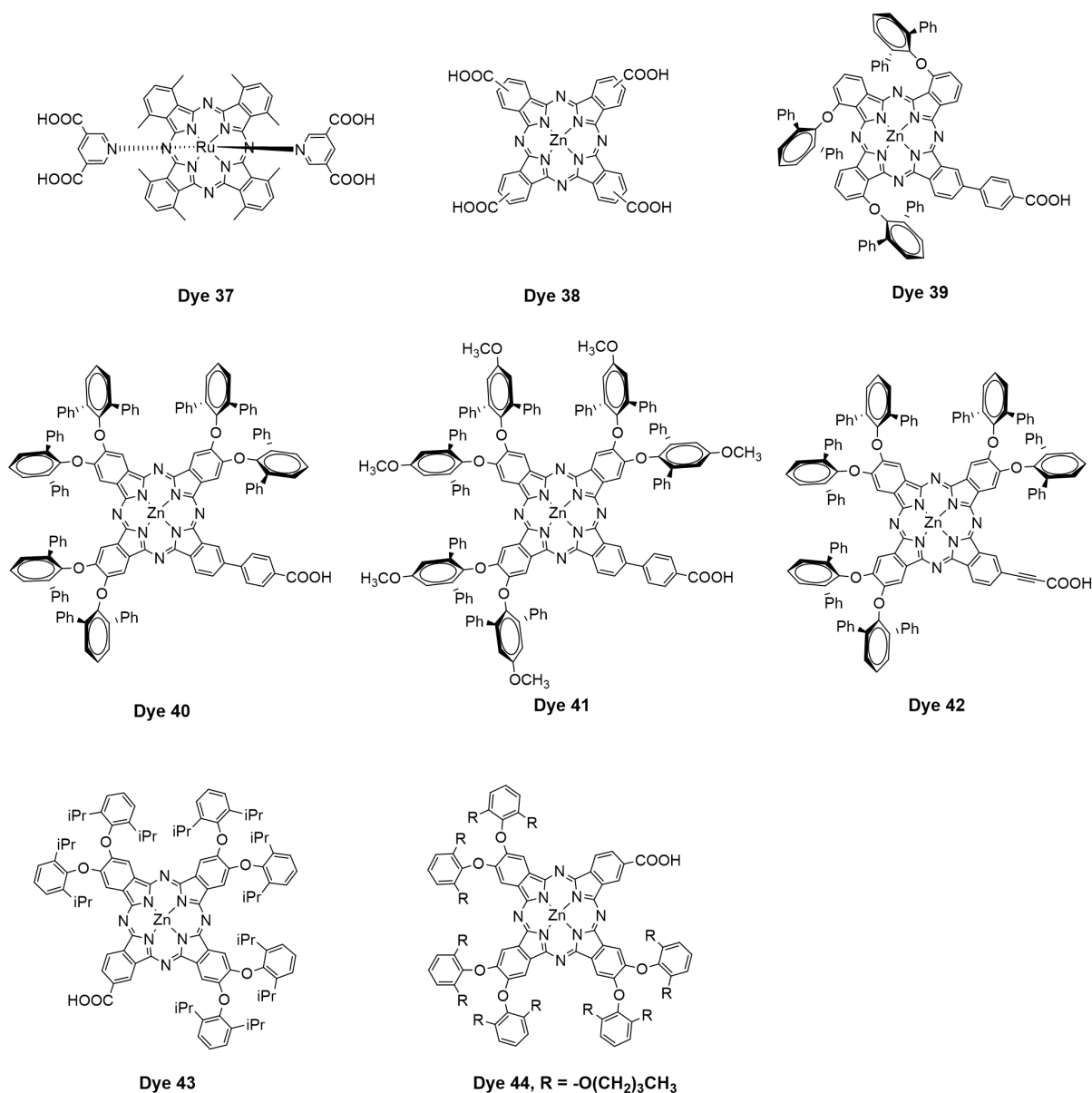


Figure II-4: Some phthalocyanine sensitizers used in DSCs.

In 1998, M. K. Nazeeruddin *et al.* reported the pioneering work relative to the design and synthesis of a ruthenium phthalocyanine photosensitizer for DSCs (see Figure II-4, dye 37) anchored to nanocrystalline TiO₂ films through axial pyridine 3,4-dicarboxylic acid ligands for DSCs. They found that very efficient quenching of the emission of the dye 37 resulted from electron injection from the excited triplet state of the phthalocyanine into the conduction band of the TiO₂. The IPCE was investigated to exceed 60% based on dye 37 sensitized solar cell device with a sandwich type cell configuration. In this study, a significantly novel pathway for attaching phthalocyanines to TiO₂ through axially attached pyridine ligands was proposed which paved the way for improvement of the near-IR response in DSCs.¹¹² Subsequently, they designed and synthesized several zinc(II) and aluminum(III)

phthalocyanines substituted by carboxylic acid and sulfonic acid groups as anchoring groups. Among these phthalocyanines, the zinc(II) 2,9,16,23-tetracarboxy-phthalocyanine (see Figure II-4, dye 38) based solar cell device showed a high IPCE of 45% at 700 nm and a power conversion efficiency of 1%.¹¹³ S. Mori *et al.* reported their synthesis of highly sterically hindered zinc phthalocyanines (see Figure II-4, dye 39 and dye 40) having three or six 2,6-diphenylphenoxy groups and proposed that the three-dimensional enlargement of the molecular structure can suppress aggregation almost completely. Through blocking of the interaction between the π -conjugated ring and I_3^- by the non-conjugated bulky substituents, the dye aggregation and recombination can be significantly prevented. The solar cell devices based on the dye 40 showed efficiency of 4.6% and IPCE of 78% at the maximum absorption of the Q band. For the first time phthalocyanine-based DSCs attained such a high power conversion efficiency without the presence of CHENO (3 α ,7 α -dihydroxy-5 β -cholic acid) as coadsorbent.¹¹⁴ Based on the former work, they further reported a novel phthalocyanine bearing an additional electron-donating methoxy group on the peripheral 2,6-diphenylphenoxy species (see Figure II-4, dye 41) which was achieved by enhancing the unsymmetrical and 3D zinc phthalocyanine structure. The maximum IPCE of the dye 41 was 72% at $\lambda=600-720$ nm, which corresponded to the Q band of zinc phthalocyanines. When used as a light harvesting dye on a TiO₂ electrode under standard solar conditions, the sterically isolated zinc phthalocyanine dye 41 showed a power conversion efficiency of 5.3%.¹¹⁵ The conjugated spacers with an anchoring group can result in significant changes in the overall power conversion efficiency for phthalocyanine sensitizers. Particularly, ethynyl bridges have been investigated to be very effective for the connection of the phthalocyanine π -system with the carboxylic anchoring group.^{92,105,107,108} In this context, M.-E. Ragoussi *et al.* developed a new zinc phthalocyanine substituted with peripheral diphenylphenoxy groups and an ethynyl bridge between the anchoring carboxy group and the phthalocyanine macrocycle (see Figure II-4, dye 42). The solar cell device based on the dye 42 showed a power conversion efficiency of 5.5% ($J_{sc} = 12.3 \text{ mA}\cdot\text{cm}^{-2}$, $V_{oc} = 638 \text{ mV}$, $FF = 0.7$) under one sun irradiation, while the increased power conversion efficiency of 6.1% was attained based on the dye 42 sensitized solar cell under $9.5 \text{ mW}\cdot\text{cm}^{-2}$ irradiation.¹¹⁶ They further optimized the devices to improve the power conversion efficiency up to 6.01% under one sun irradiation. The optimization was associated with the use of an optimized photoanode obtained, for instance, from a thicker TiO₂ film and using overnight dye sensitization.¹¹⁷ The change of the bridge between the anchoring carboxylic acid group and zinc phthalocyanine core plays a key role in the electron injection efficiency from the lowest unoccupied molecular orbital (LUMO)

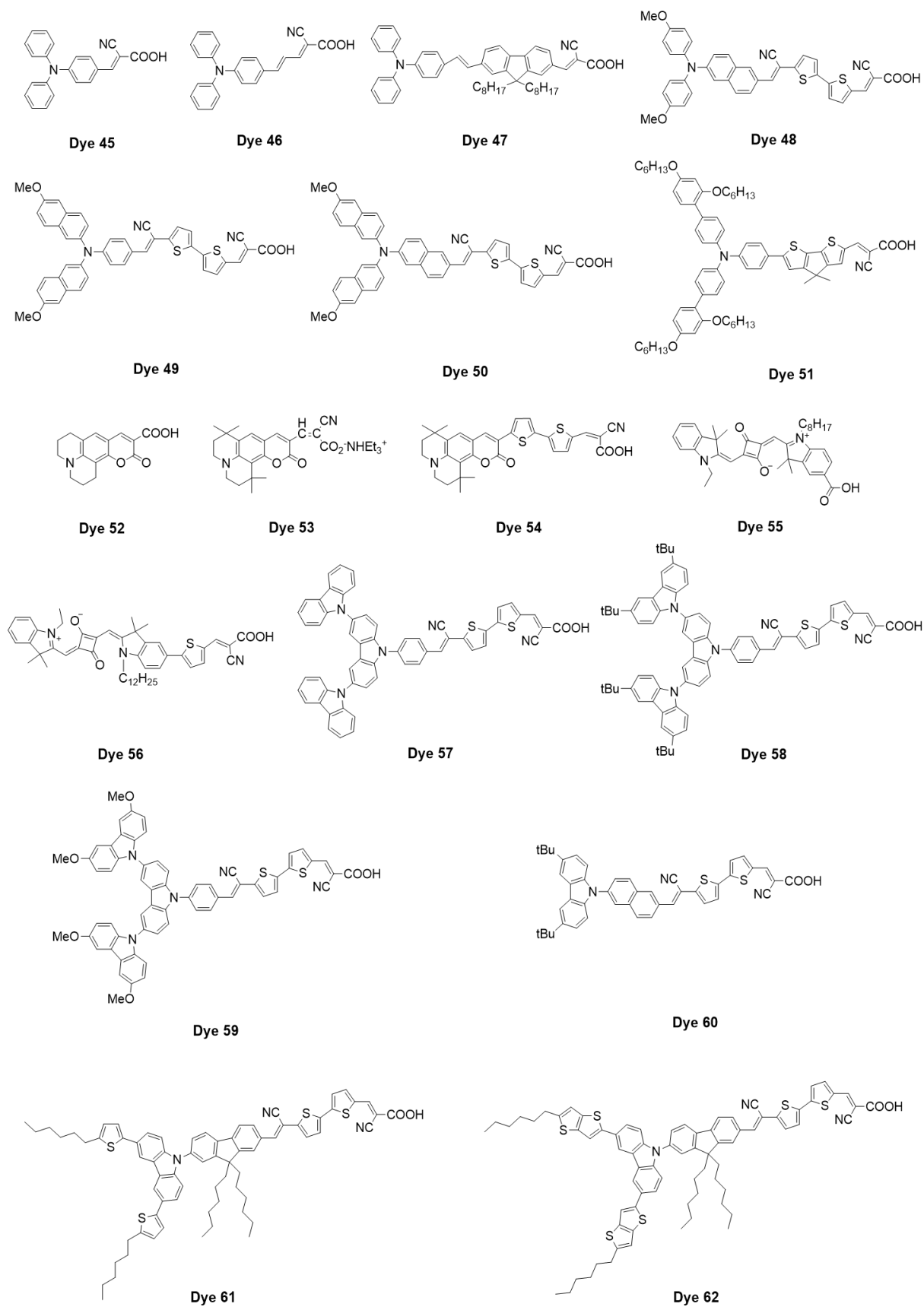
of the dye into the conduction band of TiO₂.¹¹⁸⁻¹²⁰ In this context, a series of zinc phthalocyanine sensitizers with different adsorption sites were designed and synthesized in order to investigate the dependence of adsorption site structures on the solar cell performances in zinc phthalocyanine based DSCs. Among these phthalocyanine sensitizers, the one possessing a single carboxylic acid directly attached to the zinc phthalocyanine ring and bearing six 2,6-diisopropylphenoxy units (see Figure II-4, dye 43) showed a best power conversion efficiency of 5.9% when used as a light-harvesting dye on a TiO₂ electrode under one sun condition.¹²¹ T. Ikeuchi *et al.* reported an asymmetric zinc phthalocyanine sensitizer bearing propoxy groups in the 2 and 6 positions of peripheral phenoxy units with alkyl chain substituents which was coded as PcS20 (see Figure II-4, dye 44). The 2,6-diisopropylphenoxy units were also used in order to prevent aggregation of the dye on TiO₂ surface. Under simulated AM 1.5 global sunlight, the solar cell device based on PcS20 in contact with an electrolyte containing 0.6 M DMPIImI, 0.1M LiI, 0.05 M I₂ and 0.5 M tBP in acetonitrile led to a record power conversion efficiency of 6.4% ($J_{sc} = 15.1 \text{ mA}\cdot\text{cm}^{-2}$, $V_{oc} = 600 \text{ mV}$, $FF = 0.71$). The high efficiency can be attributed to high absorption properties and the high density adsorption of PcS20 on TiO₂.¹²²

It is worth mentioning that, despite the refined characteristics and advantages compared to other dyes, the solubility of phthalocyanine sensitizers is usually poor and needs to be further improved by structural optimization in order to enhance the sensitization process. On the other hand, phthalocyanine sensitizers suffer from strong aggregation on the semiconductor surface and lack of directionality in the excited state, which unfavourably limit the power conversion efficiency of DSCs. Therefore, the conversion efficiencies attained by phthalocyanine-sensitized solar cells have not yet been able to match the values obtained by porphyrin-based devices.^{7,92,105,109-111}

II.2.3. Metal-Free Organic Dye Sensitizers

Despite the broad absorption spectra and favorable photovoltaic properties, the scarcity and high cost of metal complexes have motivated the synthesis of novel dyes, for example dyes using inexpensive metal complexes, such as zinc porphyrins and phthalocyanines or fully organic dyes, such as indoline-, coumarin-, perylene-, phenoxazine-, or triarylamine-based dyes.^{7,86-88,110,123-125} Among these alternative dyes, fully organic dyes are good candidates for photosensitizers due to their distinctive features such as high extinction coefficients, low synthetic and purification cost, tunable absorption spectra, fluorescence emission and energy levels via molecular structure tailoring and essentially no limitation of

resources.¹²⁴⁻¹²⁷ Generally, metal-free organic dyes are designed on the D- π -A system, featuring an electron donor part and an electron acceptor part bridged by a π -conjugated spacer to ensure efficient charge transfer from the ground state to the excited state. For n-type organic dyes, the electrons are injected from the excited dye into the conduction band of the semiconductor via the electron acceptor part. Therefore, the frontier molecular orbitals energy levels of the dye should match the corresponding energy levels of conduction band edge of semiconductor and electrolyte redox potential to ensure efficient electron injection and dye regeneration. The HOMO level is relative to the donor group and π -spacer bridge and the LUMO level is relative to the acceptor group and can be easily modified to tune the properties of organic dyes for photovoltaic applications.^{7,124-128} Besides the D- π -A architecture, the typical D-A- π -A and D-D- π -A have also been employed to design efficient organic dye molecules.¹²⁹⁻¹³¹ Up to date, hundreds of n-type fully organic dyes have been designed, prepared and obtained impressive efficiencies. Herein, a few metal-free organic dye molecular scaffolds such as triarylamine, coumarin, squaraine, carbazole, etc. are briefly introduced. Some representative metal-free organic photosensitizers can be found in Figure II-5.

**Figure II-5:** Some representative metal-free organic photosensitizers.

The prominent stability, electron-donating ability and aggregation resistance resulting from a non-planar molecular configuration of especially triarylamine-based photosensitizers have endowed them promising candidates for DSCs applications. Furthermore, triarylamine-based photosensitizers usually exhibit broad and intense spectral responses which can be primarily attributed to the intramolecular charge transfer process between the powerful electron-donating capability of triarylamine moieties and the electron-accepting anchoring group.¹³²⁻¹³⁴ In 2004, T. Kitamura *et al.* for the first time reported two organic dyes employing the triphenylamine unit as the electron-donating group (see Figure II-5, dye 45 and dye 46). Under irradiation of AM 1.5 simulated solar light, the dye 45 and dye 46 based solar cell devices showed the respectable efficiencies of 3.3% and 5.3%, respectively.¹³⁴ Since then, many efforts have been put in to develop various triphenylamine-based photosensitizers.^{124,132-134} For example, in 2011, H. Zhou *et al.* reported a series of new dipolar organic dyes employing triarylamine as the electron-donating group, 2-cyanoacrylic acid as the electron-withdrawing group and the fluorenevinylene as the conjugated bridge. When used as photosensitizers in DSCs, the power conversion efficiencies were in the range of 2.8%-5.5%. Among these triarylamine-based dyes, the dye with a balanced conjugated spacer (see Figure II-5, dye 47) showed the highest power conversion efficiency of 5.56% ($J_{sc} = 11.33 \text{ mA}\cdot\text{cm}^{-2}$, $V_{oc} = 860 \text{ mV}$, $FF = 0.57$) when applied in DSCs.¹³⁵ Our group also reported a series of novel organic photosensitizers based on modified triarylamine moieties (see Figure II-5, dyes 48, 49, 50). These triarylamine-based photosensitizers bearing one to three naphthyl units in place of phenyl rings were designed on the D- π -A system in order to explore the effect of the insertion of naphthyl units instead of the phenyl groups. An additional cyanovinyl unit was introduced into the conjugated spacer in order to improve the absorption wavelength of the three dyes for better light harvesting. It was found that the introduction of naphthyl units into the triarylamine core induced a slight blue-shift of the absorption maximum and a significant enhancement of the molar extinction coefficients. When employed in DSCs, the three dyes showed excellent spectral response with IPCE greater than 85% from 470 to 580 nm and overall power conversion efficiencies of 6.6% for the dye 48 ($J_{sc} = 14.0 \text{ mA}\cdot\text{cm}^{-2}$, $V_{oc} = 627 \text{ mV}$, $FF = 0.745$), 6.2% for the dye 49 ($J_{sc} = 13.9 \text{ mA}\cdot\text{cm}^{-2}$, $V_{oc} = 618 \text{ mV}$, $FF = 0.717$) and 6.4% for the dye 50 ($J_{sc} = 13.9 \text{ mA}\cdot\text{cm}^{-2}$, $V_{oc} = 625 \text{ mV}$, $FF = 0.732$).¹³⁶ Simultaneously, a number of triphenylamine-based photosensitizers were designed on the D-A- π -A and D-D- π -A architectures and showed impressive efficiencies.^{129-131,137} J.-H. Yum *et al.* reported a cyclopenta-dithiophene-bridged donor-acceptor dye (see Figure II-5, dye 51) where the triphenylamine core was functionalized by the adjacent phenyl rings with hexyloxy group in

order to suppress dye aggregation and charge recombination. When embedded in DSC devices in combination with a cobalt complex using tridentate ligands $[\text{Co}(\text{bpy-pz})_2]^{3+/2+}$ (PF6)_{3/2} as redox mediator high open-circuit voltage, ~1000 mV, along with short circuit photocurrent of $13.06 \text{ mA}\cdot\text{cm}^{-2}$, and FF of 0.77 were obtained, resulting in PCE of 10%.¹³⁸

The coumarin-based dye, coded as coumarin 343 (see Figure II-5, dye 52), was employed to explore the charge injection dynamics from the surface-bound dye to the conduction band of TiO₂ for the first time in 1996. The ultrafast fluorescence dynamics indicated that the charge injection from the surface-bound dye to the conduction band of TiO₂ proceeded on a time scale of about 200 fs, and such an excellent charge injection efficiency can be attributed to strong electronic coupling between the dye and TiO₂ energy levels.¹³⁹ From then on, coumarin-based dyes, as one of the most promising organic photosensitizers, have come into sight because their excellent photoresponse in the visible region, good long-term stability and appropriate LUMO levels matching with the conduction band of TiO₂.^{7,123-125} K. Hara *et al.* reported a novel coumarin-based dye whose carboxyl group was directly connected to the conjugated methine chain (see Figure II-5, dye 53). The structure of the dye 53 was advantageous for improving the injection of electrons into semiconductors and its cyano group connected to the methine chain and the carboxyl group might be effective for electron injection due to its strong electron acceptability. When embedded in TiO₂-based DSCs, the coumarin-based dye 53 showed a high power conversion efficiency of 5.6% ($J_{\text{sc}} = 13.8 \text{ mA}\cdot\text{cm}^{-2}$, $V_{\text{oc}} = 630 \text{ mV}$, $\text{FF} = 0.63$) under standard AM 1.5 irradiation which was comparable to the $\text{Ru}(\text{dcbpy})_2(\text{NCS})_2$ system.¹⁴⁰ The thiophene moieties can be introduced into coumarin-based dyes to improve the photovoltaic performance of dye-sensitized nanocrystalline TiO₂ solar cells. In this context, a coumarin-based dye (see Figure II-5, dye 54) endowed with a bithiophene moiety into the methine chain was reported to attain a solar-energy-to-electricity conversion efficiency of 7.7% ($J_{\text{sc}} = 14.3 \text{ mA}\cdot\text{cm}^{-2}$, $V_{\text{oc}} = 730 \text{ mV}$, $\text{FF} = 0.74$) when employed in DSCs under standard AM 1.5 sunlight, $100 \text{ mW}\cdot\text{cm}^{-2}$ irradiation.¹⁴¹ The transient absorption spectroscopy measurements of the dye 54 revealed an ultrafast electron injection (<100 fs) from the dye into the conduction band of TiO₂, which was much faster than the emission lifetime of the dye (1.0 ns), thus showing a highly efficient electron injection yield of near unity.¹⁴²

Squaraine dyes are also good candidates for photovoltaic applications due to their excellent molar absorption coefficients in green to near-IR region. Up to date, quite a number of squaraine dyes have been designed and adopted for DSCs. Some of the squaraine dyes even showed high IPCE and efficiencies comparable to ruthenium and other organic

dyes.^{7,123,143} For example, J.-H. Yum *et al.* designed and developed a novel asymmetrical squaraine sensitizer which employed a carboxylic acid group as the anchoring group (see Figure II-5, dye 55).¹⁴⁴ When embedded in a sandwich cell, the dye 55 showed a very high IPCE of 85% and an overall power conversion efficiency of 4.5% ($J_{sc} = 10.5 \pm 0.20 \text{ mA}\cdot\text{cm}^{-2}$, $V_{oc} = 603 \pm 30 \text{ mV}$, $FF = 0.71 \pm 0.03$) under standard global AM 1.5 solar condition. It was found in their study that creating directionality and inhibiting self-quenching of the excited state of the sensitizer played a key role in the unprecedented efficiency of squaraines. The synthesis and optical, electronic, and photovoltaic properties of an unsymmetrical bis(indoline) squaraine sensitizer incorporating a promising extended conjugation and a strong π -accepting carboxycyanovinyl group as a surface-anchoring group instead of a directly attached carboxylic acid (see Figure II-5, dye 56), coded as YR6, was reported by Y. Shi *et al.* The well-designed structure of the dye 56 resulted in a red-shift of the absorption maximum and the presence of additional higher-energy bands that contributed to panchromatic absorption of the dye 56. As a result, the dye 56 sensitized cell with a standard I_3/I^- liquid electrolyte showed a power conversion efficiency of 6.74% ($J_{sc} = 14.8 \text{ mA}\cdot\text{cm}^{-2}$, $V_{oc} = 642 \text{ mV}$, $FF = 0.71$) under standard global AM 1.5 simulated solar conditions.¹⁴⁵ However, most of the squaraine dyes showed low efficiencies because of their dye aggregation, lack of directionality in the excited state and low stability. Therefore, molecular engineering of near-IR squaraine-based photosensitizers with high photovoltaic properties and an improved stability remains strongly required.^{123,125,146}

Carbazoles and their derivatives have been investigated as electroluminescent, non-linear optical and photorefractive materials.^{147,148} The carbazole-based dyes are good candidates for reaching high V_{oc} values and thus constructing photovoltaic devices because of the wide band gap of carbazole.¹⁴⁹⁻¹⁵² Many efforts have been done by our group to design and synthesize various carbazole-based dyes. In particular, in 2013, a series of organic oligocarbazole-based chromophores (see Figure II-5, dyes 57 to 60) designed on the D- π -A model were reported by our group for efficient thin-film DSCs. In order to enrich the spectral response, multiple visible-light-absorbing motifs and a naphthyl group in place of a phenyl ring in the π -conjugated bridge were introduced in these chromophores. When embedded in TiO_2 -based DSCs, dyes 58 and 59 achieved power conversion efficiency values of up to 5.8% in the presence of the electrolyte Z960 under standard AM 1.5 sunlight, $100 \text{ mW}\cdot\text{cm}^{-2}$ irradiation.¹⁵³ A rational molecular engineering strategy was also proposed by our group in 2015 in order to prepare an original series of efficient carbazole-based photosensitizers for DSCs. Every of these novel carbazole-based dyes with high light-harvesting capacity contained a fluorene

core inserted in the π -conjugated skeleton of carbazole along with the addition of an auxiliary thienyl donor on the carbazole ring to strengthen the push-pull effect. When employed in DSCs with iodine-based electrolyte Z960, the dyes 61 and 62 showed excellent power conversion efficiencies up to 6.5% under standard AM 1.5 sunlight, $100 \text{ mW} \cdot \text{cm}^{-2}$ irradiation. Moreover, the solar cell devices based on the dye 61 afforded a significantly higher open-circuit photovoltage value of about 920 mV with the $\text{Co}(\text{bpy-pz})_2$ redox mediator.¹²⁶

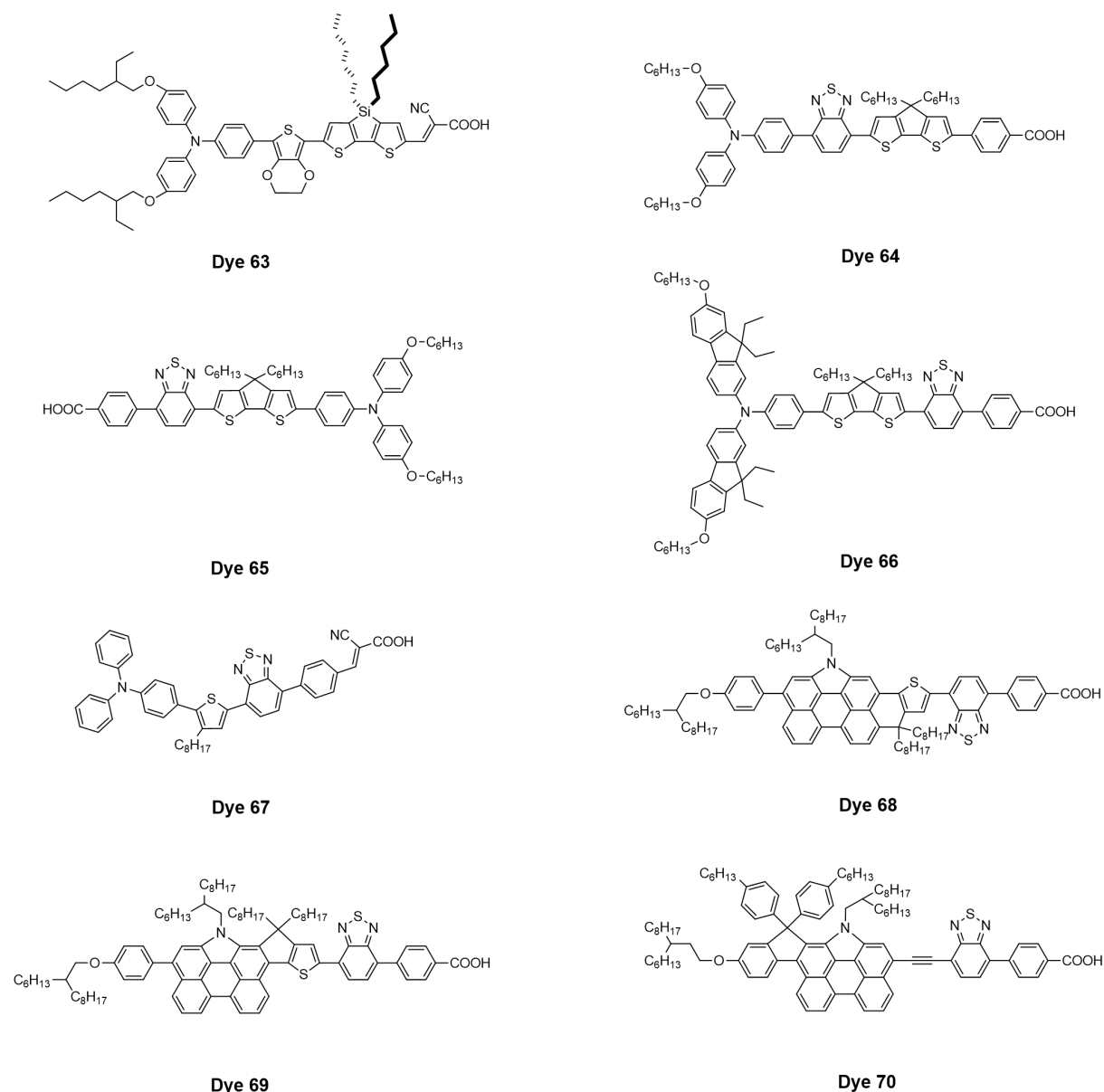


Figure II-6: Several representative metal-free organic materials used for DSCs with the cell efficiencies of $> 10\%$.

In recent years, to be more competitive in the solar cell markets, various organic materials have been investigated and used in DSCs to improve the device efficiency, enhance

its durability, and reduce the cost of production.¹⁵⁴ Several representative metal-free organic materials used for the preparation of photoanodes in DSCs with efficiencies of > 10% are shown in Figure II-6. In 2010, P. Wang *et al.* utilized a binary π -conjugated spacer of ethylenedioxythiophene and dithienosilole to construct a high molar absorption coefficient push-pull dye (see Figure II-6, dye 63).¹⁵⁵ The dye 63 endowed a nanocrystalline TiO₂ film with an evident light-harvesting enhancement, resulting in an efficiency of 10.0-10.3% under standard AM 1.5 sunlight, 100 mW·cm⁻² irradiation for DSCs with nonruthenium dyestuffs. Interestingly, a solvent-free ionic liquid cell with the dye 63 as the sensitizer exhibited an impressive efficiency of 8.9% under a low light intensity of 14.39 mW·cm⁻², making it favorable for the indoor application of flexible DSCs. In 2013, three dyes based on the chromophoric core cyclopentadithiophene-benzothiadiazole were reported by the same group (see Figure II-6, dyes 64 to 66).¹⁵⁶ When embedded in TiO₂-based DSCs, the dyes 64 and 65 exhibited power conversion efficiency values of 10.0% ($J_{sc} = 15.34 \text{ mA}\cdot\text{cm}^{-2}$, $V_{oc} = 887 \text{ mV}$, $FF = 0.728$) and 8.9% ($J_{sc} = 15.58 \text{ mA}\cdot\text{cm}^{-2}$, $V_{oc} = 813 \text{ mV}$, $FF = 0.706$) under standard AM 1.5 sunlight, 100 mW·cm⁻² irradiation, respectively. Through co-grafting their preceding organic D- π -A dye based on the di(3-hexylthiophene) linker with the dye 65 and the dye 66 to remove the penetration channels for the cobalt(III) ions which has been proved to feature a superior ability to control the interfacial charge recombination, the power conversion efficiency values of 11.2% ($J_{sc} = 18.28 \text{ mA}\cdot\text{cm}^{-2}$, $V_{oc} = 856 \text{ mV}$, $FF = 0.715$) and 11.5% ($J_{sc} = 17.85 \text{ mA}\cdot\text{cm}^{-2}$, $V_{oc} = 891 \text{ mV}$, $FF = 0.722$) were achieved under standard AM 1.5 sunlight, 100 mW·cm⁻² irradiation, respectively. This work set a new benchmark for metal-free organic DSCs. In the same year, D. Joly *et al.* reported the synthesis and complete characterization of a new purely organic sensitizer (see Figure II-6, dye 67) that can be prepared and synthetically upscaled rapidly.¹⁵⁷ Solar cells devices containing the orange dye 67 exhibited a PCE of 10.2% under standard AM 1.5 sunlight, 100 mW·cm⁻² irradiation using iodine/iodide as the electrolyte redox shuttle in the electrolyte which was among the few examples of DSC using an organic dyes and iodine/iodide redox pair to overcome the 10% efficiency barrier. Interestingly, the combination of the dye 67 with an ionic liquid electrolyte allowed the fabrication of solar cells that exhibited PCEs of up to 7.36% which were highly stable with no measurable degradation of initial performances after 2200 h of light soaking at 65°C under standard irradiation conditions. In 2015, P. Wang *et al.* reported two highly efficient metal-free perylene dyes featuring N-annulated thienobenzoperylene and N-annulated thienocyclopentaperylene, which were coplanar polycyclic aromatic hydrocarbons (see Figure II-6, dyes 68 and 69).¹⁵⁸ The dyes 68 and 69 exhibited high J_{sc} values of 19.42 and 19.64

$\text{mA}\cdot\text{cm}^{-2}$, respectively, which contributed to their corresponding higher PCEs of 11.5 and 12.0% under standard AM 1.5 sunlight, $100\text{ mW}\cdot\text{cm}^{-2}$ irradiation. Most importantly, this work was the first time that a metal-free organic dye achieved a high PCE of 12% for DSCs without any coadsorbate, which thus paved a new way for highly performing DSC dyes. Another metal-free organic dye based on an N-annulated indenoperylene electron-donor decorated with photochemically inactive segments which was further conjugated via triple bond with electron-acceptor benzothiadiazolylbenzoic acid was reported by them in the same year (see Figure II-6, dye 70).¹⁵⁹ The solar cell devices based on the dye 70 showed a high PCE of 12.5% under standard AM 1.5 sunlight, $100\text{ mW}\cdot\text{cm}^{-2}$ irradiation without use of any coadsorbate.

In addition to the metal-free organic groups referred above, many other metal-free organic photosensitizers such as indole/indoline dyes,^{129,160-163} perylene dyes,¹⁶⁴⁻¹⁶⁸ N,N-dialkylaniline dyes,¹⁶⁹⁻¹⁷¹ anthracene/heteroanthracene dyes,¹⁷²⁻¹⁷⁴ boradiazaindacene dyes,¹⁷⁵⁻¹⁷⁷ tetrahydroquinoline dyes,^{178,179} polymeric dyes,^{180,181} triphenodioxazine dyes,¹⁸² etc. have been designed, synthesized and employed in DSCs. Despite the impressive progress that has been made in the development of metal-free organic dyes, new molecular design strategies for the construction of highly efficient devices are still essential and a profound understanding of the morphology of fully organic photosensitizers is indeed necessary in order to control their photovoltaic properties.^{7,14,123-125,128,129}

II.3. Molecular Engineering of Ruthenium-Diacetylide Organometallic Complexes for n-Type DSCs

An innovative design strategy to obtain colorful dyes for efficient DSCs has been reported by our group recently. The new photosensitizers were based on organometallic complexes featuring an original D-[M]-A architecture where [M] is the electron-rich [Ru(dppe)₂] metal center (see Figure II-7).^{6,25}

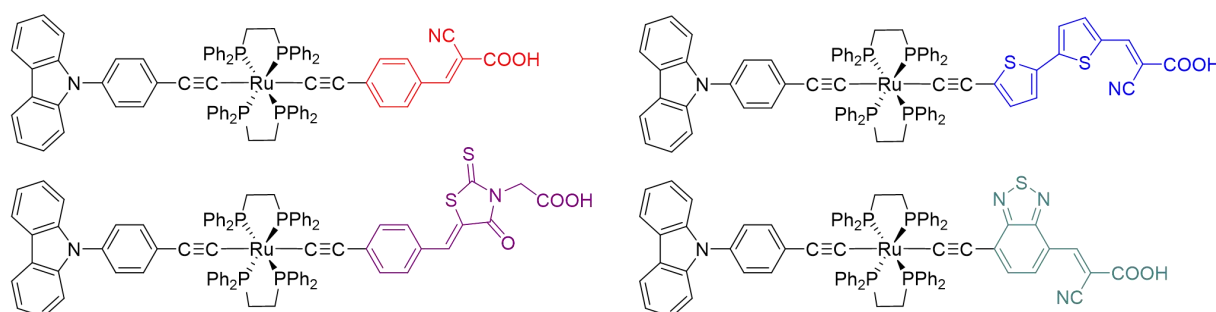


Figure II-7: Organometallic complexes featuring an original D-[M]-A architecture.^{6,25}

The flexible molecular engineering of these organometallic complexes make them good candidates to extend absorption spectra of the dyes towards low energies while keeping high molar extinction coefficient, with the view to increasing the DSSC efficiency in the near-IR region. In particular, a ruthenium-diacetylide organometallic complex endowed with a benzothiadiazole (BTD) connector was prepared accordingly and used in DSCs.²⁵ However, although the BTD unit extends the absorption spectra of organic dyes, it also hampers electron collection by causing rapid back electron transfer phenomena, *i.e.* charges injected into the conduction band of TiO₂ return to the oxidized dye molecules, thereby lowering the overall charge collection rates, photocurrent densities and power conversion efficiencies. To overcome this issue, it was shown that inserting a π -conjugated spacer between the BTD unit and the anchoring group hinders the back electron transfer phenomena.^{183,184} Several studies were reported where the D-A- π -A architecture out-performs the D- π -A design.^{185,186} Therefore this prompted us to target new low bandgap sensitizers featuring an appropriate D-[M]-A- π -A' design where [M] is the [Ru(dppe)₂] metal fragment, A the BTD unit, π an aromatic conjugated spacer and A' represents both secondary acceptor and anchoring function.

Therefore, we designed and synthesized three novel organometallic dyes for DSCs (see Figure II-8). The dye **[Ru]1** bears a phenyl spacer between the BTD unit and the carboxylic

acid anchoring group. **[Ru]2** and **[Ru]3** include either a phenyl or a thiophene π -spacer between the BTD and the cyanoacrylic acid acceptor/anchoring group. Thorough determination of the optical and electronic properties of the three new dyes is described in the following along with their photovoltaic performance in DSC devices.

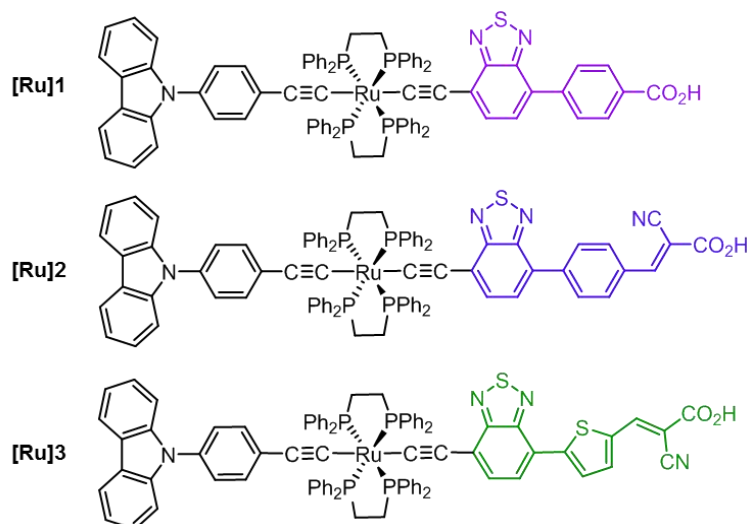
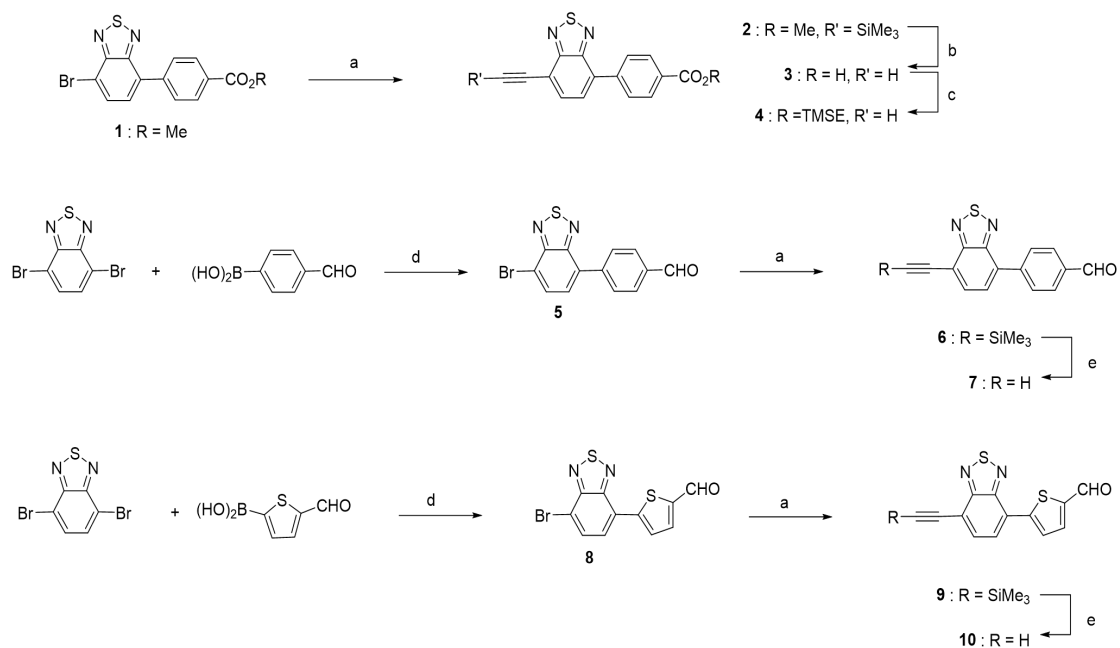


Figure II-8: Molecular structure of the Ru-diacetylide complexes **[Ru]1**-**[Ru]3**

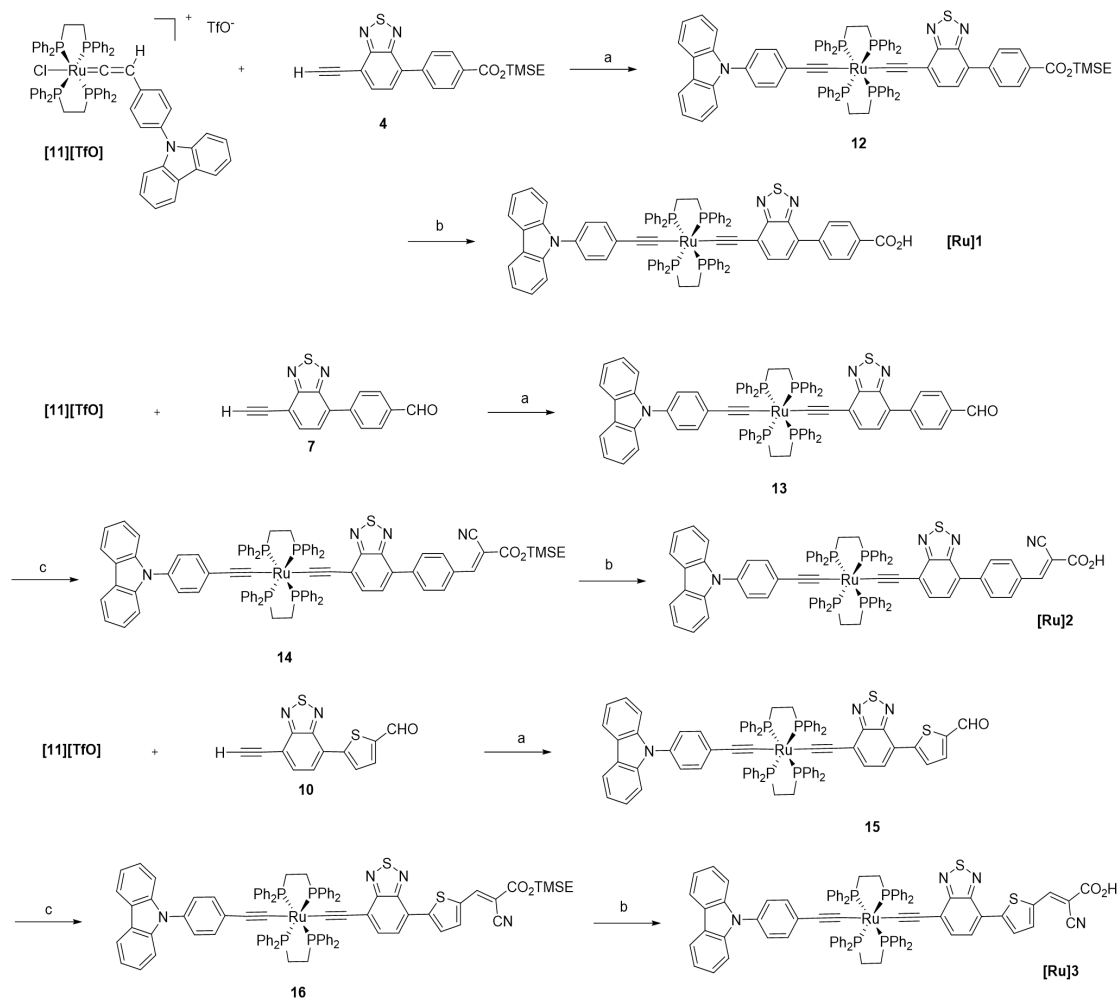
II.3.1. Synthesis of the Dyes **[Ru]1**-**[Ru]3**

The preparation of the new dissymmetric ruthenium diacetylide complexes was undertaken following already established synthesis pathway.⁸² In a first step, the activation of a terminal alkyne by the electron-deficient metal center $[\text{RuCl}(\text{dppf})_2][\text{TfO}]$ provides an intermediate metal-vinylidene complex, which further activates a second terminal alkyne to give the diacetylide backbone. Here, the previously described vinylidene moiety featuring a carbazole unit **[11][TfO]**⁶ was used to create the electron-donor part of the push-pull dyes and three benzothiadiazole-based alkyne ligands were accordingly prepared as acceptor parts. The synthetic routes to the BTD-based ligands and to the Ru-diacetylide complexes are depicted in Schemes II-1 and II-2.



Scheme II-1: Synthesis route to the benzothiadiazole-based ligands **4**, **7**, **10**. Reaction conditions: (a) Trimethylsilylacetylene, PdCl₂(PPh₃)₂, CuI, Et₃N, THF; (b) NaOH, THF/H₂O; (c) Trimethylsilylethanol, HBTU, DIPEA, DMF; (d) Pd(dppf)Cl₂, CH₂Cl₂, K₂CO₃, DMF; (e) K₂CO₃, MeOH.

The BTD- π -spacer derivatives **4**, **7** and **10** were obtained via successive palladium-catalyzed cross-coupling Sonogashira and Suzuki reactions. In the synthesis route to **[Ru]1** the carboxylic acid function was obtained by hydrolysis of the methyl ester derivative **2**, however in order to avoid side reactions with the metal center during organometallic synthesis a silyl-ester protecting group (TMSE) was introduced that was further removed under mild conditions. The cyanoacrylic acid acceptor/anchoring group in **[Ru]2** and **[Ru]3** was introduced via Knoevenagel reaction on the carbaldehyde-equipped precursor complex using 2-trimethylsilylethyl 2-cyanoacetate followed by deprotection with tetrabutylammonium fluoride (TBAF) in THF at room temperature. The three new dyes **[Ru]1**-**[Ru]3** were isolated in good overall yields.



Scheme II-2: Synthesis route to the organometallic complexes **[Ru]1-[Ru]3**. Reaction conditions: (a) NaPF_6 , Et_3N , CH_2Cl_2 ; (b) Tetrabutylammonium fluoride, THF; (c) 2-trimethylsilylethyl-2-cyanoacetate, piperidine, CHCl_3 .

All the organometallic complexes were characterized by means of ^{31}P , ^1H and ^{13}C NMR, HR-MS and FT-IR. The full data set is in accordance with the expected structure of the organometallic dyes. The *trans*-ditopic geometry of the ruthenium center in **[Ru]1-[Ru]3** and their precursors was evidenced by ^{31}P NMR as the spectra show a singlet for the four equivalent phosphorus atoms, with $\delta \approx 53$ ppm characteristic of the ruthenium-diacetylide structure.⁸² In addition, an intense band was observed in the FT-IR spectra of all the organometallic complexes at ca. 2040 cm^{-1} corresponding to the $\nu_{\text{C}=\text{C}}$ stretching modes of the σ -diacetylide metal fragment.

II.3.2. Optical and Electrochemical Properties

UV-visible electronic absorption spectra of **[Ru]1**-**[Ru]3** in dichloromethane solutions are depicted in Figure II-9a and the corresponding data are gathered in Table II-1. The spectra show intense absorption bands in the UV region at ca. 240 nm corresponding to characteristic transitions from the phosphine ligands.¹⁸⁷ Besides, as expected, broad bands are observed in the visible part corresponding to multiple transitions involving the $[\text{Ru}(\text{dppe})_2]$ metal center, thus with a strong metal-to-ligand charge transfer (MLCT) character. **[Ru]1** and **[Ru]2** spectra exhibit a broad absorption band from 450 nm to 650-700 nm with a maximum at 545 nm and 564 nm, respectively. The dye **[Ru]3** presents a small band at 448 nm and a broad band with high molecular extinction coefficient ($\epsilon \approx 33\,000\text{ M}^{-1}\cdot\text{cm}^{-1}$) covering the 500-800 nm region with a maximum at 650 nm. **[Ru]3** therefore presents a deep green coloration in solution which makes this dye a good candidate as a low-energy photon absorber in DSCs.

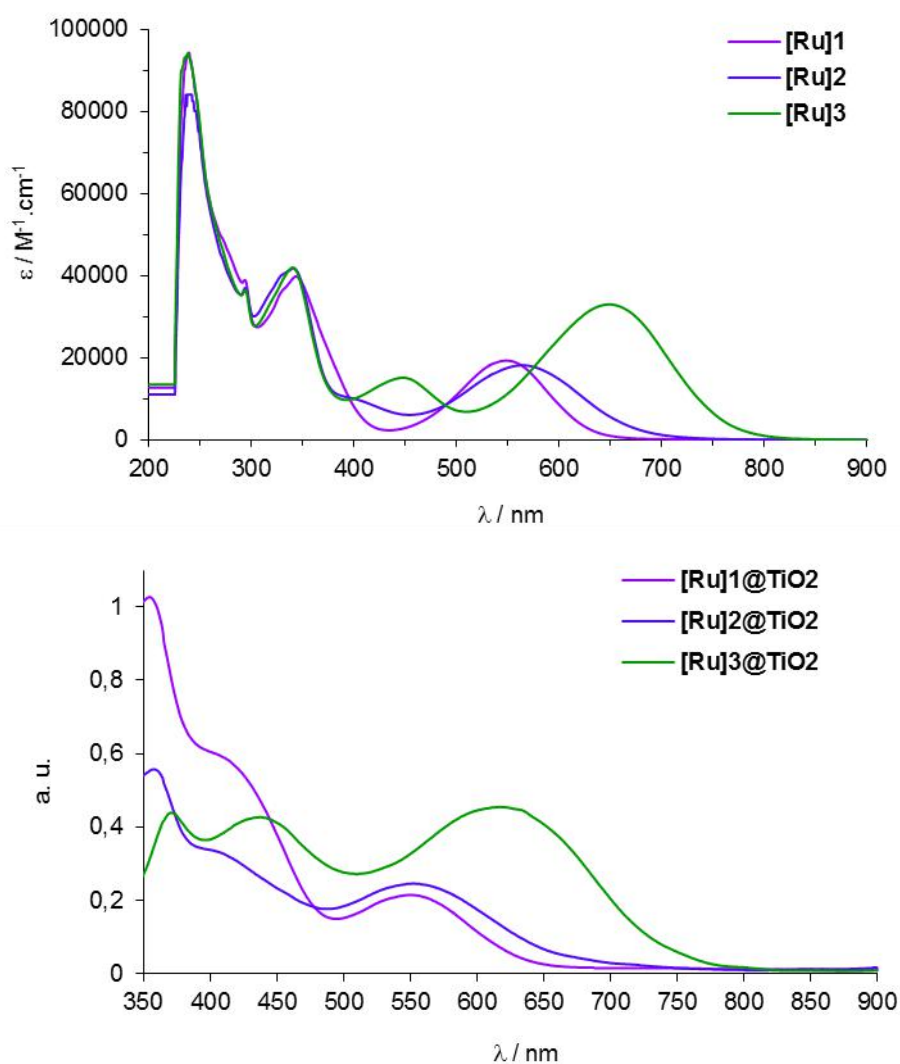


Figure II-9: (a) Electronic absorption spectra of **[Ru]1**-**[Ru]3** in CH_2Cl_2 ($C \approx 3 \times 10^{-5}\text{ M}$); (b)

Electronic absorption spectra of **[Ru]1**-**[Ru]3** adsorbed on TiO₂ transparent thin-film (3 μm) in the presence of co-adsorbent (cheno-deoxycholic acid).

The same trend is observed upon grafting the dyes on TiO₂ transparent thin-films (see Figure II-9b). The electronic spectra present broad bands in the visible region with maximum absorption around 550 nm for **[Ru]1** and **[Ru]2**, and 620 nm for **[Ru]3**. The latter again shows more intense absorption than the two other dyes and its absorption profile fully covers the visible region. Note that these measurements were done in the presence of cheno-deoxycholic acid as co-adsorbent and de-aggregating agent. This results in very little aggregation phenomena between the dye molecules on the surface and negligible shift of the main absorption band upon grafting.

Table II-1: Optical and electrochemical properties.

Dye	$\lambda_{\text{abs}}^{\text{a}} / \text{nm}$		$\epsilon / \text{M}^{-1} \cdot \text{cm}^{-1}$	$\lambda_{\text{abs}} @ \text{TiO}_2^{\text{b}} / \text{nm}$	$E_{\text{ox}}^{\text{c}} / \text{V}$	$\Delta E_{\text{opt}}^{\text{d}} / \text{eV}$	$E_{\text{ox}} - \Delta E_{\text{opt}}^{\text{e}} / \text{V}$
[Ru]1	239,	343,	94 200, 39 800,	550	+ 0.70	1.96	- 1.26
	545		20 000				
[Ru]2	240,	340,	84 000, 41 800,	554	+ 0.73	1.82	- 1.09
	564		18 200				
[Ru]3	238,	340,	94 000, 42 000,	620	+ 0.71	1.62	- 0.91
	448,	650	15 200, 33 000				

^a Absorption maxima in CH₂Cl₂ solution (C = 3 × 10⁻⁵ M). ^b Visible range absorption maximum on 3-μm TiO₂ transparent film. ^c Oxidation potentials in CH₂Cl₂ solution with FeCp*₂ as internal reference. Potentials referred to NHE by addition of 130 mV.¹⁸⁸ ^d ΔE_{opt} estimated from the onset of the absorption spectra. ^e Considering that $\Delta E_{\text{opt}} (\text{V}) = [\Delta E_{\text{opt}} (\text{eV}) / q] = [\Delta E_{\text{opt}} (\text{eV}) / 1] = \Delta E_{\text{opt}} (\text{eV})$

The redox properties of the dyes were investigated through cyclic voltammetry analyses performed in dichloromethane solutions using Bu₄NPF₆ as salt support. The corresponding voltammograms are shown in Figure II-10 and data reported in Table II-1. The three organometallic complexes undergo one reversible monoelectronic oxidation process at equivalent potential ($E_{\text{ox}} \approx +0.70 \text{ V vs. NHE}$) corresponding to the Ru^{II}→Ru^{III} oxidation process. As a consequence, the first oxidation potential of the three dyes is more positive than the Nernst potential of the conventional redox mediator used in DSCs (i. e. I⁻/I₃⁻, $E^{\circ} = +0.35 \text{ V vs. NHE}$).⁷ And thus, sufficient driving force is observed ($\geq 0.35 \text{ V}$) to ensure effective regeneration of the dye's ground-state following the photoinduced electron transfer to TiO₂.

The optical band-gap (ΔE_{opt}) of the dyes was estimated from the onset of the absorption spectra in solution, leading to $\Delta E_{\text{opt}} [\text{Ru}1] > \Delta E_{\text{opt}} [\text{Ru}2] > \Delta E_{\text{opt}} [\text{Ru}3]$. It is worth noting that **[Ru]3**, by showing an optical band-gap of 1.62 eV, appears as a low-band gap sensitizer, as expected. Finally, the difference $E_{\text{ox}} - \Delta E_{\text{opt}}$ gave us an estimation of the oxidation potential in the excited state.⁷ The values reported in Table II-1 are more negative than the conduction band edge of TiO₂ (ca. -0.50 V vs. NHE)¹⁸⁹ thus creating sufficient driving force for electron injection from the photo-excited dyes to the semiconducting oxide. In addition, reduction processes are observed in the cathodic region that can be attributed to the benzothiadiazole ligand.

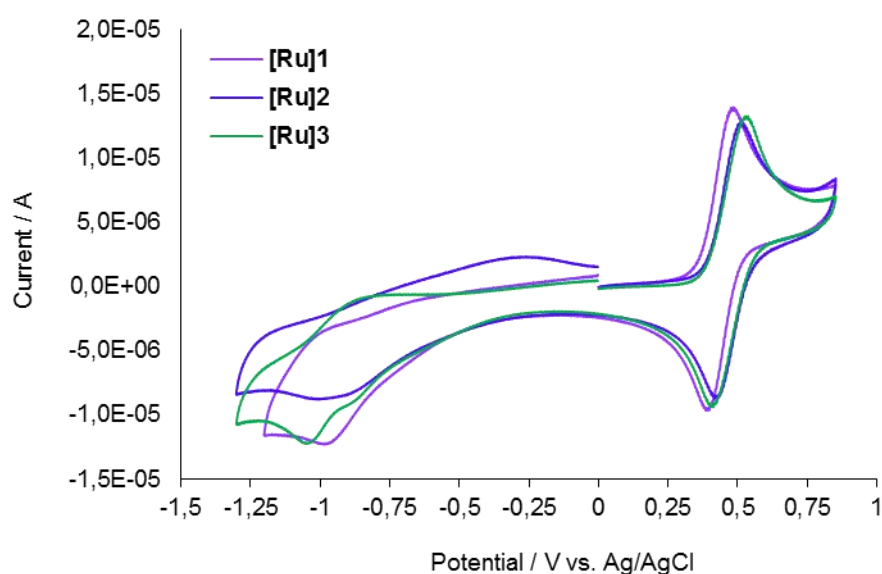


Figure II-10: Cyclic voltammograms of **[Ru]1-[Ru]3** in CH₂Cl₂ (working electrode: Pt disc; reference electrode: Ag/AgCl, counter electrode: Pt wire); salt support = 0.1 M Bu₄NPF₆; scan rate = 100 mV·s⁻¹.

II.3.3. Theoretical Calculations

The optimized geometry of complexes **[Ru]1-[Ru]3** was obtained using density functional theory (DFT) (see experimental part for details). The calculations attest the linearity of the molecular backbone. The two acetylide ligands, in trans position with regard to the [Ru(dppe)₂] fragment, form an angle close to 180°. This configuration provides a good directionality for the intramolecular charge transfer processes.

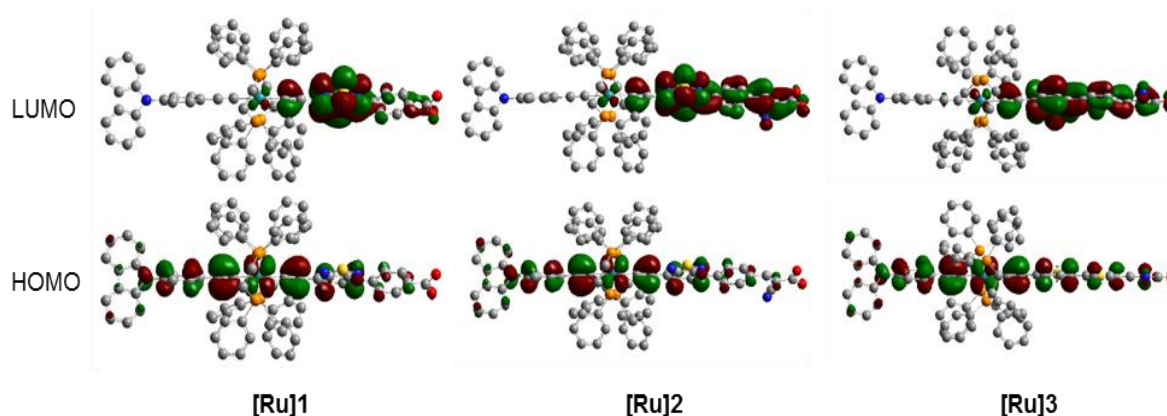


Figure II-11: Electron-density distribution of the Highest Occupied Molecular Orbital (HOMO) and Lowest Unoccupied Molecular Orbital (LUMO) of **[Ru]1**-**[Ru]3**.

Furthermore, the calculations allow a precise mapping of the electron-density of the frontier molecular orbitals. As shown in Figure II-11, the electron-density of the HOMOs is spread over the whole π -conjugated system of the dyes, from the carbazole to the remote end of the complex, with major localization on the central electron-rich $[\text{Ru}(\text{dppe})_2]$ metal fragment. Conversely, the electronic density of the LUMOs is primarily centered on the electron-withdrawing ligand bearing the benzothiadiazole motif and cyanoacrylic acid anchor. The spatial distribution of the frontier molecular orbital thus favors charge separation in the DSSC device. Upon photo-excitation of the dye an electron is promoted from the HOMO to the LUMO, efficient charge transfer to the semi-conducting metal oxide can therefore occur only if the LUMO is located close to the surface, as it is the case for **[Ru]1**-**[Ru]3**. Concomitantly, the spatial distribution of the HOMOs allows a good accessibility for the redox shuttle in order to regenerate the dye's ground-state.

Additionally, time-dependent density functional theory (TD-DFT) calculations provided information about the main transitions energy and related oscillator strength (see Figure II-12). The data are given in Table II-2. Calculations confirm that the broad absorption band observed in the visible range (see Figure II-9a) represents the envelope of several transitions, however with major contribution of the HOMO \rightarrow LUMO transition. Considering the localization of the two frontier orbitals, the main absorption band of the Ru-based dyes therefore owns a strong MLCT character. The computed transferred charge q_{CT} is close to 1 and the distance of the charge transfer is 3.2 Å for **[Ru]1** and 3.8 Å for **[Ru]2** and **[Ru]3**.

Table II-2: Theoretical data.

Dye	ΔE_{ge} /eV ^a	λ_{ge} /nm ^b	f_{ge} ^c	Transition assignment (coefficient) ^d	Λ^e	q_{CT}/e^f	$D_{CT}/\text{\AA}^g$
[Ru]1	2.04	605	0.73	H→L (0.63) ; H-2→L (0.22)	0.58	0.91	3.2
	3.47	357	0.90	H→L+1 (0.59); H-1→L+1 (0.21); H-2→L+1 (0.21)			
	4.08	304	0.82	H→L+4 (0.51); H-1→L+1 (0.24)			
[Ru]2	1.93	642	1.14	H→L (0.62) ; H-2→L (0.20)	0.58	0.90	3.8
	2.76	448	0.33	H→L+1 (0.53); H→L (-0.23); H-2→L+1 (0.22)			
	2.81	441	0.31	H-3→L (0.48); H→L+1 (0.28); H-2→L (-0.25)			
	4.07	304	1.39	H→L+4 (0.39); H→L+6 (0.29)			
[Ru]3	1.73	713	1.51	H→L (0.64) ; H-1→L (0.22)	0.60	0.84	3.8
	2.58	481	0.13	H-2→L (0.44); H→L+1 (-0.37)			
	2.64	469	0.46	H-1→L+1 (0.27); H→L+1 (0.58)			
	4.07	304	0.88	H→L+3 (-0.28); H→L+5 (0.29)			

^a ΔE_{ge} = main transition energy. ^b λ_{ge} = calculated λ_{max} . ^c f_{ge} = oscillator strength. ^d Only the transitions with coefficients higher than 0.15 are given for. ^e Λ = spatial overlap. ^f q_{CT} = quantity of transferred charge. ^g D_{CT} = distance between the barycentres of the density depletion and density increment zones related to the CT excitation.

II.3.4. Photovoltaic Properties

The dyes **[Ru]1**-**[Ru]3** were further adsorbed onto TiO₂ nanoparticulate transparent thin-films, in the presence of cheno-deoxycholic acid as co-adsorbent, and the photoanodes were incorporated in solar cell devices following reported procedure.¹⁹⁰ The photocurrent density-voltage (J/V) curves are shown in Figure II-12 and the photovoltaic parameters are gathered in Table II-3. The benchmark dye N3 (cis-bis(isothiocyanato)bis(2,2'-bipyridyl-4,4'-dicarboxylato) ruthenium as reference dye was tested under the same conditions for comparison.

First observation was that **[Ru]1** is the least effective photosensitizer of the series with $J_{sc} = 7.13 \text{ mA}\cdot\text{cm}^{-2}$, $V_{oc} = 577 \text{ mV}$ and $\text{PCE} = 3.11 \%$. The limited performance afforded by **[Ru]1** mainly arises from the low photocurrent density value which can be imputed to the carboxylic acid anchoring group. Due to the poor electron-withdrawing character of the -COOH function, the electron-density of the dye's LUMO remains principally on the BTD unit and only few electron-density is observed on the anchoring group. As a consequence, the molecular structure of this complex apparently impedes fast charge injection from the excited dye to TiO₂. Moreover, the amount of dye adsorbed on TiO₂ surface, determined by

absorption spectroscopy, indicates that the carboxylic acid anchor leads to lower dye-loading amount for **[Ru]1** ($DLA = 1.40 \times 10^{-7} \text{ mol}\cdot\text{cm}^{-2}$) than for the two other dyes. This can be ascribed to the weak acidity of **[Ru]1**. The pK_a of benzoic acid is known to be around 4 whereas pK_a of α -cyanoacrylic acid is around 1-2. Since the carboxylate group is known to form chelating and bridging linkage with TiO_2 ,⁷ the more acidic carboxylic acids are, the more stable complexes they form with the surface.¹⁹¹

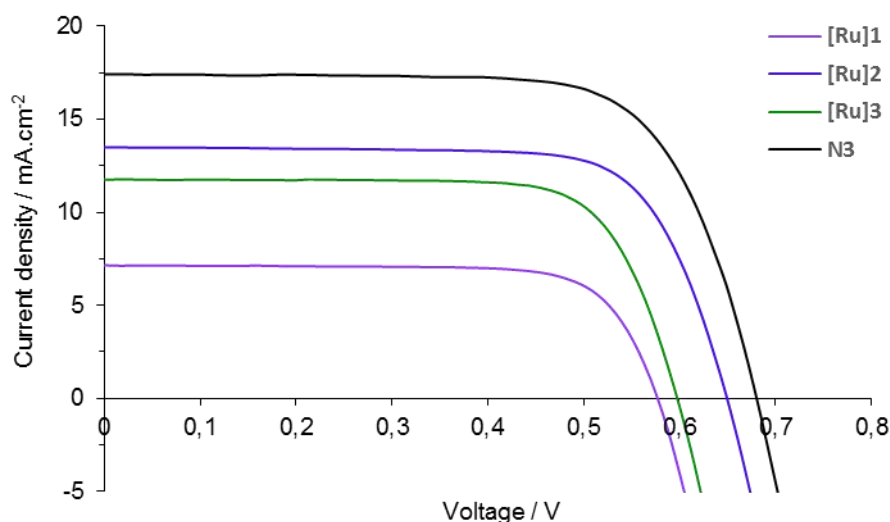


Figure II-12: J/V characteristics of **[Ru]1**-**[Ru]3** and N3 in DSCs.

Table II-3: Photovoltaic performance of DSCs using **[Ru]1**-**[Ru]3** and N3 dyes. Dye-loading amount on TiO_2 .

Dye	$J_{SC}/\text{mA}\cdot\text{cm}^{-2}$	V_{OC}/mV	$ff/\%$	$PCE/\%$	DLA ($\text{mol}\cdot\text{cm}^{-2}$)
[Ru]1	7.13	577	75.6	3.11	1.40×10^{-7}
[Ru]2	13.48	650	73.7	6.45	1.94×10^{-7}
[Ru]3	11.77	598	74.4	5.23	2.12×10^{-7}
N3	17.42	680	71.4	8.46	-

Photovoltaic data measured at full sunlight (AM 1.5G, $100 \text{ mW}\cdot\text{cm}^{-2}$): J_{sc} = short-circuit current density, V_{oc} = open-circuit voltage, ff = fill factor, PCE = power conversion efficiency. TiO_2 film thickness = $10 \mu\text{m}$ (transparent layer) + $5 \mu\text{m}$ (scattering layer). Active area = 0.159 cm^2 (defined by a mask). Data from the best of 5 devices (standard deviation on the efficiency +0.06%). DLA = dye-loading amount measured on 1 cm^2 TiO_2 electrode.

By contrast, the dye **[Ru]2** shows significantly higher performance with $J_{sc} = 13.48 \text{ mA}\cdot\text{cm}^{-2}$, $V_{oc} = 650 \text{ mV}$ and $\text{PCE} = 6.45 \%$. It is worth underlining that under the same device processing conditions the benchmark dye N3 afforded $J_{sc} = 17.42 \text{ mA}\cdot\text{cm}^{-2}$, $V_{oc} = 680 \text{ mV}$, $\text{PCE} = 8.46 \%$. Thus, considering the higher photocurrent and photovoltage values afforded by **[Ru]2**, compared to **[Ru]1**, it appears that the cyanoacrylic acid is the most appropriate anchoring group for these Ru-complexes. This is presumably due to better electronic coupling with the surface resulting in favored electron injection and limited back electron transfer phenomena. This was also confirmed by the electron-density distribution of the LUMO of **[Ru]2** which extends over the whole π -conjugated system up to the cyanoacrylic acid motif with higher electronic density on the anchoring group than in the case of **[Ru]1**, as shown on Figure II-11. Moreover, the amount of dye loaded on TiO_2 is $\sim 40 \%$ higher for **[Ru]2**, bearing the cyanoacrylic acid function ($\text{DLA} = 1.94 \times 10^{-7} \text{ mol}\cdot\text{cm}^{-2}$) than for **[Ru]1**.

Interestingly, the good performance obtained with **[Ru]2** validates the strategy consisting in the design of narrow band gap sensitizers featuring the D-[M]-A- π -A' architecture. In particular, the insertion of a phenyl ring between the BTD unit and the cyanoacrylic acid in **[Ru]2** allowed significant improvement of the V_{oc} compared to the previously reported Ru-BTD dye.²⁵ Indeed, our former Ru-BTD dye, featuring a D-[M]-A-A' architecture, *i.e.* without π -spacer, afforded $V_{oc} = 582 \text{ mV}$ compared to 650 mV for **[Ru]2**. Thus, as expected, the phenyl π -spacer acts as an effective 'non-return' barrier by impeding back electron transfer phenomena from TiO_2 to the oxidized dye. The overall PCE obtained with **[Ru]2** is also improved compared to our previous study.

The green dye **[Ru]3** also led to good performance with $J_{sc} = 11.77 \text{ mA}\cdot\text{cm}^{-2}$, $V_{oc} = 598 \text{ mV}$ and $\text{PCE} = 5.23 \%$. These values are in the same range as other green dyes for DSCs reported recently and used in combination with an iodine-based electrolyte.¹⁹²⁻¹⁹⁴ However, despite comparable dye-loading amount ($\text{DLA} = 2.12 \times 10^{-7} \text{ mol}\cdot\text{cm}^{-2}$) the photocurrent density and open circuit photovoltage values afforded by **[Ru]3** indicate lower charge injection rate and enhanced back electron transfer phenomena compared to **[Ru]2**. This behavior can be related to the LUMO of **[Ru]3** which presents slightly fewer electron density on the anchoring group than in **[Ru]2** (Figure II-11), thereby hampering fast electron injection to the semiconductor.

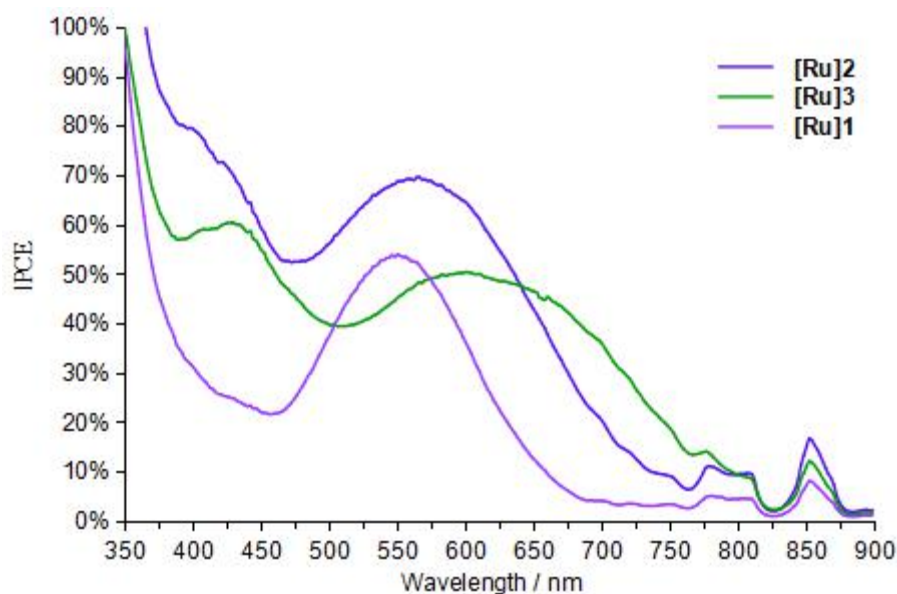


Figure II-13: IPCE spectra of [Ru]1-[Ru]3 in DSCs

Incident photon-to-current conversion efficiency (IPCE) profiles of the DSC devices encompassing [Ru]1-[Ru]3 are shown in Figure II-13. The layout of the curves is consistent with the absorption spectra of the dyes adsorbed on TiO₂ (see Figure II-9b) meaning that all the electronic transitions are involved in the device operation process and confirming low aggregation rate between the dyes on TiO₂.¹⁹⁵ The action spectrum of [Ru]2 covers a broad part of the visible from 450 nm to 750 nm with maximum 70% of incident-light conversion at about 560 nm. The spectrum of [Ru]3 extends until 800 nm with maximum 50% about 600 nm. The decrease of the green dye absorption around 500-550 nm (see Figure II-9a) logically results in lower performance in this region, this might also contribute to overall lower photocurrent density and PCE provided by [Ru]3 compared to [Ru]2.

II.3.5. Conclusions

In conclusion, three new push-pull dyes featuring the organometallic [Ru(dppe)₂] fragment were designed and successfully prepared for dye-sensitized solar cell (DSC) applications. In order to access narrow band-gap dyes with Near-IR absorption properties, our strategy consisted in modulating the electron-withdrawing part of D-[M]-A- π -A' systems where A is the benzothiadiazole (BTD) unit, π an aromatic π -spacer and A' represents both secondary acceptor and anchoring function.

This molecular design afforded efficient photosensitizers with strong absorption properties in the visible range, in particular a green dye was obtained with broad absorption

between 500 and 800 nm. The introduction of an aromatic π -spacer between the BTD and the semiconductor, by impeding charge recombination and back electron transfer from the surface, allowed improved performance of **[Ru]2** compared to our former Ru-BTD sensitizer.²⁵ Finally, the dyes **[Ru]2** and **[Ru]3**, combining BTD and cyanoacrylic acid moieties, afforded much higher performance than **[Ru]1**, endowed with a simple carboxylic acid function, thus showing that the choice of the anchoring group is of paramount importance to optimize the device operation. Overall, this study shows the relevance of finely tuned push-pull organometallic complexes for the design of narrow bandgap dyes for efficient DSCs with increased harvesting of low energy photons.¹⁹⁶

II.4. References

- 6 B. O'Regan, M. Grätzel. A low-cost, high-efficiency solar cell based on dye-sensitized colloidal TiO₂ films. *Nature*, **1991**, 353: 737-740.
- 7 S. Mathew, A. Yella, P. Gao, R. Humphry-Baker, B. F. E. Curchod, N. Ashari-Astani, I. Tavernelli, U. Rothlisberger, M. K. Nazeeruddin, M. Grätzel. Dye-Sensitized Solar Cells with 13% Efficiency Achieved Through the Molecular Engineering of Porphyrin Sensitizers. *Nature Chemistry*, **2014**, 6, 3: 242-247.
- 8 K. Kakiage, Y. Aoyama, T. Yano, K. Oya, J. Fujisawa, M. Hanaya. Highly-efficient dye-sensitized solar cells with collaborative sensitization by silyl-anchor and carboxy-anchor dyes. *Chem. Commun.*, **2015**, 51: 15894-15897.
- 9 C. Klein, M. K. Nazeeruddin, D. D. Censo, P. Liska, M. Grätzel. Amphiphilic Ruthenium Sensitizers and Their Applications in Dye-Sensitized Solar Cells. *Inorg. Chem.*, **2004**, 43, 14: 4216-4226.
- 10 J. Warnan, V.-M. Guerin, F. B. Anne, Y. Pellegrin, E. Blart, D. Jacquemin, T. Pauporté, F. Odobel. Ruthenium Sensitizer Functionalized by Acetylacetonate Anchoring Groups for Dye-Sensitized Solar Cells. *J. Phys. Chem. C*, **2013**, 117 17: 8652-8660.
- 11 S. D. Sousa, L. Ducasse, B. Kauffmann, T. Toupance, C. Olivier. Functionalization of a Ruthenium-Diacetylacetonate Organometallic Complex as a Next-Generation Push-Pull Chromophore. *Chem. Eur. J.*, **2014**, 20: 7017-7024.
- 12 A. Hagfeldt, G. Boschloo, L. C. Sun, L. Kloo, H. Pettersson. Dye-sensitized Solar Cells. *Chem. Rev.*, **2010**, 110: 6595-6663.
- 13 A. Monari, X. Assfeld, M. Beley, P. C. Gros. Theoretical Study of New Ruthenium-Based Dyes for Dye-Sensitized Solar Cells. *J. Phys. Chem. A*, **2011**, 115, 15: 3596-3603.
- 14 F. Gao, Y. Wang, D. Shi, J. Zhang, M. Wang, X. Jing, R. Humphry-Baker, P. Wang, S. M. Zakeeruddin, M. Grätzel. Enhance the Optical Absorptivity of Nanocrystalline TiO₂ Film with High Molar Extinction Coefficient Ruthenium Sensitizers for High Performance Dye-Sensitized Solar Cells. *J. Am. Chem. Soc.*, **2008**, 130, 32: 10720-10728.
- 15 R. J. Durand, S. Gauthier, S. Achelle, T. Groizard, S. Kahlal, J.-Y. Saillard, A. Barsella, N. L. Poul, F. R. L. Guen. Push-pull D- π -Ru- π -A chromophores: synthesis and electrochemical, photophysical and second-order nonlinear optical properties. *Dalton Trans.*, **2018**, 47: 3965-3975.
- 16 A. W. Hains, Z. Liang, M. A. Woodhouse, B. A. Gregg. Molecular Semiconductors in Organic Photovoltaic Cells. *Chem. Rev.*, **2010**, 110, 11: 6689-6735.
- 17 Y. Wu, W. Zhu. Organic sensitizers from D- π -A to D-A- π -A: effect of the internal

- electron-withdrawing units on molecular absorption, energy levels and photovoltaic performances. *Chem. Soc. Rev.*, **2013**, 42: 2039-2058.
- 18 J. N. Clifford, E. Martínez-Ferrero, A. Viterisi, E. Palomares. Sensitizer molecular structure-device efficiency relationship in dye sensitized solar cells. *Chem. Soc. Rev.*, **2011**, 40: 1635-1646.
- 19 P. Qin, X. Yang, R. Chen, L. Sun. Influence of π -Conjugation Units in Organic Dyes for Dye-Sensitized Solar Cells. *J. Phys. Chem. C*, **2007**, 111, 4: 1853-1860.
- 20 G. Richhariya, A. Kumar, P. Tekasakul, B. Gupta. Natural dyes for dye sensitized solar cell: A review. *Renewable and Sustainable Energy Reviews*, **2017**, 69: 705-718.
- 21 A. Listorti, B. O'Regan, J. R. Durrant. Electron Transfer Dynamics in Dye-Sensitized Solar Cells. *Chem. Mater.*, **2011**, 23: 3381-3399.
- 22 J. W. Gong, J. Liang, K. Sumathy. Review on dye-sensitized solar cells (DSSCs): Fundamental concepts and novel materials. *Renewable and Sustainable Energy Reviews*, **2012**, 16: 5848-5860.
- 23 G. Richhariya, A. Kumar, P. Tekasakul, B. Gupta. Natural dyes for dye sensitized solar cell: A review. *Renewable and Sustainable Energy Reviews*, **2017**, 69: 705-718.
- 24 L. M. Peter. Characterization and Modeling of Dye-Sensitized Solar Cells. *J. Phys. Chem. C*, **2007**, 111: 6601-6612.
- 25 A. C. Fisher, L. M. Peter, E. A. Ponomarev, A. B. Walker, K. G. U. Wijayantha. Intensity Dependence of the Back Reaction and Transport of Electrons in Dye-Sensitized Nanocrystalline TiO₂ Solar Cells. *J. Phys. Chem. B*, **2000**, 104, 5: 949-958.
- 26 N. W. Duffy, L. M. Peter, R. M. G. Rajapakse, K. G. U. Wijayantha. Investigation of the Kinetics of the Back Reaction of Electrons with Tri-Iodide in Dye-Sensitized Nanocrystalline Photovoltaic Cells. *J. Phys. Chem. B*, **2000**, 104, 38: 8916-8919.
- 27 P. Péchy, F. P. Rotzinger, M. K. Nazeeruddin, O. Kohle, S. M. Zakeeruddin, R. Humphry-Baker, M. Grätzel. Preparation of phosphonated polypyridyl ligands to anchor transition-metal complexes on oxide surfaces: application for the conversion of light to electricity with nanocrystalline TiO₂ films. *Chem. Commun.*, **1995**, 0: 65-66.
- 28 S. Anderson, E. C. Constable, M. P. Dareedwards, J. B. Goodenough, A. Hamnett, K. R. Seddon, R. D. Wright. Chemical modification of a titanium (IV) oxide electrode to give stable dye sensitisation without a supersensitiser. *Nature*, **1979**, 280: 571-573.
- 29 M. K. Nazeeruddin, P. Péchy, M. Grätzel. Efficient panchromatic sensitization of nanocrystalline TiO₂ films by a black dye based on a trithiocyanato-ruthenium complex. *Chem. Commun.*, **1997**, 0: 1705-1706.

-
-
- 30 S. D. Sousa, S. Lyu, L. Ducasse, T. Toupance, C. Olivier. Tuning visible-light absorption properties of Ru-diacetylide complexes: simple access to colorful efficient dyes for DSSCs. *J. Mater. Chem. A*, **2015**, 3: 18256-18264.
- 31 S. A. Haque, E. Palomares, B. M. Cho, A. N. M. Green, N. Hirata, D. R. Klug, J. R. Durrant. Charge Separation versus Recombination in Dye-Sensitized Nanocrystalline Solar Cells: the Minimization of Kinetic Redundancy. *J. Am. Chem. Soc.*, **2005**, 127, 10: 3456-3462.
- 32 J. B. Asbury, N. A. Anderson, E. Hao, X. Ai, T. Lian. Parameters Affecting Electron Injection Dynamics from Ruthenium Dyes to Titanium Dioxide Nanocrystalline Thin Film. *J. Phys. Chem. B*, **2003**, 107, 30: 7376-7386.
- 33 D. F. Watson, G. J. Meyer. Cation effects in nanocrystalline solar cells. *Coord. Chem. Rev.*, **2004**, 248, 13-14: 1391-1406.
- 34 Y. Tachibana, S. A. Haque, I. P. Mercer, J. E. Moser, D. R. Klug, J. R. Durrant. Modulation of the Rate of Electron Injection in Dye-Sensitized Nanocrystalline TiO₂ Films by Externally Applied Bias. *J. Phys. Chem. B*, **2001**, 105, 31: 7424-7431.
- 35 S. Ardo, G. J. Meyer. Photodriven heterogeneous charge transfer with transition-metal compounds anchored to TiO₂ semiconductor surfaces. *Chem. Soc. Rev.*, **2009**, 38: 115-164.
- 36 D. Kuciauskas, J. E. Monat, R. Villahermosa, H. B. Gray, N. S. Lewis, J. K. McCusker. Transient Absorption Spectroscopy of Ruthenium and Osmium Polypyridyl Complexes Adsorbed onto Nanocrystalline TiO₂ Photoelectrodes. *J. Phys. Chem. B*, **2002**, 106, 36: 9347-9358.
- 37 S. Altobello, R. Argazzi, S. Caramori, C. Contado, S. D. Fré, P. Rubino, C. Choné, G. Larramona, C. A. Bignozzi. Sensitization of Nanocrystalline TiO₂ with Black Absorbers Based on Os and Ru Polypyridine Complexes. *J. Am. Chem. Soc.*, **2005**, 127, 44: 15342-15343.
- 38 G. Sauvé, M. E. Cass, S. J. Doig, I. Lauermann, K. Pomykal, N. S. Lewis. High Quantum Yield Sensitization of Nanocrystalline Titanium Dioxide Photoelectrodes with *cis*-Dicyanobis (4,4'-dicarboxy-2,2'-bipyridine) osmium (II) or Tris (4,4'-dicarboxy-2,2'-bipyridine) osmium (II) Complexes. *J. Phys. Chem. B*, **2000**, 104, 15: 3488-3491.
- 39 A. Islam, H. Sugihara, K. Hara, L. P. Singh, R. Katoh, M. Yanagida, Y. Takahashi, S. Murata, H. Arakawa. Dye Sensitization of Nanocrystalline Titanium Dioxide with Square Planar Platinum(II) Diimine Dithiolate Complexes. *Inorg. Chem.*, **2001**, 40, 21: 5371-5380.
-
-

-
-
- 40 E. A. M. Geary, L. J. Yellowlees, L. A. Jack, I. D. H. Oswald, S. Parsons, N. Hirata, J. R. Durrant, N. Robertson. Synthesis, Structure, and Properties of [Pt(II)(diimine)(dithiolate)] Dyes with 3,3'-, 4,4'-, and 5,5'-Disubstituted Bipyridyl: Applications in Dye-Sensitized Solar Cells. *Inorg. Chem.*, **2005**, 44, 2: 242-250.
- 41 E. A. M. Geary, K. L. McCall, A. Turner, P. R. Murray, E. J. L. McInnes, L. A. Jack, L. J. Yellowlees, Neil Robertson. Spectroscopic, electrochemical and computational study of Pt-diimine-dithiolene complexes: rationalising the properties of solar cell dyes. *Dalton Trans.*, **2008**, 0: 3701-3708.
- 42 G. M. Hasselmann, G. J. Meyer. Diffusion-Limited Interfacial Electron Transfer with Large Apparent Driving Forces. *J. Phys. Chem. B*, **1999**, 103, 36: 7671-7675.
- 43 V. Leandri, Q. Daniel, H. Chen, L. Sun, J. M. Gardner, Lars Kloo. Electronic and Structural Effects of Inner Sphere Coordination of Chloride to a Homoleptic Copper(II) Diimine Complex. *Inorg. Chem.*, **2018**: Article ASAP.
- 44 T. Tsubomura, K. Kimura, M. Nishikawa, T. Tsukuda. Structures and photophysical properties of copper(I) complexes bearing diphenylphenanthroline and bis(diphenylphosphino)alkane: the effect of phenyl groups on the phenanthroline ligand. *Dalton Trans.*, **2015**, 44: 7554-7562.
- 45 S. Ferrere. New Photosensitizers Based upon [Fe(L)₂(CN)₂] and [Fe(L)₃] (L = Substituted 2,2'-Bipyridine): Yields for the Photosensitization of TiO₂ and Effects on the Band Selectivity. *Chem. Mater.*, **2000**, 12, 4: 1083-1089.
- 46 L. L. Jamula, A. M. Brown, D. Guo, J. K. McCusker. Synthesis and Characterization of a High-Symmetry Ferrous Polypyridyl Complex: Approaching the ⁵T₂/³T₁ Crossing Point for Fe^{II}. *Inorg. Chem.*, **2014**, 53, 1: 15-17.
- 47 G. C. Vougioukalakis, A. I. Philippopoulos, T. Stergiopoulos, P. Falaras. Contributions to the development of ruthenium-based sensitizers for dye-sensitized solar cells. *Coord. Chem. Rev.*, **2011**, 255, 21-22: 2602-2621.
- 48 M. K. Nazeeruddin, C. Klein, P. Liska, M. Grätzel. Synthesis of novel ruthenium sensitizers and their application in dye-sensitized solar cells. *Coord. Chem. Rev.*, **2005**, 249, 13-14: 1460-1467.
- 49 A. S. Polo, M. K. Itokazu, N. Y. M. Iha. Metal complex sensitizers in dye-sensitized solar cells. *Coord. Chem. Rev.*, **2004**, 248, 13-14: 1343-1361.
- 50 M. K. Nazeeruddin, A. Kay, I. Rodicio, R. Humphry-Baker, E. Mueller, P. Liska, N. Vlachopoulos, M. Grätzel. Conversion of light to electricity by cis-X₂bis(2,2'-bipyridyl-4,4'-dicarboxylate)ruthenium(II) charge-transfer sensitizers (X =
-
-

- Cl⁻, Br⁻, I⁻, CN⁻, and SCN⁻) on nanocrystalline titanium dioxide electrodes. *J. Am. Chem. Soc.*, **1993**, 115, 14: 6382-6390.
- 51 R. S. Lumpkin, E. M. Kober, L. A. Worl, Z. Murtaza, T. J. Meyer. Metal-to-ligand charge-transfer (MLCT) photochemistry: experimental evidence for the participation of a higher lying MLCT state in polypyridyl complexes of ruthenium(II) and osmium(II). *J. Phys. Chem.*, **1990**, 94, 1: 239-243.
- 52 X. Wang, A. D. Guerzo, R. H. Schmechl. Photophysical behavior of transition metal complexes having interacting ligand localized and metal-to-ligand charge transfer states. *J. Photochem. Photobiol. C: Photochemistry Reviews*, **2004**, 5, 1: 55-77.
- 53 M. K. Nazeeruddin, P. Péchy, T. Renouard, S. M. Zakeeruddin, R. Humphry-Baker, P. Comte, P. Liska, L. Cevey, E. Costa, V. Shklover, L. Spiccia, G. B. Deacon, C. A. Bignozzi, M. Grätzel. Engineering of Efficient Panchromatic Sensitizers for Nanocrystalline TiO₂-Based Solar Cells. *J. Am. Chem. Soc.*, **2001**, 123, 8: 1613-1624.
- 54 M. K. Nazeeruddin, S. M. Zakeeruddin, R. Humphry-Baker, M. Jirousek, P. Liska, N. Vlachopoulos, V. Shklover, C.-H. Fischer, M. Grätzel. Acid-Base Equilibria of (2,2' - Bipyridyl - 4,4' - dicarboxylic acid) ruthenium(II) Complexes and the Effect of Protonation on Charge-Transfer Sensitization of Nanocrystalline Titania. *Inorg. Chem.*, **1999**, 38, 26: 6298-6305.
- 55 P. Wang, S. M. Zakeeruddin, J. E. Moser, M. K. Nazeeruddin, T. Sekiguchi, M. Grätzel. A stable quasi-solid-state dye-sensitized solar cell with an amphiphilic ruthenium sensitizer and polymer gel electrolyte. *Nat. Mater.*, **2003**, 2: 402-407.
- 56 P. Wang, S. M. Zakeeruddin, I. Exnar, M. Grätzel. High efficiency dye-sensitized nanocrystalline solar cells based on ionic liquid polymer gel electrolyte. *Chem. Commun.*, **2002**, 0: 2972-2973.
- 57 P. Wang, S. M. Zakeeruddin, R. Humphry-Baker, J. E. Moser, M. Grätzel. Molecular-Scale Interface Engineering of TiO₂ Nanocrystals: Improve the Efficiency and Stability of Dye-Sensitized Solar Cells. *Adv. Mater.*, **2003**, 15: 2101-2104.
- 58 S. M. Zakeeruddin, M. K. Nazeeruddin, R. Humphry-Baker, P. Péchy, P. Quagliotto, C. Barolo, G. Viscardi, M. Grätzel. Design, Synthesis, and Application of Amphiphilic Ruthenium Polypyridyl Photosensitizers in Solar Cells Based on Nanocrystalline TiO₂ Films. *Langmuir*, **2002**, 18, 3: 952-954.
- 59 F. Sauvage, M. K. R. Fischer, A. Mishra, S. M. Zakeeruddin, M. K. Nazeeruddin, P. Bäuerle, M. Grätzel. A Dendritic Oligothiophene Ruthenium Sensitizer for Stable Dye-Sensitized Solar Cells. *ChemSusChem*, **2009**, 2: 761-768.

-
- 60 P. Wang, S. M. Zakeeruddin, J. E. Moser, R. Humphry-Baker, P. Comte, V. Aranyos, A. Hagfeldt, M. K. Nazeeruddin, M. Grätzel. Stable New Sensitizer with Improved Light Harvesting for Nanocrystalline Dye-Sensitized Solar Cells. *Adv. Mater.*, **2004**, 16, 20: 1806-1811.
- 61 D. Kuang, C. Klein, H. J. Snaith, J.-E. Moser, R. Humphry-Baker, P. Comte, S. M. Zakeeruddin, M. Grätzel. Ion Coordinating Sensitizer for High Efficiency Mesoscopic Dye-Sensitized Solar Cells: Influence of Lithium Ions on the Photovoltaic Performance of Liquid and Solid-State Cells. *Nano Lett.*, **2006**, 6, 4: 769-773.
- 62 D. Kuang, C. Klein, S. Ito, J.-E. Moser, R. Humphry-Baker, S. M. Zakeeruddin, M. Grätzel. High Molar Extinction Coefficient Ion-Coordinating Ruthenium Sensitizer for Efficient and Stable Mesoscopic Dye-Sensitized Solar Cells. *Adv. Funct. Mater.*, **2007**, 17, 1: 154-160.
- 63 S.-R. Jang, J.-H. Yum, C. Klein, K.-J. Kim, P. Wagner, D. Officer, M. Grätzel, M. K. Nazeeruddin. High Molar Extinction Coefficient Ruthenium Sensitizers for Thin Film Dye-Sensitized Solar Cells. *J. Phys. Chem. C*, **2009**, 113, 5: 1998-2003.
- 64 S. A. Haque, S. Handa, K. Peter, E. Palomares, M. Thelakkat, J. R. Durrant. Supermolecular Control of Charge Transfer in Dye-Sensitized Nanocrystalline TiO₂ Films: Towards a Quantitative Structure-Function Relationship. *Angew. Chem., Int. Ed.*, **2005**, 44, 35: 5740-5744.
- 65 S. Handa, H. Wietasch, M. Thelakkat, J. R. Durranta, S. A. Haque. Reducing charge recombination losses in solid state dye sensitized solar cells: the use of donor-acceptor sensitizer dyes. *Chem. Commun.*, **2007**, 0: 1725-1727.
- 66 C. S. Karthikeyan, H. Wietasch, M. Thelakkat. Highly Efficient Solid-State Dye-Sensitized TiO₂ Solar Cells Using Donor-Antenna Dyes Capable of Multistep Charge-Transfer Cascades. *Adv. Mater.*, **2007**, 19, 8: 1091-1095.
- 67 C. Chen, S. Wu, C. Wu, J. Chen, K. Ho. A Ruthenium Complex with Superhigh Light-Harvesting Capacity for Dye-Sensitized Solar Cells. *Angew. Chem.*, **2006**, 118: 5954-5957.
- 68 C. Chen, H. Lu, C. Wu, J. Chen, K. Ho. New Ruthenium Complexes Containing Oligoalkylthiophene-Substituted 1,10-Phenanthroline for Nanocrystalline Dye-Sensitized Solar Cells. *Adv. Funct. Mater.*, **2007**, 17, 1: 29-36.
- 69 C. Chen, S. Wu, J. Li, C. Wu, J. Chen, K. Ho. A New Route to Enhance the Light-Harvesting Capability of Ruthenium Complexes for Dye-Sensitized Solar Cells. *Adv. Mater.*, **2007**, 19, 22: 3888-3891.
-

-
-
- 70 J.-H. Yum, I. Jung, C. Baik, J. Ko, M. K. Nazeeruddin, M. Grätzel. High efficient donor-acceptor ruthenium complex for dye-sensitized solar cell applications. *Energy Environ. Sci.*, **2009**, 2: 100-102.
- 71 C.-Y. Chen, J.-G. Chen, S.-J. Wu, J.-Y. Li, C.-G. Wu, K.-C. Ho. Multifunctionalized Ruthenium-Based Supersensitizers for Highly Efficient Dye-Sensitized Solar Cells. *Angew. Chem. Int. Ed.*, **2008**, 47: 7342-7345.
- 72 F. Gao, Y. Wang, J. Zhang, D. Shi, M. Wang, R. Humphry-Baker, P. Wang, S. M. Zakeeruddin, M. Grätzel. A new heteroleptic ruthenium sensitizer enhances the absorptivity of mesoporous titania film for a high efficiency dye-sensitized solar cell. *Chem. Commun.*, **2008**, 0: 2635-2637.
- 73 Y. Cao, Y. Bai, Q. Yu, Y. Cheng, S. Liu, D. Shi, F. Gao, P. Wang. Dye-Sensitized Solar Cells with a High Absorptivity Ruthenium Sensitizer Featuring a 2-(Hexylthio)thiophene Conjugated Bipyridine. *J. Phys. Chem. C*, **2009**, 113, 15: 6290-6297.
- 74 F. Gao, Y. Cheng, Q. Yu, S. Liu, D. Shi, Y. Li, P. Wang. Conjugation of Selenophene with Bipyridine for a High Molar Extinction Coefficient Sensitizer in Dye-Sensitized Solar Cells. *Inorg. Chem.*, **2009**, 48, 6: 2664-2669.
- 75 K.-J. Jiang, N. Masaki, J.-B. Xia, S. Noda, S. Yanagida. A novel ruthenium sensitizer with a hydrophobic 2-thiophen-2-yl-vinyl-conjugated bipyridyl ligand for effective dye sensitized TiO₂ solar cells. *Chem. Commun.*, **2006**, 0: 2460-2462.
- 76 J. Faiz, A. I. Philippopoulos, A. G. Kontos, P. Falaras, Z. Pikramenou. Functional Supramolecular Ruthenium Cyclodextrin Dyes for Nanocrystalline Solar Cells. *Adv. Funct. Mater.*, **2007**, 17: 54-58.
- 77 Y. Liu, C. M. Ndiaye, C. Lagrost, K. Costuas, S. Choua, P. Turek, L. Norel, S. Rigaut. Diarylethene-Containing Carbon-Rich Ruthenium Organometallics: Tuning of Electrochromism. *Inorg. Chem.*, **2014**, 53, 15: 8172-8188.
- 78 K. Costuas, S. Rigaut. Polynuclear carbon-rich organometallic complexes: clarification of the role of the bridging ligand in the redox properties. *Dalton Trans.*, **2011**, 40: 5643-5658.
- 79 S. Rigaut. Metal complexes in molecular junctions. *Dalton Trans.*, **2013**, 42: 15859-15863.
- 80 M. P. Cifuentes, M. G. Humphrey, J. P. Morrall, M. Samoc, F. Paul, C. Lapinte, T. Roisnel. Third-Order Nonlinear Optical Properties of Some Electron-Rich Iron Mono- and Trinuclear Alkynyl Complexes. *Organometallics*, **2005**, 24, 17: 4280-4288.
- 81 H.-M. Wen, Y. Yang, X.-S. Zhou, J.-Y. Liu, D.-B. Zhang, Z.-B. Chen, J.-Y. Wang, Z.-N.
-
-

- Chen, Z.-Q. Tian. Electrical conductance study on 1,3-butadiyne-linked dinuclear ruthenium(II) complexes within single molecule break junctions. *Chem. Sci.*, **2013**, 4: 2471-2477.
- 82 O. A. Al-Owaedi, D. C. Milan, M.-C. Oerthel, S. Bock, D. S. Yufit, J. A. K. Howard, S. J. Higgins, R. J. Nichols, C. J. Lambert, M. R. Bryce, Paul J. Low. Experimental and Computational Studies of the Single-Molecule Conductance of Ru(II) and Pt(II) trans-Bis(acetylide) Complexes. *Organometallics*, **2016**, 35, 17: 2944-2954.
- 83 A. Colombo, C. Dragonetti, D. Roberto, R. Ugo, L. Falciola, S. Luzzati, D. Kotowski. A Novel Diruthenium Acetylide Donor Complex as an Unusual Active Material for Bulk Heterojunction Solar Cells. *Organometallics*, **2011**, 30, 6: 1279-1282.
- 84 W. Wu, J. Zhang, H. Yang, B. Jin, Y. Hu, J. Hua, C. Jing, Y. Long, H. Tian. Narrowing band gap of platinum acetylide dye-sensitized solar cell sensitizers with thiophene π -bridges. *J. Mater. Chem.*, **2012**, 22: 5382-5389.
- 85 D. Touchard, P. Haquette, S. Guesmi, L. L. Pichon, A. Daridor, L. Toupet, P. H. Dixneuf. Vinylidene-, Alkynyl-, and trans-Bis(alkynyl)ruthenium Complexes. Crystal Structure of trans- [Ru (NH₃) (C \equiv C-Ph) (Ph₂PCH₂CH₂PPh₂)₂] PF₆. *Organometallics*, **1997**, 16, 16: 3640-3648.
- 86 P. J. West, M. P. Cifuentes, T. Schwich, M. D. Randles, J. P. Morrall, E. Kulasekera, S. Petrie, R. Stranger, M. G. Humphrey. Syntheses and Spectroscopic, Structural, Electrochemical, Spectroelectrochemical, and Theoretical Studies of Osmium(II) Mono- and Bis-Alkynyl Complexes. *Inorg. Chem.*, **2012**, 51, 20: 10495-10502.
- 87 C. Olivier, B. Kim, D. Touchard, S. Rigaut. Redox-Active Molecular Wires Incorporating Ruthenium(II) σ -Arylacetylide Complexes for Molecular Electronics. *Organometallics*, **2008**, 27, 4: 509-518.
- 88 N. Gauthier, C. Olivier, S. Rigaut, D. Touchard, T. Roisnel, M. G. Humphrey, F. Paul. Intramolecular Optical Electron Transfer in Mixed-Valent Dinuclear Iron-Ruthenium Complexes Featuring a 1,4-Diethynylaryl Spacer. *Organometallics*, **2008**, 27, 6: 1063-1072.
- 89 G. Grelaud, M. P. Cifuentes, T. Schwich, G. Argouarch, S. Petrie, R. Stranger, F. Paul, M. G. Humphrey. Multistate Redox-Active Metalated Triarylamines. *Eur. J. Inorg. Chem.*, **2012**, 1: 65-75.
- 90 F. Nisic, A. Colombo, C. Dragonetti, E. Garoni, D. Marinotto, S. Righetto, F. D. Angelis, M. G. Lobello, P. Salvatori, P. Biagini, F. Melchiorre. Functionalized Ruthenium Dialkynyl Complexes with High Second-Order Nonlinear Optical Properties and Good

- Potential as Dye Sensitizers for Solar Cells. *Organometallics*, **2015**, 34, 1: 94-104.
- 91 J. A. A. W. Elemans, R. V. Hameren, R. J. M. Nolte, A. E. Rowan. Molecular Materials by Self-Assembly of Porphyrins, Phthalocyanines, and Perylenes. *Adv. Mater.*, **2006**, 18, 10: 1251-1266.
- 92 H. Eichhorn. Mesomorphic phthalocyanines, tetraazaporphyrins, porphyrins and triphenylenes as charge-transporting materials. *J. Porphyrins Phthalocyanines*, **2000**, 4: 88-102.
- 93 G. F. Manbeck, E. Fujita. A review of iron and cobalt porphyrins, phthalocyanines and related complexes for electrochemical and photochemical reduction of carbon dioxide. *J. Porphyrins Phthalocyanines*, **2015**, 19: 45-64.
- 94 W. M. Campbell, A. K. Burrell, D. L. Officer, K. W. Jolley. Porphyrins as light harvesters in the dye-sensitized TiO₂ solar cell. *Coord. Chem. Rev.*, **2004**, 248: 1363-1379.
- 95 T. Higashino, H. Imahori. Porphyrins as excellent dyes for dye-sensitized solar cells: recent developments and insights. *Dalton Trans.*, **2015**, 44: 448-463.
- 96 H. Imahori, T. Umeyama, S. Ito. Large π -Aromatic Molecules as Potential Sensitizers for Highly Efficient Dye-Sensitized Solar Cells. *Acc. Chem. Res.*, **2009**, 42, 11: 1809-1818.
- 97 M. V. Martínez-Díaz, G. D. L. Torre, T. Torres. Lighting porphyrins and phthalocyanines for molecular photovoltaics. *Chem. Commun.*, **2010**, 46: 7090-7108.
- 98 M. J. Griffith, K. Sunahara, P. Wagner, K. Wagner, G. G. Wallace, D. L. Officer, A. Furube, R. Katoh, S. Mori, A. J. Mozer. Porphyrins for dye-sensitized solar cells: new insights into efficiency-determining electron transfer steps. *Chem. Commun.*, **2012**, 48: 4145-4162.
- 99 L.-L. Li, E. W.-G. Diau. Porphyrin-sensitized solar cells. *Chem. Soc. Rev.*, **2013**, 42: 291-304.
- 100 K. Ladomenou, T. N. Kitsopoulos, G. D. Sharma, A. G. Coutsolelos. The importance of various anchoring groups attached on porphyrins as potential dyes for DSSC applications. *RSC Adv.*, **2014**, 4: 21379-21404.
- 101 A. Kay, M. Grätzel. Artificial photosynthesis. 1. Photosensitization of titania solar cells with chlorophyll derivatives and related natural porphyrins. *J. Phys. Chem.*, **1993**, 97, 23: 6272-6277.
- 102 S. Cherian, C. C. Wamser. Adsorption and Photoactivity of Tetra (4-carboxyphenyl)porphyrin (TCPP) on Nanoparticulate TiO₂. *J. Phys. Chem. B*, **2000**, 104, 15: 3624-3629.
- 103 Y. Tachibana, S. A. Haque, I. P. Mercer, J. R. Durrant, D. R. Klug. Electron Injection and

- Recombination in Dye Sensitized Nanocrystalline Titanium Dioxide Films: A Comparison of Ruthenium Bipyridyl and Porphyrin Sensitizer Dyes. *J. Phys. Chem. B*, **2000**, 104, 6: 1198-1205.
- 104 R. B. M. Koehorst, G. K. Boschloo, T. J. Savenije, A. Goossens, T. J. Schaafsma. Spectral Sensitization of TiO₂ Substrates by Monolayers of Porphyrin Heterodimers. *J. Phys. Chem. B*, **2000**, 104, 10: 2371-2377.
- 105 M. K. Nazeeruddin, R. Humphry-Baker, D. L. Officer, W. M. Campbell, A. K. Burrell, M. Grätzel. Application of Metalloporphyrins in Nanocrystalline Dye-Sensitized Solar Cells for Conversion of Sunlight into Electricity. *Langmuir*, **2004**, 20, 15: 6514-6517.
- 106 B. J. Brennan, M. J. L. Portolés, P. A. Liddell, T. A. Moore, A. L. Moore, D. Gust. Comparison of silatrane, phosphonic acid, and carboxylic acid functional groups for attachment of porphyrin sensitizers to TiO₂ in photoelectrochemical cells. *Phys. Chem. Chem. Phys.*, **2013**, 15: 16605-16614.
- 107 H. He, A. Gurung, L. Si. 8-Hydroxylquinoline as a strong alternative anchoring group for porphyrin-sensitized solar cells. *Chem. Commun.*, **2012**, 48: 5910-5912.
- 108 L. Si, H. He, K. Zhu. 8-Hydroxylquinoline-conjugated porphyrins as broadband light absorbers for dye-sensitized solar cells. *New J. Chem.*, **2014**, 38: 1565-1572.
- 109 C.-Y. Lin, Y.-C. Wang, S.-J. Hsu, C.-F. Lo, E. W.-G. Diau. Preparation and Spectral, Electrochemical, and Photovoltaic Properties of Acene-Modified Zinc Porphyrins. *J. Phys. Chem. C*, **2010**, 114, 1: 687-693.
- 110 G. D. L. Torre, C. G. Claessens, T. Torres. Phthalocyanines: old dyes, new materials. Putting color in nanotechnology. *Chem. Commun.*, **2007**, 0: 2000-2015.
- 111 J. Mack, N. Kobayashi. Low Symmetry Phthalocyanines and Their Analogues. *Chem. Rev.*, **2011**, 111, 2: 281-321.
- 112 V. K. Singh, R. K. Kanaparthi, L. Giribabu. Emerging molecular design strategies of unsymmetrical phthalocyanines for dye-sensitized solar cell applications. *RSC Adv.*, **2014**, 4: 6970-6984.
- 113 P. Chawla, M. Tripathi. Novel improvements in the sensitizers of dye-sensitized solar cells for enhancement in efficiency-a review. *Int. J. Energy Res.*, **2015**, 39: 1579-1596.
- 114 H. Matsuzaki, T. N. Murakami, N. Masaki, A. Furube, M. Kimura, S. Mori. Dye Aggregation Effect on Interfacial Electron-Transfer Dynamics in Zinc Phthalocyanine-Sensitized Solar Cells. *J. Phys. Chem. C*, **2014**, 118, 31: 17205-17212.
- 115 M. Ince, J.-H. Yum, Y. Kim, S. Mathew, M. Grätzel, T. Torres, M. K. Nazeeruddin. Molecular Engineering of Phthalocyanine Sensitizers for Dye-Sensitized Solar Cells. *J.*

- Phys. Chem. C*, **2014**, 118, 30: 17166-17170.
- 116 M.-E. Ragoussi, M. Ince, T. Torres. Recent Advances in Phthalocyanine-Based Sensitizers for Dye-Sensitized Solar Cells. *Eur. J. Org. Chem.*, **2013**, 2013, 29: 6475-6489.
- 117 M. K. Nazeeruddin, R. Humphry-Baker, M. Grätzel, B. A. Murrer. Efficient near IR sensitization of nanocrystalline TiO₂ films by ruthenium phthalocyanines. *Chem. Commun.*, **1998**, 0: 719-720.
- 118 M. K. Nazeeruddin, R. Humphry-Baker, M. Grätzel, D. Wöhrle, G. Schnurpfeil, G. Schneider, A. Hirth, N. Trombach. Efficient Near-IR Sensitization of Nanocrystalline TiO₂ Films by Zinc and Aluminum Phthalocyanines. *J. Porphyrins Phthalocyanines*, **1999**, 3: 230-237.
- 119 S. Mori, M. Nagata, Y. Nakahata, K. Yasuta, R. Goto, M. Kimura, M. Taya. Enhancement of Incident Photon-to-Current Conversion Efficiency for Phthalocyanine-Sensitized Solar Cells by 3D Molecular Structuralization. *J. Am. Chem. Soc.*, **2010**, 132, 12: 4054-4055.
- 120 M. Kimura, H. Nomoto, N. Masaki, S. Mori. Dye Molecules for Simple Co-Sensitization Process: Fabrication of Mixed-Dye-Sensitized Solar Cells. *Angew. Chem. Int. Ed.*, **2012**, 51: 4371-4374.
- 121 M.-E. Ragoussi, J.-J. Cid, J.-H. Yum, G. de la Torre, D. D. Censo, M. Grätzel, M. K. Nazeeruddin, T. Torres. Carboxyethynyl Anchoring Ligands: A Means to Improving the Efficiency of Phthalocyanine-Sensitized Solar Cells. *Angew. Chem. Int. Ed.*, **2012**, 51: 4375-4378.
- 122 M.-E. Ragoussi, J.-H. Yum, A. K. Chandiran, M. Ince, G. de la Torre, M. Grätzel, M. K. Nazeeruddin, T. Torres. Sterically Hindered Phthalocyanines for Dye-Sensitized Solar Cells: Influence of the Distance between the Aromatic Core and the Anchoring Group. *ChemPhysChem*, **2014**, 15: 1033-1036.
- 123 I. López-Duarte, M. Wang, R. Humphry-Baker, M. Ince, M. V. Martínez-Díaz, M. K. Nazeeruddin, T. Torres, M. Grätzel. Molecular Engineering of Zinc Phthalocyanines with Phosphinic Acid Anchoring Groups. *Angew. Chem. Int. Ed.*, **2012**, 51: 1895-1898.
- 124 M. García-Iglesias, J.-H. Yum, R. Humphry-Baker, S. M. Zakeeruddin, P. Péchy, P. Vázquez, E. Palomares, M. Grätzel, M. K. Nazeeruddin, T. Torres. Effect of anchoring groups in zinc phthalocyanine on the dye-sensitized solar cell performance and stability. *Chem. Sci.*, **2011**, 2: 1145-1150.
- 125 M. García-Iglesias, J.-J. Cid, J.-H. Yum, A. Forneli, P. Vázquez, M. K. Nazeeruddin, E. Palomares, M. Grätzel, T. Torres. Increasing the efficiency of zinc-phthalocyanine based

- solar cells through modification of the anchoring ligand. *Energy Environ. Sci.*, **2011**, 4: 189-194.
- 126 M. Kimura, H. Nomoto, H. Suzuki, T. Ikeuchi, H. Matsuzaki, T. N. Murakami, A. Furube, N. Masaki, M. J. Griffith, S. Mori. Molecular Design Rule of Phthalocyanine Dyes for Highly Efficient Near-IR Performance in Dye-Sensitized Solar Cells. *Chem. Eur. J.*, **2013**, 19: 7496-7502.
- 127 T. Ikeuchi, H. Nomoto, N. Masaki, M. J. Griffith, S. Mori, M. Kimura. Molecular engineering of zinc phthalocyanine sensitizers for efficient dye-sensitized solar cells. *Chem. Commun.*, **2014**, 50: 1941-1943.
- 128 R. K. Kanaparthi, J. Kandhadi, L. Giribabu. Metal-free organic dyes for dye-sensitized solar cells: recent advances. *Tetrahedron*, **2012**, 68, 40: 8383-8393.
- 129 A. Błaszczuk. Strategies to improve the performance of metal-free dye-sensitized solar cells. *Dyes and Pigments*, **2018**, 149: 707-718.
- 130 C.-L. Ho, W.-Y. Wong. High performance arylamine-based metallated and metal-free organic photosensitizers for dye-sensitized solar cells. *J. Photochem. Photobiol. C: Photochemistry Reviews*, **2016**, 28: 138-158.
- 131 J. Massin, L. Ducasse, M. Abbas, L. Hirsch, T. Toupance, C. Olivier. Molecular engineering of carbazole-fluorene sensitizers for high open-circuit voltage DSSCs: Synthesis and performance comparison with iodine and cobalt electrolytes. *Dyes and Pigments*, **2015**, 118: 76-87.
- 132 J. Yuan, A. Gallagher, Z. Liu, Y. Sun, W. Ma. High-efficiency polymer-PbS hybrid solar cells via molecular engineering. *J. Mater. Chem. A*, **2015**, 3: 2572-2579.
- 133 S. Namuangruk, R. Fukuda, M. Ehara, J. Meeprasert, T. Khanasa, S. Morada, T. Kaewin, S. Jungsuttiwong, T. Sudyoadsuk, V. Promarak. D-D- π -A-Type Organic Dyes for Dye-Sensitized Solar Cells with a Potential for Direct Electron Injection and a High Extinction Coefficient: Synthesis, Characterization, and Theoretical Investigation. *J. Phys. Chem. C*, **2012**, 116, 49: 25653-25663.
- 134 W. Zhu, Y. Wu, S. Wang, W. Li, X. Li, J. Chen, Z. Wang, H. Tian. Organic D-A- π -A Solar Cell Sensitizers with Improved Stability and Spectral Response. *Adv. Funct. Mater.*, **2011**, 21, 4: 756-763.
- 135 Y. Wu, W. Zhu. Organic sensitizers from D- π -A to D-A- π -A: effect of the internal electron-withdrawing units on molecular absorption, energy levels and photovoltaic performances. *Chem. Soc. Rev.*, **2013**, 42: 2039-2058.
- 136 Z. Ning, H. Tian. Triarylamine: a promising core unit for efficient photovoltaic materials.

- Chem. Commun.*, **2009**, 0: 5483-5495.
- 137 Y. Liang, Bo Peng, Jun Chen. Correlating Dye Adsorption Behavior with the Open-Circuit Voltage of Triphenylamine-Based Dye-Sensitized Solar Cells. *J. Phys. Chem. C*, **2010**, 114, 24: 10992-10998.
- 138 H. Im, S. Kim, C. Park, S.-H. Jang, C.-J. Kim, K. Kim, N.-G. Park, C. Kim. High performance organic photosensitizers for dye-sensitized solar cells. *Chem. Commun.*, **2010**, 46: 1335-1337.
- 139 T. Kitamura, M. Ikeda, K. Shigaki, T. Inoue, N. A. Anderson, X. Ai, T. Lian, S. Yanagida. Phenyl-Conjugated Oligoene Sensitizers for TiO₂ Solar Cells. *Chem. Mater.*, **2004**, 16, 9: 1806-1812.
- 140 H. Zhou, P. Xue, Y. Zhang, X. Zhao, J. Jia, X. Zhang, X. Liu, R. Lu. Fluorenylvinylenes bridged triphenylamine-based dyes with enhanced performance in dye-sensitized solar cells. *Tetrahedron*, **2011**, 67, 44: 8477-8483.
- 141 C. Olivier, F. Sauvage, L. Ducasse, F. Castet, M. Grätzel, T. Toupance. Fine-Tuning of Triarylamine-Based Photosensitizers for Dye-Sensitized Solar Cells. *ChemSusChem*, **2011**, 4: 731-736.
- 142 P. Shen, Y. Tang, S. Jiang, H. Chen, X. Zheng, X. Wang, B. Zhao, S. Tan. Efficient triphenylamine-based dyes featuring dual-role carbazole, fluorene and spirobifluorene moieties. *Org. Electron.*, **2011**, 12: 125-135.
- 143 J.-H. Yum, E. Baranoff, F. Kessler, T. moehl, S. Ahmad, T. Bessho, A. Marchioro, E. Ghadiri, J.-E. Moser, C. Yi, M. K. Nazeeruddin, Michael Grätzel. A cobalt complex redox shuttle for dye-sensitized solar cells with high open-circuit potentials. *Nat. Commun.*, **2012**, 3: 631-638.
- 144 J. M. Rehm, G. L. McLendon, Y. Nagasawa, K. Yoshihara, J. Moser, M. Grätzel. Femtosecond Electron-Transfer Dynamics at a Sensitizing Dye-Semiconductor (TiO₂) Interface. *J. Phys. Chem.*, **1996**, 100, 23: 9577-9578.
- 145 K. Hara, K. Sayama, Y. Ohga, A. Shinpo, S. Suga, H. Arakawa. A coumarin-derivative dye sensitized nanocrystalline TiO₂ solar cell having a high solar-energy conversion efficiency up to 5.6%. *Chem. Commun.*, **2001**, 0: 569-570.
- 146 K. Hara, M. Kurashige, Y. Dan-oh, C. Kasada, A. Shinpo, S. Suga, K. Sayama, H. Arakawa. Design of new coumarin dyes having thiophene moieties for highly efficient organic-dye-sensitized solar cells. *New J. Chem.*, **2003**, 27: 783-785.
- 147 K. Hara, Z.-S. Wang, T. Sato, A. Furube, R. Katoh, H. Sugihara, Y. Dan-oh, C. Kasada, A. Shinpo, S. Suga. Oligothiophene-Containing Coumarin Dyes for Efficient Dye-Sensitized

- Solar Cells. *J. Phys. Chem. B*, **2005**, 109, 32: 15476-15482.
- 148 S. Sreejith, P. Carol, P. Chithra, A. Ajayaghosh. Squaraine dyes: a mine of molecular materials. *J. Mater. Chem.*, **2008**, 18: 264-274.
- 149 J.-H. Yum, P. Walter, S. Huber, D. Rentsch, T. Geiger, F. Nüesch, F. D. Angelis, M. Grätzel, M. K. Nazeeruddin. Efficient Far Red Sensitization of Nanocrystalline TiO₂ Films by an Unsymmetrical Squaraine Dye. *J. Am. Chem. Soc.*, **2007**, 129, 34: 10320-10321.
- 150 Y. Shi, R. B. M. Hill, J.-H. Yum, A. Dualeh, S. Barlow, M. Grätzel, S. R. Marder, M. K. Nazeeruddin. A High-Efficiency Panchromatic Squaraine Sensitizer for Dye-Sensitized Solar Cells. *Angew. Chem. Int. Ed.*, **2011**, 50: 6619-6621.
- 151 G. Xia, H. Wang. Squaraine dyes: The hierarchical synthesis and its application in optical detection. *J. Photochem. Photobiol. C: Photochemistry Reviews*, **2017**, 31: 84-113.
- 152 K. Nakabayashi, H. Mori. Novel Complex Polymers with Carbazole Functionality by Controlled Radical Polymerization. *Int. J. Polym. Sci.*, **2011**, 2012: 170912.
- 153 P.-P. Li, Y. Chen, J. Zhu, M. Feng, X. Zhuang, Y. Lin, H. Zhan. Charm-Bracelet-Type Poly(N-vinylcarbazole) Functionalized with Reduced Graphene Oxide for Broadband Optical Limiting. *Chem. Eur. J.*, **2010**, 17: 780-785.
- 154 C.-Y. Chen, N. Pootrakulchote, T.-H. Hung, C.-J. Tan, H.-H. Tsai, S. M. Zakeeruddin, C.-G. Wu, M. Grätzel. Ruthenium Sensitizer with Thienothiophene-Linked Carbazole Antennas in Conjunction with Liquid Electrolytes for Dye-Sensitized Solar Cells. *J. Phys. Chem. C*, **2011**, 115, 40: 20043-20050.
- 155 J. Tang, J. Hua, W. Wu, J. Li, Z. Jin, Y. Long, H. Tian. New starburst sensitizer with carbazole antennas for efficient and stable dye-sensitized solar cells. *Energy Environ. Sci.*, **2010**, 3: 1736-1745.
- 156 K. S. V. Gupta, J. Zhang, G. Marotta, M. A. Reddy, S. P. Singh, A. Islam, L. Han, F. D. Angelis, M. Chandrasekharam, M. Pastore. Effect of the anchoring group in the performance of carbazole-phenothiazine dyads for dye-sensitized solar cells. *Dyes and Pigments*, **2015**, 113: 536-545.
- 157 G. Marotta, M. A. Reddy, S. P. Singh, A. Islam, L. Han, F. D. Angelis, M. Pastore, M. Chandrasekharam. Novel Carbazole-Phenothiazine Dyads for Dye-Sensitized Solar Cells: A Combined Experimental and Theoretical Study. *ACS Appl. Mater. Interfaces*, **2013**, 5, 19: 9635-9647.
- 158 S. D. Sousa, C. Olivier, L. Ducasse, G. L. Bourdon, L. Hirsch, T. Toupance. Oligocarbazole-Based Chromophores for Efficient Thin-Film Dye-Sensitized Solar Cells.

- ChemSusChem*, **2013**, 6: 993-996.
- 159 C.-P. Lee, C.-T. Li, K.-C. Ho. Use of organic materials in dye-sensitized solar cells. *Materials Today*, **2017**, 20, 5: 267-283.
- 160 W. Zeng, Y. Cao, Y. Bai, Y. Wang, Y. Shi, M. Zhang, F. Wang, C. Pan, P. Wang. Efficient Dye-Sensitized Solar Cells with an Organic Photosensitizer Featuring Orderly Conjugated Ethylenedioxythiophene and Dithienosilole Blocks. *Chem. Mater.*, **2010**, 22, 5: 1915-1925.
- 161 M. Zhang, Y. Wang, M. Xu, W. Ma, R. Li, P. Wang. Design of high-efficiency organic dyes for titania solar cells based on the chromophoric core of cyclopentadithiophene-benzothiadiazole. *Energy Environ. Sci.*, **2013**, 6: 2944-2949.
- 162 D. Joly, L. Pellejà, S. Narbey, F. Oswald, J. Chiron, J. N. Clifford, E. Palomares, R. Demadrille. A Robust Organic Dye for Dye Sensitized Solar Cells Based on Iodine/Iodide Electrolytes Combining High Efficiency and Outstanding Stability. *Scientific Reports*, **2013**, 4: 4033.
- 163 Z. Yao, M. Zhang, R. Li, L. Yang, Y. Qiao, P. Wang. A Metal-Free N-Annulated Thienocyclopentaperylene Dye: Power Conversion Efficiency of 12 % for Dye-Sensitized Solar Cells. *Angew. Chem. Int. Ed.*, **2015**, 54: 5994-5998.
- 164 Z. Yao, M. Zhang, H. Wu, L. Yang, R. Li, P. Wang. Donor/Acceptor Indenoperylene Dye for Highly Efficient Organic Dye-Sensitized Solar Cells. *J. Am. Chem. Soc.*, **2015**, 137, 11: 3799-3802.
- 165 M. Akhtaruzzaman, A. Islam, F. Yang, N. Asao, E. Kwon, S. P. Singh, L. Han, Y. Yamamoto. A novel metal-free panchromatic TiO₂ sensitizer based on a phenylenevinylene-conjugated unit and an indoline derivative for highly efficient dye-sensitized solar cells. *Chem. Commun.*, **2011**, 47: 12400-12402.
- 166 D. Kim, K. Song, M.-S. Kang, J.-W. Lee, S. O. Kang, J. Ko. Efficient organic sensitizers containing benzo[cd]indole: Effect of molecular isomerization for photovoltaic properties. *J. Photochem. Photobiol., A: Chem.*, **2009**, 201: 102-110.
- 167 S. Ito, S. M. Zakeeruddin, R. Humphry-Baker, P. Liska, R. Charvet, P. Comte, M. K. Nazeeruddin, P. Péchy, M. Takata, H. Miura, S. Uchida, M. Grätzel. High-Efficiency Organic-Dye-Sensitized Solar Cells Controlled by Nanocrystalline-TiO₂ Electrode Thickness. *Adv. Mater.*, **2006**, 18: 1202-1205.
- 168 T. Horiuchi, H. Miura, K. Sumioka, Satoshi Uchida. High Efficiency of Dye-Sensitized Solar Cells Based on Metal-Free Indoline Dyes. *J. Am. Chem. Soc.*, **2004**, 126, 39: 12218-12219.

-
- 169 C. Li, J.-H. Yum, S.-J. Moon, A. Herrmann, F. Eickemeyer, N. G. Pschirer, P. Erk, J. Schöneboom, K. Müllen, M. Grätzel, M. K. Nazeeruddin. An Improved Perylene Sensitizer for Solar Cell Applications. *ChemSusChem*, **2008**, 1: 615-618.
- 170 Y. Avlasevich, C. Li, K. Müllen. Synthesis and applications of core-enlarged perylene dyes. *J. Mater. Chem.*, **2010**, 20: 3814-3826.
- 171 N. Martsinovich, A. Troisi. High-Throughput Computational Screening of Chromophores for Dye-Sensitized Solar Cells. *J. Phys. Chem. C*, **2011**, 115, 23: 11781-11792.
- 172 S. Mathew, H. Imahori. Tunable, strongly-donating perylene photosensitizers for dye-sensitized solar cells. *J. Mater. Chem.*, **2011**, 21: 7166-7174.
- 173 U. B. Cappel, M. H. Karlsson, N. G. Pschirer, F. Eickemeyer, J. Schöneboom, P. Erk, G. Boschloo, A. Hagfeldt. A Broadly Absorbing Perylene Dye for Solid-State Dye-Sensitized Solar Cells. *J. Phys. Chem. C*, **2009**, 113, 33: 14595-14597.
- 174 P. Shen, X. Liu, S. Jiang, Y. Huang, L. Yi, B. Zhao, S. Tan. Effects of aromatic π -conjugated bridges on optical and photovoltaic properties of N,N-diphenylhydrazone-based metal-free organic dyes. *Org. Electron.*, **2011**, 12: 1992-2002.
- 175 S.-L. Li, K.-J. Jiang, K.-F. Shao, L.-M. Yang. Novel organic dyes for efficient dye-sensitized solar cells. *Chem. Commun.*, **2006**, 0: 2792-2794.
- 176 K. Hara, T. Sato, R. Katoh, A. Furube, T. Yoshihara, M. Murai, M. Kurashige, S. Ito, A. Shinpo, S. Suga, H. Arakawa. Novel Conjugated Organic Dyes for Efficient Dye-Sensitized Solar Cells. *Adv. Funct. Mater.*, **2005**, 15: 246-252.
- 177 C. Teng, X. Yang, C. Yang, S. Li, M. Cheng, A. Hagfeldt, L. Sun. Molecular Design of Anthracene-Bridged Metal-Free Organic Dyes for Efficient Dye-Sensitized Solar Cells. *J. Phys. Chem. C*, **2010**, 114, 19: 9101-9110.
- 178 H. Tian, X. Yang, R. Chen, Y. Pan, L. Li, A. Hagfeldt, L. Sun. Phenothiazine derivatives for efficient organic dye-sensitized solar cells. *Chem. Commun.*, **2007**, 0: 3741-3743.
- 179 K. M. Karlsson, X. Jiang, S. K. Eriksson, E. Gabrielsson, H. Rensmo, A. Hagfeldt, L. Sun. Phenoxazine Dyes for Dye-Sensitized Solar Cells: Relationship Between Molecular Structure and Electron Lifetime. *Chem. Eur. J.*, **2011**, 17: 6415-6424.
- 180 S. Hattori, K. Ohkubo, Y. Urano, H. Sunahara, T. Nagano, Y. Wada, N. V. Tkachenko, H. Lemmetyinen, S. Fukuzumi. Charge Separation in a Nonfluorescent Donor-Acceptor Dyad Derived from Boron Dipyrromethene Dye, Leading to Photocurrent Generation. *J. Phys. Chem. B*, **2005**, 109, 32: 15368-15375.
- 181 C. Y. Lee, J. T. Hupp. Dye Sensitized Solar Cells: TiO₂ Sensitization with a
-

- Bodipy-Porphyrin Antenna System. *Langmuir*, **2010**, 26, 5: 3760-3765.
- 182 M. Mao, J.-B. Wang, Z.-F. Xiao, S.-Y. Dai, Q.-H. Song. New 2,6-modified BODIPY sensitizers for dye-sensitized solar cells. *Dyes and Pigments*, **2012**, 94, 2: 224-232.
- 183 Y. Hao, X. Yang, J. Cong, A. Hagfeldt, L. Sun. Engineering of highly efficient tetrahydroquinoline sensitizers for dye-sensitized solar cells. *Tetrahedron*, **2012**, 68, 2: 552-558.
- 184 R. Chen, X. Yang, H. Tian, X. Wang, A. Hagfeldt, L. Sun. Effect of Tetrahydroquinoline Dyes Structure on the Performance of Organic Dye-Sensitized Solar Cells. *Chem. Mater.*, **2007**, 19, 16: 4007-4015.
- 185 T. Miyasaka. Toward Printable Sensitized Mesoscopic Solar Cells: Light-Harvesting Management with Thin TiO₂ Films. *J. Phys. Chem. Lett.*, **2011**, 2, 3: 262-269.
- 186 X. Liu, R. Zhu, Y. Zhang, B. Liu, S. Ramakrishna. Anionic benzothiadiazole containing polyfluorene and oligofluorene as organic sensitizers for dye-sensitized solar cells. *Chem. Commun.*, **2008**, 0: 3789-3791.
- 187 Y. Nicolas, F. Allama, M. Lepeltier, J. Massin, F. Castet, L. Ducasse, L. Hirsch, Z. Boubegiten, G. Jonusauskas, C. Olivier, T. Toupance. New Synthetic Routes towards Soluble and Dissymmetric Triphenodioxazine Dyes Designed for Dye-Sensitized Solar Cells. *Chem. Eur. J.*, **2014**, 20: 3678-3688.
- 188 S. Haid, M. Marszalek, A. Mishra, M. Wielopolski, J. Teuscher, J.-E. Moser, R. Humphry-Baker, S. M. Zakeeruddin, M. Grätzel, P. Bäuerle. Significant Improvement of Dye-Sensitized Solar Cell Performance by Small Structural Modification in π -Conjugated Donor-Acceptor Dyes. *Adv. Funct. Mater.*, **2012**, 22: 1291-302.
- 189 D.-H. Roh, K. M. Kim, J. S. Nam, U.-Y. Kim, B.-M. Kim, J. S. Kim, T.-H. Kwon. Strategy for Improved Photoconversion Efficiency in Thin Photoelectrode Films by Controlling π -Spacer Dihedral Angle. *J. Phys. Chem. C*, **2016**, 120, 43: 24655-24666.
- 190 Y. Wu, W.-H. Zhu, S. M. Zakeeruddin, M. Grätzel. Insight into D-A- π -A Structured Sensitizers: A Promising Route to Highly Efficient and Stable Dye-Sensitized Solar Cells. *ACS Appl. Mater. Interfaces*, **2015**, 7, 18: 9307-9318.
- 191 A. Yella, C.-L. Mai, S. M. Zakeeruddin, S.-N. Chang, C.-H. Hsieh, C.-Y. Yeh, M. Grätzel. Molecular Engineering of Push-Pull Porphyrin Dyes for Highly Efficient Dye-Sensitized Solar Cells: The Role of Benzene Spacers. *Angew. Chem. Int. Ed.*, **2014**, 126: 3017-3021.
- 192 R. F. Winter, K.-W. Klinkhammer, S. Zálíš. Ruthenium-Aminoallenylidene Complexes from Butatrienylidene Intermediates via an Aza-Cope Rearrangement: Synthetic,

- Spectroscopic, Electrochemical, Spectroelectrochemical, and Computational Studies. *Organometallics*, **2001**, 20, 7: 1317-1333.
- 193 J. R. Aranzaes, M.-C. Daniel, D. Astruc. Metallocenes as references for the determination of redox potentials by cyclic voltammetry—Permethyated iron and cobalt sandwich complexes, inhibition by polyamine dendrimers, and the role of hydroxy-containing ferrocenes. *Can. J. Chem.*, **2013**, 84: 288-299.
- 194 A. Hagfeldt, M. Grätzel. Light-Induced Redox Reactions in Nanocrystalline Systems. *Chem. Rev.*, **1995**, 95, 1: 49-68.
- 195 S. Ito, T. N. Murakami, P. Comte, P. Liska, Carole Grätzel, M. K. Nazeeruddin, M. Grätzel. Fabrication of thin film dye sensitized solar cells with solar to electric power conversion efficiency over 10%. *Thin Solid Films*, **2008**, 516:4613–4619.
- 196 M. Matsui, N. Tanaka, Y. Kubota, K. Funabiki, J. Jin, S. Higashijima, H. Miura, K. Manseki. Long-term stability of novel double rhodanine indoline dyes having one and two anchor carboxyl group(s) in dye-sensitized solar cells. *RSC Adv.*, **2016**, 6: 33111-33119.
- 197 A. Peddapuram, H. Cheema, R. E. Adams, R. H. Schmehl, J. H. Delcamp. A Stable Panchromatic Green Dual Acceptor, Dual Donor Organic Dye for Dye-Sensitized Solar Cells. *J. Phys. Chem. C*, **2017**, 121, 16: 8770-8780.
- 198 M. Godfroy, Cyril Aumaitre, F. Caffy, Y. Kervella, L. Cabau, L. Pellejà, P. Maldivi, S. Narbey, F. Oswald, E. Palomares, D. Joly, R. Demadrille. Dithienylpyrazine-based photosensitizers: Effect of swapping a connecting unit on optoelectronic properties and photovoltaic performances. *Dyes and Pigments*, **2017**, 146: 352-360.
- 199 Z. Shen, J. Chen, X. Li, X. Li, Y. Zhou, Y. Yu, H. Ding, J. Li, L. Zhu, J. Hua. Synthesis and Photovoltaic Properties of Powerful Electron-Donating Indeno [1, 2-b] thiophene-Based Green D-A- π -A Sensitizers for Dye-Sensitized Solar Cells. *ACS Sustainable Chem. Eng.*, **2016**, 4, 6: 3518-3525.
- 200 V. Gaidelis, E. Kamarauskas, T. Malinauskas, V. Getautis, R. Send, H. Wonneberger, I. Bruder. Relationship between measurement conditions and energy levels in the organic dyes used in dye-sensitized solar cells. *RSC Adv.*, **2015**, 5: 82859-82864.
- 201 S. Lyu, C. Bertrand, T. Hamamura, L. Ducasse, T. Toupance, C. Olivier. Molecular engineering of Ruthenium-diacetylide organometallic complexes towards efficient green dye for DSSC. *Dye and Pigments*, **2018**, 158: 326-333.

**Chapter III:
Ruthenium-Diacetylide Organometallic
Complexes for p-Type Dye Sensitizers**

III.1. General Introduction

As discussed in Chapter I, the p-DSC technology is similar by many aspects to its elder sister, the n-DSCs, but as the semiconductor is a hole transporting material the operation principle is the reverse of that occurring in classical DSCs, the photoactive electrode being the cathode. Photoexcitation of the dye promotes an electron from the HOMO level (ground-state) to the LUMO level (excited-state), thus prompting hole-carrier generation into the semiconductor valence band. The reduced sensitizer is afterwards regenerated by a redox mediator contained in the electrolyte (usually the iodine/iodide couple) and the reduced mediator is oxidized back at the counter-electrode.¹⁻⁴ Therefore, the choice of sensitizer is key to maximizing the power output of DSC devices. Ideally, with the view to develop tandem solar cells, the p-type sensitizers employed on the photocathode should absorb light in the red region of the visible spectrum, which will minimize spectral overlap with the higher energy absorbing dyes on the TiO₂ photoanode. Particularly, high molar extinction coefficients are prerequisite in p-DSCs because it is difficult to prepare thick NiO films as compared with those of TiO₂. Determined by the necessary stability of the device over a long period of time, the sensitizer should be also photochemically and electrochemically stable. More important, the reduced form of the sensitizer should remain inert toward electrophilic substances. Furthermore, high hole injection quantum yield is important for p-type dyes imposing that the reduction potential of the excited state of the sensitizer lies above the valence band edge of the semiconductor while the dye regeneration with the mediator should be thermodynamically allowed imposing that the reduction potential of the sensitizer is more negative than that of the mediator. Also, the sensitizers should be functionalized with anchoring groups in order to both graft the dyes on the semiconductor surface and provide a strong electronic coupling with the semiconductor.^{3,5,6} Up to now the performance of the p-DSC technology is still far behind that of the TiO₂ champion cells, with maximum efficiency limited to 2.51%.⁷ However, many opportunities for improvement remain because so far only little attention has been given to this technology. In this context, Ru-based diacetylide complexes again represent serious candidates for the sensitization of NiO due to their excellent optical properties and a good matching of the energy levels. Molecular engineering should undoubtedly provide new examples of organometallic chromophores suitable for the p-DSC technology.

For now, several classes of dyes were designed for p-DSCs, including push-pull organic sensitizers,⁸⁻¹⁰ perylene imides,^{7,11-13} diketopyrrolopyrroles,¹⁴ squaraines,^{15,16} 4,4-difluoro-4-bora-3a,4a-diaza-s-indacenes (BODIPYs),^{17,18} porphyrins,¹⁹⁻²¹ ruthenium²²⁻²⁵, iridium²⁶ and rhenium²⁷ coordination complexes. In this chapter, some representative p-type sensitizers are

introduced in section III.2.. Our work for the design and synthesis of novel donor- π -acceptor dyes based on organometallic ruthenium diacetylide complexes are introduced in sections III.3., III.4. and III.5. The optical and electrochemical properties, theoretical calculations as well as photovoltaic properties based on these novel dyes are also investigated and discussed.

III.2. p-Type Dye Sensitizers

As referred in Chapter II, porphyrins and their analogues are good candidates for photovoltaic applications due to their excellent photo-, electrochemical and thermal stability.²⁸⁻³² Porphyrinoids have unique absorption and photoredox properties which endow them an important role in photosynthesis.³²⁻³⁴ Some representative porphyrins used as sensitizers in NiO based p-DSCs are shown in Figure III-1.

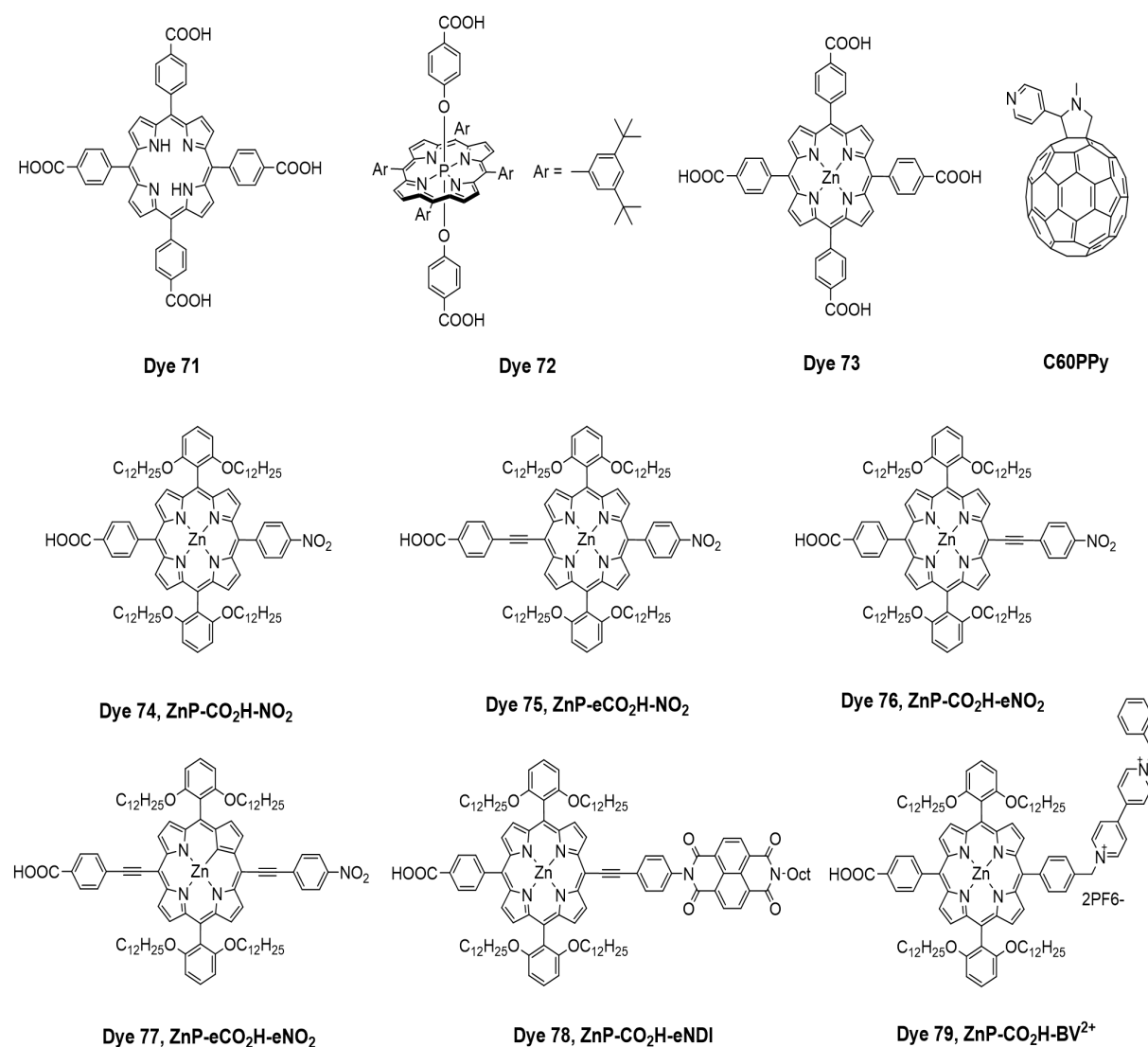


Figure III-1: Some representative porphyrins used as sensitizers in NiO based p-DSCs.

In 1999, J. He *et al.* for the first time reported a porphyrin moiety used as sensitizer and applied in a NiO based DSC.³⁵ In this study, tetrakis(4-carboxyphenyl)porphyrin (TPPC) (see Figure III-1, dye 71) as a p-type sensitizer was designed and synthesized, and subsequently adsorbed onto the nanostructured NiO film. When employed in a sandwich solar cell device with a platinized counter electrode and exposed to light from a sun simulator (light intensity: $68 \text{ mW}\cdot\text{cm}^{-2}$), the TPPC led to a short-circuit cathodic photocurrent density (J_{sc}) of $0.079 \text{ mA}\cdot\text{cm}^{-2}$, an open-circuit voltage (V_{oc}) of 98.5 mV and a very low power conversion efficiency of 0.01% . Few years later, M. Borgström *et al.* reported their work to prepare and characterize a DSC device based on the sensitization of the wide band gap p-type semiconductor NiO with a phosphorus porphyrin (see Figure III-1, dye 72).¹⁹ Although the IPCE at λ_{max} based on the dye 72 was rather low, this work was the first example of a photovoltaic cell in which a mechanism of hole photoinjection has been evidenced. A photophysical study with femtosecond transient absorption spectroscopy indicated that the light excitation of the dye 72 adsorbed on the nanocrystalline NiO electrode induced a very rapid interfacial hole injection into the valence band of NiO, occurring mainly on the 2-20 ps time scale. The low overall power conversion efficiency was attributed to the fast recombination reaction between the reduced dye 72 and the injected hole. In 2014, H. Tian *et al.* successfully adopted the supramolecular interactions based on porphyrin and fullerene derivatives to improve the photovoltaic performance of p-DSCs.²⁰ Through photoelectron spectroscopy measurements, they found that a change in binding configuration of ZnTCPP (see Figure III-1, dye 73) after co-sensitization with C60PPy (see Figure III-1, C60PPy) , which can be attributed to supramolecular interaction between ZnTCPP and C60PPy. This was the first example in which a supramolecular assembly between an electron donor ZnTCPP (dye 73) and an electron acceptor fullerene C60 (C60PPy) was employed in p-DSCs. With $\text{Co}^{2+/\beta^+}(\text{dtbp})_3$ as the electrolyte, the ZnTCPP/C60PPy-based DSC devices showed a highest efficiency of 0.13% and a highest V_{oc} of 260 mV . Several push-pull zinc porphyrin derivatives were prepared and investigated as sensitizers for NiO-based p-type DSCs by A. Maufroy *et al.* in 2015.²¹ The first series of these zinc porphyrin derivatives consisted of trans disubstituted push-pull porphyrins containing a nitrophenyl unit as an electron withdrawing group and a benzoic acid unit as an anchoring group, incorporating or not an ethynyl spacer between the trans meso aryl groups and the porphyrin core (see Figure III-1, dyes 74 to 77). The second series employed a naphthalene diimide or benzyl-viologen appended to the porphyrin as an electron acceptor (see Figure III-1, dyes 78 to 79). Despite the favorable charge transfer characteristics along with the large energy changes of the injection and

regeneration reactions, the first series of these push-pull zinc porphyrins showed a comparatively low photocurrent density in p-DSC devices. The fast charge recombination of these dyes owing to the partial delocalization of the electron density close to the surface finally resulted in the modest short-circuit current densities. For the second series, the photovoltaic performances were significantly enhanced through the introduction of a secondary electron acceptor next to the porphyrin which can be attributed to the shifted electron from the ZnP to the secondary acceptor slowing down the charge recombination. The dye 78 (ZnP-CO₂H-eNDI) exhibited a PCE of 0.056% ($J_{sc} = 1.38 \text{ mA}\cdot\text{cm}^{-2}$, $V_{oc} = 127 \text{ mV}$, $FF = 0.32$) with the I⁻/I₃⁻ electrolyte under stimulated AM1.5G solar light, $100 \text{ mW}\cdot\text{cm}^{-2}$ irradiation.

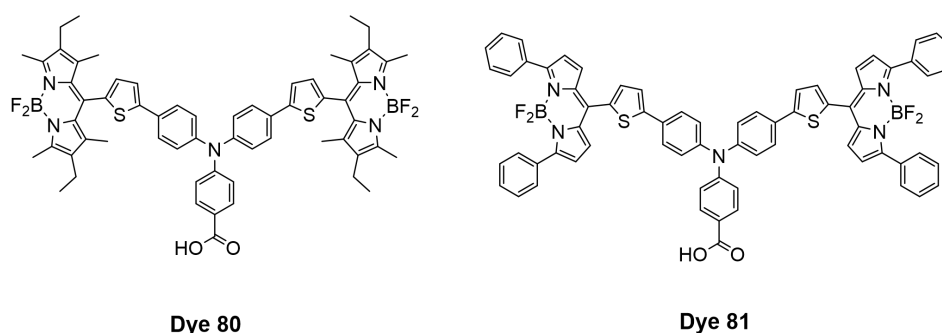


Figure III-2: Two representative structures of BODIPY dyes used as sensitizers in NiO based p-DSCs.

BODIPY sensitizers display relatively long fluorescence emission lifetimes, great photo-stability with a narrow but intense absorption band ($\sim 500 \text{ nm}$) and large fluorescence quantum yields.³⁶⁻³⁸ Therefore, a great number of BODIPY sensitizers have been designed and prepared for photovoltaic performances. Two representative structures of BODIPY dyes used as sensitizers in NiO based p-DSCs are shown in Figure III-2. In 2014, J.-F. Lefebvre *et al.* reported the first BODIPY sensitizer for promoting a long and efficient charge-separated state in p-DSCs (see Figure III-2, dye 80).¹⁷ The dye 80 consisted of a triphenylamine-thiophene motif coupled to two BODIPY moieties which was functionalized with a carboxylic acid unit as the anchoring group. The NiO-based DSC devices sensitized by the dye 80 with the I₃⁻/I⁻ as redox shuttle showed an efficiency of 0.08% ($J_{sc} = 3.15 \text{ mA}\cdot\text{cm}^{-2}$, $V_{oc} = 79 \text{ mV}$, $FF = 0.31$) and a maximum IPCE of 28% at λ_{max} . C. J. Wood *et al.* also reported an organic push-pull sensitizer with two BODIPY chromophores (see Figure III-2, dye 81).¹⁸ The dye 81 absorbed strongly in a wide range of the visible spectrum. More important, the dye 81 was investigated to be suitable for withdrawing electrons from the NiO surface based on the estimated driving forces for the charge separation process. The p-DSC devices based on the dye 81 showed an

IPCE of 53% at λ_{\max} and a PCE of 0.20% ($J_{\text{sc}} = 5.87 \text{ mA}\cdot\text{cm}^{-2}$, $V_{\text{oc}} = 106 \text{ mV}$, $\text{FF} = 0.31$).

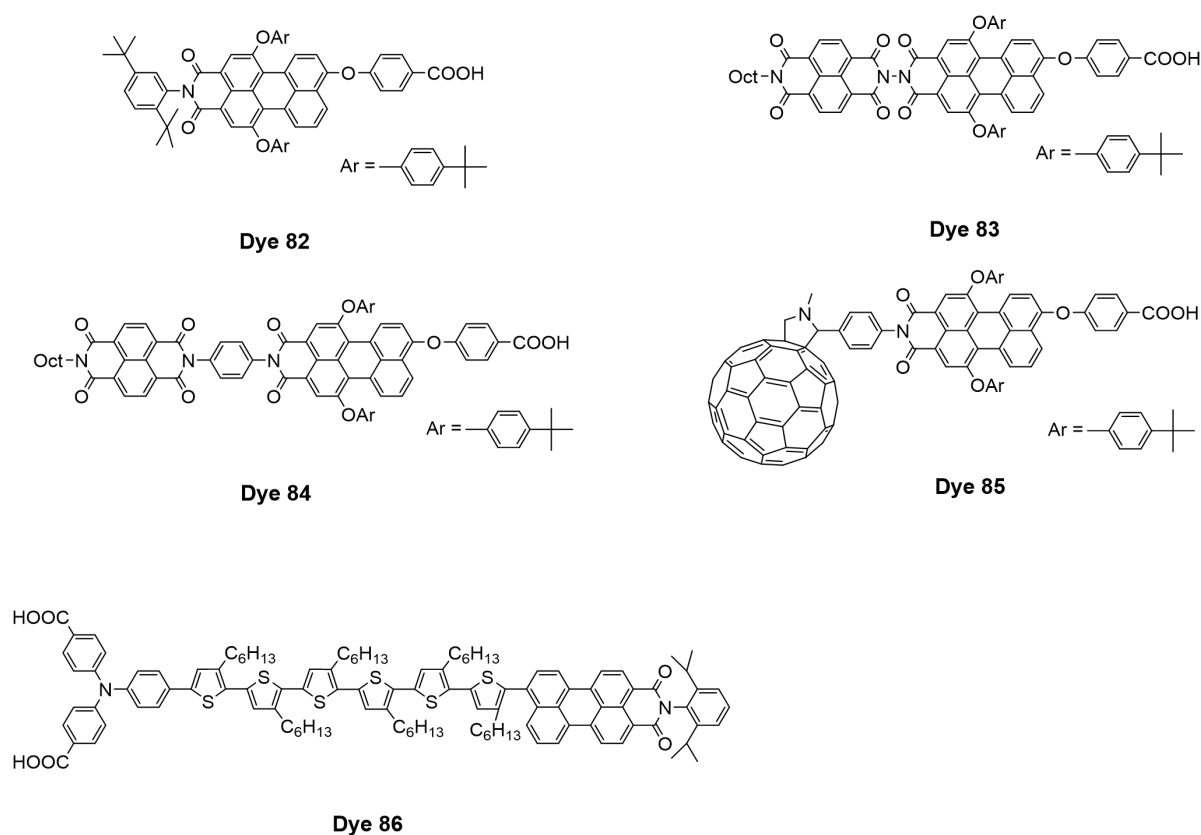


Figure III-3: Several representative perylene imide sensitizers used in p-DSCs.

Perylene imides are ideal class of high-performing dyes which exhibit excellent thermal- and photo-stability.³⁹ The perylene imide sensitizers contain imide moieties as the electron withdrawing group which makes them easily reduced either chemically or electrochemically in order to form stable radicals.^{40,41} Furthermore, the perylene imide sensitizers possess some other characteristics such as easy modification, broad absorption in the visible region and relatively high fluorescence quantum yields. Therefore, perylene imides are good candidates for p-type sensitizers and have been studied widely in last few years.^{1,40-42} Several representative perylene imide sensitizers used in p-DSCs are shown in Figure III-3. A. Morandeira *et al.* for the first time reported a perylene-imide sensitizer (PMI) and a covalently linked perylene imide-naphthalene diimide dyad (PMI-NDI) (see Figure III-3, dye 82 and dye 83).¹² For both dyes upon light excitation of the perylene imide unit, an electron shift from the valence band of NiO to the dye with an average time constant of approximately 0.5 ps was investigated. In the case of the dye 83, the excess electron was shifted further onto the naphthalene-diimide unit, producing a new charge separated state. The dye 83 displayed a substantial retardation of the charge recombination between the hole and the reduced

molecule in comparison with the dye 82. The sandwich NiO-based DSC devices sensitized by the dye 83 showed an absorbed-photon to current conversion efficiency (APCE) of 45%, which was three times higher than those sensitized by the dye 82. Based on this work, L. L. Pleux *et al.* designed and prepared two novel perylene imide sensitizers comprising a PMI moiety connected to a secondary electron accepting unit (naphthalene diimide (NDI) or fullerene (C60), see Figure III-3, dyes 84 and 85) for application in NiO-based p-DSCs.¹³ Either dye 84 or dye 85 exhibited a longer lifetime of the charge separated state by about five orders of magnitude compared to the dye 82 which can be attributed to the presence of the secondary electron acceptor group. The p-DSC devices sensitized by the dye 85 showed the highest IPCE of 57% at λ_{\max} and the J_{sc} of $1.88 \text{ mA}\cdot\text{cm}^{-2}$ with the iodide electrolyte, which were ascribed to the slightly stronger reducing power of C60 relative to NDI, resulting in more efficient reduction of the mediator in the electrolyte. In 2015, I. R. Perera *et al.* developed an electrolyte based on the tris(acetylacetonato) -iron(III)/(II) redox couple ($[\text{Fe}(\text{acac})_3]^{0/1-}$) for p-DSCs.⁷ When applied $[\text{Fe}(\text{acac})_3]^{0/1-}$ as redox mediator in p-type DSSCs in conjunction with the former reported PMI-6T-TPA sensitizer⁹ (see Figure III-3, dye 86) and incorporating a NiO blocking layer and chenodeoxycholic acid as an electrolyte additive, a world record PCE of $2.51 \pm 0.08\%$ ($J_{\text{sc}} = 7.65 \pm 0.39 \text{ mA}\cdot\text{cm}^{-2}$, $V_{\text{oc}} = 645 \pm 12 \text{ mV}$, $\text{FF} = 0.51 \pm 0.01$) was achieved.

Some sensitizers discussed above are based on the prototypical push-pull design. As referred in Chapter II, the prototypical push-pull design notoriously affords efficient charge transfer from the ground-state to the excited-state of the dye, thus enhancing its absorption properties. This design also allows reduction of the electronic recombination processes in the device. Such structure has been applied to numerous examples of organic dyes featuring various donor and acceptor parts (see Chapter II, ref. 12 and 14). Therefore, molecular engineering of push-pull organic dyes for p-DSCs can be a meaningful area of research. Several representative push-pull organic sensitizers used in p-DSCs are shown in Figure III-4.

In 2008, P. Qin *et al.* designed and prepared a novel push-pull organic dye which employed the triphenylamine moiety as the electron donor, malononitrile moiety as the electron acceptor, and a thiophene unit as the conjugated chain (see Figure III-4, dye 87).¹⁰ Through the introduction of two electron acceptor groups and the anchoring group on the donor moiety, light excitation and electron flow from the donor part to the acceptor part provided an efficient electron transfer pathway from the dye to the electrolyte. The p-type DSC devices based on the dye 87 showed an APCE of 30%, an IPCE of 18% at λ_{\max} and a PCE of 0.05% ($J_{\text{sc}} = 1.52 \text{ mA}\cdot\text{cm}^{-2}$, $V_{\text{oc}} = 110 \text{ mV}$, $\text{FF} = 0.31$) at $100 \text{ mW}\cdot\text{cm}^{-2}$ under AM 1.5

irradiation.

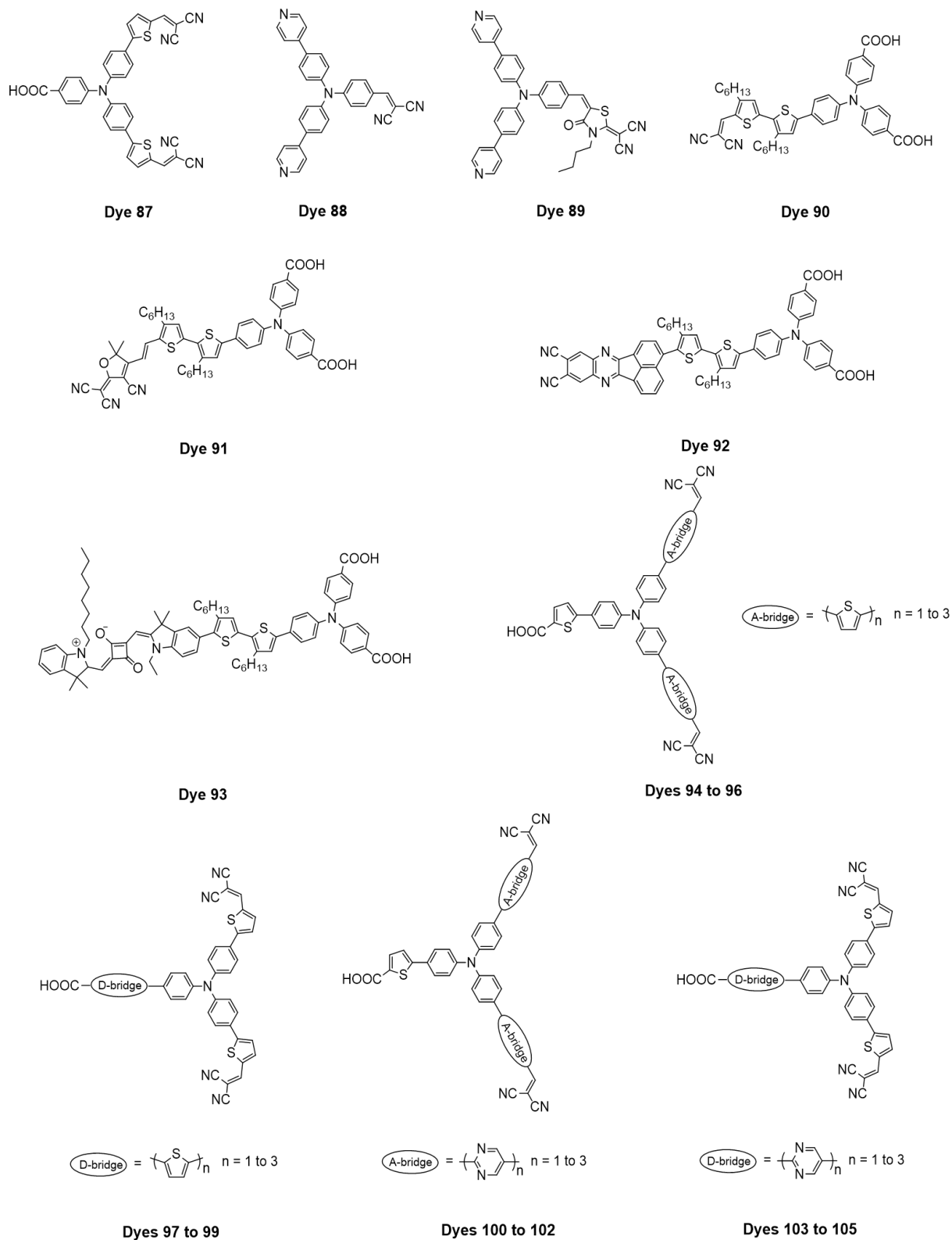
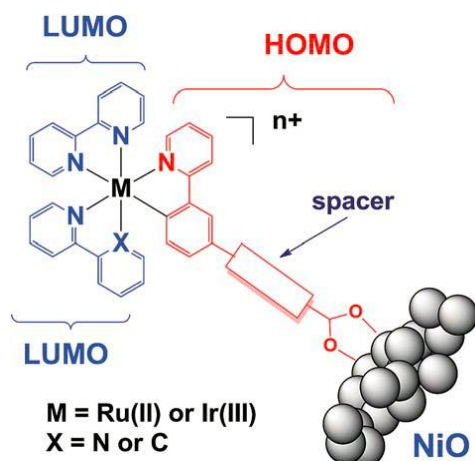


Figure III-4: Several representative push-pull organic sensitizers used in p-DSCs.

Few years later, after optimization of the NiO films (*i.e.* double layered photocathodes prepared in two steps) p-DSCs based on the same dye 87 afforded higher photocurrent density ($J_{sc} = 5.48 \text{ mA}\cdot\text{cm}^{-2}$), higher APCE and IPCE maxima (69% and 64%, respectively) and therefore a better PCE of 0.15%.⁴³ In 2013, B. Jin *et al.* first reported two examples of organic push-pull dyes based on pyridine-anchoring groups for p-DSCs (see Figure III-4, dyes 88 and 89).⁴⁴ The two dyes employed a triphenylamine moiety functionalized with pyridine groups as their electron donating groups. The dye 88 employed a malononitrile moiety as the electron accepting group while the dye 89 employed a 2-(3-butyl-4-oxothiazolidin-2-ylidene) malononitrile (BOMN) as its electron accepting group. Because of the presence of BOMN, the dye 89 was more conjugated and therefore exhibited a bathochromic shift and a larger extinction coefficient in comparison with the dye 88. The p-type DSC devices sensitized by the dye 89 showed a highest PCE of 0.14% ($J_{sc} = 2.97 \text{ mA}\cdot\text{cm}^{-2}$, $V_{oc} = 130 \text{ mV}$, $FF = 0.35$) at $100 \text{ mW}\cdot\text{cm}^{-2}$ under AM 1.5 irradiation. In 2014, M. Weidelenner *et al.* reported four novel D- π -A dyes differing in their acceptor group to study the influence of the latter on the photophysical and photovoltaic properties in NiO-based p-DSCs (see Figure III-4, dye 90 to 93).⁸ The four dyes employed a triphenylamine donating unit and a dihexylbithiophen π -bridge. The p-DSC devices sensitized by the dye 92 with an iodide-based electrolyte exhibited the highest PCE of 0.08% ($J_{sc} = 1.66 \text{ mA}\cdot\text{cm}^{-2}$, $V_{oc} = 163 \text{ mV}$, $FF = 0.28$), which can be attributed to significantly slower charge recombination process in the p-DSCs sensitized by the dye 92, due to the torsion angle between the acceptor and the donor. Although employing the strong electron-accepting tricyanofurane group, the dye 91 based p-DSCs showed a lower efficiency of only 0.01% which can be attributed to a low-lying LUMO energy level, thus resulting in an insufficient driving force for efficient dye regeneration.



Scheme III-1: Schematic representation of Ru or Ir polypyridine complexes for p-DSCs.¹

Transition metal complexes such as ruthenium and iridium polypyridine, exhibiting metal-to-ligand charge-transfer transition (MLCT), have been widely investigated as photosensitizers in n-DSCs and several good examples such as N3, Z910, CYC-B6S, CYC-B6L and others have been introduced in Chapter II. Actually, some typical ruthenium complexes such as N3 could also be employed as p-type sensitizers because their MLCT excited states are both reductants and oxidants.^{1,45} For most of the polypyridine transition metal complexes, the HOMO is positioned on the anchoring group while the LUMO is positioned on the ancillary ligands, decreasing the charge recombination by alienating the electron away from the NiO surface. Scheme III-1 represents the best performing structure of Ru or Ir polypyridine complexes for p-DSCs.¹

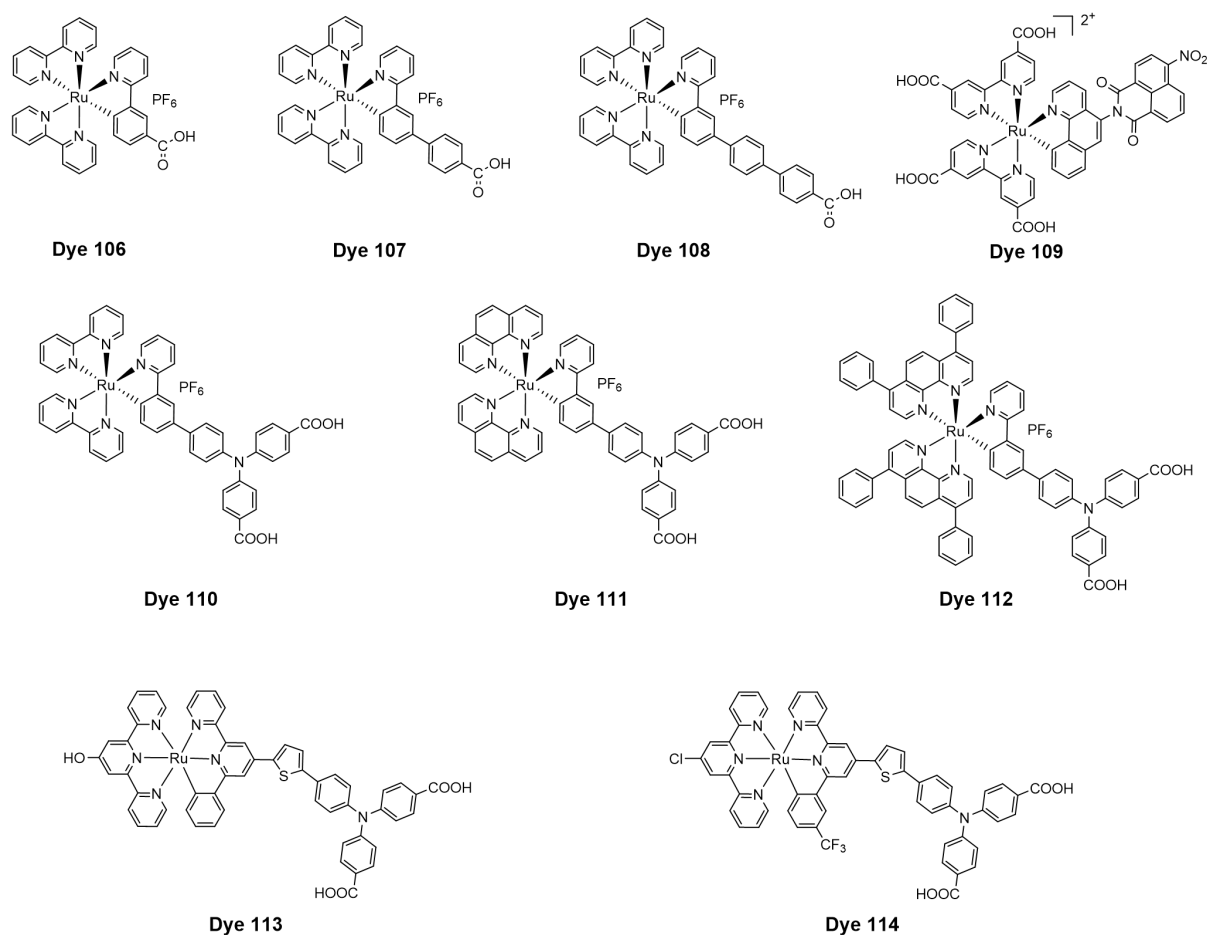


Figure III-5: Several representative ruthenium coordination complexes developed for p-DSCs.

Several other representative ruthenium coordination complexes developed for p-DSCs are shown in Figure III-5. In 2012, Z. Ji *et al.* reported the first application of cyclometalated ruthenium complexes of the type $\text{Ru}[(\text{N}^{\wedge}\text{N})_2(\text{C}^{\wedge}\text{N})]^+$ as sensitizers for p-type NiO based

DSCs (see Figure III-5, dyes 106 to 108).²² These dyes proved to be suitable for p-type sensitizers, which can be attributed to the fact that the carboxylic anchoring group attached to the phenylpyridine ligand resulted in efficient hole injection. Femtosecond transient absorption measurements and electrochemical impedance spectroscopy indicated that increasing the number of phenylene linkers resulted in enhanced hole lifetime and decreased interfacial charge recombination rate between the reduced sensitizers and the holes in the valence band of NiO. As a consequence, the NiO based p-DSC devices sensitized by the dye 108 showed a highest PCE of 0.051% ($J_{sc} = 1.84 \text{ mA}\cdot\text{cm}^{-2}$, $V_{oc} = 82 \text{ mV}$, $FF = 0.34$). J. C. Freys *et al.* also reported a donor-acceptor ruthenium polypyridyl complex bearing phenanthroline-nitronaphthalene-dicarboximide (NMI) as the ancillary ligand for p-DSCs (see Figure III-5, dye 109).²³ The presence of the electron-accepting group, NMI, which was attached to the phenanthroline of $[\text{Ru}(\text{dcb})_2(\text{NMI-phen})]^{2+}$ species resulted in long-lived charge separation between the reduced $[\text{Ru}(\text{dcb})_2(\text{NMI-phen})]^{2+}$ and the holes in NiO valence band. The NiO based DSC devices sensitized by the dye 109 showed a PCE of 0.006% ($J_{sc} = 0.16 \text{ mA}\cdot\text{cm}^{-2}$, $V_{oc} = 95 \text{ mV}$, $FF = 0.36$) with the iodine based electrolyte and a PCE of 0.020% ($J_{sc} = 0.28 \text{ mA}\cdot\text{cm}^{-2}$, $V_{oc} = 195 \text{ mV}$, $FF = 0.34$) with $\text{Co}^{\text{III/II}}(\text{dtb})_3$ electrolyte under standard AM 1.5 sunlight, $100 \text{ mW}\cdot\text{cm}^{-2}$ irradiation. In 2013, Z. Ji *et al.* reported a series of cyclometalated ruthenium sensitizers bearing triphenylamino linkers for NiO based p-DSCs (see Figure III-5, dyes 110 to 112).²⁴ The general structures of the dyes 110 to 112 consisted of $\text{Ru}[\text{N}^{\wedge}\text{N}]_2[\text{N}^{\wedge}\text{C}]$, where $[\text{N}^{\wedge}\text{N}]$ was a diimine ligand and $[\text{N}^{\wedge}\text{C}]$ was a cyclometalated ligand. The triphenylamino group was employed as a linker to bridge the ruthenium chromophore and the NiO surface in order to enhance the electronic coupling for hole injection. For the three dyes, the increasing conjugation of the $[\text{N}^{\wedge}\text{N}]$ ligands resulted in the enhancement of the extinction coefficient and the red shift of light absorption. However, the NiO based p-DSC devices sensitized by the dye 110 unexpectedly exhibited the highest PCE of 0.099% with the largest J_{sc} of $3.04 \text{ mA}\cdot\text{cm}^{-2}$ ($V_{oc} = 93 \text{ mV}$, $FF = 0.35$). Intensity-modulated photovoltage and photocurrent spectroscopies showed that the largest J_{sc} value afforded by the dye 110 was caused by slower geminate charge recombination and more efficient dye regeneration. In 2014, C. J. Wood *et al.* developed a pair of ruthenium based donor- π -chromophore sensitizers for p-DSCs (see Figure III-5, dyes 113 and 114).²⁵ Both dyes exhibited high extinction coefficients because the special ligand system dominated the optoelectronic properties of the two dyes. The p-DSCs using dye 113 sensitized nanocrystalline NiO as working electrode and an iodine-based electrolyte showed a better efficiency of 0.09% ($J_{sc} = 2.91 \text{ mA}\cdot\text{cm}^{-2}$, $V_{oc} = 96 \text{ mV}$, $FF = 0.32$) and a higher IPCE of 14% at λ_{max} compared to those using the dye 114.

However, with the cobalt electrolyte, both dyes exhibited lower efficiencies which can be ascribed to the fast rate of charge recombination reaction between the reduced dye and the holes in the NiO.

III.3. Push-Pull Ruthenium Diacetylide Complexes Including Triphenylamine Donor Moieties as New Dyes for p-Type Dye-Sensitized Solar Cells

As mentioned above, ruthenium polypyridine complexes are the archetypal dyes for solar energy conversion as they have been abundantly used for water splitting,^{46,47} and as sensitizers in conventional n-DSCs^{48,49} and more recently in p-DSCs.²²⁻²⁴ However, ruthenium organometallic dyes are less investigated for the latter purposes. We showed before that Ru-diacetylide complexes are valuable visible-light sensitizers and that they can exhibit high photoconversion efficiencies (PCEs) in conventional n-DSCs.^{50,51,52} Ruthenium diacetylide complexes are neutral molecules, they display easily tunable electronic properties and their rod-like structure enables to prepare push-pull systems. All these properties make them attractive candidates for p-DSCs, because neutral dyes can reach much higher packing density on the semiconductor than charged dyes and a strong push-pull character enhances the charge transfer band which is also favorable for charge injection.⁵³

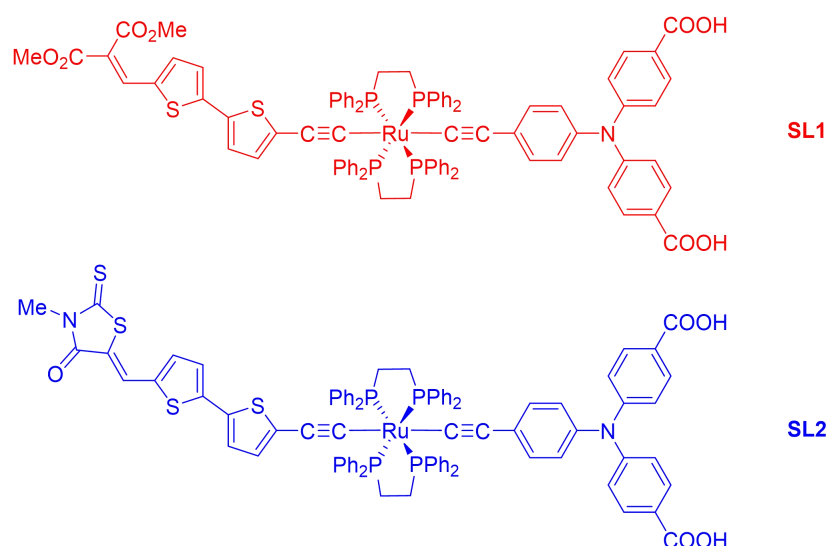


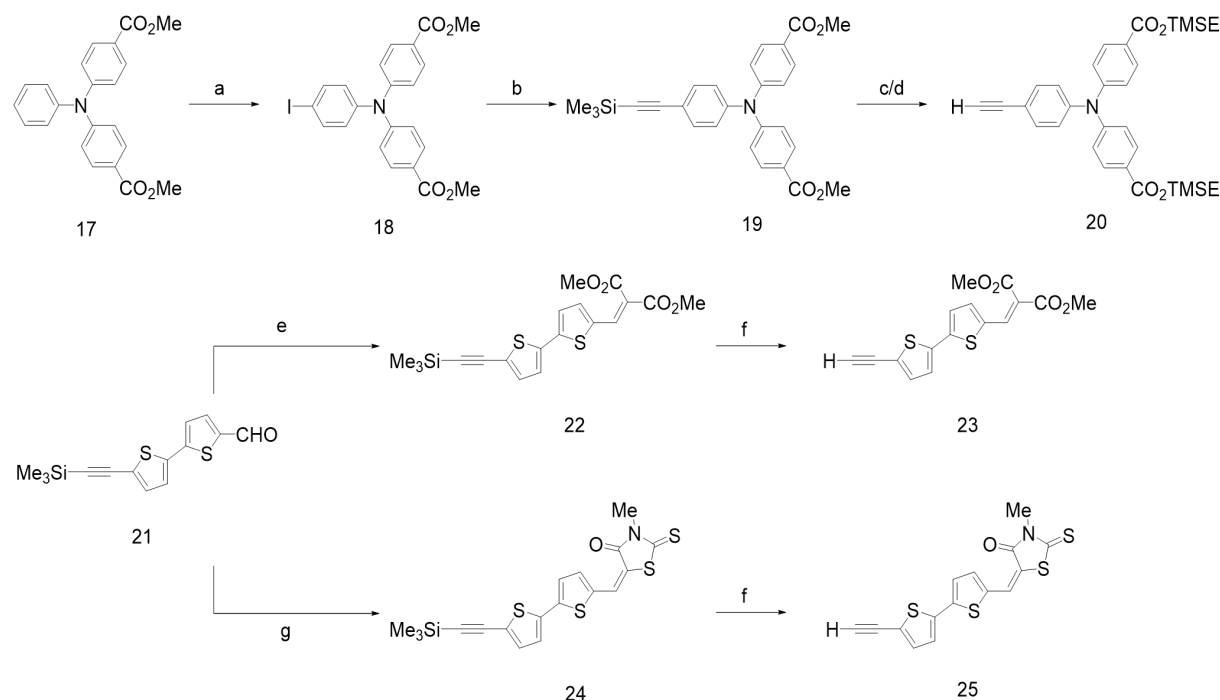
Figure III-6: Molecular structures of the push-pull organometallic dyes SL1 and SL2.

Therefore we designed and prepared the first examples of organometallic dyes based on the [Ru(dppe)₂] moiety for p-type DSCs. The molecular structure of the new photosensitizers

is depicted in Figure III-6. The bis(σ -arylacetylide) complexes **SL1** and **SL2** are endowed with a bidentate anchoring group based on a triphenylamine (TPA) as electron-donating unit and are functionalized with an electron-withdrawing group, both separated by a bithiophene linker. Dimethylmalonate and rhodanine units were investigated as acceptor moieties since this kind of electron-withdrawing groups were used with success to design dyes for solar cells (see Chapter II).

III.3.1. Synthesis of the Dyes **SL1** and **SL2**

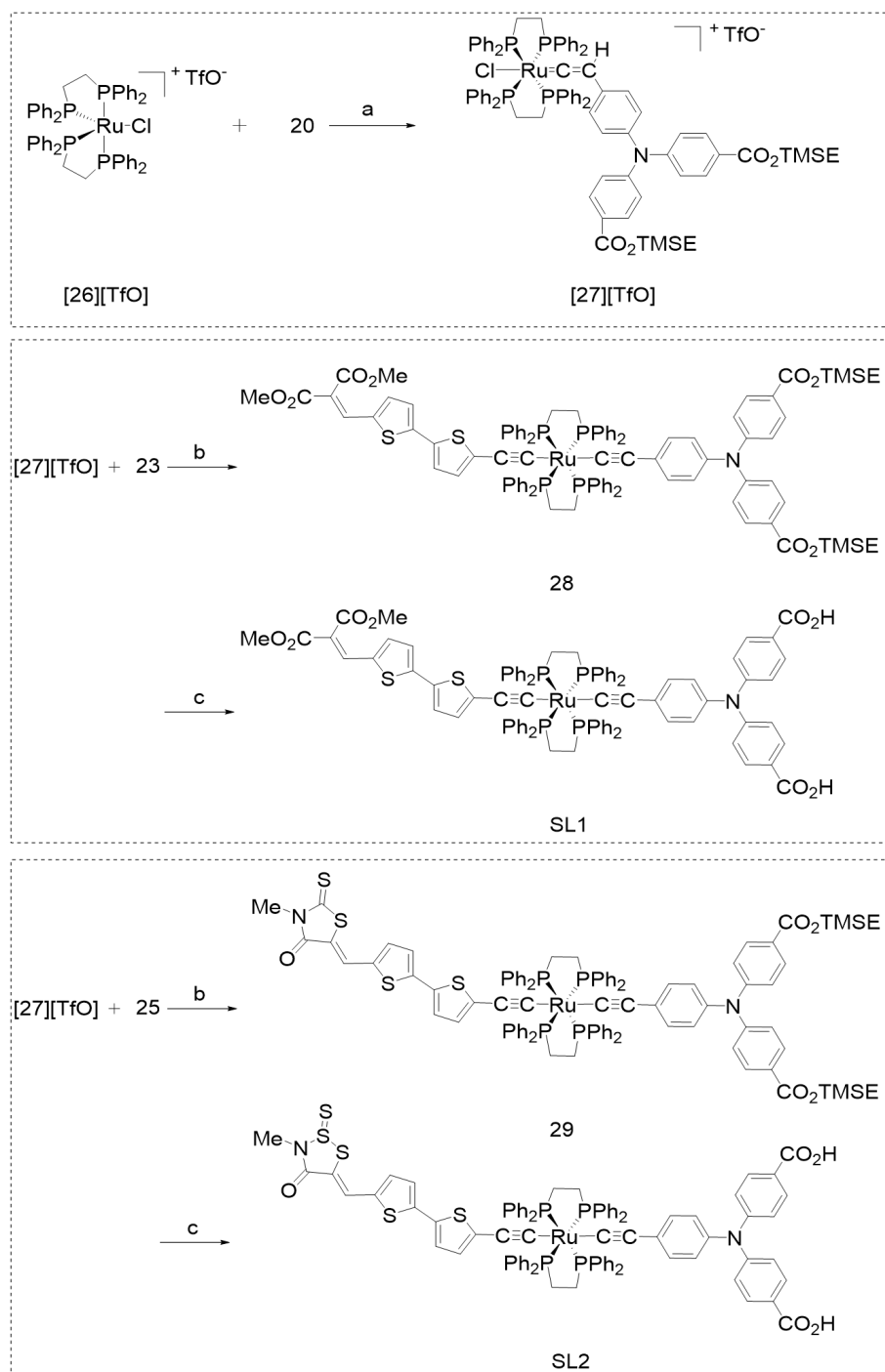
Following already established procedures, the preparation of ruthenium diacetylide complexes consists of successive activation of terminal alkynes by an electron-deficient metal center, typically $[\text{RuCl}(\text{dppe})_2][\text{TfO}]$.⁵⁴ First, the three alkyne ligands **20**, **23** and **25** were prepared following synthetic routes shown on Scheme III-2. Synthesis of the TPA-based electron-rich ligand **20** involved Sonogashira coupling reaction of the iodo-TPA derivative **18** with trimethylsilylacetylene and subsequent deprotection of the terminal alkyne. To avoid side reactions of the carboxylic acid anchoring groups with the metal center during ensuing syntheses, protection of the two COOH functions was necessary.



Scheme III-2: Synthesis of the alkyne ligands **23** and **25**. Reaction conditions: (a) ICl , $\text{Zn}(\text{OAc})_2$, dioxane; (b) trimethylsilylacetylene, $\text{PdCl}_2(\text{PPh}_3)_2$, CuI , DIPEA, THF; (c) LiOH , THF/ H_2O ; (d) trimethylsilylethanol, HBTU, DIPEA, DMF; (e) dimethyl malonate, piperidine, CHCl_3 ; (f) K_2CO_3 ,

MeOH; (g) 3-methylrodhanine, ammonium acetate, acetic acid.

A silyl-ester protecting group, *i.e.* 2-(trimethylsilyl) ethyl (TMSE), was preferably chosen rather than methyl or tertbutyl ester group as the former can be removed under mild conditions. On the other hand, synthesis of the electronwithdrawing σ -alkynyl ligands **23** and **25** was achieved through condensation of the carbaldehyde **21** with dimethyl malonate or 3-methylrodhanine, respectively.



Scheme III-3: Synthesis of the organometallic complexes **SL1** and **SL2**. Reaction conditions: (a)

CH₂Cl₂; (b) NaPF₆, Et₃N, CH₂Cl₂; (c) tetrabutylammonium fluoride, THF.

The synthetic steps to the target organometallic dyes are represented in Scheme III-3. The donor part of the dyes was first obtained by activation of the TPA-based ligand **20** by the 16-electron species [26][TfO], leading to the stable ruthenium-vinylidene intermediate [27][TfO]. Subsequent introduction of the second carbon-rich chain on the [Ru(dppe)₂] metal centre to form bis-σ-arylacetylide complexes was achieved by reacting [27][TfO] with the alkynyl ligands **23** or **25**, in the presence of a base (Et₃N) and of a non-coordinating salt (NaPF₆). Finally, the target dyes **SL1** and **SL2** were obtained in good yields after removal of the silyl-ester protecting groups, using tetrabutylammonium fluoride in THF at room temperature.

All the organometallic complexes were characterized by means of ³¹P, ¹H and ¹³C NMR, HR-MS and FTIR. The full data set is in accordance with the expected structure of the organometallic dyes. The *trans*-ditopic geometry of the ruthenium center in **SL1** and **SL2** was evidenced by ³¹P NMR as the spectra show a singlet for the four equivalent phosphorus atoms, with $\delta \approx 53$ ppm characteristic of the ruthenium-diacetylide structure.⁵⁴ In addition, an intense band was observed on the FT-IR spectra of **SL1** and **SL2** at ca. 2038 cm⁻¹ corresponding to the $\nu_{C=C}$ stretch of the σ-diacetylide metal fragment.

III.3.2. Optical and Electrochemical Properties

UV-visible absorption spectra of **SL1** and **SL2**, recorded in dichloromethane solution, are shown in Figure III-7 and the corresponding values are listed in Table III-1. The intense short wavelength absorption band observed in the UV region is characteristic of n→π* and π→π* transitions from the dppe ligands.⁵⁵ The less intense band centred around $\lambda = 360$ nm can be tentatively ascribed to electronic transitions involving the triphenylamine electron donor and the origin of this band is discussed below. However the most interesting feature of these dyes is the broad absorption band observed in the visible part of the spectrum. This intense absorption band corresponds to multiple MLCT processes, mainly stemming from the metal-centred HOMO to the LUMO located on the electron-withdrawing alkynyl ligand (see DFT calculations below). The maximum absorption wavelength, λ_{max} , of **SL1** in the visible is centred at 521 nm, making **SL1** a red pigment. Elongation of the π-conjugated system through the rhodanine acceptor group in **SL2** led to red shifted absorption band. The spectrum of **SL2** shows $\lambda_{max} = 603$ nm, hence affording blue-coloured dye-bath solution. Both dyes present a rather high molecular extinction coefficient (ϵ) of about 20 000 M⁻¹·cm⁻¹ at λ_{max} . Overall, the

good absorption properties of this couple of organometallic complexes make them good candidates for use as photosensitizers in DSCs.

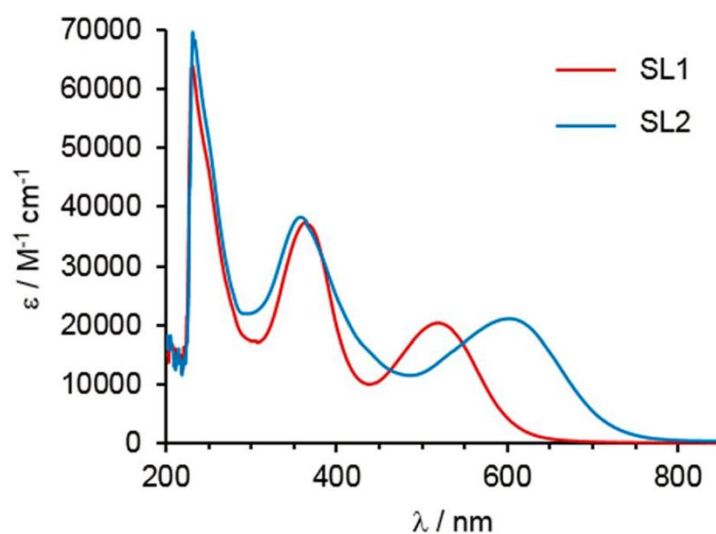


Figure III-7: Absorption spectra of **SL1** and **SL2** in CH_2Cl_2 ($C \approx 3 \times 10^{-5}$ M).

Table III-1: Optical and electrochemical properties

Dye	$\lambda_{\text{max}}^{\text{a}}$ (nm)	ϵ (M^{-1} cm^{-1})	$\lambda_{\text{em}}^{\text{b}}$ (nm)	E_{00}^{c} (eV)	$E_{\text{ox1}}^{\text{d}}$ (V)	$E_{\text{ox2}}^{\text{d}}$ (V)	$E_{\text{red}}^{\text{d}}$ (V)	$E_{\text{red}}^*^{\text{e}}$
SL1	364	37 500	618	2.18	+0.64	+1.05	-1.39	0.79
	521	20 300						
SL2	359	38 300	700	1.89	+0.54	+0.84	-1.03	0.86
	603	21 050						

^a Absorption maxima in CH_2Cl_2 solution ($C = 3 \times 10^{-5}$ M). ^b Emission maximum in CH_2Cl_2 solution ($C = 3 \times 10^{-5}$ M). ^c ΔE_{opt} estimated from the intercept of the normalized absorption and emission spectra. ^d Potentials measured in THF solution with FeCp_2 as internal reference and referred to NHE by addition of 630 mV.⁵⁶ ^e Reduction potential at the excited state estimated from $E_{\text{red}} + E_{00}$.

Although such organometallic complexes are only weakly emissive, fluorescence spectra of **SL1** and **SL2** could be recorded in dichloromethane solution (see Figure III-8). The maximum emission wavelength was detected at $\lambda_{\text{em}} = 618$ nm and $\lambda_{\text{em}} = 700$ nm for **SL1** and **SL2**, respectively. The energy of the excited state (E_{00}) was estimated from the wavelength at the intersection of the normalized absorption and emission spectra. As expected, the blue dye **SL2** presents a lower lying excited state ($E_{00} = 1.89$ eV) than that of the red dye **SL1** ($E_{00} = 2.18$ eV).

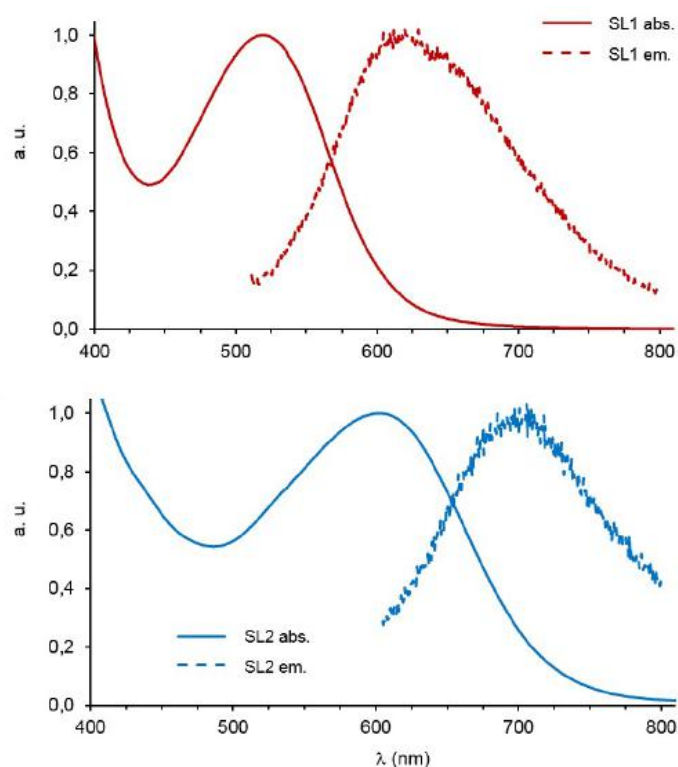


Figure III-8: Normalized electronic absorption (plain) and fluorescence emission (dashed) spectra of **SL1** and **SL2** in CH_2Cl_2 .

The electrochemical properties of **SL1** and **SL2** were investigated by cyclic voltammetry in THF solution (see Figure III-9), the corresponding data are gathered in Table III-1. In the anodic region, the voltammograms show two reversible monoelectronic processes, both stemming from oxidation of the central electron-rich π -conjugated system with strong contribution of the $[\text{Ru}(\text{dppe})_2]$ metal fragment. In the cathodic region the voltammograms feature a reversible monoelectronic reduction process mostly centered on the electron withdrawing group (acrylic ester or rodhanine). **SL1** exhibits a more cathodic reduction potential compared to that of **SL2** in agreement with the stronger withdrawing acceptor strength of rodhanine compared to acrylic ester. The calculated reduction potential of the dye at the excited state at +0.79 V and +0.86 V vs. NHE for **SL1** and **SL2**, respectively, is more positive than the valence band edge of NiO ($E_{\text{VB}} \sim +0.54$ V vs. NHE).⁵⁷ This indicates that there is a small but sufficient driving force (about 0.25-0.3 eV) for hole injection from the dye excited state into the valence band of the semiconductor (see Table 1). On the other hand, the reduction potential of the dyes is strongly negative, suggesting that regeneration of the dyes by $\text{I}_3^-/\text{I}_2^-$ ($E^\circ = -0.08$ V vs. NHE) is a very exergonic process ($|\Delta G| > 0.9$ eV) and should operate efficiently within the device.

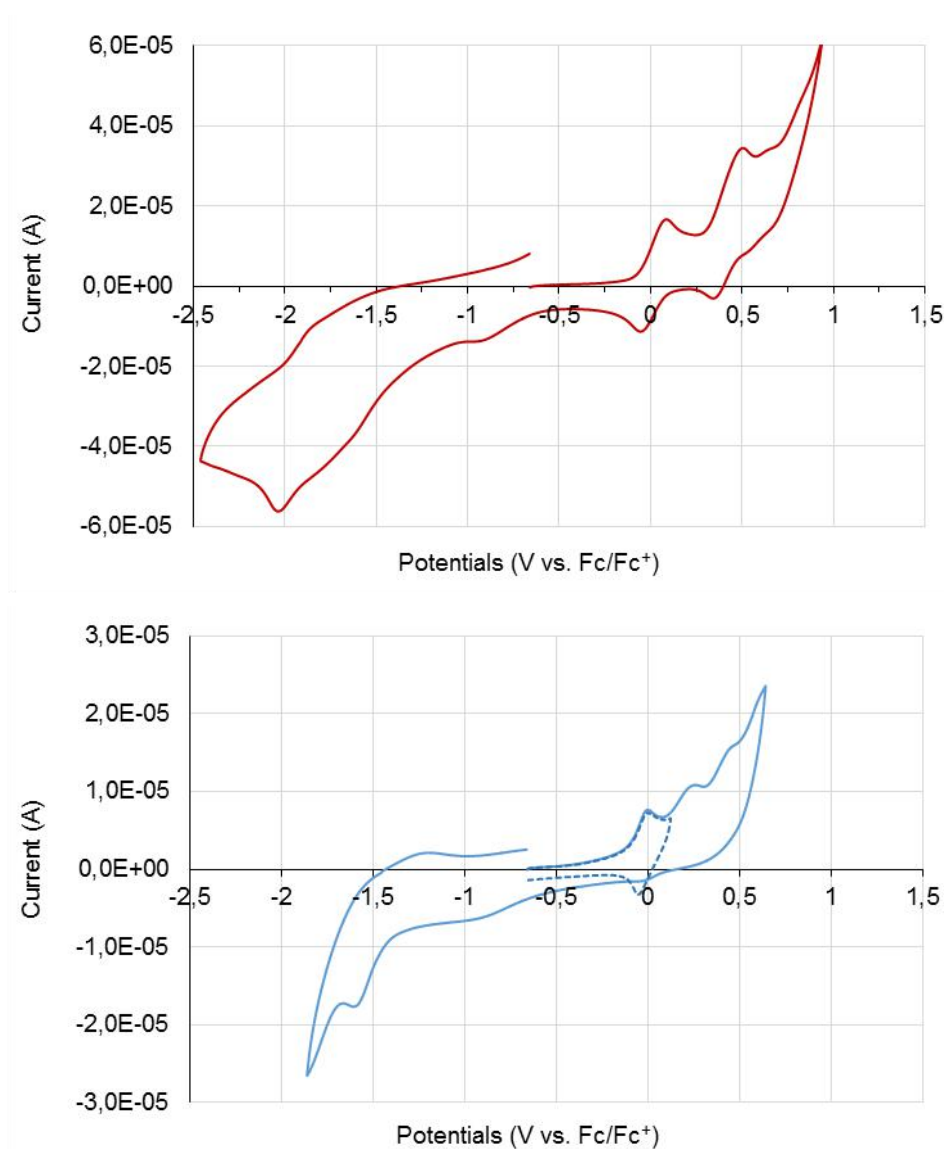


Figure III-9: Cyclic voltammograms of **SL1** and **SL2** recorded in THF/ $n\text{Bu}_4\text{NPF}_6$ (0.1M) vs. Fc/Fc^+ at 200 mV s^{-1} . The blue dotted line represents the reversibility of the first oxidation process isolated; the second oxidation process is only partly reversible.

III.3.3. Theoretical Calculations

To gain further insights into the electronic properties of **SL1** and **SL2**, the electron-density distribution of the frontier molecular orbitals (MOs) were determined by density functional theory (DFT) using the B3LYP/LANL2DZ hybrid functional. Spatial representation of the calculated transition-involved MOs is shown in Figure III-10. Theoretical calculations reveal that, for the two dyes, the HOMO is spread over the extended π -conjugated system from the triphenylamine to the bithiophene unit, with a strong

contribution of the central $C\equiv C-Ru-C\equiv C$ fragment. It also appears that, due to the presence of the two carboxylic-acid functions, the electron density at the ground-state is only partially located on the triphenylamine donor motif. Nonetheless, upon grafting the dyes on NiO one could expect that the withdrawing effect of the COOH groups will decrease and the electron density will subsequently slide towards the surface. On the other hand, the LUMO of the dyes is well localized on the electron-withdrawing part of the complexes, *i.e.* on the methylester groups in **SL1** and on the rhodanine motif in **SL2**. As a consequence, upon photoexcitation of the dye, an electron will be promoted from the metal center towards the remote part of the molecule, thus favoring electron capture by the electrolyte. Simultaneously, electron injection to the excited dye's HOMO will be possible by hopping from NiO to the triphenylamine in contact with the metal-oxide surface.

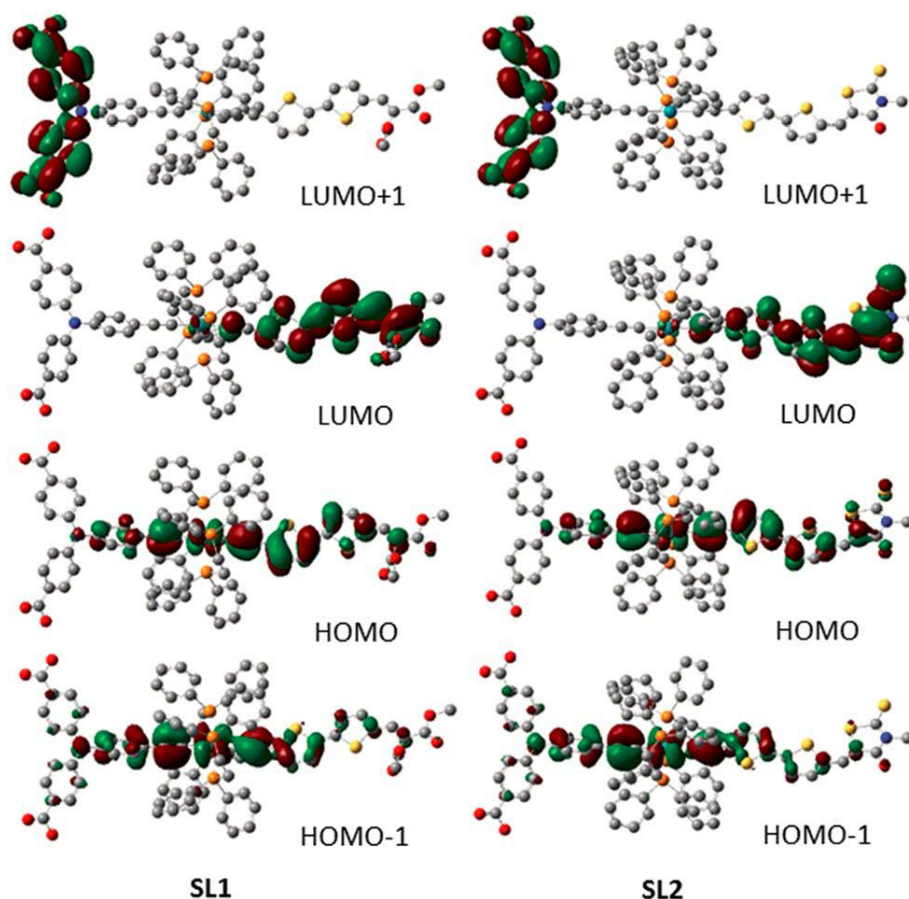


Figure III-10: Electron-density distribution of the transition-involved frontier molecular orbitals of **SL1** and **SL2**.

TD-DFT calculations were further performed in order to assess the different photoinduced electronic transitions. The simulated absorption spectra are represented in

Figure III-11 and the corresponding data are given in Table III-2. For both dyes the simulated absorption spectrum is in good agreement with the experimental one, showing two main absorption bands, one in the visible region and one around 360 nm. In accordance with the experience, the maximum wavelength calculated for the first allowed transition, λ_{ge} , is located at 544 nm for **SL1** and strongly red-shifted for **SL2**, up to 612 nm, due to increased electron withdrawing effect of rhodanine. Overall, the small deviation between the calculated and experimental data is attributable to the large size of such organometallic complexes.

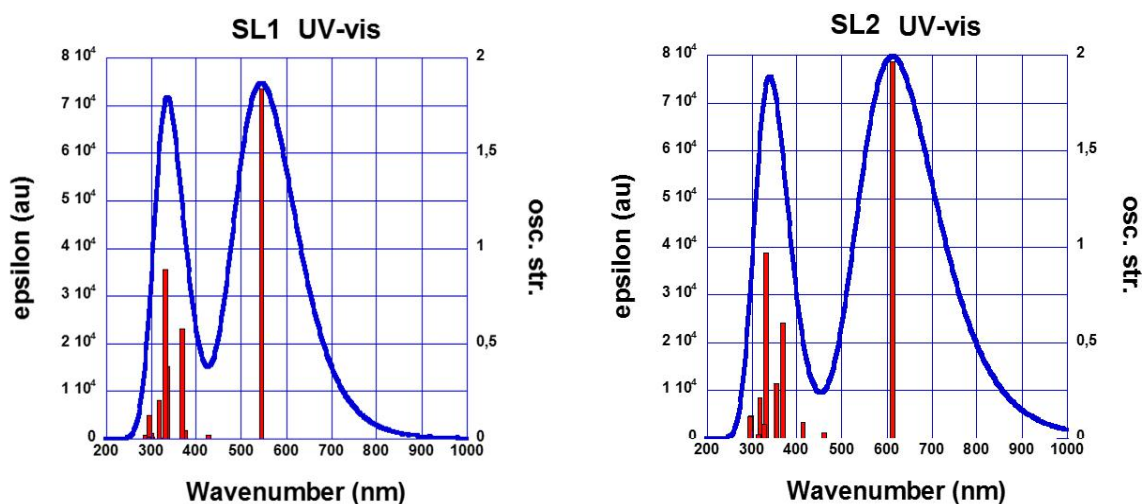


Figure III-11: TD-DFT simulated absorption spectra of **SL1** and **SL2**. Absorption bands enlarged using Gaussian functions with full-width at half-height (FWHH) of 5 nm to reproduce the experimental spectra.

Table III-2: Theoretical data

Dye	ΔE_{ge}^a (eV)	λ_{ge}^b (nm)	f_{ge}^c	Transition assignment (coefficient) ^d	Λ^e	q_{CT}/e^f	$D_{CT}/\text{\AA}^g$
SL1	2.276	544	1.842	H→L (0.62); H-1→L (-0.26)	0.59	0.88	4.7
	3.359	369	0.580	H→L+1 (-0.22); H-1→L+1 (0.56); H-2→L+1 (-0.21)			
SL2	2.024	612	1.968	H→L (0.62); H-1→L (0-0.20)	0.58	0.90	5.1
	3.371	367	0.601	H→L+1 (0.46); H-1→L+1 (-0.39); H-2→L+1 (0.23); H-3→L+1 (-0.26)			

^a ΔE_{ge} = main transition energy. ^b λ_{ge} = calculated λ_{max} . ^c f_{ge} = oscillator strength. ^d Only the transitions with coefficients higher than 0.15 are given. ^e Λ = spatial overlap. ^f q_{CT} = quantity of transferred charge. ^g D_{CT} = distance between the barycentres of the density depletion and density increment zones related to the CT excitation.

From the calculated data (Table III-2) we could further assign the origin of the main absorption bands observed on the experimental spectra. As expected, the band in the visible region owns a major HOMO \rightarrow LUMO character, but also some HOMO-1 \rightarrow LUMO character which explains the broadness of the absorption in the visible region. As shown in Figure III-10 the electronic distribution of the HOMO-1 is fairly similar to the HOMO and both orbitals are close in energy. Consequently, the observed visible absorption band owns a full MLCT character. This is confirmed by the calculated quantity of transferred charge, q_{CT} , which is almost equal to 1. The band at higher energy also stems from multiple electronic transitions mainly from the HOMO and HOMO-1 to the LUMO+1 which is entirely located on the external phenyl rings of the triarylamine motif.

III.3.4. Photovoltaic Measurements in p-Type DSCs

The photovoltaic performances of the dyes **SL1** and **SL2** were subsequently investigated in sandwich solar cells consisting of a 3 μm thick nanocrystalline layer of NiO, a platinized counterelectrode and an electrolyte based on iodide/triiodide redox couple (see Experimental part for details). The device fabrication and characterization were performed in the group of Fabrice Odobel at the University of Nantes.

The metrics of the solar cells are gathered in Table III-3 and the photoaction spectra are shown in Figure III-12.

Table III-3: Photovoltaic characteristics of the dyes **SL1** and **SL2** in p-DSC recorded under simulated solar spectrum (AM 1.5) along with dye loading on NiO film

Dye	J_{sc} ($\text{mA}\cdot\text{cm}^{-2}$)	V_{oc} (mV)	FF (%)	PCE (%)	Dye loading (nmol cm^{-2})
SL1	2.25	104	34	0.079	31.9
SL2	1.50	77	33	0.038	10.1

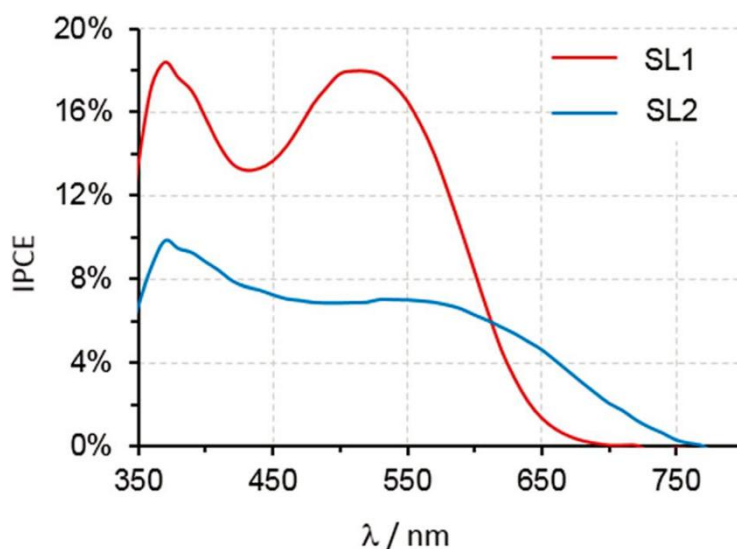


Figure III-12: Photoaction spectra of the dyes **SL1** and **SL2** in NiO based p-DSC recorded in short-circuit conditions.

The best performing dye is the red **SL1**, which produces a higher short-circuit current density (J_{sc}) and a larger open-circuit voltage (V_{oc}) than **SL2** (see Table III-3). The IPCE spectra show that **SL2** produces photocurrent above 700 nm, with a moderate efficiency, while **SL1** is more active but in a narrower bandwidth and at shorter wavelength. The IPCE is the factor of the light harvesting efficiency (LHE) by the injection quantum yield (ϕ_{inj}), the regeneration quantum yield (ϕ_{reg}) and the charge collection efficiency ($\phi_{collect}$) according to the following equation 27:

$$IPCE = LHE \times \phi_{inj} \times \phi_{reg} \times \phi_{collect} \quad (27)$$

Looking at the HOMO in **SL1** and **SL2**, we can infer that the electronic coupling of the dye excited state with the NiO valence band must be quite similar as these orbitals are roughly similarly distributed over the molecule (see Figure III-10). Moreover, the injection driving force with **SL2** is a bit larger (albeit quite close) than that of **SL1**, indicating that the injection quantum yield is certainly not the main factor controlling the IPCE. The regeneration reaction is most certainly very high as the driving force is huge in both cases (see Table III-10). Desorption experiments were made and they revealed that the dye loading is $31.9 \text{ nmol}\cdot\text{cm}^{-2}$ and $10.1 \text{ nmol}\cdot\text{cm}^{-2}$ for **SL1** and **SL2**, respectively. These values are in the same range as other NiO dyes anchored with the same group N,N-di(4-benzoic acid)phenylamine (around $10\text{-}40 \text{ nmol}\cdot\text{cm}^{-2}$)^{23,58,59} but much lower than the highly performing P1 dye ($123 \text{ nmol}\cdot\text{cm}^{-2}$).⁶⁰ Changing the anchoring group can certainly improve the dye loading of these complexes and consequently increase their photoconversion efficiency. In addition, the dye loading of **SL1** which is three fold higher than that of **SL2**, can explain the higher J_{sc} of **SL1**, which also most

certainly comes from the higher absorbance of this dye around 500 nm, where the incoming solar flux is the largest. Finally, a lower dye loading means a higher degree of naked NiO surface exposed to the electrolyte promoting more interfacial charge recombination, thus lowering the charge collection efficiency. This is evidenced by the significantly lower V_{oc} monitored for **SL2** based devices.

III.3.5. Conclusions

In this section we have described the synthesis and characterization of the first ruthenium diacetylide complexes for p-DSCs. While these dyes were not perfectly optimized yet, their photovoltaic performances were relatively high if compared with the reported ruthenium polypyridine complexes for the same application.^{22-24,25} Interestingly, these two dyes displayed moderate injection driving force while it is accepted that the density of states of NiO valence band is lower than that of TiO₂ conduction band, that is why the sensitizers for NiO must exhibit high driving force (>0.6 eV) to efficiently operate.^{61,62} We therefore anticipated that much better performing ruthenium diacetylide dyes could be developed by lowering the energy position of the HOMO levels to enhance injection Gibbs free enthalpy.

III.4. Push-Pull Ruthenium Diacetylide Complexes With Modified Electron-Donating Group

As discussed above, we reported the synthesis and characterization of the first ruthenium diacetylide complexes for p-DSCs.⁶³ However, the indicated driving force of **SL1** and **SL2** for hole injection from the dye excited state into the valence band of NiO is small. Therefore, two other Ru-based dyes based on the [Ru(dppe)₂] moiety were further designed by changing the electron-donating unit to simple phenyl and thienyl units in order to lower the HOMO energy level and to enhance the charge injection rate. The molecular structure of the two new Ru-based dyes is depicted in Figure III-13. The bis(σ -arylacetylide) photosensitizers **SL3** and **SL4** are endowed with a carboxylic acid anchoring group separated by a benzene or thiophene linker. The two dyes are functionalized with the same electron-withdrawing ligand as **SL1** bearing a dimethylmalonate group.

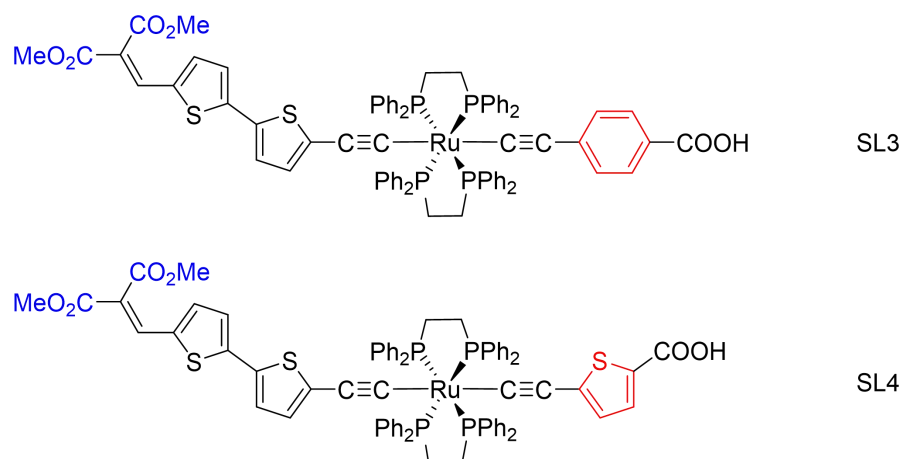
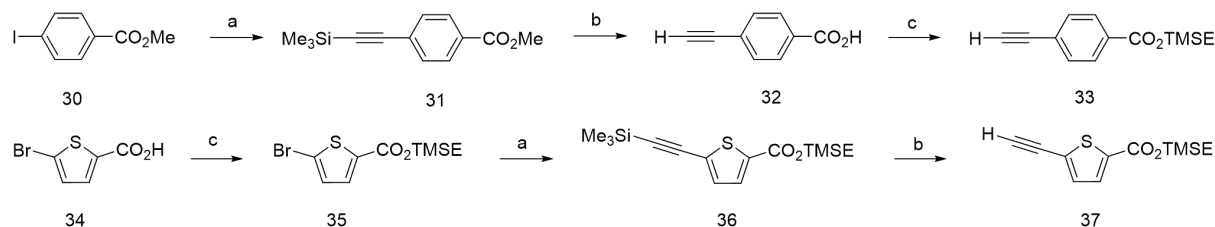


Figure III-13: Molecular structures of the push-pull organometallic dyes **SL3** and **SL4**.

The optical and electrochemical properties of two new photosensitizers **SL3** and **SL4** were assessed and theoretical calculations were performed to rationalize the experimental data. The dye **SL1** was used as the reference for comparison in photovoltaic measurements in p-DSCs.

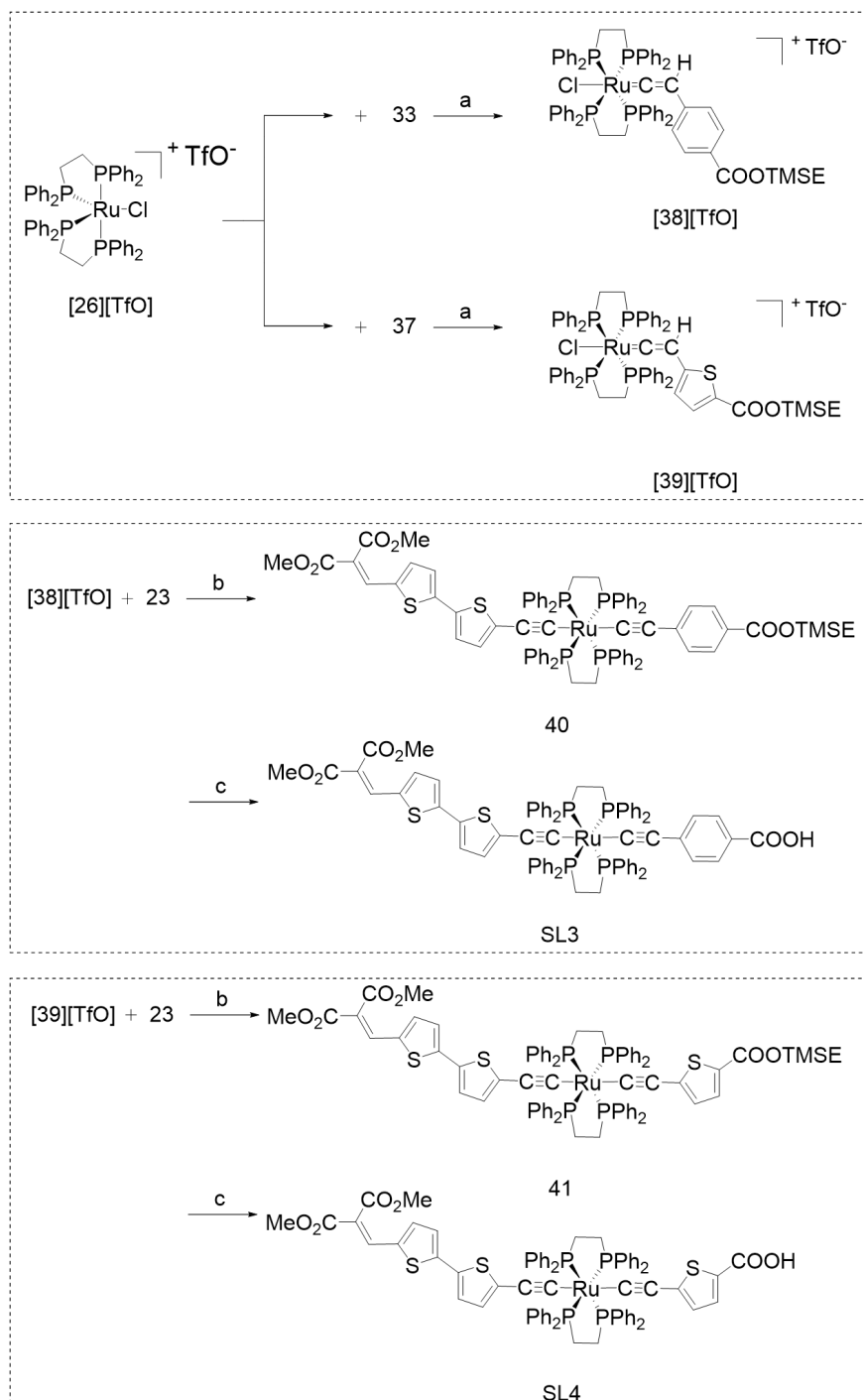
III.4.1. Synthesis of the Dyes **SL3** and **SL4**

As referred above, ruthenium diacetylide complexes **SL3** and **SL4** were prepared through already established procedures involving successive activation of terminal alkynes by the conventional electron-deficient metal center $[\text{RuCl}(\text{dppe})_2][\text{TfO}]$.⁵⁴ First, the two alkyne ligands **33** and **37** corresponding to the electron-donating units were synthesized following synthetic routes shown on Scheme III-4. To avoid side reactions of the carboxylic acid anchoring groups with the metal center during the following synthesis steps, protection of the COOH function was taken into consideration. As previously, the silyl-ester protecting group TMSE was employed for this purpose since it allows deprotection in mild conditions.



Scheme III-4: Synthesis of the alkyne ligands **33** and **37**. Reaction conditions: (a) trimethylsilylacetylene, $\text{PdCl}_2(\text{PPh}_3)_2$, CuI, Et_3N , THF; (c) K_2CO_3 , MeOH; (b) trimethylsilylethanol, HBTU, DIPEA, DMF.

Synthesis of the phenyl-containing ligand **33** involved Sonogashira coupling reaction of the bromobenzene derivative **31** with trimethylsilylacetylene and subsequent deprotection of the terminal alkyne. Analogously, synthesis of the thienyl electron-rich ligand **37** involved Sonogashira coupling reaction of the bromothiophene derivative **35** with trimethylsilylacetylene and subsequent deprotection of the terminal alkyne. Secondly, the synthesis of the electron-withdrawing σ -alkynyl ligand **23** was the same as above.



Scheme III-5: Synthesis of the organometallic complexes **SL3** and **SL4**. Reaction conditions: (a) CH_2Cl_2 ; (b) NaPF_6 , Et_3N , CH_2Cl_2 ; (c) tetrabutylammonium fluoride, THF.

The synthetic steps to the target Ru-based organometallic dyes **SL3** and **SL4** are represented in Scheme III-5. The donor part of the dye **SL3** was first obtained by activation of the phenyl-containing ligand **33** by the 16-electron species **[26][TfO]**, leading to the stable ruthenium-vinylidene intermediate **[38][TfO]** while the donor part of the dye **SL4** was obtained by activation of the thiophene-containing ligand **37** by **[26][TfO]**, leading to the stable ruthenium-vinylidene intermediate **[39][TfO]**. Subsequent introduction of the second carbon-rich chain on the $[\text{RuCl}(\text{dppe})_2]$ metal centre to form bis- σ -arylacetylide complexes was achieved by reacting either **[38][TfO]** or **[39][TfO]** with the alkynyl ligand **23** in the presence of Et_3N and of NaPF_6 . Finally, the target products **SL3** and **SL4** were obtained in good yields after removal of the silyl-ester protecting groups, using tetrabutylammonium fluoride in THF at room temperature.

All the organometallic complexes were characterized by means of ^{31}P , ^1H NMR and HR-MS. The data set is in accordance with the expected structure of the organometallic complexes. The *trans*-ditopic geometry of the ruthenium center in **SL3** and **SL4** was evidenced by ^{31}P NMR as the spectra show a singlet for the four equivalent phosphorus atoms, with $\delta \approx 52$ ppm characteristic of the ruthenium-diacetylide structure.⁵⁴

III.4.2. Optical and Electrochemical Properties

UV-visible absorption spectra of **SL3** and **SL4**, recorded in dichloromethane solution, are shown in Figure III-14 and the corresponding values are listed in Table III-4. The intense short-wavelength absorption band observed in the UV region is characteristic of $n \rightarrow \pi^*$ and $\pi \rightarrow \pi^*$ transitions from the dppe ligands.⁵⁵ More importantly, for **SL3**, the less intense band centred around $\lambda = 382$ nm can be tentatively ascribed to electronic transitions involving the phenyl-containing ligand, while for **SL4**, the intense band centred around $\lambda = 409$ nm can be tentatively ascribed to electronic transitions involving the thiophene-containing electron-donor ligand. A similar feature of these dyes is the broad absorption band observed in the visible part of the spectrum. Similarly to **SL1** and **SL2**, this intense absorption band corresponds to multiple MLCT processes, with main contribution of the photoinduced transition from the metal-centred HOMO to the LUMO located on the electron-withdrawing dimethylester moiety. The maximum absorption wavelength of **SL3** ($\lambda_{\text{max}} = 514$ nm) is similar to that of **SL4** ($\lambda_{\text{max}} = 507$ nm) due to the same electron-withdrawing group for both, which makes **SL3** and **SL4** red pigments. Both dyes present a rather high molecular extinction coefficient (ϵ) of about $20\,000 \text{ M}^{-1} \text{ cm}^{-1}$ at λ_{max} . Once again, the good absorption properties of this couple of organometallic complexes make them good candidates for use as

photosensitizers in p-DSCs.

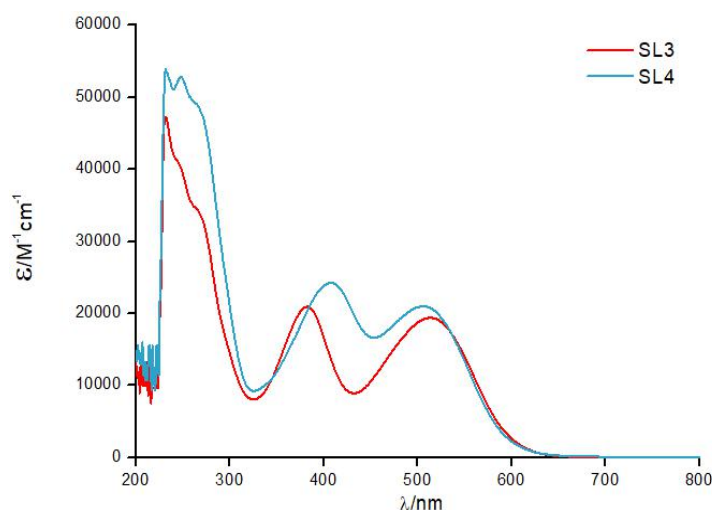


Figure III-14: Absorption spectra of **SL3** and **SL4** in CH_2Cl_2 ($C \approx 3 \times 10^{-5}$ M).

Table III-4: Optical and electrochemical properties

Dye	$\lambda_{\text{max}}^{\text{a}}$ (nm)	ϵ (M^{-1} cm^{-1})	E_{00}^{c} (eV)	E_{ox1} (V vs. FeCp^*) ^b	E_{ox2} (V vs. FeCp^*) ^b	E_{ox1} (V vs. NHE) ^b	E_{ox2} (V vs. NHE) ^b
SL1	364	37 500	2.18	-	-	+0.64	+1.05
	521	20 300					
SL3	382	20 900	2.10	+0.55	+1.19	+0.68	+1.32
	514	19 400					
SL4	409	24 200	2.10	+0.58	+1.18	+0.71	+1.31
	507	21 000					

^a Absorption maxima in CH_2Cl_2 solution ($C = 3 \times 10^{-5}$ M). ^b Potentials measured in CH_2Cl_2 solution with FeCp^*_2 as internal reference and referred to NHE by addition of 130 mV.⁵⁶

Due to the very weak emission properties of these organometallic complexes, the fluorescence spectra of **SL3** and **SL4** have not been measured. Still, the energy of the excited state (E_{00}) was estimated from the onset of their absorption spectra, leading to $E_{00} = 2.10$ eV for the two new dyes.

The electrochemical properties of **SL3** and **SL4** were investigated by cyclic voltammetry in CH_2Cl_2 solution (see Figure III-15), the corresponding data are gathered in Table III-4. In the anodic region, the voltammograms show two reversible monoelectronic processes. The first one is characteristic of the $\text{Ru}^{\text{II}} \rightarrow \text{Ru}^{\text{III}}$ oxidation process occurring in *trans*-diacetylde

complexes.⁶³ The second wave can be attributed to the central π -conjugated system. In the cathodic region no clear reduction process was observable within the window allowed by the solvent.

As expected, the modified electron-donor groups of **SL3** and **SL4** led to a first oxidation process at higher potential compared to **SL1**: $E_{\text{ox1}} = +0.68$ V (*vs.* NHE), $E_{\text{ox1}} = +0.71$ V (*vs.* NHE) and $E_{\text{ox1}} = +0.64$ V (*vs.* NHE) for **SL3**, **SL4** and **SL1**, respectively. This therefore corresponds to a lower position of the HOMO energy level, as expected.

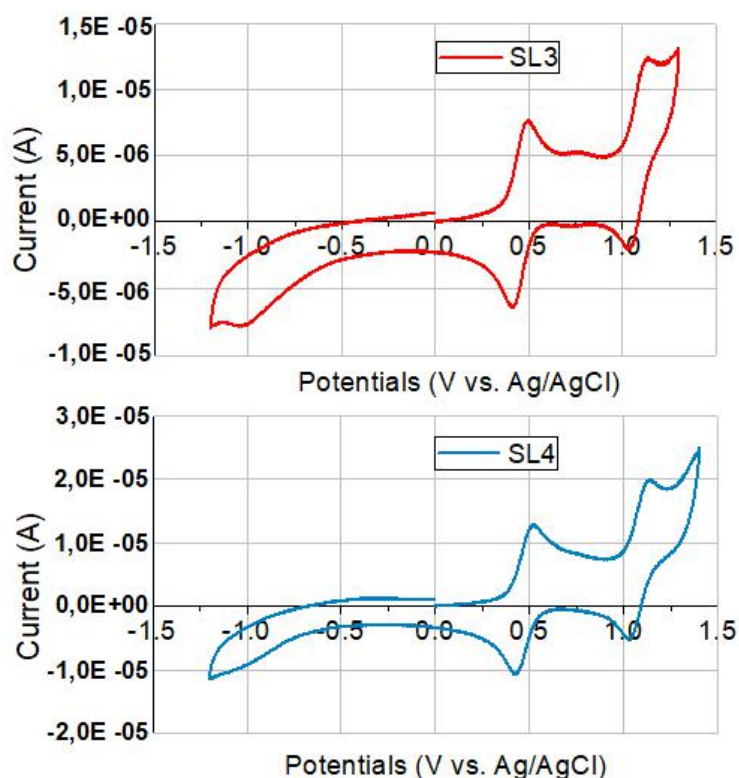


Figure III-15: Cyclic voltammograms of **SL3** and **SL4** recorded in $\text{CH}_2\text{Cl}_2/\text{nBu}_4\text{NPF}_6$ (0.1M) *vs.* Ag/AgCl at 200 mV s^{-1} .

III.4.3. Theoretical Calculations

To obtain more insights into the electronic properties of **SL3** and **SL4**, the electron-density distribution of the frontier molecular orbitals (MOs) were determined by density functional theory (DFT) using the B3LYP/LANL2DZ hybrid functional. Spatial representation of the calculated transition-involved MOs is shown in Figure III-16. Theoretical calculations revealed that, for the dye **SL3**, the HOMO includes the $[\text{Ru}(\text{dppe})_2]$ metal fragment, however no electron density is again observed on the anchoring group. For

the dye **SL4**, the HOMO is spread over the whole extended π -conjugated system, with a strong contribution of the central $C\equiv C-Ru-C\equiv C$ fragment. Moreover, the calculated HOMO energy level of the two dyes (-5.27 eV for **SL3** and -5.35 eV for **SL4**) is lower than that of **SL1** (-5.19 eV), which also suggests more efficient hole injection from the dye excited state into the valence band of NiO for both dyes compared to **SL1**. Furthermore, considering these calculations, one can also expect a slightly larger injection driving force with **SL4** than with **SL3**. Interestingly, the HOMO of **SL4** presents more electronic density on the anchoring group which is favorable to charge transfer process from NiO. On the other hand, the LUMO of the dyes is well localized on the methylester groups of the complexes. As a consequence, upon photoexcitation of the dye, an electron will be promoted from the metal center towards the remote part of the molecule, thus favoring electron capture by the electrolyte. Simultaneously, for the two dyes, electron injection to the excited dye's HOMO will be possible by transfer from NiO to the acetylide ligand in contact with the metal-oxide surface.

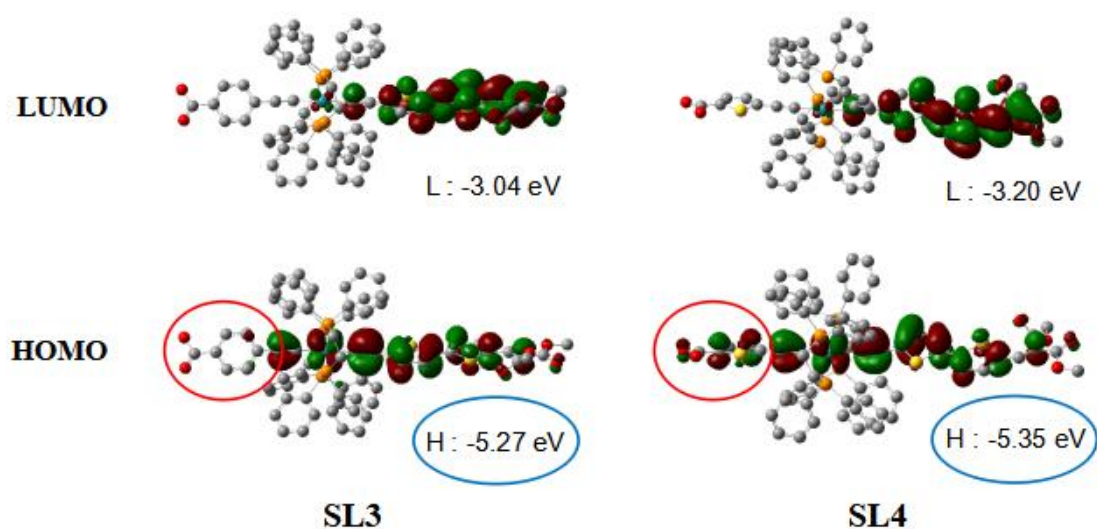


Figure III-16: Electron-density distribution of the frontier molecular orbitals of **SL3** and **SL4**.

III.4.4. Photovoltaic Measurements in p-Type DSCs

The photovoltaic performances of the dyes **SL3** and **SL4** were subsequently investigated in sandwich solar cells consisting of a 3.5 μm thick nanocrystalline layer of NiO, a platinized counter-electrode and an electrolyte based on iodide/triiodide redox couple (see Experimental part for details). The performance of the dye **SL1** was measured under the same conditions for comparison. This study was again realized in collaboration with Fabrice Odobel from the University of Nantes. The metrics of the solar cells are gathered in Table III-5.

Table III-5: Photovoltaic characteristics of the dyes **SL3** and **SL4** in p-DSC recorded under simulated solar spectrum (AM 1.5).

Dye	J_{sc} ($\text{mA}\cdot\text{cm}^{-2}$)	V_{oc} (mV)	FF (%)	PCE (%)
SL1	2.50	112.1	34.4	0.096
SL3	1.28	97.6	31.1	0.039
SL4	1.22	89.7	30.2	0.033

The photovoltaic performances of **SL1** are similar to those in section III.3.4. meaning that the data can be directly compared. The dye **SL3** showed slightly better photovoltaic performances compared to the dye **SL4**, which produces notably larger open-circuit photovoltage (V_{oc}) (see Table III-5). However, the efficiencies of the p-DSCs based on **SL3** and **SL4** are lower than those based on the reference dye **SL1**, mainly due to much lower photocurrent density values (J_{sc}). This seems to indicate that two COOH anchoring groups (**SL1**) are probably better than only one (**SL3** and **SL4**) to get a higher dye-loading amount and charge injection yield. It is worth to mention that only small intensity of coloration of the NiO-based electrode was observed after dye-bath treatment with **SL3** and **SL4**, compared to **SL1**.

III.4.5. Conclusions

In this section we have described the synthesis and characterization of two ruthenium diacetylide complexes based on the $[\text{Ru}(\text{dpppe})_2]$ moiety for p-DSCs which contain simple electron-donating groups. The introduction of either a benzene or thiophene as electron-donating units afforded lower HOMO energy levels compared to our former dye **SL1**, which was expected to enhance the charge injection rates. However, the efficiencies of the p-DSCs based on the two new dyes **SL3** and **SL4** are lower than those based on the reference dye **SL1** which can be attributed to the lower dye loading amount, and thus lower photocurrent densities. We therefore anticipated that better performing ruthenium diacetylide dyes could be developed by changing the anchoring function, for instance by using a phosphonic acid group.

III.5. Phosphonic Acid as a New Anchoring Function of Ru-Based Dyes for p-Type DSCs

As discussed above, we described the synthesis and characterization of two ruthenium diacetylide complexes based on the $[\text{Ru}(\text{dppe})_2]$ moiety for p-DSCs which contain simple electron-donating groups. However, the main drawback for these dyes is the insufficient amount of dye grafted on NiO that limits their photovoltaic performances. Therefore, another Ru-based dye was designed which included a phosphonic acid anchoring group for improving the density of dye on the photoelectrode. The molecular structure of the new dye is depicted in Figure III-17. The ruthenium diacetylide complex **SL5** is endowed with a phosphonic acid anchoring group on one side, and functionalized with a dimethylmalonate electron-withdrawing group on the other side, both separated by two bithiophene linkers and the $[\text{Ru}(\text{dppe})_2]$ electron-rich metal center.

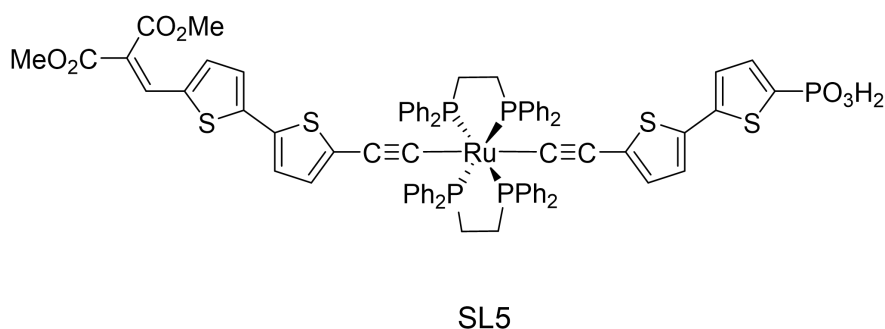
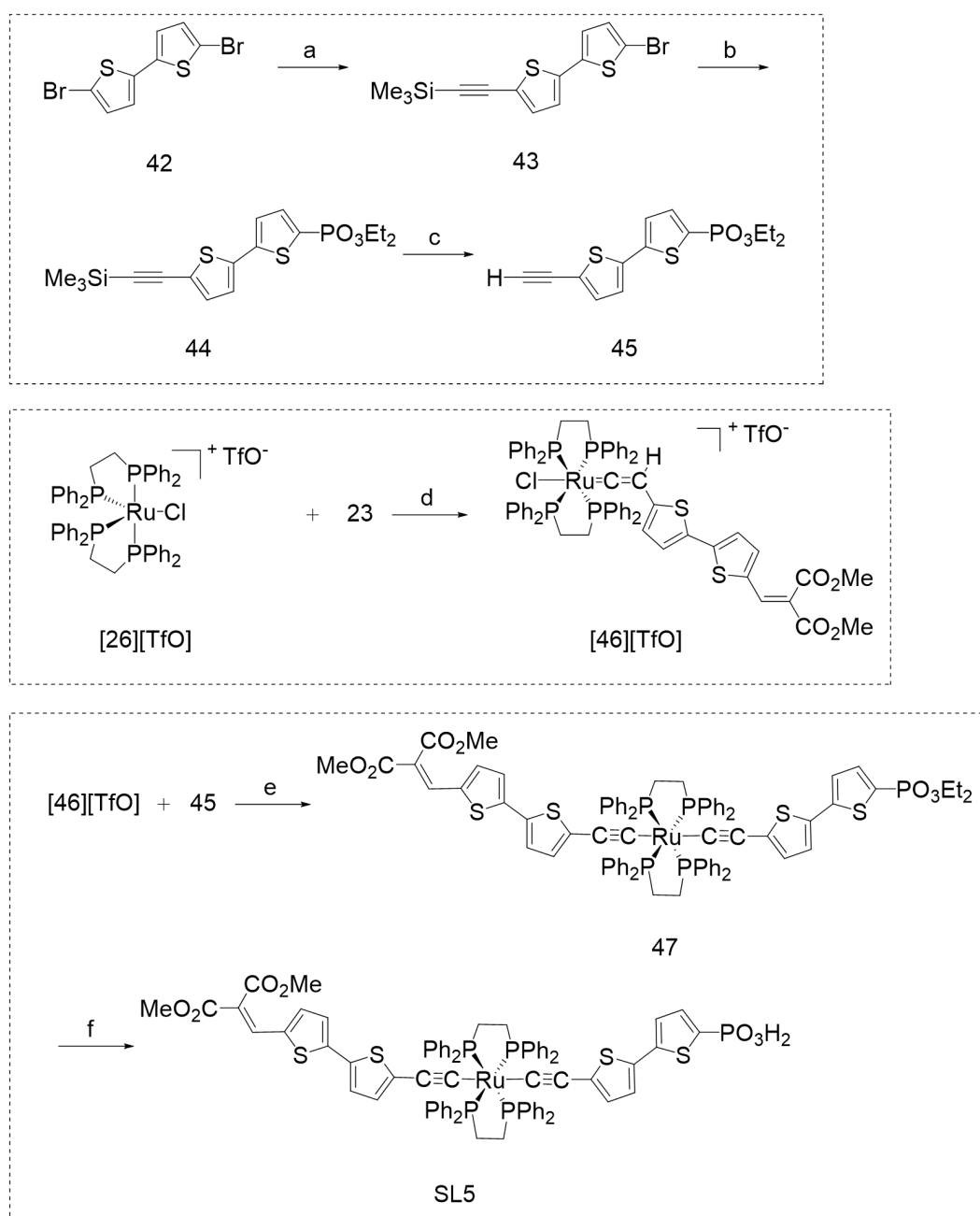


Figure III-17: Molecular structure of the push-pull organometallic dye **SL5**.

The optical and electrochemical properties of **SL5** were assessed and theoretical calculations were performed in order to rationalize the experimental data.

III.5.1. Synthesis of the Dye **SL5**

The ruthenium diacetylide complex **SL5** was prepared following the same procedures described above for **SL1-SL4**. The synthetic steps to the target organometallic complex **SL5** are represented in Scheme III-6.



Scheme III-6: Synthesis of the organometallic complex **SL5**. Reaction conditions: (a) trimethylsilylacetylene, $\text{PdCl}_2(\text{PPh}_3)_2$, CuI , DIPEA, THF; (b) diethyl phosphite, Et_3N , $\text{Pd}(\text{OAc})_2$, dppf, CH_3CN ; (c) K_2CO_3 , MeOH ; (d) CH_2Cl_2 ; (e) NaPF_6 , Et_3N , CH_2Cl_2 ; (f) N,O-bis(trimethylsilyl) acetamide, iodotrimethylsilane, CH_2Cl_2 .

First, synthesis of the alkyne ligand **45** involved Sonogashira coupling reaction of 5,5'-dibromo-2,2'-bithiophene **42** with trimethylsilylacetylene. The phosphonate group was introduced through Hiraou coupling reaction of derivative **43** with diethyl phosphite as it can generate phosphonic acid anchoring group under mild conditions. Secondly, the acceptor part of the dye **SL5** was obtained by activation of the electron-withdrawing σ -alkynyl ligand **23** by

the 16-electron species **[26][TfO]**, leading to the stable ruthenium-vinylidene intermediate **[46][TfO]**. Subsequent introduction of the second carbon-rich chain on the $[\text{Ru}(\text{dppe})_2]$ metal centre to form a bis- σ -arylacetylide complex was achieved by reacting **[46][TfO]** with the alkyne ligand **45**, in the presence of a base Et_3N and of a non-coordinating salt NaPF_6 . Finally, the target dye **SL5** was obtained in good yield through the reaction of the precursor **47** with N,O-bis(trimethylsilyl) acetamide and iodotrimethylsilane to generate the phosphonic acid anchoring group.

The organometallic complexes were characterized by means of ^{31}P , ^1H and HR-MS. The *trans*-ditopic geometry of the ruthenium center in **SL5** was again confirmed by ^{31}P NMR analyses. An additional peak was observed on the ^{31}P NMR spectra at $\delta = 11.2$ ppm and $\delta = 10.7$ ppm, for the precursor **47** and **SL5**, corresponding to the phosphonate and phosphonic acid groups, respectively.

III.5.2. Optical and Electrochemical Properties

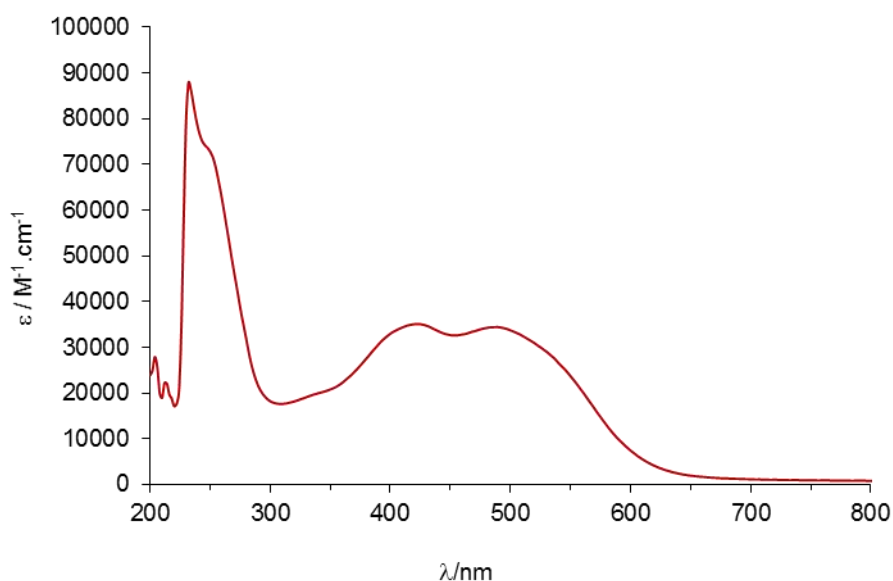


Figure III-18: Absorption spectrum of **SL5** in CH_2Cl_2 ($C \approx 3 \times 10^{-5}$ M).

The UV-visible absorption spectrum of **SL5** in dichloromethane solution is shown in Figure III-18. The corresponding values are listed in Table III-6 along with those of **SL1**, for comparison. The intense high-energy absorption band observed in the UV region correspond to $n \rightarrow \pi^*$ and $\pi \rightarrow \pi^*$ transitions from the dppe ligands.⁵⁵ The less intense band with maximum at $\lambda = 424$ nm for the dye **SL5** can be ascribed to electronic transitions involving the

polythiophene-based π -conjugated system. A broad absorption band is again observed in the visible part of the spectrum corresponding to MLCT processes, mainly stemming from the metal-centred HOMO to the LUMO located on the electron-withdrawing methylester group. This band presents a maximum absorption wavelength at $\lambda_{\text{max}} = 490$ nm with a rather high molecular extinction coefficient (ϵ) of over $34\,000\text{ M}^{-1}\text{ cm}^{-1}$. The good absorption properties of the dye **SL5** again make it a good candidate for use as photosensitizer in p-DSCs.

Table III-6: Optical and electrochemical properties of **SL5**.

Dye	$\lambda_{\text{max}}^{\text{a}}$ (nm)	ϵ ($\text{M}^{-1}\text{ cm}^{-1}$)	E_{ox1} (V	E_{ox2} (V	E_{ox1} (V	E_{ox2} (V
			vs. FeCp* ^b)	vs. FeCp* ^b)	vs. NHE) ^b	vs. NHE) ^b
SL1	364	37 500	-	-	+0.64	+1.05
	521	20 300				
SL5	424	35 100	+0.52	+1.18	+0.65	+1.32
	490	34 400				

^a Absorption maxima in CH_2Cl_2 solution ($C = 3 \times 10^{-5}\text{ M}$). ^b Potentials measured in CH_2Cl_2 solution with FeCp^*_2 as internal reference and referred to NHE by addition of 130 mV.⁵⁶

The electrochemical properties of **SL5** were investigated by cyclic voltammetry in CH_2Cl_2 solution (see Figure III-19), the corresponding data are given in Table III-6. Similarly to the dyes **SL1-SL4**, the voltammogram of **SL5** shows two reversible mono-electronic processes in the anodic region. The first one can be attributed to the $\text{Ru}^{\text{II}} \rightarrow \text{Ru}^{\text{III}}$ oxidation process while the second one can be ascribed to the central π -conjugated system.

Interestingly, the new modification made in the electron-donor group of **SL5** yielded a first oxidation process comparable to that of **SL1**: $E_{\text{ox1}} = +0.65\text{ V vs. NHE}$ and $E_{\text{ox1}} = +0.64\text{ V vs. NHE}$ for **SL5** and **SL1**, respectively. However the second oxidation process of **SL5** ($E_{\text{ox2}} = +1.32\text{ V vs. NHE}$) occurs at higher potential compared to **SL1** ($E_{\text{ox2}} = +1.05\text{ V vs. NHE}$) and is finally similar to that of **SL3** and **SL4** ($E_{\text{ox2}} = +1.32\text{ V vs. NHE}$).

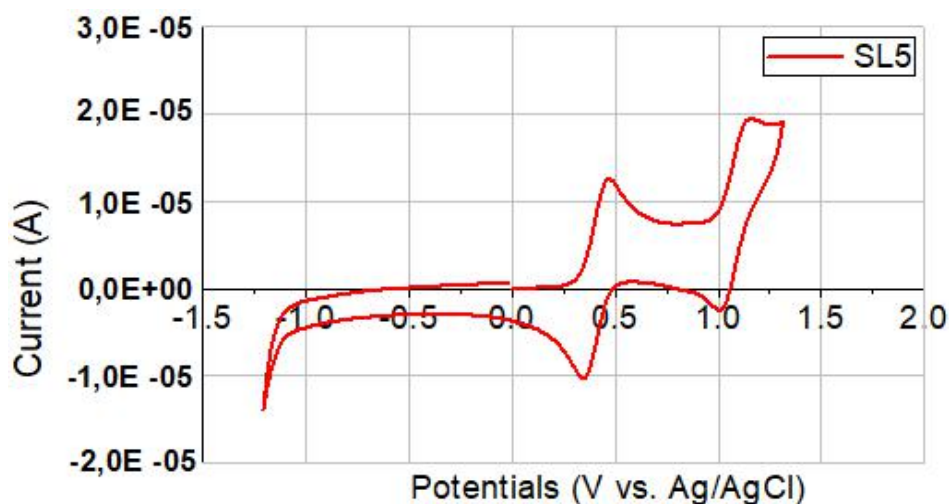


Figure III-19: Cyclic voltammograms of **SL5** recorded in $\text{CH}_2\text{Cl}_2/\text{nBu}_4\text{NPF}_6$ (0.1M) vs. Ag/AgCl at 200 mV s^{-1} .

III.5.3. Theoretical Calculations

Theoretical calculations were also performed to gain more insights into the electronic properties of **SL5**. The spatial representation of the frontier molecular orbitals is shown in Figure III-20. Theoretical calculations reveal that the HOMO of **SL5** is well spread over the extended π -conjugated system from the phosphonic acid anchoring group to the remote end of the molecular backbone, again with a strong contribution of the central $\text{C}\equiv\text{C}-\text{Ru}-\text{C}\equiv\text{C}$ fragment. On the other hand, the LUMO of **SL5** is well localized on the alkyne ligand bearing the electron-withdrawing group. It is worth underlining that the HOMO of **SL5** presents an electronic density coming very close to the surface of NiO which seems favorable to charge transfer process from the semiconducting oxide.

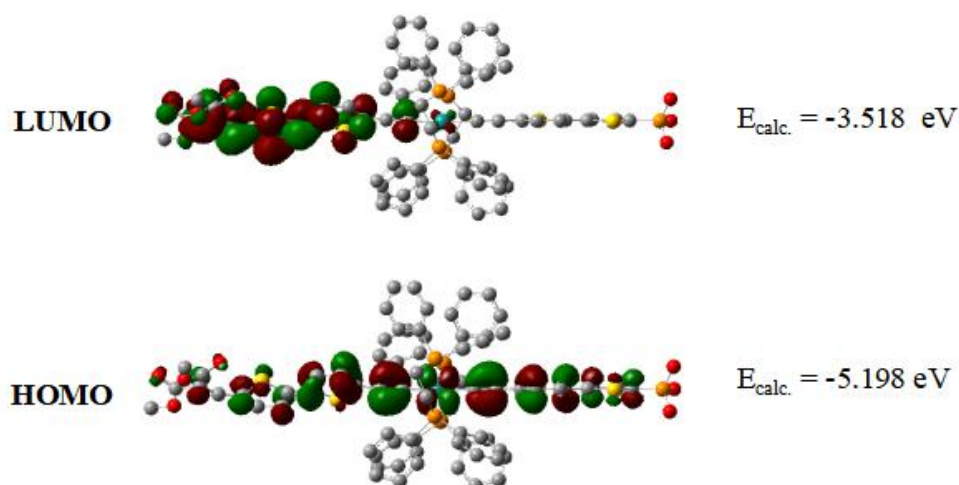


Figure III-20: Electron-density distribution of the frontier molecular orbitals of **SL5**.

III.5.4. Photovoltaic Measurements in p-Type DSCs

The photovoltaic performances of the dye **SL5** were again investigated in sandwich solar cells, in collaboration with Fabrice Odobel, under the conditions described above but also using a new disulfide/thiolate redox couple (T_2/T^-)⁶⁴ (see Experimental part for details).

The photovoltaic parameters of the solar cells are gathered in Table III-7 along with those of **SL1**, **SL3** and **SL4** for comparison.

Table III-7: Photovoltaic characteristics of the dyes **SL1**, **SL3**, **SL4** and **SL5** in p-DSCs recorded under simulated solar spectrum (AM 1.5).

Dye	Electrolyte	J_{sc} ($\text{mA} \cdot \text{cm}^{-2}$)	V_{oc} (mV)	FF (%)	PCE (%)
SL1	I_3^-/I^-	2.50	112	34	0.096
SL3	I_3^-/I^-	1.28	98	31	0.039
SL4	I_3^-/I^-	1.22	90	30	0.033
SL5	I_3^-/I^-	1.59	92	32	0.046
SL5	T_2/T^-	2.40	149	35	0.125

When the iodide/triiodide redox mediator is used, the dye **SL5** shows enhanced photovoltaic performance compared to **SL3** and **SL4**. The higher efficiency observed (PCE = 0.046%) is mainly due to a higher short-circuit photocurrent density ($J_{sc} = 1.59 \text{ mA} \cdot \text{cm}^{-2}$) that can be related to the expected higher dye-loading amount. Here, it is worth mentioning that, although it was not possible to quantify the amount of dye grafted on NiO with **SL5**, the coloration of the NiO-based electrode observed after dye-bath treatment with the phosphonic-acid dye was significantly more intense than with **SL3** and **SL4**.

Yet, the data obtained with **SL5** are lower than those previously obtained with **SL1** with the same electrolyte indicating that other phenomena might hamper the charge injection processes.

On the other hand, it is known that the triiodide/iodide redox couple suffers from two major disadvantages: 1) the electrolytes that contain triiodide/iodide corrode electrical contacts made of silver; 2) the triiodide absorbs visible light resulting in low light-harvesting efficiency.⁶⁴ Thus, the use of the disulfide/thiolate redox couple, that has negligible absorption in the visible spectral range and no corrosion properties, was examined. Moreover, this organic redox couple presents a higher standard potential compared to I_3^-/I^- ($E^\circ = 0.485 \text{ V}^{64}$ vs. $E^\circ = 0.35 \text{ V}^{65}$). This property should help to increase the photovoltage of p-type DSC devices.

Therefore, a novel electrolyte based on the disulfide/thiolate redox couple was employed with **SL5** in order to try to improve the photovoltaic performance of the dye.

Eventually, the p-DSC devices sensitized by **SL5**, combined with disulfide/thiolate-based redox mediator, showed a significantly higher open circuit voltage (V_{oc}) of 149 mV and the best efficiency of the series, PCE = 0.125%.

III.5.5. Conclusions

In this section we have described the synthesis and characterization of a new ruthenium diacetylide complex for p-DSCs. The new dye, featuring the $[Ru(dppe)_2]$ moiety, was endowed with a phosphonic acid anchoring group in the view of improving the density of dye on the photoelectrode. When using the standard iodide/triiodide redox mediator, the efficiency of p-DSC devices sensitized by **SL5** showed better performance in comparison with those sensitized by **SL3** and **SL4** which can be attributed to the enhanced dye loading amount on NiO. Moreover, the p-DSC devices sensitized by **SL5**, combined with a disulfide/thiolate-based electrolyte, eventually showed higher open-circuit photovoltage and the best performance of the series, leading to PCE = 0.125%.

III.6. General Conclusion

In this section we have described the synthesis and characterization of the first ruthenium diacetylide complexes for p-DSCs.

The first two complexes, **SL1** and **SL2**, are endowed with a bidentate anchoring group based on a triphenylamine motif as electron-donating unit (D) and functionalized with an electron-accepting group (A) connected to the $[Ru(dppe)_2]$ metal fragment by a bithiophene linker. Thus simple modification of the alkynyl ligand on the acceptor side allowed easy fine-tuning of the optical properties of the complexes, leading to red and blue dyes featuring strong visible-light absorption properties. Spectroscopic and electrochemical studies of the two dyes further confirmed suitable optical and electronic properties (*i.e.* appropriate energy levels) for use in p-type DSC devices. Additionally, theoretical calculations were performed to rationalize the experimental data. The photovoltaic performance of these dyes were subsequently investigated in NiO-based p-type DSCs, in collaboration with Fabrice Odobel (University of Nantes). Interestingly, although these dyes were not perfectly optimized yet (*i.e.* moderate electron injection driving force) their photovoltaic performances were relatively high compared with other organometallic dyes reported for the same application (*i.e.*

ruthenium polypyridine complexes).²²⁻²⁵ In our study the best performing dye (the red dye **SL1**) afforded photocurrent density of $2.25 \text{ mA} \cdot \text{cm}^{-2}$ and maximum IPCE of 18 %.

These promising results paved the way towards other finely tuned organometallic efficient dyes for such application. We indeed anticipated that much better performing ruthenium diacetylide dyes could be developed by lowering the energy position of their HOMO level in order to enhance electron injection rate from the semiconductor.

Therefore, two novel Ru-based dyes were designed and prepared, in which the electron-donating unit is replaced by a simple phenyl (**SL3**) or thiophene (**SL4**) unit. The two dyes are functionalized with the same electron-withdrawing ligand as **SL1**, the dimethylmalonate group. As expected, the use of less electron-rich units as donors afforded lower HOMO energy levels compared to the dye **SL1**, which was expected to enhance the charge injection rates. However, the efficiencies of the p-DSCs based on the two new dyes **SL3** and **SL4** were lower than those based on **SL1**, which was attributed to lower dye loading amount with the two new dyes.

We therefore looked for better a performing Ru-diacetylide dye by replacing the anchoring function. The phosphonic acid group was chosen for this purpose, in order to improve the density of dye on the photoelectrode. The complex **SL5**, endowed with a phosphonic acid anchoring group on one side, was also functionalized by the dimethylmalonate electron-withdrawing group on the acceptor side. As expected, enhanced dye loading amount on NiO was observed with **SL5**, compared to **SL3** and **SL4**. In p-DSC devices, using the standard iodide/triiodide redox mediator, the dye **SL5** showed slightly enhanced photovoltaic performance compared to **SL3** and **SL4** but lower performance than those obtained with **SL1**. However, the dye **SL5**, combined with a disulfide/thiolate-based electrolyte, eventually showed higher open-circuit photovoltage and the best performance of the series, leading to $\text{PCE} = 0.125\%$.

The good results obtained recently with **SL5** and a disulfide/thiolate-based electrolyte gave us further impetus to design a new Ru-based complex with optimized structure in view of increasing both the dye-loading amount on the electrode and the charge injection rate in p-type DSC devices. The synthesis of this new dye is currently in progress in our group, in collaboration with the group of Fabrice Odobel.

III.7. References

- 1 V. Nikolaou, A. Charisiadis, G. Charalambidis, A. G. Coutsolelos, F. Odobel. Recent advances and insights in dye-sensitized NiO photocathodes for photovoltaic devices. *J. Mater. Chem. A*, **2017**, 5: 21077.
- 2 Z. Yu, F. Li, L. C. Sun. Recent advances in dye-sensitized photoelectrochemical cells for solar hydrogen production based on molecular components. *Energy Environ. Sci.*, **2015**, 8: 760-775.
- 3 F. Odobel, L. L. Pleux, Y. Pellegrin, Errol Blart. New Photovoltaic Devices Based on the Sensitization of p-type Semiconductors: Challenges and Opportunities. *Acc. Chem. Res.*, **2010**, 43, 8: 1063-1071.
- 4 F. Odobel, Y. Pellegrin, E. A. Gibson, A. Hagfeldt, A. L. Smeigh, L. Hammarström. Recent advances and future directions to optimize the performances of p-type dye-sensitized solar cells. *Coord. Chem. Rev.*, **2012**, 256: 2414-2423.
- 5 D. Dini, Y. Halpin, J. G. Vos, E. A. Gibson. The influence of the preparation method of NiO_x photocathodes on the efficiency of p-type dye-sensitized solar cells. *Coord. Chem. Rev.*, **2015**, 304-305: 179-201.
- 6 R. Jose, A. Kumar, V. Thavasi, K. Fujihara, S. Uchida, S. Ramakrishna. Relationship between the molecular orbital structure of the dyes and photocurrent density in the dye-sensitized solar cells. *Appl. Phys. Lett.*, **2008**, 93, 023125: 1-3.
- 7 I. R. Perera, T. Daeneke, S. Makuta, Z. Yu, Y. Tachibana, A. Mishra, P. Bäuerle, C. A. Ohlin, U. Bach, L. Spiccia. Application of the Tris(acetylacetonato)iron(III)/(II) Redox Couple in p-Type Dye-Sensitized Solar Cells. *Angew. Chem., Int. Ed.*, **2015**, 54, 12: 3758-3762.
- 8 M. Weideler, S. Powar, H. Kast, Z. Yu, P. P. Boix, C. Li, K. Müllen, T. Geiger, S. Kuster, F. Nüesch, U. Bach, A. Mishra, P. Bäuerle. Synthesis and Characterization of Organic Dyes with Various Electron-Accepting Substituents for p-Type Dye-Sensitized Solar Cells. *Chem.-Asian J.*, **2014**, 9: 3251-3263.
- 9 A. Nattestad, A. J. Mozer, M. K. R. Fischer, Y. B. Cheng, A. Mishra, P. Baeuerle, U. Bach. Highly efficient photocathodes for dye-sensitized tandem solar cells. *Nature Mater.*, **2010**, 9: 31-35.
- 10 P. Qin, H. Zhu, T. Edvinsson, G. Boschloo, A. Hagfeldt, L. Sun. Design of an Organic Chromophore for P-Type Dye-Sensitized Solar Cells. *J. Am. Chem. Soc.*, **2008**, 130, 27: 8570-8571.
- 11 E. A. Gibson, A. L. Smeigh, L. L. Pleux, J. Fortage, G. Boschloo, E. Blart, Y. Pellegrin, F.

- Odobel, A. Hagfeldt, L. Hammarström. A p-Type NiO-Based Dye-Sensitized Solar Cell with an Open-Circuit Voltage of 0.35 V. *Angew. Chem., Int. Ed.*, **2009**, 48: 4402-4405.
- 12 A. Morandeira, J. Fortage, T. Edvinsson, L. L. Pleux, E. Blart, G. Boschloo, A. Hagfeldt, L. Hammarström, F. Odobel. Improved Photon-to-Current Conversion Efficiency with a Nanoporous p-Type NiO Electrode by the Use of a Sensitizer-Acceptor Dyad. *J. Phys. Chem. C*, **2008**, 112, 5: 1721-1728.
- 13 L. L. Pleux, A. L. Smeigh, E. Gibson, Y. Pellegrin, E. Blart, G. Boschloo, A. Hagfeldt, L. Hammarström, F. Odobel. Synthesis, photophysical and photovoltaic investigations of acceptor-functionalized perylene monoimide dyes for nickel oxide p-type dye-sensitized solar cells. *Energy Environ. Sci.*, **2011**, 4: 2075-2084.
- 14 L. Favereau, J. Warnan, Y. Pellegrin, E. Blart, M. Boujtita, D. Jacquemin, F. Odobel. Diketopyrrolopyrrole derivatives for efficient NiO-based dye-sensitized solar cells. *Chem. Commun.*, **2013**, 49: 8018-8020.
- 15 J. Warnan, J. Gardner, L. L. Pleux, J. Petersson, Y. Pellegrin, E. Blart, L. Hammarström, F. Odobel. Multichromophoric Sensitizers Based on Squaraine for NiO Based Dye-Sensitized Solar Cells. *J. Phys. Chem. C*, **2014**, 118, 1: 103-113.
- 16 C.-H. Chang, Y.-C. Chen, C.-Y. Hsu, H.-H. Chou, J. T. Lin. Squaraine-Arylamine Sensitizers for Highly Efficient p-Type Dye-Sensitized Solar Cells. *Org. Lett.*, **2012**, 14: 4726-4729.
- 17 J.-F. Lefebvre, X.-Z. Sun, J. A. Calladine, M. W. George, E. A. Gibson. Promoting charge-separation in p-type dye-sensitized solar cells using bodipy. *Chem. Commun.*, **2014**, 50: 5258-5260.
- 18 C. J. Wood, G. H. Summers, E. A. Gibson. Increased photocurrent in a tandem dye-sensitized solar cell by modifications in push-pull dye-design. *Chem. Commun.*, **2015**, 51: 3915-3918.
- 19 M. Borgström, E. Blart, G. Boschloo, E. Mukhtar, A. Hagfeldt, L. Hammarström, F. Odobel. Sensitized Hole Injection of Phosphorus Porphyrin into NiO: Toward New Photovoltaic Devices. *J. Phys. Chem. B*, **2005**, 109, 48: 22928-22934.
- 20 H. Tian, J. Oscarsson, E. Gabrielsson, S. K. Eriksson, R. Lindblad, B. Xu, Y. Hao, G. Boschloo, E. M. J. Johansson, J. M. Gardner, A. Hagfeldt, H. Rensmo, L. Sun. Enhancement of p-Type Dye-Sensitized Solar Cell Performance by Supramolecular Assembly of Electron Donor and Acceptor. *Sci. Rep.*, **2014**, 4: 4282.
- 21 A. Maufroy, L. Favereau, F. B. Anne, Y. Pellegrin, E. Blart, M. Hissler, D. Jacquemin, F. Odobel. Synthesis and properties of push-pull porphyrins as sensitizers for NiO based

- dye-sensitized solar cells. *J. Mater. Chem. A*, **2015**, 3: 3908-3917.
- 22 Z. Ji, G. Natu, Z. Huang, O. Kokhan, X. Zhang, Y. Wu. Synthesis, Photophysics, and Photovoltaic Studies of Ruthenium Cyclometalated Complexes as Sensitizers for p-Type NiO Dye-Sensitized Solar Cells. *J. Phys. Chem. C*, **2012**, 116, 32: 16854-16863.
- 23 J. C. Freys, J. M. Gardner, L. D'Amario, A. M. Brown, L. Hammarström. Ru-based donor-acceptor photosensitizer that retards charge recombination in a p-type dye-sensitized solar cell. *Dalton Trans.*, **2012**, 41: 13105-13111.
- 24 Z. Ji, G. Natu, Y. Wu. Cyclometalated Ruthenium Sensitizers Bearing a Triphenylamino Group for p-Type NiO Dye-Sensitized Solar Cells. *ACS Appl. Mater. Interfaces*, **2013**, 5, 17: 8641-8648.
- 25 C. J. Wood, K. C. D. Robson, P. I. P. Elliott, C. P. Berlinguette, E. A. Gibson. Novel triphenylamine-modified ruthenium(II) terpyridine complexes for nickel oxide-based cathodic dye-sensitized solar cells. *RSC Adv.*, **2014**, 4: 5782-5791.
- 26 M. Gennari, F. Légalité, L. Zhang, Y. Pellegrin, E. Blart, J. Fortage, A. M. Brown, A. Deronzier, M.-N. Collomb, M. Boujtita, D. Jacquemin, L. Hammarström, F. Odobel. Long-Lived Charge Separated State in NiO-Based p-Type Dye-Sensitized Solar Cells with Simple Cyclometalated Iridium Complexes. *J. Phys. Chem. Lett.*, **2014**, 5, 13: 2254-2258.
- 27 A. Sinopoli, F. A. Black, C. J. Wood, E. A. Gibson, P. I. P. Elliott. Investigation of a new bis(carboxylate)triazole-based anchoring ligand for dye solar cell chromophore complexes. *Dalton Trans.*, **2017**, 46: 1520-1530.
- 28 W. M. Campbell, A. K. Burrell, D. L. Officer, K. W. Jolley. Porphyrins as light harvesters in the dye-sensitised TiO₂ solar cell. *Coord. Chem. Rev.*, **2004**, 248: 1363-1379.
- 29 T. Higashino, H. Imahori. Porphyrins as excellent dyes for dye-sensitized solar cells: recent developments and insights. *Dalton Trans.*, **2015**, 44: 448-463.
- 30 M. V. Martínez-Díaz, G. D. L. Torre, T. Torres. Lighting porphyrins and phthalocyanines for molecular photovoltaics. *Chem. Commun.*, **2010**, 46: 7090-7108.
- 31 M. J. Griffith, K. Sunahara, P. Wagner, K. Wagner, G. G. Wallace, D. L. Officer, A. Furube, R. Katoh, S. Mori, A. J. Mozer. Porphyrins for dye-sensitised solar cells: new insights into efficiency-determining electron transfer steps. *Chem. Commun.*, **2012**, 48: 4145-4162.
- 32 L.-L. Li, E. W.-G. Diau. Porphyrin-sensitized solar cells. *Chem. Soc. Rev.*, **2013**, 42: 291-304.
- 33 G. Bottari, O. Trukhina, M. Ince, T. Torres. Towards artificial photosynthesis:

- Supramolecular, donor-acceptor, porphyrin- and phthalocyanine/carbon nanostructure ensembles. *Coord. Chem. Rev.*, **2012**, 256: 2453-2477.
- 34 M. K.Panda, K. Ladomenou, A. G. Coutsolelos. Porphyrins in bio-inspired transformations: Light-harvesting to solar cell. *Coord. Chem. Rev.*, **2012**, 256: 2601-2627.
- 35 J. He, H. Lindström, A. Hagfeldt, S.-E. Lindquist. Dye-Sensitized Nanostructured p-Type Nickel Oxide Film as a Photocathode for a Solar Cell. *J. Phys. Chem. B*, **1999**, 103, 42: 8940-8943.
- 36 H. Lu, J. Mack, Y. Yang, Z. Shen. Structural modification strategies for the rational design of red/NIR region BODIPYs. *Chem. Soc. Rev.*, **2014**, 43: 4778-4823.
- 37 K. Ladomenou, V. Nikolaou, G. Charalambidis, A. Charisiadis, A. G. Coutsolelos. Porphyrin-BODIPY-based hybrid model compounds for artificial photosynthetic reaction centers. *C. R. Chim.*, **2017**, 20, 3: 314-322.
- 38 H. Lu, J. Mack, T. Nyokong, N. Kobayashi, Z. Shen. Optically active BODIPYs. *Coord. Chem. Rev.*, **2016**, 318: 1-15.
- 39 C. Li, H. Wonneberger. Perylene Imides for Organic Photovoltaics: Yesterday, Today, and Tomorrow. *Adv. Mater.*, **2012**, 24: 613-636.
- 40 F. Würthner. Perylene bisimide dyes as versatile building blocks for functional supramolecular architectures. *Chem. Commun.*, **2004**, 0: 1564-1579.
- 41 D. Gosztola, M. P. Niemczyk, W. Svec, A. S. Lukas, M. R. Wasielewski. Excited Doublet States of Electrochemically Generated Aromatic Imide and Diimide Radical Anions. *J. Phys. Chem. A*, **2000**, 104, 28: 6545-6551.
- 42 S. Chen, P. Slattum, C. Wang, L. Zang. Self-Assembly of Perylene Imide Molecules into 1D Nanostructures: Methods, Morphologies, and Applications. *Chem. Rev.*, **2015**, 115, 21: 11967-11998.
- 43 L. Li, E. A. Gibson, P. Qin, G. Boschloo, M. Gorlov, A. Hagfeldt, L. Sun. Double-Layered NiO Photocathodes for p-Type DSSCs with Record IPCE. *Adv. Mater.*, **2010**, 22: 1759-1762.
- 44 B. Jin, W. Wu, X. Zhang, F. Guo, Q. Zhang, J. Hua. New Pyridine-anchoring Dyes for p-Type Dye-sensitized Solar Cells. *Chem. Lett.*, **2013**, 42: 1271-1272.
- 45 A. Nattestad, M. Ferguson, R. Kerr, Y.-B. Cheng, U. Bach. Dye-sensitized nickel(II)oxide photocathodes for tandem solar cell applications. *Nanotechnology*, **2008**, 19, 295304.
- 46 L. Duan, L. Wang, F. Li, F. Li, L. Sun. Highly Efficient Bioinspired Molecular Ru Water Oxidation Catalysts with Negatively Charged Backbone Ligands. *Acc. Chem. Res.*, **2015**, 48, 7: 2084-2096.

-
- 47 H. Li, F. Li, B. Zhang, X. Zhou, F. Yu, L. Sun. Visible Light-Driven Water Oxidation Promoted by Host-Guest Interaction between Photosensitizer and Catalyst with A High Quantum Efficiency. *J. Am. Chem. Soc.*, **2015**, 137, 13: 4332-4335.
- 48 G. C. Vougioukalakis, A. I. Philippopoulos, T. Stergiopoulos, P. Falaras. Contributions to the development of ruthenium-based sensitizers for dye-sensitized solar cells. *Coord. Chem. Rev.*, **2011**, 255: 2602-2621.
- 49 K. Kalyanasundaram, M. Grätzel. Applications of functionalized transition metal complexes in photonic and optoelectronic devices. *Coord. Chem. Rev.*, **1998**, 177: 347-414.
- 50 S. D. Sousa, L. Ducasse, B. Kauffmann, T. Toupance, C. Olivier. Functionalization of a Ruthenium-Diacetylde Organometallic Complex as a Next-Generation Push-Pull Chromophore. *Chem. Eur. J.*, **2014**, 20: 7017-7024.
- 51 S. D. Sousa, S. Lyu, L. Ducasse, T. Toupance, C. Olivier. Tuning visible-light absorption properties of Ru-diacetylde complexes: simple access to colorful efficient dyes for DSSCs. *J. Mater. Chem. A*, **2015**, 3: 18256-18264.
- 52 S. Lyu, C. Bertrand, T. Hamamura, L. Ducasse, T. Toupance, C. Olivier. Molecular engineering of Ruthenium-diacetylde organometallic complexes towards efficient green dye for DSSC. *Dye and Pigments*, **2018**, 158: 326-333..
- 53 F. Odobel, Y. Pellegrin, F. B. Anne and D. Jacquemin, Molecular engineering of efficient dyes for p-type semiconductor sensitization, in *High-Efficiency Solar Cells - Physics, Materials and Devices*, ed. Z. M. W. A. X. Wang, Springer, **2013**.
- 54 C. Olivier, B. Kim, D. Touchard, S. Rigaut. Redox-Active Molecular Wires Incorporating Ruthenium(II) σ -Arylacetylde Complexes for Molecular Electronics. *Organometallics*, **2008**, 27, 4: 509-518.
- 55 R. F. Winter, K.-W. Klinkhammer, S. Zálíš. Ruthenium-Aminoallenylidene Complexes from Butatrienylydene Intermediates via an Aza-Cope Rearrangement: Synthetic, Spectroscopic, Electrochemical, Spectroelectrochemical, and Computational Studies. *Organometallics*, **2001**, 20, 7: 1317-1333.
- 56 D. P. Hagberg, J.-H. Yum, H. Lee, F. D. Angelis, T. Marinado, K. M. Karlsson, R. Humphry-Baker, L. Sun, A. Hagfeldt, M. Grätzel, M. K. Nazeeruddin. Molecular Engineering of Organic Sensitizers for Dye-Sensitized Solar Cell Applications. *J. Am. Chem. Soc.*, **2008**, 130, 19: 6259-6266.
- 57 M. Weidelener, A. Mishra, A. Nattestad, S. Powar, A. J. Mozer, E. Mena-Osteritz, Y.-B. Cheng, U. Bach, P. Bäuerle. Synthesis and characterization of perylene-bithiophene-
-

- triphenylamine triads: studies on the effect of alkyl-substitution in p-type NiO based photocathodes. *J. Mater. Chem.*, **2012**, 22: 7366-7379.
- 58 Z. Liu, W. L. S. Topa, X. Xu, X. Zeng, Z. Zhao, M. Wang, W. Chen, F. Wang, Y.-B. Cheng, H. He. Fine Tuning of Fluorene-Based Dye Structures for High-Efficiency p-Type Dye-Sensitized Solar Cells. *ACS Appl. Mater. Interfaces*, **2014**, 6, 13: 10614-10622.
- 59 D. Ameline, S. Diring, Y. Farre, Y. Pellegrin, G. Naponiello, E. Blart, B. Charrier, D. Dini, D. Jacquemin, F. Odobel. Isoindigo derivatives for application in p-type dye sensitized solar cells. *RSC Adv.*, **2015**, 5: 85530-85539.
- 60 Y.-S. Yen, W.-T. Chen, C.-Y. Hsu, H.-H. Chou, J. T. Lin, M.-C. P. Yeh. Arylamine-Based Dyes for p-Type Dye-Sensitized Solar Cells. *Org. Lett.*, **2011**, 13, 18: 4930-4933.
- 61 Z. Liu, D. Xiong, X. Xu, Q. Arooj, H. Wang, L. Yin, W. Li, H. Wu, Z. Zhao, W. Chen, M. Wang, F. Wang, Y.-B. Cheng, H. He. Modulated Charge Injection in p-Type Dye-Sensitized Solar Cells Using Fluorene-Based Light Absorbers. *ACS Appl. Mater. Interfaces*, **2014**, 6, 5: 3448-3454.
- 62 T. Daeneke, Z. Yu, G. P. Lee, D. Fu, N. W. Duffy, S. Makuta, Y. Tachibana, L. Spiccia, A. Mishra, P. Bäuerle, U. Bach. Dominating Energy Losses in NiO p-Type Dye-Sensitized Solar Cells. *Adv. Energy Mater.*, **2015**, 5, 4: 1401387.
- 63 S. Lyu, Y. Farré, L. Ducasse, Y. Pellegrin, T. Toupance, C. Olivier, F. Odobel. Push-pull ruthenium diacetylide complexes: new dyes for p-type dye-sensitized solar cells. *RSC Adv.*, **2016**, 6: 19928-19936.
- 64 M. Wang, N. Chamberland, L. Breau, J.-E. Moser, R. Humphry-Baker, B. Marsan, S. M. Zakeeruddin, M. Grätzel. An organic redox electrolyte to rival triiodide/iodide in dye-sensitized solar cells. *Nature Chem.*, **2010**, 2: 385-389.
- 65 A. Hagfeldt, G. Boschloo, L. C. Sun, L. Kloo, H. Pettersson. Dye-sensitized Solar Cells. *Chem. Rev.*, **2010**, 110: 6595-6663.

**Chapter IV:
Organometallic Ruthenium Complexes for
NiO Sensitization and Photoelectrochemical
Applications**

IV.1. General Introduction

The development of renewable energies is a major issue to be addressed in response to the problem of profuse and environmentally friendly energy for large-scale sustainable development. A realistic energy conversion method is the use of efficient catalytic systems that can convert the energy of the sun into storable chemical fuels by splitting water into oxygen and hydrogen.¹ In particular, hydrogen presents many advantages of being produced and used as a 'solar fuel',²⁻⁴ *e.g.* it shows a high heat of combustion and can be used in fuel cells that produce a harmless combustion product, that is water.⁵ Moreover, the use of hydrogen limits the use of fossil fuels and subsequent emissions of greenhouse gases. For all these reasons, a strong incentive remains for the development of new molecular synthetic systems able to convert the solar energy into chemical fuels. For this purpose efficient catalytic systems were reported for the photogeneration of hydrogen by molecular triads using dye/catalyst molecular assemblies in association with a sacrificial electron donor (SED) such as triethylamine (TEA) or triethanolamine (TEOA) in aqueous solutions.⁶⁻⁹ Here it is worth mentioning that efficient molecular catalysts for light-driven H₂ production are mostly based on cobalt complexes or other earth-abundant metals like nickel or iron.¹⁰⁻¹³ In particular, among cobalt-based H₂-evolving catalysts, cobaloximes are candidates of choice for both efficiency and stability reasons.^{6-9,14,15} A more recent approach to convert sunlight into chemical fuel consists in building photoelectrocatalytic systems where the SED is replaced by a wide band gap semiconductor.¹⁶ For instance, the use of NiO-based photocathodes to construct dye-sensitized photoelectrochemical cells (DSPECs) sparks growing interest in the research field of solar fuel production. Thus, several examples of molecular photocatalytic H₂-evolving systems were reported for use in combination with NiO. Different strategies were developed such as a bimolecular dye/catalyst system where the dye is grafted on NiO and combined with a non-coordinated catalyst in solution,¹⁷ co-grafted bimolecular dye/catalyst systems¹⁸⁻²⁰ or layer-by-layer assembly of a dye/catalyst system on NiO electrode.²¹ Besides, a mono-molecular photocatalytic system was described involving axial coordination of the cobalt catalyst by the dye.²²

In this chapter, several representative dyes utilized in NiO-based DSPECs are reviewed. Then, our work dealing with the design and synthesis of innovative Ru-based alkynyl-allenylidene organometallic dyes and a pyridyl-functionalized Ru-diacetylide photosensitizer are described in section IV.3. and IV.4., respectively. Optical and electrochemical properties, theoretical calculations as well as photoelectrochemical properties of the organic-inorganic hybrid systems based on these novel dyes are then discussed.

IV.2. Sensitizers Utilized in NiO-Based DSPECs for Solar Hydrogen Production

Photocathodes are the key components of DSPECs, the fabrication of which is feasible by dye-sensitization of wide-band-gap p-type semiconductor oxides to drive proton reduction reactions in water splitting cells.^{23,24} Apart from the mentioned properties in section III.1. that a dye in p-DSCs should possess, the dye should also fulfil some general requirements to make functional dye-sensitized photocathodes in DSPEC devices. On one hand, the HOMO level of the dye should be more positive than the valence band position of the p-type semiconductor to facilitate efficient hole transfer after photoexcitation. On the other hand, the LUMO level of the dye should be more negative than the operation potential of the catalyst. In addition, in DSPEC devices the dyes should be strongly attached on the electrode, making it more difficult for the aqueous or the acidic media to wash the dyes off the semiconductor surface.^{1,10,16,23,24} Figure IV-1a²³ and IV-1b²⁴ show the working principle of DSPEC based on NiO photocathodes and the energy diagram of a dye-sensitized photocathode in a DSPEC, respectively.

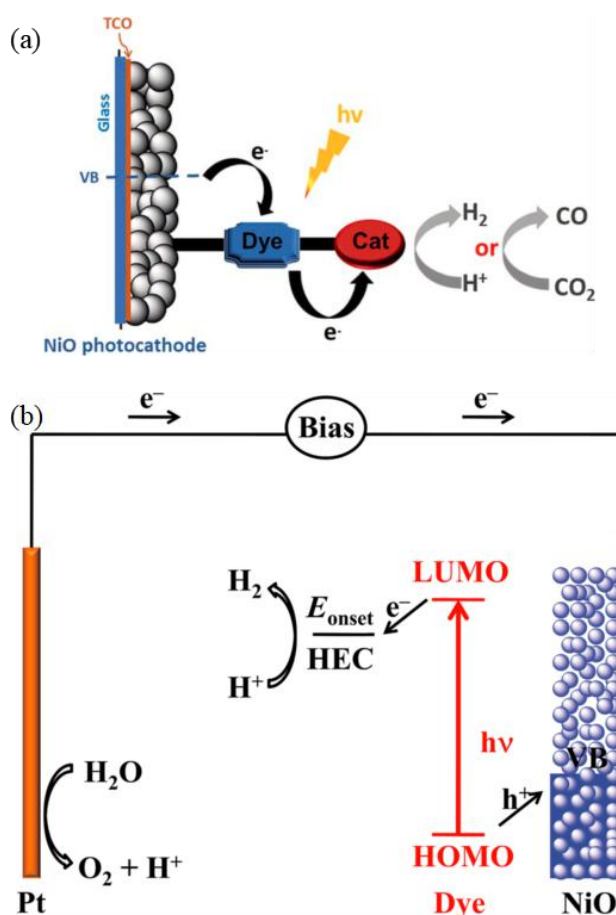


Figure IV-1: (a) Operation principle of DSPEC based on NiO photocathodes. Cat = catalyst;²³ (b)

Energy diagram of a dye-sensitized photocathode in a DSPEC. E_{onset} : the catalytic onset reduction potential of the H_2 -evolving catalyst for proton reduction.²⁴

There are three possible configuration types which are generally employed to combine a dye and a catalyst in DSPECs, as shown in Figure IV-2.²³ In the first configuration type, the catalyst is either dissolved in the reaction medium, or deposited onto the already chemisorbed dye on the surface of NiO.^{17,18,25-27} The second approach is to co-adsorb both the dye and catalyst onto the surface of NiO.^{28,29} The catalyst in this simple configuration type should be functionalized with an anchoring group. In the last strategy, the catalyst is covalently linked to the dye,³⁰⁻³³ which is our approach to design the dye **SL7** for DSPECs (see the section IV.4.). Despite its more challenging synthetic routes, the last configuration type usually provides higher overall efficiency due to the slower charge recombination reaction, the greater quantum yield for electron transfer (from the reduced dye to the catalyst) and the higher molecular organization on the surface of the NiO.²³

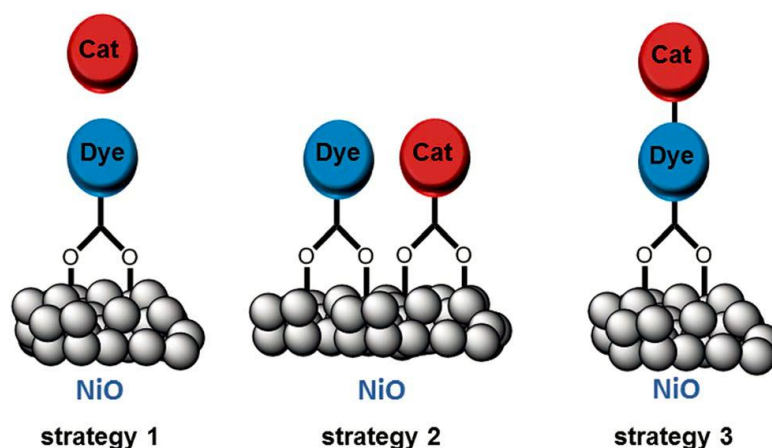


Figure IV-2: Schematic representation of the three possible configuration types that are generally employed to combine a sensitizer with a catalyst in DSPEC.²³

Some representative dyes utilized in NiO-based DSPECs for light-driven H_2 production are shown in Figure IV-3. In 2012, L. Sun *et al.* reported the first example of dye-sensitized photocathode for hydrogen generation.¹⁷ The photocathode was composed of a nano-structured NiO film sensitized with an organic D- π -A dye (see Figure IV-3, dye 115), which was then coupled with a molecular H_2 -evolving catalyst $\text{Co}(\text{dmgBF}_2)_2(\text{H}_2\text{O})_2$ (where dmgBF_2 is difluoroboryldi-methylglyoximate anion). They found that the decomposition and/or leaching of the catalyst from the electrode surface were a major reason for the photocurrent decay. In the same year, L. Hammarström *et al.* reported the first evidence of

electron transfer from the photoreduced sensitizer Coumarin-343 (see Figure IV-3, dye 116) to a proton-reducing catalyst, both bound on the surface of NiO.²⁹ Later in 2016, they prepared a photoelectrochemical device based on a photocathode, which was composed of mesoporous NiO films sensitized by the dye 116 and coupled with an iron benzene dithiolate catalyst, producing H₂ with a Faradaic efficiency of ~ 50%.²⁸ In 2013, Y. Wu *et al.* reported a photostable p-type NiO photocathode based on a bifunctional cyclometalated ruthenium sensitizer (see Figure IV-3, dye 117) and a cobaloxime catalyst for visible-light-driven water reduction to produce H₂.²² They found that the dye 117 can bind strongly to NiO in the presence of neutral water and pH 7 buffer solutions. The unprecedented stability of this photocathode was important for the practical application in solar fuel production. In 2014, L. Sun *et al.* reported for the first time a Pt-free tandem molecular photoelectrochemical cell based on the dye [Ru(bpy)₂(4,4'-(PO₃H₂)₂bpy)]²⁺ (see Figure IV-3, dye 118) with molecular Ru- and Co-catalysts immobilized on the photoanode and photocathode respectively, and successfully obtained visible light driven water splitting under pH neutral conditions.¹⁹ In 2015, F. Odobel *et al.* also reported the photoelectrochemical activity of a mesoporous NiO electrode sensitized by the dye 118 with several rhodium and cobalt H₂-evolving catalysts.²⁵ In 2016, E. Reisner *et al.* described a dye-sensitized p-type NiO-based photocathode with a hexaphosphonated Ru(2,2'-bipyridine)₃ based dye (see Figure IV-3, dye 119) and a tetraphosphonated molecular [Ni(P₂N₂)₂]²⁺ type proton reduction catalyst for the photoreduction of aqueous protons to H₂.²¹ In this study, a layer-by-layer deposition approach was employed, using Zr⁴⁺ ions to link the phosphonate units in the dye 119 and the catalyst in a supramolecular assembly on the NiO photocathode. This approach kept the dye in close proximity to the catalyst and semiconductor surface, but spatially separated the catalyst from NiO for advantageous electron transfer dynamics. Y. Wu *et al.* developed the use of an organic donor-acceptor dye (see Figure IV-3, dye 120) which prevented both dye desorption and semiconductor degradation by mimicking the hydrophobic/hydrophilic properties of lipid bilayer membranes.²⁷ The dual-functional dye 120 allowed for efficient light harvesting while also protecting the NiO surface from protons and water via its hydrophobic π linker, which therefore resulted in excellent stability in extremely acidic (pH 0) conditions. V. Artero *et al.* reported the first noble-metal free and covalent dye-catalyst assembly able to achieve photoelectrochemical visible light-driven H₂ evolution in mildly acidic aqueous conditions when grafted onto p-type NiO electrode substrate (see Figure IV-3, dye 121).³⁰ In this study, the cografting of chenodeoxycholic acid in DSPECs was found to have a strong positive influence on the photocurrent stability. In 2017, M. Chavarot-Kerlidou *et al.* reported three

different ruthenium dyes bearing either two or four methylphosphonate anchoring groups and either a bipyridine or a dipyrrophenazine ancillary ligand for solar fuel production in DSPECs (see Figure IV-3, dyes 118, 122 and 123).²⁶ They found that increasing the number of anchoring groups from two to four was beneficial for the grafting efficiency. In addition, the transient absorption study revealed that the presence of two charge recombination pathways for each of the sensitizers and evidenced a stabilized charge separated state in the dipyrrophenazine derivative, supporting its superior photoelectrochemical activity.

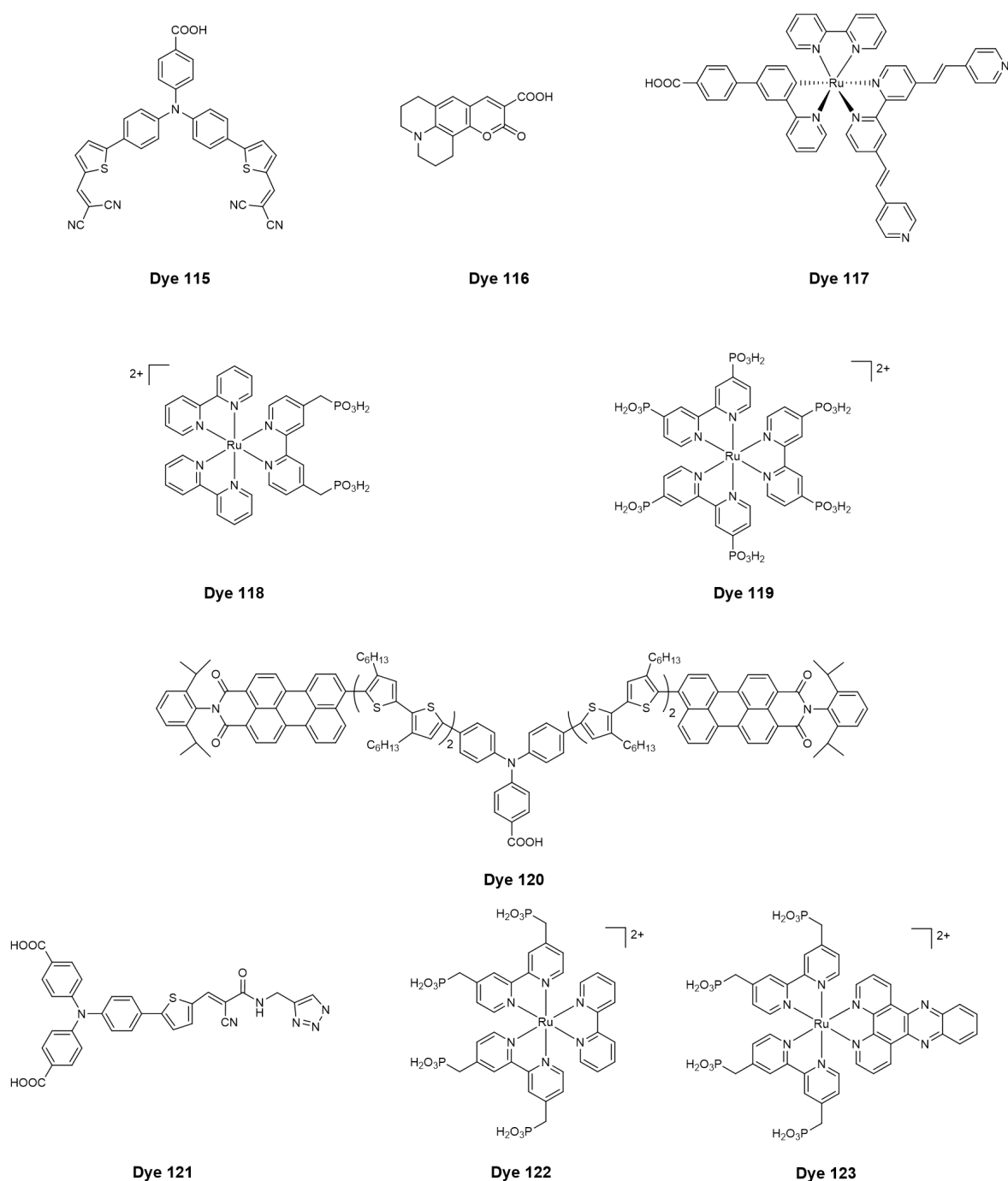


Figure IV-3: Some representative dyes utilized in NiO-based DSPECs for light-driven H₂ production.

Overall, the design of photocathodes for DSPECs has derived from the dyes used in p-type DSCs and is still in its early stage. The conditions for the efficient conversion of solar energy for hydrogen production from water splitting still need to be optimized. The enhancement of stability of the photosensitizers adsorbed onto NiO semiconductor surface for light-driven H₂ production when immersed in aqueous and acidic medium still remains full of challenges.

IV.3. Organometallic Dyes for NiO Sensitization and Photoelectrochemical Applications

In analogy to p-type DSCs,^{23,24,34,35} NiO-based photocathodes have been obtained by sensitization of nanostructured thin films with organic or metallo-organic dyes, thus displaying photoelectrochemical activity in aqueous media.^{17-19,22,36-38} In such photocathodes the dye plays a crucial role in the sunlight harvesting and the inception of electron-transfer processes. In this section, we focus on the design and preparation of innovative dye structures with suitable redox properties for this purpose. The dyes obtained were further implemented in NiO-based photocathodes and tested as photocurrent generators under pertinent aqueous conditions in association with an irreversible electron acceptor (IEA).

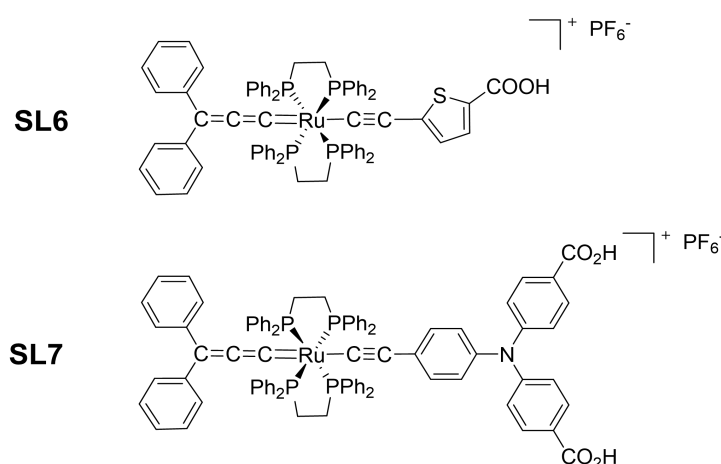


Figure IV-4: Molecular structures of the dyes SL6 and SL7.

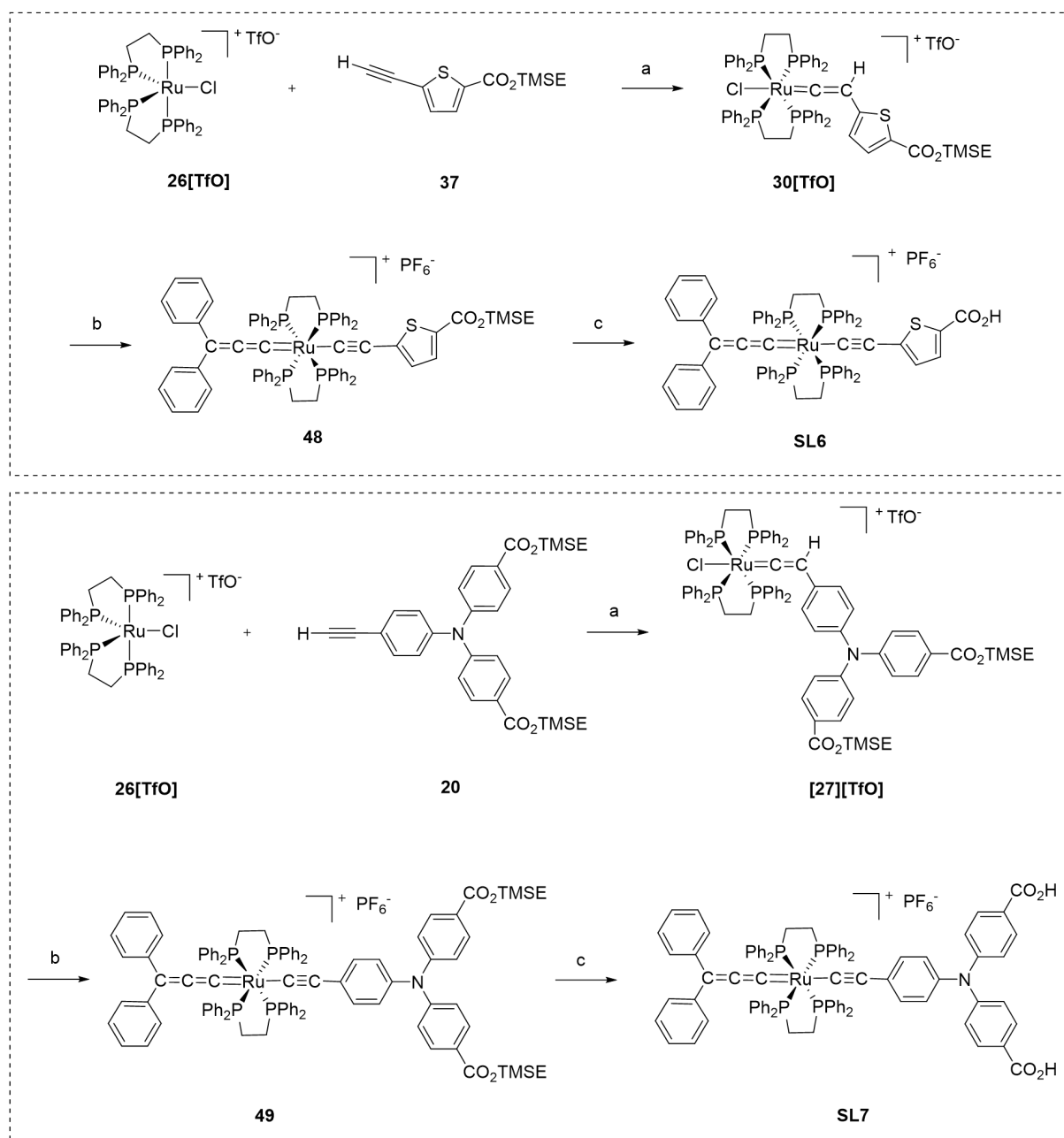
On the basis of our previous work about the preparation and study of asymmetric Ru-diacetylide complexes as efficient photosensitizers for TiO₂ in n-DSCs^{39,40} and for NiO in p-DSCs,⁴¹ we searched for a new dye design for DSPECs. Besides, another type of

organometallic complexes containing the $[\text{Ru}(\text{dppe})_2]$ core has been reported before, namely mixed alkynyl-allenylidene complexes.^{42,43} Such highly conjugated architectures intrinsically present excellent visible-light absorption properties over a broad wavelength range and low bandgap energy. Accordingly, the dyes targeted in this section present the mixed alkynyl-allenylidene structure as shown in Figure IV-4. In addition to the electron-rich $[\text{Ru}(\text{dppe})_2]$ metal centre, the photosensitizer **SL6** presents an electron-donating thiophene ring equipped with one carboxylic acid anchoring function while the dye **SL7** presents two carboxylic acid functions on a triphenylamine motif. The optical and electronic properties of the two dyes were characterized, showing that mixed alkynyl-allenylidene ruthenium complexes are promising sensitizers for NiO with the aim of producing stable photoelectrochemical systems.

IV.3.1. Synthesis of the Dyes **SL6** and **SL7**

The synthetic route towards the new dyes **SL6** and **SL7** is depicted in Scheme IV-1. The synthesis of the alkynyl ligands bearing the anchoring groups involved a Sonogashira coupling reaction of appropriate halogenated precursors with trimethylsilylacetylene and subsequent deprotection of the terminal alkyne. The carboxylic acid anchoring functions were endowed with a silyl-ester protecting group, *i.e.* 2-(trimethylsilyl)ethyl (TMSE), in order to avoid side reactions with the metal centre during the following reaction steps towards organometallic complexes. Thus, according to the general procedure previously described for the synthesis of $[\text{Ru}(\text{dppe})_2]$ metal complexes,⁴³ activation of the terminal alkynes **37** or **20** by the 16-electron species $[\text{RuCl}(\text{dppe})_2][\text{TfO}]$ (**26[TfO]**) led to the corresponding stable ruthenium-vinylidene moieties **30[TfO]** and **27[TfO]**. Subsequent reaction of the latter with a slight excess of propargyl-alcohol $\text{HC}\equiv\text{C}-\text{CPh}_2\text{OH}$, in the presence of a non-coordinating salt (NaPF_6) and a base (Et_3N), allowed substitution of the chlorine atom on the $[\text{Ru}(\text{dppe})_2]$ core and introduction of the second carbon-rich chain. Spontaneous dehydration of the alkynol ligand under these reaction conditions led to the cumulenic chain $=\text{C}=\text{C}=\text{CPh}_2$, thus affording the dye precursors **48** and **49**. Final deprotection of the silyl-ester group(s) under mild conditions, using tetrabutyl ammonium fluoride in THF at room temperature, afforded the targeted dyes **SL6** and **SL7** in good yields. All the organometallic complexes were characterized by means of ^{31}P , ^1H and ^{13}C NMR, HR-MS and FTIR. The *trans*-ditopic structure of the ruthenium center in **SL6** and **SL7** was first confirmed by ^{31}P NMR spectra, which showed a singlet for the four equivalent phosphorus atoms, with $\delta \approx 43$ ppm being

characteristic of the mixed Ru-alkynyl-allenylidene structure.^{42,43} The presence of an allenylidene carbon-rich chain was also evidenced by characteristic ¹³C NMR signals at $\delta \approx 316$ (C_α), 212 (C_β) and 162 (C_γ) ppm and by a typical intense vibration stretch ($\nu_{C=C=C}$) in the FT-IR spectra at ~ 1917 cm^{-1} . A less intense vibration stretch, characteristic of the alkynyl ligand ($\nu_{C\equiv C}$), was also observed in the FT-IR spectra at ~ 2063 cm^{-1} .



Scheme IV-1: Synthetic routes to **SL6** and **SL7**. Conditions: (a) CH_2Cl_2 ; (b) diphenyl-2-propyn-1-ol, NaPF_6 , Et_3N , CH_2Cl_2 ; (c) tetrabutylammonium fluoride, THF.

IV.3.2. Crystallographic Study

Good quality crystals were obtained by slow diffusion of pentane into a concentrated solution of complex **48** in CH₂Cl₂ solution. The crystal structure of **48** was thus resolved by X-ray diffraction analyses. Figure IV-5 shows the cationic organometallic unit from different views along with an appending triflate anion. The crystallographic data are detailed in the Experimental Part. The crystal structure of **48** confirms the *trans* position of the two carbon-rich ligands with regard to the metal centre, providing a linear arrangement of the carbon chains with a C_α-Ru-C'_α angle of 179.1(7)°. The linearity of the chains extends well beyond, over 9.27 Å from C_γ to C'_γ, with a C_γ-Ru-C'_γ angle of 178.7(2)°. The different bond lengths are consistent with the presence of a cumulenenic chain on one side and an alkynyl chain on the other side.⁴² The corresponding distances are 1.933, 1.261 and 1.364 for Ru-C_α, C_α-C_β and C_β-C_γ of the allenylidene ligand, and 2.081, 1.197 and 1.436 for Ru-C'_α, C'_α-C'_β and C'_β-C'_γ of the acetylide ligand. Note that the Ru-C_α distance is longer in the alkynyl chain than that in the cumulenenic one, and conversely C_α-C_β is much shorter in the alkynyl ligand, thus presenting a strong C≡C character. The crystal structure also shows how the metal atom and linked carbon chains are surrounded by the diphosphine ligands, which shelter the central π-conjugated system and, through their bulkiness, cause a de-aggregating effect.

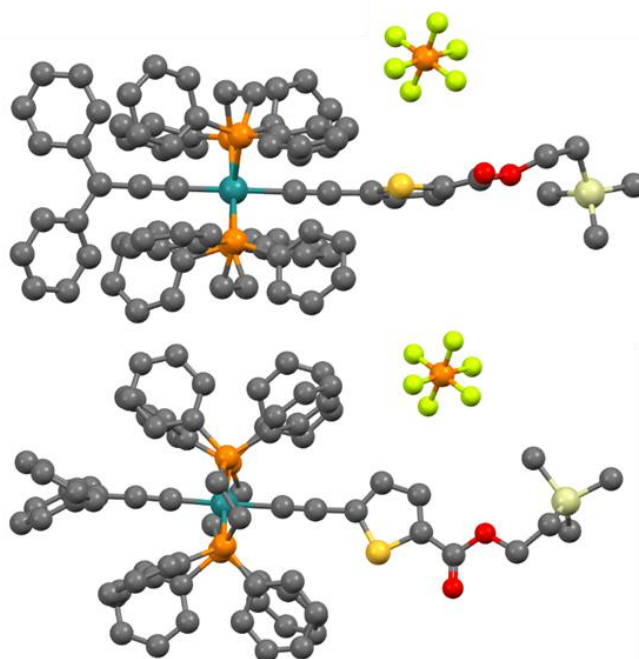


Figure IV-5: Crystal structure of **48** (top and side views). Proton and solvent molecules were removed for clarity.

IV.3.3. Optical and Electrochemical Properties

UV-visible electronic absorption spectra of the dyes, recorded in dichloromethane solution, are presented in Figure IV-6 and the corresponding data are gathered in Table IV-1. In these spectra, intense absorption bands are observed in the UV region, below 300 nm, corresponding to the $n \rightarrow \pi^*$ and $\pi \rightarrow \pi^*$ transitions characteristic of the dppe ligands.⁴⁴ The spectra also show intense absorption bands at intermediate energy with the maximum wavelength centred at 340-350 nm. These bands are tentatively attributed to transitions involving the electron-rich alkynyl ligand. The polyaromatic triphenylamine motif provides a twice more intense band ($\epsilon = 41\,000\text{ M}^{-1}\text{ cm}^{-1}$) compared to the thiophene ring ($\epsilon = 20\,100\text{ M}^{-1}\text{ cm}^{-1}$). More interestingly, the spectra of both dyes show a very broad absorption band in the visible region with the maximum wavelength located at $\lambda_{\text{max}} \approx 600\text{ nm}$ and $\epsilon \approx 12\,000\text{ M}^{-1}\text{ cm}^{-1}$. In mono-allenylidene metal complexes the transition in the visible region possesses a metal-ligand charge transfer (MLCT) character of the type $\text{Ru}^{\text{II}}(\text{d}\pi) \rightarrow \pi^*(\text{allenylidene})$.⁴⁵ Similarly, the broad absorption observed for **SL6** and **SL7** in the visible region is expected to arise from the allowed transition from one of the metal-based orbitals (HOMO) to the allenylidene-ligand-based LUMO.

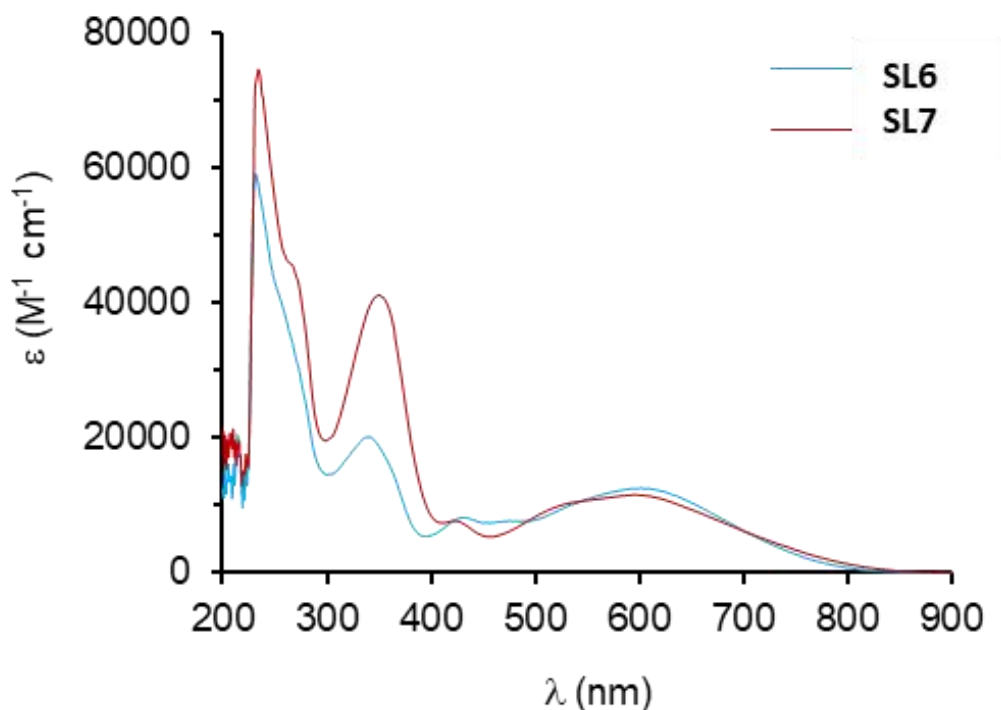


Figure IV-6: Absorption spectra of **SL6** (blue line) and **SL7** (red line) in CH_2Cl_2 ($C \sim 3 \times 10^{-5}\text{ M}$; optical pathway 1 cm).

Table IV-1: Optical and electrochemical properties.

Dye	λ_{\max} (nm)	ϵ (M ⁻¹ cm ⁻¹)	E_{0-0} ^a eV	E_{Red} ^b V	E_{LUMO} ^c / V vs. NHE	E_{LUMO} ^d eV	E_{HOMO} ^e /V vs. NHE	E_{HOMO} ^f eV
SL6	602	12 500	1.58	-0.99	-0.46	-4.11	+1.12	-5.69
	340	20 100						
SL7	598	11 500	1.53	-0.89	-0.36	-4.21	+1.17	-5.74
	350	41 000						

Absorption spectra and cyclic voltammograms were recorded in CH₂Cl₂. ^a 0-0 transition energy estimated from the onset of the absorption spectra. ^b Reduction potential in V vs. Fc⁺/Fc. ^c Estimated LUMO level in V vs. NHE, obtained from the reduction potential considering $E^{\circ}_{(\text{Fc}^+/\text{Fc})} = +0.53$ V vs. NHE.^{37,46} ^d Estimated LUMO energy in eV, considering $E^{\circ}_{(\text{Fc}^+/\text{Fc})} = -5.1$ eV.⁴⁷ ^e Estimated HOMO level in V vs. NHE, obtained from $E_{\text{LUMO}} + E_{0-0}$. ^f Estimated HOMO energy in eV, obtained from $E_{\text{LUMO}} - E_{0-0}$.

Cyclic voltammetry analyses of the organometallic complexes were performed in dichloromethane solution; the corresponding data are reported in Table IV-1. The cationic allenylidene-acetylide complexes show a well-defined reversible mono-electronic wave located at -0.99 V and -0.89 V vs. Fc⁺/Fc for **SL6** and **SL7**, respectively. This electronic process is ascribed to the reduction of the cumulenlic ligand.⁴³ Assuming that these potentials are not significantly affected when shifting from dichloromethane to acetonitrile⁴⁸ and considering that $E^{\circ}_{(\text{Fc}^+/\text{Fc})} = +0.53$ V vs. NHE in CH₃CN,^{37,46} we could estimate the LUMO energy levels of the dyes to be -4.11 eV and -4.21 eV for **SL6** and **SL7**, respectively.

The HOMO energy level was calculated accordingly by subtracting the optical bandgap energy from the LUMO energy, $E_{\text{HOMO}} = E_{\text{LUMO}} + E_{0-0}$. The HOMO energy was therefore estimated to be *ca.* -5.7 eV for **SL6** and **SL7**. As a consequence, the HOMO energy level of the dyes is lower than the edge of the valence band of NiO ($E_{\text{VB}(\text{NiO})} = -5.0$ eV),^{21,49,50} indicating that sufficient driving force exists for hole injection from the photoexcited dyes to the semiconducting metal oxide. On the other hand, the electron promoted to the LUMO upon photoexcitation is at a sufficiently high energy to be transferred to an irreversible electron acceptor (IEA) such as [Co(NH₃)₅Cl]Cl₂ ($E^{\circ}_{\text{Co(III)}/\text{Co(II)}} = -4.5$ eV).⁵¹ In that configuration, photoinduced electron transfers from NiO to the IEA, mediated by the mixed allenylidene-acetylide ruthenium complexes **SL6** and **SL7**, should be highly favourable.

IV.3.4. Theoretical Calculations

Quantum chemical calculations were performed in order to obtain information about the molecular orbital distribution and the electronic transitions occurring upon photoexcitation of the dyes **SL6** and **SL7**. These calculations were performed by Michele Pavone and Ana B. Muñoz-García from the University of Naples Federico II.

A spatial representation of the frontier molecular orbitals HOMO and LUMO calculated at the PBE0 level of theory is shown in Figure IV-7. The calculations show that the HOMO of the dyes is delocalized over the acetylide ligand bearing the thiophene (**SL6**) or triphenylamine unit (**SL7**) and on the anchoring group(s), which should greatly favour hole injection into the valence band of NiO.⁵² The HOMO also shows a strong contribution from the metal centre, and in the case of **SL6** a substantial extension onto the cumulenenic carbon chain. On the other hand, the LUMO of such mixed allenylidene-acetylide metal complexes is mainly localized on the allenylidene ligand, thus involving the external phenyl rings, the cumulenenic chain and some contribution from the metal fragment. As a consequence, the HOMO and LUMO of the dyes are well positioned on the metal complexes for hole injection into NiO on one side and electron donation to the cobalt-based electron acceptor on the other side.

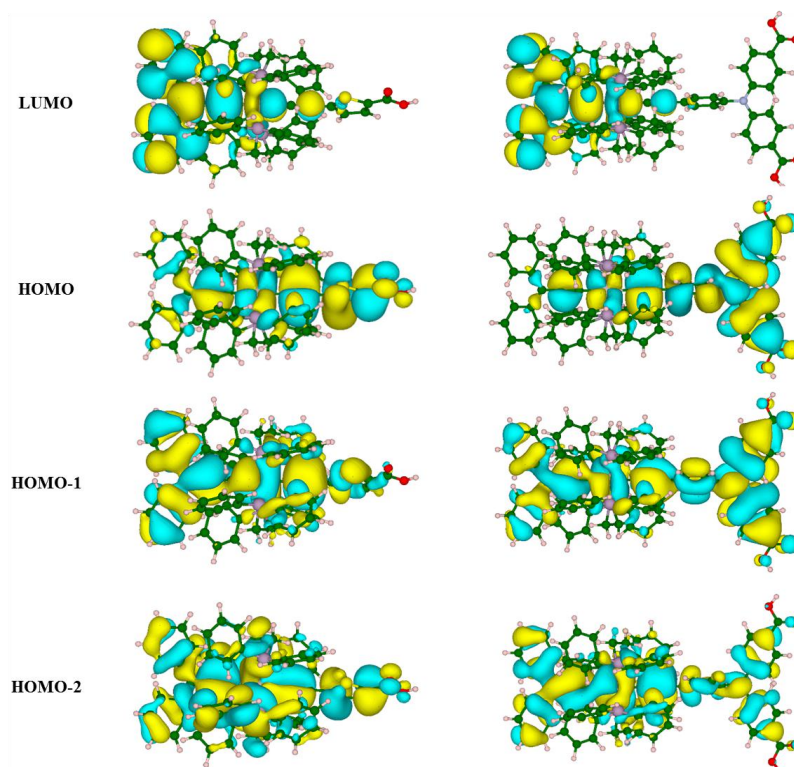


Figure IV-7: Electron-density distribution of the transition-involved frontier molecular orbitals of **SL6** (left) and **SL7** (right).

Table IV-2: DFT and TD-DFT calculated electronic properties in CH₂Cl₂.

Dye	$\Delta E_{\text{calc}}^{\text{a}}$ / eV	$\lambda_{\text{calc}}^{\text{b}}$ / nm	f^{c}	Transition assignment ^d	q_{CT} / e	D_{CT} / Å	$E_{\text{HOMO calc.}}^{\text{e}}$ / eV
[Ru]1	1.83	676	0.005	HOMO → LUMO ; HOMO-2 → LUMO	0.961	1.98	- 5.66
	2.93	423	0.841	HOMO-1 → LUMO			
[Ru]2	1.80	687	0.005	HOMO → LUMO	0.965	2.06	- 5.39
	2.93	423	0.856	HOMO-1 → LUMO ; HOMO-2 → LUMO			

^a ΔE_{calc} is the main transition energy. ^b λ_{calc} is the calculated λ_{max} . ^c f is the oscillator strength. ^d Only those transitions with coefficients higher than 0.15 are given. ^e $E_{\text{HOMO calc.}}$ is the calculated energy of the HOMO.

DFT and TD-DFT calculation parameters relative to the main photoinduced transitions are summarized in Table IV-2. In accordance with the experiment, two main transitions are predicted for **SL6** and **SL7** in the 300-800 nm region. Table IV-3 shows TD-DFT validation test of different exchange-correlation density functional models for predicting the vertical excitation energies of **SL6** dye in dichloromethane. The maximum wavelengths and oscillator factors calculated for the two main transitions are consistent with the experimental spectra; the expected small deviation between calculated and experimental data is attributable to the large size of such organometallic complexes and to the well-known limits of TD-DFT for charge-transfer excitations.⁵³ The maximum wavelength calculated for the lowest energy transition is 676 nm and 687 nm for **SL6** and **SL7**, respectively, corresponding to pure charge transfer. We have also analysed the electron-density rearrangement upon excitation (see Figure IV-8) and the computed average charge-transfer distance (DCT) was similar for both dyes, with a slightly longer extent for **SL7** than that for **SL6**. Furthermore the calculated energy of the HOMO is in good agreement with that obtained experimentally, *i.e.* $E_{\text{HOMO calc.}} = -5.6$ eV *vs.* $E_{\text{HOMO exp.}} = -5.7$ eV for **SL6** and $E_{\text{HOMO calc.}} = -5.4$ eV *vs.* $E_{\text{HOMO exp.}} = -5.7$ eV.

Table IV-3: TD-DFT validation test of different exchange-correlation density functional models for predicting the vertical excitation energies of **SL6** dye in dichloromethane.

SL6 ^(a)	1 st excitation (nm)	2 nd excitation (nm)
B3LYP	861	550
PBE0	820	525
mPW1PBE	818	524
mPW1PW91	818	524
M06-2X	753	455
CAM-B3LYP	707	448
ω B97X	696	441
LC- ω PBE	676	423
Exp.	602	340

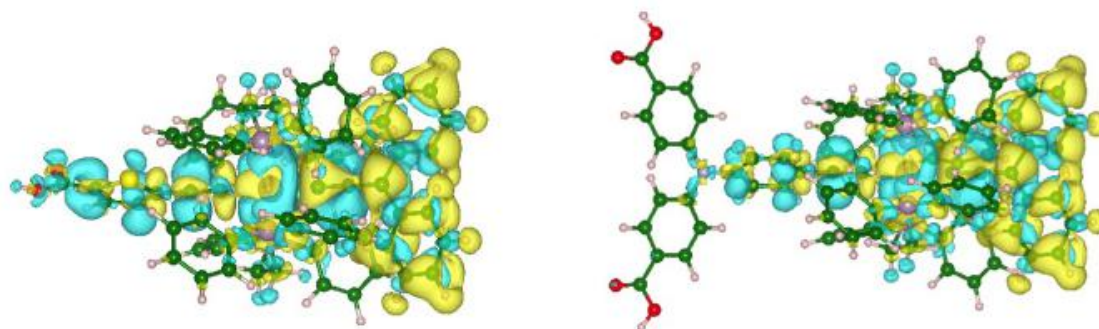


Figure IV-8: Charge density difference iso-surface plots between excited- (S1) and ground-state (S0) electron densities of **SL6** (left) and **SL7** (right). The yellow surface represents positive charge density values (*i.e.*, excited electron localization in S1), the cyan surface represents negative charge density values (*i.e.*, hole in the ground-state).

Transition assignment reveals that this low-energy transition has a major HOMO \rightarrow LUMO character whereas the transition at higher energy has a HOMO-1 \rightarrow LUMO character. These transitions therefore present a net MLCT (Metal-to-Ligand Charge Transfer) character since both HOMO and HOMO-1 strongly involve the central ruthenium-based fragment. This is further confirmed by the calculated quantity of transferred charge (q_{CT}), which is very close to 1.

IV.3.5. Electrode Preparation and Characterization

This work was realized in collaboration with the group of Dr. Vincent Artero from CEA Grenoble. The NiO substrates were purchased from Dyenamo³⁸ and sensitized by soaking in a 0.5 mM CH₃CN solution of **SL6** or **SL7** for 24 hours. The samples were rinsed with CH₃CN and dried in air before characterization. Figure IV-9a displays typical absorbance spectra of a dye-sensitized electrode, showing new features as compared with the spectrum of the blank NiO substrate (measured on the same sample before sensitization) that correspond to the absorbance of **SL6** or **SL7** dyes grafted onto the NiO surface (Figure IV-9b and c). For both dyes, a blue shift (33 nm for **SL6** and 53 nm for **SL7**) of the absorbance band is observed, in agreement with previous reports.^{47,50} These modifications result either from small structural rearrangements of the dye molecules upon grafting on the NiO substrate or from intermolecular interactions between adjacent grafted dyes.

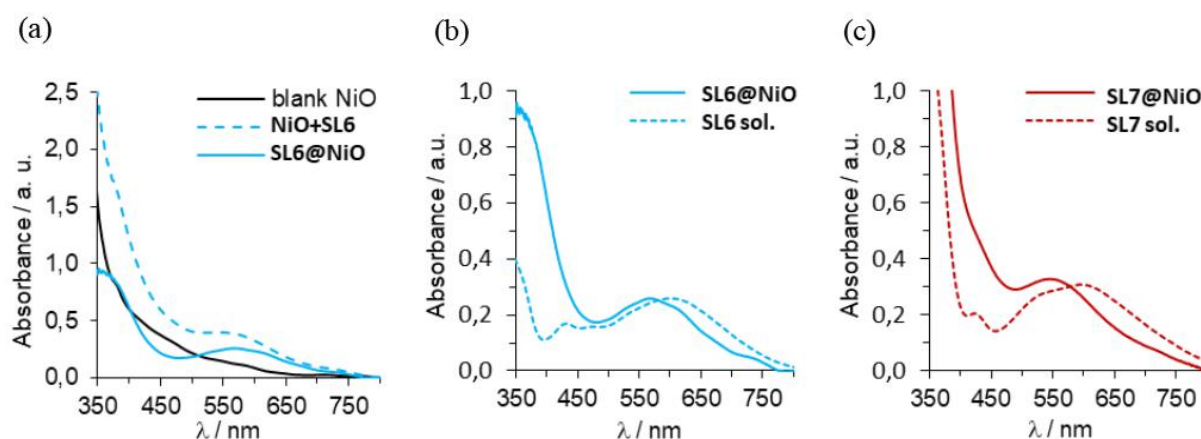


Figure IV-9: (a) Absorbance spectra of a blank NiO electrode (black line) and the same electrode after sensitization with **SL6** (dashed blue line). The difference between these two spectra is shown as a plain blue line. (b) Comparison of corrected spectra recorded on NiO films (plain blue line) and CH₂Cl₂ ($C \sim 3 \times 10^{-5}$ M; optical pathway 1 cm) solution spectra of **SL6** (dashed blue line). (c) Comparison of corrected spectra recorded on NiO films (plain red line) and CH₂Cl₂ ($C \sim 3 \times 10^{-5}$ M; optical pathway 1 cm) solution spectra of **SL7** (dashed red line).

Assuming that the dyes retain their electronic structure features upon adsorption on p-NiO.⁵⁴ and that the dye-NiO interactions do not significantly modify the molar absorbance coefficient ϵ_{\max} of the dye, the surface concentrations of **SL6** and **SL7** were estimated using the following equation:

$$\text{surf.conc.}(\text{mol} \cdot \text{cm}^{-2}) = \frac{Abs_{\max}}{1000 \times \varepsilon (M^{-1} \cdot \text{cm}^{-1})} \quad (28)$$

This methodology afforded surface concentration estimations of 21.5 ± 0.8 and $28.7 \pm 0.8 \text{ nmol} \cdot \text{cm}^{-2}$ for **SL6** and **SL7**, respectively (average values determined for 3 samples). The variation in the grafting density between the two dyes likely reflects the fact that **SL7** possesses two carboxylate anchoring groups whereas **SL6** has only one.

IV.3.6. Photoelectrochemical Properties of Dye-Sensitized NiO Films

The photoelectrochemical properties of dye-sensitized NiO films were subsequently investigated in the presence of $[\text{Co}(\text{NH}_3)_5\text{Cl}]\text{Cl}_2$ (20 mM) acting as an irreversible electron acceptor (IEA) in solution.^{37,55} The substrates were used as the working electrode in a three-electrode configuration. Potassium phosphate buffer (KPi, pH 7; 0.1 M) was used as an electrolyte and linear sweep voltammograms (LSV) were recorded under chopped-irradiation conditions (400-800 nm filtered Xe lamp light; $100 \text{ mW} \cdot \text{cm}^{-2}$) corresponding to a visible fraction of 1.5 sun (Figure IV-10a). A photocurrent was established with the onset at +0.78 V vs. NHE. Such a behaviour was directly related to the presence of **SL6** or **SL7** at the surface of the films since non-sensitized NiO films show very little photocurrent under the same conditions. This was attributed to the establishment of photoinduced electron transfers from NiO to IEA, mediated by the excited dyes. Maximum photocurrent densities ($\sim 40 \text{ } \mu\text{A} \cdot \text{cm}^{-2}$ for **SL6** and $\sim 60 \text{ } \mu\text{A} \cdot \text{cm}^{-2}$ for **SL7**) were obtained from +0.20 V vs. NHE (0 V vs. Ag/AgCl).⁵⁶

Therefore this potential was applied for the whole series of experiments described below. Under such conditions, NiO electrodes sensitized with **SL7** display a significantly higher photocurrent density ($58 \text{ } \mu\text{A} \cdot \text{cm}^{-2}$) than the same electrodes sensitized with **SL6** ($43 \text{ } \mu\text{A} \cdot \text{cm}^{-2}$) (Figure IV-10b). This difference is directly related to the observed difference in surface concentration. Indeed, if the macroscopic photocurrent ($\mu\text{A} \cdot \text{cm}^{-2}$) is divided by the Faraday constant and by the surface concentration ($\text{nmol} \cdot \text{cm}^{-2}$), similar photoinduced molecular electron transfer frequencies of 0.020 and 0.021 s^{-1} are calculated for **SL6** and **SL7**, respectively, suggesting that the two dyes have the same intrinsic efficiency for light-driven charge transfer. In the course of long-term illumination experiments, both electrodes display quite stable photocurrent values for the first 20-30 min (Figure IV-10c). After this time, the photocurrent values begin to decrease (30% after one hour for the NiO electrode sensitized by **SL7** and >50% in the case of **SL6** that only contains one anchoring carboxylate group). This

behaviour could be ascribed to both the leaching of the dye and the deposition of an insoluble product at the surface of the electrode, clogging the electrode pores and thus limiting the performances. Note that this deposit likely originates from the decomposition products of the IEA. Such an issue should not arise if a catalyst is used instead of an IEA. These observations contrast with measurements made with an analogous organic push-pull dye containing a triarylamine donor similarly anchored onto NiO through carboxylate groups.³⁷ Photocurrent values were found to be very unstable in phosphate buffer, which was ascribed to the leaching of the dye. The good stability of photocurrent at pH 7 for **SL7**-sensitized NiO electrodes therefore holds promise for the development of photoelectrodes for H₂ evolution since most molecular catalysts work under such conditions.

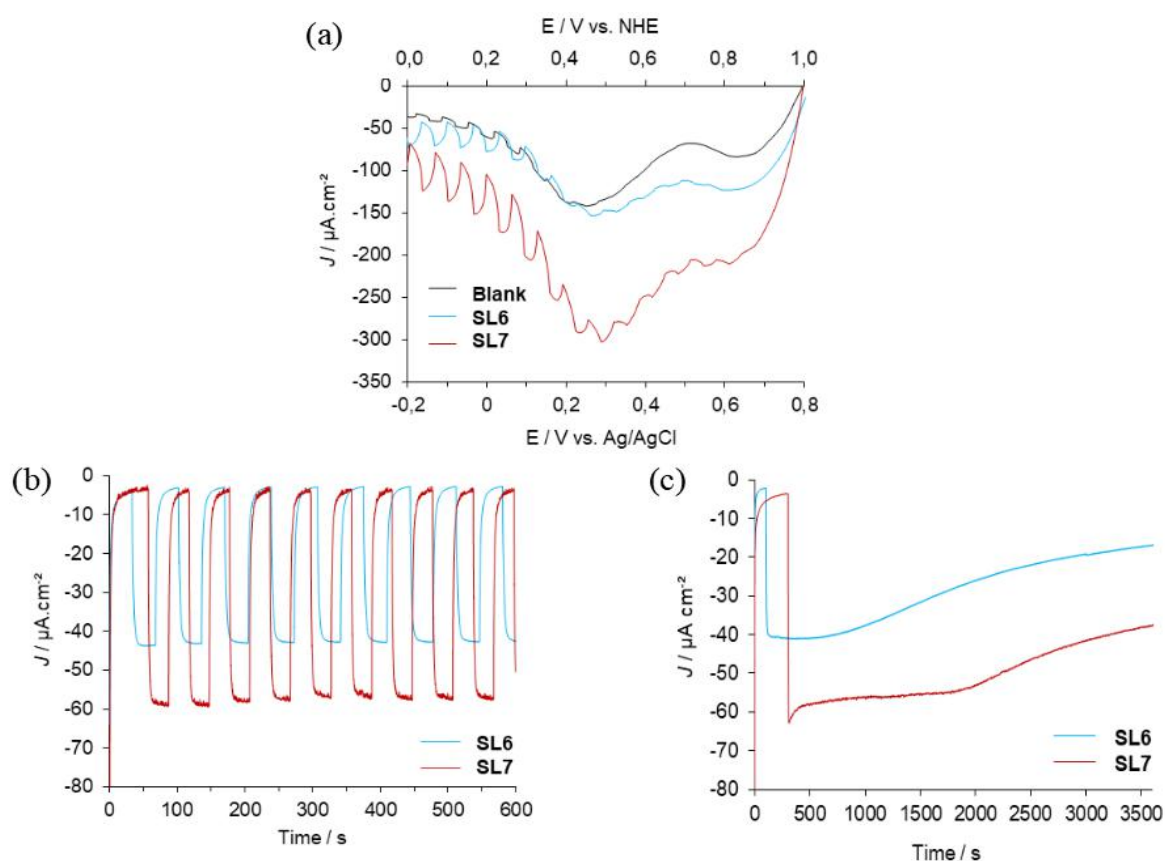


Figure IV-10: (a) Linear sweep voltammogram (10 mV s^{-1}) recorded under chopped-light on a non-sensitized NiO electrodes (black line) or NiO electrodes sensitized with **SL6** (blue line) or **SL7** (red line) in the presence of $[\text{Co}(\text{NH}_3)_5\text{Cl}]\text{Cl}_2$ (20 mM). (b) Cathodic photocurrent measurements recorded for 10 minutes under chopped-light NiO electrodes sensitized with **SL6** (blue line) or **SL7** (red line) in the presence of $[\text{Co}(\text{NH}_3)_5\text{Cl}]\text{Cl}_2$ (20 mM) in phosphate buffer (0.1 M ; pH 7) at + 0.2 V vs. NHE. (c) Cathodic photocurrent measurements recorded for 1 hour on NiO electrodes sensitized with **SL6** (blue line) or **SL7** (red line) in the presence of $[\text{Co}(\text{NH}_3)_5\text{Cl}]\text{Cl}_2$ (20 mM) at + 0.2 V vs. NHE in phosphate buffer (0.1 M ; pH 7).

IV.3.7. Conclusions

Dye-sensitized photocathodes displaying stable photoelectrochemical properties at neutral pH are targeted for the development of H₂-evolving photoelectrocatalytic cells. Tandem cells combining two dye-sensitized photoelectrodes were indeed recently shown to be capable of splitting water in the absence of any external bias.^{18,19} Optimization of the cell performances is thus required and includes the design of novel dyes. We showed in this section the relevance of push-pull organometallic dyes for the construction of photocathodes operating in water. The high stability displayed by these new dye-sensitized photocathodes in pH 7 phosphate buffer represents an important improvement compared to other photoelectrodes reported before³⁷ and held promise for the construction of H₂-evolving photoelectrodes through catalyst integration.

IV.4. Ru-diacetylide/Cobaloxime Photocatalytic System for H₂ Evolution from Dye-Sensitized Photoelectrochemical Cells

In the sections III.3. and IV.3. we have demonstrated the relevance of using [Ru(dppe)₂] organometallic complexes as photosensitizers in NiO-based photocathodes for p-type dye-sensitized solar cells and photo-electrochemical cells.^{41,57} On the other hand, in a recent study, our collaborators in the group of Dr. Vincent Artero (CEA Grenoble), reported the preparation of an innovative mono-molecular photocatalyst through covalent linkage of an organic dye and a cobalt diimine-dioxime catalyst.³⁰ Therefore we designed and prepared a new mono-molecular photocatalytic system via axial coordination of a cobalt-based H₂-evolving catalyst, *i.e.* a cobaloxime complex, to a pyridyl-functionalized Ru-diacetylide photosensitizer coded as **SL8**. Figure IV-11 shows the representation of the Ru-diacetylide/Cobaloxime photocatalytic system anchored onto NiO nanoparticulate thin-film.

The choice of the cobalt-based catalyst was motivated by the fact that, among cobaloximes, [Co(dmgbF₂)₂(OH₂)₂] is known as a stable and active H₂-evolving catalytic moiety.^{6,7,10} The new photocatalytic system was further employed for the construction of NiO-based photocathodes and subsequent H₂ generation in DSPECs under pertinent aqueous conditions.

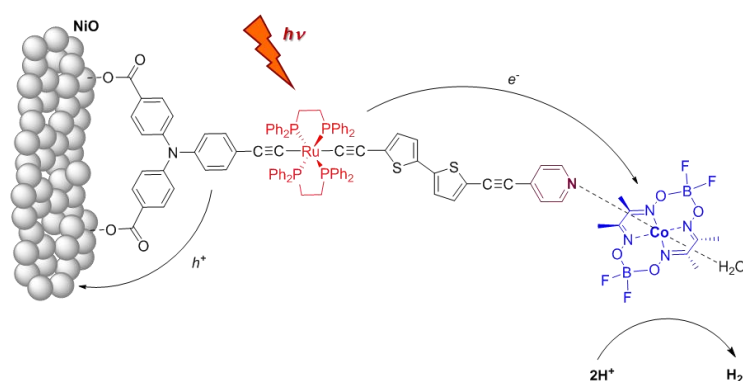


Figure IV-11: Representation of the Ru-diacetylide/Cobaloxime photocatalytic system **SL8** anchored onto NiO nanoparticulate thin-film.

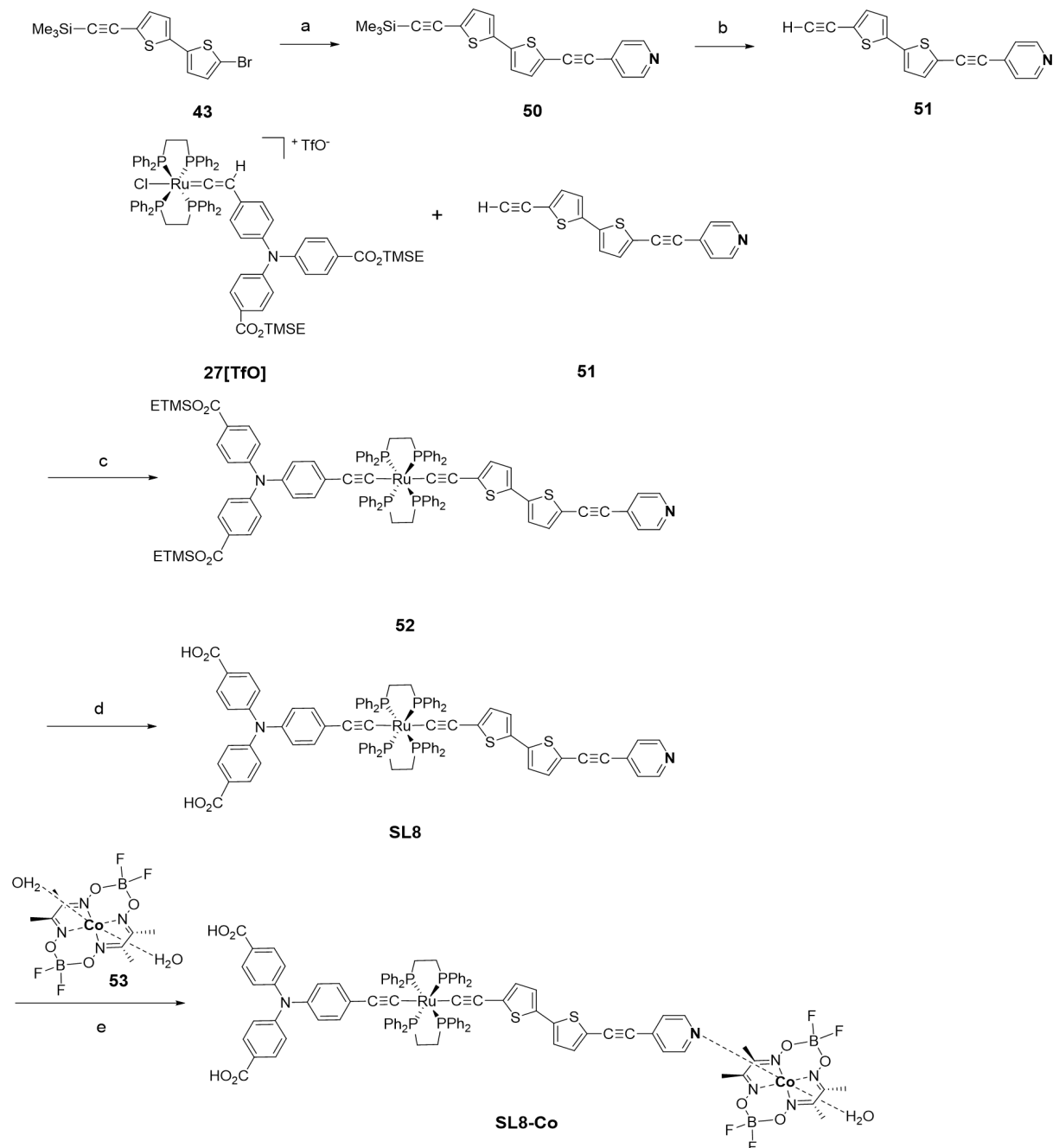
IV.4.1 Synthesis and Characterization

The synthetic route to the new photocatalytic system and the relevant precursors is depicted in Scheme IV-2. Synthesis of the alkynyl ligand bearing the pyridine coordinating group was achieved in three steps involving successive Sonogashira coupling reactions and subsequent deprotection of the alkyne function to give **51**. Then, according to established procedure for the synthesis of asymmetric [Ru(dppe)₂] diacetylide complexes,⁵⁷ the activation of the terminal alkyne of **51** by the ruthenium-vinylidene moiety **27**[TfO], described earlier,⁴¹ in the presence of a non-coordinating salt (NaPF₆) and a base (Et₃N), afforded the dialkynyl intermediate **52**. The carboxylic acid anchoring functions of **27**[TfO] were protected with silyl-ester groups, *i. e.* 2-(trimethylsilyl)ethyl (TMSE), in order to avoid side reactions with the metal centre during the different organometallic synthesis steps. Subsequent deprotection of the silyl-ester groups under mild conditions, using tetrabutyl ammonium fluoride in THF at room temperature, afforded the target photosensitizer **SL8** in good yields. Finally, the reaction of **SL8** with the cobaloxime **53**, afforded the new coordination photocatalytic system **SL8-Co**.

The Ru-based complexes **52** and **SL8** were characterized by means of ³¹P, ¹H and ¹³C NMR, HR-MS and FT-IR. The *trans*-ditopic structure of the [Ru(dppe)₂] centre was confirmed by the ³¹P NMR spectra which show a singlet for the four equivalent phosphorus atoms, with δ ≈ 53 ppm characteristic of the Ru-diacetylide structure.^{39,40,43} Characteristic peaks were observed on the infra-red spectra, at *ca.* 2195 cm⁻¹ for the ν_{C≡C} of the ethynylpyridine unit and at *ca.* 2040 cm⁻¹ corresponding to the ν_{C≡C} stretching vibration of the metal-alkynyl ligands.

Good quality NMR analysis of **SL8-Co** was impeded by the presence of the paramagnetic Co^{II} metal centre. Nonetheless, the infra-red spectrum of **SL8-Co** confirmed the preservation of the photosensitizer's structure as characteristics peaks of the ν_{C≡C} stretching

vibrations remained unchanged. Additional peaks corresponding to the cobaloxime moiety were observed at 1611 cm^{-1} ($\nu_{\text{C}=\text{N}}$), 1012 cm^{-1} ($\nu_{\text{N}-\text{O}}$) and 825 cm^{-1} ($\nu_{\text{B}-\text{O}}$). Furthermore, evidence for the formation of a coordination complex between **SL8** and the cobaloxime moiety was afforded by ESI+ HR-MS spectrometry which shows a peak at 1959.50152 corresponding to de-hydrated complex **SL8-Co** - H_2O $[\text{M} - \text{H}_2\text{O}]^+$.



Scheme IV-2: The synthetic route to the new photocatalytic system and the relevant precursors. Conditions: (a) 4-ethynylpyridine hydrochloride, $\text{PdCl}_2(\text{PPh}_3)_2$, CuI , diisopropylamine, THF; (b) K_2CO_3 , MeOH; (c) NaPF_6 , Et_3N , CH_2Cl_2 ; (d) TBAF, THF; (e) THF.

IV.4.2. Optical and Electrochemical Properties

UV-visible absorption spectra of the photocatalytic system **SL8-Co** and of the parent photosensitizer **SL8**, recorded in THF solution, are presented in Figure IV-12, the corresponding data are gathered in Table IV-4. In these spectra, intense absorption bands are observed in the UV region, below 300 nm, typical of the diphosphine ligands.⁴³ According to previous reports, the intense absorption band centered at *ca.* 355 nm can be attributed to electronic transitions involving the electron-rich triphenylamine ligand.⁴¹ What is more, a broad absorption band can be observed in the visible region with maximum wavelength at 463 nm and $\epsilon \approx 12\,000\text{ M}^{-1}\cdot\text{cm}^{-1}$. This broad band corresponds to multiple transitions involving the [Ru(dppe)₂] metal center, thus with a strong metal-to-ligand charge transfer (MLCT) character. Interestingly, the formation of the photocatalytic system through pyridyl-coordination of the cobaloxime moiety to the Ru complex **SL8** does not affect the absorption properties of the photosensitizer. The weak contribution of **53** in the electronic absorption spectrum of **SL8-Co** is totally hidden by the absorption of the dye and no significant electronic transition seems to occur between the [Ru(dppe)₂] metal center and the cobaloxime moiety. The zero-zero transition energy was estimated from the onset of the absorption spectra, leading to $E_{0-0} = 2.25\text{ eV}$ for both **SL8** and **SL8-Co**.

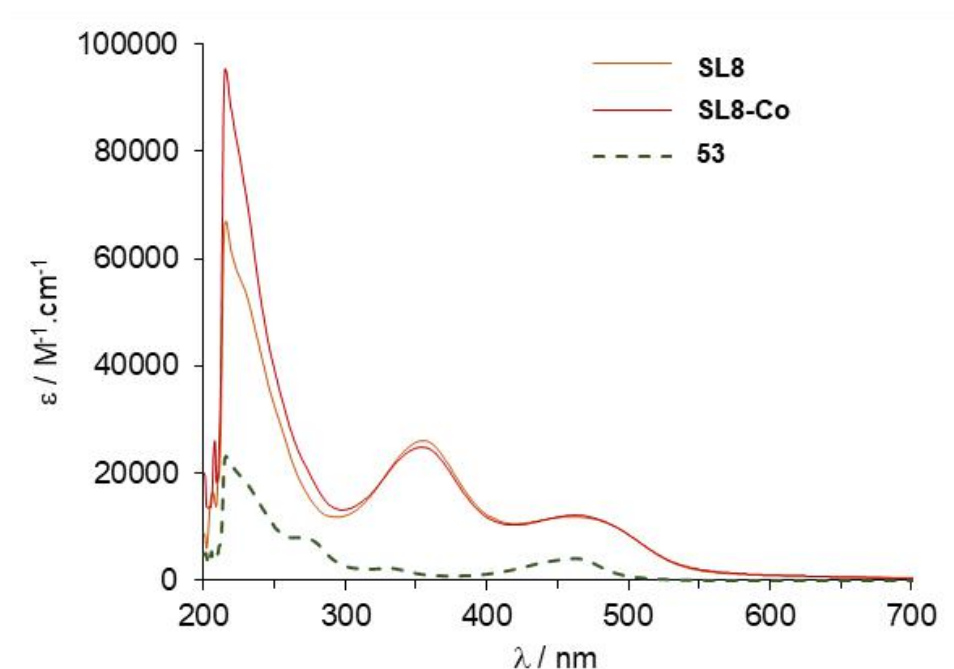


Figure IV-12: Absorption spectra of **SL8**, **SL8-Co** and **53** in THF ($C \approx 1 \times 10^{-5}\text{ M}$).

Table IV-4: Optical and electrochemical properties.

	λ_{\max} (nm)	ϵ ($\text{M}^{-1} \cdot \text{cm}^{-1}$)	E_{0-0} (eV) ^a	E_{red} (V vs. Fc ⁺ /Fc) ^b	E_{ox} (V vs. Fc ⁺ /Fc) ^b	E_{red} (V vs. NHE) ^c	E_{ox} (V vs. NHE) ^c	$E^{+/*}$ (V vs. NHE) ^d
SL8	463	11 870	2.25	-	+ 0.02	-	+ 0.75	- 1.50
	356	26 055						
SL8-Co	463	12 230	2.25	- 1.05	- 0.02	- 0.32	+ 0.71	- 1.54
	355	24 836						
53	462	4 000	-	- 1.12	-	- 0.39	-	-
	270	7 860						

Absorption spectra in THF. ^a 0-0 transition energy estimated from the onset of the absorption spectra. ^b Redox potentials in DMF solution. ^c Redox potentials referred to NHE by addition of 730 mV.⁵⁸ ^d Oxidation potential of the excited state obtained from $E_{\text{ox}}-E_{0-0}$.

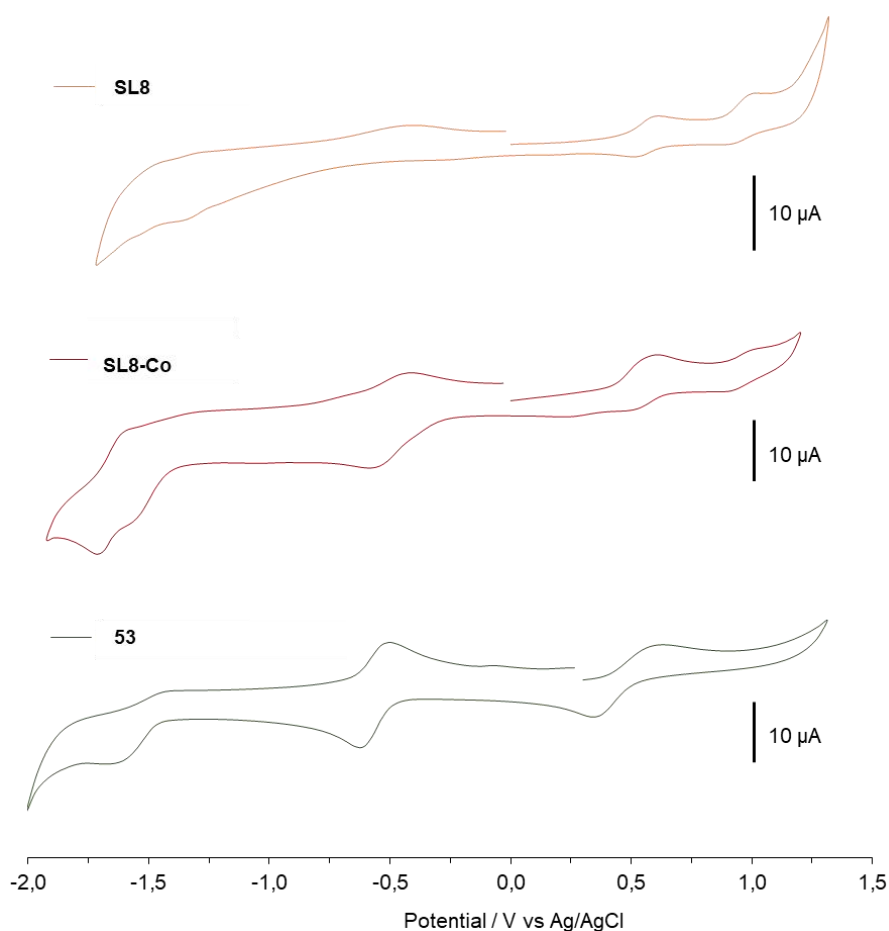


Figure IV-13: Cyclic voltammograms of **SL8**, **SL8-Co** and **53** in DMF solution. (Working electrode: Pt disc; reference electrode: Ag/AgCl, calibrated with decamethylferrocene as internal reference; counter electrode: Pt; salt support: 0.1M Bu₄NPF₆; scan rate: 100 mV·s⁻¹).

The electrochemical properties of **SL8-Co** and the parent compounds **SL8** and **53** were investigated by cyclic voltammetry in DMF solution (Figure IV-13), the corresponding data are reported in Table IV-4. The Ru-diacetylide complex **SL8** shows two reversible mono-electronic processes in the anodic region, that can be attributed to the oxidation of the electron-rich π -conjugated system of the dye, including the [Ru(dppe)₂] metal fragment. The first oxidation process occurs at +0.75 V vs. NHE. The cobaloxime **53** shows as well-defined reversible mono-electronic wave in the cathodic region, located at -0.39 V vs. NHE and corresponding to the Co^{II}→Co^I reduction process. As expected the voltammogram of **SL8-Co** displays both contributions of the Ru-based photosensitizer and of the cobalt catalyst. In the anodic part, the two oxidation waves are conserved, however the first oxidation potential of **SL8-Co** is negatively shifted upon coordination of the dye to the cobaloxime moiety, $E_{\text{ox SL8-Co}} = +0.71$ V vs. NHE. Conversely, in the cathodic part, the reduction process involving the Co core is shifted to more positive values by 70 mV, $E_{\text{red SL8-Co}} = -0.32$ vs. NHE. This positive shift of the reduction potential of a cobaloxime moiety is characteristic of the coordination by a pyridyl ligand.^{6,7} Besides, this feature provides good evidence for the formation of the coordinating photocatalytic system **SL8-Co**. The oxidation potential of the excited state was obtained by subtracting E_{0-0} to E_{ox} leading to $E^{+/*}_{\text{SL8-Co}} = -1.54$ vs. NHE. From these data, we could construct the energy diagram of a NiO-based photoelectrochemical cell designed for H₂-evolution in water and sensitized by **SL8-Co**, as displayed in Figure IV-14. This diagram shows that, upon photoexcitation, an electron can be transferred from the sensitizing part of **SL8-Co**, *i.e.* the Ru-diacetylide dye, to the Cobalt catalyst, which itself is active for the reduction of protons in H₂. Concomitantly, sufficient driving force exists for the regeneration of the catalytic system's ground-state through electron transfer from NiO ($E^0_{\text{NiO}} = +0.46$ V vs. NHE).

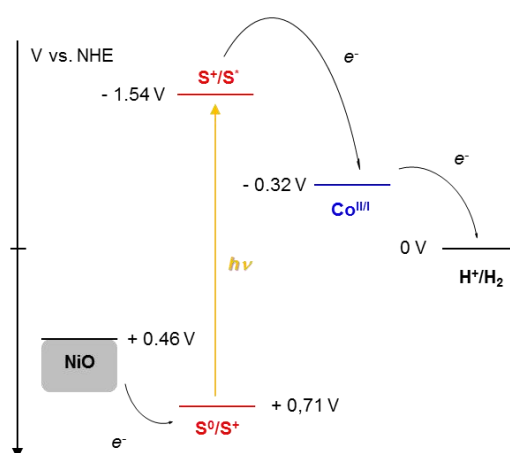


Figure IV-14: Energy diagram of a NiO-based DS-PEC including **SL8-Co** (S stands for the sensitizing part of the photocatalytic system, *i.e.* the Ru-based dye).

IV.4.3. Theoretical Calculations

Quantum chemical calculations were performed to gain deeper insight into the electron-density distribution of the frontier molecular orbitals and to assess the electronic transitions occurring upon photoexcitation of the sensitizer **SL8** and of the photocatalytic system **SL8-Co**.

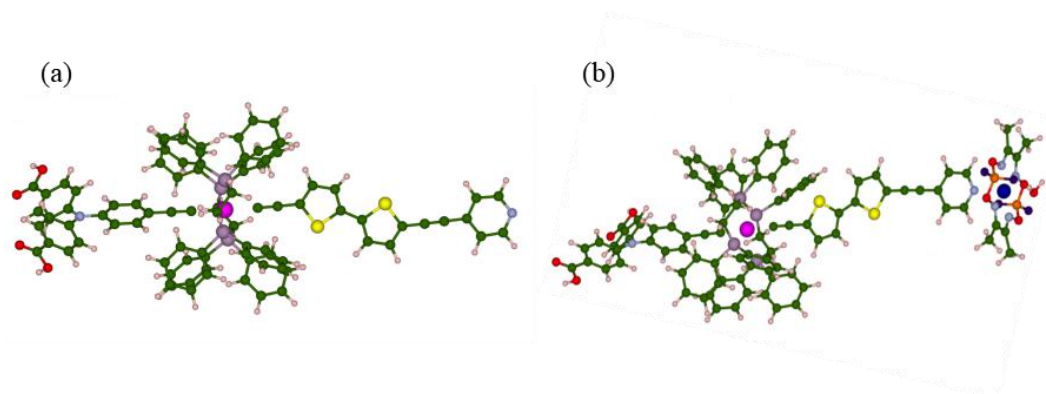


Figure IV-15: Ground-state minimum-energy molecular structures of **SL8** (a) and **SL8-Co** (b).

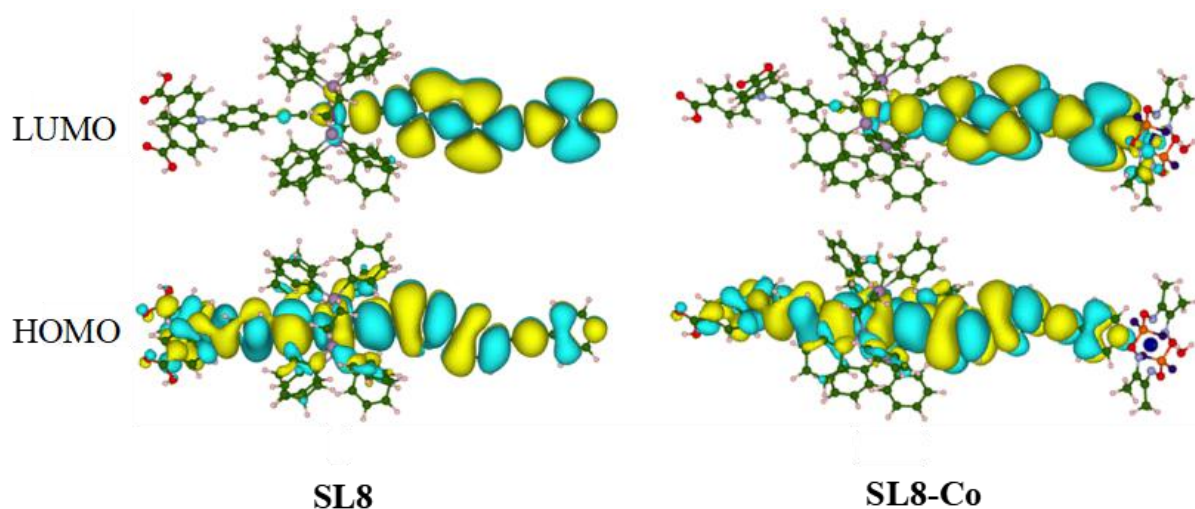


Figure IV-16: Isodensity surface plots of the HOMO and LUMO of **SL8** and **SL8-Co** (contour value set to 0.005 a.u.). Color legend: C atom green, O atom red, N atom light blue, Ru atom magenta, H atom white, S atom yellow, P light purple; isodensity positive and negative values are depicted in yellow and cyan, respectively.

The calculated ground-state minimum-energy molecular structures of **SL8** and **SL8-Co** are shown in Figure IV-15, spatial representations of the corresponding HOMO (Highest Occupied Molecular Orbital) and LUMO (Lowest Unoccupied Molecular Orbital) are represented in Figure IV-16. The calculations show that in **SL8** the HOMO is spread over the

whole π -conjugated system of the dye, including the [Ru(dppe)₂] core and the two acetylide ligands. However, significant electron-density is observed on the triphenylamine unit as well as on the two anchoring groups which favors electron transfers from NiO. On the other hand, the LUMO of the dye is localized on the electron-poor ligand bearing the pyridine ring. Good charge separation therefore occurs within this Ru-diacetylide complex. The HOMO in **SL8-Co** retains the same feature as in **SL8**, the electron density being spread over the whole π -conjugated system, but no density is observed on the cobaloxime moiety and thus, the electronic conjugation ends up at the pyridine ring. Interestingly, the LUMO in **SL8-Co** owns electron-density on the Co atom, and thus the electron transfer from the sensitizer to the catalyst is barrierless in the excited state. As a consequence, the calculations highlight the appropriate electronic density distribution of the frontier molecular orbitals in **SL8-Co**, favorable to the electron transfer processes occurring within a DSPEC.

The binding energy relative to the formation of **SL8-Co** according to equation (29) was investigated through theoretical calculations.



The calculated enthalpy of the reaction is $\Delta H = -1.14$ eV and the calculated Gibbs free-energy of the formation of the system is $\Delta G = -0.14$ eV. Both values indicate that the formation of **SL8-Co** through pyridyl-coordination of the cobaloxime **53** is strongly favoured.

TD-DFT calculation parameters relative to the main photoinduced electronic transitions are given in Table IV-5. The two main transition energies calculated for **SL8** in THF are in good accordance with the experiment, the small deviation being attributable to the large size of the complex and to some limitations of TD-DFT for charge-transfer excitation.⁵³ The transition assignment reveals that the lowest-energy transition, corresponding to $\lambda_{\text{calc}} = 445$ nm, owns a major HOMO \rightarrow LUMO character, while the higher-energy transition, corresponding to $\lambda_{\text{calc}} = 332$ nm, presents a HOMO-1 \rightarrow LUMO+1 character. The calculations give very similar results when the solvent considered is H₂O. The main transition energies calculated for **SL8-Co** in H₂O also match the experiment, the lowest-energy transition being predicted at $\lambda_{\text{calc}} = 455$ nm. TD-DFT calculation were also pursued on **SL8-CoH**, the reaction intermediate for hydrogen evolution reaction (HER).^{11,15} Interestingly the formation of the HER intermediate **SL8-CoH** does not affect the optical properties of the photocatalytic system. The two main transition energies are conserved with $\lambda_{\text{calc}} = 445$ nm and 330 nm, as well as the nature of the frontier orbitals involved in the lowest-energy transition which presents a major HOMO \rightarrow LUMO character.

Table IV-5: TD-DFT calculated electronic properties (CAM-B3LYP/SDD/6-31G(d)/PCM=THF/H₂O)

	E_{calc} /eV ^a	λ_{calc} / nm ^b	f ^c	Electronic transition assignment ^d
SL8 (THF)	2.79	445	2.023	HOMO → LUMO (72%)
	3.74	332	0.589	HOMO-1 → LUMO+1 (37%)
SL8 (H ₂ O)	2.80	443	2.013	HOMO → LUMO (71%)
	3.74	331	0.576	HOMO-1 → LUMO+1 (36%)
SL8-Co (H ₂ O)	2.73	455	2.180	HOMO → LUMO (68%)
	3.76	330	0.584	HOMO-1 → LUMO+3 (35%)
SL8-CoH (H ₂ O)	2.67	465	2.235	HOMO → LUMO (66%)
	3.76	330	0.585	HOMO → LUMO+4 (37%)

^a ΔE_{calc} = main transition energy. ^b λ_{calc} = calculated λ_{max} . ^c f = oscillator strength. ^d Main Kohn-Sham orbital contribution to the electronic transition.

IV.4.4. Electrode Preparation and Characterization - XPS Analyses

The photocatalytic system **SL8-Co** was then used to prepare a photocathode based on NiO nanoparticulate thin film designed for H₂ evolution. The F108-templated NiO electrode was prepared as previously reported.³⁰ Sensitization was achieved by soaking the semiconducting porous layer in a DMF solution of **SL8-Co** (0.5 mM) for 24 h at RT. The absorption spectrum of the sensitized electrode is depicted in Figure IV-17. An increase of absorption is observed in the 350-500 nm wavelength region as expected. The amount of dye-loading on the photoelectrode was quantified by dye desorption under mild conditions using a phenylphosphonic acid solution (1 M in DMF). The estimated quantity of dye on the 1- μm thick NiO film was estimated to be about 6.2 nmol·cm⁻², which is in the same range as those determined in previous studies using similar electrodes.^{37,41,57}

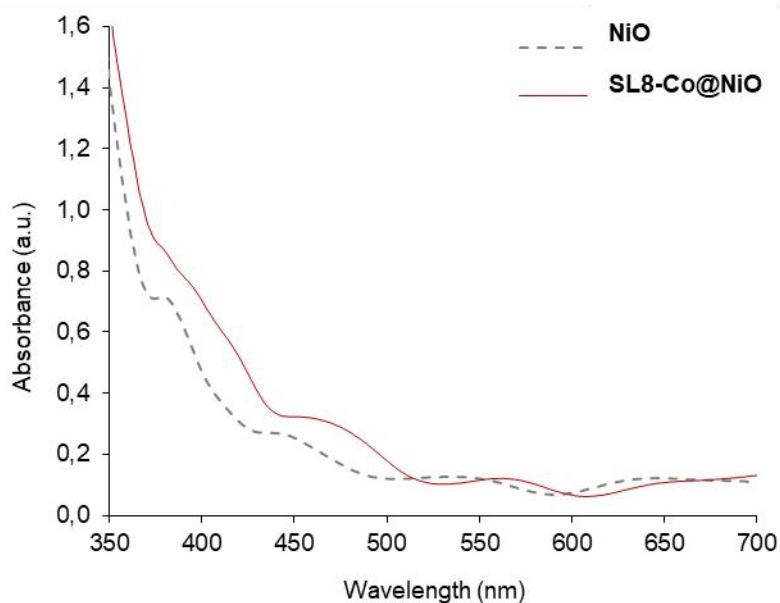


Figure IV-17: Electronic absorption spectra of blank NiO film (gray dashed) and of NiO electrode sensitized by **SL8-Co** (red).

The presence of Ru and Co atoms at the surface of NiO electrodes sensitized either with **SL8** only or **SL8-Co** was further investigated through X-ray photoelectron spectroscopy (XPS) analyses. The study was extended to pristine powders of **SL8**, **53** and **SL8-Co** for comparison. The corresponding survey spectra are shown in Figure IV-18 and IV-19.

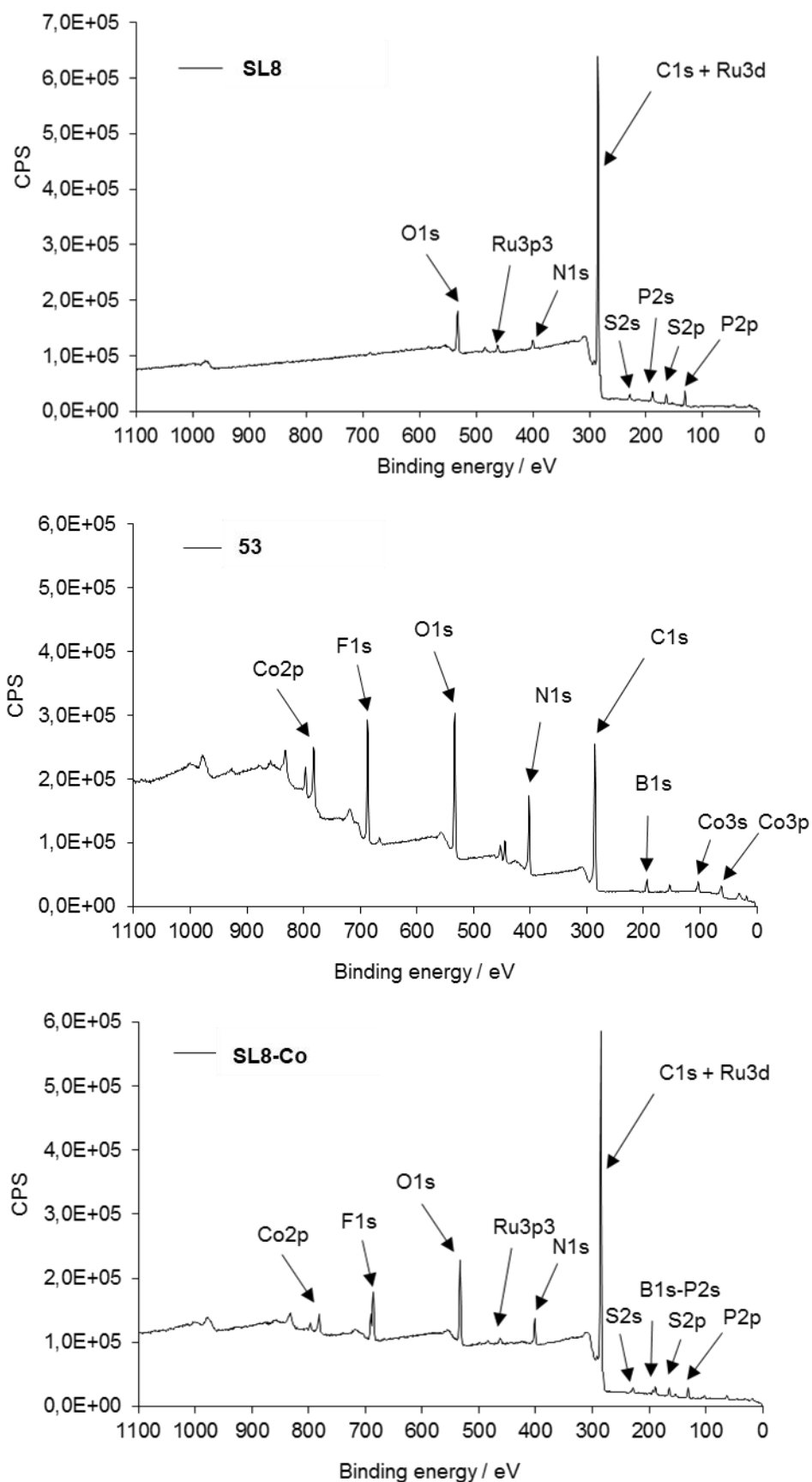


Figure IV-18: XPS survey spectra of pristine powders of SL8, 53 and SL8-Co.

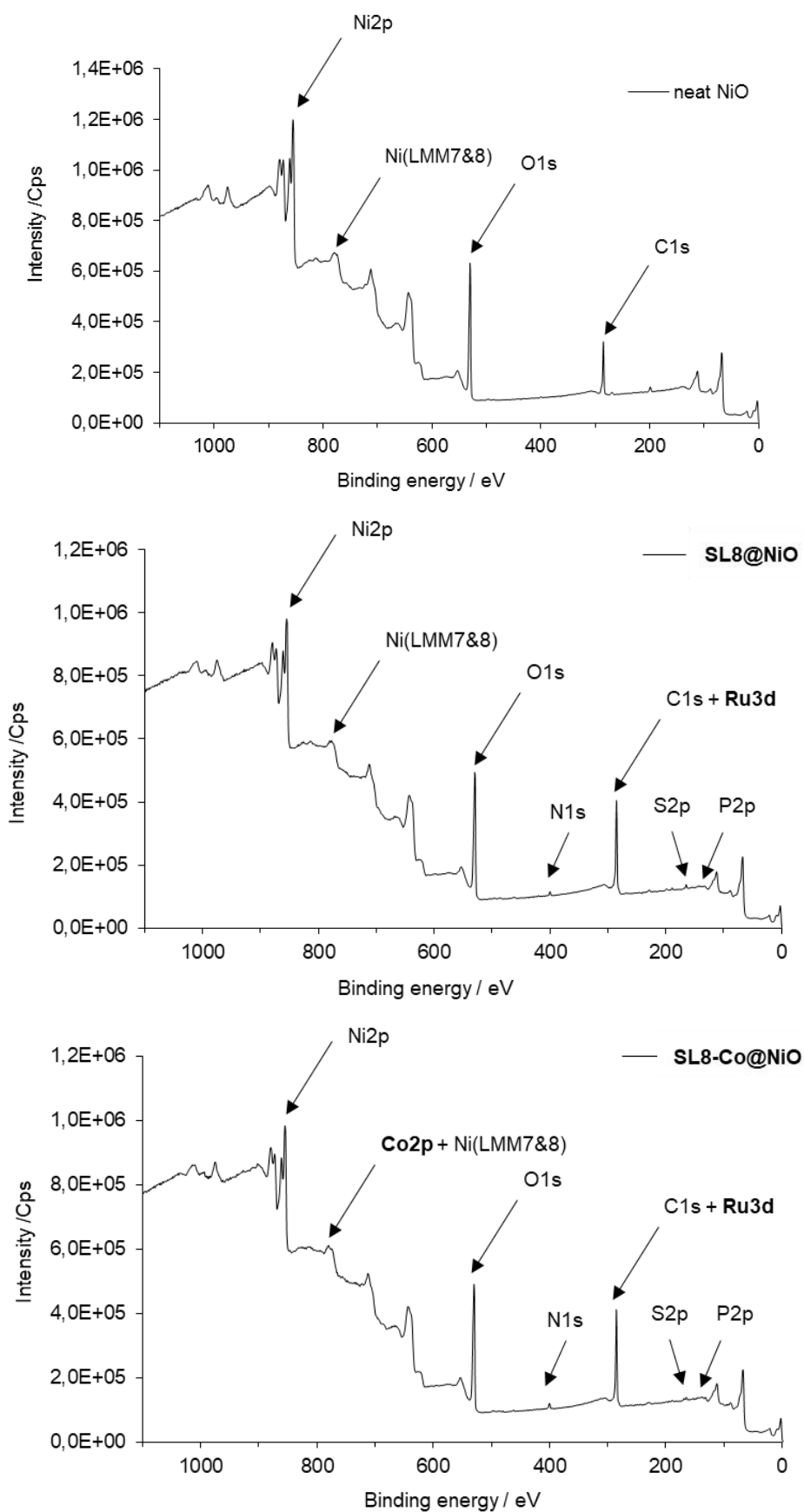


Figure IV-19: XPS survey spectra of neat NiO electrode and NiO electrodes sensitized by SL8 and SL8-Co.

The survey spectrum of pristine **SL8-Co** shows emissions of Ru, Co, C, O, N, S, P, F and B elements, the different peaks observed being assigned to Ru 3*d*, Ru 3*p*, Co 2*p*, C 1*s*, O 1*s*, N 1*s*, S 2*s*, S 2*p*, P 2*s*; P 2*p*, F 1*s* and B 1*s* core levels. This spectrum is fully consistent with XPS spectra of compounds **53** and **SL8** and confirms the chemical composition of **SL8-Co** (Figure IV-18). After chemisorption of **SL8-Co** onto NiO porous films, the survey spectrum of the resulting **SL8-Co@NiO** showed the same features along with those of NiO with peaks attributed to Ni 2*p* and Ni *LMM* Auger peaks which indicates the presence of all elements expected for **SL8-Co** chemisorbed onto NiO (Figure IV-19).

High-resolution core level spectra were recorded to further characterize the electrodes. Typical spectra in the Ru3*d*–C1*s* and Co2*p* regions are displayed in Figure IV-20.

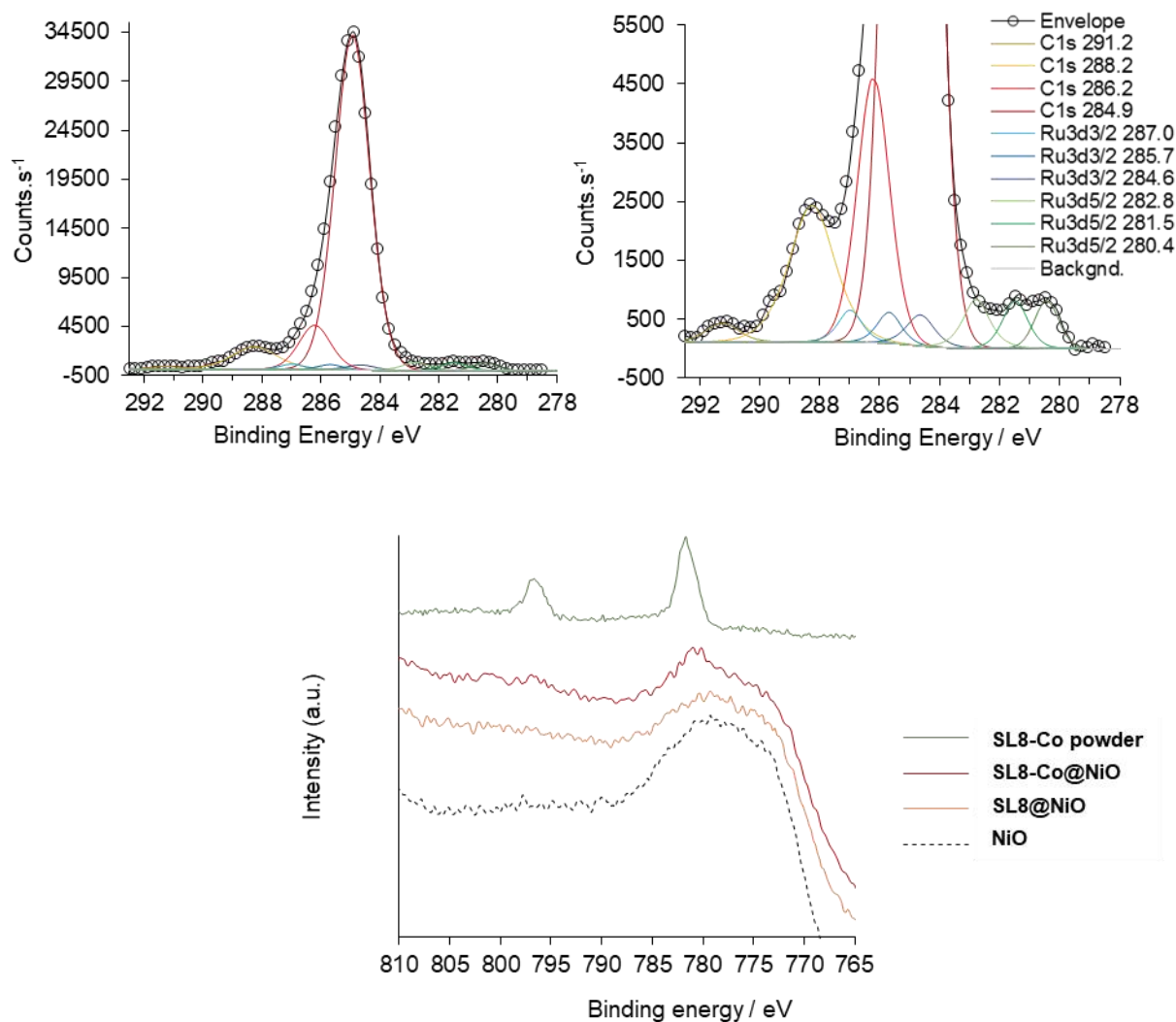


Figure IV-20: XPS core level spectra of (top) **SL8-Co@NiO** in the Ru3*d*–C1*s* region and (bottom) comparison of **SL8-Co powder**, **SL8-Co@NiO**, **SL8@NiO** and neat NiO in the Co2*p* region.

The presence of the Ru metallic centers in the XPS spectra of **SL8@NiO** and **SL8-Co@NiO** is confirmed through the signals of Ru 3p_{3/2} level at 463 eV and Ru 3d_{5/2} level at 280-282 eV, which is characteristic of Ru(II) species.^{59,60} The Ru 3d_{3/2} component overlaps the intense C 1s peak and therefore cannot be clearly resolved.

Finally, a broad band at 775 eV corresponding to Ni LMM Auger was detected in the 765-810 eV region for bare NiO and **SL8@NiO** (Figure IV-20, bottom). By contrast, new features at 780 eV and 796 eV, typical of Co 2p_{3/2} and Co 2p_{1/2} levels, along with the broad band at 775 eV were observed for **SL8-Co@NiO**. These results are fully consistent with the presence of Co(II) metal centers at the surface of the NiO electrode sensitized by **SL8-Co**.

As a consequence, XPS data clearly evidence the successful chemisorption of **SL8-Co** onto NiO electrodes.

IV.4.5. Photoelectrochemical Properties

The photocathodes **SL8-Co@NiO** were subsequently used for photocurrent generation and photoelectrochemical H₂ generation in aqueous solution (acetate buffer, pH 4.5). Linear sweep voltammograms were recorded in the dark and under visible-light irradiation (Figure IV-21). As expected a cathodic photocurrent is observed under light with a density of *ca.* 5.6 $\mu\text{A}\cdot\text{cm}^{-2}$ at -0.2 V vs. NHE (-0.4 V vs. Ag/AgCl). This behavior is due to photoinduced electron transfers from the p-type semi-conductor NiO, to the cobaloxime catalyst, through excitation of the sensitizer part in **SL8-Co**.

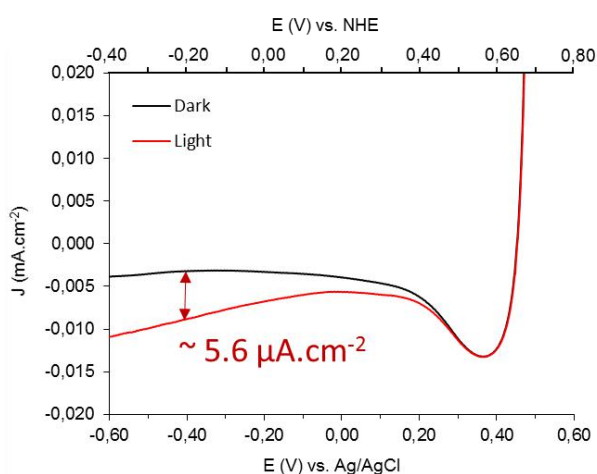


Figure IV-21: Linear sweep voltammograms (scan rate = 10 $\text{mV}\cdot\text{s}^{-1}$) of NiO electrode sensitized by **SL8-Co** recorded in acetate buffer (0.1 M, pH 4.5) in the dark (black line) or under visible-light irradiation (red line, 400-800 nm, 65 $\text{mV}\cdot\text{cm}^{-1}$, 1 sun).

Chronoamperometric measurements were performed with the photocathodes **SL8-Co@NiO** under chopped-light at different applied potentials (+0.2 V, 0.0 V, -0.2 V vs. NHE) over a period of 10 minutes showing steady-state cathodic photocurrent generation (Figure IV-22). The maximum magnitude was obtained at the most cathodic potential, *i.e.* -0.2 V vs. NHE (-0.4 V vs. Ag/AgCl), with a photocurrent density of *ca.* $3.2 \mu\text{A}\cdot\text{cm}^{-2}$ (Figure IV-23).

Thus, photoelectrochemical H_2 evolution was investigated by long-term electrolysis at an applied potential of -0.2 V vs. NHE (-0.4 V vs. Ag/AgCl) in acetate buffer (0.1 M, pH 4.5) under visible-light irradiation (1 sun). The cathodic charge passed through the photoelectrode during the course of the electrolysis was $Q = 78 \text{ mC}$ over a period of 4h30. Gas chromatographic analysis of the headspace confirmed the photo-electrochemical generation of H_2 with a faradaic efficiency of $\sim 27\%$.

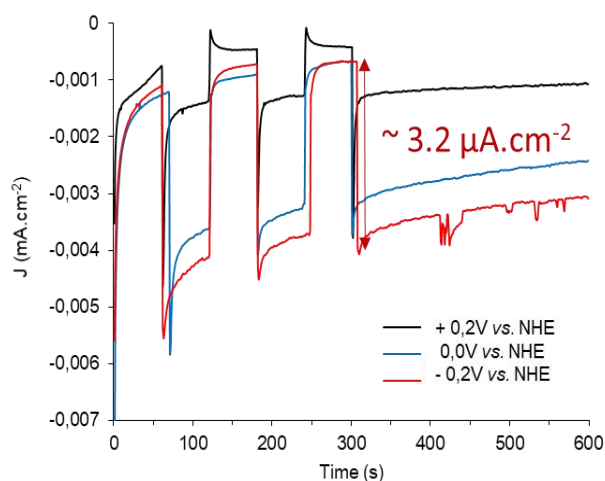


Figure IV-22: Steady-state photocurrents of NiO electrode sensitized by **SL8-Co** recorded in acetate buffer (0.1 M, pH 4.5) at an applied potential of +0.2 V, 0.0 V and -0.2 V vs. NHE under visible-light irradiation (400-800 nm, $65 \text{ mW}\cdot\text{cm}^{-2}$, 1 sun).

Control experiment using a NiO-electrode sensitized with **SL8** only confirmed steady-state photocurrent generation however with a slightly lower magnitude, *ca.* $2.4 \mu\text{A}\cdot\text{cm}^{-2}$ at -0.2 V vs. NHE, due to electron transfers from NiO to the excited dye. Long-term electrolysis over a period of 5h30 led to a cathodic charge of $Q = 144 \text{ mC}$ and an amount of H_2 close to zero was detected in the headspace with a faradaic yield of 0.3%. And thus, this confirms that the photocatalytic system **SL8-Co** is the active specie for H_2 evolution in our NiO-based DSPEC.

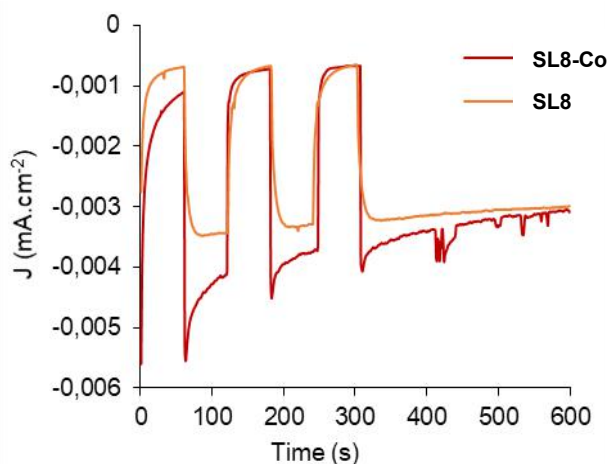


Figure IV-23: Chronoamperometric measurements under chopped-light using NiO electrodes sensitized with **SL8-Co** (red line) or **SL8** only (orange line) in acetate buffer (0.1 M, pH 4.5) at an applied potential of -0.2 V vs. NHE (-0.4 V vs. Ag/AgCl) under visible-light irradiation (400-800 nm, 65 mV·cm⁻², 1 sun).

IV.4.6. Conclusions

In this section, we designed and prepared a new mono-molecular photocatalytic system *via* axial coordination of a cobalt-based H₂-evolving catalyst on a pyridyl-functionalized Ru-diacetylide photosensitizer. The photocatalytic system **SL8-Co** showed suitable optical and electrochemical properties for use in NiO-based DSPECs. Thus this photocatalytic system was subsequently used to prepare a photocathode based on NiO nanoparticulate thin-film designed for H₂ evolution. Long-term electrolysis in acetate buffer (0.1 M, pH 4.5) and under 1 sun visible-light irradiation led to photo-electrochemical generation of H₂ with a faradaic efficiency of ~ 27%. This efficiency is comparable to other reports in the literature^{21,22,30} and thus fully validates our approach consisting in using organometallic ruthenium complexes as photoactive species to build efficient NiO-based DSPECs.

IV.5. Outlook

As discussed above, the photocatalytic system **SL8-Co**, comprising a Ru-diacetylide sensitizer in combination with a cobaloxime complex as H₂-evolving catalyst, showed a very interesting faradaic efficiency of about 27% when employed in DSPEC. Thus, we further designed a new mono-molecular photocatalytic system via coordination of a platinum-based H₂-evolving catalyst to a bipyridyl-functionalized Ru-diacetylide complex as photosensitizer. Figure IV-24 shows the representation of the new Ru-diacetylide/Platinum photocatalytic system anchored onto NiO nanoparticulate thin-film. This photocatalytic system, coded **SL9-Pt**, was prepared recently and the relevant measurements of optical and electrochemical properties as well as theoretical calculations are still in progress. The new photocatalytic system will be further employed for the construction of NiO-based photocathodes and subsequent H₂ generation in DSPECs under pertinent aqueous conditions.

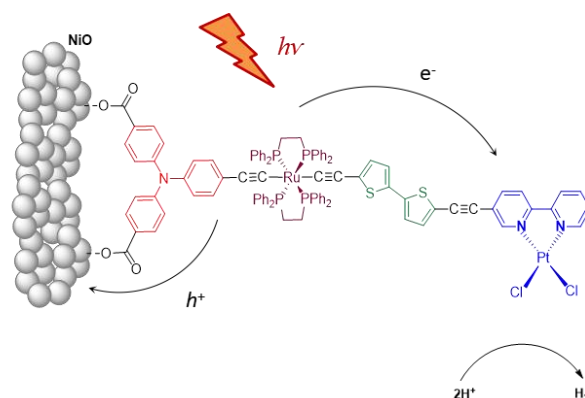


Figure IV-24: Representation of a Ru-diacetylide/Platinum photocatalytic system anchored onto NiO nanoparticulate thin-film.

IV.6. References

- 1 M. G. Walter, E. L. Warren, J. R. McKone, S. W. Boettcher, Q. Mi, E. A. Santori, N. S. Lewis. Solar Water Splitting Cells. *Chem. Rev.*, **2010**, 110, 11: 6446-6473.
- 2 H. B. Gray. Powering the planet with solar fuel. *Nature Chemistry*, **2009**, 1: 7.
- 3 N. S. Lewis, D. G. Nocera. Powering the planet: Chemical challenges in solar energy utilization. *PNAS*, **2006**, 103, 43: 15729-15735.
- 4 D. Gust, T. A. Moore, A. L. Moore. Solar Fuels via Artificial Photosynthesis. *Acc. Chem. Res.*, **2009**, 42: 1890-1898.
- 5 H. A. Gasteiger, N. M. Marković. Just a Dream-or Future Reality? *Science*, **2009**, 324: 48-49.
- 6 A. Fihri, V. Artero, M. Razavet, C. Baffert, W. Leibl, M. Fontecave. Cobaloxime-Based Photocatalytic Devices for Hydrogen Production. *Angew. Chem. Int. Ed.*, **2008**, 47: 564-567.
- 7 A. Fihri, V. Artero, A. Pereira, M. Fontecave. Efficient H₂-producing photocatalytic systems based on cyclometalated iridium- and tricarbonylrhenium-diimine photosensitizers and cobaloxime catalysts. *Dalton Trans.*, **2008**, 0: 5567-5569.
- 8 P. Du, J. Schneider, G. Luo, W. W. Brennessel, R. Eisenberg. Visible Light-Driven Hydrogen Production from Aqueous Protons Catalyzed by Molecular Cobaloxime Catalysts. *Inorg. Chem.*, **2009**, 48, 11: 4952-4962.
- 9 P. Zhang, M. Wang, C. Li, X. Li, J. Dong, L. Sun. Photochemical H₂ production with noble-metal-free molecular devices comprising a porphyrin photosensitizer and a cobaloxime catalyst. *Chem. Commun.*, **2010**, 46: 8806-8808.
- 10 V. Artero, M. Chavarot-Kerlidou, M. Fontecave. Splitting Water with Cobalt. *Angew. Chem. Int. Ed.*, **2011**, 50: 7238-7266.
- 11 J. R. McKone, S. C. Marinescu, B. S. Brunshwig, J. R. Winkler, H. B. Gray. Earth-abundant hydrogen evolution electrocatalysts. *Chem. Sci.*, **2014**, 5: 865-878.
- 12 N. Queyriaux, R. T. Jane, J. Massin, V. Artero, M. Chavarot-Kerlidou. Recent developments in hydrogen evolving molecular cobalt(II)-polypyridyl catalysts. *Coord. Chem. Rev.*, **2015**, 304-305: 3-19.
- 13 N. Coutard, N. Kaeffer, V. Artero. Molecular engineered nanomaterials for catalytic hydrogen evolution and oxidation. *Chem. Commun.*, **2016**, 52: 13728-13748.
- 14 J. L. Dempsey, B. S. Brunshwig, J. R. Winkler, H. B. Gray. Hydrogen Evolution Catalyzed by Cobaloximes. *Acc. Chem. Res.*, **2009**, 42, 12: 1995-2004.
- 15 K. L. Mulfort, D. M. Tiede. Supramolecular Cobaloxime Assemblies for H₂

- Photocatalysis: An Initial Solution State Structure-Function Analysis. *J. Phys. Chem. B*, **2010**, 114, 45: 14572-14581.
- 16 J. Willkomm, K. L. Orchard, A. Reynal, E. Pastor, J. R. Durrant, E. Reisner. Dye-sensitized semiconductors modified with molecular catalysts for light-driven H₂ production. *Chem. Soc. Rev.*, **2016**, 45: 9-23.
- 17 L. Li, L. Duan, F. Wen, C. Li, M. Wang, A. Hagfeldt, L. Sun. Visible light driven hydrogen production from a photo-active cathode based on a molecular catalyst and organic dye-sensitized p-type nanostructured NiO. *Chem. Commun.*, **2012**, 48: 988-990.
- 18 F. Li, K. Fan, B. Xu, E. Gabrielsson, Q. Daniel, L. Li, L. Sun. Organic Dye-Sensitized Tandem Photoelectrochemical Cell for Light Driven Total Water Splitting. *J. Am. Chem. Soc.*, **2015**, 137, 28: 9153-9159.
- 19 K. Fan, F. Li, L. Wang, Q. Daniel, E. Gabrielsson, L. Sun. Pt-free tandem molecular photoelectrochemical cells for water splitting driven by visible light. *Phys. Chem. Chem. Phys.*, **2014**, 16: 25234-25240.
- 20 P. Meng, M. Wang, Y. Yang, S. Zhang, L. Sun. CdSe quantum dots/molecular cobalt catalyst co-grafted open porous NiO film as a photocathode for visible light driven H₂ evolution from neutral water. *J. Mater. Chem. A*, **2015**, 3: 18852-18859.
- 21 M. A. Gross, C. E. Creissen, K. L. Orchard, E. Reisner. Photoelectrochemical hydrogen production in water using a layer-by-layer assembly of a Ru dye and Ni catalyst on NiO. *Chem. Sci.*, **2016**, 7: 5537-5546.
- 22 Z. Ji, M. He, Z. Huang, U. Ozkan, Y. Wu. Photostable p-Type Dye-Sensitized Photoelectrochemical Cells for Water Reduction. *J. Am. Chem. Soc.*, **2013**, 135, 32: 11696-11699.
- 23 V. Nikolaou, A. Charisiadis, G. Charalambidis, A. G. Coutsolelos, F. Odobel. Recent advances and insights in dye-sensitized NiO photocathodes for photovoltaic devices. *J. Mater. Chem. A*, **2017**, 5: 21077.
- 24 Z. Yu, F. Li, L. C. Sun. Recent advances in dye-sensitized photoelectrochemical cells for solar hydrogen production based on molecular components. *Energy Environ. Sci.*, **2015**, 8: 760-775.
- 25 C. E. Castillo, M. Gennari, T. Stoll, J. Fortage, A. Deronzier, M.-N. Collomb, M. Sandroni, F. Légalité, E. Blart, Y. Pellegrin, C. Delacote, M. Boujtita, F. Odobel, P. Rannou, S. Sadki. Visible Light-Driven Electron Transfer from a Dye-Sensitized p-Type NiO Photocathode to a Molecular Catalyst in Solution: Toward NiO-Based Photoelectrochemical Devices for Solar Hydrogen Production. *J. Phys. Chem. C*, **2015**,

- 119, 11: 5806-5818.
- 26 N. Queyriaux, R. A. Wahyuono, J. Fize, C. Gablin, M. Wächtler, E. Martinez, D. Léonard, B. Dietzek, V. Artero, M. Chavarot-Kerlidou. Aqueous Photocurrent Measurements Correlated to Ultrafast Electron Transfer Dynamics at Ruthenium Tris Diimine Sensitized NiO Photocathodes. *J. Phys. Chem. C*, **2017**, 121, 11: 5891-5904.
- 27 K. A. Click, D. R. Beauchamp, Z. Huang, W. Chen, Y. Wu. Membrane-Inspired Acidically Stable Dye-Sensitized Photocathode for Solar Fuel Production. *J. Am. Chem. Soc.*, **2016**, 138, 4: 1174-1179.
- 28 L. J. Antila, P. Ghamgosar, S. Maji, H. Tian, S. Ott, L. Hammarström. Dynamics and Photochemical H₂ Evolution of Dye-NiO Photocathodes with a Biomimetic FeFe-Catalyst. *ACS Energy Lett.*, **2016**, 1, 6: 1106-1111.
- 29 J. M. Gardner, M. Beyler, M. Karnahl, S. Tschierlei, S. Ott, L. Hammarström. Light-Driven Electron Transfer between a Photosensitizer and a Proton-Reducing Catalyst Co-adsorbed to NiO. *J. Am. Chem. Soc.*, **2012**, 134, 47: 19322-19325.
- 30 N. Kaeffer, J. Massin, C. Lebrun, O. Renault, M. Chavarot-Kerlidou, V. Artero. Covalent Design for Dye-Sensitized H₂-Evolving Photocathodes Based on a Cobalt Diimine-Dioxime Catalyst. *J. Am. Chem. Soc.*, **2016**, 138, 38: 12308-12311.
- 31 G. Sahara, H. Kumagai, K. Maeda, N. Kaeffer, V. Artero, M. Higashi, R. Abe, O. Ishitani. Photoelectrochemical Reduction of CO₂ Coupled to Water Oxidation Using a Photocathode with a Ru(II)-Re(I) Complex Photocatalyst and a CoO_x/TaON Photoanode. *J. Am. Chem. Soc.*, **2016**, 138, 42: 14152-14158.
- 32 G. Sahara, R. Abe, M. Higashi, T. Morikawa, K. Maeda, Y. Ueda, O. Ishitani. Photoelectrochemical CO₂ reduction using a Ru(II)-Re(I) multinuclear metal complex on a p-type semiconducting NiO electrode. *Chem. Commun.*, **2015**, 51: 10722-10725.
- 33 Y. Kou, S. Nakatani, G. Sunagawa, Y. Tachikawa, D. Masui, T. Shimada, S. Takagi, D. A. Tryk, Y. Nabetani, H. Tachibana, H. Inoue. Visible light-induced reduction of carbon dioxide sensitized by a porphyrin-rhenium dyad metal complex on p-type semiconducting NiO as the reduction terminal end of an artificial photosynthetic system. *J. Catal.*, **2014**, 310: 57-66.
- 34 F. Odobel, L. L. Pleux, Y. Pellegrin, Errol Blart. New Photovoltaic Devices Based on the Sensitization of p-type Semiconductors: Challenges and Opportunities. *Acc. Chem. Res.*, **2010**, 43, 8: 1063-1071.
- 35 F. Odobel, Y. Pellegrin. Recent Advances in the Sensitization of Wide-Band-Gap Nanostructured p-Type Semiconductors. Photovoltaic and Photocatalytic Applications. *J.*

- Phys. Chem. Lett.*, **2013**, 4, 15: 2551-2564.
- 36 L. Tong, A. Iwase, A. Nattestad, U. Bach, M. Weidelener, G. Götz, A. Mishra, P. Bäuerle, R. Amal, G. G. Wallace, A. J. Mozer. Sustained solar hydrogen generation using a dye-sensitized NiO photocathode/BiVO₄ tandem photo-electrochemical device. *Energy Environ. Sci.*, **2012**, 5: 9472-9475.
- 37 J. Massin, M. Bräutigam, N. Kaeffer, N. Queyriaux, M. J. Field, F. H. Schacher, J. Popp, M. Chavarot-Kerlidou, B. Dietzek, V. Artero. Dye-sensitized PS-*b*-P2VP-templated nickel oxide films for photoelectrochemical applications. *Interface Focus*, **2015**, 5, 3: 20140083.
- 38 C. J. Wood, G. H. Summers, C. A. Clark, N. Kaeffer, M. Braeutigam, L. R. Carbone, L. D'Amario, K. Fan, Y. Farré, S. Narbey, F. Oswald, L. A. Stevens, C. D. J. Parmenter, M. W. Fay, A. L. Torre, C. E. Snape, B. Dietzek, D. Dini, L. Hammarström, Y. Pellegrin, F. Odobel, L. Sun, V. Artero, E. A. Gibson. A comprehensive comparison of dye-sensitized NiO photocathodes for solar energy conversion. *Phys. Chem. Chem. Phys.*, **2016**, 18: 10727-10738.
- 39 S. D. Sousa, L. Ducasse, B. Kauffmann, T. Toupance, C. Olivier. Functionalization of a Ruthenium-Diacetylide Organometallic Complex as a Next-Generation Push-Pull Chromophore. *Chem. Eur. J.*, **2014**, 20: 7017-7024.
- 40 S. D. Sousa, S. Lyu, L. Ducasse, T. Toupance, C. Olivier. Tuning visible-light absorption properties of Ru-diacetylide complexes: simple access to colorful efficient dyes for DSSCs. *J. Mater. Chem. A*, **2015**, 3: 18256-18264.
- 41 S. Lyu, Y. Farré, L. Ducasse, Y. Pellegrin, T. Toupance, C. Olivier, F. Odobel. Push-pull ruthenium diacetylide complexes: new dyes for p-type dye-sensitized solar cells. *RSC Adv.*, **2016**, 6: 19928-19936.
- 42 D. Touchard, P. Haquette, A. Daridor, A. Romero, P. H. Dixneuf. Novel Ruthenium Allenylidene and Mixed Alkynyl Allenylidene Complexes: Crystal Structure of *trans*-[(Ph₂PCH₂CH₂PPh₂)₂Ru(C≡CPh)(=C=C=CPh₂)]PF₆. *Organometallics*, 1998, 17, 18: 3844-3852.
- 43 C. Olivier, B. Kim, D. Touchard, S. Rigaut. Redox-Active Molecular Wires Incorporating Ruthenium(II) σ -Arylacetylide Complexes for Molecular Electronics. *Organometallics*, **2008**, 27, 4: 509-518.
- 44 R. F. Winter, K.-W. Klinkhammer, S. Zálíš. Ruthenium-Aminoallenylidene Complexes from Butatrienylidene Intermediates via an Aza-Cope Rearrangement: Synthetic, Spectroscopic, Electrochemical, Spectroelectrochemical, and Computational Studies.

- Organometallics*, **2001**, 20, 7: 1317-1333.
- 45 O. Pélerin, C. Olivier, T. Roisnel, D. Touchard, S. Rigaut. A ruthenium(II) allenylidene complex with a 4,5-diazafluorene functional group: A new building-block for organometallic molecular assemblies. *J. Organomet. Chem.*, **2008**, 693: 2153-2158.
- 46 T. N. Huan, E. S. Andreiadis, J. Heidkamp, P. Simon, E. Derat, S. Cobo, G. Royal, A. Bergmann, P. Strasser, H. Dau, V. Artero, M. Fontecave. From molecular copper complexes to composite electrocatalytic materials for selective reduction of CO₂ to formic acid. *J. Mater. Chem. A*, **2015**, 3: 3901-3907.
- 47 M. Weidelener, S. Powar, H. Kast, Z. Yu, P. P. Boix, C. Li, K. Müllen, T. Geiger, S. Kuster, F. Nüesch, U. Bach, A. Mishra, P. Bäuerle. Synthesis and Characterization of Organic Dyes with Various Electron-Accepting Substituents for p-Type Dye-Sensitized Solar Cells. *Chem.-Asian J.*, **2014**, 9: 3251-3263.
- 48 Table 6.2, p. 158 in *Handbook of reference electrodes*, ed. G. Inzelt, A. Lewenstam, F. Scholz, Springer-Verlag, Berlin, Heidelberg, **2013**.
- 49 G. Boschloo, A. Hagfeldt. Spectroelectrochemistry of Nanostructured NiO. *J. Phys. Chem. B*, **2001**, 105: 3039-3044.
- 50 M. Weidelener, A. Mishra, A. Nattestad, S. Powar, A. J. Mozer, E. Mena-Osteritz, Y.-B. Cheng, U. Bach, P. Bäuerle. Synthesis and characterization of perylene-bithiophene-triphenylamine triads: studies on the effect of alkyl-substitution in p-type NiO based photocathodes. *J. Mater. Chem.*, **2012**, 22: 7366-7379.
- 51 W. Chen, F. N. Rein, R. C. Rocha. Homogeneous Photocatalytic Oxidation of Alcohols by a Chromophore-Catalyst Dyad of Ruthenium Complexes. *Angew. Chem., Int. Ed.*, **2009**, 48: 9672-9675.
- 52 Y. Pellegrin, L. L. Pleux, E. Blart, A. Renaud, B. Chavillon, N. Szuwarski, M. Boujtita, L. Cario, S. Jobic, D. Jacquemin, F. Odobel. Ruthenium polypyridine complexes as sensitizers in NiO based p-type dye-sensitized solar cells: Effects of the anchoring groups. *J. Photochem. Photobiol., A*, **2011**, 219: 235-242.
- 53 T. L. Bahers, C. Adamo, I. Ciofini. A Qualitative Index of Spatial Extent in Charge-Transfer Excitations. *J. Chem. Theory Comput.*, **2011**, 7, 8: 2498-2506.
- 54 A. B. Muñoz-García, M. Pavone. Structure and energy level alignment at the dye-electrode interface in p-type DSSCs: new hints on the role of anchoring modes from ab initio calculations. *Phys. Chem. Chem. Phys.*, **2015**, 17: 12238-12246.
- 55 W. Hamd, M. Chavarot-Kerlidou, J. Fize, G. Muller, A. Leyris, M. Matheron, E. Courtin, M. Fontecave, C. Sanchez, V. Artero, C. Laberty-Robert. Dye-sensitized nanostructured

-
- crystalline mesoporous tin-doped indium oxide films with tunable thickness for photoelectrochemical applications. *J. Mater. Chem. A*, **2013**, 1: 8217-8225.
- 56 We note that such values are much lower than those typically measured in non-aqueous electrolytes as previously reported: F. Bella, C. Gerbaldi, C. Barolo, M. Grätzel. Aqueous dye-sensitized solar cells. *Chem. Soc. Rev.*, **2015**, 44: 3431-3473.
- 57 J. Massin, S. L. Lyu, M. Pavone, A. B. Muñoz-Garcia, B. Kauffmann, T. Toupance, C. Olivier. Design and synthesis of novel organometallic dyes for NiO sensitization and photo-electrochemical applications. *Dalton Trans.*, **2016**, 45: 12539-12547.
- 58 J. R. Aranzaes, M.-C. Daniel, D. Astruc. Metallocenes as references for the determination of redox potentials by cyclic voltammetry-Permethyated iron and cobalt sandwich complexes, inhibition by polyamine dendrimers, and the role of hydroxy-containing ferrocenes. *Can. J. Chem.*, **2006**, 84: 288-299.
- 59 G. Grelaud, N. Gauthier, Y. Luo, F. Paul, B. Fabre, F. Barrière, S. Ababou-Girard, T. Roisnel, M. G. Humphrey. Redox-Active Molecular Wires Derived from Dinuclear Ferrocenyl/Ruthenium(II) Alkynyl Complexes: Covalent Attachment to Hydrogen-Terminated Silicon Surfaces. *J. Phys. Chem. C*, **2014**, 118, 7: 3680-3695.
- 60 A. Mulas, Y.-M. Hervault, X. He, E. D. Piazza, L. Norel, S. Rigaut, C. Lagrost. Fast Electron Transfer Exchange at Self-Assembled Monolayers of Organometallic Ruthenium(II) σ -Arylacetylide Complexes. *Langmuir*, **2015**, 31, 25: 7138-7147.

Chapter V: General Conclusion

The main objective of this work was i) the design and synthesis of new colorful dyes based on organometallic complexes featuring the original D-[M]-A architecture where [M] is the electron-rich [Ru(dppe)₂] metal center for n-type DSCs and p-type DSCs, ii) the characterization their optical and electronic properties as well as their photovoltaic performance in TiO₂-based n-type devices and NiO-based p-type devices, respectively. Following this work, our aim was to widen the scope of applications of these organometallic sensitizers to NiO-based DSPEC for H₂ evolution.

Thus, on the basis of previous works led in our group, the Chapter II describes the synthesis and study of a novel series of dyes for n-type DSCs. In particular, three new push-pull dyes featuring the organometallic [Ru(dppe)₂] fragment were designed and successfully prepared for DSC applications. In order to access narrow band-gap dyes with Near-IR absorption properties, our strategy consisted in modulating the electron-withdrawing part of D-[M]-A- π -A' systems where A is the benzothiadiazole (BTD) unit, π represents an aromatic π -spacer and A' represents both secondary acceptor and anchoring function. This molecular design afforded efficient photosensitizers with strong absorption properties in the visible range, in particular a green dye was obtained with broad absorption between 500 and 800 nm. The introduction of an aromatic π -spacer between the BTD and the semiconductor, by impeding charge recombination and back electron transfer from the surface, allowed improved performance of **[Ru]2** compared to the Ru-BTD sensitizer reported before. Finally, the dyes **[Ru]2** and **[Ru]3**, combining BTD and cyanoacrylic acid moieties, afforded much higher performance than **[Ru]1**, endowed with a simple carboxylic acid function, thus showing that the choice of the anchoring group is of paramount importance to optimize the device operation. Overall, this study shows the relevance of finely tuned push-pull organometallic complexes for the design of narrow bandgap dyes for efficient DSCs with increased harvesting of low energy photons.

In the Chapter III we describe the synthesis and characterization of the first ruthenium diacetylide complexes for p-type DSCs. The first two complexes, **SL1** and **SL2**, were endowed with a bidentate anchoring group based on a triphenylamine motif as electron-donating unit (D) and functionalized with an electron-accepting group (A) connected to the [Ru(dppe)₂] metal fragment by a bithiophene linker. Simple modification of the alkynyl ligand on the acceptor side allowed easy fine-tuning of the optical properties of the complexes, leading to red and blue dyes with strong visible-light absorption properties. Spectroscopic and electrochemical studies of the two dyes confirmed suitable optical and electronic properties (*i.e.* appropriate energy levels) for use in p-type DSC devices. Theoretical calculations were

performed to rationalize the experimental data. The photovoltaic performance of these dyes were subsequently investigated in NiO-based p-type DSCs, in collaboration with Dr. Fabrice Odobel (University of Nantes). Interestingly, although these two dyes were not perfectly optimized (*i.e.* moderate electron injection driving force) their photovoltaic performances were relatively high compared with other organometallic dyes reported for the same application (*i.e.* ruthenium polypyridine complexes). In our study the best performing dye (the red dye **SL1**) afforded photocurrent density of $2.25 \text{ mA}\cdot\text{cm}^{-2}$ and maximum IPCE of 18 %. These promising results paved the way towards other finely tuned organometallic efficient dyes for such application. We indeed anticipated that better performing ruthenium diacetylide dyes could be developed by lowering the energy position of their HOMO level in order to enhance electron injection rate from the semiconductor.

Therefore, two novel Ru-based dyes were designed and prepared, in which the electron-donating unit was replaced by a simple phenyl (**SL3**) or thiophene (**SL4**) unit. The two dyes were functionalized with the same electron-withdrawing ligand as **SL1**, the dimethylmalonate group. As expected, the use of less electron-rich units as donors afforded lower HOMO energy levels compared to the dye **SL1**, which was expected to enhance the charge injection rates. However, the efficiencies of p-DSCs based on **SL3** and **SL4** were lower than those based on **SL1**, which was attributed to lower dye loading amount with the two new dyes.

We therefore looked for a better performing Ru-diacetylide dye by replacing the anchoring function. The phosphonic acid group was chosen for this purpose, in order to improve the density of dye on the photoelectrode. The complex **SL5**, endowed with a phosphonic acid anchoring group on one side, was also functionalized by the dimethylmalonate electron-withdrawing group on the acceptor side. As expected, enhanced dye loading amount on NiO was observed with **SL5**, compared to **SL3** and **SL4**. In p-DSC devices, using the standard iodide/triiodide redox mediator, the dye **SL5** showed slightly enhanced photovoltaic performance compared to **SL3** and **SL4** but lower performance than those obtained with **SL1**. However, the dye **SL5**, combined with a disulfide/thiolate-based electrolyte, eventually showed higher open-circuit photovoltage and the best performance of the series, leading to $\text{PCE} = 0.125\%$.

On the basis of the good results obtained with **SL5** and a disulfide/thiolate-based electrolyte, we eventually designed new Ru-based complexes with optimized structure in view of increasing both the dye-loading amount on the electrode and the charge injection rate in p-type DSC devices. The synthesis of new dyes is thus currently in progress in our group,

in collaboration with the group of Dr. Fabrice Odobel.

Our third objective was to extend the scope of application of ruthenium-based organometallic sensitizers to NiO-based DSPEC for H₂ evolution.

Thus, the Chapter IV describes the design, preparation and study of innovative organometallic chromophores featuring an original π -conjugated structure for binding onto a semi-conducting metal oxide in view of photochemical applications. In particular, we explored the use of mixed allenylidene-acetylide ruthenium complexes for the photosensitization of NiO and photocurrent generation in dye-sensitized photoelectrochemical devices.

The new dyes present a highly conjugated structure including the [Ru(dppe)₂] metal fragment with a delocalized allenylidene ligand on one side and a σ -alkynyl ligand bearing an electron-rich group, *i. e.* thiophene or triphenylamine unit, and one or two anchoring functions, on the other side. The optoelectronic, electrochemical and photoelectrochemical properties of the two dyes were systematically investigated. A broad photoresponse was observed with absorption maximum at 600 nm. Furthermore, the X-ray crystal structure of one precursor was obtained and theoretical calculations were performed in order to address the photophysical properties of the new dyes. These photosensitizers were further implemented into NiO-based photocathodes and tested as photocurrent generators under pertinent aqueous conditions in association with [Co(NH₃)₅Cl]Cl₂ as an irreversible electron acceptor. The dye-sensitized photocathodes provided good photocurrent densities (40-60 $\mu\text{A}\cdot\text{cm}^{-2}$) at neutral pH in phosphate buffer and a high stability was observed for both dyes.

Overall, this study evidenced the relevance of push-pull organometallic dyes for the construction of photocathodes operating in water.

Thus, following this work, we designed and prepared a new mono-molecular photocatalytic system via axial coordination of a cobalt-based H₂-evolving catalyst (*i.e.* cobaloxime) on a pyridyl-functionalized Ru-diacetylide photosensitizer. The photocatalytic system **SL8-Co** showed suitable optical and electrochemical properties for use in NiO-based DSPECs. Thus photocathodes based on NiO nanoparticulate thin-film were prepared using our this [Ru-Co] photocatalytic system. Long-term electrolysis in acetate buffer (0.1 M, pH 4.5) and under 1 sun visible-light irradiation led to photoelectrochemical generation of H₂ with a faradaic efficiency of $\sim 27\%$. This efficiency, comparable to other reports in the literature,¹⁻³ fully validated our approach consisting in using organometallic ruthenium complexes as photoactive species to build efficient NiO-based DSPECs.

Finally, we recently designed a new mono-molecular photocatalytic system via

coordination of a platinum-based H₂-evolving catalyst to a bipyridyl-functionalized Ru-diacetylide complex as photosensitizer. The optical and electrochemical properties of this new photocatalytic system are currently under investigations, then the new photocatalytic system will be employed for the construction of NiO-based photocathodes and subsequent H₂ generation in DSPECs.

References

- 1 Z. Ji, M. He, Z. Huang, U. Ozkan, Y. Wu. Photostable p-Type Dye-Sensitized Photoelectrochemical Cells for Water Reduction. *J. Am. Chem. Soc.*, **2013**, 135, 32: 11696-11699.
- 2 N. Kaeffer, J. Massin, C. Lebrun, O. Renault, M. Chavarot-Kerlidou, V. Artero. Covalent Design for Dye-Sensitized H₂-Evolving Photocathodes Based on a Cobalt Diimine-Dioxime Catalyst. *J. Am. Chem. Soc.*, **2016**, 138, 38: 12308-12311.
- 3 J. Massin, M. Bräutigam, N. Kaeffer, N. Queyriaux, M. J. Field, F. H. Schacher, J. Popp, M. Chavarot-Kerlidou, B. Dietzek, V. Artero. Dye-sensitized PS-*b*-P2VP-templated nickel oxide films for photoelectrochemical applications. *Interface Focus*, **2015**, 5, 3: 20140083.

Chapter VI: Experimental Part

VI.1. Materials and Methods

The reactions were carried out under inert atmosphere using Schlenk techniques. Solvents were dried from appropriate drying agents (sodium for pentane, diethyl ether and THF; calcium hydride for dichloromethane, chloroform and methanol) and freshly distilled under nitrogen before use. All reagents were obtained from commercially available sources and used without further purification.

[**11**][TfO]¹, the alkynyl ligands **7** and **10**,² [RuCl(dppe)₂][TfO] (**[26][TfO]**)³ and 5'-trimethylsilylethynyl-[2,2']-bithiophene-5-carbaldehyde (**21**)⁴ were synthesized according to literature procedures.

¹H NMR, ¹³C NMR and ³¹P NMR analyses were performed on Bruker Avance I 300 MHz, Avance II 400 MHz and Avance III 600 MHz spectrometers. Chemical shift values are given in ppm with reference to solvent residual signals. HR-MS analyses were performed by the CESAMO (Bordeaux, France). Field desorption (FD) measurements were carried out on a TOF mass spectrometer AccuTOF GCv using an FD emitter with an emitter voltage of 10 kV. One to two microliters solution of the compound were deposited on a 13 μm emitter wire. FT-IR spectra were recorded on a Perkin Elmer Spectrum 100 spectrometer using KBr pellets. UV-visible absorption spectra were recorded on a UV-1650PC SHIMADZU spectrophotometer. Cyclic voltammetry analyses were performed using a potentiostat/galvanostat Autolab PGSTAT100 and a three-electrode system (working electrode: Pt disc; reference electrode: Ag/AgCl, calibrated with decamethylferrocene as internal reference; counter electrode: Pt) with 0.1M Bu₄NPF₆ as salt support at a scan rate of 100 to 400 mV·s⁻¹. Potentials were afterwards referred to NHE by addition of 130 mV.⁵

DFT and TD-DFT calculations for [**Ru**]**1**-[**Ru**]**3** and **SL1**-**SL5** were performed by Dr. Laurent Ducasse (ISM, Bordeaux) with Gaussian09.⁶ B3LYP/LANL2DZ optimized geometries in vacuo conditions were used to perform TD-DFT calculations using the LANL2DZ basis set together with the MPW1K XC functional containing 42.8% of HF exchange,⁷ while taking into account the solvent within the integral equation formalism of the polarizable continuum model (IEF-PCM).^{8,9}

DFT and TD-DFT calculations for **SL6**, **SL7**, **SL8** and **SL8-Co** were performed by Dr. Michele Pavone and Dr. Ana-Belen Muñoz-García (University of Naples) with the Gaussian09 suite of programs for quantum chemistry.⁶ The PBE0 hybrid density functional¹⁰ for ground state calculations was employed, including the semi-empirical dispersion term proposed by Grimme (D3BJ).¹¹ The standard Pople's 6-31G(d,p) basis set,¹² for H, C, N, O, P, and S atoms, and the SDD effective core potential and basis set for Ru¹³ provided the best

compromise between accuracy and computational feasibility. The polarizable continuum model (PCM) of solvation¹⁴ has been applied to model the dichloromethane solvent. The Ru-based dyes under investigation have been purposely designed to undergo electronic excitation with long-range intra-molecular charge transfer from the ground to the excited states. This represents the worst-case scenario for the state-of-the-art time-dependent DFT (TD-DFT) methods.¹⁵ Thus in Chapter IV several density functional models were tested for the TD-DFT calculations (see Table IV-3) and the long-range corrected LC- ω PBE density functional was chosen.¹⁶ Analysis of electron density rearrangement upon vertical excitation has been performed according to the charge-transfer indexes developed by Ciofini and coworkers.¹⁷

X-ray photoelectron spectroscopy surface analyses were performed at PLACAMAT (UMS 3626) with a K-Alpha spectrometer (ThermoFisher Scientific) for powders pressed onto indium foil. The monochromatized AlK α source ($h\nu=1486.6\text{eV}$) was activated with a spot size 200 μm in diameter. The full spectra (0-1100 eV) were obtained with a constant pass energy of 200 eV and high resolution spectra with a constant pass energy of 40 eV (dwell time 200 ms). Fitting and quantitative analyses of XPS spectra were performed using the AVANTAGE software (ThermoFisher Scientific).

VI.2. Synthesis

VI.2.1. Synthetic Routes to the Dyes [Ru]1-[Ru]3

Synthesis of 4. To the residue of **3** was added HBTU (437 mg, 1.15 mmol), DMF (15 mL), DIPEA (836 μL , 4.80 mmol) and 2-(trimethylsilyl)ethanol (227 μL , 1.58 mmol). The reaction mixture was stirred for 18h at RT. The reaction mixture was evaporated to dryness. The residue was dissolved in CH_2Cl_2 and the solution was washed with saturated NH_4Cl aqueous solution. The organic phase was evaporated to dryness. After adsorbed on silica gel in advance, the crude solid was purified by silica gel chromatography with CH_2Cl_2 as an eluent, to afford **4** as a red-brown solid in 35 % yield (117 mg, 0.30 mmol). ^1H NMR (300 MHz, CDCl_3): δ 8.20 (2H, d, $^3J_{\text{H-H}} = 8.3$ Hz), 8.02 (2H, d, $^3J_{\text{H-H}} = 8.3$ Hz), 7.91 (1H, d, $^3J_{\text{H-H}} = 7.3$ Hz), 7.74 (1H, d, $^3J_{\text{H-H}} = 7.3$ Hz), 4.47 (2H, t, $^3J_{\text{H-H}} = 8.3$ Hz), 3.66 (1H, s), 1.17 (2H, t, $^3J_{\text{H-H}} = 8.5$ Hz), 0.10 (9H, s). ^{13}C NMR (300 MHz, CDCl_3): 166.5, 155.5, 152.9, 141.0, 134.4, 133.9, 130.9, 129.9, 129.3, 128.0, 115.6, 84.3, 79.4, 63.6, 17.5, -1.2. CI-HRMS (m/z): 381.1096 [M-H] $^+$ (calcd. 381.1093 for $\text{C}_{20}\text{H}_{21}\text{N}_2\text{O}_2\text{SSi}$).

Synthesis of 7. Compound **6** (200 mg, 0.594 mmol) and K_2CO_3 (82 mg, 0.59 mmol) were dissolved in MeOH (150 mL). The mixture was stirred for 2h at RT. The reaction mixture was diluted with H_2O and the product was extracted with CH_2Cl_2 . The organic phase was dried with MgSO_4 and evaporated to dryness to afford **7** as a red solid in 99 % yield (155 mg, 0.58 mmol). ^1H NMR (300 MHz, CDCl_3): δ 10.11 (1H, s), 8.12 (2H, m), 8.05 (2H, m), 7.91 (1H, m), 7.76 (1H, d, $^3J_{\text{H-H}} = 7.4$ Hz), 3.67 (1H, s). ^{13}C NMR (300 MHz, CDCl_3): 191.9, 155.6, 153.6, 142.7, 134.4, 133.9, 132.6, 130.1, 130.1, 128.3, 116.0, 84.6, 79.3. CI-HRMS (m/z): 264.0357 [M] $^-$ (calcd. 264.0357 for $\text{C}_{15}\text{H}_8\text{N}_2\text{OS}$).

Synthesis of 10. To compound **9** (176 mg, 0.514 mmol) and K_2CO_3 (71 mg, 0.51 mmol) were added MeOH (150 mL). The mixture was stirred for 2h at RT. The reaction mixture was diluted with H_2O and the product was extracted with EtOAc. The organic phase was dried with MgSO_4 and evaporated to dryness to afford **10** as a red solid in 96 % (133 mg, 0.49 mmol). ^1H NMR (300 MHz, CDCl_3): δ 9.99 (1H, s), 8.24 (1H, d, $^3J_{\text{H-H}} = 4.1$ Hz), 7.96 (1H, d, $^3J_{\text{H-H}} = 7.5$ Hz), 7.87 (1H, d, $^3J_{\text{H-H}} = 6.9$ Hz), 7.86 (1H, d, $^3J_{\text{H-H}} = 4.1$ Hz), 3.71 (1H, s). ^{13}C NMR (300 MHz, CDCl_3): δ 183.4, 155.3, 152.2, 147.9, 144.3, 137.5, 133.8, 130.0, 126.5, 126.0, 117.6, 84.2, 80.1. CI-HRMS (m/z): 269.9923 [M] $^-$ (calcd. 269.9922 for $\text{C}_{13}\text{H}_6\text{N}_2\text{OS}_2$).

Synthesis of 12. To a solution of [**11**][**TfO**] (300 mg, 0.22 mmol, 1 equiv.), compound **4** (100 mg, 0.26 mmol, 1.2 equiv.) and NaPF_6 (74 mg, 0.44 mmol, 2 equiv.) in dry CH_2Cl_2 (25 mL) and under inert atmosphere, was added distilled Et_3N (92 μL , 0.66 mmol, 3 equiv.). The reaction mixture was stirred for 24h at RT. The organic phase was further washed with degassed water and evaporated to dryness. Precipitation from a CH_2Cl_2 /pentane mixture afforded pure **12** as a purple solid in 72 % yield (244 mg, 0.16 mmol). ^{31}P NMR (120 MHz, CDCl_3): δ = 53.8. ^1H NMR (300 MHz, CDCl_3): δ = 8.15 (m, 6H), 7.71 (m, 8H), 7.52 (d, 1H, $^3J_{\text{H-H}} = 7.6$ Hz), 7.45-7.38 (m, 12H), 7.31-7.19 (m, 8H), 7.06-6.95 (m, 14H), 6.78-6.73 (m, 8H), 6.33 (d, 1H, $^3J_{\text{H-H}} = 7.6$ Hz), 4.46 (m, 2H), 2.96 (m, 4H), 2.72 (m, 4H), 1.17 (m, 2H), 0.10 (s, 9H). ^{13}C NMR (100 MHz, CD_2Cl_2): δ = 166.8, 157.5, 153.9, 153.0, 142.9, 141.5, 137.6, 137.2, 134.9, 134.8, 134.5, 134.4, 133.8, 132.8, 131.5, 131.3, 130.1, 129.9, 129.7, 129.6, 129.3, 129.2, 128.8, 127.5, 127.3, 126.6, 126.4, 126.3, 126.2, 123.9, 123.5, 120.5, 120.0, 118.0, 117.4, 110.3, 63.5, 31.9, 17.7, -1.3. HR-MS FD^+ (m/z): 1543.3676 [M] $^+$ (calcd. 1543.3656 for $[\text{C}_{92}\text{H}_{79}\text{N}_3\text{O}_2\text{P}_4\text{RuSSi}]^+$). FT-IR (KBr): $\nu_{\text{C=C}} = 2034$ cm^{-1} , $\nu_{\text{C=O}} = 1711$ cm^{-1} , $\nu_{\text{P-Ph}} = 1097$ cm^{-1} .

Synthesis of [Ru]1. To a solution of **12** (240 mg, 0.15 mmol, 1 equiv.) in dry THF (22 mL) and under inert atmosphere was added TBAF (1M sol. in THF, 0.23 mL, 1.5 equiv.). The reaction mixture was stirred overnight at RT. After removal solvent the resulting solid was dissolved in CH₂Cl₂ and thoroughly washed with degassed citric acid aqueous solution (10 % m) and pure water. The organic phase was evaporated to dryness and the solid was further washed with pentane. Slow crystallization from a CH₂Cl₂/pentane mixture afforded pure **[Ru]1** as a purple powder in 78 % yield (175 mg, 0.12 mmol). ³¹P NMR (240 MHz, THF-d₈): δ = 53.1. ¹H NMR (600 MHz, THF-d₈): δ = 8.27 (d, 2H, ³J_{H-H} = 7.8 Hz), 8.17 (d, 4H, ³J_{H-H} = 7.8 Hz), 7.85 (m, 8H), 7.71 (d, 1H, ³J_{H-H} = 7.3 Hz), 7.49-7.39 (m, 14H), 7.28-7.25 (m, 6H), 7.16 (d, 2H, ³J_{H-H} = 7.8 Hz), 7.11-7.07 (m, 12H), 6.81 (m, 8H), 6.46 (d, 1H, ³J_{H-H} = 7.3 Hz), 3.10 (m, 4H), 2.82 (m, 4H). ¹³C NMR (100 MHz, THF-d₈): δ = 168.2, 158.9, 155.1, 154.4, 143.8, 142.6, 139.0, 138.4, 136.1, 135.6, 134.2, 132.6, 132.3, 131.4, 131.2, 131.1, 131.0, 130.6, 130.4, 129.9, 129.8, 128.7, 128.4, 127.6, 127.5, 127.1, 125.2, 125.0, 121.5, 121.1, 119.5, 118.5, 111.3, 33.1. HR-MS FD⁺ (m/z): 1443.2971 [M]⁺ (calcd. 1443.2948 for [C₈₇H₆₇N₃O₂P₄RuS]⁺). FT-IR (KBr): ν_{C≡C} = 2037 cm⁻¹, ν_{C=O} = 1728 cm⁻¹, ν_{P-Ph} = 1095 cm⁻¹.

Synthesis of 13. To a solution of **[11][TfO]** (270 mg, 0.2 mmol, 1 equiv.), compound **7** (58 mg, 0.22 mmol, 1.1 equiv.) and NaPF₆ (67 mg, 0.4 mmol, 2 equiv.) in dry CH₂Cl₂ (20 mL) and under inert atmosphere, was added distilled Et₃N (85 μL, 0.6 mmol, 3 equiv.). The reaction mixture was stirred for 24h at RT. The organic phase was further washed with degassed water and evaporated to dryness. Precipitation from a CH₂Cl₂/pentane mixture afforded pure **13** as a purple solid in 75 % yield (215 mg, 0.15 mmol). ³¹P NMR (120 MHz, CD₂Cl₂): δ = 53.8. ¹H NMR (300 MHz, CD₂Cl₂): δ = 10.13 (s, 1H), 8.28 (d, 2H, ³J_{H-H} = 8.3 Hz), 8.19 (d, 2H, ³J_{H-H} = 7.7 Hz), 8.06 (d, 2H, ³J_{H-H} = 8.3 Hz), 7.76 (m, 8H), 7.60 (d, 1H, ³J_{H-H} = 7.6 Hz), 7.50-7.25 (m, 20H), 7.11-7.01 (m, 14H), 6.84-6.78 (m, 8H), 6.37 (d, 1H, ³J_{H-H} = 7.6 Hz), 3.01 (m, 4H), 2.77 (m, 4H). ¹³C NMR (100 MHz, CD₂Cl₂): δ = 192.1, 157.6, 154.3, 153.8, 144.5, 141.4, 137.5, 137.1, 135.5, 134.8, 134.3, 133.6, 132.8, 131.3, 130.1, 129.9, 129.6, 129.4, 129.3, 128.8, 127.6, 127.3, 126.5, 126.2, 125.9, 124.3, 123.5, 120.5, 120.0, 118.1, 117.8, 110.3, 31.9. HR-MS FD⁺ (m/z): 1427.3022 [M]⁺ (calcd. 1427.3022 for [C₈₇H₆₇N₃OP₄RuS]⁺). FT-IR (KBr): ν_{C≡C} = 2033 cm⁻¹, ν_{C=O} = 1697 cm⁻¹, ν_{P-Ph} = 1093 cm⁻¹.

Synthesis of 14. To a solution of **13** (188 mg, 0.13 mmol, 1 equiv.) and 2-trimethylsilylethyl 2-cyanoacetate (49 mg, 0.26 mmol, 2 equiv.), in dry CHCl₃ (20 mL) and under inert atmosphere, was added piperidine (52 μL, 0.52 mmol, 4 equiv.). The reaction

mixture was refluxed for 48h. The organics were further washed with degassed water and evaporated to dryness. Precipitation from a CH₂Cl₂/pentane mixture afforded pure **14** as a purple solid in 72 % yield (150 mg, 0.094 mmol). ³¹P NMR (120 MHz, CDCl₃): δ = 53.7. ¹H NMR (300 MHz, CDCl₃): δ = 8.30 (s, 1H), 8.25 (d, 2H, ³J_{H-H} = 8.4 Hz), 8.16 (d, 4H, ³J_{H-H} = 7.7 Hz), 7.73 (m, 8H), 7.58 (d, 1H, ³J_{H-H} = 7.6 Hz), 7.48-7.21 (m, 20H), 7.08-6.98 (m, 14H), 6.81-6.76 (m, 8H), 6.35 (d, 1H, ³J_{H-H} = 7.6 Hz), 4.45 (m, 2H), 2.98 (m, 4H), 2.67 (m, 4H), 1.18 (m, 2H), 0.11 (s, 9H). ¹³C NMR (100 MHz, CD₂Cl₂): δ = 163.2, 157.5, 155.4, 154.3, 153.8, 143.5, 141.4, 137.5, 137.1, 134.7, 134.3, 133.7, 132.8, 131.7, 131.3, 130.6, 130.0, 129.7, 129.6, 129.4, 129.3, 128.8, 128.6, 127.6, 127.3, 126.5, 126.1, 125.7, 124.4, 123.5, 120.5, 120.0, 118.1, 116.3, 110.2, 102.6, 65.4, 31.9, 17.6, -1.4. HR-MS FD⁺ (m/z): 1594.3813 [M]⁺ (calcd. 1594.3790 for [C₉₅H₈₀N₄O₂P₄RuSSi]⁺). FT-IR (KBr): ν_{C=N} = 2220 cm⁻¹, ν_{C=C} = 2032 cm⁻¹, ν_{C=O} = 1722 cm⁻¹, ν_{P-Ph} = 1092 cm⁻¹.

Synthesis of [Ru]2. To a solution of **14** (150 mg, 0.094 mmol, 1 equiv.) in dry THF (18 mL) and under inert atmosphere was added TBAF (1M sol. in THF, 0.14 mL, 1.5 equiv.). The reaction mixture was stirred overnight at RT. After removal solvent the resulting solid was dissolved in CH₂Cl₂ and thoroughly washed with degassed citric acid aqueous solution (10 % m) and pure water. The organics were evaporated to dryness and the solid was further washed with pentane. Slow crystallization from a CH₂Cl₂/pentane mixture afforded pure **[Ru]2** as a deep violet powder in 75 % yield (105 mg, 0.07 mmol). ³¹P NMR (240 MHz, THF-d₈): δ = 53.5. ¹H NMR (600 MHz, THF-d₈): δ = 8.39 (d, 2H, ³J_{H-H} = 7.9 Hz), 8.36 (s, 1H), 8.23 (d, 2H, ³J_{H-H} = 7.9 Hz), 8.17 (d, 4H, ³J_{H-H} = 7.4 Hz), 7.83 (m, 8H), 7.77 (d, 1H, ³J_{H-H} = 7.4 Hz), 7.48-7.38 (m, 14H), 7.27-7.05 (m, 19H), 6.80 (m, 8H), 6.45 (d, 1H, ³J_{H-H} = 7.3 Hz), 3.09 (m, 4H), 2.81 (m, 4H). ¹³C NMR (200 MHz, THF-d₈): δ = 164.9, 158.8, 156.0, 155.0, 153.4, 143.5, 142.5, 138.9, 138.3, 136.0, 135.8, 135.5, 135.0, 134.1, 132.5, 132.2, 131.3, 131.2, 130.6, 130.3, 130.2, 129.8, 128.6, 128.3, 127.5, 127.3, 127.0, 125.4, 124.8, 121.6, 121.4, 121.0, 119.5, 119.0, 117.8, 111.2, 33.0. HR-MS FD⁺ (m/z): 1450.3182 [M-CO₂]⁺ (calcd. 1450.3158 for [C₈₉H₆₈N₄P₄RuS]⁺). FT-IR (KBr): ν_{C=N} = 2212 cm⁻¹, ν_{C=C} = 2031 cm⁻¹, ν_{C=O} = 1705 cm⁻¹, ν_{P-Ph} = 1093 cm⁻¹.

Synthesis of 15. To a solution of **[11][TfO]** (337 mg, 0.25 mmol, 1 equiv.), compound **10** (74 mg, 0.275 mmol, 1.1 equiv.) and NaPF₆ (84 mg, 0.5 mmol, 2 equiv.) in dry CH₂Cl₂ (30 mL) and under inert atmosphere, was added distilled Et₃N (105 μL, 0.75 mmol, 3 equiv.). The reaction mixture was stirred for 24h at RT. The organics were further washed with degassed

water and evaporated to dryness. Precipitation from a CH₂Cl₂/pentane mixture afforded pure **15** as a blue solid in 70 % yield (250 mg, 0.17 mmol). ³¹P NMR (120 MHz, CDCl₃): δ = 53.6. ¹H NMR (300 MHz, CDCl₃): δ = 9.96 (s, 1H), 8.18 (s, 1H), 8.16 (d, 2H, ³J_{H-H} = 8.3 Hz), 7.78 (m, 9H), 7.78-7.04 (m, 35H), 6.75 (m, 8H), 6.22 (d, 1H, ³J_{H-H} = 7.6 Hz), 2.99 (m, 4H), 2.74 (m, 4H). ¹³C NMR (100 MHz, CD₂Cl₂): δ = 183.3, 159.9, 157.3, 152.8, 150.8, 142.4, 141.5, 137.7, 137.6, 137.1, 134.9, 134.3, 133.2, 133.0, 131.4, 130.1, 129.5, 129.0, 128.7, 127.7, 127.4, 126.7, 126.3, 125.1, 123.6, 120.6, 120.1, 119.7, 119.4, 118.7, 110.4, 32.0. HR-MS FD⁺ (m/z): 1433.2634 [M]⁺ (calcd. 1433.2585 for [C₈₅H₆₅N₃OP₄RuS₂]⁺). FT-IR (KBr): ν_{C=C} = 2027 cm⁻¹, ν_{C=O} = 1659 cm⁻¹, ν_{C=C (Thiophene)} = 1433 cm⁻¹, ν_{P-Ph} = 1096 cm⁻¹.

Synthesis of 16. To a solution of **15** (200 mg, 0.14 mmol, 1 equiv.) and 2-trimethylsilylethylcyano-ethanoate (52 mg, 0.28 mmol, 2 equiv.), in dry CHCl₃ (20 mL) and under inert atmosphere, was added piperidine (56 μL, 0.56 mmol, 4 equiv.). The reaction mixture was refluxed for 48h. The organics were further washed with degassed water and evaporated to dryness. Precipitation from a CH₂Cl₂/pentane mixture afforded pure **16** as a green solid in 45 % yield (100 mg, 0.06 mmol). ³¹P NMR (120 MHz, CDCl₃): δ = 53.6. ¹H NMR (300 MHz, CDCl₃): δ = 8.35 (s, 1H), 8.28 (d, 1H, ³J_{H-H} = 4.1 Hz), 8.16 (d, 2H, ³J_{H-H} = 7.7 Hz), 7.85 (d, 1H, ³J_{H-H} = 4.1 Hz), 7.81 (m, 8H), 7.76 (d, 1H, ³J_{H-H} = 7.8 Hz), 7.50-7.42 (m, 4H), 7.35-7.23 (m, 16H), 7.10-7.03 (m, 14H), 6.78-6.73 (m, 8H), 6.18 (d, 1H, ³J_{H-H} = 7.8 Hz), 4.42 (m, 2H), 3.00 (m, 4H), 2.74 (m, 4H), 1.17 (m, 2H), 0.10 (s, 9H). ¹³C NMR (100 MHz, CD₂Cl₂): δ = 163.8, 162.3, 157.3, 152.9, 151.6, 146.7, 141.6, 139.7, 137.6, 137.1, 135.2, 135.0, 134.3, 133.1, 131.5, 130.2, 129.8, 129.6, 129.1, 127.8, 127.5, 126.8, 126.3, 125.4, 123.7, 120.7, 120.1, 119.5, 119.2, 117.1, 110.5, 97.6, 65.2, 32.1, 18.2, -1.2. HR-MS FD⁺ (m/z): 1600.3284 [M]⁺ (calcd. 1600.3329 for [C₉₃H₇₈N₄O₂P₄RuS₂Si]⁺). FT-IR (KBr): ν_{C=N} = 2214 cm⁻¹, ν_{C=C} = 2024 cm⁻¹, ν_{C=O} = 1712 cm⁻¹, ν_{C=C (Thiophene)} = 1432 cm⁻¹, ν_{P-Ph} = 1093 cm⁻¹.

Synthesis of [Ru]3. To a solution of **16** (90 mg, 0.056 mmol, 1 equiv.) in dry THF (9 mL) and under inert atmosphere was added TBAF (1M sol. in THF, 67 μL, 0.067 mmol, 1.2 equiv.). The reaction mixture was stirred overnight at RT. After removal solvent the resulting solid was dissolved in CH₂Cl₂ and thoroughly washed with degassed citric acid aqueous solution (10 % m) and pure water. The organics were evaporated to dryness and the solid was further washed with pentane. Slow crystallization from a CH₂Cl₂/pentane mixture afforded pure **[Ru]3** as a green powder in 73 % yield (61 mg, 0.041 mmol). ³¹P NMR (240 MHz, THF-d₈): δ = 53.4. ¹H NMR (600 MHz, THF-d₈): δ = 8.43 (s, 1H), 8.36 (d, 1H, 3J_{H-H} = 4.1

Hz), 8.17 (d, 2H, $^3J_{\text{H-H}} = 7.8$ Hz), 7.98 (d, 1H, $^3J_{\text{H-H}} = 4.1$ Hz), 7.92 (d, 1H, $^3J_{\text{H-H}} = 7.7$ Hz), 7.90 (m, 8H), 7.49 (d, 2H, $^3J_{\text{H-H}} = 8.2$ Hz), 7.44-7.38 (m, 12H), 7.28-7.25 (m, 6H), 7.49 (d, 2H, $^3J_{\text{H-H}} = 8.3$ Hz), 7.13-7.05 (m, 12H), 6.79 (m, 8H), 6.36 (d, 1H, $^3J_{\text{H-H}} = 7.7$ Hz), 3.12 (m, 4H), 2.81 (m, 4H). ^{13}C NMR (200 MHz, THF-d8): $\delta = 164.9, 162.4, 158.4, 153.8, 151.6, 146.9, 142.5, 140.0, 138.9, 138.1, 136.6, 136.1, 135.3, 134.3, 134.0, 132.5, 131.2, 131.1, 130.4, 129.9, 129.7, 128.7, 128.4, 127.8, 127.6, 127.1, 126.1, 124.9, 121.5, 121.0, 120.8, 120.2, 117.6, 111.2, 100.0, 33.0$. HR-MS FD^+ (m/z): 1456.2767 $[\text{M-CO}_2]^+$ (calcd. 1456.2745 for $[\text{C}_{87}\text{H}_{66}\text{N}_4\text{P}_4\text{RuS}_2]^+$). FT-IR (KBr): $\nu_{\text{C}\equiv\text{N}} = 2212$ cm^{-1} , $\nu_{\text{C}\equiv\text{C}} = 2018$ cm^{-1} , $\nu_{\text{C}=\text{O}} = 1704$ cm^{-1} , $\nu_{\text{C}-\text{C}}$ (Thiophene) = 1430 cm^{-1} , $\nu_{\text{P-Ph}} = 1092$ cm^{-1} .

VI.2.2. Synthetic Routes to the Dyes SL1 and SL2

Synthesis of 17. Methyl 4-bromobenzoate (4.30 g, 20 mmol, 4 equiv.), cesium carbonate (4.89 g, 15 mmol, 3 equiv.), palladium(II) acetate (67 mg, 0.3 mmol, 6%) and aniline (0.45 mL, 5.0 mmol, 1 equiv.) were sequentially introduced in a Schlenk flask under nitrogen. Then dry toluene (50 mL) and tri-tert-butyl-phosphine (0.14 mL, 0.6 mmol, 12%) were added sequentially. The suspension was heated at 90 °C for 3 days. After that, the reaction mixture was diluted with CHCl_3 and filtered. The resulting solution was evaporated to dryness. The crude product was purified on silica gel column (pentane/ethyl acetate (9 : 1, v/v)) to obtain **17** as a pale yellow powder in 63% yield (1.14 g, 3.15 mmol). ^1H NMR (300 MHz, CDCl_3): $\delta = 7.90$ (d, 4H, $^3J_{\text{H-H}} = 9.0$ Hz), 7.35 (t, 2H, $^3J_{\text{H-H}} = 15.0$ Hz), 7.22-7.14 (m, 3H), 7.08 (d, 4H, $^3J_{\text{H-H}} = 9.0$ Hz), 3.89 (s, 6H). ^{13}C NMR (75 MHz, CDCl_3): $\delta = 166.7, 151.1, 146.1, 131.1, 129.9, 126.6, 125.5, 124.2, 122.5, 52.1$.

Synthesis of 18. Zinc acetate (0.25 g, 1.4 mmol, 1 equiv.) was introduced in a Schlenk tube (Schlenk tube A) under nitrogen. Dry dioxane (3 mL) and iodine monochloride (0.45 g, 2.8 mmol, 2 equiv.) were sequentially introduced in the Schlenk tube and stirred at RT for 15 min. At the same time, compound **17** (0.50 g, 1.4 mmol, 1 equiv.) was dissolved in dry dioxane (3 mL) in another Schlenk tube (Schlenk tube B). The solution of Schlenk tube B was subsequently added into Schlenk tube A with a syringe. The solution was stirred at RT overnight. The reaction mixture was poured into saturated aqueous $\text{Na}_2\text{S}_2\text{O}_3$ solution (30 mL) to remove the excess of iodine monochloride and extracted with CH_2Cl_2 . After drying on MgSO_4 , the organic layer was evaporated to give **18** as a red-brown powder in 87% yield (0.58 g, 1.2 mmol). ^1H NMR (300 MHz, CDCl_3): $\delta = 7.92$ (d, 4H, $^3J_{\text{H-H}} = 9.0$ Hz), 7.63 (d, 2H, $^3J_{\text{H-H}} = 9.0$ Hz), 7.08 (d, 4H, $^3J_{\text{H-H}} = 9.0$ Hz), 6.89 (d, 2H, $^3J_{\text{H-H}} = 9.0$ Hz), 3.89 (s, 6H). ^{13}C

NMR (75 MHz, CDCl₃): δ = 166.6, 150.6, 146.0, 138.9, 131.2, 127.9, 124.8, 123.3, 122.8, 88.9, 52.1.

Synthesis of 19. To a solution of **18** (0.48 g, 1.0 mmol, 1 equiv.), PdCl₂(PPh₃)₂ (35 mg, 0.05 mmol, 2.5%) and copper(I) iodide (5 mg, 0.025 mmol, 5%) in dry THF (6 mL) under nitrogen, were added Et₃N (6 mL) and (trimethylsilyl)acetylene (0.21 mL, 1.5 mmol, 1.5 equiv.). The solution was stirred at RT for 6 h. After evaporation of the solvent, the resulting crude product was purified on silica gel column (CH₂Cl₂/pentane (8 : 1, v/v)) to obtain **19** as a pale yellow powder in 70% yield (0.32 g, 0.70 mmol). ¹H NMR (300 MHz, CDCl₃): δ = 7.92 (d, 4H, ³J_{H-H} = 9.0 Hz), 7.42 (d, 2H, ³J_{H-H} = 9.0 Hz), 7.08 (d, 4H, ³J_{H-H} = 9.0 Hz), 7.04 (d, 2H, ³J_{H-H} = 9.0 Hz), 3.89 (s, 6H), 0.25 (s, 18H). ¹³C NMR (75 MHz, CDCl₃): δ = 166.5, 150.5, 146.2, 133.4, 131.1, 125.3, 124.7, 123.2, 123.0, 119.3, 104.4, 94.7, 52.0, -0.03.

Synthesis of 20. Compound **19** (0.68 g, 1.5 mmol, 1 equiv.) and lithium hydroxide monohydrate (0.63 g, 15.0 mmol, 10 equiv.) were introduced into a round-bottom flask under air and dissolved in a mixture of THF (8 mL) and distilled water (2 mL). The suspension was stirred at RT for 6 h. The reaction mixture was acidified with 10% aqueous citric acid until pH 4. THF was subsequently removed through rotary evaporator and the resulting mixture was extracted with ethyl acetate. The organic layer was further washed with water, dried over MgSO₄ and evaporated to dryness. The crude product was obtained as a pale yellow powder in 83% yield (0.45 g, 1.25 mmol) and used without further purification. ¹H NMR (300 MHz, DMSO-d₆): δ = 12.81 (s, 2H), 7.89 (d, 4H, ³J_{H-H} = 9.0 Hz), 7.48 (d, 2H, ³J_{H-H} = 9.0 Hz), 7.10 (m, 6H), 3.57 (s, 1H). The intermediate compound (0.45 g, 1.25 mmol, 1 equiv.) was dissolved in dry DMF (10 mL) under nitrogen atmosphere, and HBTU (1.18 g, 3.1 mmol, 2.5 equiv.), 2-(trimethylsilyl)ethanol (0.72 mL, 5 mmol, 4 equiv.) and N,N-diisopropylethylamine (2.17 mL, 12.5 mmol, 10 equiv.) were added subsequently. The solution was stirred at RT for 48 h. After dilution with CH₂Cl₂ (20 mL), the reaction mixture was washed with saturated aqueous NH₄Cl solution and water, and then dried over MgSO₄ and evaporated to dryness. The crude product was purified on silica gel column (CH₂Cl₂/pentane (1 : 1, v/v) to CH₂Cl₂) to obtain **20** as a pale yellow powder in 65% yield (0.45 g, 0.81 mmol). ¹H NMR (300 MHz, CD₂Cl₂): δ = 7.92 (d, 4H, ³J_{H-H} = 9.0 Hz), 7.44 (d, 2H, ³J_{H-H} = 9.0 Hz), 7.11 (d, 4H, ³J_{H-H} = 9.0 Hz), 7.08 (d, 2H, ³J_{H-H} = 9.0 Hz), 4.40 (m, 4H), 3.14 (s, 1H), 1.12 (m, 4H), 0.08 (s, 18H). ¹³C NMR (75 MHz, CD₂Cl₂): δ = 166.3, 150.8, 147.2, 133.9, 131.3, 125.9, 125.6, 123.6, 118.3, 83.5, 77.6, 63.4, 17.7, -1.40.

Synthesis of 22. To a solution of 5'-trimethylsilylethynyl-[2,2']bithiophene-5-carbaldehyde (**21**) (0.25 g, 0.86 mmol, 1 equiv.) in dry CHCl₃ (50 mL) under nitrogen, were added piperidine (0.34 mL, 3.44 mmol, 4 equiv.) and dimethyl malonate (0.2 mL, 1.72 mmol, 2 equiv.). The solution was heated at reflux for 24 h and then evaporated to dryness. The crude product was purified on silica gel column (pentane/ethyl acetate (9 : 1, v/v)) to obtain **22** as an orange powder in 74% yield (0.26 g, 0.64 mmol). ¹H NMR (300 MHz, CD₂Cl₂): δ = 7.80 (s, 1H), 7.29 (d, 1H, ³J_{H-H} = 4.0 Hz), 7.16 (d, 1H, ³J_{H-H} = 4.0 Hz), 7.15 (s, 1H), 7.14 (s, 1H), 3.92 (s, 3H), 3.80 (s, 3H), 0.25 (s, 9H). ¹³C NMR (75 MHz, CDCl₃): δ = 166.5, 164.8, 143.2, 137.4, 136.6, 135.7, 134.9, 133.6, 124.8, 124.4, 123.7, 120.8, 101.4, 96.9, 53.0, 52.8, -0.2.

Synthesis of 23. Compound **22** (0.26 g, 0.64 mmol, 1 equiv.) was dissolved in dry THF (10 mL) under nitrogen atmosphere. Potassium carbonate (7 mg, 0.054 mmol, 0.1 equiv.) was subsequently added and the suspension was stirred at RT for 24 h. The reaction mixture was then concentrated, poured into pure water and the solution was extracted with CH₂Cl₂. After drying over MgSO₄, the organic layer was evaporated to dryness to afford **23** in 69% yield (0.15 g, 0.44 mmol). ¹H NMR (300 MHz, CDCl₃): δ = 7.82 (s, 1H), 7.26 (d, 1H, ³J_{H-H} = 4.0 Hz), 7.17 (d, 1H, ³J_{H-H} = 3.9 Hz), 7.12 (d, 1H, ³J_{H-H} = 4.0 Hz), 7.09 (d, 1H, ³J_{H-H} = 3.9 Hz), 3.94 (s, 3H), 3.83 (s, 3H), 3.45 (s, 1H). ¹³C NMR (75 MHz, THF-d₈): δ = 166.4, 164.8, 143.0, 138.4, 137.3, 136.3, 135.2, 134.8, 125.7, 125.4, 123.4, 122.7, 85.1, 76.8, 52.6, 52.4.

Synthesis of 24. In a Schlenk flask under nitrogen were sequentially introduced 5'-trimethylsilylethynyl-[2,2']bithiophene-5-carbaldehyde (**21**) (0.25 g, 0.86 mmol, 1 equiv.), 3-methyl rhodanine (0.14 g, 0.95 mmol, 1.1 equiv.), ammonium acetate (0.02 g, 0.26 mmol, 0.3 equiv.) and acetic acid (5 mL). The reaction mixture was left under stirring at 120 °C for 3 h. After cooling down to RT the reaction mixture was filtered and the solid was dissolved in CH₂Cl₂. The resulting solution was washed with pure water and then evaporated to dryness. The crude product was purified on silica gel column (CH₂Cl₂/pentane (1 : 1, v/v)) to obtain **24** as an orange powder in 63% yield (0.23 g, 0.54 mmol). ¹H NMR (300 MHz, CDCl₃): δ = 7.82 (s, 1H), 7.30 (d, 1H, ³J_{H-H} = 4.0 Hz), 7.20 (d, 1H, ³J_{H-H} = 4.0 Hz), 7.15 (s, 2H), 3.51 (s, 3H), 0.26 (s, 9H). ¹³C NMR (75 MHz, CDCl₃): δ = 192.1, 167.4, 144.4, 137.1, 136.9, 135.2, 133.7, 125.4, 125.0, 124.1, 123.2, 120.9, 101.8, 96.8, 31.4, -0.2.

Synthesis of 25. Compound **24** (0.23 g, 0.54 mmol, 1equiv.) was dissolved in a mixture of dry THF (8 mL) and dry MeOH (2 mL) under nitrogen atmosphere. Potassium carbonate (7 mg, 0.054 mmol, 0.1 equiv.) was subsequently added and the suspension was stirred at RT for 24 h. The reaction mixture was then concentrated, poured into pure water and the solution was extracted with CH₂Cl₂. After drying over MgSO₄, the organic layer was evaporated to dryness to afford **25** as a dark red powder in 72% yield (0.14 g, 0.39 mmol). ¹H NMR (300 MHz, DMSO-d₆): δ = 8.07 (s, 1H), 7.75 (s, 1H), 7.58 (s, 1H), 7.52 (s, 1H), 7.41 (s, 1H), 4.80 (s, 1H), 3.39 (s, 3H). ¹³C NMR (75 MHz, CDCl₃): δ = 192.3, 167.2, 143.8, 137.1, 135.2, 134.3, 125.7, 124.9, 124.7, 123.2, 122.5, 121.1, 83.4, 76.1, 31.2.

Synthesis of [27][TfO]. In a Schlenk tube under inert atmosphere, [RuCl(dppe)₂][TfO] (**[26][TfO]**) (1.08 g, 1 mmol, 1 equiv.) and **20** (0.67 g, 1.2 mmol, 1.2 equiv.) were dissolved in dry CH₂Cl₂ (50 mL). The mixture was stirred for 24 h at RT. After removal of the solvent, the crude product was washed with freshly distilled pentane (2 × 40 mL). Precipitation from a CH₂Cl₂/pentane mixture afforded pure **[27][TfO]** as a light brown powder in 93% yield (1.52 g, 0.93 mmol). ³¹P NMR (120 MHz, CDCl₃): δ = 35.8 (s, PPh₂). ¹H NMR (300 MHz, CDCl₃): δ = 7.87 (d, 4H, ³J_{H-H} = 8.7 Hz), 7.34-7.07 (m, 40H), 6.88 (d, 4H, ³J_{H-H} = 8.7 Hz), 6.24 (d, 2H, ³J_{H-H} = 8.1 Hz), 5.63 (d, 2H, ³J_{H-H} = 8.1 Hz), 4.93 (s, 1H), 4.40 (m, 4H), 2.92 (m, 8H), 1.12 (m, 4H), 0.08 (s, 18H). ¹³C NMR (100 MHz, CD₂Cl₂): δ = 360.5, 166.6, 151.1, 144.2, 134.7, 134.5, 133.9, 133.1, 132.1, 131.9, 131.7, 131.6, 131.5, 131.2, 129.6, 129.4, 129.0, 128.8, 128.7, 126.8, 126.4, 125.5, 124.6, 124.0, 123.2, 122.8, 109.7, 63.6, 29.4, 17.9, -1.1. HR-MS FD⁺ (m/z): 1490.3749 [M]⁺ (calcd. 1490.3876 for [C₈₄H₈₇ClNO₄P₄RuSi₂]⁺). FT-IR (KBr): ν_{C=C} = 1630 cm⁻¹.

Synthesis of 28. To a solution of **[27][TfO]** (230 mg, 0.14 mmol, 1 equiv.), compound **23** (52 mg, 0.156 mmol, 1.1 equiv.) and NaPF₆ (47 mg, 0.28 mmol, 2 equiv.) in dry CH₂Cl₂ (15 mL) and under inert atmosphere, was added distilled Et₃N (63 mL, 0.42 mmol, 3 equiv.). The reaction mixture was stirred for 24 h at RT. The organics were further washed with degassed water and evaporated to dryness. Precipitation from a CH₂Cl₂/pentane mixture afforded pure **28** as a red solid in 89% yield (224 mg, 0.1125 mmol). ³¹P NMR (120 MHz, CDCl₃): δ = 53.4. ¹H NMR (300 MHz, CDCl₃): δ = 7.94 (d, 4H, ³J_{H-H} = 8.8 Hz), 7.88 (s, 1H), 7.68 (m, 8H), 7.30-6.97 (m, 39H), 6.76 (d, 2H, ³J_{H-H} = 8.6 Hz), 6.92 (d, 2H, ³J_{H-H} = 8.6 Hz), 6.10 (d, 1H, ³J_{H-H} = 3.8 Hz), 4.42 (m, 4H), 4.00 (s, 3H), 3.85 (s, 3H), 2.62 (m, 8H), 1.14 (m, 4H), 0.10 (s, 18H). ¹³C NMR (100 MHz, CD₂Cl₂): δ = 166.5, 165.2, 151.3, 149.1, 146.2,

141.5, 137.7, 137.4, 136.9, 135.9, 134.7, 134.1, 132.9, 131.9, 131.4, 131.0, 129.4, 129.0, 128.6, 128.1, 127.6, 126.5, 125.8, 124.6, 122.4, 119.6, 117.6, 109.8, 63.1, 53.0, 52.8, 31.7, 30.1, 17.6, -1.3. HR-MS FD^+ (m/z): 1785.4190 $[\text{M}]^+$ (calcd. 1785.4214 for $[\text{C}_{100}\text{H}_{97}\text{NO}_8\text{P}_4\text{RuS}_2\text{Si}_2]^+$). FT-IR (KBr): $\nu_{\text{C}=\text{C}} = 2040 \text{ cm}^{-1}$, $\nu_{\text{C}=\text{O}} = 1709 \text{ cm}^{-1}$, $\nu_{\text{C}=\text{C}} (\text{Thiophene}) = 1432 \text{ cm}^{-1}$, $\nu_{\text{C}-\text{O}} = 1265 \text{ cm}^{-1}$, $\nu_{\text{P}-\text{Ph}} = 1098 \text{ cm}^{-1}$, $\nu_{\text{Si}-\text{C}} = 836 \text{ cm}^{-1}$.

Synthesis of SL1. To a solution of **28** (180 mg, 0.10 mmol, 1 equiv.) in dry THF (10 mL) and under inert atmosphere was added TBAF (1 M sol. in THF, 0.25 mL, 0.25 mmol, 2.5 equiv.). The reaction mixture was stirred overnight at RT. After removal of the solvent the resulting solid was dissolved in CH_2Cl_2 and thoroughly washed with degassed citric acid aqueous solution (10% m) and pure water. The organics were evaporated to dryness and the solid was further washed with pentane. Slow crystallization from a CH_2Cl_2 /pentane mixture afforded pure **SL1** as a red powder in 83% yield (132 mg, 0.083 mmol). ^{31}P NMR (120 MHz, THF- d_8): $\delta = 53.1$. ^1H NMR (300 MHz, THF- d_8): $\delta = 7.86$ (d, 4H, $^3J_{\text{H}-\text{H}} = 8.7$ Hz), 7.79 (s, 1H), 7.58 (m, 8H), 7.26-7.03 (m, 23H), 6.95-6.87 (m, 16H), 6.83 (d, 2H, $^3J_{\text{H}-\text{H}} = 8.5$ Hz), 6.67 (d, 2H, $^3J_{\text{H}-\text{H}} = 8.5$ Hz), 6.0 (d, 1H, $^3J_{\text{H}-\text{H}} = 3.8$ Hz), 3.90 (s, 3H), 3.75 (s, 3H), 2.53 (m, 8H). ^{13}C NMR (100 MHz, THF- d_8): $\delta = 164.2, 162.4, 149.1, 146.2, 143.5, 139.5, 135.1, 134.9, 132.9, 132.5, 131.9, 131.3, 131.0, 129.1, 128.9, 127.3, 126.8, 126.5, 125.8, 125.1, 124.1, 123.7, 123.1, 122.7, 120.1, 119.9, 117.9, 114.4, 107.7, 49.7, 49.4, 29.3, 27.7$. HR-MS FD^+ (m/z): 1585.2713 $[\text{M}]^+$ (calcd. 1585.2795 for $[\text{C}_{90}\text{H}_{73}\text{NO}_8\text{P}_4\text{RuS}_2]^+$). FT-IR (KBr): $\nu_{\text{C}=\text{C}} = 2038 \text{ cm}^{-1}$, $\nu_{\text{C}=\text{O}} = 1717\text{-}1681 \text{ cm}^{-1}$, $\nu_{\text{C}=\text{C}} (\text{Thiophene}) = 1434 \text{ cm}^{-1}$, $\nu_{\text{C}-\text{O}} = 1265 \text{ cm}^{-1}$, $\nu_{\text{P}-\text{Ph}} = 1095 \text{ cm}^{-1}$.

Synthesis of 29. The same procedure as for **28** was applied using **[27][TfO]** (130 mg, 0.08 mmol), **25** (33 mg, 0.095 mmol), NaPF_6 (27 mg, 0.16 mmol), CH_2Cl_2 (15 mL) and Et_3N (37 mL, 0.24 mmol). Pure **29** was obtained as a blue solid in 92% yield (139 mg, 0.077 mmol). ^{31}P NMR (120 MHz, CDCl_3): $\delta = 53.2$. ^1H NMR (300 MHz, CDCl_3): $\delta = 8.02$ (d, 4H, $^3J_{\text{H}-\text{H}} = 8.7$ Hz), 7.97 (s, 1H), 7.77 (m, 8H), 7.43-7.09 (m, 42H), 7.01 (d, 2H, $^3J_{\text{H}-\text{H}} = 8.5$ Hz), 6.85 (d, 2H, $^3J_{\text{H}-\text{H}} = 8.5$ Hz), 6.19 (d, 1H, $^3J_{\text{H}-\text{H}} = 3.8$ Hz), 4.50 (m, 4H), 3.63 (s, 3H), 2.71 (m, 8H), 1.22 (m, 4H), 0.19 (s, 18H). ^{13}C NMR (150 MHz, CD_2Cl_2): $\delta = 192.6, 167.3, 166.1, 151.0, 150.6, 147.3, 141.1, 136.9, 136.6, 136.1, 134.6, 134.3, 133.8, 132.3, 131.5, 131.0, 130.6, 129.0, 128.9, 128.7, 127.8, 127.2, 127.1, 126.5, 126.1, 125.9, 125.6, 124.3, 123.2, 122.0, 118.6, 117.5, 110.0, 62.8, 31.4, 31.2, 17.3, -1.7$. HR-MS FD^+ (m/z): 1800.3617 $[\text{M}]^+$ (calcd. 1800.3602 for $[\text{C}_{99}\text{H}_{94}\text{N}_2\text{O}_5\text{P}_4\text{RuS}_4\text{Si}_2]^+$). FT-IR (KBr): $\nu_{\text{C}=\text{C}} = 2035 \text{ cm}^{-1}$, $\nu_{\text{C}=\text{O}} = 1706 \text{ cm}^{-1}$, $\nu_{\text{C}=\text{C}} (\text{Thiophene}) = 1419 \text{ cm}^{-1}$, $\nu_{\text{C}-\text{O}} = 1270 \text{ cm}^{-1}$, $\nu_{\text{P}-\text{Ph}} = 1098 \text{ cm}^{-1}$, $\nu_{\text{Si}-\text{C}} = 834 \text{ cm}^{-1}$.

Synthesis of SL2. Same procedure as for **SL1** was applied using **29** (100 mg, 0.056 mmol), TBAF (1 M sol. in THF, 0.11 mL, 0.11 mmol) and THF (10 mL). Pure **SL2** was obtained as a blue powder in 71% yield (63 mg, 0.039 mmol). ^{31}P NMR (120 MHz, CD_2Cl_2): $\delta = 53.2$. ^1H NMR (300 MHz, CD_2Cl_2): $\delta = 7.81$ (s, 1H), 7.80 (d, 4H, $^3J_{\text{H-H}} = 8.5$ Hz), 7.77 (m, 8H), 7.35 (d, 1H, $^3J_{\text{H-H}} = 3.6$ Hz), 7.18-6.89 (m, 38H), 6.83 (d, 2H, $^3J_{\text{H-H}} = 8.3$ Hz), 6.72 (d, 2H, $^3J_{\text{H-H}} = 8.3$ Hz), 6.09 (d, 1H, $^3J_{\text{H-H}} = 3.6$ Hz), 3.37 (s, 3H), 2.54 (m, 8H). ^{13}C NMR (150 MHz, THF-d8): $\delta = 192.1, 166.7, 166.1, 151.0, 150.2, 146.9, 141.4, 137.0, 136.7, 136.1, 134.7, 134.3, 133.8, 133.7, 132.8, 131.0, 130.8, 130.6, 129.0, 128.7, 128.5, 127.9, 127.7, 127.0, 126.4, 125.6, 124.8, 124.6, 123.1, 122.0, 118.8, 117.4, 110.1, 31.2, 30.4, 29.6$. HR-MS FD^+ (m/z): 1600.2244 [M] $^+$ (calcd. 1600.2183 for $[\text{C}_{89}\text{H}_{70}\text{N}_2\text{O}_5\text{P}_4\text{RuS}_4]^+$). FT-IR (KBr): $\nu_{\text{C=C}} = 2034 \text{ cm}^{-1}$, $\nu_{\text{C=O}} = 1705\text{-}1686 \text{ cm}^{-1}$, $\nu_{\text{C=C (Thiophene)}} = 1420 \text{ cm}^{-1}$, $\nu_{\text{C-O}} = 1283 \text{ cm}^{-1}$, $\nu_{\text{P-Ph}} = 1097 \text{ cm}^{-1}$.

VI.2.3. Synthetic Routes to the Dyes SL3 and SL4

Synthesis of 31. Methyl 4-iodobenzoate (6.55 g, 25 mmol), $\text{PdCl}_2(\text{PPh}_3)_2$ (175 mg, 0.25 mmol) and copper(I) iodide (95 mg, 0.5 mmol) were dissolved in dry THF (25 mL) and Et_3N (25 mL). Trimethylsilylacetylene (2.7 g, 27.5 mmol) was added and the solution was stirred at RT for 16 h. After evaporation of the solvent, the resulting crude product was purified on silica gel column (ethyl acetate/petroleum ether (95:5, v/v)) to obtain **31** as a white powder in 92% yield (5.35 g, 23 mmol). ^1H NMR (CDCl_3 , 300 MHz): 7.97 (d, 2 H, $^3J_{\text{H-H}} = 6$ Hz), 7.52 (d, 2 H, $^3J_{\text{H-H}} = 6$ Hz), 3.91 (s, 3H), 0.26 (s, 9H).

Synthesis of 32. Compound **31** (3.5 g, 15 mmol) was dissolved in dry MeOH (200 mL) under nitrogen atmosphere. Potassium carbonate (6.24 g, 45 mmol) was added and the suspension refluxed for 24 h. The reaction mixture was then poured into 10% aqueous HCl solution (400 mL). A white precipitate was obtained that was filtered and dried under vacuum to afford **32** as a yellow powder in 92% (2.02 g, 13.75 mmol). ^1H NMR (CDCl_3 , 300 MHz): 8.06 (d, 2 H, $^3J_{\text{H-H}} = 12$ Hz), 7.59 (d, 2H, $^3J_{\text{H-H}} = 12$ Hz), 3.26 (s, 1H).

Synthesis of 33. Compound **32** (1.86 g, 12.75 mmol), HBTU (5.8 g, 15.3 mmol) and N,N-diisopropylethylamine (11.1 mL, 63.7 mmol) were dissolved in DMF (28 mL) under nitrogen atmosphere. Trimethylsilylethanol (2.75 mL, 19.11 mmol) was added and the solution stirred at RT for 24 h. After removal of the solvent and dilution in CH_2Cl_2 (200 mL) the

reaction mixture was washed with saturated aqueous NH_4Cl solution and water, and then dried over MgSO_4 and evaporated to dryness. The crude product was purified on silica gel column ($\text{CH}_2\text{Cl}_2/\text{pentane}$ (1:1, v/v) to CH_2Cl_2) to obtain **33** as a pale yellow oil in 72 % yield (2.42 g, 9.22 mmol). ^1H NMR (CDCl_3 , 300 MHz): 8.00 (d, 2H, $^3J_{\text{H-H}} = 12$ Hz), 7.55 (d, 2H, $^3J_{\text{H-H}} = 12$), 4.42 (m, 2H), 3.22 (s, 1H), 1.13 (m, 2H), 0.07 (s, 9H).

Synthesis of 35. 5-Bromo-2-thiophenecarboxylic acid (1.0 g, 4.8 mmol, 1 equiv.) was dissolved in dry DMF (15 mL) under nitrogen atmosphere, and HBTU (2.20 g, 5.8 mmol, 1.2 equiv.), 2-(trimethylsilyl)ethanol (0.97 mL, 6.7 mmol, 1.4 equiv.) and *N,N*-diisopropylethylamine (4.21 mL, 24.2 mmol, 5 equiv.) were added subsequently. The solution was stirred at RT for 24 h. After dilution with CH_2Cl_2 (20 mL), the reaction mixture was washed with saturated aqueous NH_4Cl solution and water, and then dried over MgSO_4 and evaporated to dryness. The crude product was purified on silica gel column ($\text{CH}_2\text{Cl}_2/\text{pentane}$ (1 : 1, v/v) to CH_2Cl_2) to obtain **35** as a pale yellow powder in 77% yield (1.14 g, 3.72 mmol). ^1H NMR (300 MHz, CD_2Cl_2): $\delta = 7.52$ (d, 1H, $^3J_{\text{H-H}} = 6.0$ Hz), 7.10 (d, 1H, $^3J_{\text{H-H}} = 3.0$ Hz), 4.37 (m, 2H), 1.10 (m, 2H), 0.08 (s, 9H).

Synthesis of 36. To a solution of **35** (1.28 g, 4.18 mmol, 1 equiv.), $\text{PdCl}_2(\text{PPh}_3)_2$ (73.3 mg, 0.1 mmol, 2.5%) and copper(I) iodide (39.8 mg, 0.2 mmol, 5%) in dry THF (50 mL) under nitrogen, were added Et_3N (50 mL) and (trimethylsilyl)acetylene (0.65 mL, 4.6 mmol, 1.1 equiv.). The solution was stirred at RT for 12 h. After evaporation of the solvent, the resulting crude product was purified on silica gel column ($\text{CH}_2\text{Cl}_2/\text{pentane}$ (8 : 1, v/v)) to obtain **36** as a pale yellow powder in 76% yield (1.03 g, 3.17 mmol). ^1H NMR (300 MHz, CD_2Cl_2): $\delta = 7.60$ (d, 1H, $^3J_{\text{H-H}} = 6.0$ Hz), 7.17 (d, 1H, $^3J_{\text{H-H}} = 6.0$ Hz), 4.37 (m, 2H), 1.10 (m, 2H), 0.25 (s, 9H), 0.08 (s, 9H).

Synthesis of 37. Compound **36** (1.36 g, 4.18 mmol, 1equiv.) was dissolved in dry MeOH (30 mL) under nitrogen atmosphere. Potassium carbonate (57.6 mg, 0.418 mmol, 0.1 equiv.) was subsequently added and the suspension was stirred at RT for 24 h. The reaction mixture was then concentrated, poured into pure water and the solution was extracted with CH_2Cl_2 . After drying over MgSO_4 , the organic layer was evaporated to dryness to afford **37** as a dark red powder in 78% yield (0.82 g, 3.26 mmol). ^1H NMR (300 MHz, CDCl_3): $\delta = 7.62$ (d, 1H, $^3J_{\text{H-H}} = 6.0$ Hz), 7.20 (d, 1H, $^3J_{\text{H-H}} = 6.0$ Hz), 4.38 (m, 2H), 3.44 (s, 1H), 1.10 (m, 2H), 0.07 (s, 9H). ^{13}C NMR (75 MHz, CDCl_3): $\delta = 161.63, 135.18, 133.38, 132.79, 128.29, 83.68, 76.38,$

63.96, 17.46, -1.31.

Synthesis of [38][TfO]. In a Schlenk tube under inert atmosphere, [RuCl(dppe)₂][TfO] ([26][TfO]) (0.55 g, 0.51 mmol, 1 equiv.) and **33** (0.15 g, 0.61 mmol, 1.2 equiv.) were dissolved in dry CH₂Cl₂ (25 mL). The mixture was stirred for 24 h at RT. After removal of the solvent, the crude product was washed with freshly distilled pentane (2 × 30 mL). Precipitation from a CH₂Cl₂/pentane mixture afforded pure [38][TfO] as a red powder in 88% yield (0.60 g, 0.45 mmol). ³¹P NMR (120 MHz, CD₂Cl₂): δ = 38.0 (s, PPh₂). ¹H NMR (300 MHz, CD₂Cl₂): δ = 7.41-7.08 (m, 42H), 5.70 (d, 2H, ³J_{H-H} = 6 Hz), 4.35 (m, 2H), 3.56 (m, 1H), 2.89 (m, 8H), 1.09 (m, 2H), 0.09 (s, 9H).

Synthesis of [39][TfO]. In a Schlenk tube under inert atmosphere, [RuCl(dppe)₂][TfO] ([26][TfO]) (0.89 g, 0.83 mmol, 1 equiv.) and **37** (0.25 g, 0.99 mmol, 1.2 equiv.) were dissolved in dry CH₂Cl₂ (25 mL). The mixture was stirred for 24 h at RT. After removal of the solvent, the crude product was washed with freshly distilled pentane (2 × 30 mL). Precipitation from a CH₂Cl₂/pentane mixture afforded pure [39][TfO] as a red powder in 88% yield (1.0 g, 0.75 mmol). ³¹P NMR (120 MHz, CD₂Cl₂): δ = 39.4 (s, PPh₂). ¹H NMR (300 MHz, CD₂Cl₂): δ = 7.61 (d, 2H, ³J_{H-H} = 3 Hz), 7.47-7.11 (m, 40H), 5.37 (m, 1 H), 4.34 (m, 2H), 2.85 (m, 8H), 1.08 (m, 2H), 0.08 (s, 9H).

Synthesis of 40. To a solution of [38][TfO] (0.5 g, 0.38 mmol, 1 equiv.), compound **23** (0.15 g, 0.46 mmol, 1.2 equiv.) and NaPF₆ (0.13 g, 0.75 mmol, 2 equiv.) in dry CH₂Cl₂ (30 mL) and under inert atmosphere, was added distilled Et₃N (0.16 mL, 1.13 mmol, 3 equiv.). The reaction mixture was stirred for 24 h at RT. The organics were further washed with degassed water and evaporated to dryness. Precipitation from a CH₂Cl₂/pentane mixture afforded pure **40** as a red solid in 88% yield (0.49 g, 0.33 mmol). ³¹P NMR (120 MHz, CDCl₃): δ = 53.2. ¹H NMR(300 MHz, CDCl₃): δ = 7.87 (s, 1H), 7.82 (d, 2H, ³J_{H-H} = 9 Hz), 7.53-6.94 (m, 44H), 6.73 (d, 2H, ³J_{H-H} = 9 Hz), 4.41 (m, 2H), 3.99 (s, 3H), 3.85 (s, 3H), 2.61 (m, 8H), 1.15 (m, 2H), 0.11 (s, 9H). MS APCI⁺ (m/z): 1475.3 [M+H]⁺ (calcd. 1474.2847 for [C₈₂H₇₆O₆P₄RuS₂Si]⁺).

Synthesis of 41. The same procedure as for **40** was applied using [39][TfO] (0.6 g, 0.45 mmol), **23** (0.18 g, 0.54 mmol), NaPF₆ (0.15 g, 0.90 mmol), CH₂Cl₂ (30 mL) and Et₃N (0.19 mL, 1.35 mmol). Pure **41** was obtained as a blue solid in 91% yield (0.61 g, 0.42 mmol). ³¹P

NMR (120 MHz, THF-d8): $\delta = 52.2$. ^1H NMR (300 MHz, THF-d8): $\delta = 7.84$ (s, 1H), 7.81-6.61 (m, 46H), 4.37 (m, 2H), 3.96 (s, 3H), 3.81 (s, 3H), 2.57 (m, 8H), 1.27 (m, 2H), 0.09 (s, 9H). HR-MS APCI⁺ (m/z): 1480.2435 [M]⁺ (calcd. 1480.2405 for [C₈₀H₇₄O₆P₄RuS₃Si]⁺).

Synthesis of SL3. To a solution of **40** (0.22 g, 0.15 mmol, 1 equiv.) in dry THF (20 mL) and under inert atmosphere was added TBAF (1 M sol. in THF, 0.22 mL, 0.22 mmol, 1.5 equiv.). The reaction mixture was stirred for 24 h at RT. After removal of the solvent the resulting solid was dissolved in CH₂Cl₂ and thoroughly washed with degassed citric acid aqueous solution (10% m) and pure water. The organics were evaporated to dryness and the solid was further washed with pentane. Slow crystallization from a CH₂Cl₂/pentane mixture afforded pure **SL3** as a red powder in 79% yield (0.16 g, 0.083 mmol). ^{31}P NMR (120 MHz, CD₂Cl₂): $\delta = 52.5$. ^1H NMR (300 MHz, CD₂Cl₂): $\delta = 7.84$ (m, 4H), 7.53-6.97 (m, 40H), 6.79 (d, 3H, $^3J_{\text{H-H}} = 9$ Hz), 6.23 (d, 2H, $^3J_{\text{H-H}} = 3$ Hz), 3.96 (s, 3H), 3.81 (s, 3H), 2.65 (m, 8H). HR-MS ESI⁺ (m/z): 1374.2156 [M]⁺ (calcd. 1374.2138 for [C₇₇H₆₄O₆P₄RuS₂]⁺).

Synthesis of SL4. Same procedure as for **SL3** was applied using **41** (0.21 g, 0.14 mmol), TBAF (1 M sol. in THF, 0.22 mL, 0.22 mmol) and THF (25 mL). Pure **SL4** was obtained as a red powder in 69% yield (0.14 g, 0.10 mmol). ^{31}P NMR (120 MHz, CD₂Cl₂): $\delta = 52.2$. ^1H NMR (300 MHz, CD₂Cl₂): $\delta = 7.83$ (s, 1H), 7.63 (d, 1H, $^3J_{\text{H-H}} = 6$ Hz), 7.47-7.01 (m, 43H), 6.24 (m, 2H), 3.96 (s, 3H), 3.81 (s, 3H), 2.63 (m, 8H). HR-MS ESI⁺ (m/z): 1380.1716 [M]⁺ (calcd. 1380.1702 for [C₇₅H₆₂O₆P₄RuS₃]⁺).

VI.2.4. Synthetic Routes to the Dye SL5

Synthesis of 43. To a solution of 5,5'-Dibromo-2,2'-bithiophene **42** (0.60 g, 1.85 mmol, 1 equiv.), PdCl₂(PPh₃)₂ (65.0 mg, 0.09 mmol, 2.5%) and copper(I) iodide (8.8 mg, 0.045 mmol, 5%) in dry THF (10 mL) under nitrogen, were added diisopropylamine (10 mL) and (trimethylsilyl)acetylene (0.24 mL, 1.67 mmol, 0.9 equiv.). The solution was stirred at RT for 1 h. After evaporation of the solvent, the resulting crude product was purified on silica gel column (hexane) to obtain **43** as an earth yellow powder in 52% yield (0.33 g, 0.96 mmol). ^1H NMR (300 MHz, CD₂Cl₂): $\delta = 7.12$ (d, 1H, $^3J_{\text{H-H}} = 3.83$ Hz), 7.00 (d, 1H, $^3J_{\text{H-H}} = 3.89$ Hz), 6.98 (d, 1H, $^3J_{\text{H-H}} = 3.83$ Hz), 6.95 (d, 1H, $^3J_{\text{H-H}} = 3.89$ Hz), 0.25 (s, 9H). ^{13}C NMR (75 MHz, CD₂Cl₂): $\delta = 138.45, 138.03, 133.86, 131.33, 124.90, 124.09, 122.71, 112.06, 100.86, 97.23, 0.15$.

Synthesis of 44. To a solution of **43** (0.71 g, 2.07 mmol, 1 equiv.), palladium acetate (4.64 mg, 0.02 mmol, 1.0%) and dppf (12.6 mg, 0.023 mmol, 1.1%) in dry CH₃CN (15 mL) under nitrogen, were added diethyl phosphite (0.32 mL, 2.48 mmol, 1.2 equiv.) and Et₃N (0.37 mL, 2.69 mmol, 1.3 equiv.). The reaction mixture was refluxed for 24 h and then evaporated to dryness. The organics were further washed with degassed water, extracted with ethyl acetate. Subsequently, the solution was washed with brine for two times. After evaporation of the solvent, the resulting crude product was purified on silica gel column (ethyl acetate/hexane (4 : 1, v/v)) to obtain **44** as a yellow powder in 52% yield (0.60 g, 1.5 mmol). ³¹P NMR (120 MHz, CD₂Cl₂): δ = 10.3. ¹H NMR (300 MHz, CD₂Cl₂): δ = 7.50 (m, 1H), 7.23 (m, 1H), 7.14 (m, 2H), 4.12 (m, 4H), 1.33 (m, 6H), 0.25 (s, 9H). ¹³C NMR (75 MHz, CD₂Cl₂): δ = 137.60, 137.45, 133.96, 129.17, 125.38, 125.27, 125.16, 123.84, 101.34, 97.04, 63.19, 63.12, 16.53, 16.44, 0.20.

Synthesis of 45. Compound **44** (0.14 g, 0.34 mmol, 1 equiv.) was dissolved in dry MeOH (10 mL) under nitrogen atmosphere. Potassium carbonate (4.72 mg, 0.034 mmol, 0.1 equiv.) was subsequently added and the suspension was stirred at RT for 24 h. The reaction mixture was then concentrated, poured into pure water and the solution was extracted with ethyl acetate. After drying over MgSO₄, the organic layer was evaporated to dryness to afford **45** as a yellow powder in 89% yield (0.10 g, 0.30 mmol). ³¹P NMR (120 MHz, CD₂Cl₂): δ = 10.2. ¹H NMR (300 MHz, CD₂Cl₂): δ = 7.50 (m, 1H), 7.23 (m, 2H), 7.15 (d, 1H, ³J_{H-H} = 3.0 Hz), 4.13 (m, 4H), 3.51 (s, 1H), 1.33 (m, 6H). ¹³C NMR (75 MHz, CD₂Cl₂): δ = 144.35, 144.24, 137.88, 137.46, 134.55, 129.36, 125.22, 122.54, 83.24, 76.60, 63.22, 63.15, 16.54, 16.45.

Synthesis of [46][TfO]. In a Schlenk tube under inert atmosphere, [RuCl(dppe)₂][TfO] (**[26][TfO]**) (1.082 g, 1.0 mmol, 1 equiv.) and **23** (0.40 g, 1.2 mmol, 1.2 equiv.) were dissolved in dry CH₂Cl₂ (25 mL). The mixture was stirred for 24 h at RT. After removal of the solvent, the crude product was washed with freshly distilled pentane (2 × 30 mL). Precipitation from a CH₂Cl₂/pentane mixture afforded pure **[46][TfO]** as a red powder in 92% yield (1.30 g, 0.92 mmol). ³¹P NMR (120 MHz, CD₂Cl₂): δ = 39.1 (s, PPh₂). ¹H NMR (300 MHz, CD₂Cl₂): δ = 7.79 (s, 1H), 7.42-6.77 (m, 45H), 3.92 (s, 3H), 3.81 (s, 3H), 2.87 (m, 8H). HR-MS APCI⁺ (m/z): 1264.1550 [M-H]⁺ (calcd. 1264.531 for [C₆₈H₅₉ClO₄P₄RuS₂]⁺).

Synthesis of 47. To a solution of **[46][TfO]** (0.51 g, 0.36 mmol, 1 equiv.), compound **45** (0.14 g, 0.43 mmol, 1.2 equiv.) and NaPF₆ (0.12 g, 0.72 mmol, 2 equiv.) in dry CH₂Cl₂ (25

mL) and under inert atmosphere, was added distilled Et₃N (0.20 mL, 1.44 mmol, 4 equiv.). The reaction mixture was stirred for 24 h at RT. The organics were further washed with degassed water and evaporated to dryness. Precipitation from a CH₂Cl₂/pentane mixture afforded pure **47** as a red solid in 87% yield (0.48 g, 0.31 mmol). ³¹P NMR (120 MHz, CD₂Cl₂): δ = 52.1 (s, PPh₂), 11.25 (s, PO₃Et₂). ¹H NMR (300 MHz, CD₂Cl₂): δ = 7.83 (s, 1H), 7.52-6.91 (m, 48H), 4.14 (m, 4H), 3.96 (s, 3H), 3.81 (s, 3H), 2.63 (m, 8H), 1.36 (m, 6H). HR-MS APCI⁺ (m/z): 1554.1990 [M]⁺ (calcd. 1554.1965 for [C₈₂H₇₃O₇P₅RuS₄]⁺).

Synthesis of SL5. To a solution of **47** (0.16 g, 0.1 mmol, 1 equiv.) in dry CH₂Cl₂ (20 mL) and under inert atmosphere was added N,O-bis(trimethylsilyl) acetamide (0.27 mL, 1.1 mmol, 11 equiv.). The reaction mixture was stirred for 1 h at RT. Subsequently, the mixture was cooled at -20 °C and iodotrimethylsilane was added dropwise. The reaction mixture was again stirred for 1 h at -20 °C and 1 h at RT. After removal of the solvent, the mixed CH₃CN/H₂O (7/3, 10 mL) was added and the solution was stirred 1 h at RT. The solvents were subsequently removed by vacuum. Slow crystallization from a CH₂Cl₂/pentane mixture afforded pure **SL5** as a red powder in 73% yield. ³¹P NMR (120 MHz, CD₂Cl₂): δ = 49.3 (s, PPh₂), 10.7 (s, PO₃H₂). ¹H NMR (300 MHz, CD₂Cl₂): δ = 7.83 (s, 1H), 7.57-6.57 (m, 48H), 3.95 (s, 3H), 3.82 (s, 3H), 2.71 (m, 8H). HR-MS (*awaiting for FD analysis equipment*).

VI.2.5. Synthetic Routes to the Dye SL6 and SL7

Synthesis of 30[TfO]. In a Schlenk tube under an inert atmosphere, [RuCl(dppe)₂][TfO] (**26[TfO]**) (865 mg, 0.8 mmol, 1 equiv.) and **37** (300 mg, 1.2 mmol, 1.5 equiv.) were dissolved in dry CH₂Cl₂ (50 mL). The mixture was stirred for 24 h at RT. After removal of the solvent, the crude product was washed with freshly distilled pentane (2 × 40 mL). Precipitation from a CH₂Cl₂/pentane mixture afforded pure **30[TfO]** as a light brown powder in 63% yield (670 mg, 0.5 mmol). ³¹P NMR (120 MHz, CDCl₃): δ = 36.8 (s, PPh₂). ¹H NMR (300 MHz, CDCl₃): δ = 7.35–7.11 (m, 41H), 5.65 (d, 1H, ³J_{H-H} = 3.7 Hz), 4.65 (s, 1H), 4.26 (m, 2H), 2.91 (m, 8H), 1.06 (m, 2H), 0.07 (s, 9H). ¹³C NMR (100 MHz, CD₂Cl₂): δ = 360.5, 198.2, 163.5, 161.5, 136.0, 134.6, 134.1, 133.8, 133.7, 133.1, 132.1, 131.9, 131.7, 131.6, 131.5, 131.2, 129.6, 129.4, 129.0, 128.8, 128.7, 126.8, 126.4, 125.5, 124.6, 124.0, 121.8, 119.7, 103.2, 63.3, 29.0, 17.3, -1.4. HR-MS FD⁺ (m/z): 1185.2146 [M]⁺ (calcd. 1185.2092 for [C₆₄H₆₄ClO₂SP₄RuSi]⁺). FT-IR (KBr): ν_{C=C} = 1623 cm⁻¹.

Synthesis of 48. To a solution of **30[TfO]** (335 mg, 0.25 mmol, 1 equiv.), NaPF₆ (84 mg,

0.5 mmol, 2 equiv.) and 1,1-diphenyl-2-propyn-1-ol (104 mg, 0.5 mmol, 2 equiv.) in dry CH₂Cl₂ (30 mL) under a nitrogen atmosphere was added Et₃N (140 μL, 1 mmol, 4 equiv.). The solution was stirred at RT for 48 h. The reaction mixture was washed with water and evaporated to dryness. The resulting solid was afterwards washed with pentane and dried to afford **48** as a deep blue powder in 80% yield (296 mg, 0.20 mmol). ³¹P NMR (120 MHz, CDCl₃): δ = 43.7 (s, PPh₂), -144.2 (sept, PF₆). ¹H NMR (300 MHz, CDCl₃): δ = 7.66 (t, 2H, ³J_{H-H} = 7.4 Hz), 7.65 (d, 1H, ³J_{H-H} = 3.7 Hz), 7.24-7.16 (m, 18H), 7.04-6.78 (m, 30H), 6.37 (d, 1H, ³J_{H-H} = 6 Hz), 4.44 (m, 2H), 2.90 (m, 8H), 1.16 (m, 2H), 0.13 (s, 9H). ¹³C NMR (100 MHz, CD₂Cl₂): δ = 316.1, 210.2, 163.2, 162.1, 144.2, 135.1, 133.5, 133.3, 133.0, 132.9, 132.6, 131.7, 131.1, 130.9, 130.7, 130.5, 129.2, 128.6, 128.3, 127.7, 63.5, 29.2, 17.4, -1.4. HR-MS FD⁺ (m/z): 1339.3087 [M]⁺ (calcd. 1339.3094 for [C₇₉H₇₃O₂SP₄RuSi]⁺). FT-IR (KBr): ν_{C=C} = 2062 cm⁻¹, ν_{C=C-C} = 1925 cm⁻¹, ν_{C=O} = 1691 cm⁻¹, ν_{P-Ph} = 1088 cm⁻¹, ν_{P-F} = 839 cm⁻¹.

Synthesis of SL6. To a solution of **48** (125 mg, 0.08 mmol, 1 equiv.) in dry THF (12 mL) under a nitrogen atmosphere was added tetrabutylammonium fluoride (163 μL, 1 M in THF, 2 equiv.). The solution was stirred at RT for 20 h. After evaporation of the solvent, the resulting solid was dissolved in CH₂Cl₂ and the solution was washed with 10% aqueous citric acid and water. The solvent was evaporated and the solid was recrystallized by slow diffusion from a CH₂Cl₂/pentane solvent mixture to afford **SL6** as a deep blue powder in 72% yield (83 mg, 0.06 mmol). ³¹P NMR (120 MHz, CDCl₃): δ = 43.5 (s, PPh₂), -144.4 (sept, PF₆). ¹H NMR (300 MHz, CDCl₃): δ = 7.66 (t, 2H, ³J_{H-H} = 7.4 Hz), 7.61 (d, 1H, ³J_{H-H} = 3.7 Hz), 7.33-6.79 (m, 48H), 6.42 (d, 1H, ³J_{H-H} = 3.7 Hz), 3.01 (m, 4H), 2.80 (m, 4H). ¹³C NMR (100 MHz, CD₂Cl₂): δ = 316.0, 213.2, 165.9, 161.9, 144.6, 139.6, 135.5, 135.0, 133.8, 133.7, 133.6, 133.1, 133.0, 132.4, 131.1, 130.8, 130.7, 129.3, 128.6, 128.4, 127.9, 127.5, 29.5. HR-MS FD⁺ (m/z): 1239.2368 [M]⁺ (calcd. 1239.2386 for [C₇₄H₆₁O₂SP₄RuSi]⁺). FT-IR (KBr): ν_{C=C} = 2039 cm⁻¹, ν_{C=C-C} = 1917 cm⁻¹, ν_{C=O} = 1688 cm⁻¹, ν_{P-Ph} = 1094 cm⁻¹, ν_{P-F} = 837 cm⁻¹.

Synthesis of 49. To a solution of **27[TfO]** (164 mg, 0.1 mmol, 1 equiv.), NaPF₆ (34 mg, 0.2 mmol, 2 equiv.) and 1,1-diphenyl-2-propyn-1-ol (42 mg, 0.2 mmol, 2 equiv.) in dry CH₂Cl₂ (10 mL) under a nitrogen atmosphere was added Et₃N (60 μL, 4 equiv.). The solution was stirred at RT for 48 h. The reaction mixture was diluted with CH₂Cl₂ up to 30 mL. The organics were washed with water and evaporated to dryness. The resulting solid was afterwards washed with pentane and dried to afford **49** as a deep blue powder in 89% yield (160 mg, 0.089 mmol). ³¹P NMR (120 MHz, CDCl₃): δ = 43.3 (s, PPh₂), -144.2 (sept, PF₆). ¹H

NMR (300 MHz, CDCl₃): δ = 7.98 (d, 4H, ³J_{H-H} = 8.8 Hz), δ = 7.87 (t, 2H, ³J_{H-H} = 7.4 Hz), 7.30-6.77 (m, 56H), 4.43 (m, 4H), 2.88 (m, 8H), 1.14 (m, 4H), 0.1 (s, 18H). ¹³C NMR (100 MHz, CD₂Cl₂): δ = 316.3, 212.9, 166.4, 162.4, 151.2, 144.7, 144.0, 140.9, 134.0, 133.8, 133.7, 133.5, 132.4, 131.4, 131.2, 130.9, 130.6, 129.4, 128.7, 128.3, 126.1, 125.3, 120.9, 63.4, 29.5, 17.7, -1.3. HR-MS FD⁺ (m/z): 1644.5029 [M]⁺ (calcd. 1644.4899 for [C₉₉H₉₆NO₄P₄RuSi₂]⁺). FT-IR (KBr): $\nu_{\text{C=C}}$ = 2064 cm⁻¹, $\nu_{\text{C=C=C}}$ = 1919 cm⁻¹, $\nu_{\text{C=O}}$ = 1706 cm⁻¹, $\nu_{\text{P-Ph}}$ = 1098 cm⁻¹, $\nu_{\text{P-F}}$ = 839 cm⁻¹.

Synthesis of SL7. To a solution of **49** (250 mg, 0.140 mmol, 1 equiv.) in dry THF (30 mL) under a nitrogen atmosphere was added tetrabutylammonium fluoride (307 μ L, 1 M in THF, 2.2 equiv.). The solution was stirred at RT for 24 h. After evaporation of the solvent, the resulting solid was dissolved in CH₂Cl₂ and the mixture was washed with 10% aqueous citric acid and pure water and then dried to afford **SL7** as a deep blue powder in 76% yield (179 mg, 0.106 mmol). ³¹P NMR (120 MHz, CD₂Cl₂): δ = 43.2 (s, PPh₂), -142.6 (sept, PF₆). ¹H NMR (300 MHz, CD₂Cl₂): δ = 7.94 (d, 4H, ³J_{H-H} = 8.7 Hz), δ = 7.64 (t, 2H, ³J_{H-H} = 7.4 Hz), 7.28-6.77 (m, 56H), 2.99 (m, 4H), 2.81 (m, 4H). ¹³C NMR (100 MHz, CD₂Cl₂): δ = 317.6, 214.1, 166.9, 162.6, 151.6, 145.1, 144.6, 141.6, 135.9, 135.4, 134.9, 134.6, 133.9, 132.6, 131.8, 131.6, 131.2, 130.7, 129.7, 129.3, 129.0, 128.6, 126.0, 125.3, 123.3, 121.5, 29.6. HR-MS ESI⁺ (m/z): 1444.3406 [M]⁺ (calcd. 1444.3449 for [C₈₉H₇₂NO₄P₄Ru]⁺). FT-IR (KBr): $\nu_{\text{C=C}}$ = 2063 cm⁻¹, $\nu_{\text{C=C=C}}$ = 1917 cm⁻¹, $\nu_{\text{C=O}}$ = 1714-1681 cm⁻¹, $\nu_{\text{P-Ph}}$ = 1095 cm⁻¹, $\nu_{\text{P-F}}$ = 838 cm⁻¹.

VI.2.6. Synthetic Routes to the Dye SL8 and SL8-Co

Synthesis of 50. Compound **43** (0.758 g, 2.22 mmol, 1 equiv.), 4-ethynylpyridine hydrochloride (0.3719 g, 2.66 mmol, 1.2 equiv.), PdCl₂(PPh₃)₂ (77.9 mg, 0.11 mmol, 5%) and copper(I) iodide (10.6 mg, 0.056 mmol, 2.5%) were introduced in a Schlenk flask under nitrogen and dissolved in a mixture of diisopropylamine (15 mL) and dry THF (15 mL). The solution was stirred at RT for 24 h. After evaporation of the solvent, the mixture was dissolved with ethyl acetate and washed with water. The resulting crude product was evaporated to dryness and purified on silica gel column (ethyl acetate/pentane (8:2, v/v)) to give **50** as a yellow powder in 79 % yield (0.636 g, 1.75 mmol). ¹H NMR (300 MHz, CD₂Cl₂): δ = 8.59 (s, 2H), 7.37 (d, 2H, ³J_{H-H} = 5.80 Hz), 7.28 (d, 1H, ³J_{H-H} = 3.88 Hz), 7.15 (d, 1H, ³J_{H-H} = 3.86 Hz), 7.13 (d, 1H, ³J_{H-H} = 3.88 Hz), 7.09 (d, 1H, ³J_{H-H} = 3.85 Hz), 0.25 (s, 9H). ¹³C NMR (75 MHz, CD₂Cl₂): δ = 150.22, 139.77, 137.99, 134.76, 133.98, 131.04, 125.39, 124.74,

123.34, 121.57, 114.17, 101.27, 97.19, 92.18, 87.11, 0.16.

Synthesis of 51. Compound **50** (0.513 g, 1.41 mmol, 1 equiv.) and potassium carbonate (0.019 g, 0.14 mmol, 0.1 equiv.) were dissolved in distilled methanol (25 mL) under nitrogen. The mixture was stirred at RT for 24 h before being poured into water. The organic phase was recovered with ethyl acetate and evaporated to dryness. The crude product was purified by chromatography on silica gel (ethyl acetate/pentane (8:2, v/v)) to afford **51** as an orange powder in 72 % yield (0.2976 g, 1.02 mmol). ^1H NMR (300 MHz, CD_2Cl_2): δ = 8.60 (m, 2H), 7.37 (m, 2H), 7.29 (d, 1H, $^3J_{\text{H-H}} = 3.83$ Hz), 7.21 (d, 1H, $^3J_{\text{H-H}} = 3.82$ Hz), 7.14 (d, 1H, $^3J_{\text{H-H}} = 3.91$ Hz), 7.11 (d, 1H, $^3J_{\text{H-H}} = 3.87$ Hz), 3.51 (s, 1H). ^{13}C NMR (75 MHz, THF-d8): δ = 150.72, 139.83, 138.21, 135.19, 134.64, 130.86, 125.35, 125.18, 122.88, 121.88, 117.80, 92.49, 86.76, 84.76, 76.78.

Synthesis of 52. Compounds **27**[TfO] (0.500 g, 0.31 mmol, 1 equiv.), **51** (0.106 g, 0.37 mmol, 1.2 equiv.) and NaPF_6 (0.102 g, 0.61 mmol, 2 equiv.) were dissolved in dry CH_2Cl_2 under nitrogen atmosphere. Et_3N (0.17 mL, 1.22 mmol, 4 equiv.) was subsequently added and the suspension was stirred at RT for 36 h. The reaction mixture was then diluted with CH_2Cl_2 and washed with pure water. The organic phase was evaporated to dryness. The resulting solid was washed with pentane and dried under reduced pressure to afford **52** as a red powder in 74 % yield (0.393 g, 0.23 mmol). ^{31}P NMR (120 MHz, CD_2Cl_2): δ = 52.5. ^1H NMR (300 MHz, CD_2Cl_2): δ = 8.59 (m, 2H), 8.00-6.79 (m, 56H), 4.39 (m, 2H), 2.51 (m, 8H), 1.12 (m, 2H), 0.08 (s, 9H). ^{13}C NMR (200 MHz, THF-d8): δ = 204.17, 195.29, 166.97, 165.93, 150.69, 135.17, 134.69, 131.93, 131.84, 131.69, 131.57, 131.35, 129.48, 129.26, 127.80, 126.66, 126.42, 125.21, 124.96, 122.81, 122.39, 118.82, 117.92, 110.00, 91.81, 87.80, 67.78, 63.15, 62.85, 54.62, 31.99, 30.16, 17.94, 1.12, -1.62. HR-MS FD^+ (m/z): 1744.4719 [M] $^+$ (calcd. 1744.4213 for $[\text{C}_{101}\text{H}_{94}\text{N}_2\text{O}_4\text{P}_4\text{RuS}_2\text{Si}_2]^+$). FT-IR (KBr): $\nu_{\text{C}=\text{C}} = 2196$ cm^{-1} , $\nu_{\text{C}=\text{C}} = 2040$ cm^{-1} , $\nu_{\text{C}=\text{O}} = 1709$ cm^{-1} , $\nu_{\text{P-Ph}} = 1099$ cm^{-1} , $\nu_{\text{Si-C}} = 836$ cm^{-1} .

Synthesis of SL8. To a solution of **52** (470 mg, 0.27 mmol, 1 equiv.) in dry THF (50 mL) and under inert atmosphere was added TBAF (1M sol. in THF, 1.08 mL, 1.08 mmol, 4 equiv.). The reaction mixture was stirred at RT for 24 h. After removal of the solvent the resulting solid was dissolved in CH_2Cl_2 and thoroughly washed with degassed citric acid aqueous solution (10 % m) and then pure water. The organics were evaporated to dryness to afford **SL8** as a dark red powder in 69 % yield (0.288 g, 0.19 mmol). ^{31}P NMR (120 MHz, CD_2Cl_2):

$\delta = 52.9$. ^1H NMR (300 MHz, THF- d_8): $\delta = 10.82$ (s, 2H), 8.56 (m, 2H), 7.97-6.85 (m, 60H), 2.47 (m, 8H). ^{13}C NMR (100 MHz, THF- d_8): 166.21, 165.98, 151.02, 150.29, 150.02, 142.08, 141.11, 137.17, 136.76, 134.42, 133.92, 131.93, 132.35, 131.20, 131.11, 131.03, 130.85, 130.70, 129.74, 128.67, 128.47, 128.30, 127.86, 126.98, 126.34, 125.82, 125.56, 124.97, 124.64, 124.56, 124.42, 124.19, 123.73, 123.61, 123.50, 122.00, 121.57, 29.74. HR-MS FD^+ (m/z): 1544.2713 $[\text{M}]^+$ (calcd. 1544.2794 for $[\text{C}_{91}\text{H}_{70}\text{N}_2\text{O}_4\text{P}_4\text{RuS}_2]^+$). FT-IR (KBr): $\nu_{\text{C}=\text{C}} = 2195 \text{ cm}^{-1}$, $\nu_{\text{C}=\text{C}} = 2039 \text{ cm}^{-1}$, $\nu_{\text{C}=\text{O}} = 1709\text{-}1701 \text{ cm}^{-1}$, $\nu_{\text{P-Ph}} = 1099 \text{ cm}^{-1}$.

Synthesis of SL8-Co. To a solution of **SL8** (30.8 mg, 0.02 mmol, 1 equiv.) in dry THF (10 mL) and under inert atmosphere was added **53** (8.7 mg, 0.02 mmol, 1 equiv.). The reaction mixture was stirred at RT for 4 h. After removal of the solvent, the resulting solid was further dried under vacuum to afford **SL8-Co** as a dark red powder in quantitative yield (39 mg). ^{31}P NMR (120 MHz, CD_2Cl_2): $\delta = 52.9$. HR-MS ESI^+ (m/z): 1959.5015 $[\text{M-H}_2\text{O}]^+$ (calcd. 1959.3553 for $[\text{C}_{101}\text{H}_{88}\text{B}_2\text{CoF}_4\text{N}_6\text{O}_8\text{P}_4\text{RuS}_2]^+$). FT-IR (KBr): $\nu_{\text{C}=\text{C}} = 2194 \text{ cm}^{-1}$, $\nu_{\text{C}=\text{C}} = 2039 \text{ cm}^{-1}$, $\nu_{\text{C}=\text{O}} = 1714\text{-}1684 \text{ cm}^{-1}$, $\nu_{\text{C}=\text{N}} = 1611 \text{ cm}^{-1}$, $\nu_{\text{P-Ph}} = 1098 \text{ cm}^{-1}$, $\nu_{\text{N-O}} = 1012 \text{ cm}^{-1}$, $\nu_{\text{B-O}} = 825 \text{ cm}^{-1}$.

VI.3. Photovoltaic Characterization

VI.3.1. DSC Preparation and Characterization for [Ru]1-[Ru]3

FTO-coated conducting glass substrates (NSG10, 10 ohm/ \square , thickness 3.2 mm, XOPFisica) were cleaned by using successive ultrasonic treatments in an alkaline detergent solution and in ethanol. The conducting glass substrates were afterwards treated by 40 mM TiCl_4 aqueous solution at 70°C for 30 min in order to create an ultra-thin TiO_2 blocking layer. The photoanodes were prepared by screen-printing method using commercially available titania pastes. TCO substrates were first coated with a transparent layer, composed of 20 nm anatase TiO_2 nanoparticles (Solaronix, Ti-Nanoxide T/SP). The screen-printing step was repeated three times to get an approximate thickness of 10 μm . A diffusing layer, made of 250 to 400 nm TiO_2 particles (Solaronix, Ti-Nanoxide R/SP) was then deposited on top of the working electrode. The thickness of this scattering layer was of 5 μm (as determined by cross-sectional SEM images). The photoanodes were treated by gradual heating under air at 325 °C (5 min), 375 °C (5 min), 450 °C (15 min) and 500 °C (15 min). The resulting films were further treated with 40 mM TiCl_4 aqueous solution at 70 °C for 30 min followed by annealing at 500 °C for 30 min. After cooling down to 40 °C, the electrodes were immersed

into 0.3 mM dye solutions in dichloromethane containing 1 mM of cheno-deoxycholic acid as co-adsorbent. Under these conditions, the sensitization time was optimized to 16 hours in the dark. Platinized counter-electrodes were prepared by drop-casting a solution of H_2PtCl_6 (5 mM in ethanol) on FTO-glass substrates (TCO22-7, 7 ohm/\square , thickness 2.2 mm, Solaronix). Thermal decomposition of the complex under air flow, at 500 °C for 30 min, afforded sufficient amount of Pt nanoparticles. The photoanode and counter-electrode were assembled using a hot-melt Surlyn polymer gasket (25 μm , Dupont). The electrolyte was introduced into the cell by vacuum backfilling through a hole drilled in the counter-electrode. The device was finally sealed with Surlyn gasket and glass plate cover. The composition of the electrolyte Z960 is as follows: 0.03 M iodine, 0.05 M lithium iodide, 1.0 M 1,3-dimethylimidazolium iodide, 0.8 M 4-tert-butylpyridine and 0.1 M guanidinium thiocyanate in acetonitrile/valeronitrile 85:15. Photovoltaic performance of the DSCs were measured by using a black mask with an aperture area of 0.159 cm^2 . The device was illuminated by AM1.5G solar simulator (Newport Oriel Sol3A) calibrated with a certified Si-based solar cell (Newport Oriel, 91150V) to provide an incident irradiance of 100 $\text{mW}\cdot\text{cm}^{-2}$ at the surface of the solar cells. The J-V measurements were performed using a Keithley model 2400 digital source meter by applying independently external voltage to the cell and by measuring the photo-generated current out from the cell. Action spectra of incident photon-to-current conversion efficiency (IPCE) were realized using a Xe lamp associated with a monochromator (Triax 180, Jobin Yvon) to select and increment wavelength irradiation to the cell. No bias light was employed to illuminate the cell. The current produced was measured by steps of 5 nm after 2 s of radiation exposure with a Keithley 6487 picoammeter in order to be in steady state conditions. The incident photon flux was measured with a 6-in. diameter calibrated integrated sphere and a silicon detector.

VI.3.2. DSC Preparation and Characterization for SL1-SL5

For the p-type photovoltaic devices, conductive glass substrates (F-doped SnO_2) were purchased from Solaronix (TEC15, sheet resistance 15 ohm/\square). The latter were successively cleaned by sonication in soapy water, then acidified ethanol for 10 min before being fired at 450 °C for 30 min. Once cooled down to room temperature, a dense layer of NiO was deposited on the FTO plates by spin coating a solution of nickel acetate (0.5 M) and triethanolamine (0.5 M) in methoxyethanol (2000 RPM, 30s) and firing at 500 °C for 30 min. Mesoporous NiO was then screen printed on the latter substrates using a home-made paste. Briefly, the NiO screen-printing paste was produced by preparing a slurry of 3 g of NiO

nanopowder (Inframmat) suspended in 10 mL of distilled ethanol and ball-milled (500 rpm) for 24 h. The resulting slurry was mixed in a round-bottom flask with 10 mL of 10 wt% ethanolic ethyl cellulose (Sigma Aldrich) solution and 20 mL terpineol, followed by slow ethanol removal by rotary evaporation. The dried film was calcined in air at 400 °C for 30 min. Once back at room temperature, the substrates were treated in a nickel acetate ethanolic solution (20 mM) with 1 mM triethanolamine at 60 °C for 30 min and subsequently fired at 200 °C for 30 min. The prepared NiO electrodes for the dyes SL1 to SL5 were finally soaked while still hot (80 °C) in a 0.3 mM solution of each dye during 16 h. A mixture of distilled acetonitrile and methanol was used (9/1, v/v) for each bath. Platinum counter electrodes were prepared by drop casting a few drops of an isopropanol solution of hexachloroplatinic acid in distilled isopropanol (10 mg per mL) on FTO plates (TEC7, Solaronix). Substrates were then fired at 375 °C for 30 min. The photocathode and the counter electrode were placed on top of each other and sealed using a thin transparent film of Surlyn polymer (DuPont, 25 mm) as spacer. A drop of electrolyte was introduced through a predrilled hole in the counter electrode by vacuum backfilling. The electrolyte for the dyes SL1 to SL5 is composed of: 0.6 M 1,2-dimethyl-3-butylimidazolium iodide, 0.03 M I₂, 0.5 M 4-tert-butylpyridine and 0.1 M guanidinium thiocyanate in acetonitrile. The hole was then sealed by a glass stopper with Surlyn gasket. The cell had an active area of 0.25 cm². Specially, another novel electrolyte using disulfide/thiolate (T₂/T⁻) molecules as redox mediators was employed for the dye SL5 to improve the photovoltaic performances.¹⁸

VI.4. Determination of Dye-loading Amounts

A solution of dye (0.3 mM) and cheno-deoxycholic acid (1 mM) in dichloromethane was prepared and utilized to sensitize a nanoparticulate TiO₂ thin-film (thickness = 6.8 μm ; surface area = 1 cm²) as described above. UV-visible absorption spectrum of the dye solution was recorded prior to and after sensitization. The amount of dye loaded onto TiO₂ was deduced from the difference between the two sets of data.

VI.5. Crystallographic Study for Compound 48

Data collection was performed at the IECB X-ray facility (UMS3033) on a high flux microfocus Rigaku (MM007, 1.2 kW) rotating anode at the copper α wavelength. The experimental setup is composed of osmic Varimax mirrors and a semi-cylindrical R-Axis spider IP detector. The crystal was mounted on a cryo-loop after quick soaking on Paratone-N

oil from Hampton research and flash-frozen at 123K. The diffractometer has a partial chi geometry goniometer allowing omega-scan data collections. The data were processed with the CrystalClear suite version 2.1b25¹⁹. The crystal structure was solved using direct methods implemented in SHELXT²⁰ and was refined using SHELXL 2013 version²¹. Full-matrix least-squares refinement were performed on F2 for all unique reflections, minimizing $w(\text{Fo}^2 - \text{Fc}^2)$, with anisotropic displacement parameters for non-hydrogen atoms. Hydrogen atoms were positioned in idealized positions and refined with a riding model, with Uiso constrained to 1.2 Ueq value of the parent atom (1.5 Ueq when CH3). The positions and isotropic displacement parameters of the remaining hydrogen atoms were refined freely. The RIGU command was used to restrain parts of the molecule as rigid groups and restrain their displacement parameters. The terminal ester group is disordered in this crystal structure and two positions have been modeled. Data statistics are presented in Table VI-1 and in the cif file CCDC 1460734.

Table VI-1: X-Ray data statistics for compound **48**.

Crystal System	Monoclinic	ρ , g·cm ⁻³	1.292
Space Group	P2 ₁ /c	λ , E	3.499
Z	4	θ min	6.528
Unit Cell Parameters a, Å	15.5292(3)	θ max	63.674
Unit Cell Parameters b, Å	18.0323(5)	Radiation	1.54187
Unit Cell Parameters c, Å	27.1454(19)	Reflections Measured	38290
Unit Cell Parameters α , °	90	Reflections Unique ([Fo > 2 σ Fo])	9556
Unit Cell Parameters β , °	92.228(7)	Parameters/restraints	795/136
Unit Cell Parameters γ , °	90	GOF	1.127
Temperature, K	123	R1 (I>2 σ (I))	00658
Volume, Å ³	7595.7(6)	wR2 (all data)	0.1734
FW, g·mol ⁻¹	1477.22	CCDC#	CCDC 1460734

VI.6. Electrode preparation method for SL6 and SL7

NiO electrodes (thickness 1.5 μm) on TCO glass were purchased from Dyenamo AB, Stockholm, Sweden. UV-visible absorbance spectra of the sensitized films were recorded on an Agilent Cary 60 UV-Vis spectrometer equipped with a solid sample holder. Film sensitization. NiO electrodes were soaked in a 0.5 mM solution of **SL6** or **SL7** in MeCN for 24 h on an orbital stirring table. The electrodes were rinsed with MeCN and dried in air.

Film sensitization. NiO electrodes were soaked in a 0.5 mM solution of **SL6** or **SL7** in MeCN for 24 h on an orbital stirring table. The electrodes were rinsed with MeCN and dried in air.

Photoelectrochemical measurements. Chronoamperometric and linear sweep voltammograms were recorded with a Biologic SP 300 potentiostat under nitrogen at room temperature using a previously described specific cell in a three-electrode configuration.²² The NiO electrode is clamped on the cell, serving as both a working electrode and a window. The surface of the working electrode in contact with the electrolyte is 0.42 cm^2 . A Ti wire and Ag/AgCl (3 M KCl) have been used as the counter-electrode and the reference electrode, respectively. We used potassium phosphate buffer (0.1 M; pH = 7) as an electrolyte and $[\text{Co}(\text{NH}_3)_5\text{Cl}]\text{Cl}_2$ (20 mM) as an irreversible electron acceptor. The $[\text{Fe}(\text{CN})_6]^{3-}/[\text{Fe}(\text{CN})_6]^{4-}$ couple ($E^\circ = 0.244$ V vs. Ag/AgCl, calculated at 0.425 V vs. NHE in 0.1 M potassium phosphate buffer at pH = 7; $E^\circ = 0.200$ V vs. Ag/AgCl, recorded at 0.412 V vs. NHE in 0.1 M sodium acetate buffer at pH = 4.5)²³ was then used for the standardization of the measurements in aqueous solution. Photoelectrodes were back-illuminated with a 300 W ozone-free xenon lamp (Newport) operated at 280 W, coupled to a water-filled Spectra-Physics 6123NS liquid filter for elimination of IR radiation ($\lambda > 800$ nm) and a Spectra-Physics 59472 UV cut-off filter ($\lambda > 400$ nm). Irradiance at the substrate surface was calibrated at 100 $\text{mW}\cdot\text{cm}^{-2}$ using a Newport PM1918-R power-meter.

VI.7. Electrochemical and Photoelectrochemical Measurements for SL8-Co and SL8-Co@NiO

Electrochemical and photoelectrochemical data were acquired with a Biologic VSP 300 potentiostat. Electrochemical measurements were conducted in a three-electrode cell. The working electrode was a glassy carbon electrode in the reduction potential window and a Pt one in the oxidation potential window. The reference electrode was made of a Ag/AgCl wire dipped into a KCl 3 M solution, separated from the supporting electrolyte by a Vycor® frit,

and denoted below as Ag/AgCl. The counter electrode was a Pt wire. The supporting electrolyte was 0.1 M nBu₄NPF₆ in dry DMF. The supporting electrolyte was degassed with a flow of N₂ at least for 5 min before the measurements. The N₂ flow was removed from the solution but let in the headspace of the cell for the duration of the experiment. The concentration of the compound of interest was 1 mM. Cyclic voltammograms were typically recorded at a scan rate of 100 mV·s⁻¹. The potential of the reference electrode was calibrated after each experiment by adding in the supporting electrolyte an internal reference (ferrocene for organic solvent, K₄FeCN₆ for aqueous solution), the potential of which was measured against the Ag/AgCl reference (0.43V for ferrocene and 0.24V for K₄FeCN₆).

Irradiation was carried out with a 300W ozone-free Xe lamp (Newport) operated at 280 W and mounted with a water-filled Spectra-Physics 6123NS liquid filter for elimination of IR ($\lambda > 800$ nm) irradiation and a Spectra-Physics 59472 UV cut-off filter ($\lambda < 400$ nm). The power density was calibrated using a Newport PM1918-R power-meter. The photocurrent measurements were carried out in a specifically designed three-electrode cell, using the NiO-sensitized film as the working electrode (1.2 to 2 cm²), Ag/AgCl as the reference electrode and a Pt wire as the counter electrode. The counter electrode compartment was separated from the cathodic one by a Vycor® frit. The supporting electrolyte was a 0.1 M 2-(N-morpholino)ethanesulfonic acid (MES)/0.1 M NaCl buffer at pH 5.5. The solution was degassed with nitrogen for 30 minutes prior to use. In a typical experiment, the volume of supporting electrolyte was 4.0 mL and the headspace was 2.4 mL. The photocathode was illuminated with a power density of 65 mW·cm⁻² (*ca.* one sun). The amounts of evolved hydrogen were determined by sampling aliquots of the headspace in a Perkin Elmer Clarus 580 gas chromatograph equipped with a molecular sieve 5 Å column and a TCD detector.

VI.8. References

- 1 S. D. Sousa, L. Ducasse, B. Kauffmann, T. Toupance, C. Olivier. Functionalization of a Ruthenium-Diacetylide Organometallic Complex as a Next-Generation Push-Pull Chromophore. *Chem. Eur. J.*, **2014**, 20: 7017-7024.
- 2 H. Feng, R. Li, Y. Song, X. Li, B. Liu. Novel D- π -A- π -A coumarin dyes for highly efficient dye-sensitized solar cells: Effect of π -bridge on optical, electrochemical, and photovoltaic performance. *J. Power Sources*, **2017**, 345: 59-66.
- 3 J. R. Polam, L. C. Porter. Ru(II) Complexes Containing Chelating Phosphine Ligands. Synthesis, Characterization, and X-Ray Crystal Structures of Dichlorobis(1,2-bis(diphenylphosphino)ethane)Ru(II) and the Coordinatively Unsaturated Trigonal-bipyramidal Cation, Chlorobis-(1,2-bis(diphenylphosphino)ethane)Ru(II). *J. Coord. Chem.*, **1993**, 29: 109-119.
- 4 J.-L. Song, P. Amaladass, S.-H. Wen, K. K. Pasunooti, A. Li, Y.-L. Yu, X. Wang, W.-Q. Deng, X.-W. Liu. Aryl/hetero-arylethyne bridged dyes: the effect of planar π -bridge on the performance of dye-sensitized solar cells. *New J. Chem.*, **2011**, 35: 127-136.
- 5 J. R. Aranzaes, M.-C. Daniel, D. Astruc. Metallocenes as references for the determination of redox potentials by cyclic voltammetry-Permethylylated iron and cobalt sandwich complexes, inhibition by polyamine dendrimers, and the role of hydroxy-containing ferrocenes. *Can. J. Chem.*, **2013**, 84: 288-299.
- 6 M. J. Frisch, G. W. Trucks, H. B. Schlegel, G. E. Scuseria, M. A. Robb, J. R. Cheeseman, G. Scalmani, V. Barone, B. Mennucci, G. A. Petersson, H. Nakatsuji, M. Caricato, X. Li, H. P. Hratchian, A. F. Izmaylov, J. Bloino, G. Zheng, J. L. Sonnenberg, M. Hada, M. Ehara, K. Toyota, R. Fukuda, J. Hasegawa, M. Ishida, T. Nakajima, Y. Honda, O. Kitao, H. Nakai, T. Vreven, J. A. Montgomery, J. E. Peralta, F. Ogliaro, M. Bearpark, J. J. Heyd, E. Brothers, K. N. Kudin, V. N. Staroverov, R. Kobayashi, J. Normand, K. Raghavachari, A. Rendell, J. C. Burant, S. S. Iyengar, J. Tomasi, M. Cossi, N. Rega, J. M. Millam, M. Klene, J. E. Knox, J. B. Cross, V. Bakken, C. Adamo, J. Jaramillo, R. Gomperts, R. E. Stratmann, O. Yazyev, A. J. Austin, R. Cammi, C. Pomelli, J. W. Ochterski, R. L. Martin, K. Morokuma, V. G. Zakrzewski, G. A. Voth, P. Salvador, J. J. Dannenberg, S. Dapprich, A. D. Daniels, A. Farkas, J. B. Foresman, J. V. Ortiz, J. Cioslowski, D. J. Fox. Gaussian 09, Revision A.02, *Gaussian, Inc., Wallingford CT*, **2009**.
- 7 B. J. Lynch, P. L. Fast, M. Harris, D. G. Truhlar. Adiabatic Connection for Kinetics. *J. Phys. Chem. A*, **2000**, 104, 21: 4811-4815.
- 8 J. Tomasi, M. Persico. Molecular Interactions in Solution: An Overview of Methods

-
-
- Based on Continuous Distributions of the Solvent. *Chem. Rev.*, **1994**, 94, 7: 2027-2094.
- 9 J. Tomasi, B. Mennucci, R. Cammi. Quantum Mechanical Continuum Solvation Models. *Chem. Rev.*, **2005**, 105, 8: 2999-3094.
- 10 C. Adamo, V. Barone. Toward reliable density functional methods without adjustable parameters: The PBE0 model. *J. Chem. Phys.*, **1999**, 110: 6158-6169.
- 11 S. Grimme, S. Ehrlich, L. Goerigk. Effect of the damping function in dispersion corrected density functional theory. *J. Comput. Chem.*, **2011**, 32: 1456-1465.
- 12 V. A. Rassolov, M. A. Ratner, J. A. Pople, P. C. Redfern, L. A. Curtiss. 6-31G* basis set for third-row atoms. *J. Comput. Chem.*, **2001**, 22: 976-984.
- 13 D. Andrae, U. Haeussermann, M. Dolg, H. Stoll, H. Preuss. Energy-adjusted ab initio pseudopotentials for the second and third row transition elements. *Theor. Chem. Acc.*, **1990**, 77: 123-141.
- 14 G. Scalmani, M. J. Frisch. Continuous surface charge polarizable continuum models of solvation. I. General formalism. *J. Chem. Phys.*, **2010**, 132: 114110.
- 15 A. Dreuw, M. Head-Gordon. Failure of Time-Dependent Density Functional Theory for Long-Range Charge-Transfer Excited States: The Zincbacteriochlorin-Bacteriochlorin and Bacteriochlorophyll-Spheroidene Complexes. *J. Am. Chem. Soc.*, **2004**, 126: 4007-4016.
- 16 O. A. Vydrov, G. E. Scuseria. Assessment of a long-range corrected hybrid functional. *J. Chem. Phys.*, **2006**, 125: 234109.
- 17 A. B. Muñoz-García, M. Pavone. Structure and energy level alignment at the dye-electrode interface in p-type DSSCs: new hints on the role of anchoring modes from ab initio calculations. *Phys. Chem. Chem. Phys.*, **2015**, 17: 12238-12246.
- 18 M. Wang, N. Chamberland, L. Breau, J.-E. Moser, R. Humphry-Baker, B. Marsan, S. M. Zakeeruddin, M. Grätzel. An organic redox electrolyte to rival triiodide/iodide in dye-sensitized solar cells. *Nature Chemistry*, **2010**, 2: 385-389.
- 19 CrystalClear (Rigaku/MS, **2006**)
- 20 G. M. Sheldrick. SHELXT - Integrated space-group and crystal-structure determination. *Acta Cryst. A*, **2015**, A71: 3-8.
- 21 G. M. Sheldrick. A short history of SHELX. *Acta Cryst. A*, **2008**, A64: 112-122.
- 22 J. Massin, M. Bräutigam, N. Kaeffer, N. Queyriaux, M. J. Field, F. H. Schacher, J. Popp, M. Chavarot-Kerlidou, B. Dietzek, V. Artero. Dye-sensitized PS-*b*-P2VP-templated nickel oxide films for photoelectrochemical applications. *Interface Focus*, **2015**, 5, 3: 20140083.
-
-

- 23 J. E. O'Reilly. Oxidation-reduction potential of the ferro-ferricyanide system in buffer solutions. *Biochim. Biophys. Acta*, **1973**, 292: 509-515.

Annexes

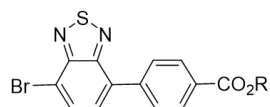
Abbreviations

AM: air mass	FD: field desorption
a-Si: amorphous silicon	FF: fill factor
AcN: acrylonitrile	FTO: fluorine doped tin oxide
APCE: absorbed-photon to current conversion efficiency	HBTU: N,N,N',N'-Tetramethyl-O-(1H-benzotriazol-1-yl)uronium hexafluorophosphate
AU: astronomical unit	HDI: human development index
BODIPY: boron-dipyrromethene	HOMO: highest occupied molecular orbital
BTD: benzothiadiazole	IEA: irreversible electron acceptor
CB: conduction band	IPCE: incident photon-to-current conversion efficiency
CIGS: Copper Indium Gallium Selenide	ITO: indium tin oxide
CIS: Copper indium diselenide	J-V: density-voltage
CNFs: carbon nanofibers	LHE: light-harvesting efficiency
CNTs: single wall carbon nanotubes	LSV: linear sweep voltammograms
CODATA: Committee on Data for Science and Technology	LUMO: lowest unoccupied molecular orbital
c-Si: crystalline silicon	MePN: 3-methoxypropionitrile
CTO: cadmium stannate	MLCT: metal-to-ligand charge-transfer
DFT: density functional theory	mono-Si: monocrystalline silicon
DIPEA: N,N-diisopropylethylamine	MOs: molecular orbitals
DLA: dye-loading amount	NDI: naphthalene diimide
DMF: dimethylformamide	NIR: near infrared
DOS: density of states	NMBI: N-methylbenzimidazole
DPA: 1-decylphosphonic acid	NMI: phenanthroline-nitronaphthalene-dicarboximide
dppf: 1,1'-bis(diphenylphosphino)ferrocene	NMP: N-methylpyrrolidone
dppe: 1,2-bis(diphenylphosphino)ethane	NREL: The National Renewable Energy Laboratory
DSC(s): dye-sensitized solar cell(s)	n-DSC(s): n-type dye-sensitized solar cell(s)
DSPEC(s): dye-sensitized photo-electrochemical cell(s)	NHE: normal hydrogen electrode
EC: ethylene carbonate	PAN: polyacrylonitrile
ECNs: electrospun carbon nanofibers	PC: propylene carbonate
EIS: electrochemical impedance spectroscopy	
EQE: external quantum efficiency	

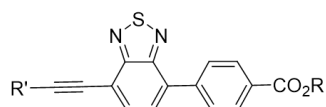
PCE(s): power conversion efficiency (efficiencies)	TMSE: 2-(trimethylsilyl)ethanol
PCM: polarizable continuum model	UV: ultraviolet
p-DSC(s): p-type dye-sensitized solar cell(s)	XPS: X-ray photoemission spectroscopy
PEDOT: poly(3,4-ethylenedioxythiophene)	ZAO: aluminum doped zinc oxide
PEDOT-PSS: poly(3,4-ethylenedioxythiophene) polystyrenesulfonate	ZTO: zinc stannate
PEDOTTsO: poly(3,4-ethylenedioxythiophene)-toluenesulfonate	
PEN: polyethylene naphthalate	
PET: polyethylene terephthalate	
PMI: perylene-imide	
PMMA: poly(methyl methacrylate)	
poly-Si: polycrystalline silicon	
PSC(s): perovskite solar cells	
PV: photovoltaic	
PVB: polyvinyl butyral	
RT: room temperature	
SED: sacrificial electron donor	
SEM: scanning electron microscope	
SHE: standard hydrogen electrode	
SoG-Si: solar grade silicon	
spiro-OMeTAD: 2,2',7,7'-tetrakis(N,N-di-p-methoxyphenylamine)9,9'-spirobifluorene	
TBAF: tetrabutylammonium fluoride	
TBP: 4-tert-butylpyridine	
TCO: transparent conducting oxide	
TD-DFT: time-dependent density functional theory	
TEA: triethylamine	
TEOA: triethanolamine	
TfO: trifluoromethanesulfonate anion	
THF: tetrahydrofuran	
TMSA: trimethylsilylacetylene	

Formulas

Chapter II:

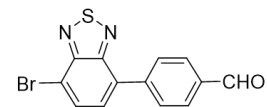


1

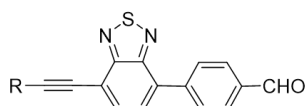
2 : R = Me, R' = SiMe₃

3 : R = H, R' = H

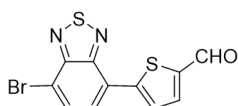
4 : R = TMSE, R' = H



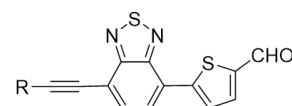
5

6 : R = SiMe₃

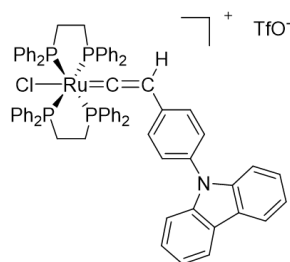
7 : R = H



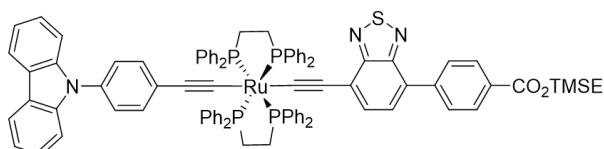
8

9 : R = SiMe₃

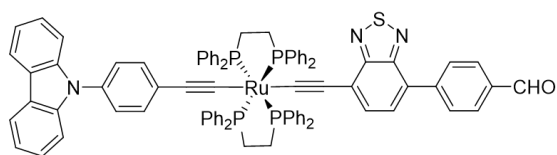
10 : R = H



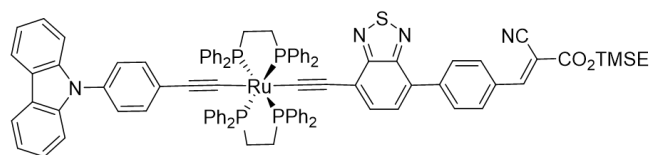
[11][TfO]



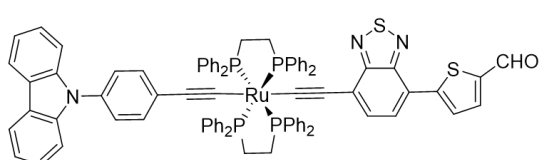
12



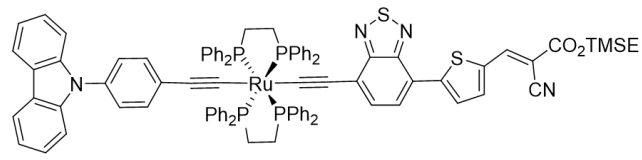
13



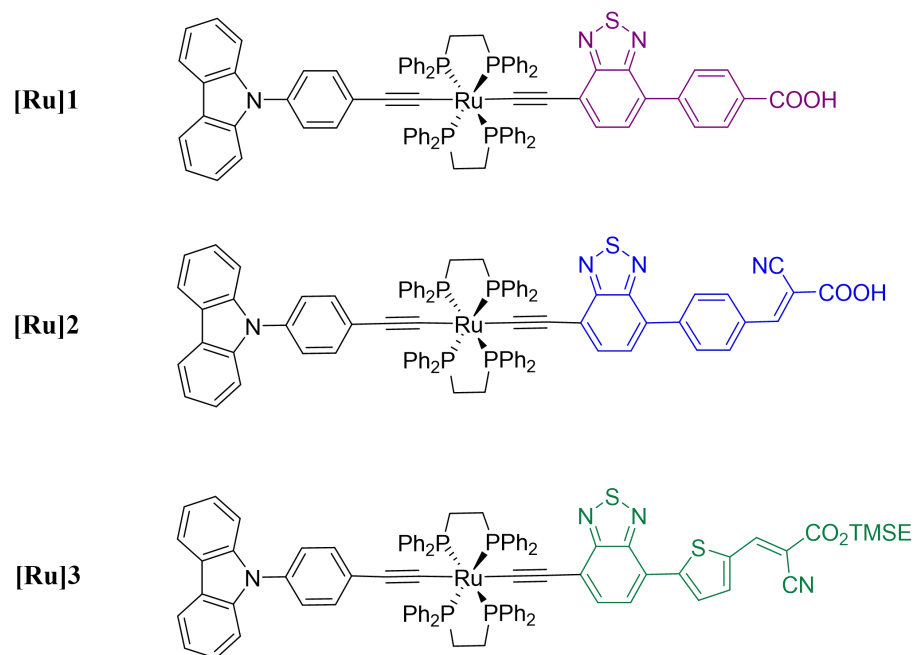
14



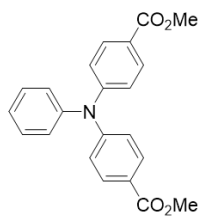
15



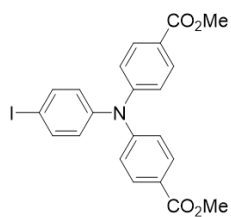
16



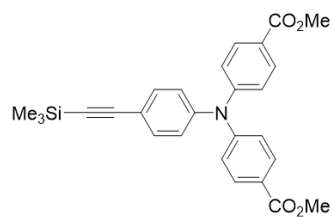
Chapter III:



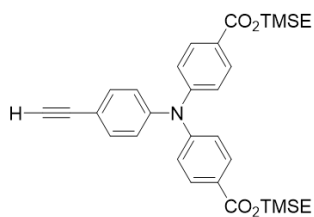
17



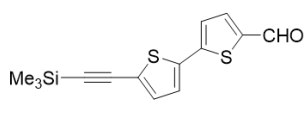
18



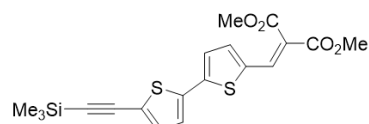
19



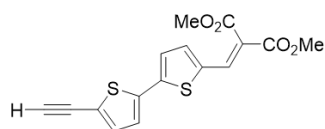
20



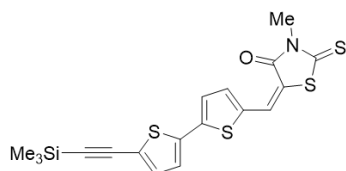
21



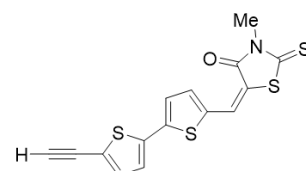
22



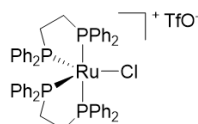
23



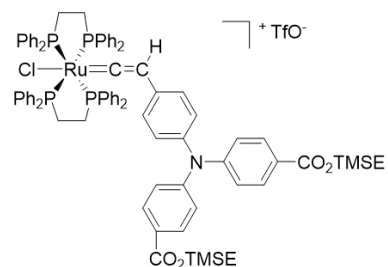
24



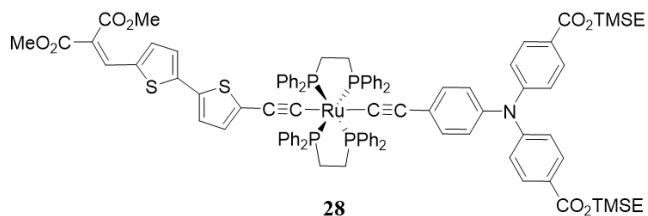
25



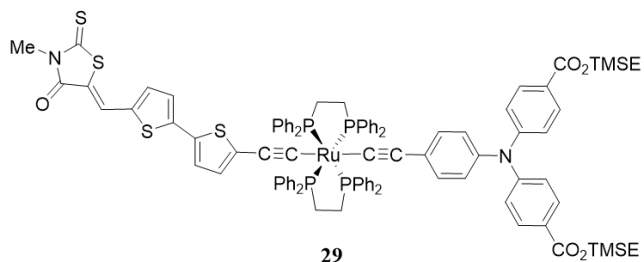
[26][TfO]



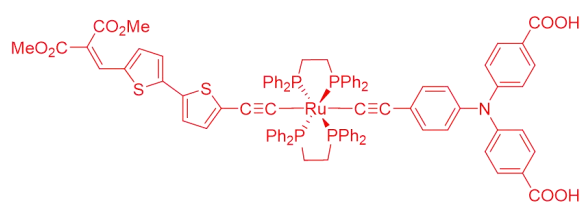
[27][TfO]



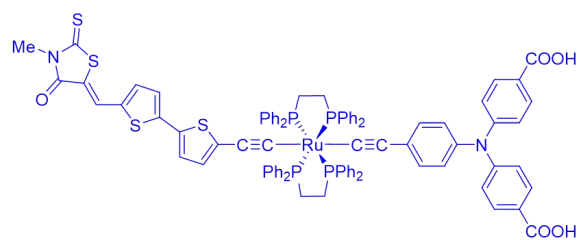
28



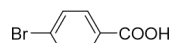
29



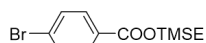
SL1



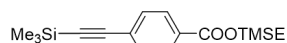
SL2



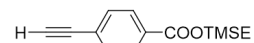
30



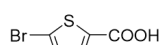
31



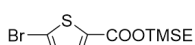
32



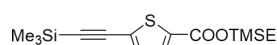
33



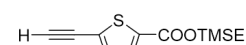
34



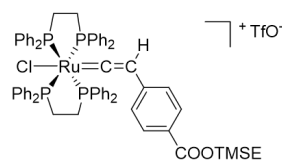
35



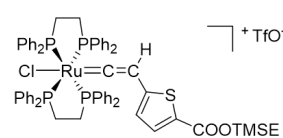
36



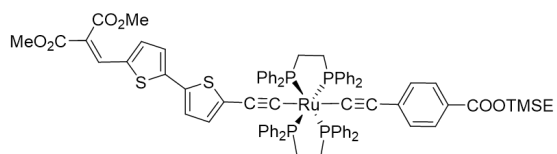
37



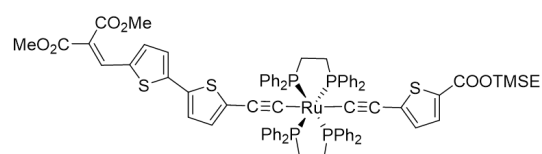
[38][TfO]



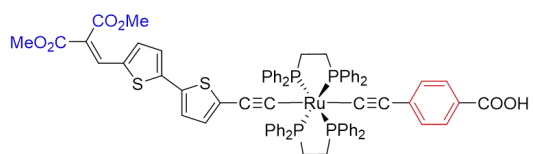
[39][TfO]



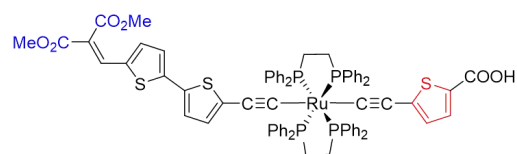
40



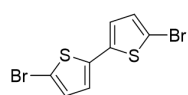
41



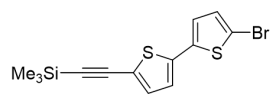
SL3



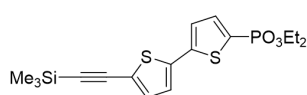
SL4



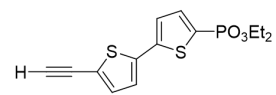
42



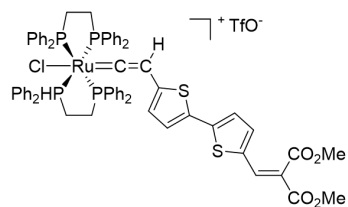
43



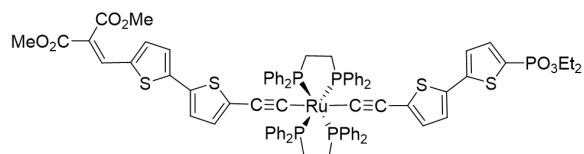
44



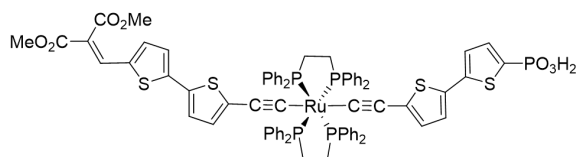
45



[46][TfO]

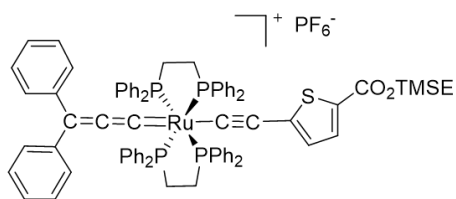


47

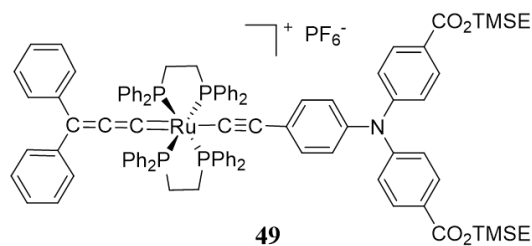


SL5

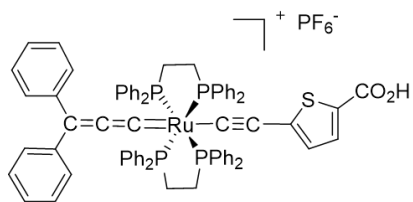
Chapter VI:



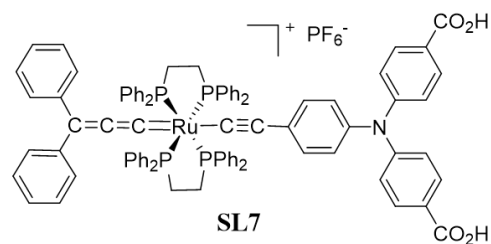
48



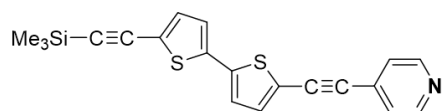
49



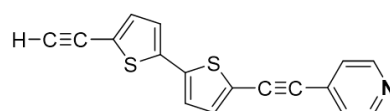
SL6



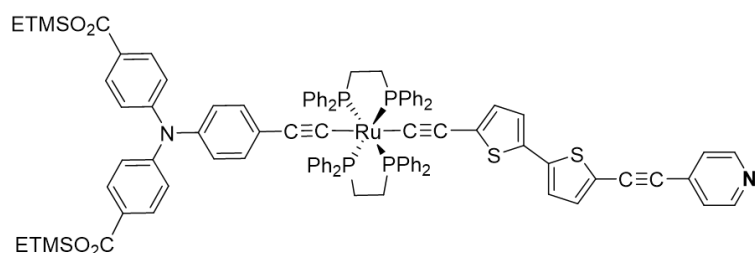
SL7



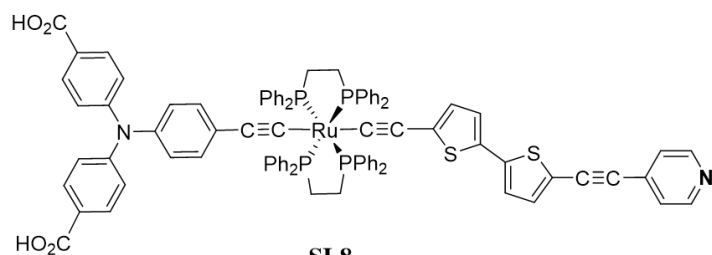
50



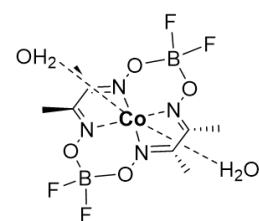
51



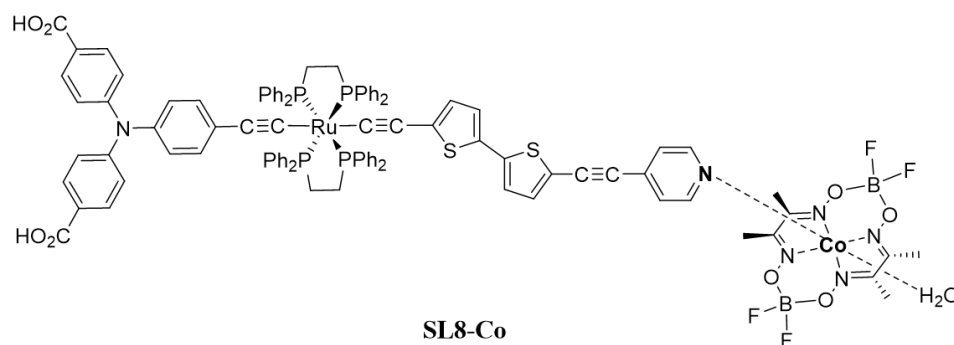
52



SL8



53



SL8-Co

Published Articles

- 1 S. D. Sousa, **S. Lyu**, L. Ducasse, T. Toupance, C. Olivier. Tuning visible-light absorption properties of Ru-diacetylde complexes: simple access to colorful efficient dyes for DSSCs. *J. Mater. Chem. A*, **2015**, 3: 18256-18264.
- 2 **S. Lyu**, C. Bertrand, T. Hamamura, L. Ducasse, T. Toupance, C. Olivier. Molecular engineering of Ruthenium-diacetylde organometallic complexes towards efficient green dye for DSSC. *Dye and Pigments*, **2018**, 158: 326-333.
- 3 **S. Lyu**, Y. Farré, L. Ducasse, Y. Pellegrin, T. Toupance, C. Olivier, F. Odobel. Push-pull ruthenium diacetylde complexes: new dyes for p-type dye-sensitized solar cells. *RSC Adv.*, **2016**, 6: 19928-19936.
- 4 J. Massin, **S. Lyu**, M. Pavone, A. B. Muñoz-Garcia, B. Kauffmann, T. Toupance, C. Olivier. Design and synthesis of novel organometallic dyes for NiO sensitization and photo-electrochemical applications. *Dalton Trans.*, **2016**, 45: 12539-12547.
- 5 **S. Lyu**, J. Massin, M. Pavone, A. B. Muñoz-García, C. Labrugère, T. Toupance, M. Chavarot-Kerlidou, V. Artero, C. Olivier. Ru-diacetylde/Cobaloxime photocatalytic system for H₂ evolution from dye-sensitized photoelectrochemical cells. In process.